UNIVERSITY OF NAPOLI "FEDERICO II"

DOCTORATE SCHOOL IN
INDUSTRIAL ENGINEERING

PH.D. THESIS IN
AEROSPACE ENGINEERING

SMART MORPHING CONCEPTS AND APPLICATIONS FOR ADVANCED LIFTING SURFACES

by

Silvestro BARBARINO

ADVISOR
Prof. Eng. Leonardo LECCE

Dept. Of Aerospace Engineering
(DIAS)

CO-ADVISOR
Dr. Antonio CONCILIO

Italian Aerospace Research Centre
(CIRA)

Napoli (ITALY), November 2009

Abstract

SMART MORPHING CONCEPTS AND APPLICATIONS FOR ADVANCED LIFTING SURFACES

by

Silvestro BARBARINO

Doctor of Philosophy in Aerospace Engineering

University of Napoli "Federico II" - ITALY

ADVISOR - Prof. Eng. Leonardo LECCE (DIAS)

CO-ADVISOR - Dr. Antonio CONCILIO (CIRA)

The aim of this thesis has been the study and implementation of structural solutions for the local or global change of airplanes wing geometry (adaptive wing): they may lead to an increase in aerodynamic efficiency and reduced operating costs and maintenance, as well as the structural complexity through the use of "smart" materials. In particular, attention has been paid to three parameters: the formation of a dorsal bump, the trailing edge curvature and the airfoil chord. Innovative aspects of this research concern the use of "smart" materials with an high structural integration and the development of solutions in full scale for use on regional civil transportation aircrafts.

Developed methodologies have been both theoretical-numerical, to simulate the thermo-mechanical behaviour of Shape Memory Alloys (SMA) and its integration into a Finite Element approach in commercial software, and application-experimental, with the manufacture of prototypes and tests in laboratory.

Major achievements included the construction and validation in laboratory of several original morphing architectures for load-bearing surfaces. The full functionality against the requirements and a discrete numerical-experimental correlation has been demonstrated. One of the investigated solutions is based on an innovative actuator based

on SMA: its use in the aeronautical field, however, is one of many possible applications. Novelty of the studies and interest shown by the industrial partner (Alenia Aeronautica) have conducted at the request of an European patent (patent pending), and further funding of such studies to proceed with industrialization of the proposed architectures (TIAS project).

Napoli (ITALY), November 30 2009

Acknowledgements

"Morphing Team" in Napoli, from left to right: Salvatore, Rosario, me, Antonio, Leonardo.

I would also like to thank all my colleagues of both the Aerospace Engineering department (DIAS) at University of Napoli and the Smart Structure Laboratory at CIRA for their help, benevolence, and countless technical and funny discussions through all the PhD: in particular thanks to Igor, Luigi, Crispino, Barbara, Andrea, Antonio G., Antonio C., Gianluca, Angela. Thanks for making this experience memorable.

My dear gratitude goes to the PhD coordinator too, Prof. Antonio Moccia, for his reliable support, unlimited courteousness and innumerable counsels.

And the doctoral experience would have not been the same without my dear colleague and friend Monica: we started the PhD together and could share many occurrences; thanks for walking next to me in this journey.

Then, I would like to thank Prof. Farhan Gandhi of the Aerospace Engineering department at the Pennsylvania State University for hosting me three months in the US at the Penn State Vertical Lift Research Center of Excellence (VLRCOE): it has been an amazing experience and I really got excited about the lab and the work done there. Of course, I have to express my appreciation to all the guys of VLRCOE who made my time at Penn State an enjoyable one: in particular, many thanks to my new friends abroad Maryam, Mihir, Gabriel, Raimond.

To my sisters and all my everyday friends, thank you for always being there for me, and giving me the opportunity to get away (sometimes) from my work!

I would like to dedicate this thesis to my parents, without whom I would not have been able to pursue my educational goals: they have given me guidance, encouragement and endless support, and spurred me to new heights!

Contents

FIXED WING AIRCRAFTS

List of Figures

Chapter 3 – Shape Memory Alloys: State of the Art

Chapter 4 – Former Application: Transonic Bump

PAPER "Wing Shape Control through an SMA-Based Device"

Chapter 5 – Variable Camber Morphing Flap: Preliminary Research
ENGLISH TRANSLATION OF AIDAA 2007 PAPERS

PAPER "Wing camber control architectures based on SMA: numerical investigations"

PAPER "Design of an Actuation Architecture Based on SMA Technology for Wing Shape Control"

PAPER "A Novel SMA-based Concept for Airfoil Structural Morphing"

PAPER "Airfoil Morphing Architecture Based on Shape Memory Alloys"

Chapter 6 – Variable Camber Morphing Flap: SMA Actuator Development

PAPER "A Novel Smart Actuator for Airfoil Structural Morphing: Design and Optimization"

PAPER "A Novel Smart Actuator for Airfoil Structural Morphing:

Test Campaign and Numerical Correlation"

Chapter 7 – Variable Camber Morphing Flap: Smart Flap

Chapter 8 – Variable Chord Morphing Blade

perpendicular junctions solution.

List of Tables

PAPER "Design of an Actuation Architecture Based on SMA Technology for Wing Shape Control"

PAPER "A Novel SMA-based Concept for Airfoil Structural Morphing"

PAPER "Airfoil Morphing Architecture Based on Shape Memory Alloys"

Chapter 6 – Variable Camber Morphing Flap: SMA Actuator Development

PAPER "A Novel Smart Actuator for Airfoil Structural Morphing: Design and Optimization"

PAPER "A Novel Smart Actuator for Airfoil Structural Morphing:

Test Campaign and Numerical Correlation"

Chapter 7 – Variable Camber Morphing Flap: Smart Flap

Chapter 8 – Variable Chord Morphing Blade

Nomenclature

3.A.S.	Active Aeroelastic Aircraft Structures (EU Project)
A.A.W.	Active Aeroelastic Wing (NASA Project)
A.B.S.	Acrylonitrile Butadiene Styrene
A.D.I.F.	Adaptive Wing Project (EADS-Airbus, DaimlerChrysler, DLR)
A.F.I.T.	Air Force Institute of Technology
A.F.R.L.	Air Force Research Laboratory
A.F.T.I.	Advanced Fighter Technology Integration (NASA Program)
A.H.P.A.	Active Hinge Pin Actuator
A.L.I.C.E.	Air Launched Integrated Counter-Measure, Expendable
A.M.P.	Aircraft Morphing Program (NASA Program)
A.o.A.	Angle of attack
A.P.V.E.	Adaptive Planform Vehicle Experiment
A.T.B.	Active Twist Blade
B.I.G. B.L.U.E.	Baseline Inflatable Wing Glider, Balloon-Launched Unmanned Experiment
B.V.I.	Blade Vortex Interaction
C.A.P.E.	Canister for Air Payload Ejections (Dept. of Defence Space Test Program)
C.F.R.P.	Carbon Fibres Reinforced Plastics
C.H.E.M.	Cold-Hibernated Elastic Memory
C.I.R.A.	Italian Aerospace Research Centre
C.R.G.	Cornerstone Research Group
C.T.D.	Composite Technology Development
D.A.R.P.A.	Defense Advanced Research Projects Agency
D.E.C.S.M.A.R.	Deployable Elastic Composite SMA Reinforced
D.I.A.S.	Dept. of Aerospace Engineering, Univ. of Napoli "Federico II"
D.L.R.	Deutschen Zentrum für Luft- und Raumfahrt
D.o.D.	Department of Defence

D.S.C.	Differential Scanning Calorimetry
E	Young elastic modulus
E.A.D.S.	European Aeronautic Defence and Space
E.A.P.	Electro Active Polymer
F.E.A.	Finite Element Analysis
F.E.M.	Finite Element Method
F.L.Y.R.T.	Flying Radar Target
F.S.M.A.	Ferromagnetic Shape Memory Alloy (also known as Magnetic SMA)
H.A.L.E.	High Altitude, Long Endurance
H.A.Z.	Heat Affected Zone
H.E.C.S.	Hyper-Elliptic Cambered Span
I.D.E.P.F.C.	Inter-Digitated Electrode Piezoelectric Fiber Composite
I.R.C.S.	Intelligent Responsive Composite Structures
L.F.S.A.	Lightweight Flexible Solar Array
M.A.R.	Mission Adaptive Rotor
M.A.R.S.	Mars Aircraft Realization System
M.A.S.	Morphing Aircraft Structures (D.A.R.P.A. Program)
M.A.V.	Micro Air Vehicle
M.A.W.	Mission Adaptive Wing
M.F.C.	Macro Fiber Composite
M.I.T.	Massachusetts Institute of Technology
M.i.T.E.	Miniature Trailing Edge Effectors
M.P.U.A.V.	Multi-Purpose Unmanned Aerial Vehicle
M.S.M.A.	Magnetic Shape Memory Alloy (also known as Ferromagnetic SMA)
N.A.S.A.	National Aeronautics and Space Administration
N.I.A.C.	NASA Institute for Advanced Concepts
NiTiNOL	Commercial name for one of the most diffused Ni-Ti SMA
N.R.L.	Naval Research Laboratory
O.S.U.	Oklahoma State University
P.B.P.	Post-Buckled Precompressed
P.D.E.	Partial Differential Equation
P.M.N.	Lead Magnesium Niobate (electro-strictive material)

P.V.D.F.	Polyvinylidenefluoride (polymeric piezo-electric material)
P.Z.T.	Lead Zirconate Titanate (piezo-ceramic material)
Q.B.C.L.M.	Quaternary-Binary Cross Linked Mechanism
R.I.	Rigidizable Inflatable
R.I.G.E.X.	Rigidizable Inflatable Get-Away-Special Experiment
R.M.A.	Rubber Muscle Actuator
R.P.T.	Rhombohedral Phase Transformation (also known as **R-Phase)**
R.R.B.	Reconfigurable Rotor Blade
S.A.M.P.S.O.N.	Smart Aircraft and Marine Project System Demonstration
S.A.W.	Seamless Aeroelastic Wing
S.E.S.	Strain Energy Shuttle
S.E.T.E.	Static Extended Trailing Edge
S.I.C.S.A.	Sasakawa International Center for Space Architecture
S.I.M.	Stress-Induced Martensite
S.M.A.	Shape Memory Alloy
S.M.A.H.C.	Shape Memory Alloy Hybrid Composite
S.M.E.	Shape Memory Effect
S.M.P.	Shape Memory Polymer
S.U.A.V.E.	Stowable Unmanned Air Vehicle Engineering
Terfenol-D	Terbium-Iron-Naval Ordnance Laboratori-Dysprosium (magneto-strictive material)
T.I.I.M.S.	Texas Institute for Intelligent Bio-Nano Materials and Structures for Aerospace Vehicles
T.W.I.S.C.A.	Twistable Section Closed by Actuation
U.A.V.	Unmanned Aerial Vehicle
U.C.A.V.	Unmanned Combat Air Vehicle
U.F.O.	Unidentified Flying Object
U.M.A.A.V	Unmanned Morphing Aerial Attack Vehicle
U.S.A.F.	United States Air Force
V.A.F.N.	Variable Area Fan Nozzle
V.G.C.	Variable Geometry Chevrons
V.L.R.C.O.E.	Vertical Lift Research Centre of Excellence
Z.I.F.	Zero Insertion Force

- *Chapter 1* -

Introduction

1 WHAT IS MORPHING AND WHY IS IT INTERESTING?*

Morphing is not easy to do, otherwise it would have already been done, and even to define. It is easier to say what it is not: morphing is not aliens or UFOs, and it is not Terminator. Nor is it airplane torture: scientists are not trying to take a perfectly good airplane and do "evil" things to it.

Today airplanes change shape all the time: something as simple as leading and trailing flaps, landing gear, a variable incidence nose make the airplane change shape or adapt to its environment, so morphing is not exactly a new science.

Morphing is more like a paradigm; three words can be used to summarize it:

- *adaptability*, making the airplane much more versatile, much more resilient to a wide variety of flight conditions (nowadays airplanes are already pretty adaptive);

- *multi-point*, trying to accommodate very diverse and even sometimes contradictory mission scenarios, trying to fly supersonically and subsonically with the same amount of efficiency, without burning a lot of fuel (long range strike efficiently);

- *efficient*, leading to mechanically simpler aeronautical structures, capable of a better efficiency in terms of weight, volume, energy, manufacture and maintenance costs, etc.

Other definitions of morphing take into account the state change (according to DARPA and AFRL), the real-time adaptation to enable multi-point optimized performance (as from NATO RTO Technical Team on Morphing Vehicles), and many others (large shape change, smooth shape change, reconfigurable aircraft, adaptive wings, etc.).

---

* = freely inspired to Mrs. A.M. McGowan (NASA Langley) lecture in [1].

The previously discussed efficiency point, in particular, opens to a whole new set of questions about morphing: what is the cost of shape change? is it worth it?

A first answer can be obtained looking at the F-14 Tomcat variable sweep mechanism (Figure 1), which "costs" 5.000 pounds on the airplane: after a system study was done, this additional weight more than bought its way onto the airplane for the capability that the Navy got from the F-14.

Figure 1: F-14 Tomcat: variable sweep mechanism in the extended (left) and retracted (right) position.

So, shape change is not actually the goal of morphing, it is just one technology approach; morphing is about the mission and the mission requirements that can be fulfilled by means of morphing strategies.

The function of the morphing mechanisms is to enable the aircraft's mission (Figure 2, [1]).
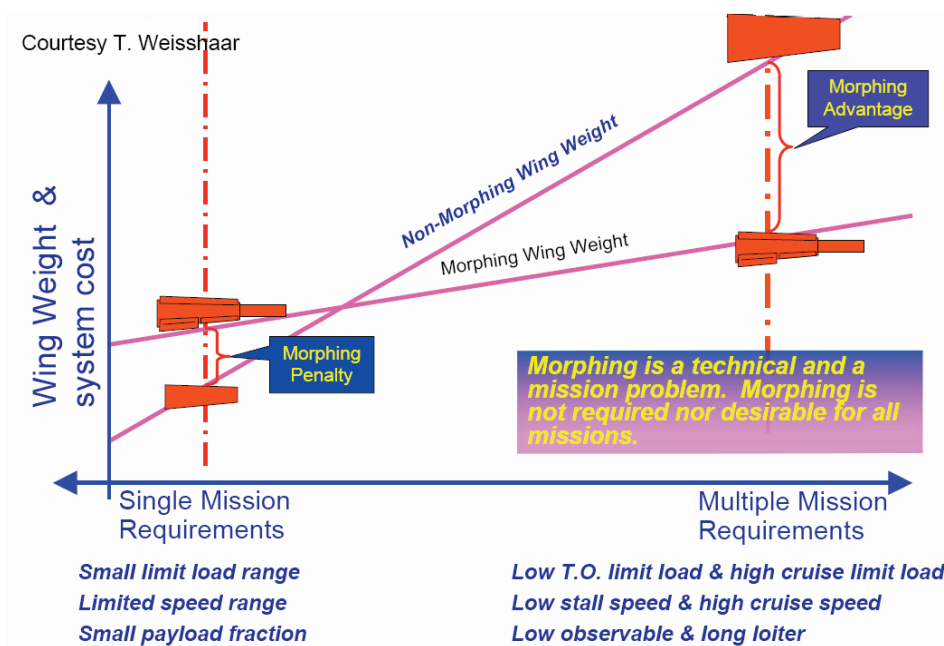
Figure 2: Wing weight and system cost prediction according to the airplane mission requirements. [1]

If an aircraft has to accomplish a single type of mission, system cost is not going to be a problem; however, if it has to satisfy multiple mission requirements, the wing must be basically sized to do everything is desired, and it's going to cost a lot, be very heavy and very large, leading to a weight penalty. From a morphing perspective, only a multi-mission scenario actually saves weight over having a fixed wing. The "cost" of the morphing may be added weight and complexity at the sub-system level; however, these sub-system "costs" enable less weight and greater performance at a vehicle level.

An example can help in understanding this: retractable landing gear. In the aeronautical field, everyone knows that for aircrafts flying past about 110-120 knots there is the need for landing gear that retracts: below that speed, it does not buy its way onto the airplane because this system costs and weights a lot; if flying past 110-120 knots, the airplane has got to have it on there, and it will pay the weight and the complexity penalty.

This is basically the same thing for morphing wings: engineers have to know if they are going to design morphing mechanisms in the airplane according to the position of the knee in Figure 2 and where their aircraft is going to be placed. The F-14, absolutely, at a single condition, it certainly costs more; however, for the mission scenarios it was designed to go to, it actually saved weight in the long run.

So, morphing is a technical and a mission problem: it's not required for everything, nor is it desirable for all missions. Aircraft morphing is most importantly about what the designer is trying to do WITH the aircraft, and secondly about what the designer is trying to do TO the aircraft. Any aircraft design should always be focused on the most efficient way to enable the mission.

Morphing techniques and mechanism have been widely inspired by nature. The first example of this is the Wright Flyer (Figure 3, [2]), in which the Wright brothers turned and twisted the wings by means of cables: their inspiration was from birds.

One of the biggest break-troughs the Wright Brothers made was actually studying the empanada or the tail section of a bird: the birds land widely by twisting and bending their tail section; they cannot land very well if the tails are cut off or if stay fixed. It only takes moving a few tail feathers for them to be able to do so, so adaptability is a big deal to a birds' manoeuvrability, and the Wright Brothers in fact pointed that out in many of their early studies ("Learning the secret of flight from a bird was a good deal like learning the secret of magic from a magician. After you once know the trick and know what to look for, you see things that you did not notice when you did not know exactly what to look for", Orville Wright, [3]).
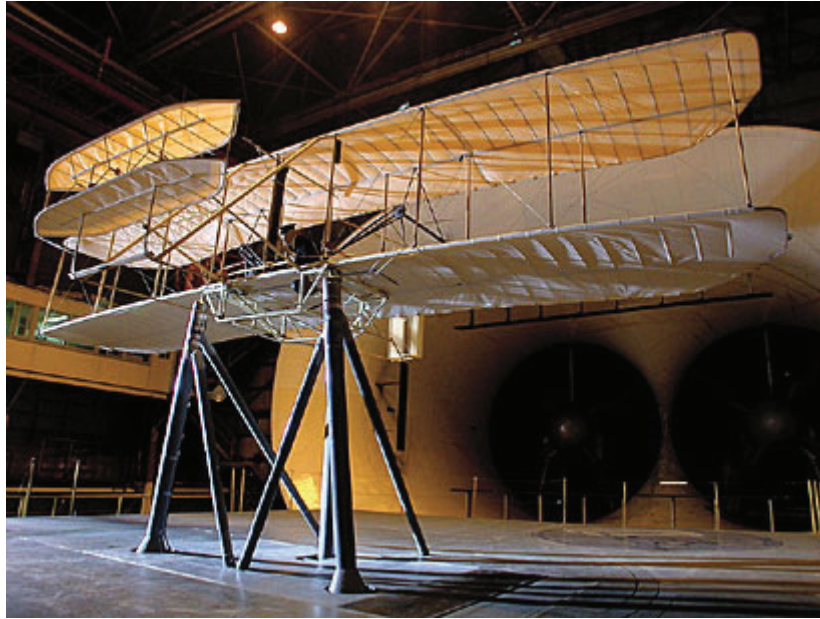
Figure 3: "The Wright Experience" project: Wright Flyer replica during wind tunnel tests. [2]

After the first flights, designers started searching for ways to optimize both aircraft efficiency and performance. Typically, wings are designed to best perform in a single specific flight condition, but suffer from lower efficiency in the others. These penalties can be reduced by the deflection of hinged control surfaces, which alter the local camber and, thus, the aerodynamic field around the airfoil.

Starting from 1980, many researchers investigated the adoption of suitable actuators and shape changing structures implementing the so called "smart" materials, to improve flight characteristics and performance by adapting the wing shape to the multiple specific flight conditions that an aircraft can encounter during a typical mission (Figure 4).
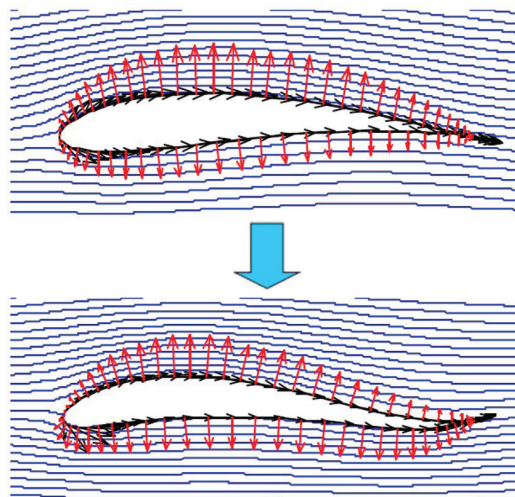
Figure 4: Example of shape change of an airfoil which modifies the aerodynamic forces and moments.

Smart systems, or systems which can sense and react to their environment autonomously, represent the future of aerospace technology. A smart structure usually involves the presence of distributed actuators and sensors, together with one or more microprocessors that analyze the sensors' output and use the control theory to command actuators. This is then used to apply local displacements or strains to change the structural behaviour. By adopting the smart materials within the smart system paradigm, structural elements can be suited not only to carry loads, but also to provide actuation.

Among the smart materials, such as piezo-ceramics, magneto-rheological fluids, magneto-strictive and electro-strictive materials, etc., Shape Memory Alloys have been preferred in many applications due to their combined high recoverable strain and force levels. In this research field, many applications can be found for the active control of noise and vibrations, modification of damping characteristics, aero-elastic tailoring, shape and internal stress field control of structural elements, development of smart actuators, deployable structures, etc.; studies have been carried out in fields such as aerospace, civil, mechanical, automotive, biomedical, robotics, etc.. Many of them will be presented in the next chapters.

However, again, aircraft morphing means different things to different people. Today the research is generally focused on seamless structural wing shape adaptation, inspired by biological life. Nevertheless, the "aerodynamic" shape of airfoil can effectively be the same as the "structural" shape of the airfoil: following this definition, also flow control techniques (active/passive ventilation, synthetic jets, etc.) can be counted in the morphing research scenario.

As a summary of the lessons learned in the large amount of literature work developed worldwide and challenges for future morphing aircrafts, one may conclude:

- morphing does not always pays off, designers have to know when to morph;
- understanding the mission assistance level requirements, as shape change is not the goal but one good approach to fulfil mission requirements;
- designing and modelling the morphing concept can be difficult, and usually requires a good dose of creativity for addressing application issues in an innovative way, together with good optimization tools and the right criteria to select the best concept;
- innovative structures and materials must work with other disciplines to enable the final design to fly;

- skin issues must be addressed to accommodate the shape change and expected higher aerodynamic performance;

- control systems exploiting the new capabilities (as distributed actuation and sensing) must be developed, without increasing the difficulty for the pilot to fly.

Moreover, what is really important to understand is "one size does not fit all", that is several morphing strategies and solutions have to be developed to fit the single aircraft type and mission requirements: a good morphing concept for a given airplane may not fit well the needs of another one. Criteria to select the best solution must be suitably taken into account: for instance, weight can be a key factor for concepts in the early stages, as shown in Figure 5, [1]. Basically it represents how much the wing weighs versus how much it can carry: a morphing concept must be in the weight efficient region, otherwise it is not worth it. After weight requirements are met, functionality can be another important criteria; subsequently, multi-dimensional criterion may be applied.
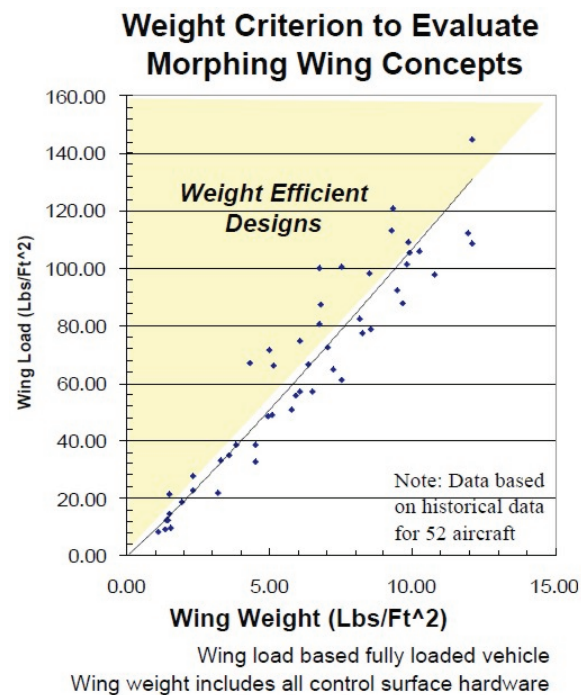
Figure 5: Wing weight vs wing load chart based on a historical average of 52 airplanes. [1]

Morphing airplane concepts have continued to evolve for over a century. Aircrafts fly today and are a pretty mature technology. However, they are not complete with the kind of things scientist can do or new materials can allow: the next century of flight can be even more exciting than the first one, and with morphing technologies developing nowadays so fast, it is entirely possible. Nature still has a lot going on.

motor it would never have worked, because we tried, by the way.

2 OVERVIEW OF THE WORK STRUCTURE

In this research study, aeronautical "structural" morphing has been considered, focused on seamless structural wing shape adaptation, inspired by biological life.

Available literature (Chapter 2) shows that international interest in the aeronautical field is focused in the morphing of specific wing parameters, such as leading or trailing edge curvature, wing torsion, wing span change, etc., each capable of generating aerodynamic advantages or better adaptability over a traditional design.

Moreover, to overcame weight, mechanical complexity and costs penalties introduced by morphing architectures, many of these solutions adopt smart materials as actuators. Among them, Shape Memory Alloys have attracted a lot of attention and are present in many applications, due to their favourable force/volume or force/weight ratio: state of the art about SMAs features, numerical modelling and characterization is presented in Chapter 3.

The chief objective of this dissertation is to propose plausible architectural solutions for changing different geometrical parameters of an airfoil; many of them integrate Shape Memory Alloys within the structure, having both actuation and load-bearing role.

In particular, three airfoil parameters have been taken into account:

- airfoil (upper) **bump**;
- airfoil **camber** at trailing edge (morphing flap);
- airfoil **chord**.

The formation of an airfoil upper bump is one of the first experiences in the morphing field done by the author and researchers at CIRA: it represents one of the less invasive possible morphing techniques, not affecting the wing primary load-bearing structure, and capable of introducing some benefits in transonic regime (Chapter 4).

Then, activities moved towards a greater level of integration and interaction within the wing structure, trying to substitute a traditional hinged flap with a variable camber trailing edge, also known as morphing flap (Chapter 5). In particular, literature showed a dearth of real scale applications of morphing technologies with smart materials to civil transportation class aircrafts. Basing on the partnership with Alenia Aeronautica Spa industry (which founded part of these activities), innovative concepts for a morphing flap have been conceived, suitable for real scale regional transportation aircrafts; expertise at CIRA in modeling and characterization of Shape Memory Alloys allowed for an high integration of these alloys both as actuators and structural load-bearing

elements. Results of this collaboration brought to the design and manufacture of a SMA-based actuator (Chapter 6) and a morphing flap architecture highly integrating such an actuator device (Chapter 7). Moreover, these research activities have raised great interest in the industrial partner (Alenia): a patent is pending on both devices (Appendix) and further studies and collaborations are currently starting.

Finally, new research activities started in the branch of variable chord are presented (Chapter 8). Chord morphing has the power to increase the airfoil surface and, so, its lifting capability. Something similar already happens for high lift devices on transportation aircrafts, where the typical single/double slotted solution for trailing edge flaps allow not only to increase wing curvature, but also its chord (that is, wing area). The possibility to match the greater aerodynamic efficiency of a morphing flap with an airfoil chord (wing area) increase could lead to even better aerodynamic performance. In this work, an early concept has been studied and manufactured for a morphing rotorcraft blade, basing on a three-month collaboration with Prof. F. Gandhi of the Aerospace Engineering department at the Pennsylvania State University (with particular reference to the Vertical Lift Research Centre of Excellence (VLRCOE)).

The thesis, where possible, has been produced as a collection of publications (both on journals and to conferences). However, due to the patent pending on some of the presented activities and prototypes, pieces of the research activities have not been published yet at the moment of writing: for this reason, some chapters will be offered as traditional reports.

Therefore, the dissertation is organized as follows:

- ***Chapter 2*** treats the worldwide state of the art in morphing technologies through a survey of aeronautical applications that can be found in literature, focused in the optimization of specific wing parameters, using traditional actuators or Shape Memory Alloys;

- ***Chapter 3*** overviews the Shape Memory Alloys micromechanics and macroscopic behaviour, together with material modelling and characterization; then, current applications in various fields exploiting either the super-elastic or shape memory effect are presented, jointly with new discovered materials in the "shape memory" field;

- *Chapter 4* introduces the first studied morphing application, focused on the bump formation on the upper wing skin for transonic drag reduction (paper): a device integrating Shape Memory Alloys has been designed, manufactured and tested;

- *Chapter 5* reviews some preliminary studies carried out to identify possible morphing solutions, actuated by SMAs elements, to produce a camber change localized to the aft part of a wing airfoil, so to mimic a trailing edge flap: several architectures are presented and numerical results discussed (various papers);

- *Chapter 6* presents the conceived SMA-based smart actuator, explaining in great detail its design features and all the considerations, numerical simulations and optimizations which brought to the final prototype, experimentally tested and characterized (two papers);

- *Chapter 7* shows in detail an application of the developed smart actuator to a real scale morphing architecture able to mimic a trailing flap: after numerical simulations, the solution has been built and prototype tested also in presence of static loads;

- *Chapter 8* deals with the other morphing parameter taken into account in this research, that is airfoil chord, introducing an early concept for a morphing rotorcraft blade, its design constraints and the realized prototype;

- *Chapter 9* closes and comments on the work presented, discussing also future developments.

Finally, an *Appendix* is present, reproducing the patent communication from the European Patent Office with all the details.

3 REFERENCES

[1] McGowan A.M., 2008, "*Morphing Background and Historical Perspective*" – Invited lecturer at the Advanced Course on Morphing Aircrafts – Materials, Mechanisms and Systems, November 17-20 2008, Lisbon, Portugal

[2] Project "The Wright Experience", website: http://www.wrightexperience.com/

[3] Dalton S., 2004, "*The Miracle of Flight*" – Firefly Books, 184pp, ISBN 1-552-09378-6

- *Chapter 2* -

Morphing Applications in Aeronautics:
State of the Art

1 INTRODUCTION

Aircrafts are the result of the human desire to fly, as suggested by the observation of nature and other life forms, which highlighted its feasibility while being denied to human beings. So, making a virtue of necessity, adventurers, scientists, engineers, or just mainly humans with a dream, began to design the first flying machines: even today, though, nature has much to teach us and continuously inspires research.

By directly comparing actual aircrafts with nature creations, today designers seek inspiration, in order to achieve the same simplicity, elegance and efficiency that characterize the animal species and thousands of years of biological evolution: namely, what attracts designers is the integration between structure and function that characterizes the birds wings [1] (Figure 1).

Landing   Loitering   Fast Cruise

Figure 1: Different flight conditions of a bird and associated wing geometry changes. [1]

To create an aircraft capable of varying the wing shape, and thus its function, it is necessary to adopt a flexible and adaptive structure. This solution always led to penalties in terms of cost, complexity and weight in former aircrafts, although in certain circumstances these were overcome by the benefits attained at the overall system level: airplanes like the F-14 "Tomcat" and the "Tornado" are good examples. Recent developments in the field of "intelligent" materials can overcome these penalties.

From an historical point of view, as early as 1890 the French aviation pioneer Clement Ader had proposed a bat wing for an airplane that could reduce its size to half or one third of its total deployment. Among the first examples of "polymorphic" aircrafts, the Pterodactyl IV designed by Geoffrey Hill at Westland flew in 1931, or the Russian fighter IS-1 which flew in 1940, able to switch from manoeuvrable biplane to faster monoplane. A brief historical overview is shown in Figure 2.
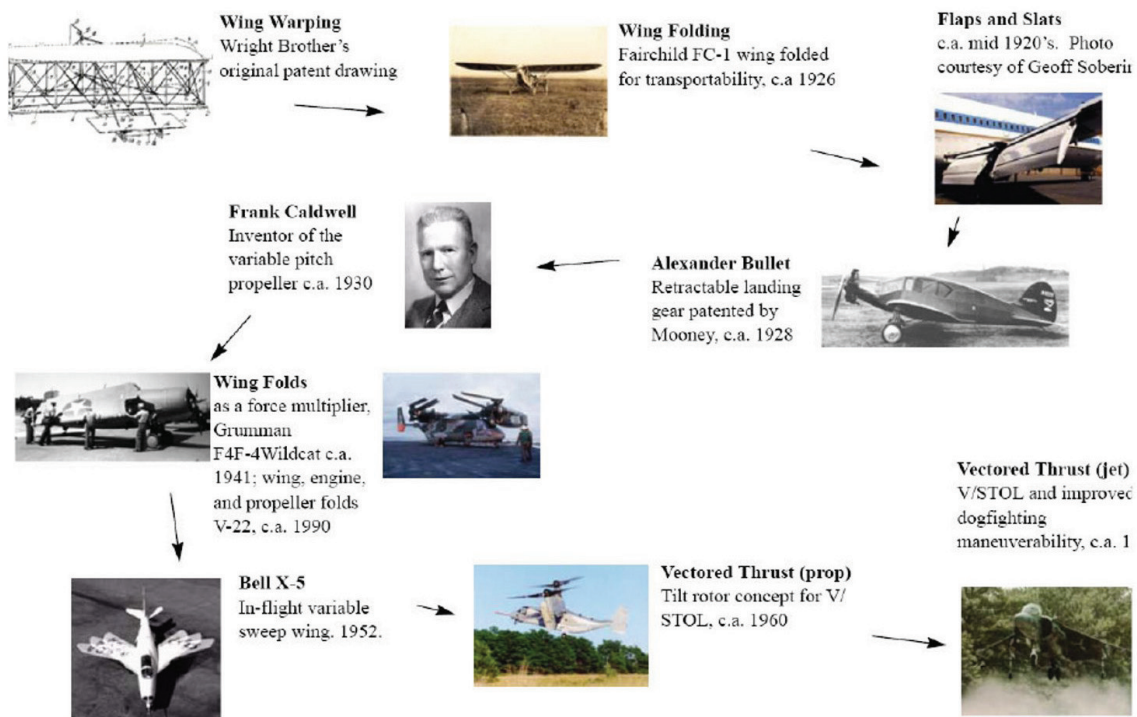
Figure 2: Historical examples of morphing technologies. [1]

The ability of a wing surface to change its geometry (morphing) during flight has been of great interest to researchers and designers over the years: an adaptive wing allows to diminish the number of compromises that a designer is forced to accept to ensure the operation of the airplane in multiple flight conditions [2]. Figure 3 shows a typical mission profile for a civil transportation aircraft (Airbus A-340): as shown by the diagrams, for a selected aircraft and flight mission, there are still several flight conditions to be addressed.
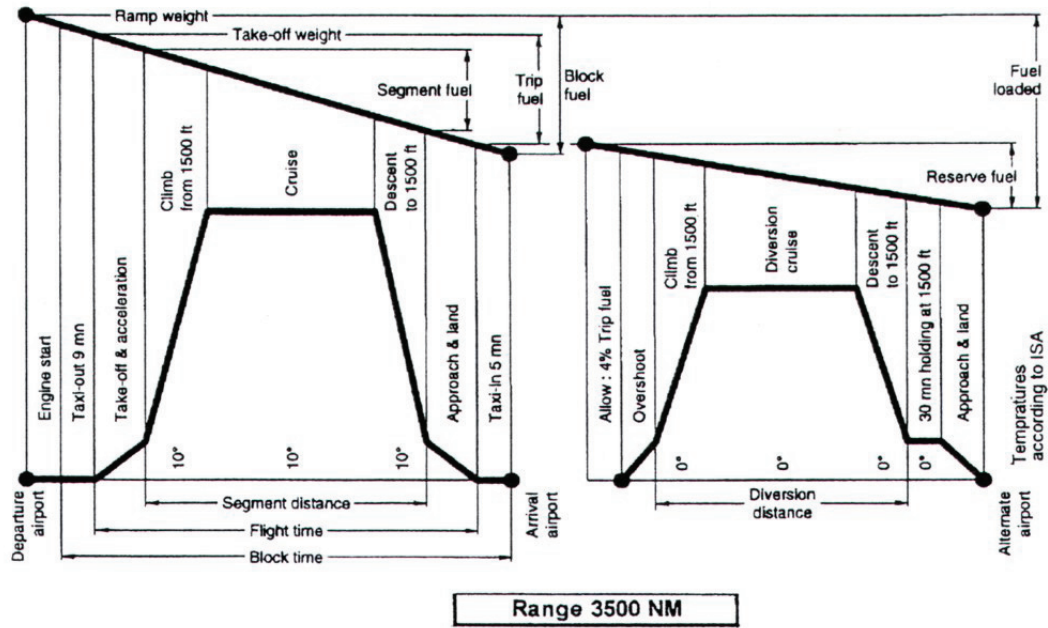
Figure 3: Example of mission profile for a commercial aircraft, A-340. [3]

By using an adaptive wing, whose geometry varies according to changing circumstances of external aerodynamic loads, it is possible to fully explore the potential of airflow in each part of the aircraft mission profile, resulting in an increase of aerodynamic performance during cruising flight as well as during manoeuvre, and in a more efficient structural design [4-8]; therefore, having to choose at the design stage between high efficiency or high manoeuvrability, as the need to consider aerodynamic optimization for a single flight condition would no longer be necessary (Figure 4).
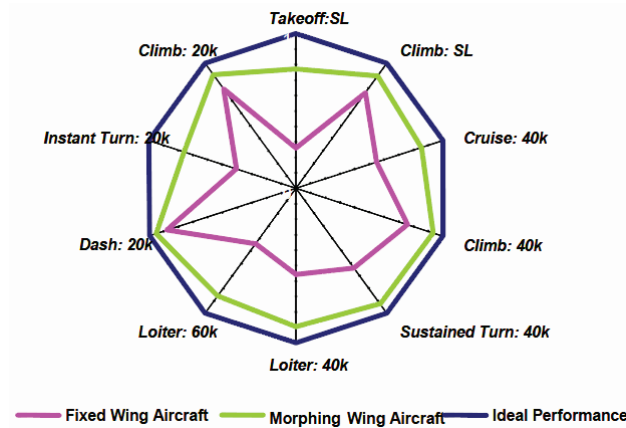
Figure 4: Spider plot comparison of fixed and morphing wing aircraft. [9]

For this reason, many companies and universities follow a multidisciplinary optimization and systems approach to morphing solutions, also focusing on the integration of computational fluid dynamics (CFD) and computational structural dynamics (CSD) models for geometric optimization; moreover, morphing wing(s)

airfoil and configuration geometry, design methodology, effectors, flight control, aero-elasticity and stability are taken into consideration too (an overview can be found in [10]).

Moreover, estimated 1% reduction in airfoil drag would save the U.S. fleet of wide-body transport aircraft $140 million/year, at fuel cost of 0.70 $ / gal (source NASA Dryden Studies). For a medium-range transport aircraft with an adaptive wing, the projected fuel saving should be about 3-5%, depending on mission distance.

Usually in literature this possibility to change the wing shape is also referred to by the name **M.A.W.** (*Mission Adaptive Wing*).

At present, the use of multiple aerodynamic devices (such as flaps, slats, etc.) represents a simplification of such general idea: the use of traditional control systems (with a fixed geometry and / or location) allows to obtain high aerodynamic performance in a fixed range and for a fixed number of flight conditions; when the aircraft comes out of that range, these traditional systems can be neutral or negatively influence the development of aerodynamics, with obvious consequences (lower efficiency).

Moreover, the conventional hinged mechanisms are effective in controlling the airflow, but they are not efficient, as the hinges and other junctions usually create discontinuities in the surface, resulting in unwanted fluid dynamic phenomena.

As pointed out by Renken [11], since 1920 the airplanes have used devices that can increase the lift during landing and takeoff; however, with the aircraft weight gain and growing cruise speed, also the wing structural stiffness increased due to multiple aero-elastic phenomena (divergence, flutter, etc..): this has led to the use of control surfaces such as ailerons and / or flaps in place of wing twist. Only starting by the second half of the '70 researchers seriously resumed the idea of a variable wing shape: most of this research was based on two concepts, namely the active control of the curvature along the wing span and the implementation of flexible wings, able to exploit the aero-elastic forces to obtain the desired deformations (wing shapes).

To date many studies have been targeted to the variation of the wing shape and they have been focused to achieve several objectives, as the control of shock waves during transonic flight conditions, control of turbulence, the wake (laminar flow separation), vortex, active control of flutter, etc.. [2] (Figure 5).

The adaptive wing can therefore provide a significant increase of performance of the airplane. However, the realization of such an aircraft poses new design challenges: traditional standards of design based on the realization of lightweight and extremely

rigid structures must be abandoned, in which the airfoil profile and wing shape is dictated by the optimization of aerodynamics at fixed flight conditions, to undertake the development of innovative structures that are inherently deformable and continuously adaptable, in real time and during flight, according to the operational conditions and requirements imposed by the mission.
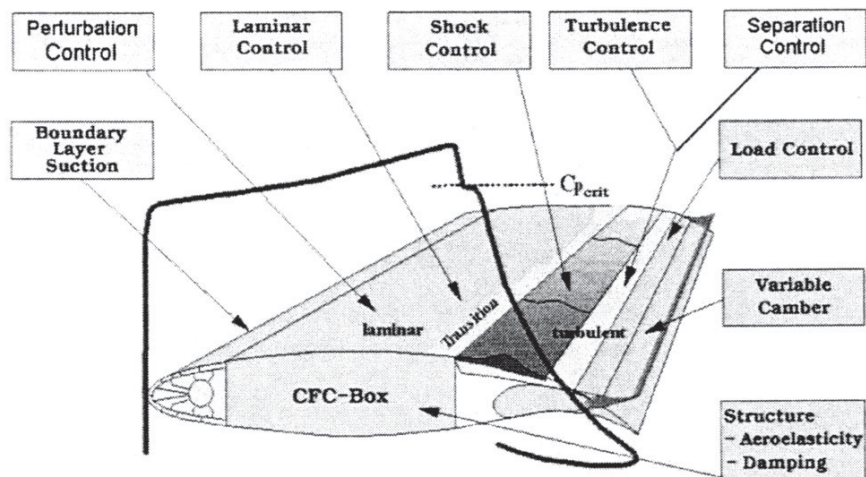
Figure 5: Typical issues that can be dealt with by using the airfoil shape change. [2]

Obviously, the opportunity to realize a morphing wing is tied to the availability of materials and implementing solutions that guarantee in all circumstances the necessary deformation of the structure while keeping unharmed the essential characteristics of structural integrity and load bearing capability. Precisely in this context, the Shape Memory Alloys (as part of the SMART materials family) may be the solution for the realization of distributed actuators within the wing structure capable of providing local shape modifications.

This chapter will mainly focus on the adaptive wing concept as designed to optimize the geometry (or shape) of the airfoil (Figure 6) from a structural perspective: the aerodynamic shape change (active flow control) techniques will not be discussed. Many research activities incurred so far will be presented, dealing with the variation of the wing shape (globally, its portions or specific parameters) in order to improve the aerodynamics efficiency, exploitability of the free-stream airflow or to simply replace traditional control surfaces with more effective ones.

In particular, great attention will be paid to solutions aimed at increasing aerodynamic efficiency by means of an airfoil with variable shape: that is, the wing itself (of some part) is able to deform in order to vary the aerodynamic forces and moments, reaching a new shape "adapted" to the selected flight condition and carrying out the appropriate

control tasks; in addition, since the morphing can be implemented continuously and gradually, it is possible to get several benefits over conventional control surfaces that, when deployed, create discontinuity or additional obstacles to the airflow, causing additional resistance (Figure 7).
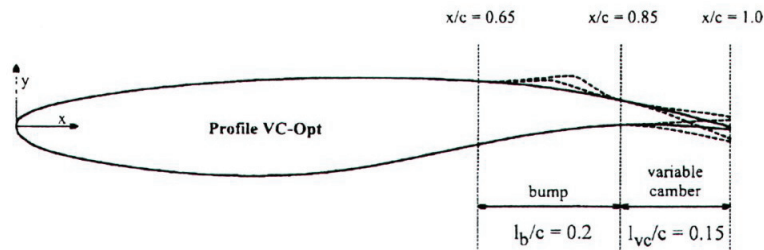
Figure 6: Example of adaptive wing. [12]
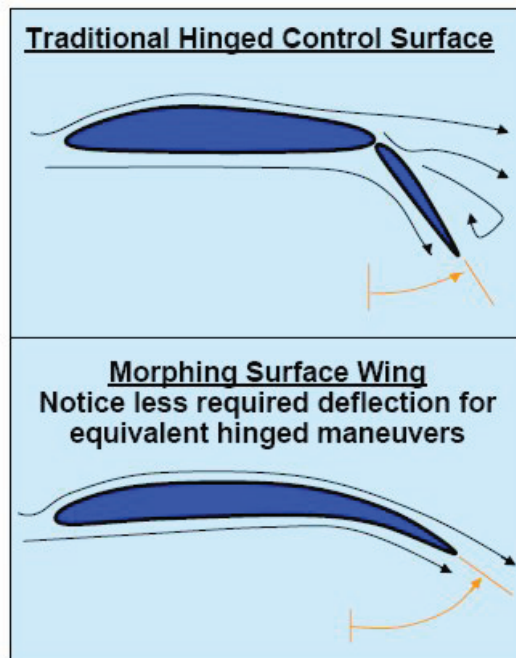
Figure 7: Comparison between traditional actuation and wing morphing.

2 METHODOLOGIES FOR STRUCTURAL WING MORPHING

In this section different methods for realizing the adaptive wing will be discussed, as a result of the earlier studies found in the literature. Research activities carried out on wing morphing by means of Shape Memory Alloys (SMA) will be presented in the next paragraph.

At present, several studies are underway aimed at understanding the potential of adaptive wing technologies: these new technologies have the ability to alter substantially the shape and size of the wing, which can lead to many benefits. Aircraft wings that can change their geometry during different flight condition can maximize the efficiency and performance of the airplane [1], intended as increased payload or range, noise or weight reduction, less polluting emissions, etc.

The idea of changing the wing shape or geometry is far from new. Referring to the Wright Flyer, the first heavier than air aircraft with an engine, it could change the curvature of the wing by means of some cables actuated directly by the pilot. There are examples of newer aircraft, like the "F-14 Tomcat" fighter or the European "Tornado" (Figure 8), which can alter the wing sweep angle to obtain, from time to time, good performance at high or low speed (alleviating the problems of compressibility).
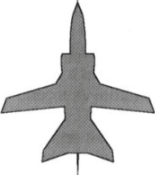
	25 deg	45 deg	67 deg
CONFIGURATION			
MANEUVERABILITY	BETTER	AVERAGE	WORST
STALL VELOCITY	LOW	MEDIUM	HIGH
MAX VELOCITY (MACH NUMBER)	LOW (0.73)	MEDIUM (0.88)	HIGH (2.2+)

Figure 8: Sweep angle change for the military aircraft Tornado.

Even when a commercial airplane deploys its conventional flaps, in practice is changing the geometry of the wings. However, these examples of geometry changes are still limited, with narrow benefits compared with those which can be obtained employing a wing that is inherently deformable and adaptable in many ways or by changing several parameters.

Some efforts in the construction of an airplane that can also change the wing geometry, as for the F-14 or Tornado, led to some penalties in terms of weight, cost and maintenance, sustainable only for high performance/military aircrafts. Recent developments in the SMART materials field may allow to overcome these limitations and enhance the benefits coming from similar design solutions [13].

There are many ways to vary the geometry of a wing, main subject of several researches.

Wing Local or global Variable Camber (VC)

The need for wing curvature change arises from the possibility, in the subsonic regime, to adjust continuously the airfoil geometry at different flight conditions, thus increasing the Lift / Drag ratio [14]; the more are the possible intermediate configurations to gradually change this geometry, the greater are the occurring aerodynamic benefits.

The wing camber can change only on specific parts (leading or trailing edge) or in a global manner, letting the entire wing act as an unique control surface. Moreover, some applications also realized a small curvature change on the wing upper surface to increase the aircraft performance in transonic regime [2].

Although the idea of changing the wing camber was born simultaneously with the first airplanes, it is far from simple to design devices capable of achieving the necessary deformation and suitable control systems: many patents and researches have been carried out in this regard.

Probably, the first example in literature of a variable camber wing has been presented by **Parker** [15] in 1920 (Figure 9). This concept involved changing the wing configuration through aerodynamic loads on the wing. This scheme divided the wing into three sections using two wing spars, one at the leading edge and the other at the two-third chord. The portion of the wing between the spars was flexible and the portion aft of the second spar was rigid. The ribs were allowed to slide over the rear spar. Thus, when the wing was placed under aerodynamic load the portion between the spars was carried upward while the rear portion being rigid and fixed to it, moved downward resulting in a camber wing. The wing was covered with fabric continuously except where the flexible channel was connected to the tailpiece, a 1-inch space was left open to allow the lower portion of the fixed tail to slide to when the wing was deformed. The

wind tunnel test results showed that the wing had a maximum lift coefficient of 0.76 and minimum drag of 0.007.
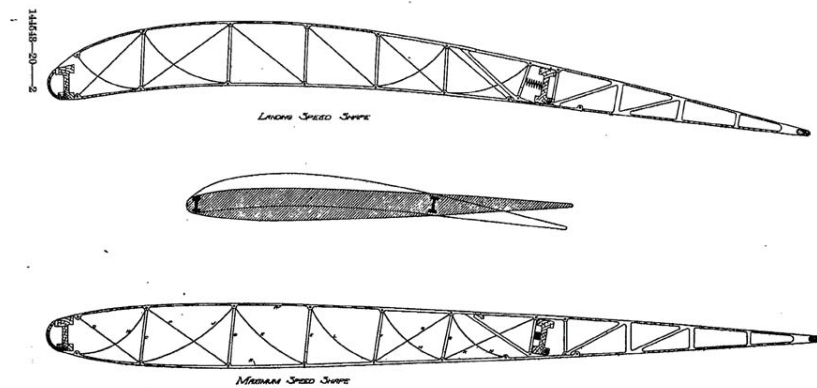
Figure 9: Parker variable camber wing. [15]

In 1978 **Frost & al.** [16] filed a patent for the camber change of a wing trailing edge by means of a suitably designed internal structure, actuated by screws connected by articulated joint: the surface panels are supposed to be flexible and the entire structure behaves like a flexible beam (Figure 10).
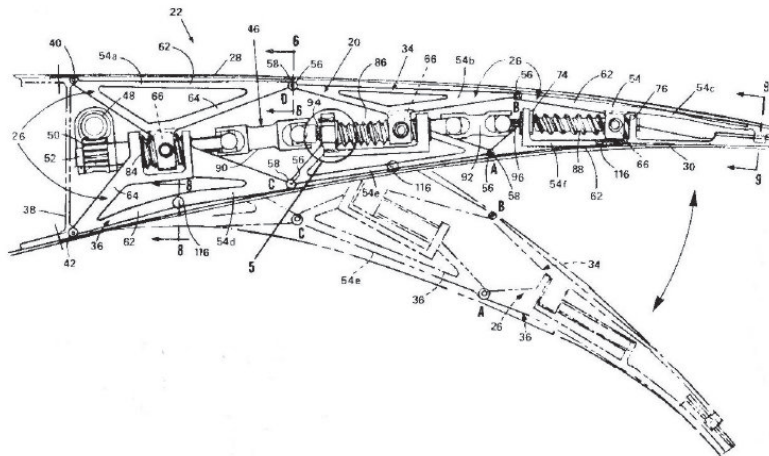
Figure 10: Patent of a wing trailing edge with internal actuation mechanism based on screws connected by articulated joint. [16]

Actuation of the connected screws could induce an opposite translation between the upper and lower parts, leading to the desired deflection of the trailing edge.

A similar concept has been patented by **Statkus** [17], in which two separate groups, constituted by four separate leverages each, can control the curvature of a leading edge (Figure 11): one group manages the horizontal and vertical displacement of the internal structure, while the second one regulates the rotation angle and the applied moment to the flexible surface skin.
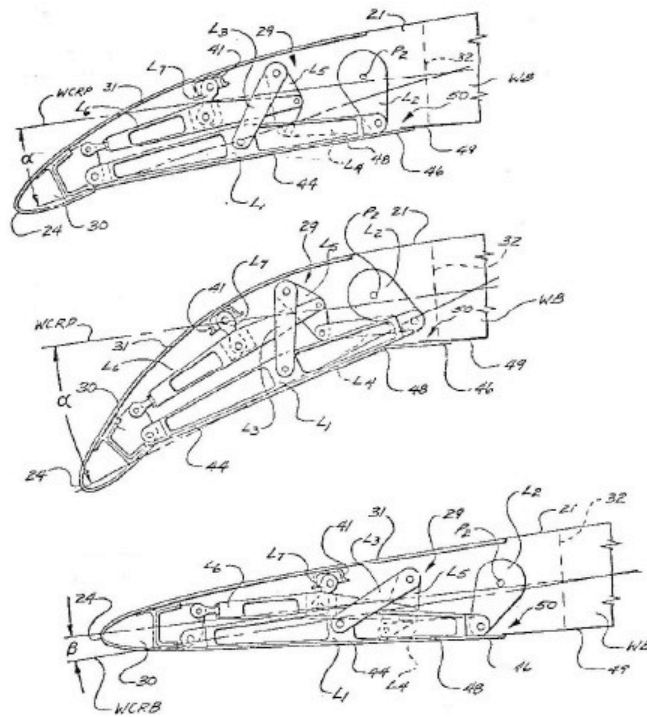
Figure 11: Patent of a wing trailing edge with internal actuation mechanism based on leverages. [17]

A more recent patent has been issued to **<u>Perez</u>** in 2002 [18], who conceived a mechanism for adjusting the curvature of airfoils, based on a plurality of torsion boxes connected by means of a drive chord, the length of which may be changed using a control command (Figure 12).
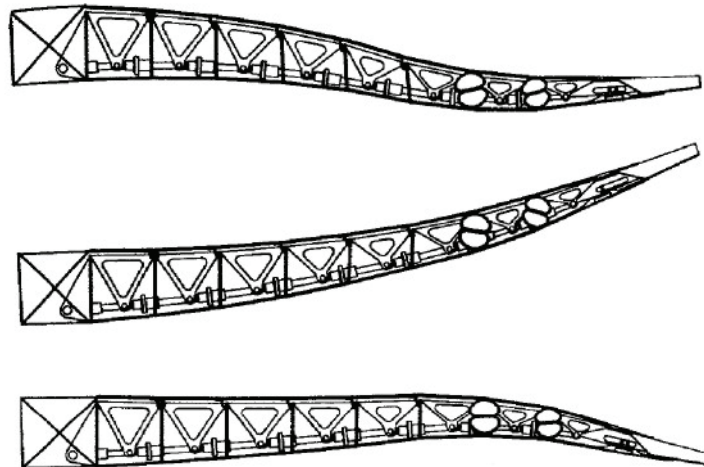
Figure 12: Patent of a mechanism for adjusting the curvature of airfoils. [18]

Starting from mid '80, Boeing accepted the challenge of integrating, on board a military aircraft, a device capable of controlling the wing curvature by means of an automated control system, so as to optimize performance according to the external wing pressure

loads: this program, named **A.F.T.I.** (Advanced Fighter Technology Integration)/F-111, was promoted by NASA in collaboration with the USAF (Figure 13 and Figure 14) [19].
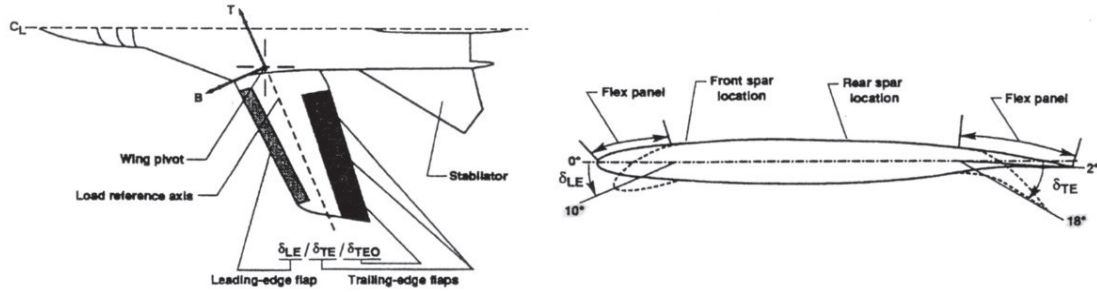
Figure 13: Drawing of structural changes applied to a F-111A military aircraft for the AFTI program. [19]

| (a) | (b) |
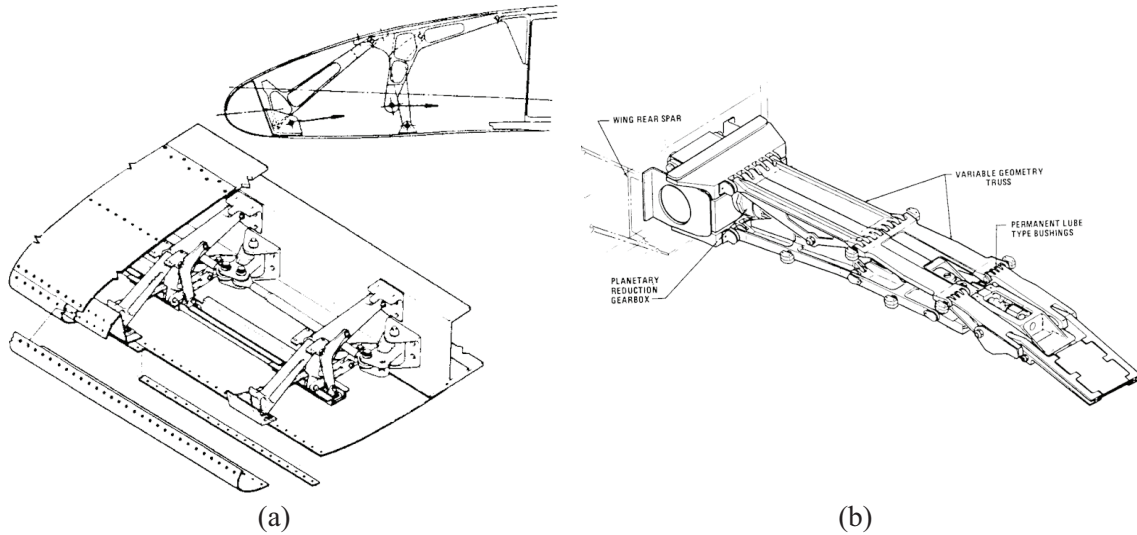
Figure 14: General Dynamics F111-MAW: (a) leading edge and (b) trailing edge schematics. [21]

The F-111 wing was suitably modified, adopting six independent sections for the trailing edge (three for each wing, based on sliding panels for the lower surface and flexible panels made of glass fibre for the upper one) and two for the leading edge in flexible composite; all these surfaces were commanded by electro-hydraulic actuators.

The automated control system was able of managing four different operating modes [20], to achieve several optimized conditions basing on measurements of dynamic pressure, normal acceleration, Mach number and onboard fuel:

- the *Maneuver Camber Control* (MCC) mode maximized the Lift / Drag ratio;
- the *Cruise Camber Control* (CCC) mode maximized the cruise speed at appropriate conditions of altitude and engine throttle;

- the *Maneuver Load Control* (MLC) mode measured the aerodynamic moment generated by the wing and optimized its curvature to "move" as much air-load as possible to the wing root;

- the *Maneuver Enhancement/Gust Alleviation* (MEGA) mode maximized the aircraft responsiveness to the pilot commands.

Flight tests were conducted on the AFTI/F111 aircraft (Figure 15) and confirmed the performance increase: 20-30% range enhancement, 20% aerodynamic efficiency growth, 15% increase of wing air-load at a constant bending moment [21].

Figure 15: F-111A modified aircraft for the AFTI program promoted by NASA. [21]

Researchers at the University of Maryland [22] have designed and implemented a multi-section wing model (Figure 16) **<u>mandrin-type</u>**, based on the NACA 0012 airfoil, capable of variable curvature.
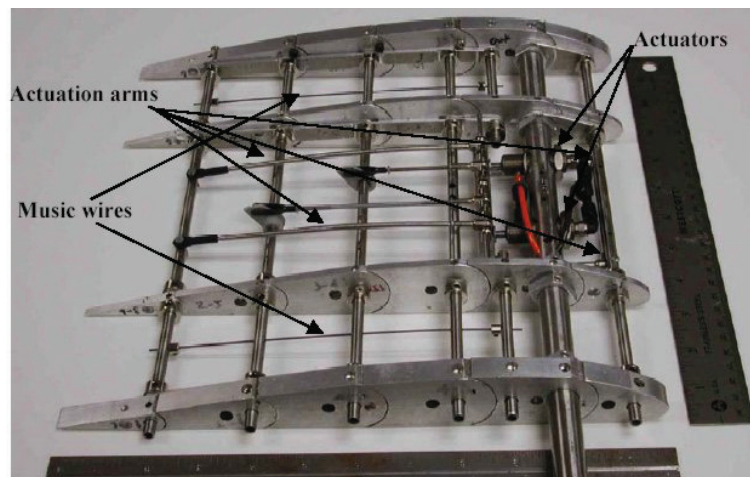
Figure 16: Variable curvature wing designed by the University of Maryland. [22]

Each rib is divided into six sections, each able to rotate up to 5 deg with respect with the previous one without significant discontinuities on the wing surface; the camber change is obtained by means of pneumatic actuators. Wind tunnel tests showed that the lift produced by a similar wing is comparable to that of the same one piece airfoil, but the surface drag is higher due to the increased required flexibility of the skin.

Monner & al. [23], within the ADIF project carried out by EADS-Airbus, DaimlerChrysler F&T and DLR, developed a typical example of "*Compliant Structure*", that is a one piece structure which is able to spread forces so that it can deform in predetermined areas and result rigid to deformation elsewhere (Figure 17). So, the trailing edge is constituted of a flexible structure realized with plate elements connected with a cinematic mechanism, as illustrated in Figure 18.

Each rib is actuated in a single point: the rotation of the commanded plate element is gradually transferred by means of the mechanism to the other elements, to obtain the desired shape. This solution is actually under development for a possible application on the Airbus A-340 aircraft.
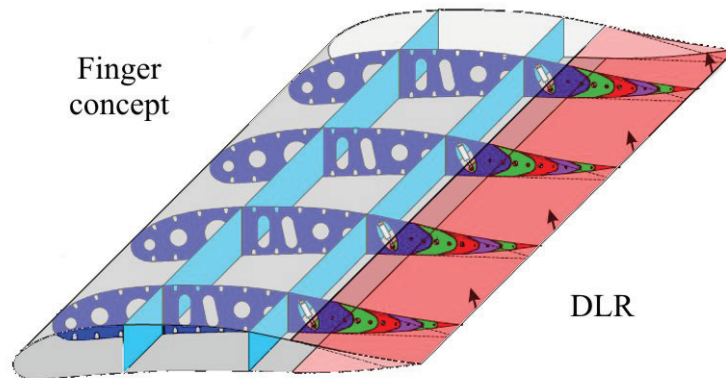
Figure 17: Example of "Compliant Structure" developed at DLR. [23]
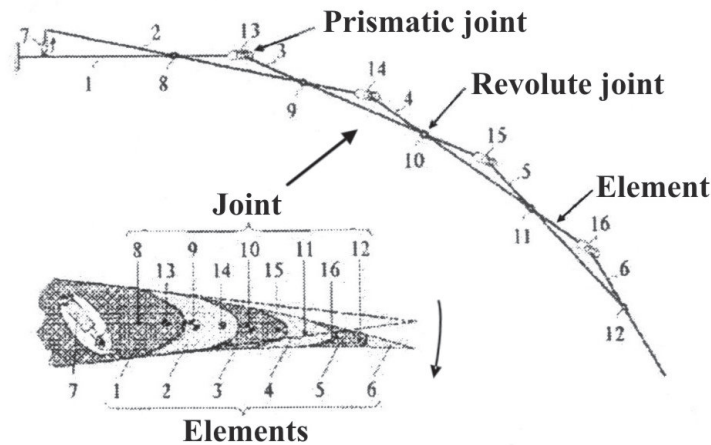
Figure 18: Cinematic mechanism of the actuation system developed at DLR. [23]

Basing on a similar idea, the Second University of Napoli developed and simulated a servo-actuated articulated rib [24] (Figure 19).

<table>
<tr><td>(a)</td><td>(b)</td></tr>
</table>
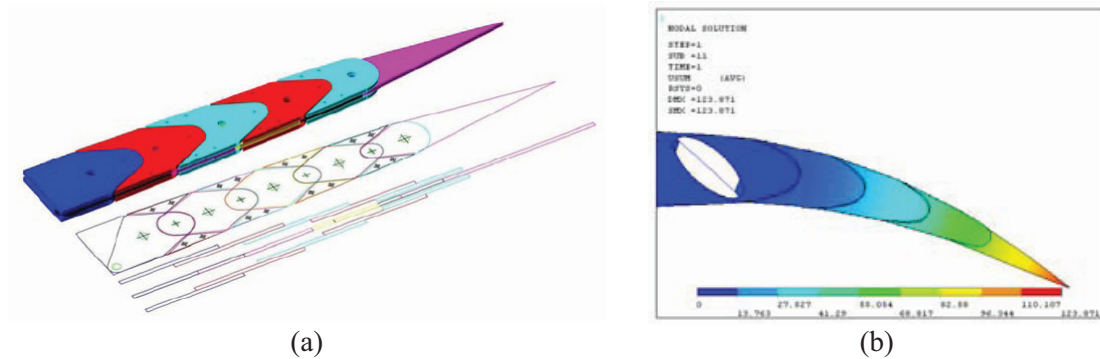
Figure 19: Servo-actuated articulated rib developed at the Second University of Napoli: (a) schematics of rigid parts and (b) FE simulation. [24]

<u>Baker & Friswell</u> [25-27] presented a concept for active wing morphing in the form of variable camber control by the application of a variable geometry truss structure. The Kagome truss pattern is shown to offer a geometry that after modification satisfies the requirements of static and kinematic determinacy; thus by replacing selected members with linear actuators structural form may be altered without resistance. A simple 14 element truss forming the trailing edge between 0.6c and c (c = 100mm) of a NACA 0012 aerofoil is illustrated in Figure 20. Each of the 14 elements provides a possible location for actuator substitution with the goal of replicating either the illustrated shape or geometry objective forms. Both of the objectives are defined by the deformation of the mean line resulting in a trailing edge deflection that would require 10 deg equivalent flap angle.
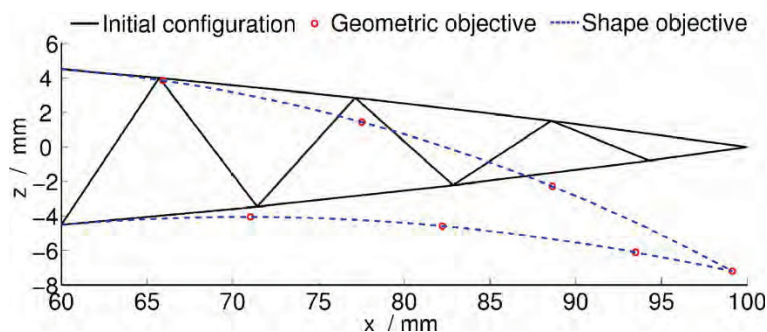
Figure 20: The 14 element trailing edge in its initial configuration, and the target geometry and approximate target shape. [27]

After this first study, a similar trailing edge geometry has been adopted for two statically and kinematically determinate truss structures comprising 1752 elements, and referred to as 'A' and 'B' (Figure 21). Each structure is geometrically identical and

topologically similar; the difference being the connectivity of elements adjacent to the surface
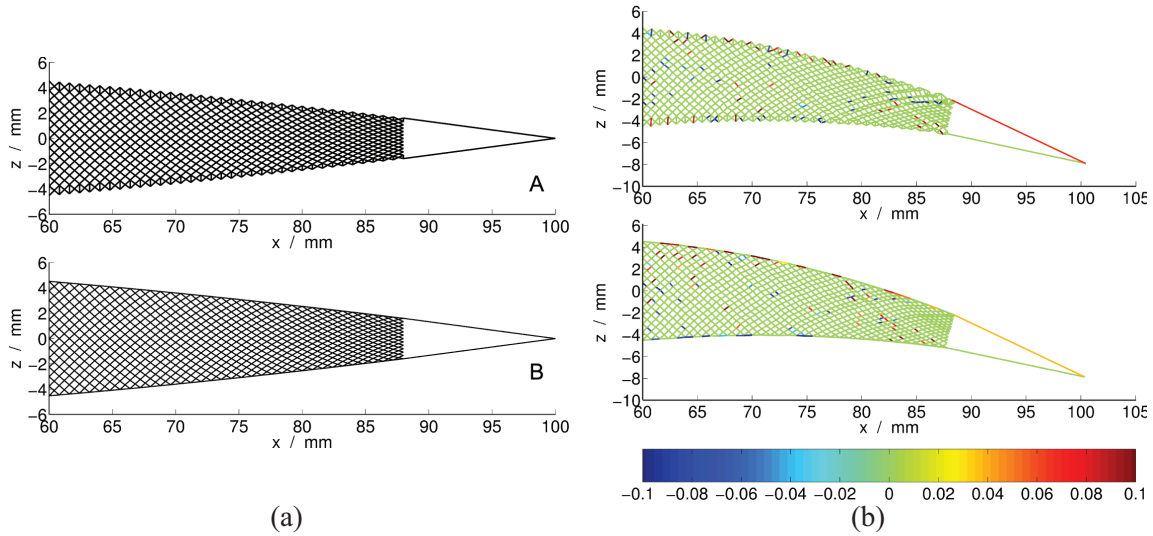
Figure 21: 1752 element truss structures with identical geometry: (a) trusses topology and (b) with 88 actuators located using the GA and the shape objective (element shade refers to the applied strain). [27]

<u>Ricci</u> [28] at Polytechnic of Milano developed a rotating rib concept capable of gapless camber variation (Figure 22): this has been achieved by an internal hinge to which the trailing edge rib is attached; both the upper and lower skins are allowed to glide over the rib contour (they are not connected at the trailing edge). As a proof-of-concept, a wing section has been built equipped with 4 rotating ribs, having 1.4m of span and 0.622m of chord, driven by 4 servo-actuators; a maximum rotation of +/- 5.5deg was demonstrated.
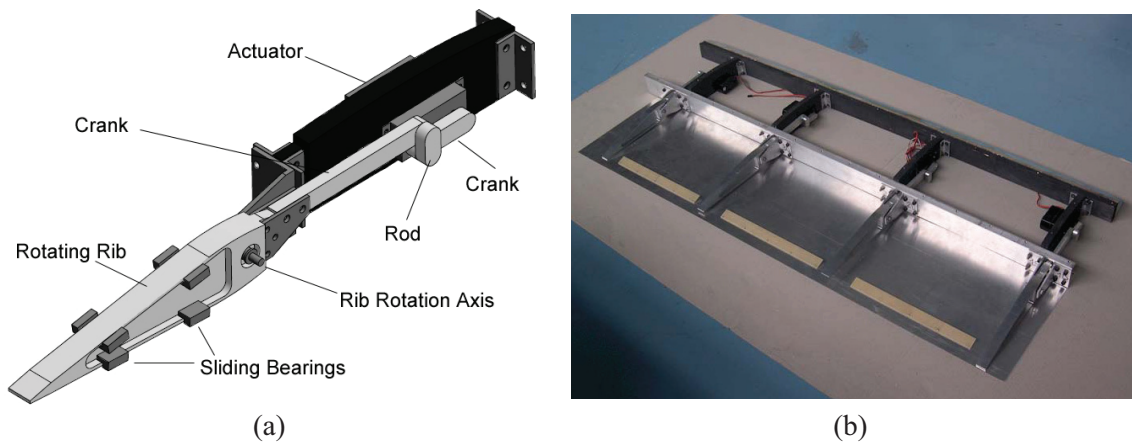
Figure 22: Rotating rib concept: (a) rib details and (b) proof-of-concept wing section. [28]

<u>Perera & Guo</u> [29] of Cranfield University investigated the optimal design of a Seamless Aeroelastic Wing (SAW) structure for a light weight aircraft. Attention was firstly paid to a design concept of a hinge-less flexible trailing edge control surface and

its eccentuator actuation mechanism (Figure 23). By creating an innovative sliding trailing edge and improving an existing curved torque beam design, the SAW camber can be varied in a desirable shape with minimum control power demand (an open trailing edge has been considered for this purpose). This design concept has been simulated numerically and demonstrated by a test model (based on a NACA 0015 airfoil section of 200 mm chordwise and 100 mm spanwise). Since the wing loading is relatively small for a small scale aircraft, strength and flutter are not the major design constraints for weight saving. Due to a large sweptback angle, significant bending-torsion coupling makes the bending stiffness play a very important role in the aeroelastic stability. As a result, the control efficiency becomes a main concern in the wing design. The subsequent effort has been therefore made to optimise the wing structure configuration and aeroelastic tailoring. The results showed that an initial base line example structural weight can be reduced by approximately 30% under the strength criteria. The resulting reduction of the wing box stiffness and aeroelastic stability have been improved by applying aeroelastic tailoring.
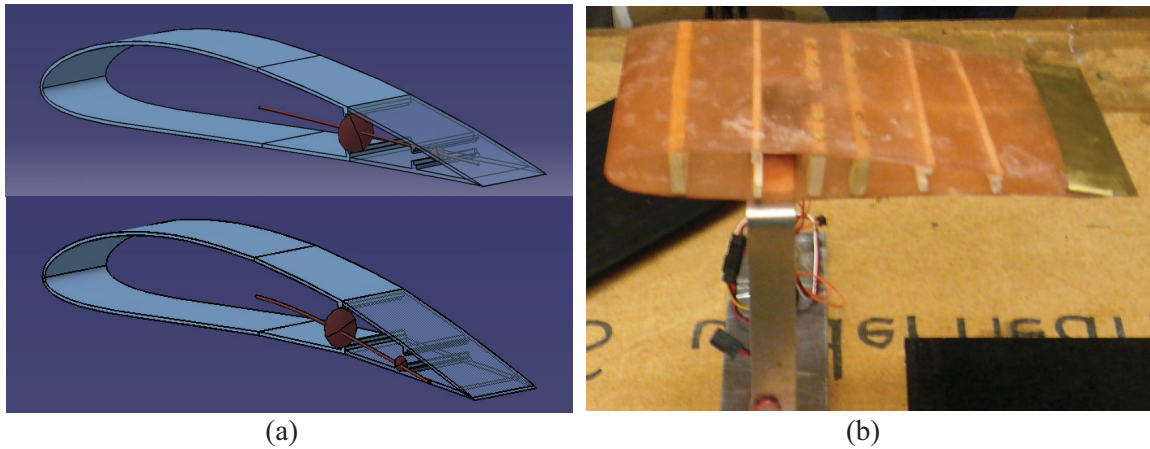
Figure 23: SAW structure: (a) schematic of curved beam disk actuation mechanism and (b) experimental prototype. [29]

In recent years, the development of innovative materials allowed the adoption of new techniques for wing morphing, enabling the substitution of traditional servo or hydraulic actuation mechanisms with more integrated and lighter actuation elements made of "**SMART**" materials.

Austin & al. [30] proposed an adaptive trailing edge actuated by magneto-strictive material (Terfenol-D), which provide wing morphing through the internal structure displacement (Figure 24).
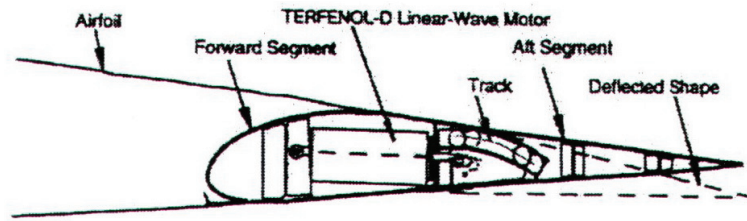
Figure 24: Trailing edge control by means of magneto-strictive materials. [30]

Geissler & al. [31], instead, adopted piezoelectric material as actuation element for a morphing leading edge (Figure 25): however, in this case the leading edge is an independent element able to rotate around an internal hinge. This technique has been conceived and adopted also for rotorcraft morphing on helicopters, due to the small size of actuators. (see next paragraphs)
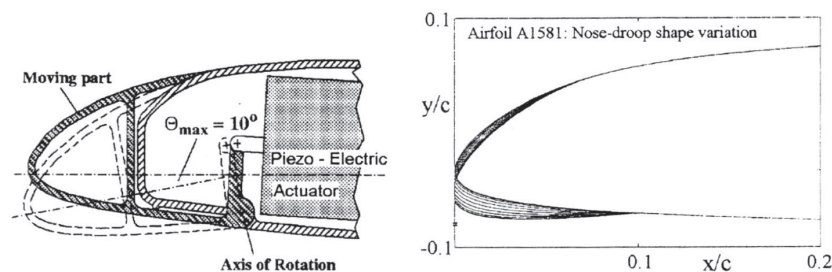
Figure 25: Trailing edge control by means of piezoelectric materials. [31]

Munday & Jacob [32] developed a wing with conformal curvature, characterized by a piezoelectric actuator internally mounted in a position so to alter the upper surface shape of the airfoil, resulting in a variation of the effective curvature: this way the airfoil thickness can be modified and the position of its maximum value changed along the airfoil (Figure 26). The piezoelectric actuator (Thunder) allows for a continuously variable movement, thus resulting in both a static and dynamic shape change control.
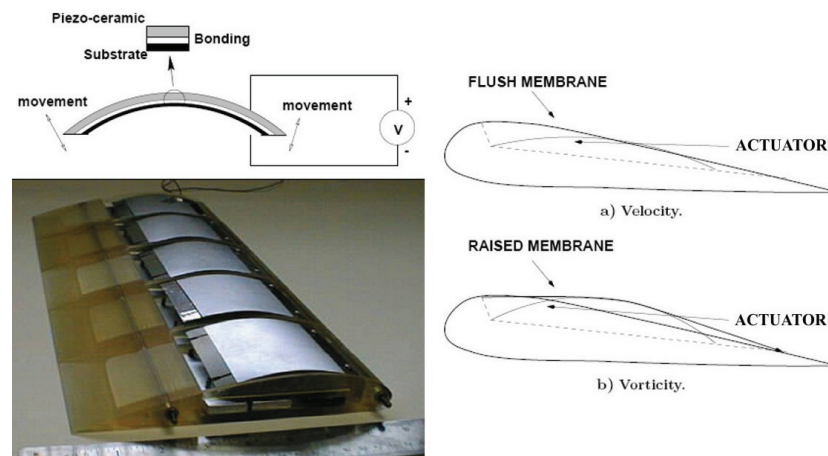
Figure 26: Curvature control with piezoelectric material. [32]

Vos & al. [33] employed post-buckled precompressed (PBP) piezoelectric bender actuators in a deformable wing structure to manipulate its camber distribution and thereby induce roll control on a subscale UAV. Bench tests showed that, with a wing chord of 145 mm and an axial compression of 70.7 gmf mm−1, deflection levels increased by more than a factor of 2 to 15.25 deg peak-to-peak, with a corner frequency of 34 Hz (an order of magnitude higher than conventional subscale servo-actuators) for under 100 mW of total power consumption (Figure 27). A 1.4 m span subscale UAV has been equipped with two PBP morphing panels at the outboard stations, each measuring 230 mm in span. Flight testing has been carried out, showing a 38% increase in roll control authority and 3.7 times greater control derivatives compared to conventional ailerons.

(a)   (b)
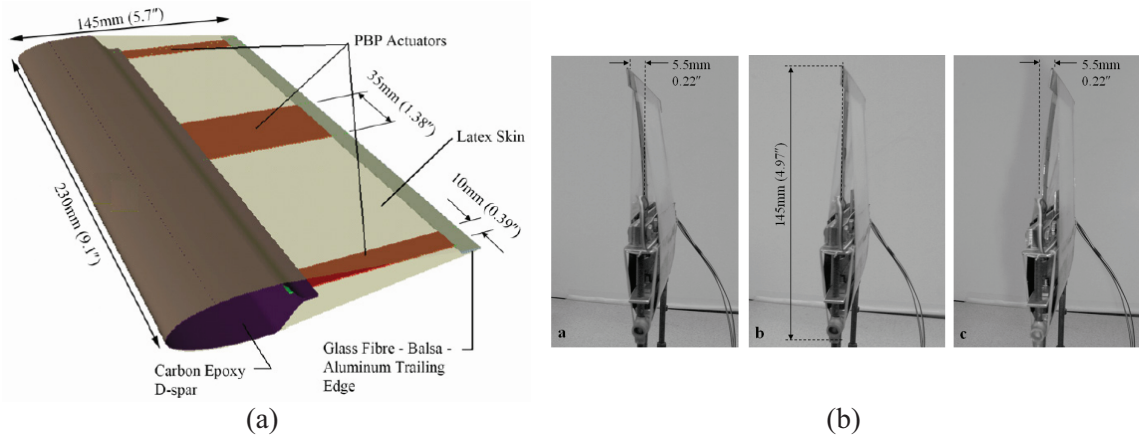
Figure 27: Morphing wing actuated by PBP: (a) schematics and (b) prototype during quasi-static bench tests. [33]

So far some examples of local wing camber change have been shown, which try to "emulate" traditional control surfaces. However, the concept itself of adaptive wing foreshadows a geometry change of the entire wing, in order to better control the aerodynamic forces and their distribution, and completely eliminate traditional control surfaces, allowing for new designs [34]. Among these, some studies rely on the entire wing twist to generate the appropriate control moments (especially in terms of rolling). However, as one could expect, these designs require a greater wing flexibility: this also explains why most researchers find interesting to work on model aircrafts.

The interest towards the study of **M.A.V.s** (Micro Aerial Vehicles) and their morphing capabilities is connected with the recent and increasing development of UAVs, which share with the former some flight conditions: as insects and birds, they fly at low Reynolds and Mach numbers (Figure 28) [35].
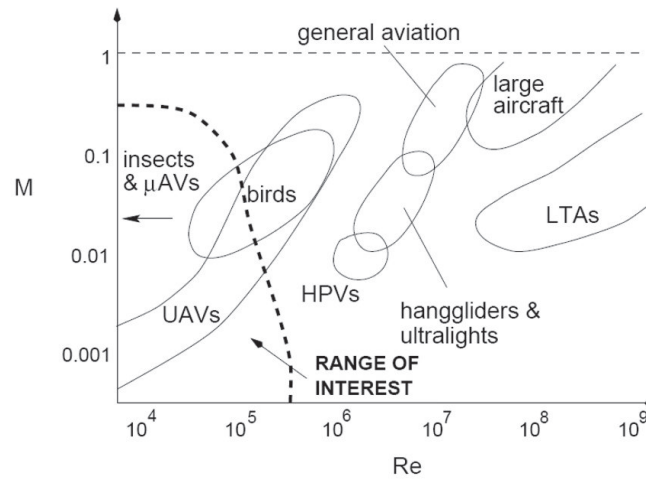
Figure 28: Typical operating regions for several aircrafts. [35]

Some researchers at University of Florida [36] have developed a fleet of MAVs, with carbon fiber fuselage and wings in thin flexible sheets (Figure 29).

The **wing twisting** is obtained by means of torsion bars (one for each wing), implemented by servos inside the fuselage. The attained rolling speed is much higher than the yaw one, indicating that almost pure roll control through wing twist is possible [37, 38]. In fact, these model aircrafts show a high agility and manoeuvrability, which makes them hard to manage remotely.
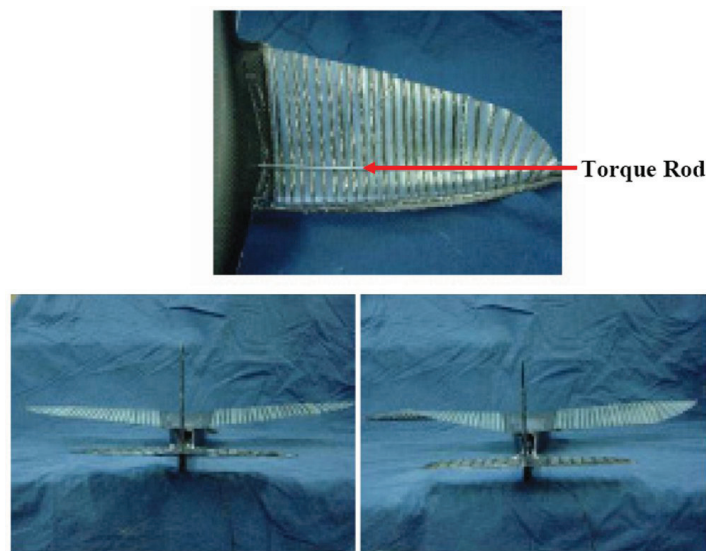
Figure 29: Micro Aerial Vehicle with twisting wings for roll control. [36]

Bilgen & al. [39] at Virginia Polytechnic Institute developed an experimental, theoretical and computational evaluation of a remotely piloted morphing wing aircraft (Figure 30) using smart materials. A type of piezo-ceramic composite actuator commonly known as Macro Fiber Composite (MFC) is used for wing morphing. The

MFC actuators have been implemented on a swept wing, 0.76 m wingspan aircraft weighing about 0.8 kg. The experimental vehicle has been flown using two MFC patches in an elevator/aileron (elevon) configuration: the flexible composite wing design provided excellent impact resistance; a 0.93 rad/s roll rate has been observed during the flight tests. The continuous surface of the MFC actuated composite wing produced lower drag and wider actuation bandwidth; moreover, it reduced the moment of inertia of the vehicle.
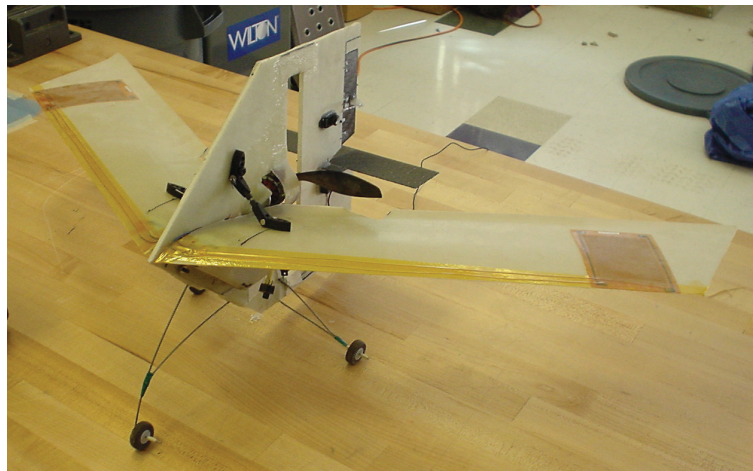
Figure 30: Fabricated micro air vehicle on ground. [39]

In a more recent work [40], the same authors focused on a bi-directional variable camber airfoil design employing MFCs. In this case, airfoil employs two active surfaces and a single four-bar (box) mechanism as the internal structure. The airfoil produces deflection in both directions from a flat camber line. Wind tunnel results showed comparable effectiveness to conventional actuation systems. MFCs demonstrated adequate control authority for aerodynamic shape control. The concept showed adequate stiffness at a tested flow speed of 15 m/s. An average lift coefficient increase of 1.67 has been observed purely due to peak-to-peak actuation voltage.

Lind & al. [41] at the University of Florida developed another radio controlled aircraft that can dramatically change the wing shape during flight, as birds do (Figure 31).

In this way, pressure gradients can be altered due to the wing shape change, or the relative position between pressure centre and gravity centre can be modified, changing the aircraft performance (stability vs. agility). In this implementation, two servo motors were involved in the wings twist to control the roll moment, while other two were implicated in the change of the wings front geometry.

(a)   (b)
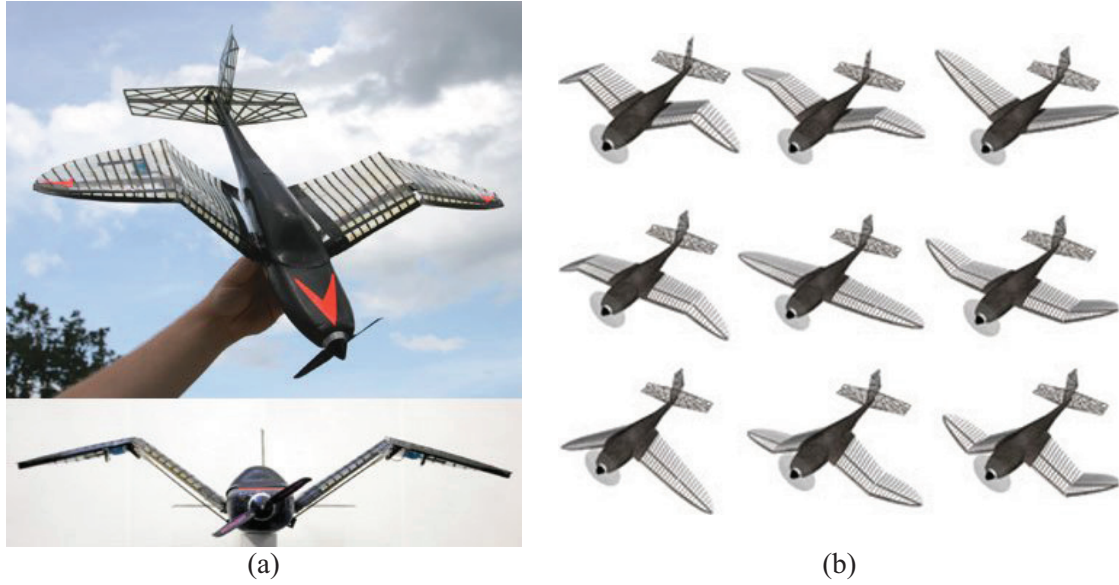
Figure 31: Variable gull-wing morphing aircraft possible configurations. [41]

Wickramasinghe & al. [42] designed a MAV with the capability to hover vertically like a rotary-wing vehicle through a flight manoeuvre known as prop-hanging. The proposed design provides the range superiority of a fixed-wing aircraft with the hover capabilities of a rotary-wing aircraft to accomplish a variety of missions. The hover manoeuvre requires roll control of the fixed-wing aircraft through differential aileron deflection to maintain its orientation. The adopted smart wing structure consists of a composite spar and ailerons that have bimorph active ribs consisting of piezo-ceramic fiber actuators with interdigitated electrodes (Figure 32). Actuation is enhanced by preloading the piezo-ceramic fiber actuators with a compressive axial load. The preload is exerted on the actuators through a passive latex or Electro Active Polymer (EAP) skin that wraps around the airfoil.
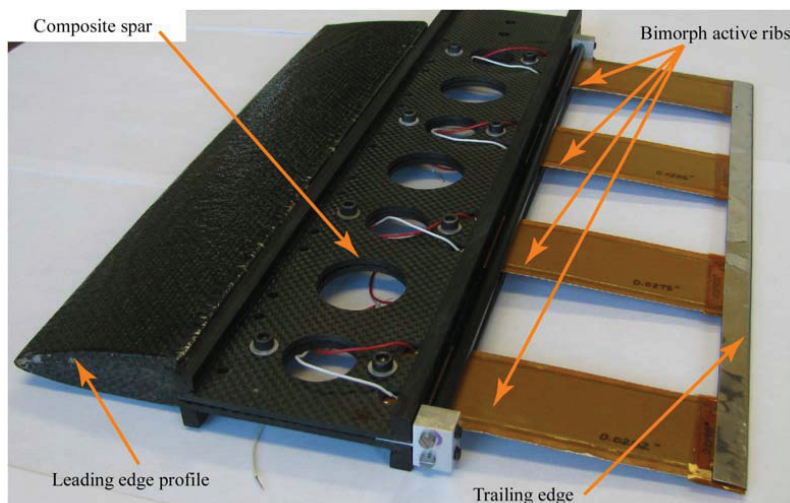
Figure 32: Smart wing hardware model with active ribs. [42]

An EAP skin would further enhance the actuation by providing a electrostatic effect of the dielectric polymer. The experimental results validated the analytical and FEM models used to analyze the performance of the smart wing design for MAV applications. The maximum deflection of 9.4 deg measured for 1500 Vpp at 1 Hz showed good agreement with analytical results. Application of axial compressive preload through 4 rubber bands has increased the deflection to 11.7 deg.

NASA Langley also pursued wing concepts that allowed unprecedented shape changes without surface discontinuities through internal efforts [43, 44]. An example is shown in Figure 33. In this concept, referred to as the **<u>fish bone concept</u>**, the main load-bearing component resembles the spinal cord of a fish covered with an elastomeric material to transfer pressure loads to the main structure. The trailing edge ribs can deflect up to ± 20 deg in camber and ± 25 deg span-wise. Likewise, the leading edge ribs can deflect ± 25 deg in camber and ± 20 deg span-wise. Although the configuration was built for the assessment and the demonstration of the structural concept and not for wind tunnel testing, the departure from conventional design practices is fostering new ideas for improved designs that can provide a technology pull for new smart materials and technologies.

(a)   (b)
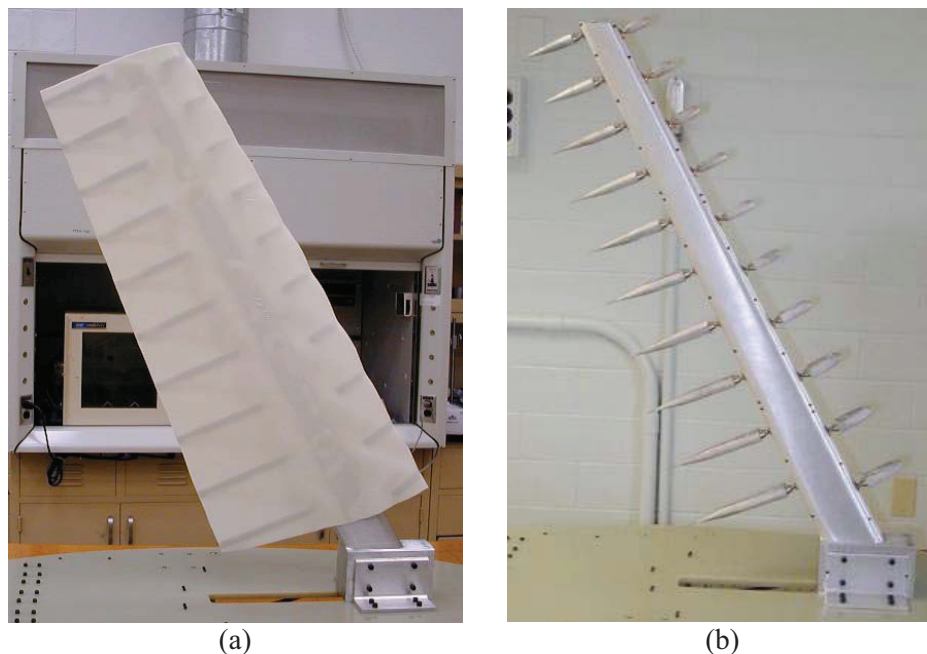
Figure 33: NASA fish bone wing concept: (a) with and (b) without skin. [44]

The idea of an **<u>Active Aero-elastic Wing</u>** (AAW) is based on the incorporation, in the existing aircrafts, of a flexible wing to make them lighter and increase the roll performance (Figure 34) [45, 46]: it can be considered a modern reinterpretation of the

control system used by the Wright brothers. By combining the movement of control surfaces on the leading and trailing edge of the wings, it is possible to change the pressure distribution on the wings surface, causing the twist: the improved performance of such wings can be attributed to the taking advantage of aero-elastic deformations.
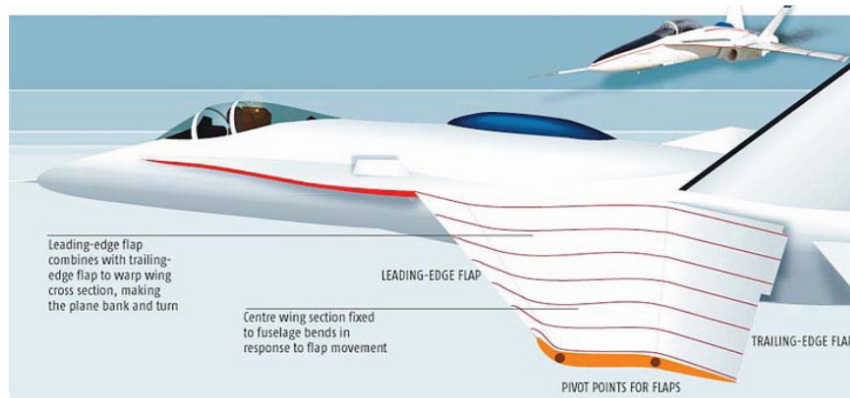
Figure 34: The Active Aero-elastic Wing (AAW) idea makes the entire wing a control surface. [45]

In November 2002, a modified F/A-18 (Figure 35) successfully flew on the north-east of the NASA Dryden Flight Research Center in Edwards, California: it was equipped with experimental wings, extremely flexible and lightweight, designed to improve the handling characteristics of high performance military aircraft.

This study, a collaboration between NASA Dryden, Boeing's Phantom Works and AFRL, showed the improvements attainable in controlling the roll moment by means of wing twisting (induced by the various aerodynamic control surfaces) on a full-scale piloted aircraft.
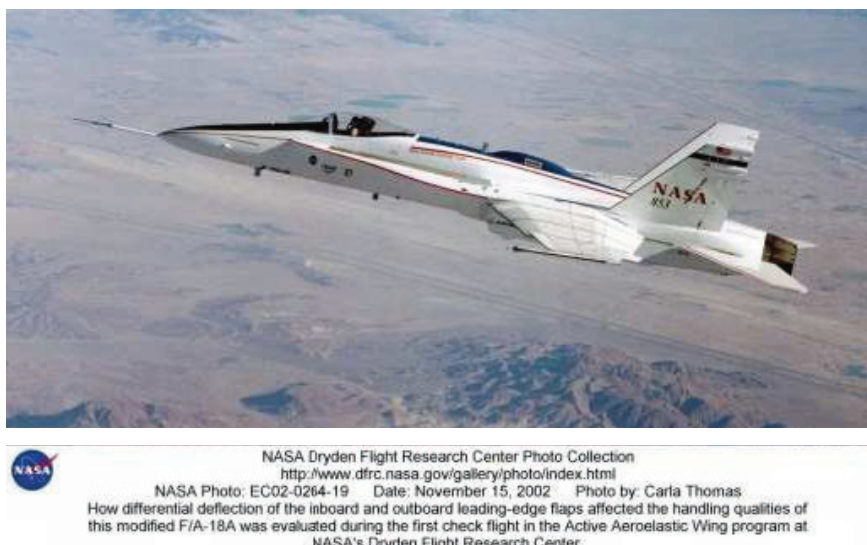
Figure 35: Modified F/A-18A for the AAW (Active Aeroelastic Wing) program promoted by NASA during an experimental flight.

With a similar focus, in 2003 the project **3AS** (Active Aero-elastic Aircraft Structures) involved a consortium of 15 European partners in the aerospace industry, partially funded by the European Community, having as objective to develop innovative structural design concepts to improve the aircraft efficiency: rather than building extremely rigid and heavy structures, that resist to aero-elastic deformations, research activities were deepened towards how to take advantage of such existing deformations.

The exploitation of aero-elastic effects allows for the use of the aerodynamic loads to produce the required deformations, thus leading to a reduction in structural weight, aerodynamic drag, etc. [47]: this requires a deep understanding of the interaction between the structure and aerodynamic loads.

One idea aimed at increased efficiency for an UAV has been proposed by **Gano & Renaud** [48], which adopts the concept of adaptive wing (Figure 36) in order to change the airfoil thickness. The concept is that, as the mission goes on and the aircraft burns fuel, it is possible to decrease the volume of the wing tanks, thus inducing a thickness reduction and thereby a drag diminution (Figure 37).
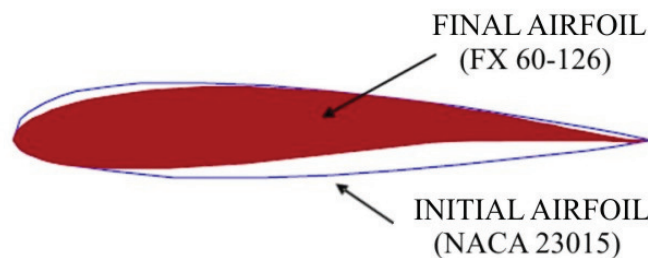
Figure 36: Concept of a variable (according to fuel consumption) thickness airfoil. [48]
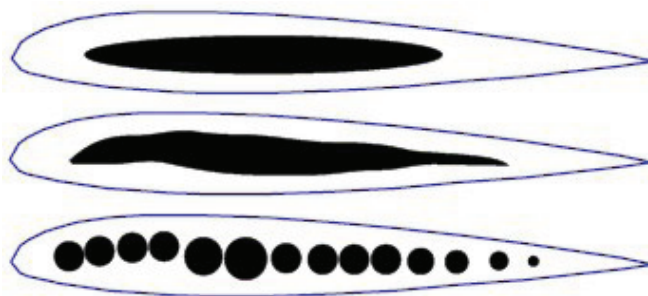
Figure 37: Several possible configurations for the fuel shells. [48]

Peel & al. [49] developed two generations of a student morphing wing project. A very simple morphing wing was fabricated in phase one: the nose was able to elastically camber down ~ 25 deg and the tail 20 deg. Actuation was provided by three pneumatic Rubber Muscle Actuators (RMA) that produce high contractive forces. The second

generation wing fabrication methodology shows smooth elastic cambering and no buckling or waviness in the skins (airfoil 20 inch in chord and a 13 inch span-wise). To eliminate lower skin buckling the front lower skin is much stiffer and slides against the rigid wing box: simple guides that slide in wing box slots are attached to the skin. The rear skin is attached rigidly to the lower wing box and slides against the tail section. The semi-rigid lower wing skin slides out beyond the tail, effectively increasing wing area, somewhat like a fowler flap. In this case, the nose cambered down 23 deg and the tail cambered down to 15 deg (Figure 38).
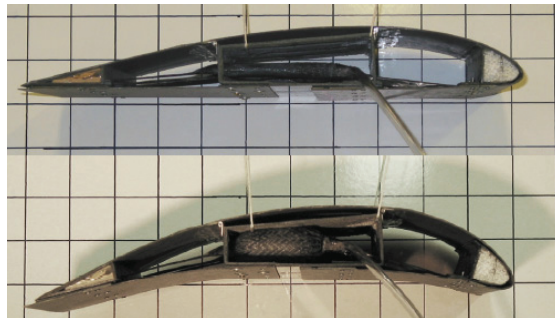
Figure 38: Second generation morphing wing actuation (on a 2 inch grid). [49]

Recent studies on variable airfoil camber have been carried out also by **<u>Flexsys Inc.</u>** [50], focusing especially on aerodynamic smoothness of the developed morphing solutions (Figure 39 and Figure 40). FlexSys has developed the world's first functional, seamless, hinge-free wing whose trailing and/or leading edges morph on demand to adapt to different flight conditions. With Air Force funding, FlexSys has built working prototypes, and demonstrated their performance in wind tunnels. A fully instrumented model was flight tested in 2006. This ground-breaking shape-morphing technology has proven to be lightweight, power efficient, and durable.

(a) (b) (c)
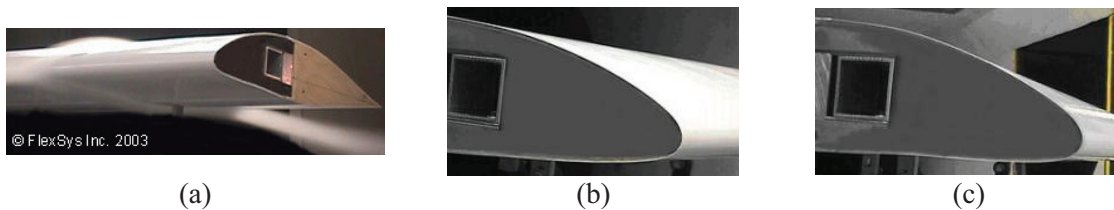
Figure 39: Flexsys morphing leading edge: (a) scheme, (b) undeformed and (c) deformed. [50]

(a) (b) (c)
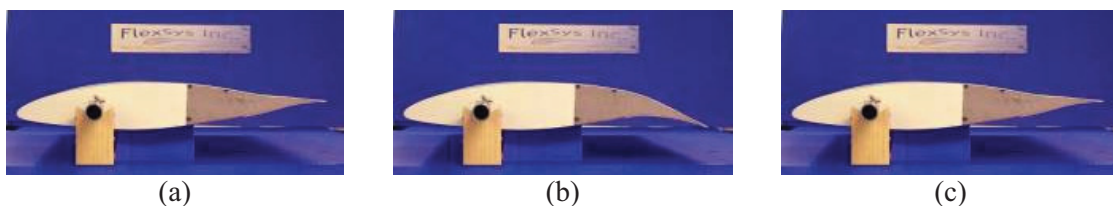
Figure 40: Flexsys morphing trailing edge: (a) scheme, (b) +10 deg and (c) –10 deg actuation. [50]

Wildschek & al. [51] from EADS proposed an all-composite morphing trailing edge design for flying wing aircraft control. An adaptive wing demonstrator with an all-electric actuation system is investigated (Figure 41). This multi-functional morphing trailing edge is shown to provide full control authority, such as roll, pitch, yaw, and load control, high lift, and airbrake function at the same time (Figure 42). The advantage compared to conventional control surfaces thereby is, that the flap function for roll and pitch, the crocodile flap function for yaw and airbrake, as well as the spoiler function for gust and maneuver load control, and high lift are provided by one control device, since all modes can be combined arbitrarily. The morphing structure is pre-designed with simplified assumptions on the aerodynamic forces for the 2.5g load case (regarding static strength), as well as for the 1g cruise (regarding sufficient stiffness). Moreover, the required actuator force against vertical trailing edge displacement/equivalent deflection angle respectively is computed for a subsequent design of the electric actuation system. With the proposed morphing trailing edge device a maximum deflection angle of over 35 deg is achievable.
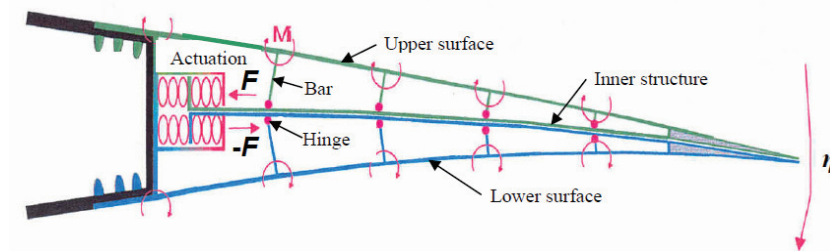
Figure 41: The morphing trailing edge concept developed at EADS. [51]
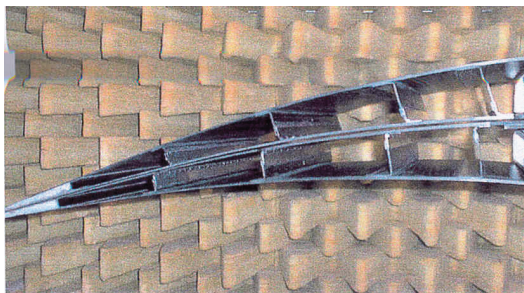
Flap mode for pitch and roll control.
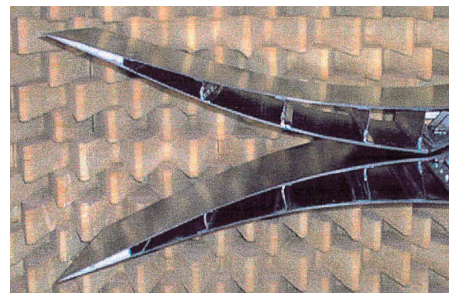
Crocodile flap mode for yaw control and air brake.
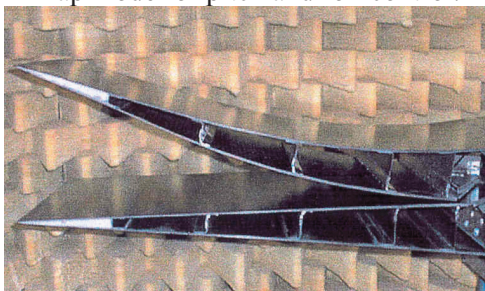
Spoiler mode for gust load alleviation.
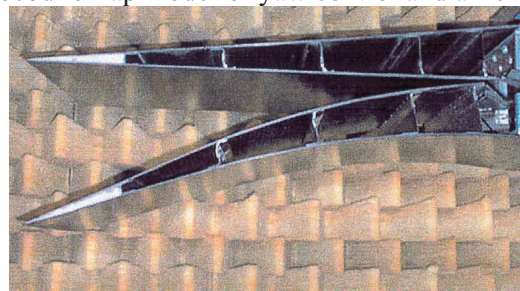
High lift mode, i.e. widening of the trailing edge

Figure 42: Deflection modes of the proposed morphing trailing edge device developed at EADS. [51]

A research study focused, instead, on the leading edge morphing has been carried out by **Monner & al.** [52] based on a collaboration between DLR and EADS within the SmartLED project. A concept of a smart leading edge device has been developed (Figure 43), which, due to systems solutions, delivers an alternative to the droop nose device as used for the A380: it has been developed starting from the Dornier Patent DE 2907912 and introducing a suitable optimization process. The main emphasis of this new device is to realize a structure/system solution for a smooth leading surface, which can be deflected into a typical high lift application: a deflection of 20 deg has been selected as target. A seamless and gapless high lift device at the wing's leading edge has the potential for reduction of airframe noise as well as for drag.

(a)   (b)
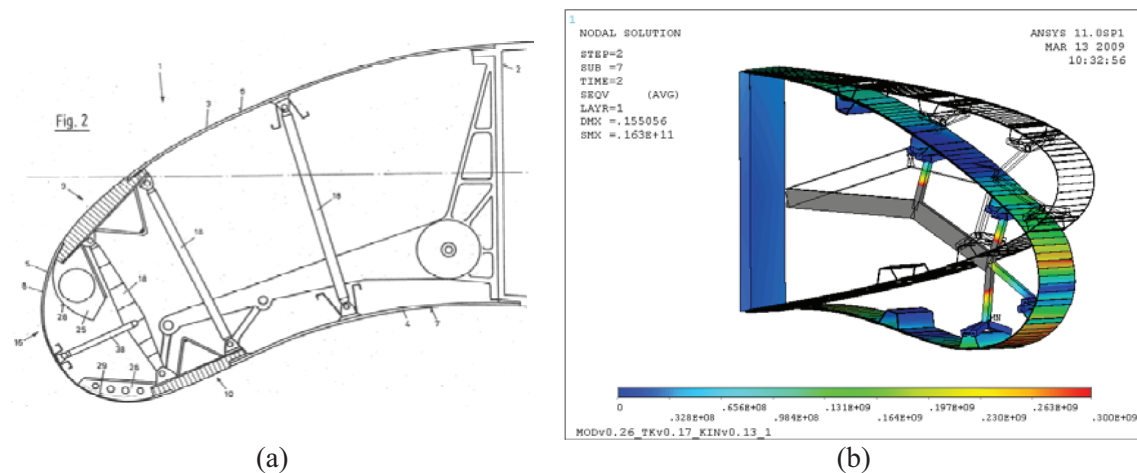
Figure 43: Seamless and gapless concept of a Smart Droop Nose: (a) Dornier Patent DE 2907912 and (b) numerical investigation. [52]

Inflatable wings

Inflatable wings represent one of the most successful implementations of morphing, allowing large changes in wing shape.

They are the ideal solution in situations when the airplane is not in use and wings need to be folded: so, although inflatable wings of different sizes are easily achievable, they acquire particular importance for UAVs, since for these aircraft reduced stowage spaces is an appreciated feature; moreover, the weight / volume ratio is particularly advantageous for inflatable wings when compared to foldable wings [53]. The main disadvantage associated with inflatable wings is the lack of actuators for roll control (ailerons): this shortage may be overcome in various ways, including using the wing twist; moreover, in almost all cases it is necessary to keep a constant pressure input to maintain the inflated shape during flight.

A survey on inflatable wing structures has been presented by **Norris & Pulliam** [54]. Although the concept of inflatable wings was born about a hundred years ago, their development only occurred in recent decades. Inflatable wings have been successfully demonstrated in 1950 by **Goodyear GA-468**, developed as a military rescue aircraft. Many other aircraft have been developed up to 1970 with the lightweight **Stingray** (the developer proposed to inflate the wings for more lift with helium) (Figure 44).

Goodyear Model GA-468 Inflatoplane   **Stingray**
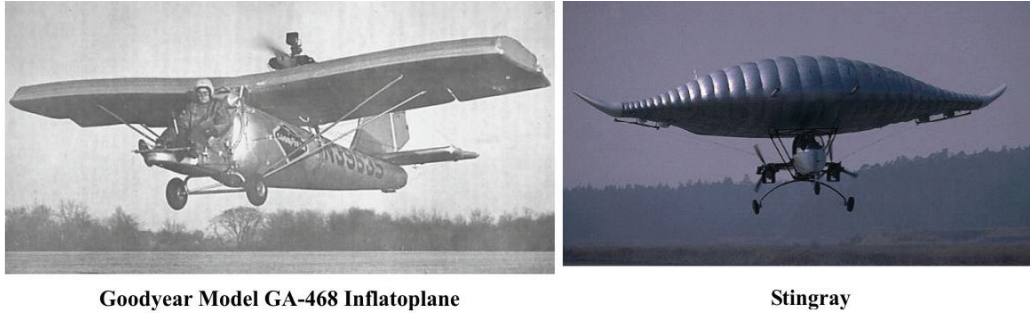
Figure 44: Examples of inflatable wings aircrafts. [53]

Starting from 1970, many UAVs were developed, as the "**Apteron**" by ILC Dover Inc., which flew successfully but was never put into production; since then many projects have been developed based on inflatable wings [55].

In 2001, researchers from NASA Dryden conducted several test flights with the U.A.V. "**I2000**" [56] (Figure 45), equipped with inflatable wings whose curvature could be changed in response to a pressure input: they were characterized by inflatable tubes surrounded by sponge which helped in defining the airfoil shape (Figure 46). Wind tunnel tests done at NASA Dryden Flight Research Center assessed that inflatable wings have a similar behaviour of solid wings with similar dimensions and geometry.
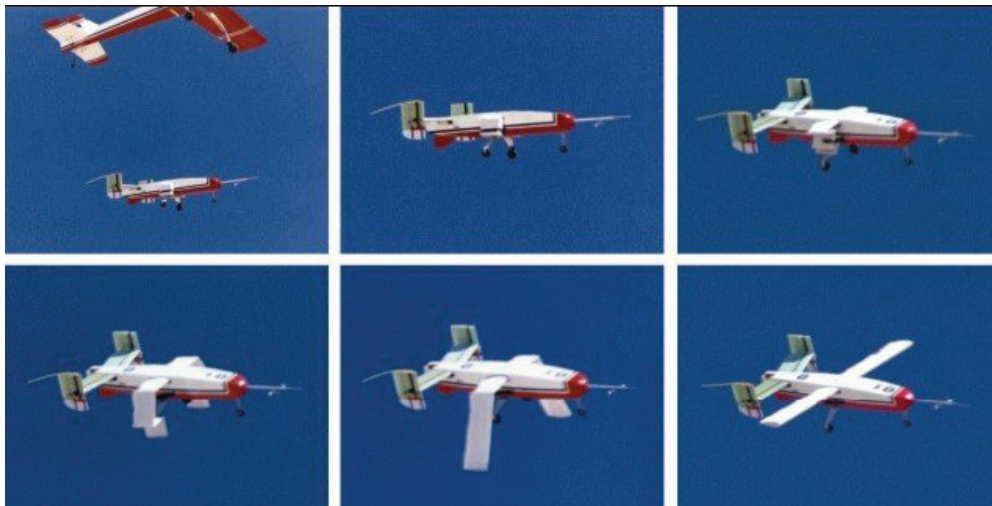
Figure 45: Sequence of the deployment in flight of I2000 inflatable wings. [56]
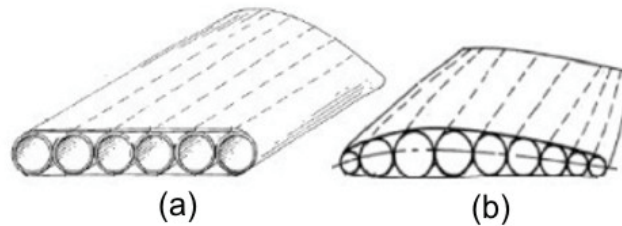
Figure 46: Wing morphing concept for inflatable wings: (a) normal inflated status and (b) differential inflated condition. [56]

This 64 inch span inflatable wing contains five high pressure inflatable cylindrical spars than run span wise from tip to tip and the chord is 7.25 inch. Between the spars and to the trailing edge of the wing is open-cell foam bonded to the spars and to a rip-stop nylon outer skin. Additionally, a rib at each tip rigidly connects all the spars to establish wing torsional stiffness. Thermally activated adhesives are used to bond the spars, foam, and the nylon skin into a contiguous wing structure. The airfoil profile is a NACA0021 and does not contain any control surfaces, therefore, full three axis control was affected only by the tail control surface. This inflatable wing consists of a manifold at the center of the wing to hold the wing spars in position. A small commercial off-the- shelf tank (COTS) with a volume of approximately 35 cubic inches was selected as the high pressure tank source. Nitrogen gas was selected as the gas source at 1800 psig and was reduced to a wing pressure between 150 psig to 300 psig using an adjustable pressure regulator. By using this high pressure inflation system, the inflatable wing can be rapidly deployed on the ground or in the flight within less than a second.

Recent studies carried out at the University of Kentucky [53] have developed two different types of inflatable wings: one at constant pressurization, which is needed to maintain the expanded wing shape, and another one capable of **stiffening after inflation**. In this second case, wings are made of a composite material that becomes rigid after exposure to ultraviolet light [57, 57] (Figure 47).
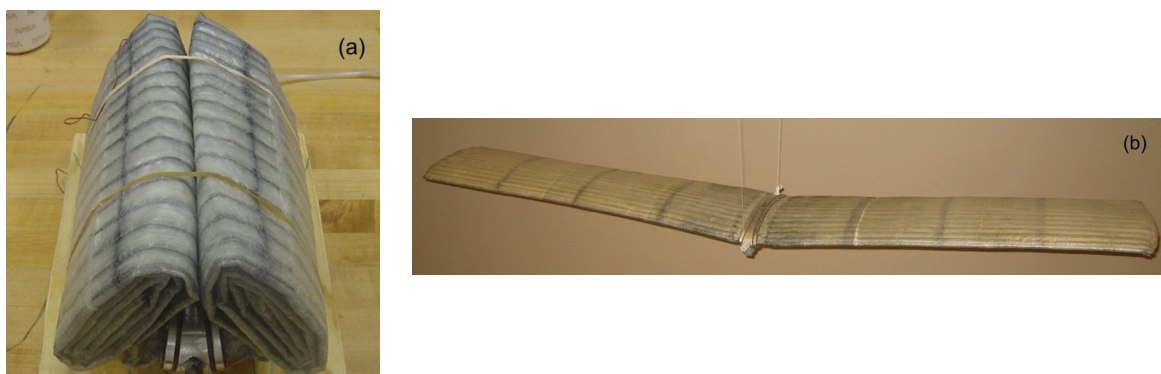
Figure 47: Inflatable wing: (a) packed condition and (b) inflated configuration (stiffened). [53]

The Mars Aircraft Realization System (**M.A.R.S.**), is the part of the program at Oklahoma State University (OSU) to develop, construct and test airplane designs for flight on planet Mars [59]. It is a component of BIG BLUE V. BIG BLUE (Baseline Inflatablewing Glider, Balloon-Launched Unmanned Experiment) is a high-altitude experiment (Figure 48) developed, designed, built, conducted and evaluated primarily by undergraduate students in the College of Engineering at the University of Kentucky (UK). The goal of BIG BLUE is to demonstrate the feasibility of inflatable wings for flight in the low-density atmosphere of planet Mars. While most designs use folding wings, MARS uses inflatable wings to overcome the packing problem in the spacecraft carrier.

Figure 48: BIG BLUE aero-model. [59]

In the high altitude flight test discussed herein, the completed and semi-autonomous aircraft ascends via weather balloon to a targeted altitude of 100,000 feet in order to simulate the density present in the Martian atmosphere. The inflatable wings are inflated to a minimum of around 5 psig and a release mechanism is triggered that allows the aircraft to parachute to an altitude of 5,000 feet above ground level, where it is flown under autonomous guidance, and then lands under human control. The inflatable wings have been manufactured by ILC Dover, Inc. out of polyurethane coated rip-stop nylon. The airfoil profile is NACA 4318, which is similar to the wing profile presented in this paper. Each wing semi-span has a root chord of 19.5 inches and a tip chord of 13.5 inches with a semi-span of 36 inches. The wings have been constructed in two semi-spans such that they could be mounted externally to a fuselage, but they did not include mounting attachments. The wings have been attached to a balsa sandwich wing mount using a light weight low temperature fiberglass tape with a silicon based adhesive. The wing mounts have been in turn connected to one another using two carbon fiber rods. Full three axis control has been affected only by the tail control surface. A small scuba air tank was selected as the pressure tank source. The fuselage has been initially constructed out of a composite using a balsa sandwich. While this design has been used for low altitude flight testing, later designs used a composite with a card stock sandwich to reduce weight and was used for the high altitude mission.

Other studies focus on inflatable wings capable of **twisting or bending**, thereby eliminating the problems of lack of roll control: in many cases the adoption of Shape Memory wires was used, upon thermal activation, to perform the wing camber change (obviously in these circumstances have not been used stiffened inflatable wings) [60, 61] (Figure 49).
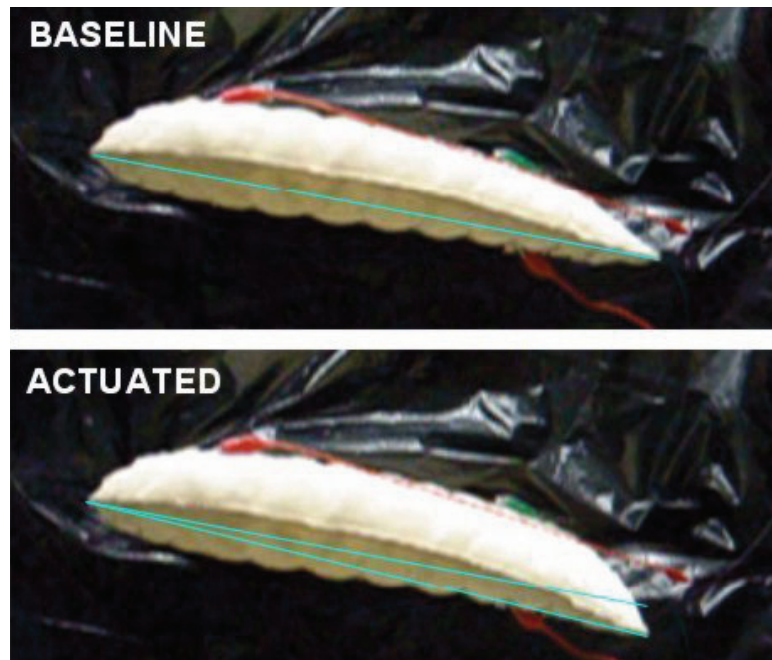
Figure 49: Inflatable wing with variable curvature actuated by SMA wires. [53]

An investigation of the feasibility of aspect ratio morphing using inflatable wings is presented also by **Kheong & Jacob** [62]. Studies have been carried out for an inflatable wing manufactured from polyurethane fabric that varies the aspect ratio of a small unmanned vehicle from approximately 3.4 to over 8.5, an 150% increase (Figure 50). Overall flight performance of an electric-powered aircraft integrated with the inflatable wing was analytically predicted. Successful flight tests have been carried out at both low aspect ratio configuration and pre-inflated flight for high aspect ratio configuration. Static deployment tests have been conducted using a light-weight/low-flow-rate inflation system. At this stage, this system was not yet ready to be fully integrated for an in-flight inflation test. However, wind tunnel deployment tests using a smaller scale inflatable wing have been conducted to investigate the deployment behaviour of slow inflation at a variety of dynamic pressures and angles of attack. The resulting deployment tests in the wind tunnel showed that the wing fully deployed in all cases. Furthermore, all deployment tests took about the same amount of time to achieve its final wing shape at the required in-flight pressure.

<div align="center">(a)   (b)</div>
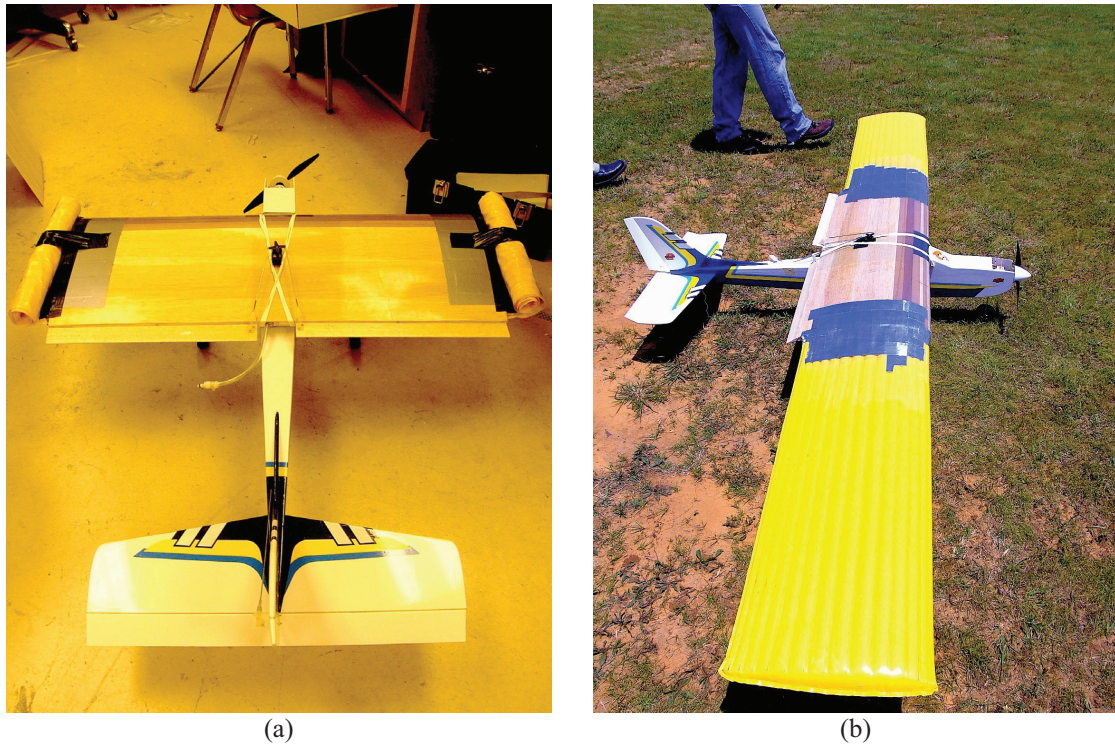
Figure 50: Test vehicle with inflatable wings: (a) low aspect ratio and (b) high aspect ratio configuration. [62]

Another work has been carried out by **Scott & al.** [63] sponsored by DARPA on the development of a novel low-stored-volume wing for high-altitude aircraft. The key innovation is the development of a hybrid design incorporating a telescoping and load-bearing spar within an inflatable wing. Primary benefits of the approach include significantly lower required inflation pressures and lower overall system weight.

The overall goal is to develop a low-stowed volume wing design with projected vehicle L/D > 27 at altitudes ranging from 60.000 to 75.000 ft.
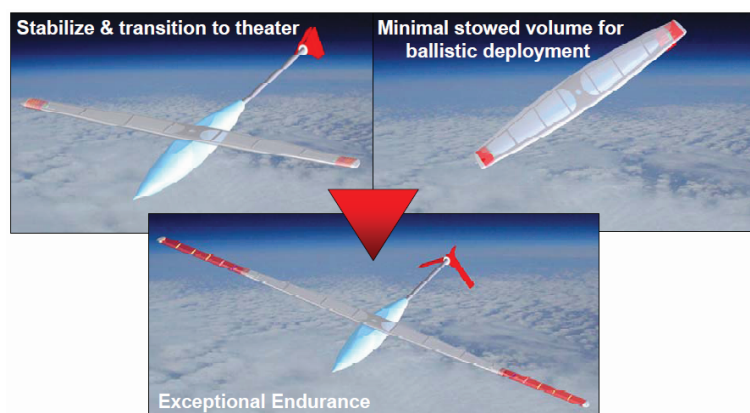
Figure 51: Stowable Unmanned Air Vehicle Engineering (SUAVE) concept of operation. [63]

As illustrated in Figure 51, the sequence from initial ballistic delivery to complete vehicle deployment is as follows: aircraft is separated from a rocket in the stowed

position either by mechanical means or a parachute; the tail deploys and the rigid wing rotates 90 degrees to provide a stable craft capable of weathering the deployment dynamics. Lastly, the span extensions deploy, giving the vehicle 4 times the span of the stowed rigid wing. The pivoting wing configuration with deployable span extensions is a low stowed volume solution that efficiently embraces the spatial constraints of the launch vehicle. Focus has been given to the design of the hybrid span extendable wing. The design of high-aspect-ratio wings is driven by the ability to sustain substantial root bending moments: to bear these bending moments with a purely inflatable wing, very high (50 to 100 psi) pressurization would be required, thus resulting in enormous requirements for the skin fabric and the vehicle's regulatory systems. The hybrid approach utilizes "ribfoils" and tension wires to support the skin, thereby reducing the chamber pressure to the minimum required for maintaining the airfoil profile. The telospar serves as the primary load path in addition to deploying the wing section (Figure 52).
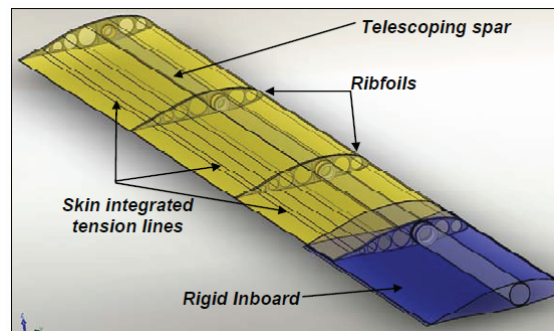
Figure 52: Hybrid span extension schematics. [63]

The telospar (hybrid structural actuator) concept proven viable in a series of deployment tests, in ambient and vacuum conditions. System level studies concluded that this deployed span design would reduce pressurization requirements by almost an order of magnitude, reducing wing weight by 25-35% (as compared to a purely inflatable Vectran baffled wing).

Another similar study on HALE (High Altitude Long Endurance) aircrafts with hybrid inflatable-rigidizable wings has been developed by **Haight & al.** [64], adopting Ultraviolet (UV) light rigidizable inflatable wings activated by means of internal LED light sources (Figure 53).

As compared to current purely inflatable wing designs, there are many benefits of an inflatable-rigidizable wing that lend to its use in long-duration high-AR wing systems, including no make-up gas, lower aeroelasticity, and higher stiffness. The latter two

characteristics allow the wings to have lower deflection and higher L/D (i.e., thinner or higher AR wings that withstand the loading conditions can be built). Higher wing L/D ultimately leads to lower fuel consumption and longer endurance UAVs. However, there are some distinct disadvantages, including higher system complexity than purely inflatable systems (UV light source) and inflatable/rigidizable wings are heavier than purely inflatable systems. Also, upon deployment, the inflatable-rigidizable systems will most likely require a parachute descent while the material deploys and cures so that there are no distortions from aero loading in the wings during the rigidization period. This leads to the "snap cure" requirement for the UV resin system.
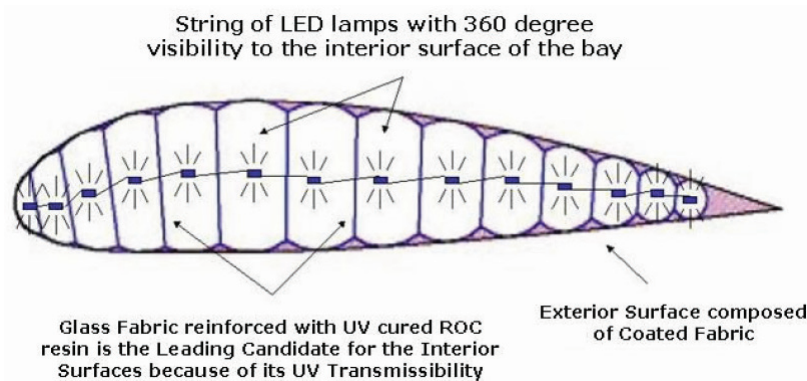
Figure 53: Cross section of inflatable wing concept with internal baffling scheme and internal LED light sources for UV rigidization of resins. [64]

Endurance requirement of only 7-15 hours for the requested application led to the consideration that completely rigidizing the wings may not provide enough benefit (in terms of make-up gas) to justify using them. So, a hybrid inflatable/rigidizable wing system has been selected and is based on the idea that only certain areas of the inflatable wing structure should be rigidized to minimize weight and maximize stiffness. The hybrid concept has similar advantages and disadvantages as the inflatable-rigidizable system; however, it is a lower weight option and retains a larger degree of damage tolerance from wind gusting due to the compliance of the inflatable portion. The hybrid wing concept involves the inclusion of rigidizable composite reinforcement panels strategically within the wing spar construction (Figure 54).

The manufacturing design involved placement of UV rigidizing prepregs in some spars and flex circuit mounted UV LEDs (also designed by ATI) in adjacent spars to provide the light required to rigidize the system. The halfspan prototype, as designed, with LEDs mounted every 6.35 cm (2.5 in.) on the flex circuits, could be operated using standard aircraft voltage at a total system weight of 1.05 kg. A weight reduction of

approximately 45% could be immediately realized by switching to lighter weight, higher power LEDs, thereby allowing the use of LEDs spaced at 5 in.
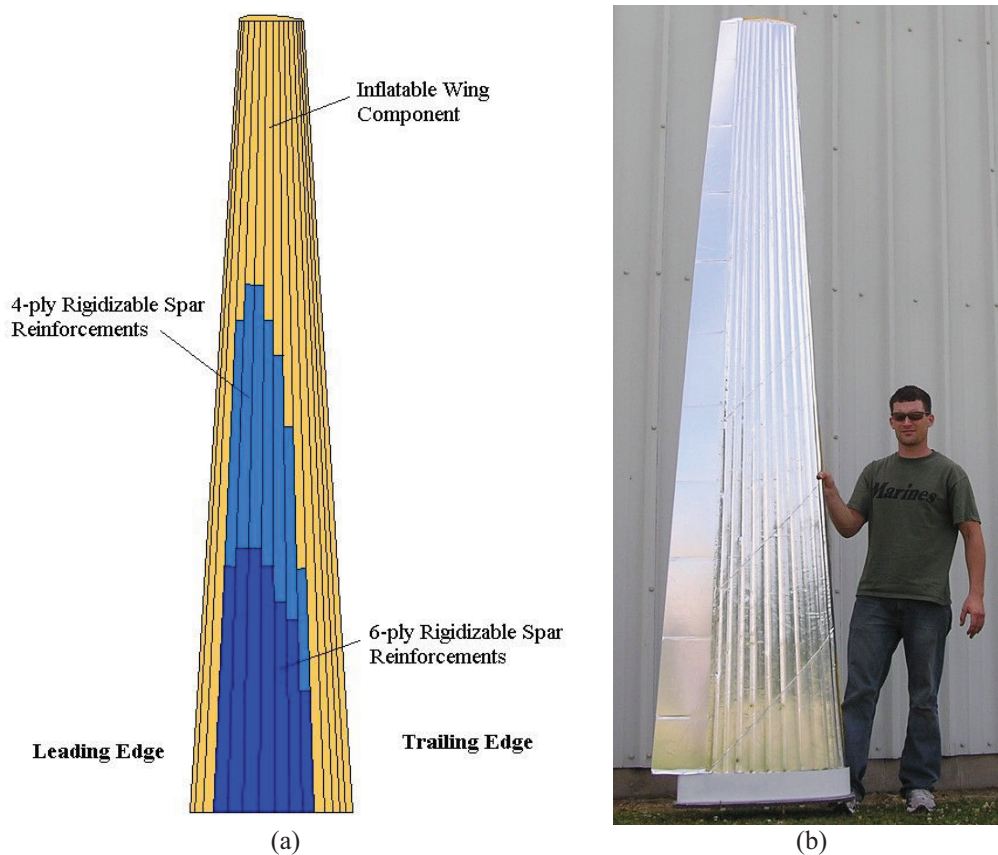
Figure 54: Hybrid Inflatable Wing Prototype: (a) composite panel distribution and (b) completed wing.

[64]

Wing span change

Airplanes able to vary the wing span may have good aerodynamic efficiency over a wide speed range because of the wing are change. Typical examples are military aircraft with variable geometry wings (where variable geometry, f.i., only means the change of the sweep angle of the leading edge with the airflow), as the "Tornado" or the F-14 "Tomcat".

Today there are several ongoing studies on the wing span change, focused especially on telescopic wings, that is aircrafts equipped with wings made of several section, each extensible or retractable according to the performance requirement. So, it is possible to have great wing surfaces when flying at low speed, to reduce fuel consumption, or high manoeuvrability at high speeds, closing the wings.

Proposals for telescopic wings can be found already in the early 40s. However, there is not much evidence of devices ever built. Recently, in 1997, the **Gevers Aircraft Inc**.

company designed a telescopic wing, capable of variable span, for use on a six-seat amphibious aircraft (Figure 55) [65]: when "closed", the wings allow for high cruise speeds, while they guarantee higher performance at lower speeds and fully expanded.
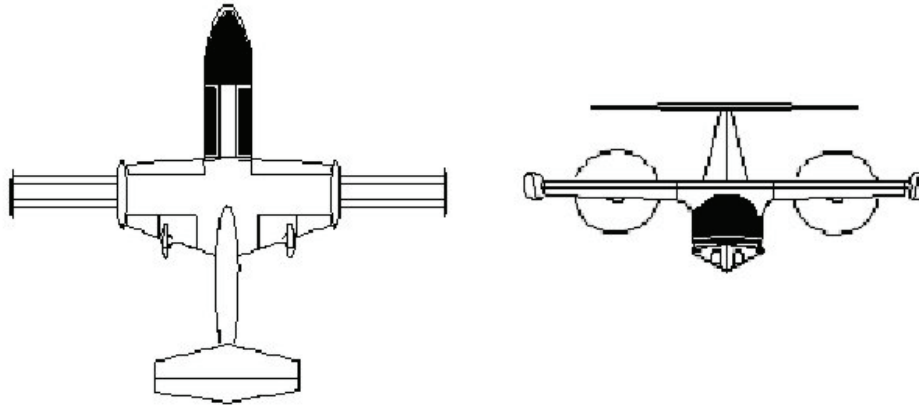
Figure 55: Gevers concept for an aircraft with a variable span wing. [65]

In 1990, the Naval Research Laboratory built and tested an experimental non-recoverable ship-launched expendable radar decoy named **F.L.Y.R.T.** (Flying Radar Target) [66], as shown in Figure 56. The first test flight occurred in September 1993. Flyrt was launched with rigid folded wings and tail surfaces from a MK 36 launcher by using a solid-propellant rocket motor, which burned for about 1.6 seconds. The fully expanded rigid wing has a span of 2.4 meters and weight of 60kg. Immediately after launch, the tail fins were unfolded mechanically to control the vehicle during ascent. After the booster had been jettisoned, the UAV coasted to the apogee of the launch trajectory, where the rigid wings were unfolded and the electric motor started. A total of 13 drones were built before the program ended, and the decoy successfully demonstrated the defense of a variety of ships against simulated radar threats.
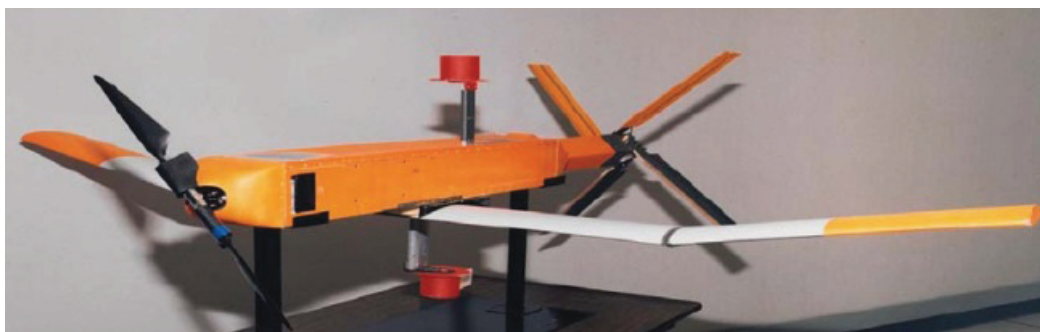
Figure 56: Flying Radar Target UAV. [66]

The same concept applies to the **U.M.A.A.V.** (Morphing Unmanned Aerial Attack Vehicle) developed by AeroVisions Inc. [67] within the "Morphing Aircraft Structures"

program organized by DARPA. The wing span is inversely proportional to the cruise speed, and allows for several operating conditions: from loitering to fast cruise to high speed attack. Figure 57 shows the different configurations for the radio controlled demonstrator.
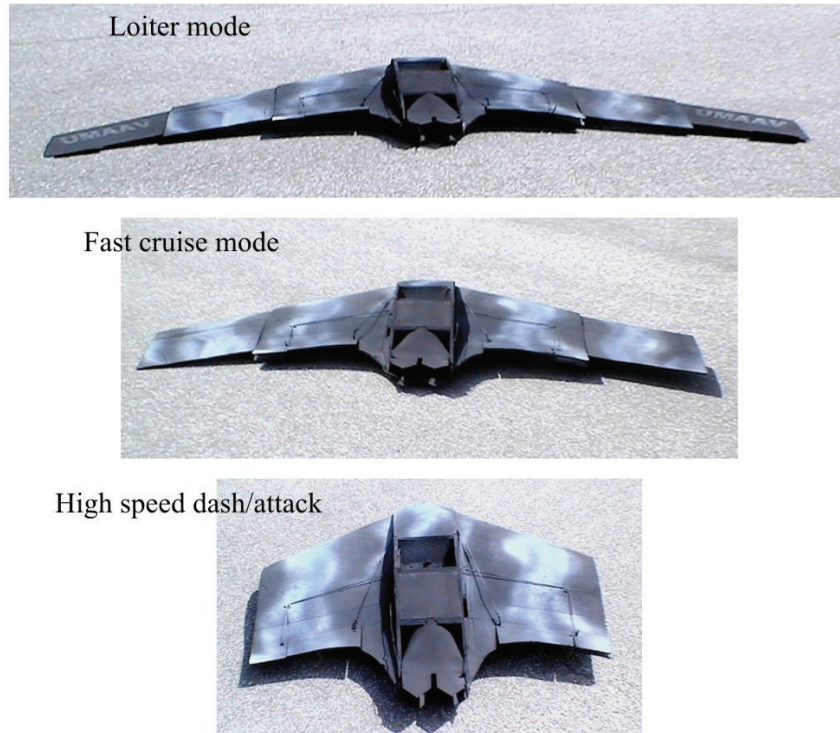
Figure 57: AeroVisions UMAAV with variable span wing. [67]

A similar concept based on telescopic wings has been carried out by **Leite & al.** [68]. The morphing wing consists of a variable span wing which allows airfoil shape change of all wing sections simultaneously between two different airfoils. The telescopic wing can continuously change the wing span as it has an inner wing that slides in and out of the outer wing (Figure 58). The wing can also change the airfoil shape independently of the span variation: it is assumed that it can only change between two different and specific airfoils (Eppler 434 and NACA 0012).
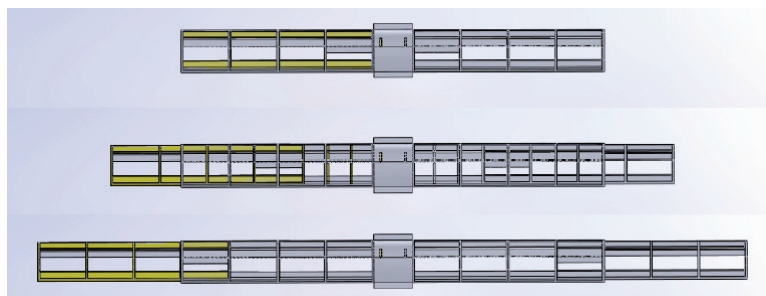
Figure 58: Span increase mechanism for an UAV. [68]

The structural solution adopted to achieve the morphing capability consists of a hollow outer wing which supports loadings having leading and trailing edge composite carbon fibre reinforcement as well as composite carbon fibre reinforcements evenly spaced along the span to substitute conventional ribs. The inner wing is a normal wing with fixed ribs and a fixed spar.

The University of Maryland [69] is developing a small scale morphing aspect ratio wing, as shown in Figure 59, using an inflatable telescopic spar that may be possible to develop a UAV with variable aspect ratio wings. The telescopic wing consists of three concentric circular aluminum tubes of decreasing diameter and increasing length that deploy under pressure to produce various wingspan configurations. This wing could extend or retract its span from 7 inches to 15 inches. However, such a wing has only been tested in wind tunnels at a range of Reynolds numbers and not yet fully designed for actual flight testing due to the complexity of the telescoping mechanism.
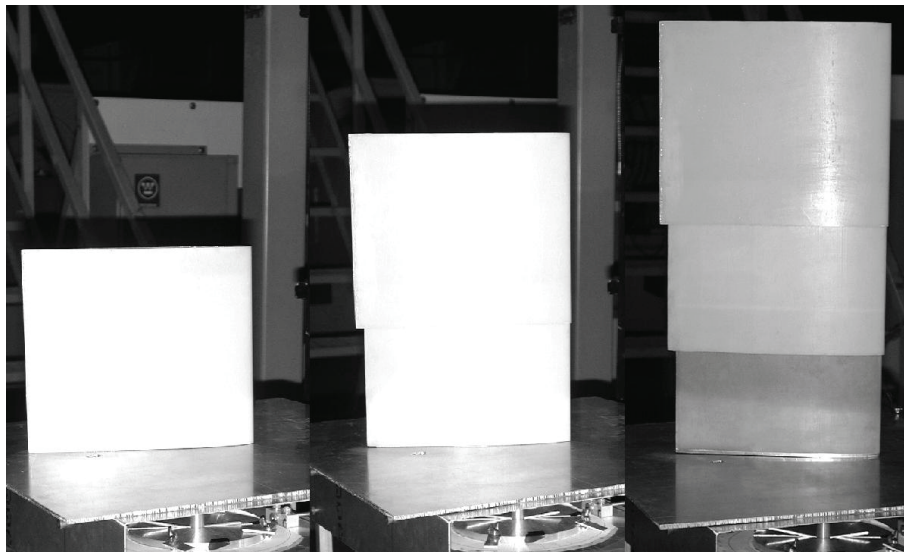
Figure 59: Morphing wing using inflatable telescopic spar. [69]

An alternative design for variable sweep wings has been investigated by **<u>Mattioni & al.</u>** [70]. It consists of a two-spar, CFRP (carbon fibres reinforced plastics) wing, with truss-like ribs. The spar-web is a shell structure laminated using an unsymmetric stack sequence in order to take advantage of the residual stress field developed during the curing process, resulting in increased transverse curvature of the spar. The effect of this curvature is twofold: to increase the moment of inertia to withstand bending stresses and, under certain loading conditions, to behave like an elastic hinge to allow the sweep angle of the wing to change (Figure 60). The experimental model achieved successfully both backward and forward sweep angles (Figure 61).
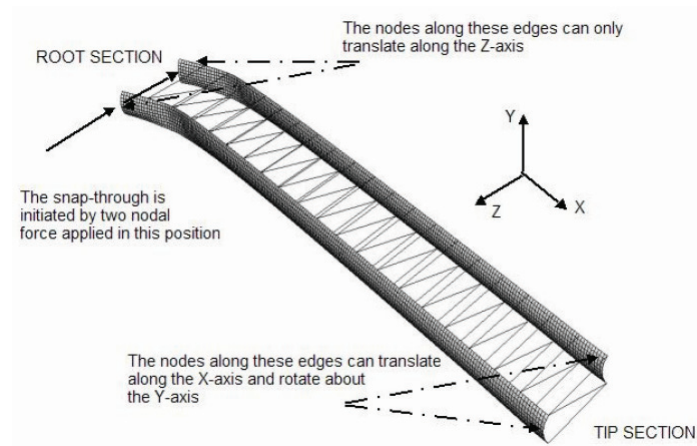
Figure 60: Wing box structure schematics. [70]

| (a) | (b) | (c) |
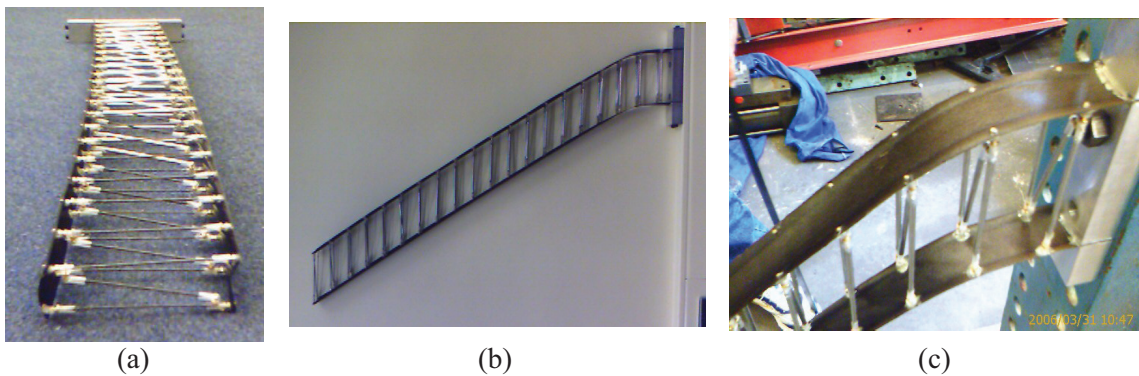
Figure 61: Experimental truss-rib: (a) prototype, (b) swept configuration and (c) snap area detail. [70]

A.L.I.C.E. (Air Launched Integrated Counter-measure, Expendable) [71] is an unmanned platform developed by AFRL Vehicle Research Section that can be air launched from a tactical aircraft at speeds up to 0.8 Mach and altitudes up to 45,000 ft. The design is shown in Figure 62. After launched from the tactical aircraft, ALICE glides using tail control surfaces until it reaches a speed of approximately 250 knots.

Figure 62: AFRL – ALICE concept. [71]

The rigid wing and propeller then deploy and the heavy fuel engine starts. ALICE will cruise approximately 200 nautical miles in one hour before the outer rigid wing panels deploy for loiter. In the loiter mode, it will operate at 65 knots with a two hour

endurance and carry a 25 lb payload. Research efforts included development of the polymorphic wing, a JP-8 fueled rotary engine, a high efficiency starter/generator, a folding variable pitch propeller, and an advanced EW payload.

Neal III & al. [72] at the Virginia Polytechnic Institute studied the design and development of the MORPHEUS wind tunnel model (Figure 63), within the adaptive planform vehicle experiment (APVE), that combines large and small wing shape variations for fundamental research in modelling and control of morphing air vehicles. MORPHEUS is capable of planform morphing for mission adaptation, and control morphing for vehicle manoeuvring. Planform variations include major changes in wingspan, sweep, and tail configuration such that the aspect ratio, planform area, and static margin are significantly modified. Control morphing refers to smaller motions that alter lesser portions of the flow-field to manoeuvre without significantly affecting the aircraft dynamics. For MORPHEUS this consists of independent wing twist, which replaces elevons on conventional vehicles.

| (a) | (b) | (c) |
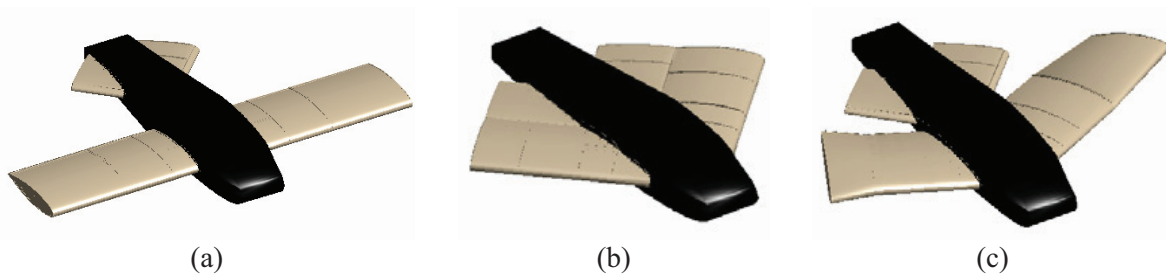
Figure 63: MORPHEUS concept: (a) loiter, (b) dash and (c) asymmetric manoeuvring configurations. [72]

In this same area (span morphing) can be inserted the **A.M.P.** (Aircraft Morphing Program) of NASA and the **M.A.S**. (Morphing Aircraft Structures) program of DARPA that have been engaged in a large-scale cooperation for the development of an airplane with an adaptive wing [9, 73].

The research program at DARPA aims to achieve an airplane wing that can drastically change its shape, so as to meet, within the same mission, the conflicting requirements of loitering at low speeds on a particular area and a high manoeuvrability at transonic speeds: an UAV having similar characteristics would present a great adaptability to many different missions and be able to perform multiple functions. Such an aircraft would have the advantages of several different platforms: those of a fighter plane, fast and with high manoeuvrability at high speed (but low aerodynamic efficiency), combined with those typical of a surveillance aircraft, aerodynamically efficient but not

particularly fast and manoeuvrable; in addition, one could decide when to prefer one or the other characteristics [74]. This brings immediate benefits in those missions where different skills are generally required, and thus involve multiple aircraft: a similar aircraft would be able to carry out the mission alone, with a great reduction of costs and resources involved. DARPA is currently developing two parallel projects.

The Lockheed Martin project called "**Agile Hunter**" (Figure 64) [43, 75] involves the design and implementation of an UAV with the ability to fold the inner sections of the wing (also called Z-wing) near the fuselage, so as to hide part of the area and reduce drag during the transonic flight at low altitude: in fact, the wing folds into two parts that rotate in the opposite way during the deployment or withdrawal (Figure 65).

Figure 64: Lockheed Martin "Agile Hunter" prototype. [74]
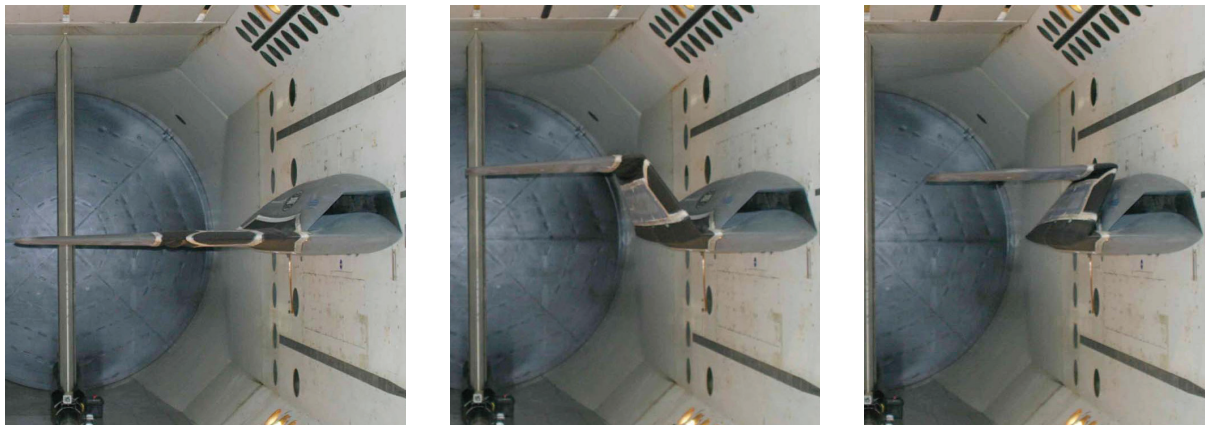
Figure 65: Lockheed Martin prototype wing deployment during wind tunnel tests. [43]

Benefits of such a design are summarized in Figure 66; data measured in wind tunnel tests is showed in Figure 67. In particular, at Mach 0.6 a morphing capability from 0 to 130 deg is demonstrated over 65 second period (with a controllable, reliable and precise actuation), with angle of attack (AoA) adjusted to maintain lift and inboard motor torque near zero [76, 77]. The Z-Wing program has been stopped after the company experienced several problems during the initial flight testing.
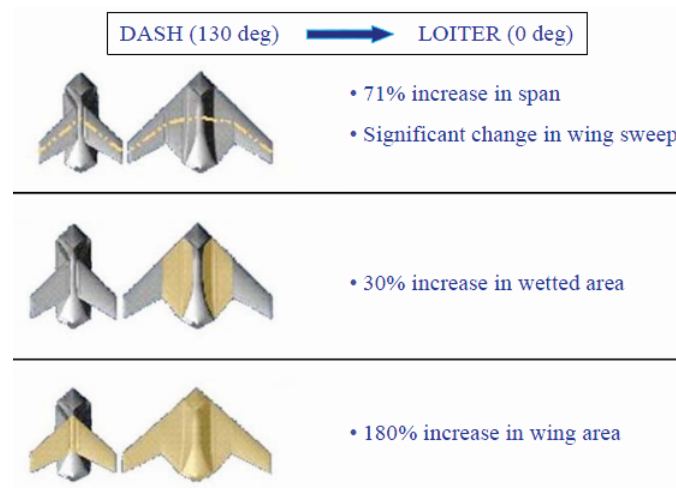
Figure 66: Key mission performance drivers for the morphing vehicle. [75]
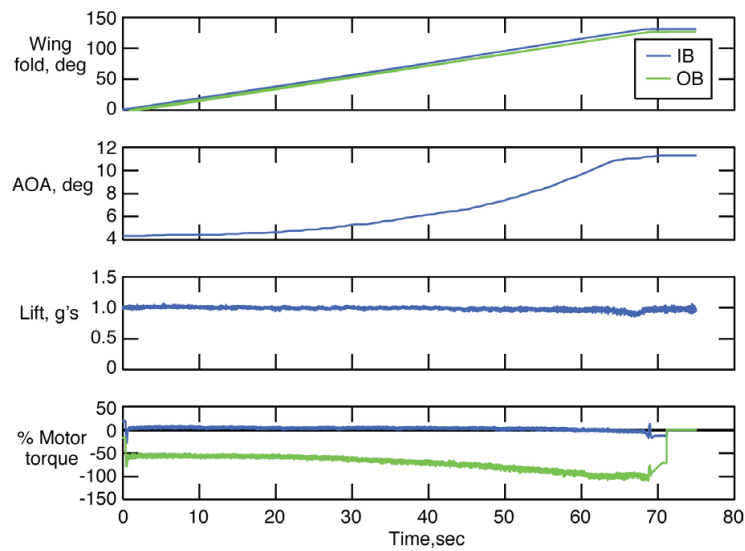
Figure 67: Lockheed Martin prototype wind tunnel measurements. [77]

Hinges around which revolve the two wing portions are covered with silicone-based materials, to ensure a continuous and aerodynamically smooth surface (Figure 68).
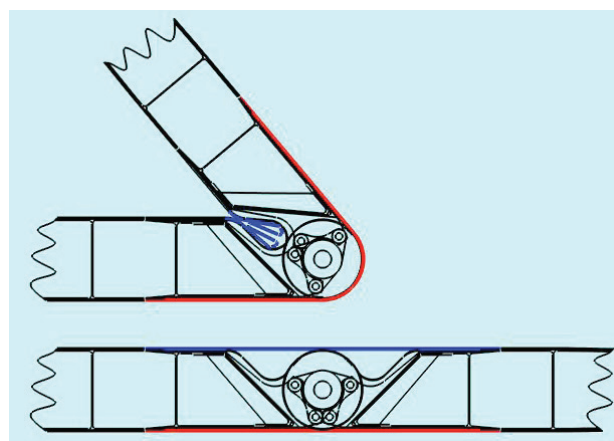
Figure 68: Lockheed Martin prototype: hinge details. [78]

However, studies are already underway for the adoption of a Shape Memory Polymer, namely Veritex (Figure 69), a composite based on Veriflex produced by CRG Inc.) [79]: when heated, these materials become elastic allowing for the rotation around the hinges; when cooled, they stiffen; finally, they "remember" their original shape when reheated again [80].
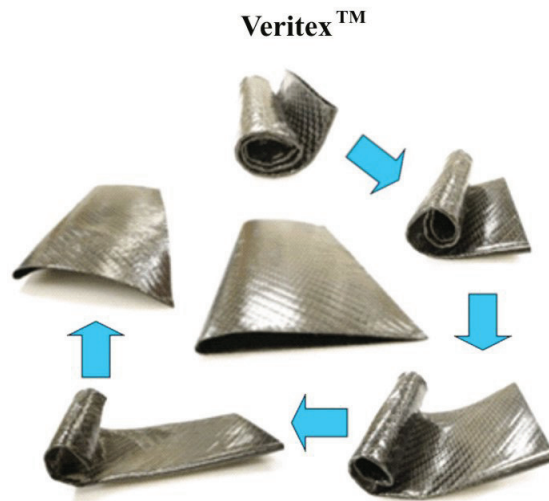
Figure 69: Veritex wing sample working cycle: when heated the wing unfolds and recovers its initial shape. [79]

A Multi-Purpose Unmanned Aerial Vehicle (**M.P.U.A.V.**) was also briefly considered by Lockheed Martin called The Cormorant [10] as shown in Figure 70. The idea is that the drone could handle all-weather reconnaissance, battle damage assessment, or specialized mission support for the submarine. This UAV could be launched from a submarine, then perform wing shaping for a different mission and return to the boat.

Figure 70: The Cormorant concept by Lockheed Martin. [10]

The NextGen Aeronautics design, instead, has a wing structure capable of being transformed from a high-span configuration for slow speed flights to a configuration with reduced wing span to fly at high speeds (Figure 71 and Figure 72). This UAV was

originally referred to as a "BatWing" but has since been named **MFX-1** by NextGen. In this solution, the wing is based on a moveable truss-like structure that can be handled by appropriate actuators, so as to adjust the wing span, area and shape (Figure 73). The metallic wing structure is then covered with silicone elastomer reinforced with titanium or steel to prevent unwanted deformations: the real problem is to attack these surfaces together; an alternative approach could be based on the use of sliding panels.

Figure 71: NextGen Aeronautics design schematics. [74]

High Lift	Climb	Cruise	Loiter	Dash/Maneuver
Wing design L/D ratio 1.45 b/2 = 8.8 ft. S = 17.0 ft^2	Wing design L/D ratio 1.39 b/2 = 9.8 ft. S = 22.8 ft^2	Wing design L/D ratio 1.23 b/2=7.2 ft. S = 15.8 ft^2.	Wing design L/D ratio 1.60 b/2 =9.8 ft. S =17.4 ft^2	Wing design L/D ratio 1.00 b/2 = 7.2 ft. S = 23.9 ft^2

b = wing semi-span
S = wing semi-span area

Figure 72: NextGen Aeronautics design various operative configurations. [43]

(a)   (b)
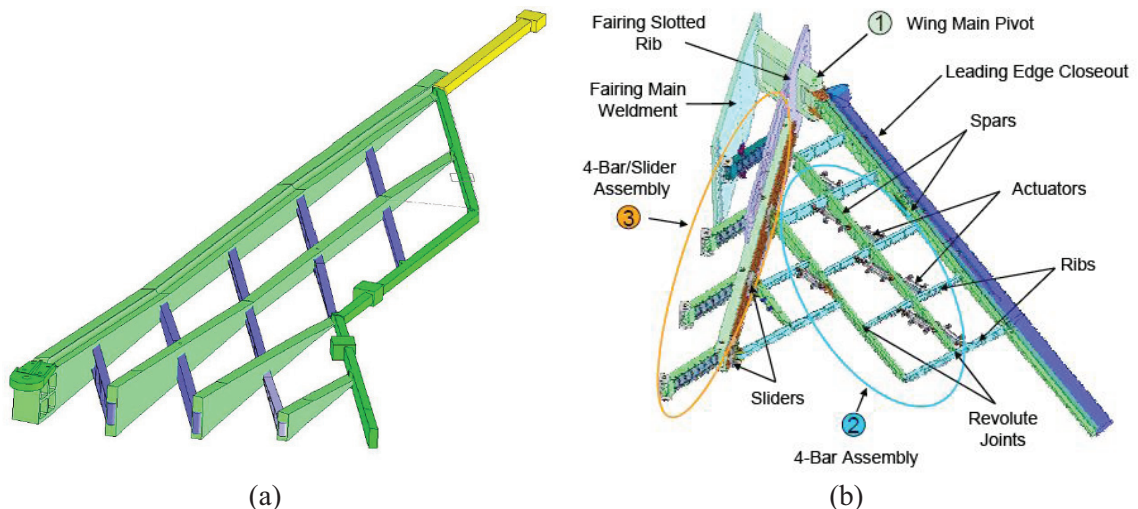
Figure 73: NextGen Aeronautics "batwing" design. [81]

The MFX-1 wing features several technical innovations including innovative flexible wing skin designs which can undergo strains in excess of 100 percent while withstanding air loads of up to 400 pounds per square foot, and kinematic, light-weight, wing substructure which enables the wing to morph. The geometry change is implemented using an efficient, internal electro-mechanical actuation system.

In August of 2006, NextGen successfully flight tested MFX-1 in Camp Roberts, California. The UAV sustained an area change of 40 percent, span change of 30 percent and sweep varying from 15 to 35 degrees while in flight. It also attained airspeeds of about 100 knots during the test cycle. This was the first recorded successful test of an aircraft that morphed during flight [81] (Figure 74 and Figure 75).

Figure 74: NextGen Aeronautics half MXF-1 wind tunnel tests. [43]

Figure 75: NextGen Aeronautics flying MFX-1. [10]

After the success of MFX-1, NextGen developed a larger 300 pound morphing UAV named MFX-2. MFX-2 used twin jet engines for propulsion and also encompassed a flight control system that allowed autonomous flight. A September 2007 flight test of the aircraft once

again garnered success while demonstrating a 40 percent change in wing area, 73 % change in span and 177 % change in aspect ratio.

Another way to interpret wing span morphing is based on Hyper Elliptic Cambered Span (**H.E.C.S.**) wings that are being developed since 2003 by NASA.

University of Virginia has designed a HECS wing based on several segments [82]. This wing can increase its planform area in 10% to 15% and reduce drag by augmenting the Oswald coefficient. It is made by several segments that fold, creating an approximated elliptic cambered span (Figure 76a). This mechanism uses only one actuator at the wing root; the motion is then transmitted by Quaternary-Binary Cross Linked Mechanism (QBCLM). Cornell University developed also a HECS wing [83] very similar to Virginia University's one (Figure 76b), but it is actuated by smart material alloy wires. This option revealed to be more energy efficient.

| (a) | (b) |
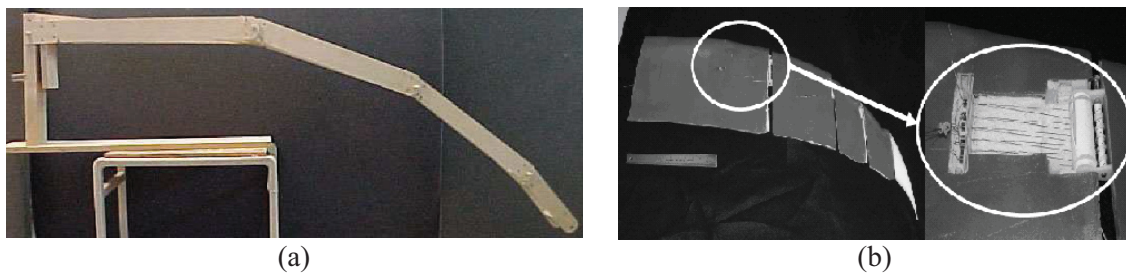
Figure 76: HECS wing: (a) Virginia University and (b) Cornell University prototypes. [83]

It is obvious that such morphing capabilities require careful optimization studies: if the aircraft future is based on emulation of the birds flight, with the ability to alter substantially the wing shape, then it becomes necessary to determine in real time and during flight the configuration that best suits the operating conditions [84, 85].

3 ADAPTIVE WING ACTUATED BY SMA

The possibility of changing the airfoil shape by means of Shape Memory Alloys is very attractive: by directly implementing these materials within the structural elements, an actuation capability is integrated within the structure, with significant benefits in terms of:

➢ weight, because there is no need for the traditional hydraulic lines for the control surfaces actuation;

➢ reliability and maintenance, as it reduces the number of required components;

➢ structural and aerodynamic efficiency, as the use of SMA can allow for both load bearing and deformable structures, with the possibility of implementing a continuous, gradual, adaptive, in real-time actuation.

However, the use of SMA for morphing wing applications is still in an experimental phase: what makes these technologies inapplicable in a commercial context is the lack of an established modelling, suitable for engineering design on a large scale, as well as the intrinsic limits of shape memory materials, for which the ratio of applied force / application rate is rather limited. Many studies, therefore, are still facing small model aircraft or aircraft (such as U.A.V.s).

Alasty & al. [86] studied the effect of a variable shape wing applied to an ultra-light aircraft, in order to improve aerodynamic efficiency and flight control. Given the size (less than a meter of wing span) and the low weight of this aircraft, the use of Shape Memory alloys has proven more appropriate than traditional actuators thanks to the favourable characteristics of a high strength and low weight, as well as a reduced footprint. The structure was made of balsa wood with nylon sticks; wings were composed of two parts, a rigid front element and a deformable rear, as shown in Figure 77.
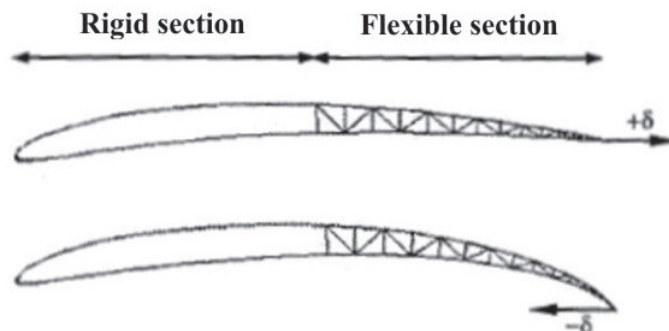
Figure 77: Sketch for a morphing wing for an ultra-light vehicle. [86]

Actuators in SMA are used in pairs, so each wire acts in opposition to another: this concept is often found in the literature with the name of antagonistic configuration. Conclusions made from the authors demonstrate an increment of manoeuvrability characteristics of the radio controlled aircraft with respect to previous works.

Benavides & Correa [87] at University of Missouri-Rolla realized a wing section, based on the simmetric Gottingen 776 airfoil (Figure 78), having a deformable trailing edge actuated by SMA wires: during wind tunnel tests it has been verified the improvement in terms of Lift / Drag ratio and lift coefficient of this solution with respect to a traditional one.

The wing section used six NiTiNOL wires that could pull, upon electrical activation, the upper part of the wing trailing edge downward: in this manner, the thrust produced by the upper pat induces a deformation of the lower surface, with a deflection equivalent to that produced by a flap. Following the cooling of the SMA wires, ten springs carry the profile to its initial configuration.

Figure 78: Wing section with deformable trailing edge actuated by SMA wires. [87]

Song & Ma [88] used SMA wires to control the flap movement of a model airplane wing mainly to achieve weight reduction (Figure 79). Two SMA actuators are used: one to move the flap up and the other to move the flap down; by alternatively activating the SMA actuators, the flap can stay at a desired position. A sliding mode based nonlinear robust controller is designed and implemented on a real-time data acquisition and control platform to control the position of the flap. Experimental results show that a high control accuracy has been achieved for both the position regulation and tracking tasks, even with uncertainties and disturbances.
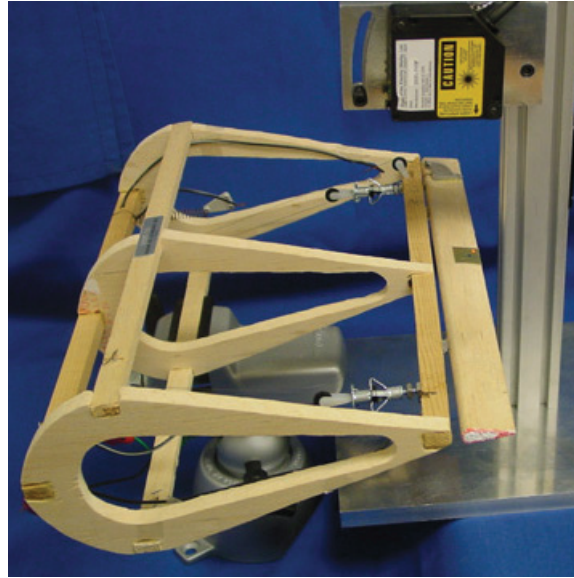
Figure 79: Wing model with the SMA actuated flap. [88]

Another study on morphing flaps actuated by SMA wires has been developed **Seow & al.** [89]. The prototype consisted of 2 ribs with aluminum rods as spars, and instead of a conventional hinge, metallic shims have been used to allow the deflections: SMA wires could be positioned in four different anchoring points (Figure 80). Flexible skins have been also explored and experimented. Glass fiber composite bonded to 0.5mm thick silicon rubber sheet (hybrid skin) and overlapping glass fiber composite have been made and tested on the prototype. Calculation to handle the aerodynamic load has been also performed. Finally the controllability of the prototype has been also investigated, including the measurement and estimation of power consumption, and dependence of heating and cooling time on input variations. A wing prototype has been designed and fabricated (Figure 81), and actuation of the flap has been successfully demonstrated using two Ø0.185mm SM495 wires, achieving an actuation angle of 5.2 deg. Larger deflection angle of 15 deg has been also achieved with a single Ø0.5mm SM495.
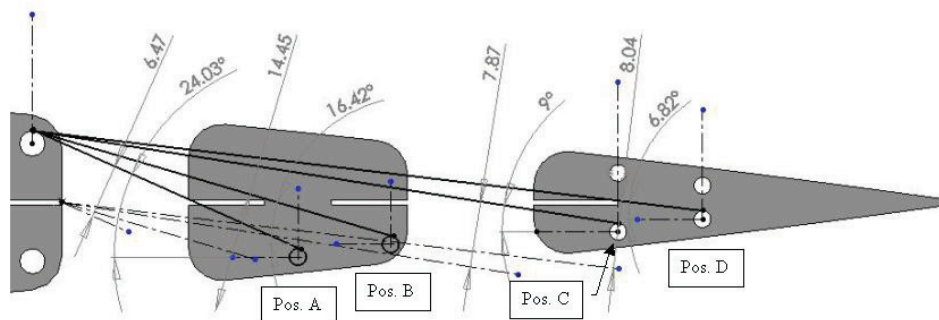
Figure 80: Four investigated anchoring positions for SMA. [89]

<table>
<tr><td>(a)</td><td>(b)</td><td>(c)</td></tr>
</table>
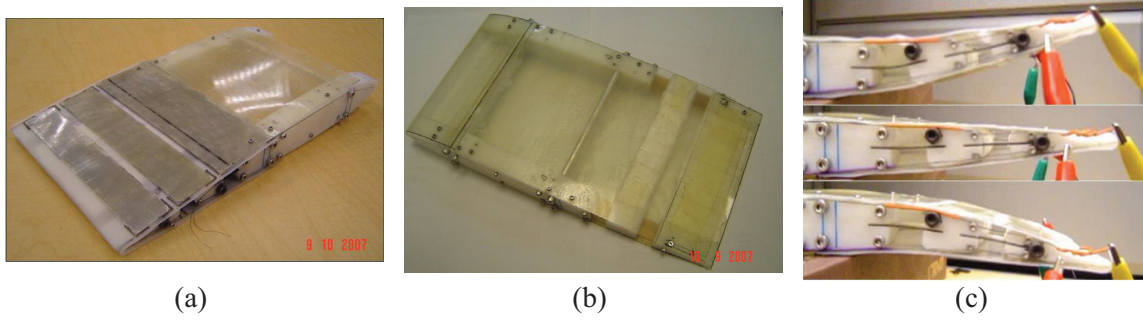
Figure 81: Morphing flap prototype: (a) with hybrid skin, (b) with overlapping skin and (c) testing. [89]

Eggleston & al. [90] experimented the use of SMA wires on a model aircraft (after having also explored the idea of using torsion bars in SMA) for the roll control on a morphing wing.

The first concept developed for the variation of the wing curvature was based on NiTiNOL wires: a polyurethane rod is connected to a wood element (representative of the wing box) and is bent due to the SMA wires activation, connected to it through four Flexane sheets; the rod exercises the elastic recovery when the wires are not heated, returning to the initial configuration. Having more wires on both sides of the rod, it can be alternatively deflected to one side or the other (simulating an aileron) (Figure 82a).
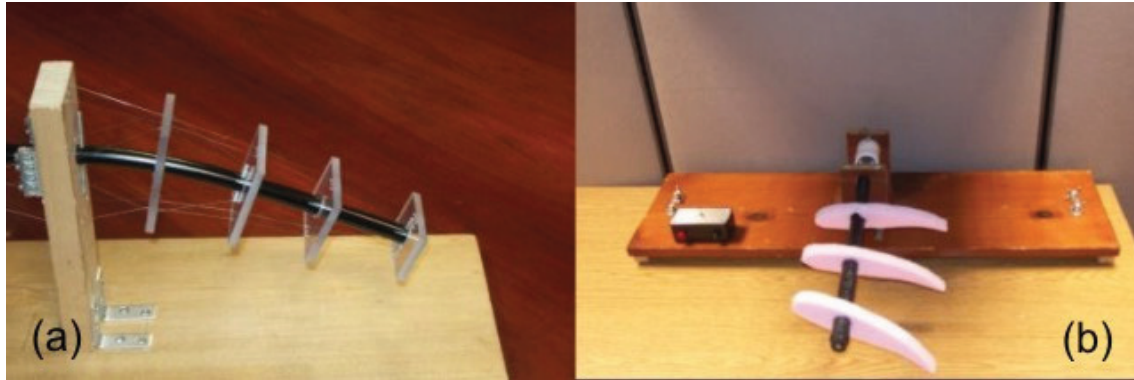
Figure 82: Morphing wing concepts: (a) actuation through SMA wires, (b) actuation through an SMA torque tube. [90]

The second idea (Figure 82b) is aimed at the wing twist, and is based on the use of a wooden rod constrained on one side, with a rubber coating and then a PVC pipe that encloses everything and is linked to the SMA wires wrapped around the rubber layer: this way, upon activation, the rod is subject to torsion.

The final chosen configuration is similar to the first model (Figure 83). The wings are stiffened by Plexiglas elements, where SMA wires are arranged on both sides (through aluminum supports that are needed to prevent the Plexiglas overheating upon activation).
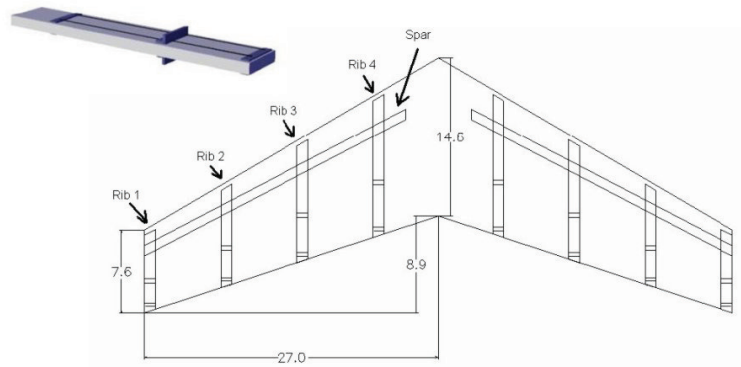
Figure 83: Conceptual layout of the adaptive wing structure. [90]

The final model aircraft is shown in Figure 84: from wind tunnel tests, it showed a significant improvement in aerodynamic characteristics.
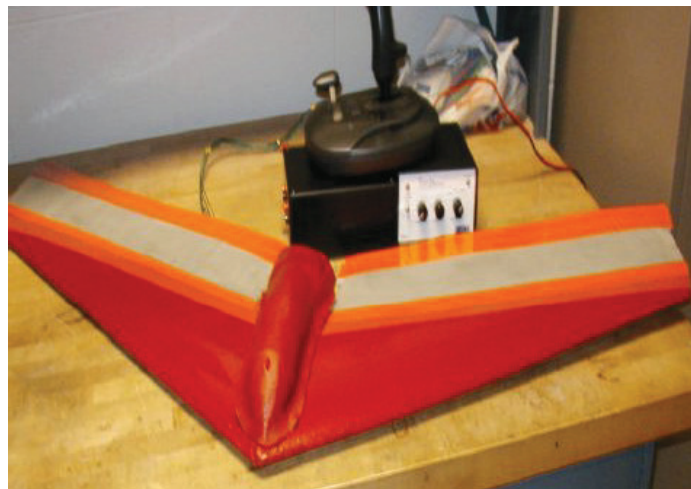
Figure 84: Ultra-light aircraft with adaptive wings. [90]

Mirone [91] at the University of Catania (Italy) investigated ability of the wing to modify its cross section assuming the shape of two different airfoils and to the possibility of deflecting the profiles near the trailing edge in order to obtain hingeless control surfaces. The actuation is provided by one-way shape memory alloy wires eventually coupled to springs (Figure 85 and Figure 87). The points to be actuated along the profiles and the displacements to be imposed are selected so that they satisfactorily approximate the change from an airfoil to the other and to result in an adequate deflection of the control surface; the actuators and their performances are designed so that an adequate wing stiffness is guaranteed, in order to prevent excessive deformations and undesired airfoil shape variations due to aerodynamic loads. Two prototypes have been realised incorporating the variable airfoil (Figure 86) and the hingeless aileron (Figure 88) features respectively, and the verification of their shapes in both the actuated and non-actuated states.
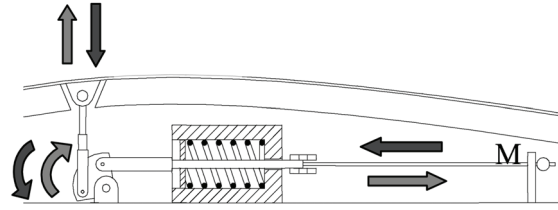
Figure 85: Actuator layout for the wing cross section morphing. [91]
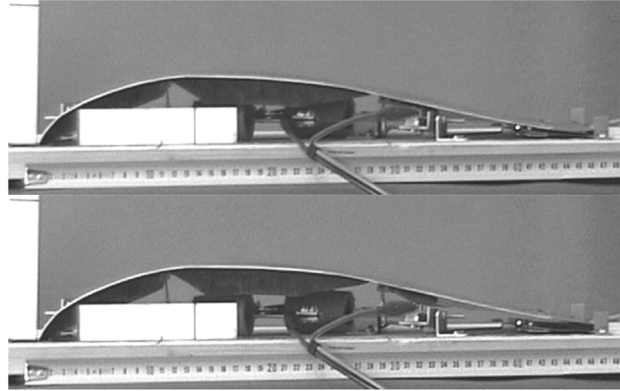
Figure 86: Un-actuated (top) and actuated (bottom) prototype with different cross sections. [91]
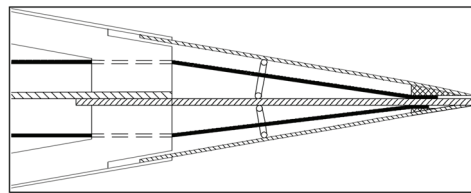
Figure 87: Actuator layout for the wing trailing edge morphing. [91]
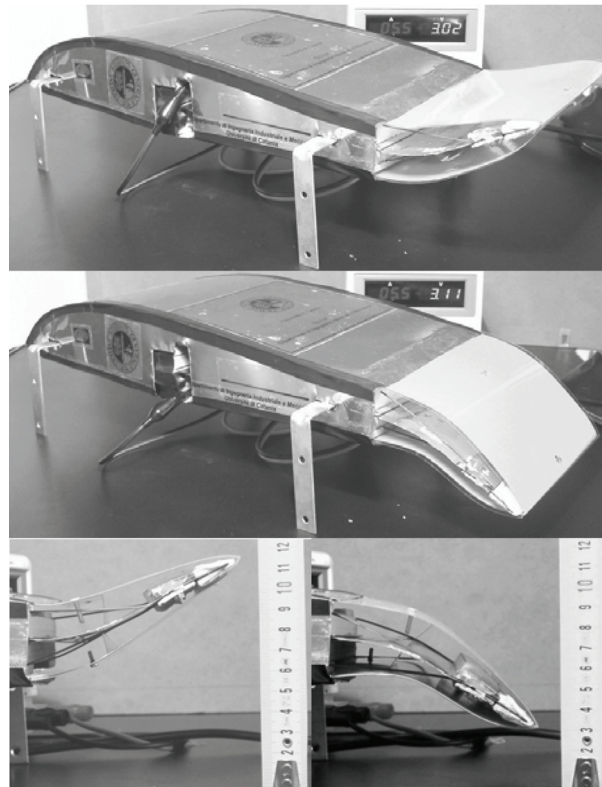
Figure 88: Activated hingeless wing model. [91]

The comparison of the real wing profiles with the theoretical airfoils coordinates has shown a good performance of the actuation system, which is also able to ensure a structural stiffness adequate to the considered airflow pressure load. A significant trailing edge displacement, close to 10% of the wing chord, is achieved in the experimental tests.

A different method to change wing camber has been studied by **Brailovski & al.** [92], who considered a morphing wing concept designed for subsonic cruise flight conditions combining three principal subsystems: a flexible extrados, a rigid intrados and an actuator group located inside the wing box (Figure 89). Using weighed evaluation of the aerodynamic and mechanical performances in the framework of the multi-criteria optimization procedure, an adaptive structure consisting of 4-ply flexible extrados powered by two individually controlled actuators has been designed. The forces these actuators must provide in order to fit target wing profiles are calculated for a given flexible structure and given flight conditions. Each actuator includes linear SMA active elements with one extremity connected, through a cam transmission system, to the flexible extrados and other extremity connected to the rigid structure of the wing through a bias spring. To meet the functional requirements of the application, the geometry (length and cross-section) of the SMA active elements and the bias spring characteristics are calculated.
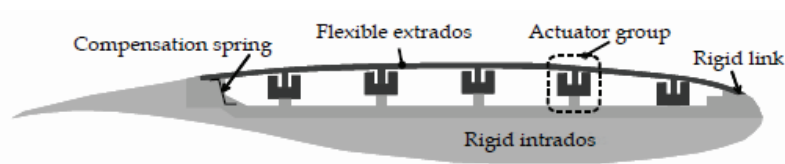
Figure 89: Conceptual design of the morphing laminar wing. [92]

Kudva & al. [93, 94] have worked on SMA applications for a morphing wing on a more extensive way. In particular, they developed those concepts which have then been implemented in the "Smart Wing" program sponsored by DARPA (see later in this section). They mainly focused on the wing torsion (through an SMA torsion tube) and the leading and trailing edge actuation (with SMA wires).

The wing twist was obtained using two concentric SMA torque tubes, one of which tied to the wing tip and the other to the aircraft body: by means of a relative rotation the entire wing can undergo a twisting action (Figure 90a).

Instead, to achieve the hingeless aileron, SMA wires were adopted in an antagonistic configuration (Figure 90b): the aerodynamic surfaces to be controlled (either upper or

lower one) internally integrate SMA wires, ensuring a two-way antagonistic deflection. Figure 91 shows in more detail what has been achieved.
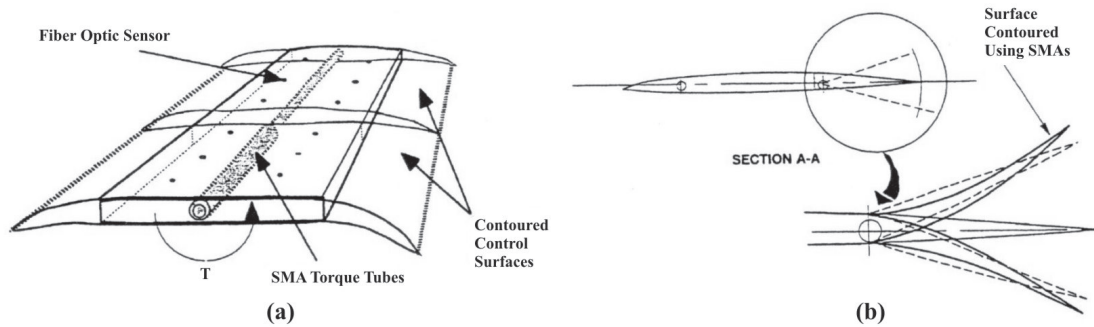
Figure 90: Smart Wing program: (a) wing model and wing twist actuation through SMA torque tube, (b) trailing edge model and actuation with SMA wires. [93, 94]

Due to the considerable complexity of the thermo-mechanical behaviour of SMAs, a fiber optic interferometric system was implemented for determining the actual deformation.
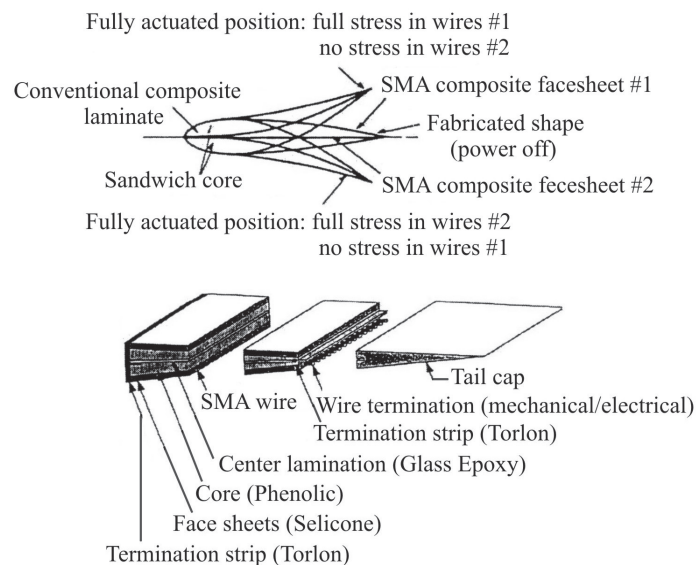
Figure 91: Details of the adaptive trailing edge. [93, 94]

Surely one of the most interesting studies carried out to date in terms of integration of Shape Memory Alloys within a morphing wing has been developed under the "**Smart Wing**" program by the cooperation of DARPA, AFRL, NASA and Northrop Grumman [95-97], aimed at the realization of an UCAV (Unmanned Combat Air Vehicle) (Figure 92). Starting from what has already been described (see Kudva & al.), this experimental study implemented both concepts of SMA tubes to attain wing twist and flexible leading and trailing edges actuated by SMA wires (Figure 93 and Figure 94).
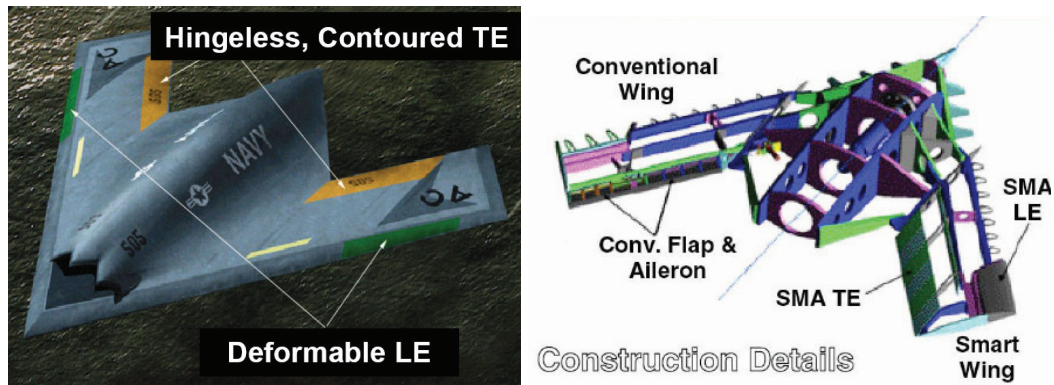
Figure 92: UCAV developed in the "Smart Wing" program. [93, 94]
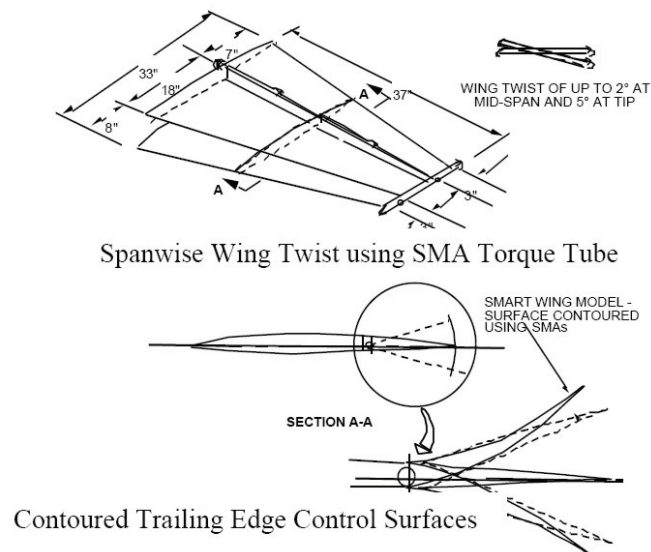
Figure 93: Details of the UCAV adaptive wing. [93, 94]
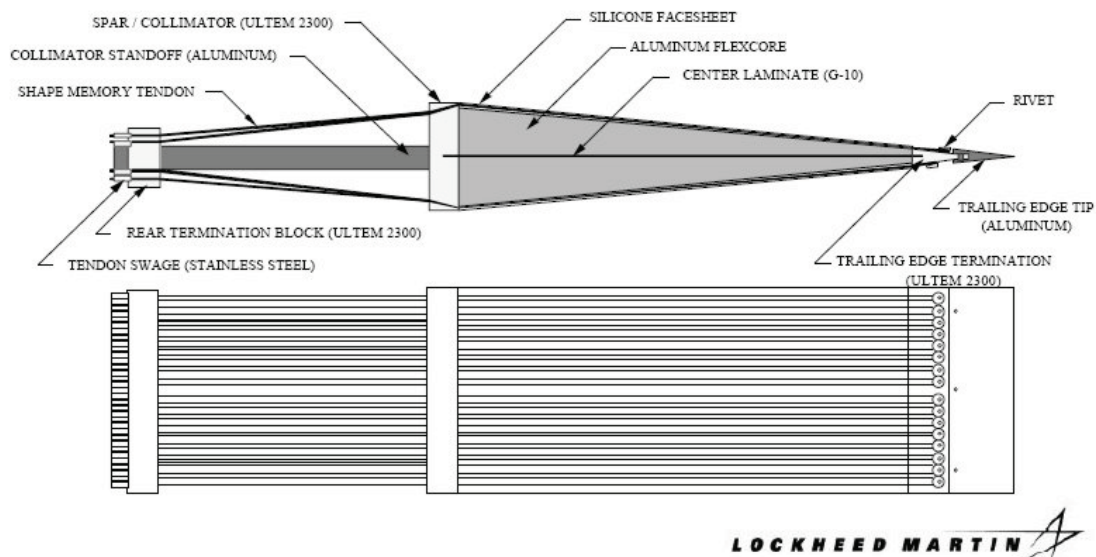
Figure 94: Manufacture details of the UCAV trailing edge actuated by SMA wires. [93, 94]

The choice of an antagonistic configuration for the SMA wires actuating the wing edges was no accident: though a single set of wires could be sufficient for actuation and the

single central laminate adequate to restore the structure at rest upon cooling, this solutions showed a better efficiency under static loads (Figure 95). The mid laminate also provides the necessary support for the SMA wires termination and constraint, in addition to being the load-bearing structural element of the wing edge; the aerodynamic surface is then defined by means of Flexcore filling and an elastomeric skin (Figure 96 and Figure 97).
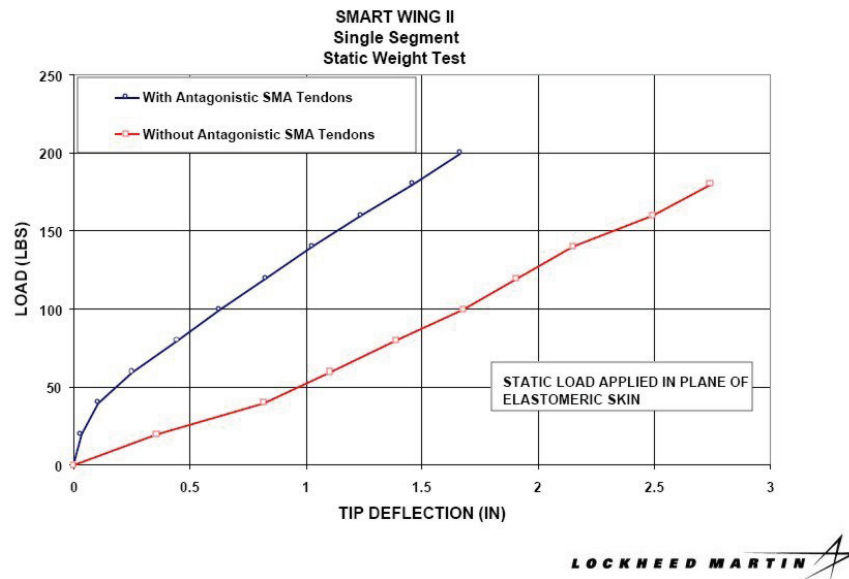
Figure 95: Static weight test for the trailing edge with SMA wires. [93, 94]
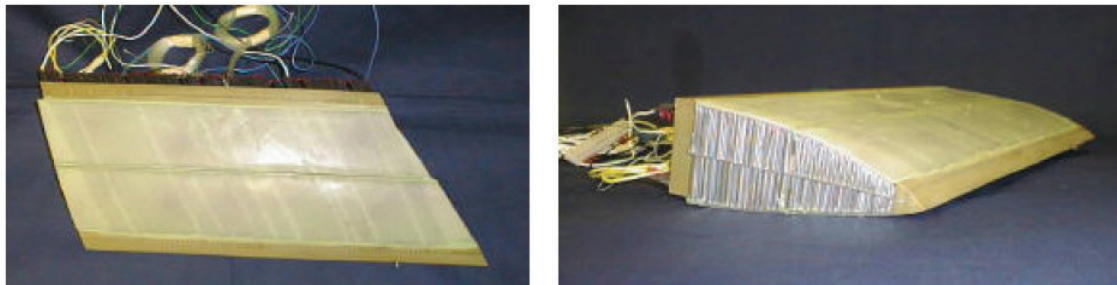
Figure 96: UCAV leading edge manufacture. [93, 94]

Figure 97: UCAV trailing edge manufacture. [93, 94]

From wind tunnel tests, it was noticed an improvement between 8% and 12% in lift and roll control over a traditional wing. A wing twist up to 5 deg was also attained, together with a deflection of up to 4.5 deg for the leading edge and 15 deg for the trailing edge (Figure 98 and Figure 99).
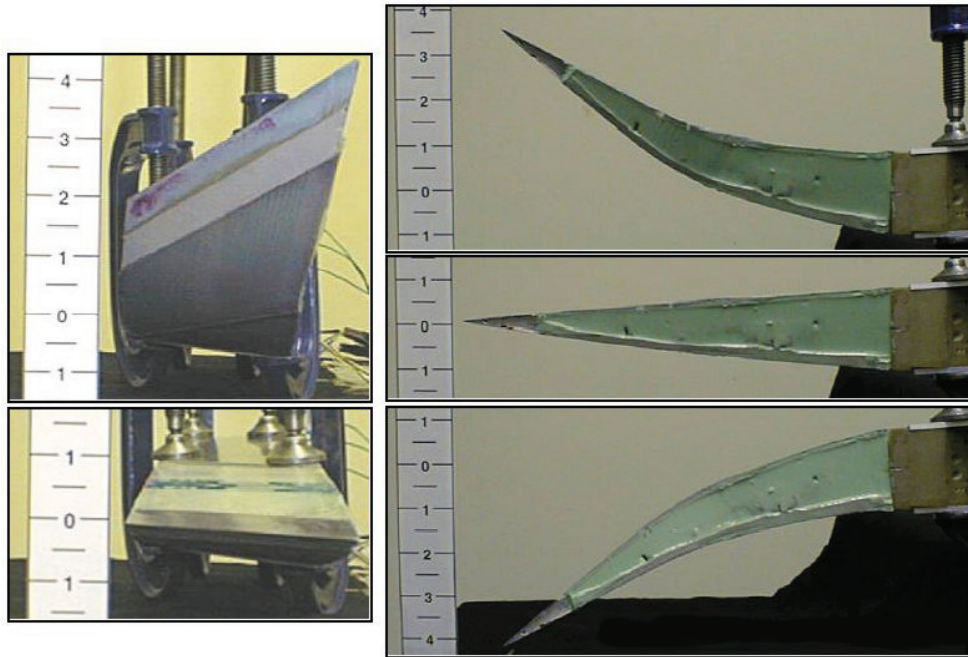
Figure 98: Experimental tests on the trailing edge tip deflection. [93, 94]

Figure 99: UCAV trailing edge deflection tests. [93, 94]

A study on the morphing wing was conducted by **T.I.I.M.S.** (Texas Institute for Intelligent Bio-Nano Materials and Structures for Aerospace Vehicles) [98] on a NACA 0015 airfoil made of ABS plastic, whose structure was divided into three independent

sections, each able to rotate freely with respect to the others by means of concentric tubes, so as to attain wing twisting (Figure 100).

To actuate the three independent wing sections, NiTiNOL ribbons and wires were used. Each section is equipped with two SMA ribbons and an aluminium strip with a SMA wire, to achieve the actuator shown in Figure 101. The combined strength of the SMA ribbons and wires under thermal activation is able to generate a twisting moment, allowing for a relative rotation between two consecutive wing sections and a global wing twist effect (also if attained by means of rigid discrete sections). Figure 102 shows the actuator position within the three wing sections: with only two actuators for section, an experimental rotation of 5.5 deg was measured for each section.
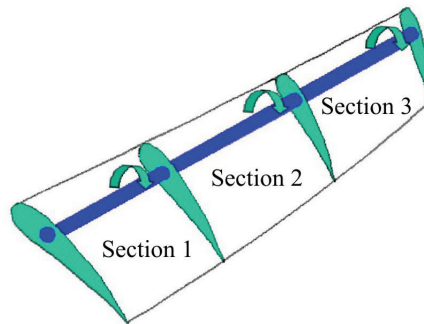
Figure 100: Concept developed at TIIMS for the adaptive wing. [98]
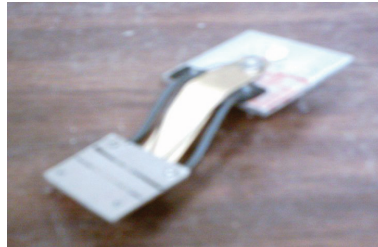
Figure 101: Actuator developed at TIIMS for the adaptive wing, comprised of an aluminium strip and SMA wires. [98]
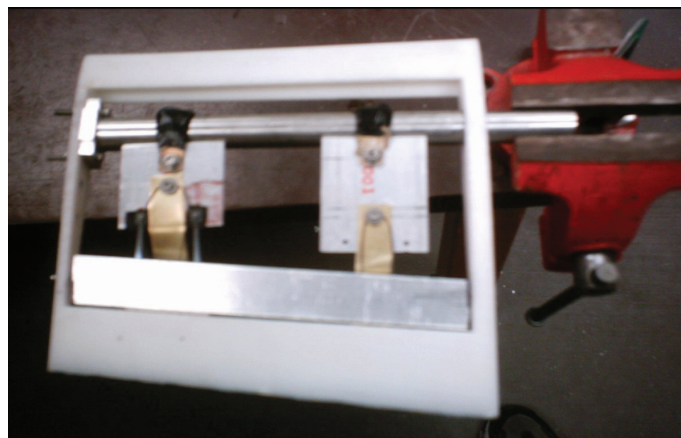
Figure 102: Wing section prototype adopted for the experimental tests. [98]

Also in China the adoption of SMAs for morphing applications is gaining momentum [99]. A SMA torsion actuator based on NiTi wires and a thin-walled tube have been developed for the adaptive wing demonstration system. The angle of attack of a wing model with the SMA torsion actuator could be changed continuously up to 15 deg in 1 second. A novel smart wing rib has been researched, with the swing angles capable of reaching +/-10 deg (Figure 103).
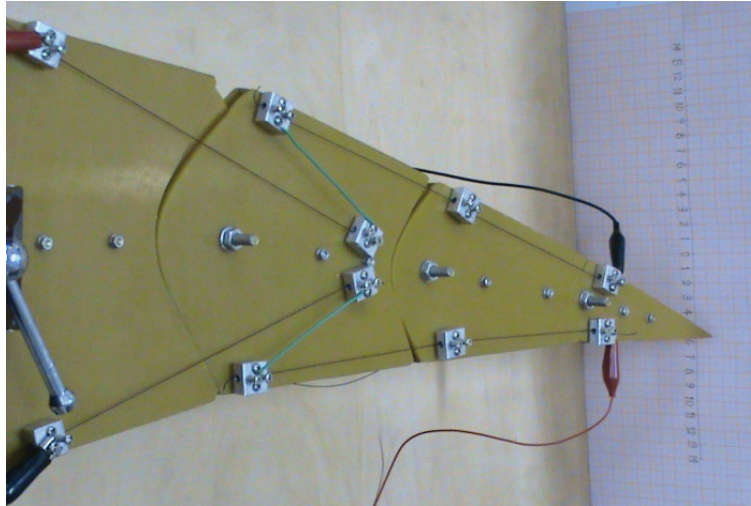
Figure 103: Smart wing ribs actuated by SMA wires. [99]

The Aerospace Engineering Department (**D.I.A.S.**) at University "Federico II" of Naples, in collaboration with the Italian Aerospace Research Center (**C.I.R.A.**), also conducted some studies in the morphing wing field, with particular reference to a "Hingeless Wing" concept for an U.A.V. [100, 101].

The main focus of the study was to create, on the selected *NACA 63_2-415 airfoil,* a morphing leading edge capable of 10 deg deflection, as obtained by aerodynamic optimizations for take-off and landing conditions. To achieve this deflection, an actuation system based on seven SMA wires was adopted together with a three hinge mechanism (Figure 104), and a partial return of the lower surface in the airfoil itself was allowed (the ventral area of the leading edge is not attached to the front spar, but free to slide in the wing). Accommodating the SMA wires along the wing span allowed for greater available length and volume: this way, a sufficient number of wires could be placed according to the requested actuation forces (estimated by a F.E. analysis in 336N under maximum external loads) and their action calibrated.

Figure 105 shows some details about the three hinge mechanism: it is constrained to the wing front spar on one side (fixed hinge) and to a suitable structural element on the

other (free hinge); upon activation, the two hinges get closer and the skin undergoes a suitable curvature.
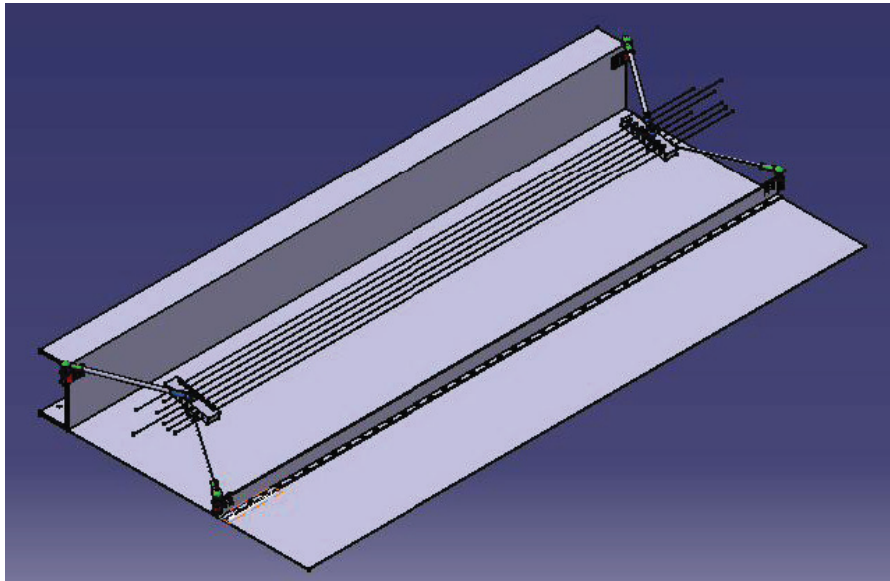
Figure 104: Leading edge CAD model developed at CIRA. [100, 101]
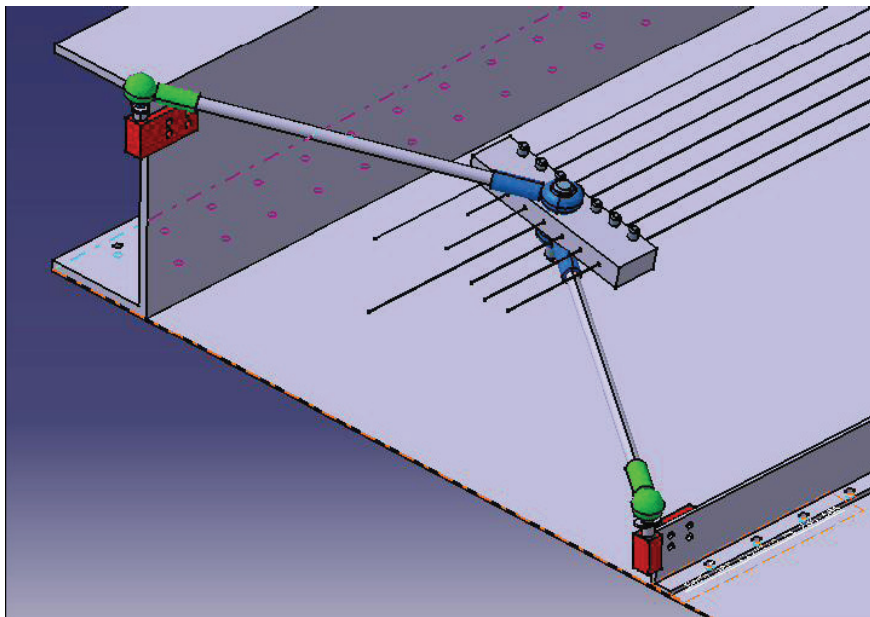
Figure 105: Detail of the three hinge arc system adopted for actuation. [100, 101]

4 OTHER MORPHING AEROSPACE APPLICATIONS

In the previous paragraphs, many studies have been illustrated regarding aeronautical morphing, focused on the variation of main geometrical parameters of a fixed wing. However, the idea of changing the shape of an aerodynamic surface is of great interest nowadays and spread in all the branches of aerospace field: in this paragraph, some applications not centred on geometry change of fixed wing aircrafts will be discussed.

Winglets

Wingtip devices aim the reduction of induced drag, which is responsible for 30-40% of the total drag of a transport-aircraft at long-range cruise condition and for considerably downgrading the climb performance of an aircraft. Winglets alongside with tip tanks, raked wingtips, aligned fans belong to this class of devices. In the case of winglets, the reduction of the induced drag is accomplished by acting like a small sail whose lift component generates a traction force, draining energy from the tip vortices [102]. The wingtip might be considered a dead zone regarding to the aerodynamic efficiency, because it generates lots of drag and no significant lift. The winglet contributes to accelerate the airflow at the tip in such a way that it generates lift and improves the wing loading distribution, which is related to the induced drag. In addition, the aircraft will fly at a slightly lower angle of attack for the same lift coefficient.

Despite the benefits of winglets, there are some drawbacks that need to be addressed. For example, the bending moment at the wing root is higher and may require additional structural wing reinforcements. The winglet also generates viscous and induced drag, which should be minimized and obviously avoiding offsetting the induced-drag reduction caused by the winglet itself on the configuration. Winglets could also contribute to slightly worsening of the aircraft Dutch-roll.

Considering the large amount of investigations on suitable winglet design and aerodynamic performance evaluation [103-113], together with the necessity to adapt its geometry to the different flight conditions an aircraft can encounter in its mission, morphing technologies and smart materials have been focused also in the development of active or adaptive winglets: in this case, the main advantage of morphing techniques is related to the low invasiveness in traditional structures, whose main load-bearing

elements can be designed traditionally, and the greater aerodynamic benefits that can be achieved.

Studies in this regard have been carried out at the Univ. of Bristol [114-117], with a pair of **winglets with adaptive cant angle**, independently actuated, mounted at the tips of a flying wing. Computations and wind tunnel tests (Figure 106) demonstrate that variable cant angle winglet appears to be a multi-axis effector with a favourable coupling in pitch and roll with regard to turning manoeuvres.

(a)   (b)
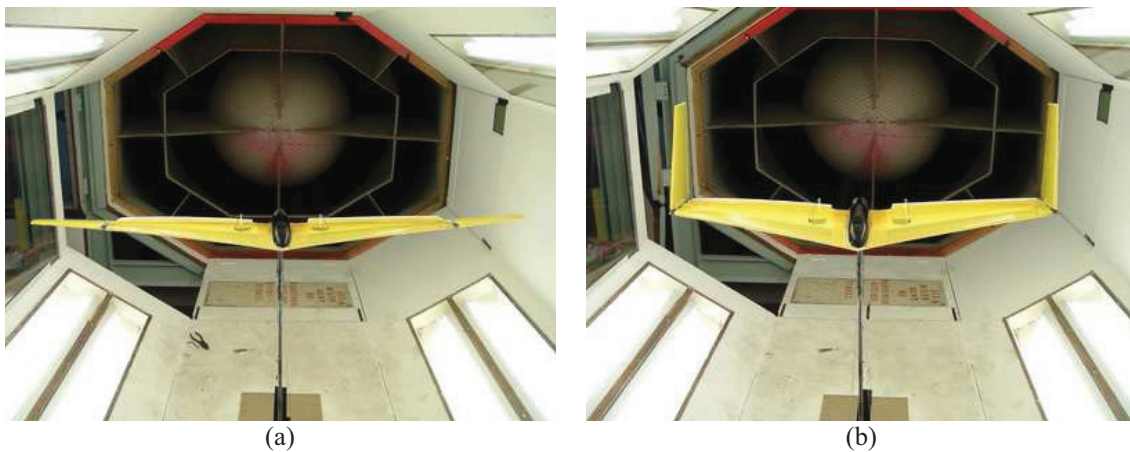
Figure 106: Experimental model as mounted in the wind-tunnel with (a) both winglets planar and (b) both winglets upright. [114]

The investigated concept appears also to be a promising alternative to conventional control surfaces such as ailerons, elevators and rudders as far as basic manoeuvres are concerned. However, a single pair of adaptive winglets cannot substitute for all the conventional control surfaces at the same time if one wants to get a full control envelope: an alternative is to use a second pair of adaptive winglets on top of the first one to control the aircraft in pitch without elevators (Figure 107 and Figure 108).
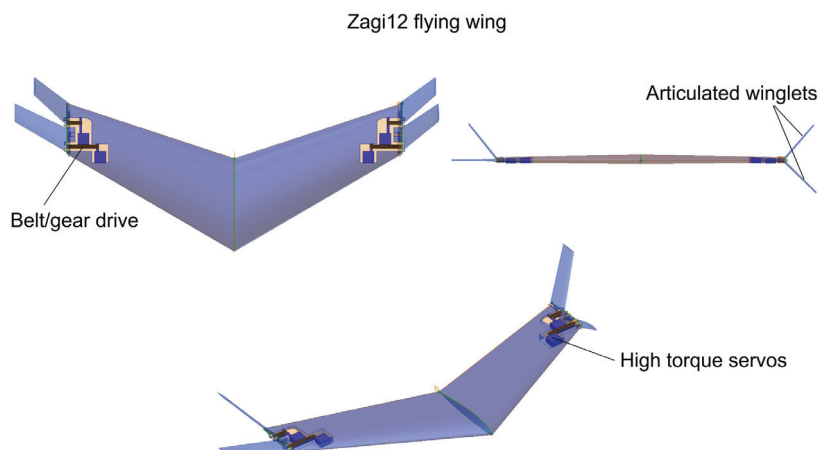
Figure 107: Wind tunnel model schematics of adaptive winglet prototype. [115]

(a)   (b)

Figure 108: Experimental model as mounted in the wind-tunnel: (a) front and (b) rear view. [115]

Moreover, further studies are focused on the development of a small-scale flying wing with active winglets from its actual discrete surfaces concept [118], actuated via single torque actuator, to a seamless continuous concept actuated via a distribution of actuators (Figure 109).
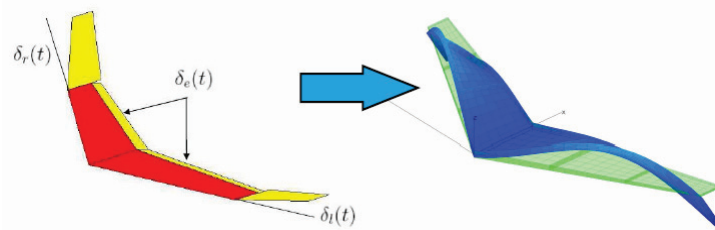
Figure 109: Discrete and continuous wing morphing concept. [A67]

Some investigations on active winglets have been done also by **Shelton & al.** [119]. The feasibility of using an all-moving wing tip device for passive gust loads alleviation has been demonstrated on a number of simulated models and also in some preliminary experiments by **Miller & al** [120] (Figure 110).

Figure 110: Load alleviation device using an all-moving wing tip. [120]

Through consideration of the attachment position and torsional stiffness it is possible to obtain loads alleviation without degradation of aero-elastic stability for a wide range of gust lengths. The incorporation of an adaptive stiffness capability in the device would enable roll control to be feasible for applications such as large flexible HALE aircraft. It would also be feasible to use the adaptive stiffness capability to trim the device so that it maintained the some orientation as the wing-tip, thus improving performance throughout the flight envelope.

Propulsion systems: inlets, nozzles, chevrons

The usefulness of active materials in tailoring propulsion systems has been demonstrated through the Smart Aircraft and Marine Project System DemonstratiON (**<u>S.A.M.P.S.O.N.</u>**) program [121]. One of the uses of SMAs in this program has been to change the geometry of an F-15 engine inlet. The shock structure inside the inlet of an air-breathing hypersonic (or scramjet) engine is controlled largely by the inlet geometry: the ability to change that geometry in flight allows for the control of flow behaviour and the enhancement of engine performance. The inlet must compress and decelerate the entering air to speeds and pressures appropriate for combustion. Typically, this deceleration is achieved through a series of oblique shocks in the inlet and the isolator. The geometry of the inlet determines the structure of these oblique shocks, and therefore the amount of compression and the total energy loss as the flow is decelerated.
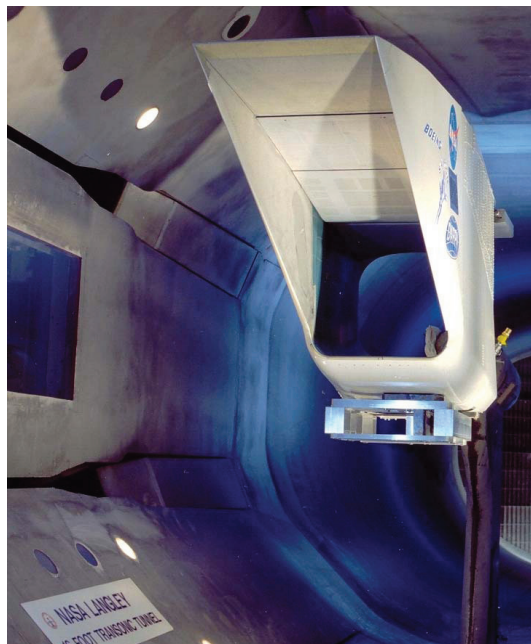
Figure 111: The SAMPSON F-15 inlet cowl as installed in the NASA Langley Transonic Wind Tunnel. [122]

The experiment conducted within the SAMPSON program has been carried out on a full scale F-15 inlet, and the experimental setup arranged at NASA Langley can be seen in Figure 111 and Figure 112 [122, 123]. A total force of approximately 26.700N has been achieved through the use of SMA bundles containing 34 wires/rods. This generated force rotated the inlet cowl through 9 deg. Another concept tested by the SAMPSON program has been the concept of changing the shape of the inlet lip through a more complex system of SMA actuation.

(a)   (b)
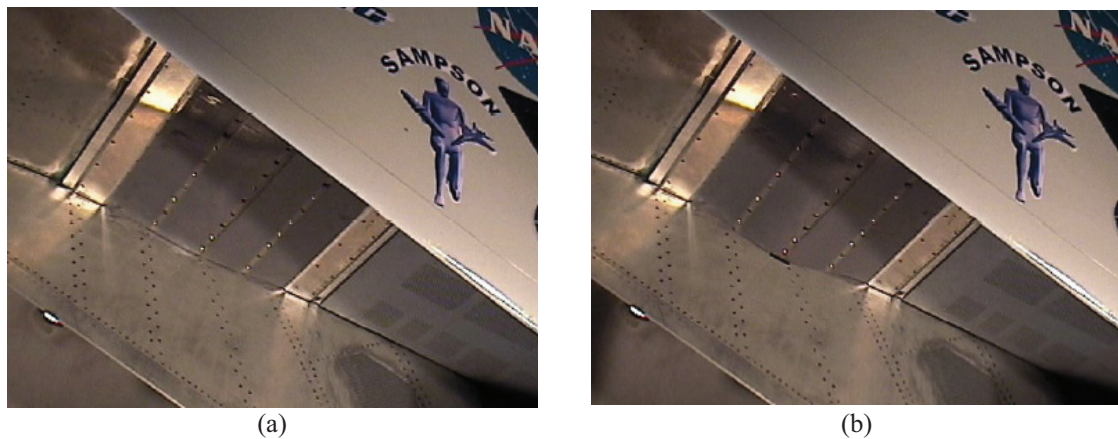
Figure 112: Photograph of adaptive wall installed in SAMPSON inlet: (a) wall stored and (b) wall deployed configuration. [123]

A similar study has been done by **Timpano & al.** [124] on a morphing inlet based on cellular-core sandwich panels, which provide a useful platform for aerodynamic shape change without introducing seals or gaps into the structure. A morphing supersonic nozzle has been designed, built, and tested in wind tunnel (Figure 113). The nozzle has the capability of changing its aerodynamic shape smoothly and continuously during operation, thus changing the Mach number in the test section of the nozzle: seven actuators (linear stepper motors) have been used to achieve the three prescribed shapes.

(a)   (b)
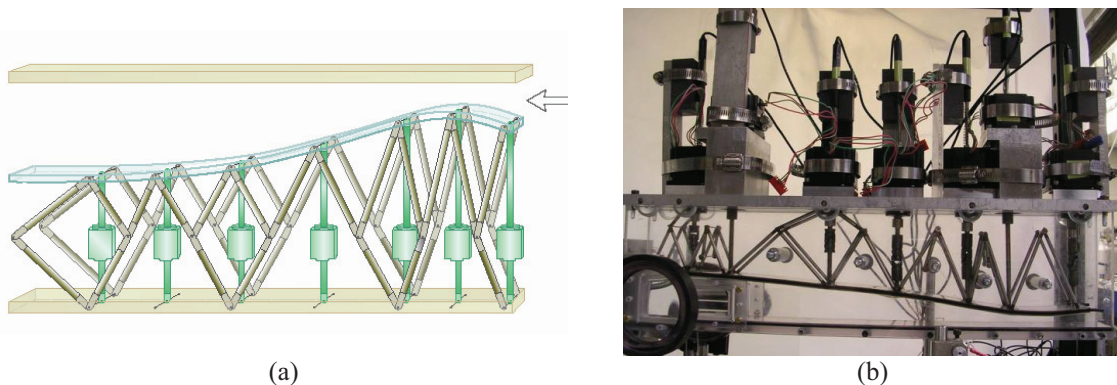
Figure 113: Morphing nozzle (half-nozzle configuration): (a) schematics and (b) prototype with potentiometers. [124]

A variable area exhaust nozzles for a jet engine, actuated by means of SMAs, has been investigated by **Song & al.** [125]. A significant reduction in noise and improved fuel consumption can be achieved by varying the area of a commercial jet engine's fan nozzle. A larger diameter at takeoff and approach can reduce jet velocity reducing noise. Adjusting the diameter in cruise, to account for operating conditions such as varying Mach number and altitude, can optimize fan loading and reduce fuel consumption. The difficulty of using SMA actuators for controlling variable area exhaust nozzles lies in the fact that the temperature near the exhaust nozzle is far higher than the transformation temperature of an SMA actuator. Due to the flexibility and small volume of SMA wire actuators, they have been remotely replaced away from the exhaust nozzle area, in a region where the temperature is lower than that of its transformation temperature (Figure 114). Experimental results on the proof-of-concept prototype demonstrate that the proposed design meets the desired area variation specifications (Figure 115) and shows the promise of a lightweight and simple exhaust nozzle design by using shape-memory alloy actuators.

(a)   (b)
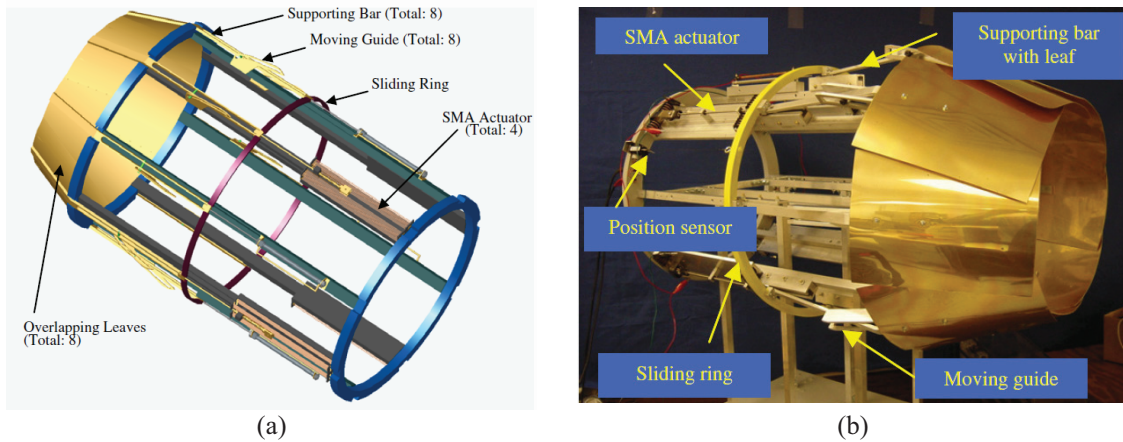
Figure 114: Variable area exhaust nozzle model: (a) schematics and (b) prototype. [125]

(a)   (b)
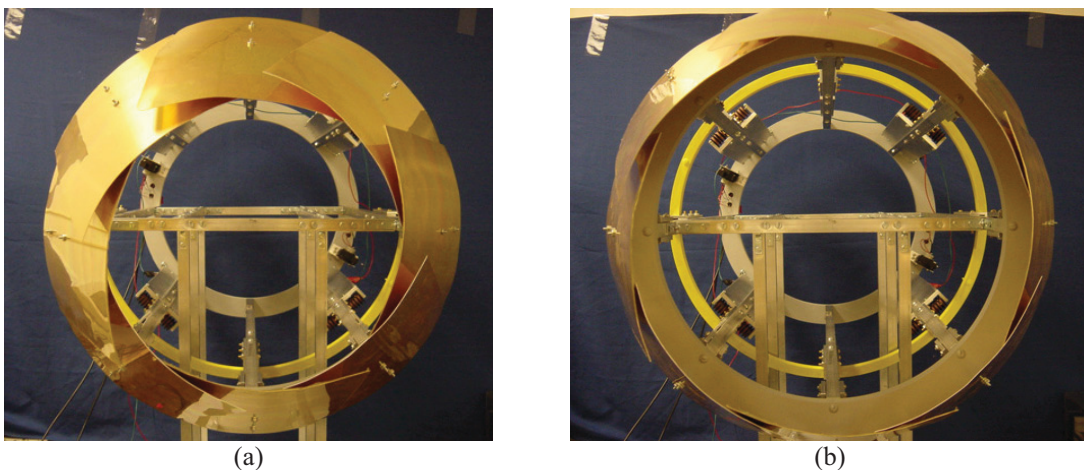
Figure 115: Exhaust nozzle experimental prototype: (a) fully closed and (b) fully open state. [125]

A similar study has been carried out by Boeing [126], with two examples of Variable Area Fan Nozzles (**V.A.F.N.**) employing SMA flexure actuators that have been built and tested (the first was a scaled version used for noise tests and the second was a full scale functional display).

Figure 116 shows a scaled variable area jet nozzle capable of a 20% area change. Shape Memory Alloy flexure actuators were used to position 12 interlocking panels at the nozzle exit. The nozzle has an outlet diameter of 7 cm (2.75"). There are 12 interlocking Aluminum panels that make up the last 2.86 cm (1.125") of the nozzle. SMA actuators designed to expand and contract the nozzle when heated are attached to alternating panels. The interlocks and actuator forces are designed such that each panel's edge stays in contact with the edges of the adjoining panels. A SMA actuator, made of Ni-40Ti (60% by wt. Nickel), was attached to each panel. The actuator base is attached to the support ring and the tip is attached near the free end of each panel. A small resistive heater is bonded on the surface of each actuator. The expanding actuators are trained to curve away from the center-line of the nozzle when heated pulling the panel tip with it.

(a)   (b)
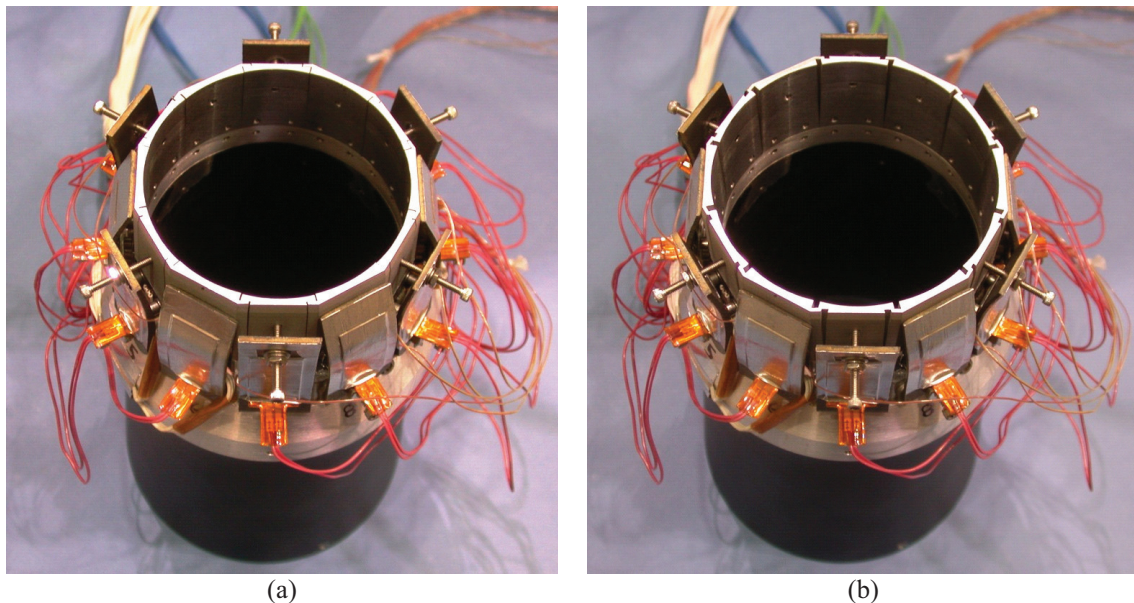
Figure 116: Scale model variable area nozzle: (a) contracted and (b) expanded by 20%. [126]

The contracting actuators are trained to bend towards the center-line when heated, pushing the panel tip into the nozzle flow (Figure 117). The actuators were 1.9cm wide (0.75") x 4.4cm long (1.75") and tapered from 2 mm (0.08") thick at the base and 1 mm (0.04") thick at the tip. A closed loop control system was used to maintain a range of constant diameters with varying flow conditions and to vary the diameter under constant flow conditions. Acoustic data by side line microphones and flow field measurements at

several cross sections using PIV showed significant effect on the flow and noise reduction.
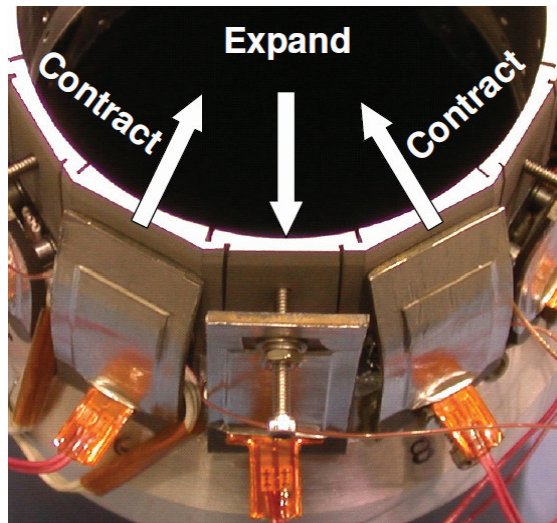
Figure 117: Variable area nozzle configuration. [126]

Engine noise levels during take off and landing have become more highly regulated worldwide. To reduce this noise, some designers are installing chevrons onto engines to mix the flow of exhaust gases and reduce engine noise. Research is being performed into methods by which SMA beam components can be embedded inside chevrons. The SMA beams bend the chevrons into the flow during low-altitude flight or low speed flight, thereby increasing mixing and reducing noise; during high-altitude, high speed flight, these SMA beam components cool into martensite, thereby straightening the chevrons and increasing engine performance [127]. The current Boeing design for these variable geometry chevrons (**V.G.C.**) can be seen in Figure 118 and details are illustrated in Figure 119.
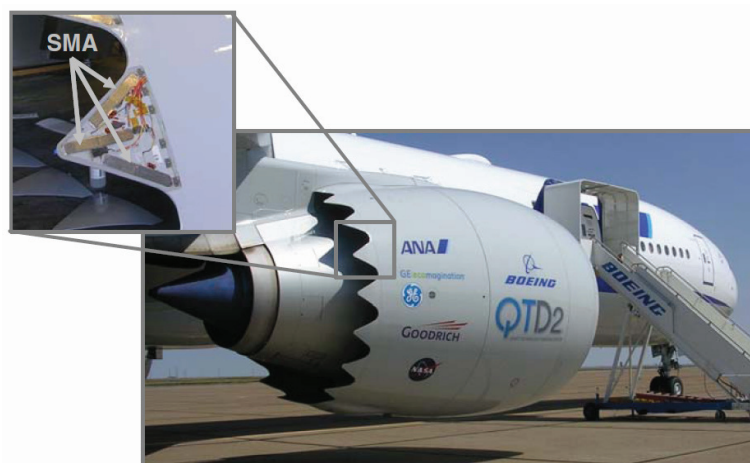
Figure 118: Boeing variable geometry chevron, flight testing. [128]
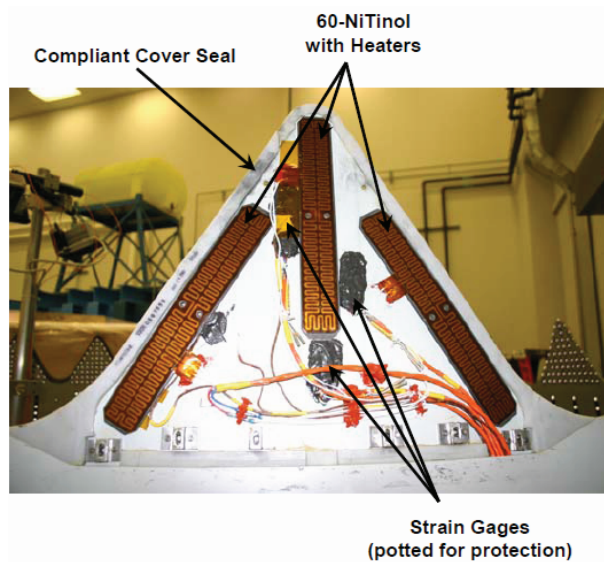
Figure 119: Individual chevron components. [128]

Variable Geometry Chevrons (VGCs) have been successfully flight tested on a Boeing 777-300ER with GE-115B engines, demonstrating full-scale aerostructure morphing using shape memory alloy actuators. Chevrons, serrated aerodynamic devices along the trailing edge of a jet nozzle, have been shown to greatly reduce jet noise by encouraging advantageous mixing of the free, fan, and primary streams.

A different solution to the **active chevron** problem has been proposed by NASA. In this design, SMA strips are installed on each side of the chevron centroid during the fabrication process [129]. Upon heating, the SMA strips contract alternately, leading to asymmetric stresses within the chevrons and therefore create a bending moment.

Helicopter rotor blades

Aeronautical engineers have faced a plethora of issues in their path to obtaining stable flight of rotary-wing aircraft. A major component of these issues has to do with the complex flow field that a rotor blade is exposed to: even in hover, each section of the rotor blade is exposed to a different oncoming flow velocity; engineers have designed the blade to have a pre-built twist which compensates for the varying flow velocity. However, the optimum amount of this pre-twist varies with flight condition: considering this fact, classical rotor blade designs are therefore actually a compromise and not an optimum design.

Aside from the performance issues that plague rotating wing aircraft, the rotor blades emanate a significant amount of vibration and noise as well. These problems are caused by a number of factors including the increased asymmetrical loading of the rotor disk as well as blade tip shocks that occur with increasing speed. Furthermore, the noise

emitted by the rotor blades is compounded by the interaction of the blades with the tip vortices of the proceeding blades (BVI noise), Figure 120. These problems, while not necessarily imperative to performance improvements, are essential to be solved in order to obtain a "smooth" ride.
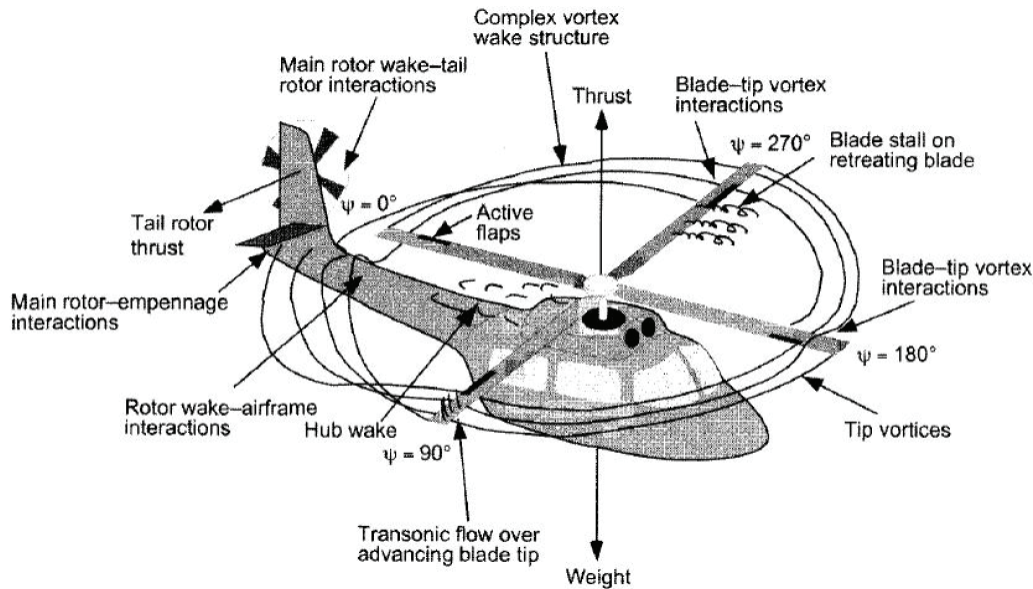
Figure 120: Complex flow-field of an helicopter. [130]

As for aircrafts, current researches focus on improvements in terms of increased speed, payload and manoeuvrability, along with reductions in costs, vibrations and noise.

These are among the objectives of the DARPA Mission Adaptive Rotor (**M.A.R.**) initiative, which will kick off by the end of 2009 [131]. The program aims to develop "on-the-fly" morphing rotor technology and demonstrate the benefits of actively reconfiguring the rotor in flight: DARPA has identified a wide range of potential ways of reconfiguring the rotor in flight, including varying blade diameter, sweep and chord; morphing tip shapes and variable camber airfoils; variable blade twist, anhedral/dihedral, tip speed, stiffness and damping. DARPA is looking for technologies that can increase rotorcraft payload by 30% and range by 40%, while reducing acoustic detection range by 50% and vibration by 90% over the fixed geometry rotors.

Some studies can be found in literature which illustrate the aerodynamic and acoustic benefits of an active twist rotor [132-134], the rotor power reduction in presence of trailing edge flaps [135] or the envelope expansion using extendable chord sections [136]. Many researches are focused on how to achieve these morphing characteristics from a structural perspective, focusing on specific geometrical parameters. Some solutions for rotor twist have been presented by **Riemenschneider & al.** [137]; warp

induced systems to obtain the variable twist of rotor blades have been investigated by **Mistry** [138], focusing on the use of an I-beam spar situated within the blade which acts as both a load bearing member and the actuating mechanism (through the application of differential axial loads, Vlasov bimoments) or via the forced warping of the skin (actuated using a mechanism based on the power screw concept) (Figure 121).

| (a) | (b) |
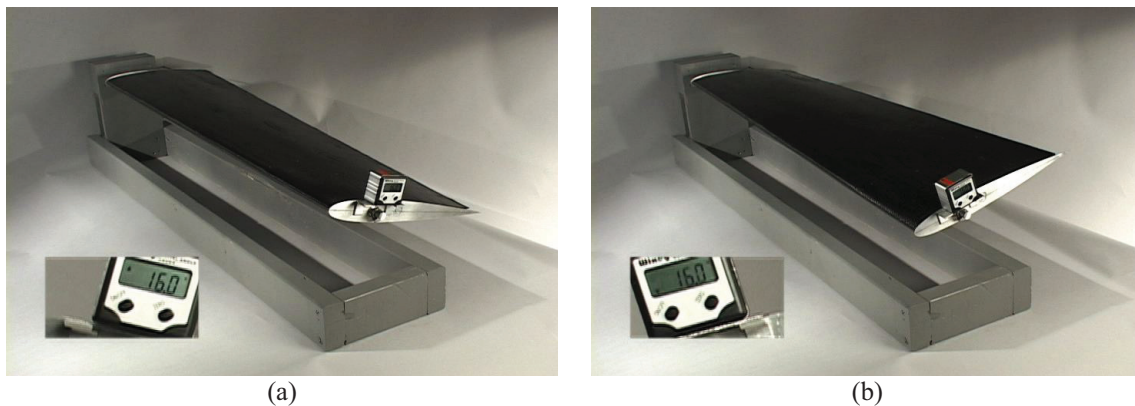
Figure 121: Warp induced variable twist for a rotor blade: (a) nose up and (b) nose down state. [138]

Another example on rotor blade twisting obtained by means of Shape Memory Alloys has been developed within the Reconfigurable Rotor Blade (**R.R.B.**) program funded by NAVAIR, with a goal of demonstrating the potential to improve rotorcraft performance by optimizing the configuration of major structures in flight [139, 140].

The NiTi actuation system employed 55-Nitinol (Ni-55Ti) rotary actuators in a quarter scale rotor blade. The actuators have been integrated into the rotor blade as structural elements controlling blade twist. The basic concept of the RRB is illustrated in Figure 122, which shows an actuator assembly in red located inside the spar near the root of the blade. The passive torque tube in blue transmits the torque from the actuator assembly to the tip of blade causing the blade to twist. A lightweight spring mechanism, the Strain Energy Shuttle, provided an energy storage element between the SMA actuator and the passive torque tube. The Strain Energy Shuttle reduced the actuator system weight by half. Figure 123 shows the actuator system before assembly in the rotor blade. In 2007 the actuator has been tested in the V/STOL Wind Tunnel using a ¼ scale three blade hub assembly mounted on the Boeing Advanced Rotor Test Stand. The wind tunnel test was a high-fidelity assessment of the SMA actuator. It represents one of the first attempts to incorporate SMAs into an actuator which provides more than 60 in-lb of torque and 30 in-lb of energy and is able to withstand a rotor environment. The actuator provided approximately 250 twist transitions during 75 hours of testing with no loss of performance or operational anomalies.

(a)   (b)
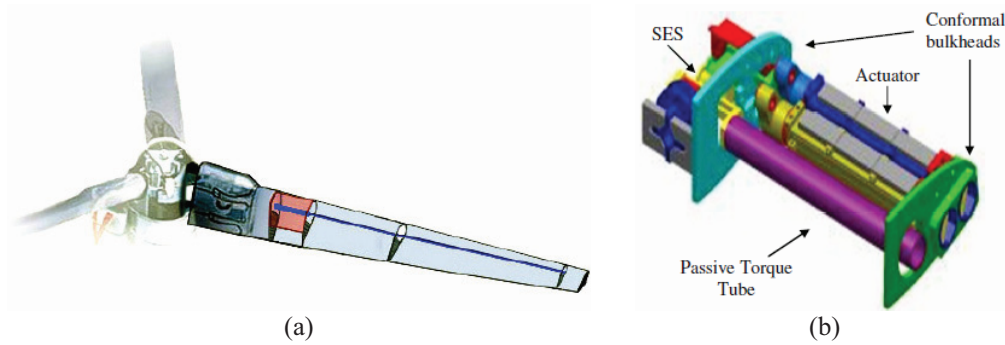
Figure 122: Reconfigurable Rotor Blade (RRB) program: (a) blade system showing placement of actuator system (red region) at base of rotor, b) schematic of actuator system, including antagonistic actuators (blue and yellow), passive torque tube (purple), and strain energy shuttle (SES). [126]
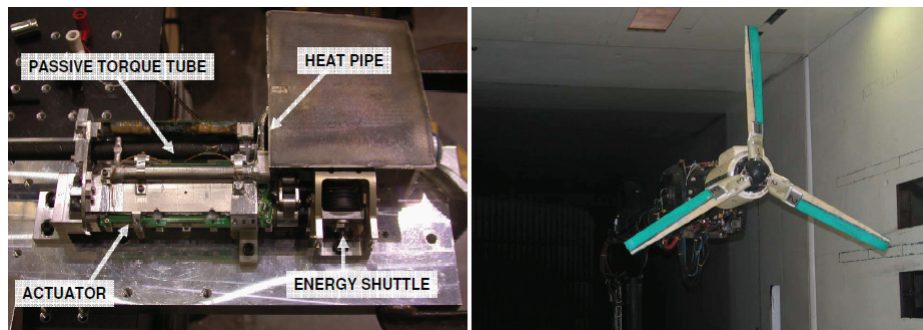
Figure 123: Reconfigurable Rotor Blade (RRB): actuator system prior to installation (left) and ¼ scale rotor blade in Boeing V/STOL Tunnel (right). [126]

Chord morphing over a blade section has been studied by **<u>Leon & al.</u>** [136], demonstrating the feasibility of a Static Extended Trailing Edge (SETE) constituted by a rigid plate able of coming out of the airfoil (Figure 124).

(a)   (b)
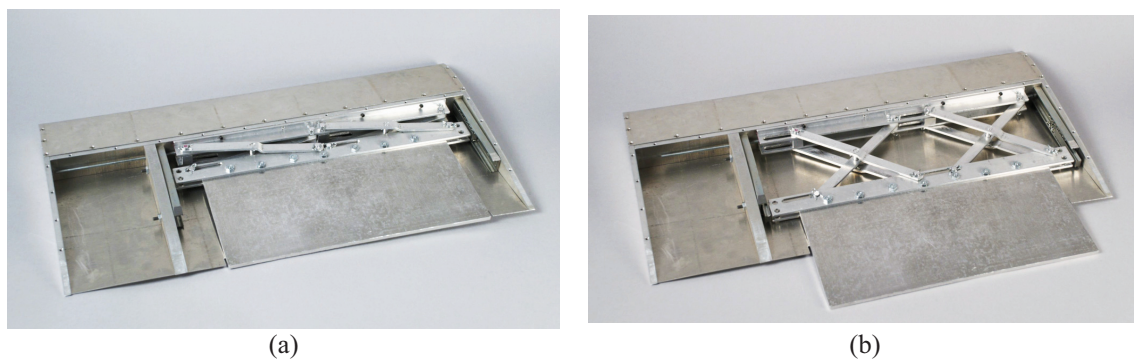
Figure 124: X truss commanding the SETE, in (a) fully retracted and (b) fully extended configuration. [136]

To improve lift coefficient of a blade airfoil, also Miniature Trailing-edge Effector (MiTE) have been considered by **<u>Thiel & Lesieutre</u>** [141] (Figure 125). A MiTE is an active Gurney flap (a small tab on the lower surface of the airfoil near the trailing edge) which, when deployed perpendicular to the flow, increases the maximum lift coefficient

of an airfoil section [142]; in this study, a bimorph actuator was couples with the proposed proof-of-concept prototype.

(a)   (b)
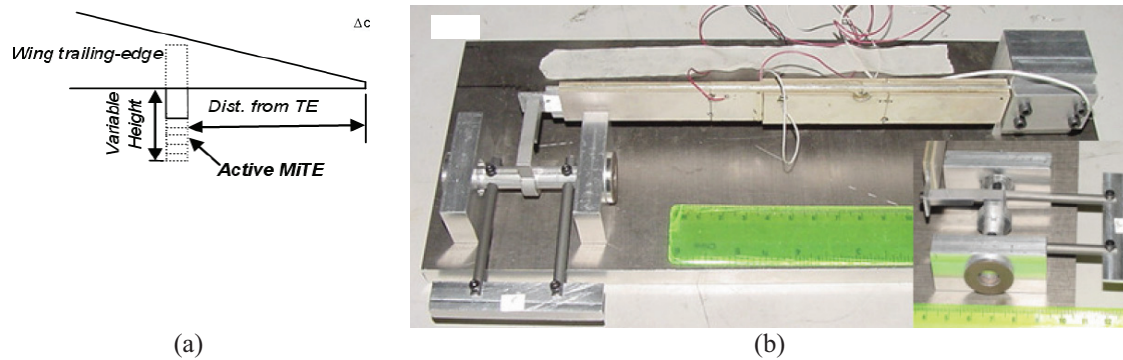
Figure 125: MiTE flap: (a) schematic and (b) experimental prototype. [141]

Also variable span has been studied by **Prabhakar & al.** [143], actuated by centrifugal force: a scaled prototype has been built (Figure 126) which upon RPM increase of the main rotor undergoes span morphing accordingly (the amount can be calibrated during the design phase).
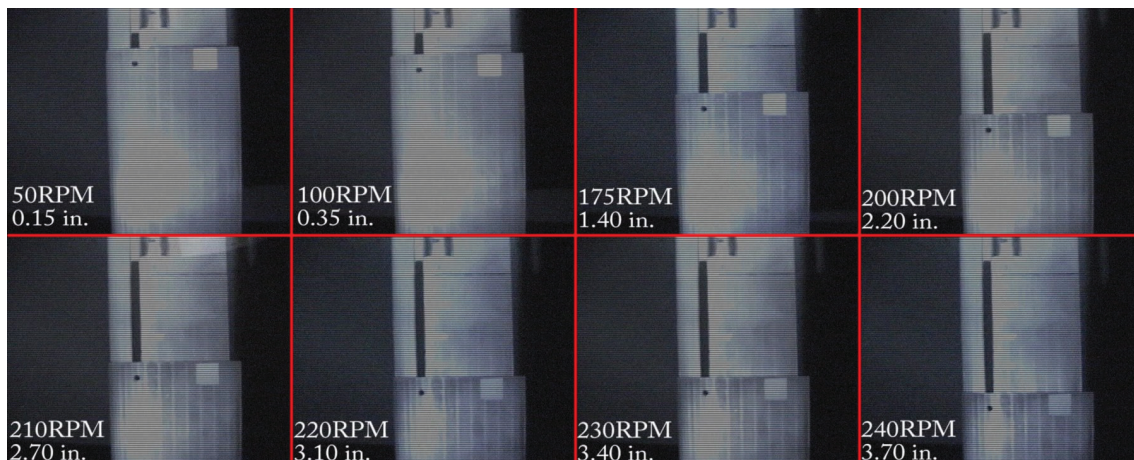
Figure 126: Variable span rotor blade actuated by variable RPM. [143]

More than any other system, the structural, mechanical and aerodynamic complexity and the interdisciplinary nature of rotorcraft offer numerous opportunities for the application of smart materials with the potential for substantial payoffs in system effectiveness.

Currently, considerable research is focused on the application of smart-structures technology to rotor systems to improve their performance and effectiveness. Three types of smart-rotor concepts are under development: leading- and trailing-edge flaps actuated with smart material actuators, controllable camber/twist blades with embedded piezoelectric elements/fibers, and active blade tips actuated with tailored smart actuators

(Figure 127). For flap actuation, actuators range from piezobimorphs [144, 145], piezostacks [146-150], and piezoelectric/magnetostrictive-induced composite coupled systems [151-158] (Figure 128 and Figure 129).
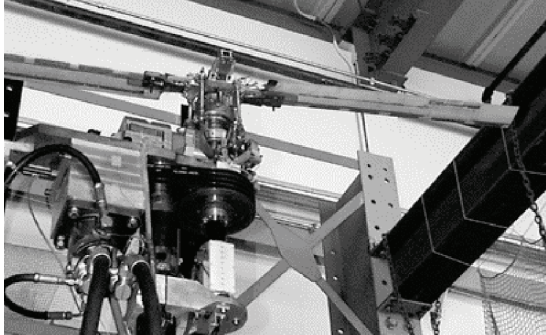
Froude-scale rotor model (6 ft diam) on hover tower with piezobimorph-actuated flaps.
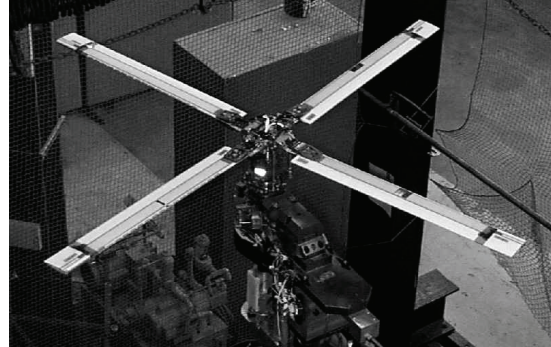
Smart tip rotor model (diam 6 ft) on hover stand, actuated with composite bending-torsion coupling and piezos.

Figure 127: Smart rotor development at Alfred Gessow Rotorcraft Center. [159]
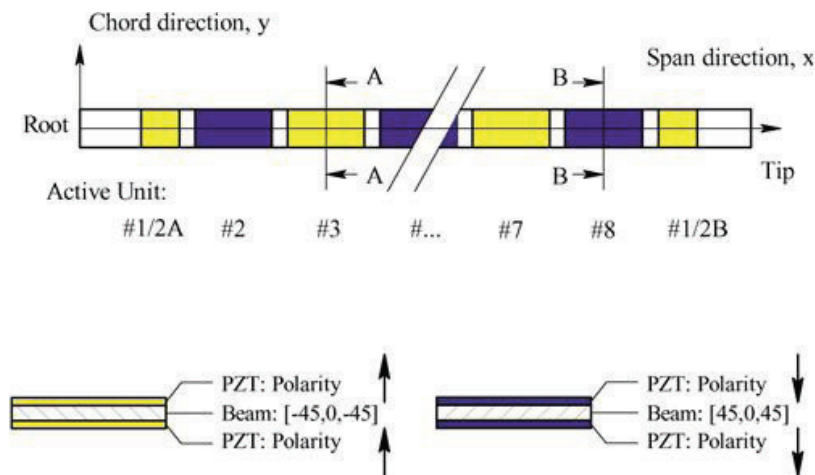
Figure 128: Bending-twist coupled actuator beam active twist concept. [151]
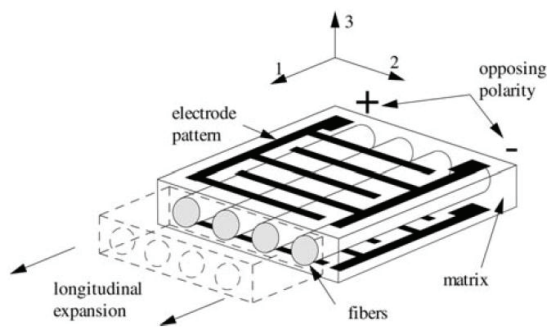
Inter-Digitated Electrode Piezoelectric Fiber Composite (IDEPFC) schematic. [154]
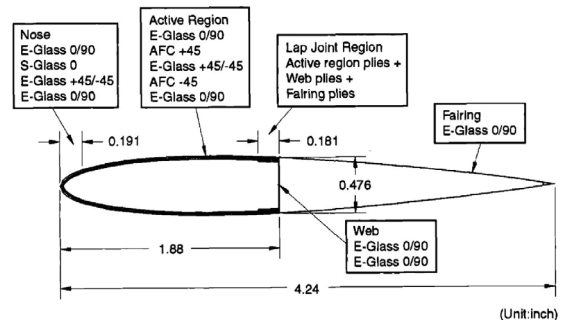
NASA/ARMY/MIT Prototype blade schematic. [156]

Figure 129: Active fiber composite rotor blade. [151]

Camber variation of the blade airfoil (conformable airfoil), instead, has been investigated by **Gandhi & al.** [160] as an alternative to trailing-edge flaps used for active helicopter vibration reduction through high-frequency changes in camber (Figure

131). Piezostacks were adopted as actuators of a chord-wise series of compliant-mechanism units (Figure 130) constituting the morphing blade; a trailing-edge deflection of 6.0 mm (a 4.6-deg equivalent trailing-edge flap angle) were predicted, resulting in a lift increase of 17–22%.
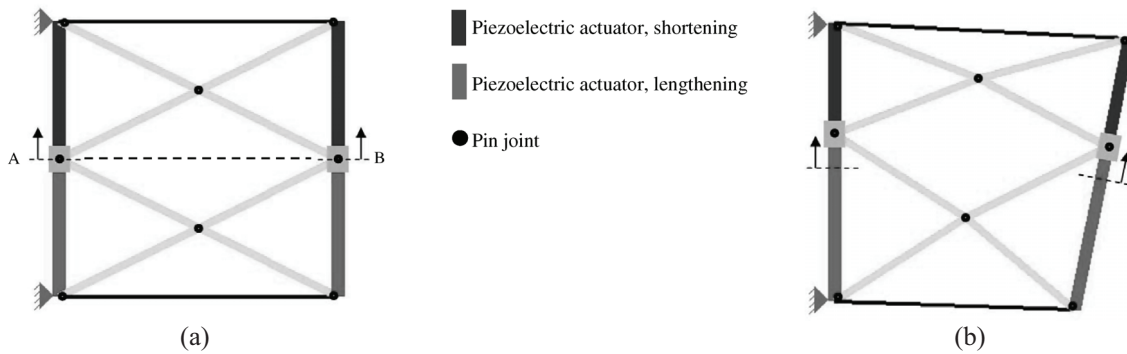
Figure 130: Compliant-mechanism units: (a) rest and (b) actuated configuration. [160]
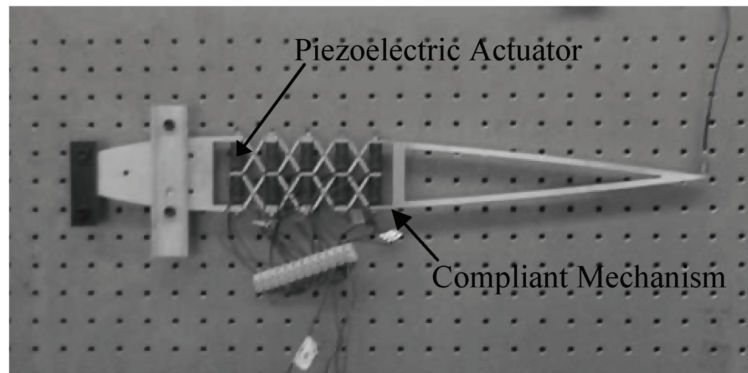
Figure 131: Assembled compliant blade prototype with piezostack actuators. [160]

A TWIstable Section Closed by Actuation (**T.W.I.S.C.A.**) concept has been developed jointly by DLR and ONERA for the Active Twist Blade (ATB) project [161].
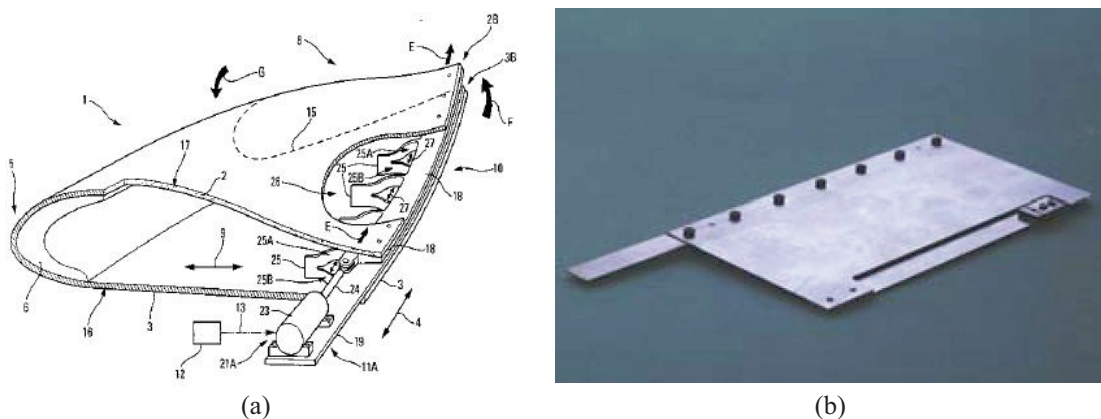
Figure 132: TWIstable Section Closed by Actuation (TWISCA) active twist rotor concept. [161]

This concept utilizes the warp-twist coupled behavior of beams to produce the twist of rotor blades and is intended for high frequency, low amplitude twist changes of the

beam. The concept utilized an open section spar at the leading edge of the blade (Figure 132a). A mini-prototype model for this concept was developed which utilized a PZT actuator at the trailing edge (Figure 132b). This model was able to produce a tip twist of approximately 0.7 degrees for an input voltage of almost 800 V.

Boeing's **Smart active rotor**, with piezoelectric actuated blade flaps (Figure 133), was tested in wind tunnel at NASA's Ames Research Center in 2008, demonstrating a more than 80% reduction in vibration and the potential for zero vibration at the hub [162].

Figure 133: Boeing's Smart Rotor with piezoelectric actuated on-blade flaps. [162]

Epps & Chopra [163, 164] systematically investigated the development of an SMA-actuated trailing-edge tab for in-flight blade tracking (Figure 134). This wing section was tested in the open-jet wind tunnel, and tab deflections of the order of 20 deg were obtained at a speed of 120 ft/s. This concept appears promising for full-scale rotor tracking: **Singh & Chopra** [165] improved this design and successfully tested it in the wind tunnel for a repeatable open-loop and closed-loop performance.
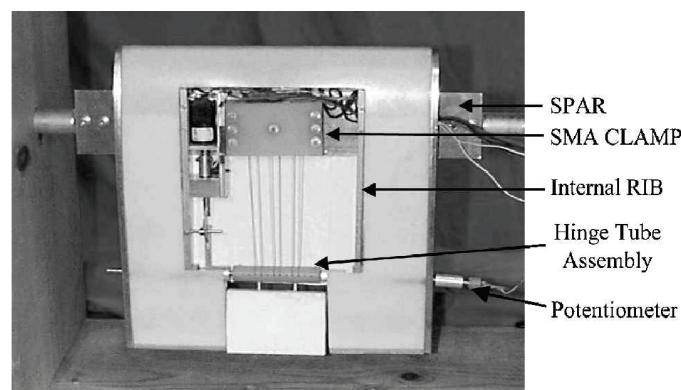
Figure 134: Blade tab actuated with shape memory alloys. [164]

Ameduri et al. [166], within the European "Friendcopter" project, studied how to achieve blade twist through a SMA based device suitably integrated along spanwise direction (Figure 135). A max angular rotation of 6 deg was reached on an experimental prototype, with a transmitted corresponding moment of 21.6 Nm.

(a) (b)
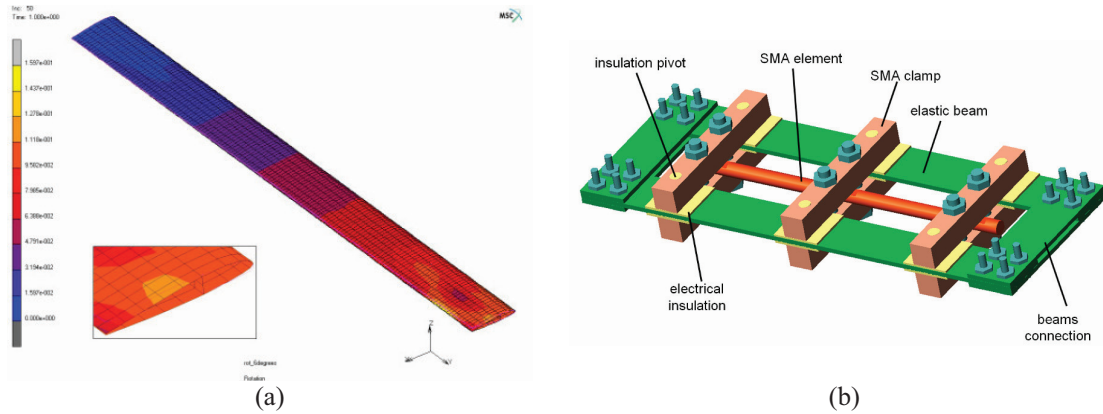
Figure 135: Active blade twist actuated with an integrated spanwise SMA: (a) FE blade twisting simulation (contour of rotation angle) and (b) torque demonstrator sketch. [166]

The Boeing Company has been actively developing a robust solid state Active Hinge Pin Actuator (**A.H.P.A.**) that can reliably apply high torque and angular displacement with a low space, weight, and power burden. It uses Shape Memory Alloy (SMA) technology adapted and developed into a solid-state actuator [167]. Previous research has shown that small tabs on the rotor blades can reduce blade-vortex interaction (BVI) noise; however, these tabs also increase drag and decrease overall performance. The ideal solution is to integrate deployable tabs on the rotor blade that can be extended when quiet operation is desired and stowed when they are not needed.

(a) (b)
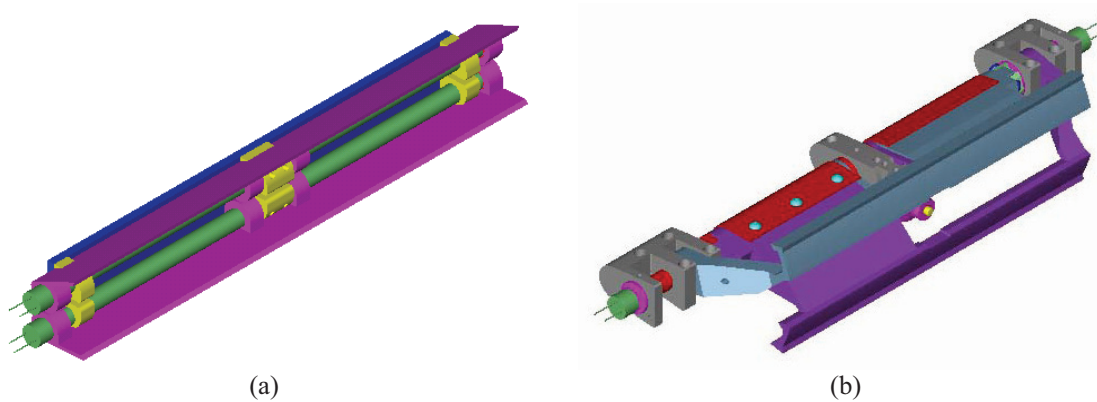
Figure 136: Active Hinge Pin Actuator (AHPA): (a) two torque tubes solution that each control one flap, and (b) double acting hinge. [167]

This application demonstrates the integration of a compact, low-cost, reproducible, rugged and efficient torsional actuator that can survive the harsh rotor blade

environment. An AHPA was developed that meets the displacement, force, and frequency requirements of a BVI noise reduction tab within acceptable weight and size limits. Two deployment device configurations were built and tested in both a centrifuge and 2D wind tunnel (Figure 136 and Figure 137).

<div align="center">(a)   (b)</div>
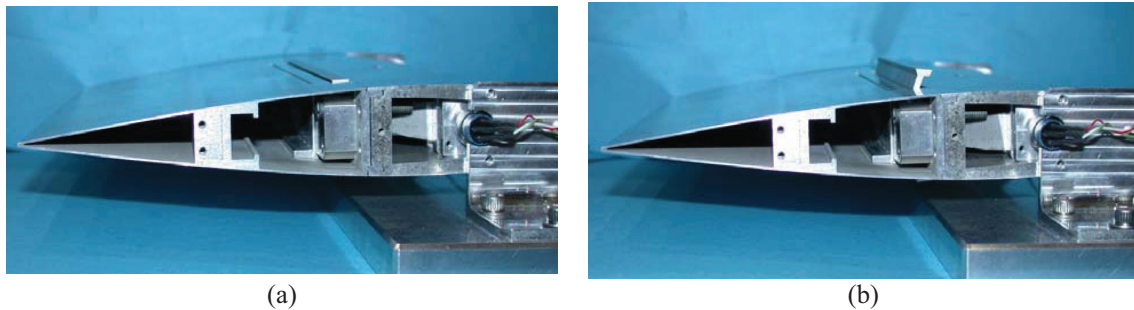
Figure 137: NACA0015 Blade Section with Integrated Double Acting Hinge: (a) stowed and (b) deployed. [167]

The **FlexSys Inc.** [50] variable geometry leading edge for rotorcraft creates a seamless upper surface and has a sliding joint on the lower surface (Figure 138). The structure is made of Titanium and is capable of 10 deg LE droop at once per rev. The compliant system is designed to withstand air loads and inertial loads (600gs) for 220 million morphing cycles. This technology enables the delay of dynamic stall on the retreating blade and requires 126 Watts/ft span with a weight of 4.3Lbs/ft.

Figure 138: FlexSys Adaptive Leading Edge for Rotorcraft (patent pending). [50]
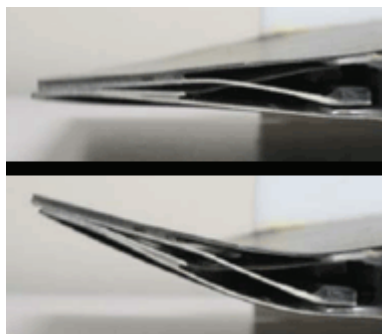
Figure 139: FlexSys Adaptive Trailing Edge for Rotorcraft (patent pending). [50]

Instead, the FlexSys variable geometry trailing edge for rotorcraft (Figure 139) is capable of 1 cycle/rev large deflection for cyclic control and 5 cycles/rev for vibration control. The 10% chord FlexSys compliant flap has equivalent aero performance as a 15% conventional flap and consumes 20% less power than a conventional TE flap. These benefits give FlexSys the technological edge for rotorcraft active blade technology.

Daynes & al. [168] from University of Bristol presented the design and wind tunnel testing results of a full scale helicopter rotor blade section with an electromechanically actuated bistable trailing edge flap, developed under the Intelligent Responsive Composite Structures (IRCS) program. The bistability of the flap derives from the use of bistable composite material. The flap system is designed to change between these two positions when the helicopter moves between hover and forward flight conditions. The bistability of the flap system means that the electromechanical actuator is only required to do work to transit between these two stable states, not to maintain the states. The use of bistable composites as aerodynamic surfaces was proven to be possible, and stable trailing edge deflections of 0 deg and 10 deg were achieved (Figure 140). The wind tunnel model clearly demonstrated a significant change in lift coefficients compared to the standard airfoil section when the flap was deflected. The mass increase for the integration of the actuated bistable flap system was approximately 6.3 kg per 1 m span flap of standard NACA 24016 rotor blade section, with the active components of the actuator itself weighing 2.5 kg. The flap system was able to actuate within 0.05 s. The proposed flap design may also have dynamic applications for rotorcraft vibration/noise reduction which have yet to be explored.

(a) (b)
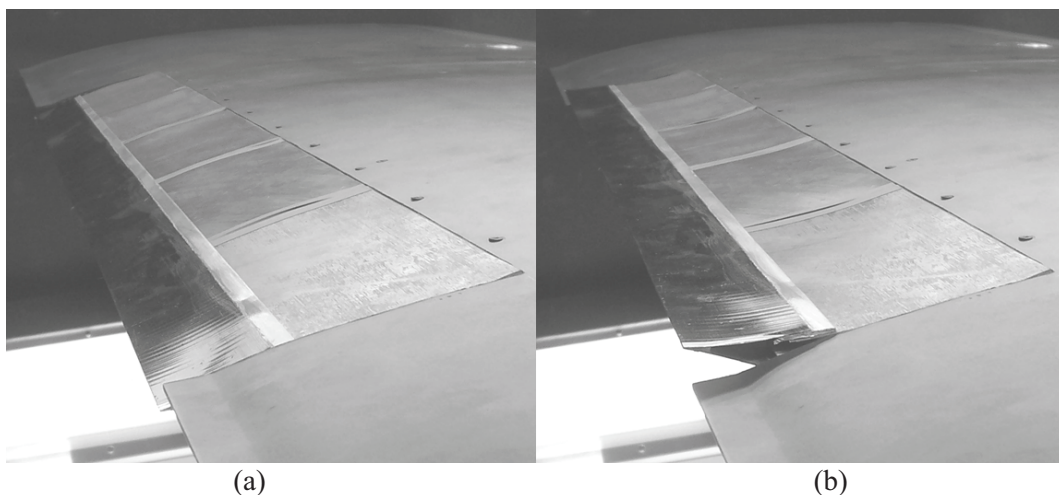
Figure 140: IRCS bistable airfoil when (a) flap at 0 deg and (b) flap at 10 deg. [168]

Space applications

Morphing applications are of great interest also in the space field especially due to size and volume constraints at launch. For this reason, morphing technologies are mainly focused on deployable structures, with particular reference to inflatable structures and trusses.

A comparison of several inflatable structures for space applications can be found in **Bell** [169]. Pressurized "soft" membrane structures can offer important advantages for space habitat applications (volume-efficient launch packaging, large diameter interior volumes that increase as a function of the radius squared rather than relying upon linear extension, flexible conformability for use as connectors between imperfectly aligned "hard" modules). Inflatable modules also present certain special constraints and requirements compared with conventional hard shell structures. One of the most significant of these relates to problematic pre-integration of hardware and utility systems, requiring that hook-ups be undertaken manually following inflation by flight crew. Some innovative concepts developed by Sasakawa International Center for Space Architecture (**S.I.C.S.A.**) are shown in Figure 141.
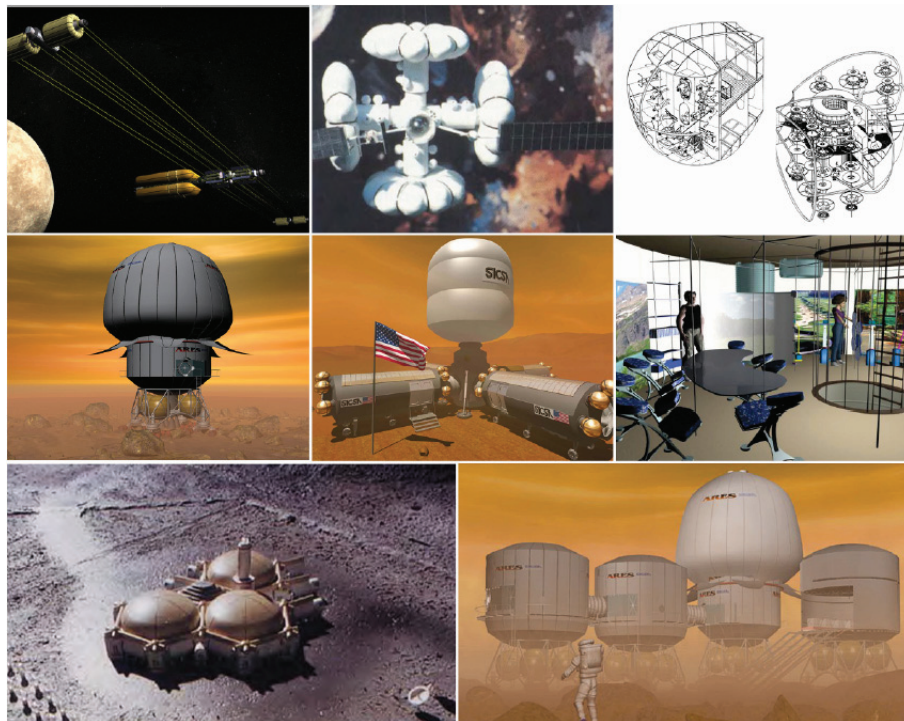
Figure 141: SICSA's Inflatable Structures concepts. [169]

Owens & al. [170] at the Air Force Institute of Technology (AFIT) developed the Rigidizable Inflatable Get-Away-Special Experiment (RIGEX) to demonstrate the feasibility of using rigidizable, inflatable, technology for space structures.

RIGEX autonomously deployed and captured the structural characteristics of three rigidizable, inflatable tubes while in the space environment: the three identical tubes were made from carbon fibers in a thermoplastic resin (Figure 142). RIGEX was designed to fly in the DoD's Space Test Program's Canister for All Payload Ejections (CAPE) container within the Space Shuttle Orbiter's payload bay. RIGEX completed successfully its mission on March 26, 2008 after being in orbit for 16 days.

It has been designed to test the deployment and structural characteristics of three 20-inch long rigidizable inflatable tubes. Each tube is composed of a three ply carbon fiber material in a proprietary polyurethane resin (called by L'Garde Inc. as L5). The L5 material is designed to remain rigid while below a specified glass transient temperature (Tg) and once heated above Tg the material softens. For RIGEX, the Tg value was set at 125ºC. To demonstrate this technology on orbit, ovens successively heated each tube above Tg. The tubes were then inflated, cooled (hardened), vented and excited using piezoelectric patches. The patch, along with a tri-axial accelerometer mounted at the free end of the cantilevered tube, provided on-orbit modal characterization data. Digital cameras provided photographic documentation of the deployment process.

(a)   (b)
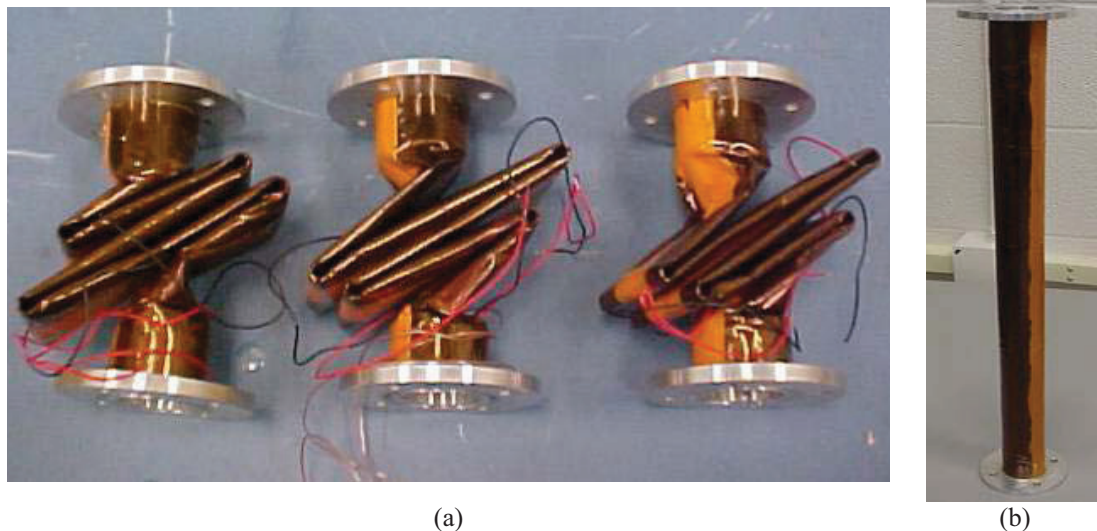
Figure 142: Inflatable, Rigidizable tubes: (a) folded for flight and (b) deployed configuration. [170]

<u>Sofla & al.</u> [171] developed a rotational joint for use in shape morphing. The joint is a chain mechanism comprising up to six pivoted linkages that provide a compact mechanism for the connection of up to six structures at a node (Figure 143).

The joint mechanism has a total of three degrees of freedom leading to interrelationship of the six rotation angles at the pivots: by knowing three of the angles as input, the other three rotation angles are determined. Twenty different arrangements for the joint

mechanism are possible for any set of three known angles, making the joint capable of having several different shapes. The hexa-pivotal joint is easy to manufacture and can be fabricated to the desired size and strength. Having no offset between the links is another advantage of the joint which makes it easily programmable for precise positioning applications (Figure 144).

(a) (b)
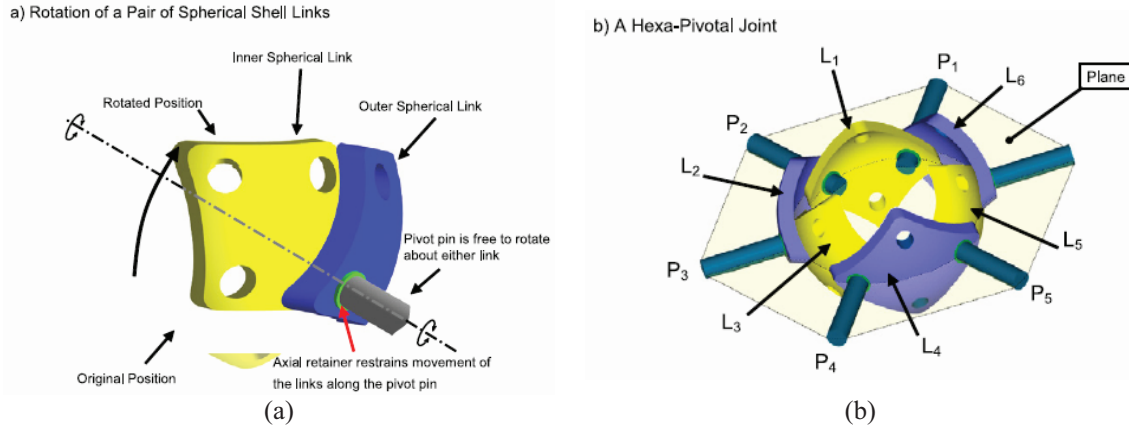
Figure 143: Rotational joint scheme: (a) two concentric spherical links detail and (b) a hexa-pivotal joint consisting of six spherical links. [171]
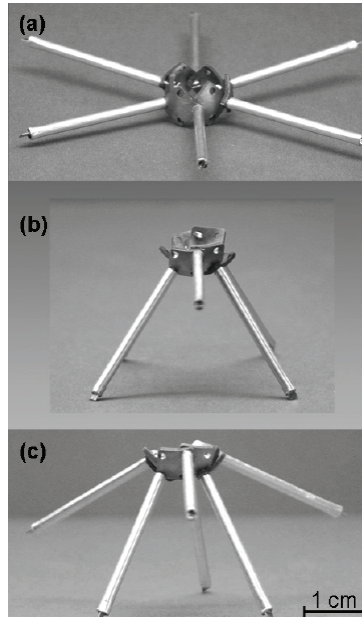
Figure 144: Three symmetric arrangement of a hexa-pivotal joint. [171]

Many other deployable truss-like structures useful for space applications have been studied by **You** [172] (mostly inspired by Japanese origami) and **Ramrakhyani** [173, 174] (Figure 145).

The structural concept underlying the latter approach is a compliant cellular truss, with tendons used as active elements capable of achieving continuous stable deformations over a large range of aircraft shapes. The members of the truss are connected through

compliant joints such that only modest bending moments can be transmitted from one member to another. Actuation is achieved by pulling on one set of cables while controlling the release of another, so that the stability of the structure is maintained in any intermediate position. The tendon-actuated compliant truss can be made to behave locally, and temporarily, as a compliant mechanism, by releasing appropriate cables. As a result, in the absence of aerodynamic forces, the structure can be morphed using relatively low forces.
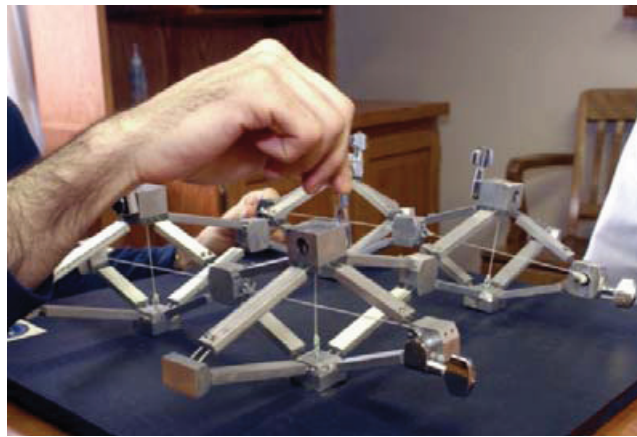
Figure 145: Compliant cellular truss prototype from Penn State University. [173]

Also in this field, the adoption of smart materials is considered mandatory to overcome many of the limitations (weight, size, complexity, etc.) of traditional approaches based on electromechanical mechanisms and mechanically expandable booms.

DARPA and NASA have recognized ultra-lightweight shape memory Rigidizable Inflatable (**R.I.**) structures as an enabling technology for future space and interplanetary missions requiring large space systems [175]. The enabling feature is the ability of the material to be compacted very tightly; extremely large structures can be stowed into existing launch vehicles or smaller launchers. The objective of the RI structures is to achieve the advantages of both high strength and high compaction of mechanical and inflatable structures respectively. SMP technology, a branch of the RI structures, provides a means of reconfiguration at the material level similar to inflatable structures, capable of high compaction; and at the same time offers high stiffness similar to state-of-the-art rigid composite structures. SMP structures permit tight packing by altering the stiffness of the material; thus, reconfiguration is at the material level by folding it. In other word, structure can be reconfigured for stowage and deployment without additional hardware such as hinges or rotational joints. Figure 146 shows a deployable Shape Memory Polymer composite truss developed at **ILC Dover**.
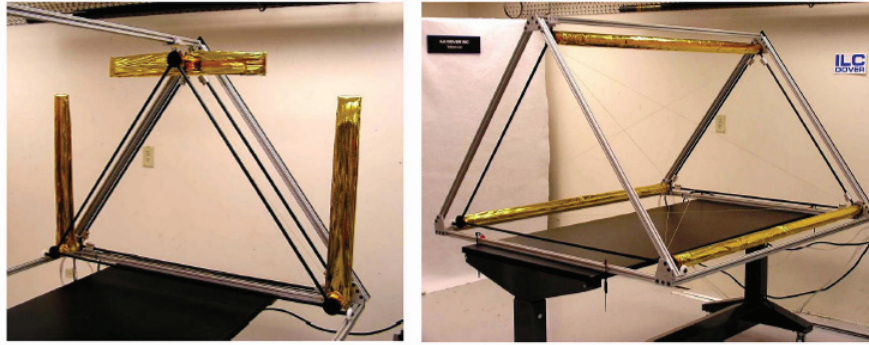
Figure 146: Shape Memory Polymer composite truss in packed (left) and deployed (right) configurations. [175]

The development of structures made of cold-hibernated elastic memory (CHEM) technology is one of the most recent results of the quest for simple, reliable, and low-cost self-deployable structures. These lightweight foam structures are deployed via shape memory and the foam's elastic recovery. The key to this technology is the use of shape-memory-polymer material in open-cell foam structures or sandwich structures made of shape-memory-polymer foam cores and polymeric laminated-composite skins. **Sokolowski & al.** [176] presented an overview of the current applications of CHEM technology for space deployable structures and a comparison among mechanical, inflatable, and elastic memory-deployable structures. In particular, an application for improving solar-sail technology has been studied. This advanced membrane concept provides a simple end-to-end process for stowing, deployment, and rigidization and avoids the complexities by eliminating booms, deployable mechanisms, launch restraints, inflation, and control systems.

Instead, an application of SMAs for the deployment of membrane mirrors for spaceborne telescopes has been illustrated by **Polard & Jenkins** [177].

Morphing investigations more similar to aeronautical ones regard the development of variable geometry decelerators for planetary entry trajectory modulation, as from **Kwok & Pellegrino** [178].

Entry trajectory can be significantly improved to reduce entry range errors and alleviate deceleration peaks if the hypersonic aerodynamic performance of the decelerator is tunable during flight. Two structural concepts featuring a segmented shell and a sphere-cone corrugated surface have been demonstrated (Figure 147) to obtain a variable cone angle change of 10 deg; a foldable bar structure (Figure 148) has been adopted for actuation. Structural analysis of a 4.5 m diameter decelerator based on the corrugated shell concept predicts a peak stress of 540 MPa under the elastic deformation resulting from a 7 deg cone angle reduction and 3 deg increment, plus peak pressure loads typical

of a Mars entry mission. The total radial actuation force reaches a maximum value of 134 kN when the cone angle is maximised.

<table>
<tr><td>(a)</td><td>(b)</td></tr>
</table>
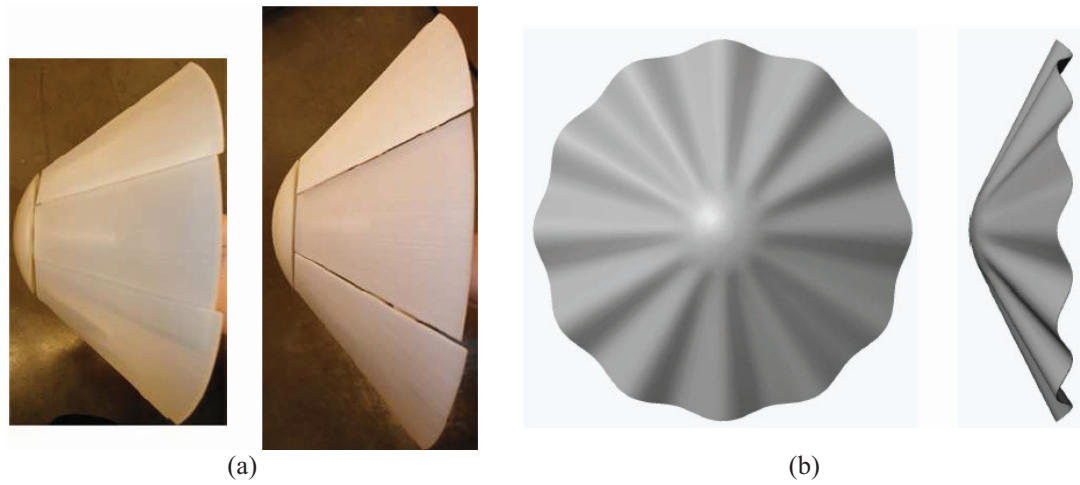
Figure 147: Aeroshell concepts: (a) segmented and (b) corrugated surfaces. [178]

<table>
<tr><td>(a)</td><td>(b)</td></tr>
</table>
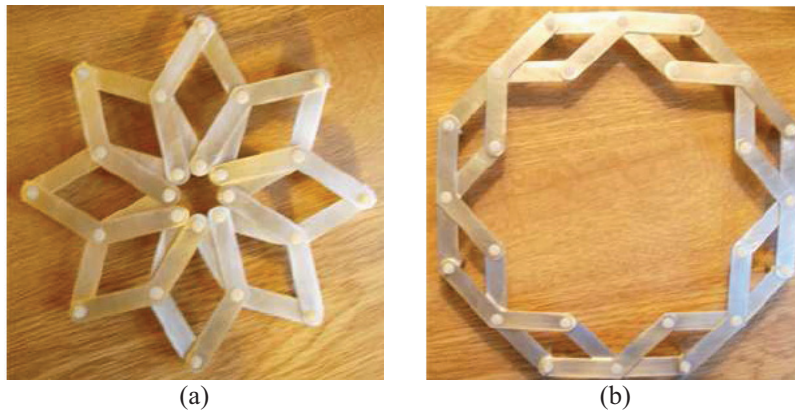
Figure 148: Aeroshell actuation foldable bar structure: (a) retracted and (b) expanded configuration.

[178]

Finally, some early studies begin to appear for aircrafts having adaptive wings thought as automatic robots to be sent to other planets, like the "Daedalon" developed by **Lafleur & al.** [179] and sponsored by N.I.A.C. (NASA Institute for Advanced Concepts). The morphing wing concept is here assumed to integrate the re-entry phase into the Martian atmosphere with the flight, before touch-down: in this manner, in addition to increase the aerodynamic efficiency at different stages of descent, it is possible to avoid the typical constraints associated with packaging of the wings.

The mission (Figure 149) provides that, once the initial more intense descent into the atmosphere finishes, Daedalon can get rid of its thermal shield and starts its wing morphing (in a continuous manner, in a 10 minutes time range) from an initial configuration suited for the high initial speeds, up to a final configuration suitable for propelled flight in the Martian atmosphere at Mach 0.7 and 500 m altitude: in this way it

is possible to search for the most suitable landing site (it is expected a flight range of 54 minutes). According to this study, the morphing wing is operated through spars (six along the wing span and two along its longitudinal axis; other four spars go down, to support the thermal shield) able to rotate and having telescopic capabilities (Figure 150); the wing is not characterized by surfaces that can deform, but is also assuming telescopic or sliding panels that can overlap or unfold.

Figure 149: Hypothetical mission profile for Daedalon during descent on Mars. [179]
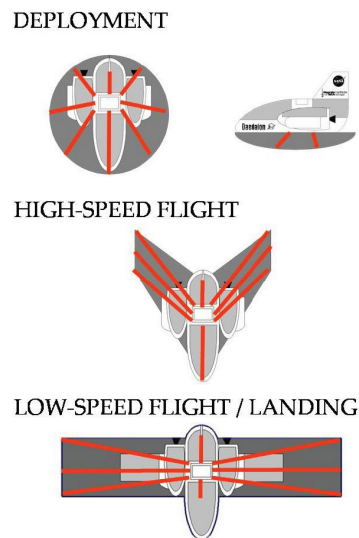
Figure 150: Morphing wing concepts for Daedalon. [179]

5 MORPHING SKINS

Historically, the wing skin on early aircraft was made of fabric; however, with increasing flight speeds and hence aerodynamic loads, stiffer and more robust materials were needed. Today, the majority of aircrafts uses stiffened metallic (typically aluminium alloy) panels as an outer skin, although high specific strength and stiffness fibre reinforced polymer composites in the form of glass or carbon fibre/epoxies are increasingly being employed. The stiffeners are usually Z or T-shaped. The panels are supported by ribs in the chordwise direction and by spars in the spanwise direction. Propellers or rotor blades often include a sandwich structure with a honeycomb core and metallic or composite faces. While most of the axial and bending loads are counteracted by the stringers, ribs and spars, the skin needs to withstand a combination of tensile, compression and shear forces (semi-monocoque structures i.e. stressed skin concept) and needs to be able to distribute the aerodynamic pressure loads to the underlying structure. This highlights the difficulties inherent in replacing the current stiff and strong skins with a more flexible solution, needed for morphing applications.

A morphing skin can be envisaged as an aerodynamic fairing to cover an underlying morphing structures. In this case, the skin must be able to withstand a change in shape in at least one of the following two ways: change in camber or in surface area. This shape change can be instigated either by external or integrated actuators, which in the latter case would make the skin self-actuating or active (and potentially "smart"). An adaptive structure can be defined as possessing the ability to change shape whilst maintaining a continuous form, whereas a passive structure, such as a hinged aileron, has discrete components which move relative to each other. A smart structure is able to sense external stimuli (pressure, velocity, density or temperature change), process the information and respond in a controlled manner, in real-time.

The major problematic, when a morphing skin is chosen, is its smoothness. In literature, many investigated morphing solutions exhibit a skin with many wrinkles: however, from an aerodynamic point of view, this can represent a source for undesired drag increase (which could also cause the morphing configuration to be less effective than a traditional one).

The morphing skin can be realized either by materials that exhibit specific properties or by means of innovative structural concepts. In this paragraph, a review of suitable materials, concepts and structures that can be used for a morphing skin are illustrated.

Morphing skins tailoring material properties

Elastomers (or rubbers) are a class of polymer with a low density of cross-links [180]. Hence they have the ability to undergo large elastic deformations without permanent changes in shape. However, the few cross-links give them a memory effect so that they return to their original shape on unloading [181]. Many studies mention elastomers as being a promising solution for morphing skins [181-183]. As an example, in the DARPA Smart Wing programme, a high strain-to-failure silicone skin was used [183]. The low tensile modulus of elastomers (~ 0.5 to 50MPa) makes them easily deformable up to 1000% (elongation at break) of their original length. At the same time, the load required is relatively low; tensile strength can have values up to around 50MPa [180]. Since the stress-strain curve of elastomers is non-linear, its modulus of elasticity varies with strain, strain rate and temperature. Below the glass transition temperature (T_g) polymers behave like glass and are brittle; above T_g they are in a rubbery state. Hence the T_g for useful elastomers to be used as stretchable morphing skins must be well below their operation temperature range. A further property exhibited in general by polymers is visco-elasticity, which means that when subjected to a load the strain does not occur instantly (i.e. the strain is time dependent) [180].

While these properties potentially make elastomers good candidates for flexible skins, they are unsuitable for carrying loads, which means that it would be difficult to design elastomeric skins that can sustain and transfer aerodynamic loads to the underlying structure [181]. At the same time, working against the strain of the material should be avoided as much as possible, since it is likely that it will induce fatigue problems as well as requiring excessive actuation power to hold the deformed skin in place.

Kikuta [13] is one of the few investigators that experimentally tested a few thermoplastic polyurethanes, co-polyesters and woven materials that are commercially available to investigate the materials' viability as morphing skins. According to the author's results, none of the selected materials satisfy all of the requirements of a morphing skin: a material that was able to strain and recover well was not able to carry a high load and vice versa. The best polymer tested was found to be Tecoflex® 80A (thermoplastic polyurethane). A suggestion was made to combine a material like Spandura® (woven material) with a polyurethane like Tecoflex® 80A, that way the high strength required would be achieved by the fibres and the elasticity by the polymer.

Auxetics are materials that have a negative Poisson's ratio: when stretched, they become thicker perpendicularly to the applied force (Figure 151). This occurs due to

their hinge-like structures which flex when stretched. Such materials are expected to have interesting mechanical properties such as high energy absorption and fracture resistance. Auxetics may be useful in applications such as body armor, packing material, knee and elbow pads, robust shock absorbing material, and sponge mops.
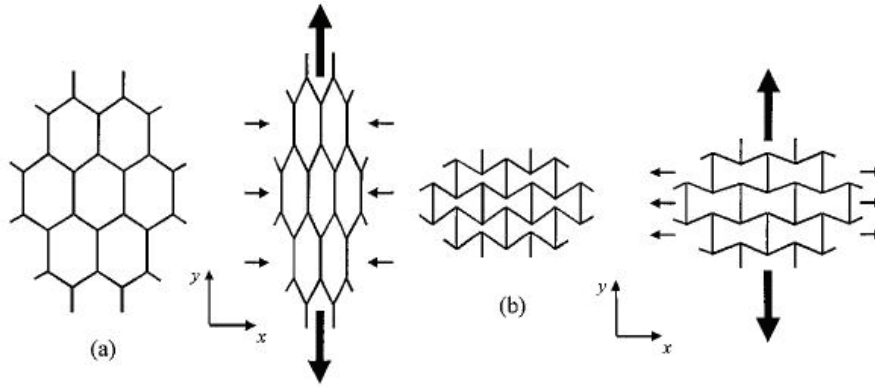
Figure 151: (a) Positive Poisson's ratio honeycomb; (b) Auxetic honeycomb.

Research on a morphing aerofoil concept using a hexagonal chiral honeycomb structure (a cellular network featuring a negative Poisson effect) was conducted by Bornengo & al. [184]. Finite element analysis (FEA) of a chiral honeycomb made from acrylonitrile butadiene styrene (ABS) plastic and used as concept for a Formula 1 car wing box predicted a trailing edge deflection of 5 mm due to the pressure distribution of the air flow. Wei & Edwards [185] looked at ways of making composite materials with auxetic inclusions in order to improve the low modulus of elasticity in auxetic materials.

Gandhi and his collaborators in many studies [186-189] suggest using zero-Poisson's ratio cellular structures as morphing skins. They present an analytical model and a FE model that shows that by using hybrid (negative and positive Poisson's ratio materials) and accordion cellular honeycomb cores, the Poisson's ratio is zero and hence would be ideal for morphing. Additionally these honeycombs give low in-plane and high out-of-plane stiffness.

A novel cellular platform, inspired by the amorphous silica configurations, has been investigated by Lira & al. [190] and called "SILICOMB". Their work was concerned with the investigation of the in-plane mechanical and dielectric properties of a novel centresymmetric cellular structure. Multiple geometry parameters to be used to design the honeycomb are identified and discussed.

Auxetic polymer foams appear to offer some potential for use as a "gap filling" material in a morphing application. Due to their low modulus they can be easily deformed whilst simultaneously expanding when elongated. An example would be to use such materials

between a hinged aileron and the main wing of an aircraft to maintain a smooth aerodynamic profile and minimise drag.

Multi-stable composites (Figure 152) could potentially be used for morphing skin applications. Multi-stability of thin laminates, a property usually considered unfavourable, is due to residual stresses forming during the cure cycle of a non-symmetric lay-up or due to Gaussian curvature effects. Generally bi-stable composites exhibit large deformations but only require low actuation forces. This makes them in the current form difficult to use as morphing skins, since aerodynamic loads may be greater than the forces needed to snap the laminates from one stable configuration to the other. However, there are still many phenomena related to these materials currently not clearly understood and object of researches, such as how different parameters (fibre angle, lay-up sequence, ply geometry) affect multi-stability and how they interact. Solving these questions may allow multi-stable laminates as a viable option for morphing skins.
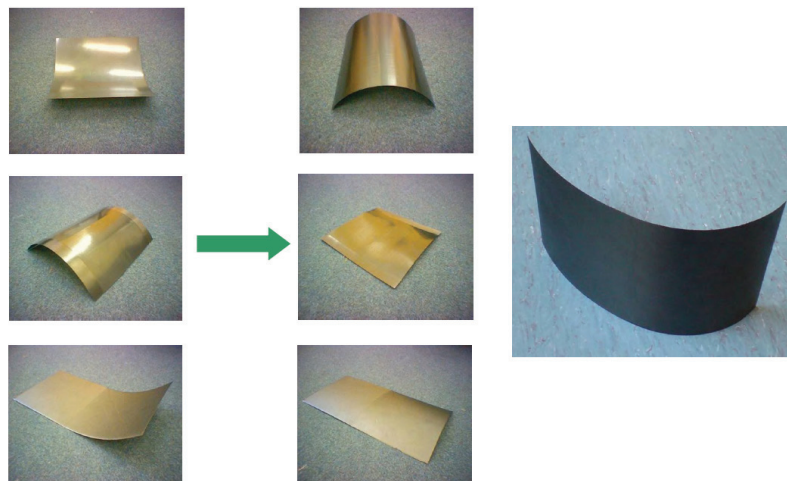
Figure 152: Multi-Stable Composite.

Great interest has been posed by the international scientific community on these materials, as illustrated by the works of Hyer [191-192], Kebadze & al. [193], Hufenbach & al. [194] and Iqbal & Pellegrino [195]. The research on multi-stable composite and its applications at the University of Bristol is documented for example in Weaver [196], Potter & al. [197], Mattioni & al. [198], who mentioned the use of snap-through buckling as a deployment mechanism in anisotropic composite structures.

Norman & al. [199] manufactured multi-stable corrugated panels made from copper-beryllium alloy via cold working. Bi-stable panels consisted of corrugated state and a coiled state parallel to the corrugations that occurs when the corrugations are pressed flat the panel. Tri-stable panels have two states where the panel is twisted along an axis

not aligned with the corrugations in two different directions and a coiled state like the bi-stable panels. Applications could include flexible display screens or roll-able keyboards, or adaptive wings/skin panels for UAVs and spacecrafts. Although these panels have been manufactured in metal, there should be no reason why similar multi-stable composite corrugated panels could not be made. Furthermore this work is interesting since it combines anisotropy and multi-stability.

Shape Memory Alloys (SMA) are metal alloys able to recover their original shape after large deformations [200]. Depending upon the alloy material properties and the external conditions, shape recovery can occur in two ways: Shape Memory Effect and Super-elasticity or Pseudo-elasticity. They will be discussed in great detail in the next Chapter. Some researchers have embedded SMA actuators in laminates to obtain self-actuating structures. So for example, Zheng & al. [201] embedded prestrained SMA TiNiCu wires into a glass/epoxy and a Kevlar®/epoxy prepreg. Dano & Hyer [202] attached SMA wires to a bi-stable composite plate to initiate snap-through phenomena. The wires could not be directly surface mounted but rather attached to supports in order have a larger moment arm. Barrett & Gross [203] embedded SMA wires in a very-low-modulus silicone matrix (no additional reinforcements were used). Cellular structures made from SMA have also been investigated by Shaw & al. [204].

In many applications SMAs are used as actuators of suitably designed morphing structures.

Shape Memory Polymers (SMP) are polymeric smart materials that have the ability to return from a deformed state (temporary shape) to their original (permanent) shape induced by an external stimulus (trigger), such as temperature change [200, 205].

In addition to temperature change, the shape memory effect of SMPs can also be triggered by an electric or magnetic field, UV light or a change in pH. As well as polymers in general, SMPs also cover a wide property-range from stable to biodegradable, from soft to hard, and from elastic to rigid, depending on the structural units that constitute the SMP. SMPs include thermoplastic and thermoset (covalently cross-linked) polymeric materials. SMPs are known to be able to store up to three different shapes in memory [200, 205, 206] (Figure 153).

Polymers exhibiting a shape memory effect have both a current (temporary) form and a stored (permanent) form. Once the latter has been manufactured by conventional methods, the material is changed into another, temporary form by processing through heating, deformation, and finally, cooling. The polymer maintains this temporary shape

until the shape change into the permanent form is activated by a predetermined external stimulus. The secret behind these materials lies in their molecular network structure, which contains at least two separate phases.
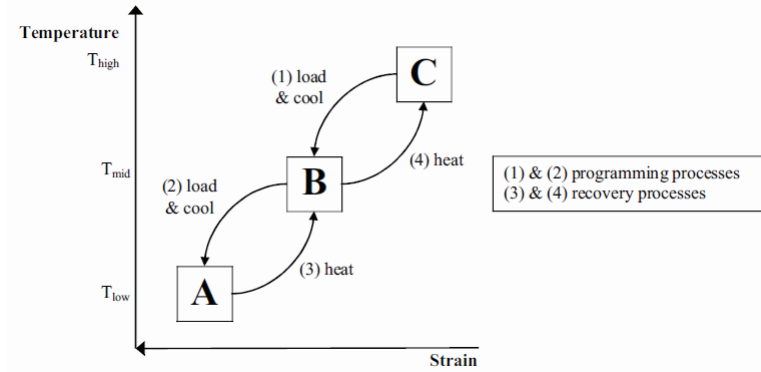
Figure 153: Temperature-strain diagram of triple-shape SMPs. [206]

SMPs can be elongated up to 1100% [207] and their mechanical properties can be varied over a wide range. Potential applications include: self-repairing auto bodies, kitchen utensils, switches, sensors, intelligent packing, tools and medical applications. However, not many applications have been implemented to date since only a few SMPs have been investigated and even less are available on the market.

SMPs may also be useful in the production of aircrafts which would morph during flight. In the previous paragraphs, it has been already illustrated the Lockheed Martin "Agile Hunter" which could drastically change its wing shape.

Perkins & al. [208, 209] gave an overview of research carried out by Cornerstone Research Group (CRG) [210], whose aim is to come up with a wing that can increase its lift by 80% and that can morph between different configurations within 1 second. Three main products have been developed, based on a fully-cured thermoset SMP that can change shape due to a thermo-molecular relaxation rather than a thermally-induced crystalline phase transformation as with SMA. The first product is Veriflex® which is the styrene based SMP itself (Figure 154): it was used as a skin material for a morphing aerofoil section. The second is VeritexTM (Figure 155), which is a composite that can be fabricated with nearly any fibre type and with Veriflex® as the matrix resin. And finally CRG's third product is a low-density foam based on Veriflex® called VerilyteTM (Figure 156). It could be used as core material in a sandwich structure that can be reshaped when soft at high temperature and carry out structural functions at low temperature. The method used by the manufacturer to heat the SMP is electrical resistive heating using nichrome wires.

Figure 154: Veriflex® honeycomb structure self-recovering under an IR heat lamp. [208]
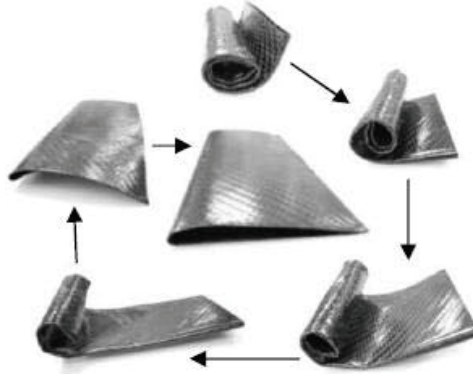
Figure 155: Veritex^{TM} aerofoil self-recovering from rolled state.
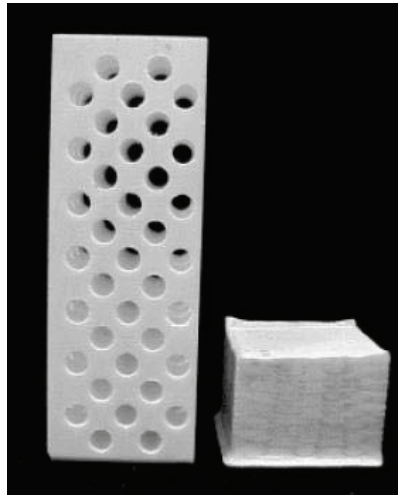
Figure 156: Verilyte^{TM}.

Keihl & al. [2] believe that SMPs are an attractive and promising solution for morphing skins since the multiple stable state abilities of SMPs allow them to easily change shape and once cooled to resist appreciable loads.

McKnight & Henry [212, 213] used SMPs to achieve variable stiffness materials for reconfigurable structures. In their first paper they design a laminate with constant and variable stiffness elements. The function of the constant stiffness elements is to carry the structural loads while the function of the variable stiffness element is to provide variable connectivity between the constant stiffness elements. In the structural mode, the variable stiffness elements rigidly connect the stiff elements which creates high stiffness (similar to traditional structural composites). In the morphing mode, the

variable stiffness material becomes soft leaving the stiff elements effectively disconnected. In this mode large axial, shear and bending deformations can be achieved (Figure 157). They used high yield spring steel for the stiff elements and a thin film polyurethane SMP (produced by Mitsubishi Heavy Industries., Diaplex 5510 [213]) for the variable stiffness elements to manufacture their samples. The key design variables were length and thickness of stiff elements, spacing of elements, thickness of variable stiffness elements, fraction of stiff elements within segmented layer and volume fraction of stiff elements.
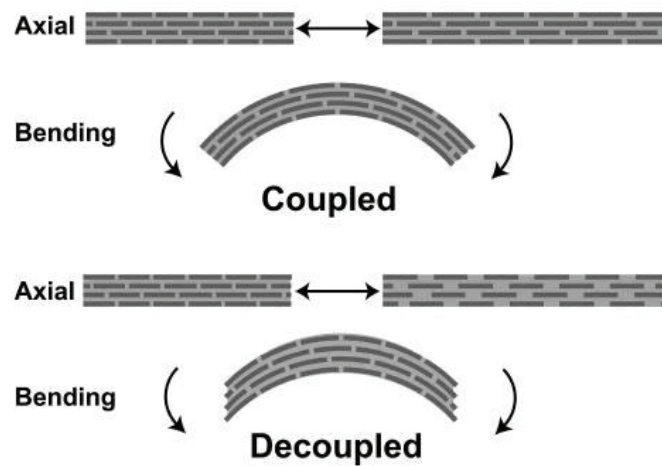
Figure 157: High stiffness (top) and low stiffness (bottom) structure. [212]

Tupper & al. [214] presented **elastic memory composite** (EMC) materials which are traditional fibre reinforced composites with a polymer resin that exhibits shape memory properties.

Lake & Campbell [215] list current available Tembo® SMP resins made by the US company Composite Technology Development (CTD) [216]: most of the research found in literature has been actually focused on the characterization and adoption of such material.

Another idea for morphing sking investigated in literature is given by the coupling of a flexible modified honeycomb substructure (f.i., an auxetic one), capable of handling out-of-plane loads without greatly adding to the in-plane stiffness, with a soft, thin silicone elastomer sheet with orthotropic carbon fiber reinforcement, called a **flexible matrix composite** (FMC), that could then be bonded to the substructure. Related research with FMC materials can also be found in [188]. Reinforcing carbon fibers controlling the major axis Poisson's ratio of the sheet would limit the FMC to 1-D shape change. The combined FMC sheet and honeycomb substructure form a complete

morphing "skin". Bubert & al. [217] investigated such a concept (Figure 158), evaluating a number of elastomers, composite arrangements, and substructure configurations which led to the selection of the most appropriate components. The developed prototype morphing skin demonstrated 100% uniaxial extension accompanied by a 100% increase in surface area. Results from out-of-plane pressure loading showed that out-of-plane deflection of less than 0.1-in can be maintained at various levels of area change under pressures of up to 200 psf.

(a)   (b)
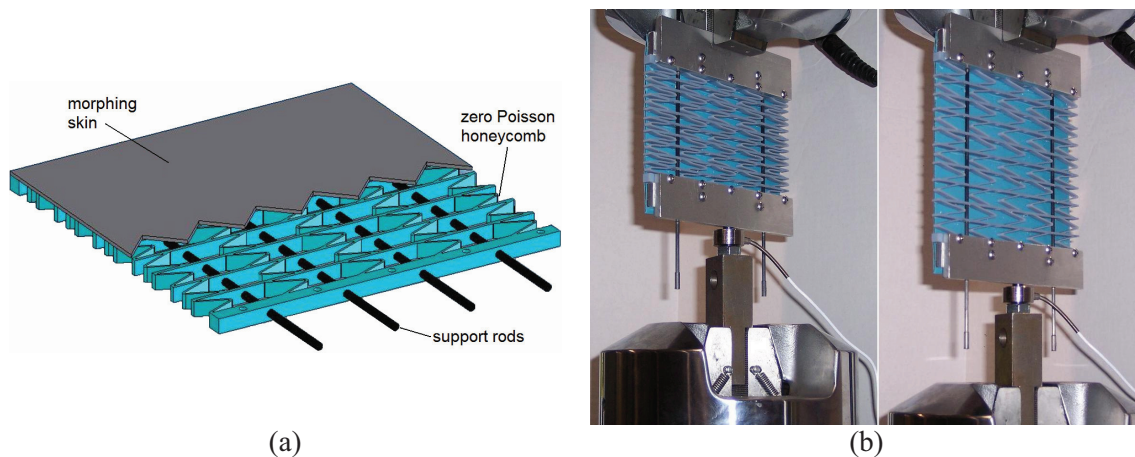
Figure 158: Reinforced morphing skin: (a) schematics and (b) experimental testing. [217]

<u>Metal Rubber</u> [219] is a broad, informal name for several conductive plastic polymers with metal ions, produced by NanoSonic Inc. in cooperation with Virginia Tech (Figure 159). This self-assembling nanocomposite is ultra flexible and durable to high and low pressures, temperatures, tensions, most chemical reactions, and retains all of its physical and chemical properties upon being returned to a ground state. The possible uses of such a product include superior body armor, durable electronic sensors, various aerospace-building materials, and alternate commercial building materials.
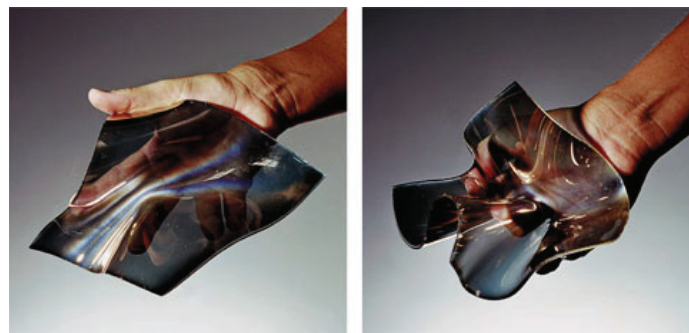
Figure 159: NanoSonic Metal Rubber. [219]

Morphing skins tailoring innovative structural concepts

Skins for morphing applications can also take advantage of innovative structural concepts to accomplish their objective of an adaptive, high strain capability together with structural load-bearing requirements.

Deployable structures allow big surface area changes which are desirable during change from high to low speed flight configuration (e.g. trailing edge flap deployment during landing). There are different classes of deployable structures: rollable, collapsible, foldable, inflatable and overlapping/stacked/nested structures; many examples have already been presented in the previous paragraphs.

In order to change the form of a structure with minimal actuation force it needs to be relatively soft in the direction the structure will be deformed in. This is where **stiffness tailoring** comes in useful i.e. designing the structure in such a way that low stiffness is present in the planes where deformation occurs and high stiffness is present in the planes where loads need to reacted against. Materials that exhibit such a radical variation in stiffness for two orthogonally opposed directions are called (extreme) orthotropic structures [182, 219].

Many researches are present in this field. Potter & Wisnom's [219] aim was to design and manufacture composite components with minimal torsional rigidity but with high bending stiffness for which a potential application would be a bearingless rotor hub for a heavy helicopter. Murray & al. [188] presented results from simple analytical and experimental analysis on reinforced elastomeric skin called flexible matrix composite membrane. They suggested using this composite as skins for one-dimensional wing morphing i.e. chord/camber or span morphing. Yokozeki & al. [182] demonstrated the use of corrugated composite sheets as a candidate material for flexible wing skins (Figure 160).
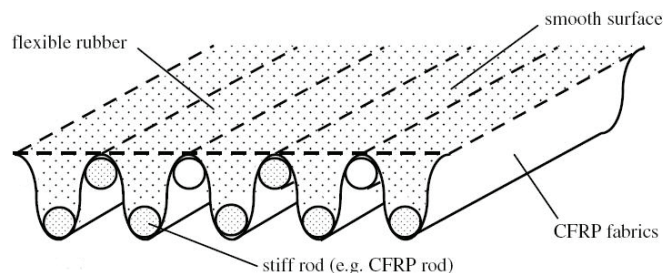
Figure 160: Reinforced corrugated structure with elastomeric surface. [182]

Butler [220] also picked up Yokozeki & al.'s idea by manufacturing and testing corrugated composite laminate specimen made from Kevlar/914 pre-preg.

Another structural concept, inspired by fish skins, is the idea of **segmented structures**. Ramrakhyani & al. [221] explained that due to the multiple discrete elements, called scales, which slide relative to each other, such a structure can deform (Figure 161).

This arrangement provides a high local lateral stiffness i.e. on their on own the scales are fairly stiff and hence can transmit the loads via myotomes (muscles) to the underlying structure (vertebral structure) while overall the structure can deform. However a significant aerodynamic concern is the non-continuous profile where the scales overlap. A detailed description of the morphology and functions of fish scales can be found in Varma [223], Long & al. [222] and Bechert & al. [224].
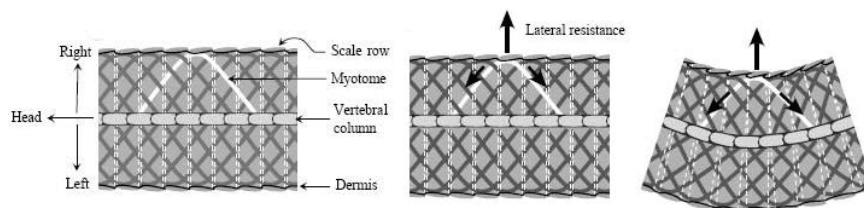
Figure 161: Function model of fish scales. [222]

Ramrakhyani & al. [221] suggested the use of **folded inner skins** (Figure 162), that provide lateral support to very flexible outer skins e.g. elastomers, as a potential morphing skin solution. The folded inner skins would expand and contract with the main-load bearing substructure.

They also mention using a **multilayered skin** (Figure 163) that consists of multiple thin layers of conventional material (e.g. metal or composite) that are not bonded together. In this configuration transverse shear stresses are not transmitted from one layer to another which reduces bending stiffness compared to a monolithic skin — in effect the through-thickness shear modulus is very low. This allows large bending curvatures to develop but the skin can withstand the same tensile loads as a monolithic structure of the same thickness.
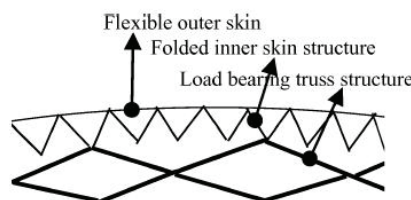
Figure 162: Folded inner skins. [221]

Figure 163: Multilayered skin. [221]

6 CONCLUSIONS

As it can be seen from this bibliographic research, most solutions for wing morphing have regarded small aircrafts, radio controlled scale models or UAVs (Unmanned Aerial Vehicle).

Among these studies, the most promising make extensive use of the SMART materials (SMA, piezoelectric, flexible composites, etc.). As regards the use of Shape Memory alloys, to date they have generally been adopted in the form of wires due to modelling and manufacturing limitations.

At the end of this overview of morphing wing technologies, the following conclusions can be done:

➢ wing morphing is a promising technology, because it allows to fully explore the aerodynamic potential of an aircraft wings by enabling the wing shape adaptability to the several flight conditions that can be encountered in a typical mission profile;

➢ the opportunity of taking advantage of aero-elastic deformations can allow for performance and manoeuvrability increase, in addition to a structural efficiency improvement;

➢ new design criteria must be adopted for wing morphing, usually antithetical to the traditional ones, which allow for highly deformable or compliant structures;

➢ many actual studies are focused on the exposed aerodynamic surfaces, which must be deformable while ensuring a smooth skin for flow continuity and complying with the structural integrity;

➢ the development of innovative SMART materials, their commercial availability and modelling assessment can only enlarge future perspectives on wing morphing applied to real aircrafts;

➢ as of today, Shape Memory Alloys allow for highly integrated actuation systems within the wing structure, but their relatively low actuation energy constrained many works to model aircrafts or UAVs, also because of the use of SMAs in the form of wires only;

➢ considering the actual studies on wing morphing with SMAs, benefits in terms of maintenance, weight reduction, cost and complexity reduction seem clear, thus justifying more researches in this field.

According to studies at NASA, it will take another 20-30 years before skies could be furrowed by aircraft more and more similar to birds (Figure 164), having wings with no attached control surfaces and that can change their shape in a smart way.

Figure 164: Artistic concept for a future morphing UAV conceived at NASA.

7 REFERENCES

[1] Browman J., Sanders B., Weisshaar T., 2002, "*Evaluating the Impact of Morphing Technologies on Aircraft Performance*" – AIAA Journal 2002-1631

[2] Stanewsky E., 2001, "*Adaptive Wing and Flow Control Technology*" – Progress in Aerospace Sciences, Elsevier Science Ltd., vol.37, pp.583-667

[3] DASA-Airbus DA-Report, 1999, No. EF-069/99

[4] Siclari M.J., Van Nostrand W., Austin F., 1996, "*The Design of Transonic Airfoil Sections for an Adaptive Wing Concept Using a Stochastic Optimization Method*" – 34th Aerospace Sciences Meeting and Exhibit, Reno, NV, AIAA 1996-0329

[5] Smith S.B., Nelson D.W., 1990, "*Determination of the Aerodynamic Characteristics of the Mission Adaptive Wing*" – AIAA Journal, vol.27, no.11

[6] Thornton S.V., 1993, "*Reduction of Structural Loads Using Maneuver Load Control on the Advanced Fighter Technology Integration (AFTI)/F-111 Mission Adaptive Wing*" – NASA TM 4526

[7] Szodruch J., 1985, "*The Influence of Camber Variation on the Aerodynamics of Civil Transport Aircraft*" – 23rd Aerospace Sciences Meeting, Reno, NV, AIAA 85-0353

[8] Martins A.L., Catalano F.M., 1998, "*Viscous Drag Optimization for a Transport Aircraft Mission Adaptive Wing*" – 21st ICAS Congress, Melbourne, Australia, Paper A98-31499

[9] Browman J., Sanders B., Cannon B., Kudva J., Joshi S., Weisshaar T., 2007, "*Development of Next Generation Morphing Aircraft Structures*" – 48th AIAA/ASME/ASCE/AHS/ASC Structures, Structural Dynamics, and Materials Conference, April 23-26, Honolulu, Hawaii, AIAA J. 2007-1730

[10] Rodriguez A.R., 2007, "*Morphing Aircraft Technology Survey*" – 45th AIAA Aerospace Sciences Meeting and Exhibit, January 8-11, Reno, Nevada, AIAA J. 2007-1258

[11] Renken J.H., 1985, "*Mission – Adaptive Wing Camber Control Systems for Transport Aircraft*" – 3rd Applied Aerodynamics Conference, Colorado Springs, CO, AIAA 85-5006

[12] Richter K., Rosemann H., 1999, "*Numerical Investigation of Transonic Airfoil Drag Reduction by the Combined Application of a Contour Bump and Variable Rear Camber*" – DLR Internal Report IB 223-1999 A 31

[13] Kikuta M.T., 2003, "*Mechanical Properties of Candidate Materials for Morphing Wings*" – Master's thesis, University of Virginia, Blacksburg, VA

[14] Spillman, J., 1992, "*The Use of Variable Camber to Reduce Drag, Weight and Costs of Transport Aircraft*" – Aeronautical Journal, Gennaio 1992, vol.96, pp.1-8

[15] Parker H.F., 1920, "*The Parker Variable Camber Wing*" – Annual Report National Advisory Committee for Aeronautics, report no.77

[16] Frost & al., 1978, "*Airfoil Variable Cambering Device and Method*" – United States Patent no.4,247,066, General Dynamics Corporation, Fort Worth, TX

[17] Statkus F.D., 1980, "*Continuous Skin Variable Camber Airfoil Edge Actuating Mechanism*" – United States Patent No. 4,351,502, The Boeing Company, Seattle, WA

[18] Perez J., 2002, "*Mechanism for at least Regionally Adjusting the Curvature of Airfoil Wings*" – United States Patent No. 2002/0100842 A1

[19] Bonnema K.L., Smith S.B., 1988 – AFTI/F-111 Mission Adaptive Wing Flight Research Program, San Diego, California, pp.155–161

[20] DeCamp R.W., Hardy R., 1984, "*Mission Adaptive Wing Advanced Research Concepts*" – AIAA Journal 84-2088

[21] Smith S.B., Nelson D.W., 1989, "*Determination of the Aerodynamic Characteristics of the Mission Adaptive Wing*" – 6th Applied Aerodynamics Conference, Williamsburg, VA, AIAA J. 88-2556

[22] Poonsong P., 2004, "*Design and Analysis of a Multi-Section Variable Camber Wing*" – Master's thesis, University of Maryland, MD

[23] Monner H.P., Bein T., Hanselka H., Breitbach E., 1998, "*Design Aspects of the Adaptive Wing – The Elastic Trailing Edge and the Local Spoiler Bump*" – Royal Aeronautical Society, Multidisciplinary Design and Optimization, London, October 1998

[24] Santangelo M., Iuspa L., Blasi L., 2006, "*Analisi Cineto-Statica di una Struttura Alare Adattiva Hingeless*" – Proceedings of XXXV Convegno Nazionale Associazione Italiana per l'Analisi delle Sollecitazioni (AIAS), September 13-16, Polytechnic University of Marche, in italian

[25] Baker D., Friswell M.I., 2006, "*Design of a Compliant Aerofoil using Topology Optimisation*" – Proceedings of the International Workshop on Smart Materials and Structures (Cansmart 2006), October 12-13, Toronto, Canada

[26] Baker D., Friswell M.I., Lieven N.A.J., 2005, "*Active Truss Structures for Wing Morphing*" – Proceddings of II ECCOMAS Thematic Conference on Smart Structures and Materials, July 18-21, Lisbon, Portugal

[27] Baker D., Friswell M.I., 2008, "*The Design of Morphing Aerofoils using Compliant Mechanisms*" – Proceedings of 19th International Conference on Adaptive Structures and Technologies, October 6-9, Ascona, Switzerland

[28] Ricci S., 2008, "*Adaptive Camber Mechanism for Morphing Experiences at DIA-PoliMI*" – Advanced Course on Morphing Aircraft Materials, Mechanisms and Systems, November 17-20, Lisbon, Portugal, invited lecturer

[29] Perera M., Guo S., 2009, "*Optimal Design of a Seamless Aeroelastic Wing Structure*" – 50th AIAA/ASME/ASCE/AHS/ASC Structures, Structural Dynamics, and Materials Conference, May 4-7, Palm Springs, California, AIAA J. 2009-2195

[30] Austin F., Siclari M.J., Van Nostrand W., Weisensel G.N., Kottamasu V., Volpe G., 1997, "*Comparison of Smart Wing Concepts for Transonic Cruise Drag Reduction*" – SPIE 1997, p.3044

[31] Geissler W., Sobieczky H., Trenker M., 2000, "*New Rotor Airfoil Design Procedure for Unsteady Flow Control*" – 26th European Rotorcraft Forum, September 2000, The Hague, Holland, Paper no.31

[32] Munday D., Jacob J., 2001, "*Active Control of Separation on a Wing with Conformal Camber*" – AIAA Journal 2001-0293

[33] Vos R., Barrett R., De Breuker R., Tiso P., 2007, "*Post-buckled precompressed elements: a new class of control actuators for morphing wing UAVs*" – Smart Materials and Structures, vol.16, pp.919-926

[34] Inman D.J., 2001, "*Wings: Out of the Box. Determining Actuator Requirements for Controlled Morphing Air Vehicles – Aerodinamic Loads*" – DARPA Technology Interchange Meeting, Wright Patterson Air Force Base, November 2001, Dayton, Ohio

[35] Santhanakrishnan A., Nan Jou Pern, Ramakumar K., Simpson A., Jacob J.D., 2005, "*Enabling Flow Control Technology for Low Speed UAVs*" – AIAA Journal 2005-6960

[36] Boothe K., 2004, "*Dynamic Modeling and Flight Control of Morphing Air Vehicles*" – Master's thesis, University of Florida, FL

[37] Garcia H., Abdulrahim M., Lind R., 2003, "*Roll Control for a Micro Air Vehicle using Active Wing Morphing*" – AIAA Guidance, Navigation and Control Conference, Austin, TX, August 2003, AIAA Journal 2003-5347

[38] Garcia H., Abdulrahim M., Lind R., 2005, "*Flight Characteristics of Shaping the Membrane Wing of a Micro Air Vehicle*" – Journal of Aircraft, vol.42, no.1

[39] Bilgen O., Kochersberger K., Diggs E.C., Kurdila A.J., Inman D.J., 2007, "*Morphing Wing Aerodynamic Control via Macro-Fiber-Composite Actuators in an Unmanned Aircraft*" – AIAA Infotech@Aerospace 2007 Conference and Exhibit, May 7-10, Rohnert Park, California, AIAA J. 2007-2741

[40] Bilgen O., Kochersberger K.B., Inman D.J., Ohanian III O.J., 2009, "*Novel, Bi-Directional, Variable Camber Airfoil via Macro-Fiber Composite Actuators*" – 50th AIAA/ASME/ASCE/AHS/ASC Structures, Structural Dynamics, and Materials Conference, May 4-7, Palm Springs, California, AIAA J. 2009-2133

[41] Rick Lind, Università della Florida, sito web: http://aemes.mae.ufl.edu/~rick/

[42] Wickramasinghe V.K., Chen Y., Martinez M., Kernaghan R., Wong F., "*Design and Verification of a Smart Wing for an Extremely-Agile Micro-Air-Vehicle*" – 50th AIAA/ASME/ASCE/AHS/ASC Structures, Structural Dynamics, and Materials Conference, May 4-7, Palm Springs, California, AIAA J. 2009-2132

[43] McGowan A.M., 2008, "*Overview: Morphing Activities in the USA*" – Advanced Course on Morphing Aircraft Materials, Mechanisms and Systems, November 17-20, Lisbon, Portugal, invited lecturer

[44] McGowan A.R., Horta L.G., Harrison J.S., Raney D.L., 1999, "*Research Activities within NASA's Morphing Program*", RTO Meeting Proceedings 36 (AC/323(AVT)TP/17) from the RTO AVT Specialists' Meeting on "Structural Aspects of Flexible Aircraft Control*", Ottawa (AL-CAN), October 1999

[45] Pendleton E., 2000, "*Active Aeroelastic Wing*" – AFRL Technology Horizons, vol.1, no.2, June 2000, pp.27-28

[46] Wilson J.R., 2002, "*Active Aeroelastic Wing: A New/Old Twist On Flight*" – Aerospace America, vol.40, no.99, pp.34–37

[47] Thornton S.V., 1993, "*Reduction of Structural Loads Using Maneuver Load Control on the Advanced Fighter Technology Integration (AFTI)/F-111 Mission Adaptive Wing*" – NASA TM 4526

[48] Gano S.E., Renaud J.E., 2002, "*Optimized Unmanned Aerial Vehicle with Wing Morphing for Extended Range and Endurance*" – 9th AIAA/ISSMO Symposium

and Exhibit on Multidisciplinary Analisys and Optimization, AIAA Journal 2002-5668

[49] Peel L.D., Mejia J., Narvaez B., Thompson K., Lingala M., 2008, "*Development of a Simple Morphing Wing Using Elastomeric Composites as Skins and Actuators*" – Proceedings of ASME Conference on Smart Materials, Adaptive Structures and Intelligent Systems (SMASIS 2008), October 28-30, Ellicott City, Maryland, paper SMASIS2008-544

[50] Flexsys Inc., website: http://www.flxsys.com/index.shtml

[51] Wildschek A., Grünewald M., Maier R., Steigenberger J., Judas M., Deligiannidis N., Aversa N., 2008, "*Multi-Functional Morphing Trailing Edge Device for Control of All-Composite, All-Electric Flying Wing Aircraft*" – The 26th Congress of International Council of the Aeronautical Sciences (ICAS), September 14-19, Anchorage, Alaska, AIAA J. 2008-8956

[52] Monner H.P., Kintscher M., Lorkowski T., Storm S., 2009, "*Design of a Smart Droop Nose as Leading Edge High Lift System for Transportation Aircrafts*" – 50th AIAA/ASME/ASCE/AHS/ASC Structures, Structural Dynamics, and Materials Conference, May 4-7, Palm Springs, California, AIAA J. 2009-2128

[53] Simpson A., Jacob J., Smith S., 2005, "*Inflatable and Warpable Wings for Meso-scale UAVs*" – AIAA Journal 2005-7161

[54] Norris R.K., Pulliam W.J., 2009, "*Historical Perspective on Inflatable Wing Structures*" – 50th AIAA/ASME/ASCE/AHS/ASC Structures, Structural Dynamics, and Materials Conference, May 4-7, Palm Springs, California, AIAA J. 2009-2145

[55] Cadogan D., Smith T., Lee R., Scarborough S., Graziosi D., 2003, "*Inflatable and Rigidizable Wing Components for Unmanned Aerial Vehicles*" – 44th AIAA/ASME/ASCE/AHS/ASC Structures, Structural Dynamics and Materials Conference, Norfolk, VA, AIAA Journal 2003-6630

[56] Murray J.E., Pahle J.W., Thornton S.V., Vogus S., Frackowiak T., Mello J.D., Norton B., 2002, "*Ground and Flight Evaluation of a Small-Scale Inflatable-Winged Aircraft*" – 40th Aerospace Sciences Meeting & Exhibit, Reno, NV, AIAA Journal 2002-0820

[57] Lin J.K., Sapna G.H., Cadogan D.P., Scarborough S.E., 2002, "*Inflatable Rigidizable Isogrid Boom Development*" – 43rd AIAA/ASME/ASCE/AHS/ASC

Structures, Structural Dynamics, and Materials Conference and Exhibit, AIAA Gossamer Spacecraft Forum, Denver, CO, AIAA Journal 2002-1297

[58] Allred R., Hoyt A., Harrah L., McElroy P., Scarborough S., Cadogan D., 2004, "*Light Curing Rigidizable Inflatable Wing*" – 45th AIAA/ASME/ASCE/ AHS/ASC Structures, Structural Dynamics and Materials Conference, Palm Springs, CA, AIAA Journal 2004-1809

[59] Chandler J., Jacob J., 2007, "*Design and Flight Testing of a Mars Aircraft Prototype Using Inatable Wings*" – 58th International Astronautical Congress, September 27, Hyderabad, India

[60] Simpson A., Jacob J., 2005, "*Aerodynamic Control of an Inflatable Wing Using Wing Warping*" – 35th AIAA Fluid Dynamics Conference and Exhibit, Toronto, Ontario, Canada, AIAA Journal 2005-5133

[61] Simpson A., Coulombe N., Jacob J., Smith S., 2005, "*Morphing of Inflatable Wings*" – 46th AIAA/ASME/ASCE/AHS/ASC Structures, Structural Dynamics and Materials Conference, Austin, Texas, AIAA Journal 2005-2110

[62] Kheong L.W., Jacob J.D., 2008, "*In Flight Aspect Ratio Morphing Using Inflatable Wings*" – 46th AIAA Aerospace Sciences Meeting and Exhibit, January 8-11, 2008, Reno, Nevada, AIAA J. 2008-425

[63] Scott M.J., Jacob J.D., Smith S.W., Asheghian L.T., Kudva J.N., 2009, "*Development of a Novel Low Stored Volume High-Altitude Wing Design*" – 50th AIAA/ASME/ASCE/AHS/ASC Structures, Structural Dynamics, and Materials Conference, May 4-7, Palm Springs, California, AIAA J. 2009-2146

[64] Haight A.E.H., Jacob J.D., Scarborough S.E., Gleeson D., 2009, "*Hybrid Inflatable/Rigidizable Wings for High Altitude Applications*" – 50th AIAA/ASME/ASCE/AHS/ASC Structures, Structural Dynamics, and Materials Conference, May 4-7, Palm Springs, California, AIAA J. 2009-2148

[65] Gevers Aircraft Inc., 1997, "*Multi-Purpose Aircraft*", United States Patents Office, Patent Number 5,645, 250

[66] Munson K., 2000, "*Jane's Unmanned Aerial Vehicles and Targets*", Jane's, issue 15

[67] AeroVisions Inc., website: http://www.canosoarus.com/05UMAAV/UMAAV01.htm

[68] Leite A., Vale J., Lau F., Suleman A., 2009, "*Development of Morphing Strategies for Flight Demonstrator RPV*" – 50th AIAA/ASME/ASCE/AHS/ASC

Structures, Structural Dynamics, and Materials Conference, May 4-7, Palm Springs, California, AIAA J. 2009-2134

[69] Blondeau J., Pines D., 2004, "*Pneumatic Morphing Aspect Ratio Wing*" – 45th AIAA/ASME/ASCE/AHS/ASC Structures, Structural Dynamics and Materials Conference, Palm Springs, California, AIAA Journal 2004-1808

[70] Mattioni F., Gatto A., Weaver P.M., Friswell M.I., Potter K.D., 2006, "*The application of residual stress tailoring of snap-through composites for variable sweep wings*" – 47th AIAA/ASME/ASCE/AHS/ASC Structures, Structural Dynamics, and Materials Conference, May 1-4, Newport, Rhode Island, AIAA J. 2006-1972

[71] AFRL Vehicle Research Section, Air Launched Integrated Countermeasure, Expendable (ALICE), website: http://www.nrl.navy.mil/vrs/factsheets/index.php

[72] Neal III D.A., Farmer J., Inman D.J., 2006, "*Development of a Morphing Aircraft Model for Wind Tunnel Experimentation*" – 47th AIAA/ASME/ASCE/AHS/ASC Structures, Structural Dynamics, and Materials Conference, May 1-4, Newport, Rhode Island, AIAA J. 2006-2141

[73] Roth B.D., Crossley W.A., 2003, "*Application of Optimization Techniques in the Conceptual Design of Morphing Aircraft*" – AIAA Journal 2003-6733

[74] Flight Group - Airline Industry news, aviation jobs & airline recruitment, website: http://www.flightinternational.com/Articles/2005/09/13/Navigation/190/201485/Strange+shapes.html

[75] Bye D.R., McClure P.D., 2007, "*Design of a Morphing Vehicle*" – 48th AIAA/ASME/ASCE/AHS/ASC Structures, Structural Dynamics, and Materials Conference, April 23-26, Honolulu, Hawaii, AIAA J. 2007-1728

[76] Love M.H., Zink P.S., Stroud R.L., Bye D.R., Rizk S., White D., 2007, "*Demonstration of Morphing Technology through Ground and Wind Tunnel Tests*" – 48th AIAA/ASME/ASCE/AHS/ASC Structures, Structural Dynamics, and Materials Conference, April 23-26, Honolulu, Hawaii, AIAA J. 2007-1729

[77] Ivanco T.G., Scott R.C., Love M.H., Zink S., Weisshaar T.A., 2007, "*Validation of the Lockheed Martin Morphing Concept with Wind Tunnel Testing*" – 48th AIAA/ASME/ASCE/AHS/ASC Structures, Structural Dynamics, and Materials Conference, April 23-26, Honolulu, Hawaii, AIAA J. 2007-2235

[78] Canfield B., 2008, "*Overview: Morphing Activities in the USA*" – Advanced Course on Morphing Aircraft Materials, Mechanisms and Systems, November 17-20, Lisbon, Portugal, invited lecturer

[79] Cornerstone Research Group Inc., website: http://www.crgrp.net/veriflex.htm

[80] Perkins D.A., Reed J.L., Havens E., 2004, "*Morphing Wing Structures for Loitering Air Vehicles*" – 45th AIAA/ASME/ASCE/AHS/ASC Structures, Structural Dynamics & Materials Conference, Palm Springs, California, AIAA Journal 2004-1888

[81] Flanagan J.S., Strutzenberg R.C., Myers R.B., Rodrian J.E., 2007, "*Development and Flight Testing of a Morphing Aircraft, the NextGen MFX-1*" – 48th AIAA/ASME/ASCE/AHS/ASC Structures, Structural Dynamics, and Materials, April 23-26, Honolulu, Hawaii, AIAA J. 2007-1707

[82] Stubbs M.D., 2003, "*Kinematic Design and Analysis of a Morphing Wing*" – Master thesis, Virginia Polytechnic Institute and State University, December 2003

[83] Manzo J.E., "*Analysis and design of a hyper elliptical cambered span morphing aircraft wing*" – Master thesis, Cornell University, 2006

[84] Lu K.J., Kota S., 2003, "*Parameterization Strategy for Optimization of Shape Morphing Compliant Mechanisms Using Load Path Representation*" – ASME 2003 Design Engineering Technical Conferences and Computers and Information in Engineering Conference, Chicago, Illinois

[85] Li H., Figliola R.S., 2004, "*Exergy Based Design Methodology for Airfoil Shape Optimization*" – 10th AIAA/ISSMO Multidisciplinary Analysis and Optimization Conference, Albany, New York, AIAA Journal 2004-4632

[86] Alasty A., Alemohammad S.H., Khiabani R.H., Khalighi Y., 2004, "*Maneuverability Improvement for an Ultra Light Airplane Model Using Variable Shape Wing*" – AIAA Atmospheric Flight Mechanics Conference and Exhibit, Providence, Rhode Island, AIAA Journal 2004-4831

[87] Benavides J.C., Correa G., 2004, "*Morphing Wing Design Using Nitinol Wire*" – University of Missouri-Rolla (UMR), Intelligent System Center, website: http://isc.mst.edu/reu/2004indprojects/2004-6.html

[88] Song G., Ma N., 2007, "*Robust control of a shape memory alloy wire actuated flap*" – Smart Materials and Structures, vol.16, pp.N51-N57

[89] Seow A.K., Liu Y., Yeo W.K., 2008, "*Shape Memory Alloy as Actuator to Deflect a Wing Flap*" – 49th AIAA/ASME/ASCE/AHS/ASC Structures, Structural

Dynamics, and Materials Conference, April 7-10, Schaumburg, IL, AIAA J. 2008-1704

[90] Eggleston G., Hutchison C., Johnston C., Koch B., Wargo G., Williams K., 2002, "*Morphing Aircraft Design Team*" – Virginia Tech Aerospace Engineering Senior Design Project

[91] Mirone G., 2007, "*Design and demonstrators testing of adaptive airfoils and hingeless wings actuated by shape memory alloy wires*" – Smart Structures and Systems, vol.3, no.1, pp.89-114

[92] Brailovski V., Terriault P., Coutu D., Georges T., Morellon E., Fischer C., Bérubé S., 2008, "*Morphing Laminar Wing with Flexible Extrados Powered by Shape Memory Alloy Actuators*" – Proceedings of ASME Conference on Smart Materials, Adaptive Structures and Intelligent Systems (SMASIS 2008), October 28-30, Ellicott City, Maryland, paper SMASIS2008-377

[93] Kudva J.N., Lockyer A.J., Appa K., 1996, "*Adaptive Aircraft Wing*" – AGARD SMP Lecture series 205, Smart Structures and Materials: Implications for Military Aircraft of New Generation, AGARD-LS-205

[94] Kudva J.N., Jardine P., Martin C., Appa K., 1996, "*Overview of the ARPA/WL "Smart Structures and Material Development – Smart Wing" Contract*" – SPIE, vol.2721

[95] Kudva J.N., Carpenter B., 2000, "*Smart Wing Program*" – DARPA Technology Interchange Meeting, June 2000

[96] Kudva J.N., 2001, "*Overview of the DARPA/AFRL/NASA Smart Wing Phase II Program*" – Smart Structures and Materials Conference, USA, SPIE n.4332-48, pp.383-389

[97] Florance J.P., Burner A.W., Fleming G.A., Hunter C.A., Graves S.S., 2003, "*Contributions of the NASA Langley Research Center to the DARPA/AFRL/NASA/Northrop Grumman Smart Wing Program*" – 44th AIAA/ASME/ASCE/AHS Structures, Structural Dynamics and Materials Conference, Norfolk, Virginia, AIAA Journal 2003-1961

[98] Gonzalez L., Rediniotis O., 2005, "*Morphing Wing Using SMA*" – T.I.I.M.S. 3rd Annual Meeting

[99] Lv H., Leng J., Du S., 2009, "*A Survey of Adaptive Materials and Structures Research in China*" – 50th AIAA/ASME/ASCE/ASH/ACS Structures, Structural

Dynamics, and Materials Conference, May 4-7, Palm Springs, California, AIAA J. 2009-2389

[100] Lecce L., 2004, "*Deliverable 4 - Relazione di progetto del dimostratore bidimensionale*" – Dep.t internal report no.04/64, Dep.t of Aeronautical Design, University of Napoli "Federico II", Napoli, in italian

[101] Lemme M., Caruso A., 2004, "*Deliverable 3 - Modellazione FEM del dimostratore bidimensionale di un bordo d'attacco deformabile con attuazione tramite fili di SMA*" – Dep.t internal report no.04/72, Dep.t of Aeronautical Design, University of Napoli "Federico II", Napoli, in italian

[102] De Mattos B.S., Macedo A.P., Da Silva Filho D.H., 2003, "*Considerations about Winglet Design*" – 21st Applied Aerodynamics Conference, June 23-26, Orlando, Florida, AIAA J. 2003-3502

[103] Smith M.J., Komerath N., Ames R., Wong O., 2001, "*Performance Analysis of a Wing with Multiple Winglets*" – AIAA Journal 2001-2407

[104] Maughmer M.D., Swan T.S., Willits S.M., 2002, "*Design and Testing of a Winglet Airfoil for Low-Speed Aircraft*" – Journal of Aircraft, vol.39, no.4, pp.654-661

[105] Soltani M.R., Ghorbanian K., Nazarinia M., 2004, "*Flow Analysis Over and Behind a Wing with Different Winglet Shapes*" – 42nd AIAA Aerospace Sciences Meeting and Exhibit, January 5-8, Reno, Nevada, AIAA J. 2004-723

[106] Ogurek D.J., Ashworth J., 2004, "*Experimental Investigation of Various Winglet Designs for a Wing in Ground Effect*" – 22nd Applied Aerodynamics Conference and Exhibit, August 16-19, Providence, Rhode Island, AIAA J. 2004-4720

[107] Daccache E., Lee T., 2007, "*Effect of a Winglet on Normal Blade-Vortex Interaction*" – Journal of Aircraft, vol.44, no.1, pp.264-273

[108] Ning S.A., Kroo I., 2008, "*Tip Extensions, Winglets, and C-wings: Conceptual Design and Optimization*" – 26th AIAA Applied Aerodynamics Conference, August 18-21, Honolulu, Hawaii, AIAA J. 2008-7052

[109] Mann A, Elsholz E., 2005, "*The M-DAW Project Investigations in Novel Wing Tip Device Design*" – 43rd AIAA Aerospace Sciences Meeting and Exhibit, January 10-13, Reno, Nevada, AIAA J. 2005-461

[110] Hantrais-Gervois J.-L., Rapin M., 2006, "*Aerodynamic and Structural Behaviour of a Wing Equipped with a Winglet at Cruise*" – 44th AIAA Aerospace Sciences Meeting and Exhibit, January 9-12, Reno, Nevada, AIAA J. 2006-1489

[111] Elsholz E., Barakat S., 2006, "*CFD Analysis of Twist Correction on Commercial Aircraft Wing with Different Tip Devices in ETW Windtunnel*" – 44th AIAA Aerospace Sciences Meeting and Exhibit, January 9-12, Reno, Nevada, AIAA J. 2006-513

[112] Allen A., Breitsamter C., 2008, "*Transport Aircraft Wake Influenced by a Large Winglet and Winglet Flaps*" – Journal of Aircraft, vol.45, no.2, pp.686-699

[113] Slingerland R., Verstraeten J.G., 2008, "*Drag Characteristics for Optimally Span-loaded Planar, Wingletted, and C-wings*" – 46th AIAA Aerospace Sciences Meeting and Exhibit, January 7-10, Reno, Nevada, AIAA J. 2008-161

[114] Bourdin P., Gatto A., Friswell M.I., 2006, "*The Application of Variable Cant Angle Winglets for Morphing Aircraft Control*" – 24th Applied Aerodynamics Conference, June 5-8, San Francisco, California, AIAA J. 2006-3660

[115] Bourdin P., Gatto A., Friswell M.I., 2007, "*Potential of Articulated Split Wingtips for Morphing-Based Control of a Flying Wing*" – 25th AIAA Applied Aerodynamics Conference, June 25-28, Miami, FL, AIAA J. 2007-4443

[116] Ameri N., Lowenberg M.H., Friswell M.I., 2007, "*Modelling the Dynamic Response of a Morphing Wing with Active Winglets*" – AIAA Atmospheric Flight Mechanics Conference and Exhibit, August 20-23, Hilton Head, South Carolina, AIAA J. 2007-6500

[117] Ursache N.M., Melin T., Isikveren A.T., Friswell M.I., 2007, "*Morphing Winglets for Aircraft Multi-phase Improvement*" – 7th AIAA Aviation Technology, Integration and Operations Conference (ATIO), September 18-20, Belfast, Northern Ireland, AIAA J. 2007-7813

[118] Ameri N., Livne E., Lowenberg M.H., Friswell M.I., 2008, "*Modelling Continuously Morphing Aircraft for Flight Control*" – AIAA Guidance, Navigation and Control Conference and Exhibit, August 18-21, Honolulu, Hawaii, AIAA J. 2008-6966

[119] Shelton A., Tomar A., Prasad J.V.R., Smith M.J., Komerath N., 2004, "*Active Multiple Winglets for Improved UAV Performance*" – 22nd Applied Aerodynamics Conference and Exhibit, August 16-19, Providence, Rhode Island, AIAA J. 2004-4968

[120] Miller S., Vio G.A., Cooper J.E., 2009, "*Development of an Adaptive Wing Tip Device*" – 50th AIAA/ASME/ASCE/AHS/ASC Structures, Structural Dynamics,

and Materials Conference, May 4-7, Palm Springs, California, AIAA J. 2009-2121

[121] Pitt D., Dunne J., White E., Garcia E., 2001, "*SAMPSON smart inlet SMA powered adaptive lip design and static test*" – Proceedings of the 42nd AIAA Structures, Structural Dynamics, and Materials Conference, Seattle, WA, April 16-20, pp.1-11

[122] Wax S., Fischer G., Sands R., 2003, "*The past, present, and future of DARPAs investment strategy in smart materials*" – Journal of the Minerals, Metals, and Materials Society, vol.55, no.12, pp.17-23

[123] Pitt D.M., Dunne J.P., White E.V., 2002, "*Design and Test of a SMA Powered Adaptive Aircraft Inlet Internal Wall*" – 43rd AIAA/ASME/ASCE/AHS/ASC Structures, Structural Dynamics, and Materials Conference, April 22-25, Denver, Colorado, AIAA J. 2002-1356

[124] Timpano K.H., Zaidi S., Martinelli L., Miles R.B., Steeves C.A., Evans A.G., 2008, "*Design and Test of a Morphing Supersonic Nozzle*" – 46th AIAA Aerospace Sciences Meeting and Exhibit, January 7-10, Reno, Nevada, AIAA J. 2008-851

[125] Song G., Ma N., Lee H.-J., Arnold S., 2007, "*Design and control of a proof-of-concept variable area exhaust nozzle using shape-memory alloy actuators*" – Smart Materials and Structures, vol.16, pp.1342-1347

[126] Calkins F.T., Mabe J.H., Ruggeri R.T., 2008, "*Overview of Boeing's Shape Memory Alloy Based Morphing Aerostructures*" – Proceedings of ASME Conference on Smart Materials, Adaptive Structures and Intelligent Systems (SMASIS 2008), October 28-30, Ellicott City, Maryland, paper SMASIS2008-648

[127] Mabe J., Cabell R., Butler G., 2005, "*Design and control of a morphing chevron for takeoff and cruise noise reduction*" – Proceedings of the 26th Annual AIAA Aeroacoustics Conference, Monterey, CA, pp. 1-15

[128] Mabe J.H., Calkins F.T., Butler G.W., 2006, "*Boeing's variable geometry chevron, morphing aerostructure for jet noise reduction*" – 47th AIAA/ASME/ASCE/AHS/ASC Structures, Structural Dynamics and Materials Conference, Newport, Rhode Island, pp.1-19, AIAA J. 2006-2142

[129] Turner T.L., Buehrle R.D., Cano R.J., Fleming G.A., 2006, "*Modeling, fabrication, and testing of a SMA hybrid composite jet engine chevron concept*" – Journal of Intelligent Material Systems and Structures, vol.17, pp.483-497

[130] Leishman G., 2006, *"Principles of Helicopter Aerodynamics"* – Cambridge University Press

[131] Warwick G., 2009, *"Morphing Methods"* – Aviation Week & Space Technology, October 5, 2009, p.55

[132] Boyd Jr., Douglas D., 2009, *"Aerodynamic and Acoustic Study of an Active Twist Rotor using a Loosely Coupled CFD/CSD Method"* – 35th European Rotorcraft Forum, Hamburg, Germany, September 22-25, article 1160

[133] Bailly J., Delrieux Y., 2009, *"Improvement of Noise Reduction and Performance for a Helicopter Model Rotor Blade by Active Twist Actuation"* – 35th European Rotorcraft Forum, Hamburg, Germany, September 22-25, article 1157

[134] Zhang Q., Hoffmann F., 2009, *"Benefit Studies for Rotor with Active Twist Control Using Weak Fluid-Structure Coupling"* – 35th European Rotorcraft Forum, Hamburg, Germany, September 22-25, article 1217

[135] Leon O., Gandhi F., 2009, *"Rotor Power Reduction using Multiple Spanwise-Segmented Optimally-Actuated Trailing-Edge Flaps"* – 35th European Rotorcraft Forum, Hamburg, Germany, September 22-25, article 1309

[136] Leon O., Hayden E., Gandhi F., 2009, *"Rotorcraft Operating Envelope Expansion Using Extendable Chord Sections"* – Proceedings of the American Helicopter Society 65th Annual Forum, Grapevine, Texas, May 27-29

[137] Riemenschneider J., Opitz S., Wierach P., Mercier des Rochettes H., Buchaniek L., Joly D., 2009, *"Structural design and testing of Active Twist Blades – A comparison"* – 35th European Rotorcraft Forum, Hamburg, Germany, September 22-25, article 1163

[138] Mistry M.P., 2008, *"Induced Warp Systems to Obtain Active Twist of Rotor Blades"* – Master thesis, The Pennsylvania State University, State College

[139] Ruggeri R.T., Bussom R.C., Arbogast D.J., 2008, *"Development of a ¼-scale NiTinol actuator for reconfigurable structures"* – SPIE Smart Materials and Structures, paper 6930-21

[140] Bushnell G.S., Arbogast D.J., Ruggeri R.T., 2008, *"Shape control of a morphing structure (rotor blade) using a shape memory alloy actuator system, future of SMA"* – SPIE Smart Materials and Structures, paper 6928-95

[141] Thiel M.R., Lesieutre G.A., 2009, *"New Actuation Methods for Miniature Trailing-Edge Effectors for Rotorcraft"* – 50th AIAA/ASME/ASCE/AHS/ASC

Structures, Structural Dynamics, and Materials Conference, May 4-7, Palm Springs, California, AIAA J. 2009-2104

[142] Kinzel M.P., Maughmer M.D., Lesieutre G.A., 2007, "*Miniature Trailing-Edge Effectors for Rotorcraft Performance Enhancements*" – Journal of the American Helicopter Society, vol.52, no.2, pp.146-158

[143] Prabhakar T., Gandhi F., McLaughlin D., 2007, "*A Centrifugal Force Actuated Variable Span Morphing Helicopter Rotor*" – 63rd Annual AHS International Forum and Technology Display, Virginia Beach, VA, May 1-3. Also at the AHS International/Korean Society for Aeronautical and Space Sciences International Forum on Rotorcraft Multidisciplinary Technology, Seoul, Korea, October 15-17, 2007

[144] Koratkar N.A., Chopra I., 2000, "*Development of a Mach-Scaled Model with Piezoelectric Bender Actuated Trailing-Edge Flaps for Helicopter Individual Blade Control (IBC)*" – AIAA Journal, vol.38, no.7, pp.1113-1124

[145] Koratkar N.A., Chopra I., 2001, "*Wind Tunnel Testing of a Mach-Scaled Rotor Model with Trailing-Edge Flaps*" – Smart Materials and Structures, vol.10, no.1, pp.1-14

[146] Lee T., 1999, "*Design of High Displacement Smart Trailing Edge Flap Actuator Incorporating Dual-Stage Mechanical Stroke Amplifiers for Rotors*" – Ph.D. Dissertation, Dept. of Aerospace Engineering, University of Maryland, College Park, December 1999

[147] Lee T., Chopra I., 2001, "*Design of Piezostack-Driven Trailing-Edge Flap Actuator for Helicopter Rotors*" – Smart Materials and Structures, vol.10, no.1, pp.15-24

[148] Lee T., Chopra I., 2001, "*Wind Tunnel Test of Blade Sections with Piezoelectric Trailing-Edge Flap Mechanism*" – Proceedings of the 57th Annual Forum of the American Helicopter Society, vol.2, American Helicopter Society, Alexandria, VA, pp.1912-1923

[149] Straub F.K., Ngo H.T., Anand V., Domzalski D.B., 2001, "*Development of a Piezoelectric Actuator for Trailing-Edge Flap Control for Full Scale Rotor System*" – Smart Materials and Structures, vol.10, no.1, pp.25-34

[150] Janker P., Kloppel V., Hermle F., Lorkowski T., Storm S., Christmann M., Wettemann M., 1999, "*Development and Evaluation of a Hybrid Piezoelectric*

Actuator for Advanced Flap Control Technology" – 25th European Rotorcraft Forum (ERF 1999), Rome, September

[151] Bernhard A.P.F., Chopra I., 2001, "*Analysis of a Bending-Torsion Coupled Actuator for a Smart Rotor with Active Blade Tips*" – Smart Materials and Structures, vol.10, no.1, pp.35-52

[152] Rogers J.P., Hagood N.W., 1997, "*Design and Manufacture of an Integral Twist-Actuated Rotor Blade*" – Proceedings of the 38th AIAA/ASME/ASCE/AHS/ASC Structures, Structural Dynamics, and Materials Conference and Adaptive Structures Forum, AIAA, Reston, VA

[153] Derham R.C., Hagood N.W., 1996, "*Rotor Design Using Smart Materials to Actively Twist Blades*" – Proceedings of the 52nd Annual Forum, vol.2, American Helicopter Society, Alexandria, VA, pp.1242-1252

[154] Cesnik C.E.S., Shin S.J., 2001, "*On the twist performance of a multiple-cell active helicopter blade*" – Smart Materials and Structures, vol.10, no.1, pp. 53-61

[155] Cesnik C.E.S., Shin S.J., Wilbur M.L., 2001, "*Dynamic Response of Active Twist Rotor Blades*" – Smart Materials and Structures, vol.10, no.1, pp.62-76

[156] Shin S.J., 2001, "*Integral Twist Actuation of Helicopter Rotor Blades for Vibration Reduction*" – Ph.D. thesis, Massachusetts Institute of Technology

[157] Shin S.J., Cesnik C.E.S., Hall S.R., 2002, "*Control of Integral Twist-Actuated Helicopter Blades for vibration Reduction*" – Proceedings of the 58th American Helicopter Society Annual Forum, vol. 2, American Helicopter Society, Alexandria, VA, pp.2122-2134

[158] Kovalovs A., Barkanov E., Gluhihs S., 2007, "*Active Twist of Model Rotor Blades with D-Spar Design*" – Transport, vol.22, no.1, pp.38-44, ISSN 1648-4142

[159] Chopra I., 2002, "*Review of State of Art of Smart Structures and Integrated Systems*" – AIAA Journal, vol.40, no.11, pp.2145-2187

[160] Gandhi F., Frecker M., Nissly A., 2008, "*Design Optimization of a Controllable Camber Rotor Airfoil*" – AIAA Journal, vol.46, no.1, pp.142-153

[161] Riemenschneider J., Keye S., Wierach P., Mercier des Rochettes H., 2004, "*Overview of the Common DLR/ONERA Project 'Active Twist Blade' (ATB)*" – 30th European Rotorcraft Forum, Marseilles, France, September 14-16, pp.20.1-9

[162] Straub F., Anand V.R., Birchette T., Lau B.H., 2009, "*SMART Rotor Development and Wind Tunnel Test*" – 35th European Rotorcraft Forum 2009 (ERF 2009), Hamburg, Germany, September 22-25, article 1200

[163] Epps J.J., Chopra I., 2000, "*In-Flight Tracking of Helicopter Rotor Blades Using Shape Memory Alloy Actuators*" – Proceedings of the 56th American Helicopter Society Annual Forum, Vol. 1, American Helicopter Society, Alexandria, VA, pp.328-343

[164] Epps J.J., Chopra I., 2001, "*In-Flight Tracking of Helicopter Rotor Blades Using Shape Memory Alloy Actuators*" – Smart Materials and Structures, vol.10, no.1, pp.104-111

[165] Singh K., Chopra I., 2002, "*Design of an Improved Shape Memory Alloy Actuator for Rotor Blade Tracking*" – Proceedings of the 2002 Society of Photo-Optical Instrumentation Engineers' North American Symposium on Smart Structures and Materials, vol.4701, Society of Photo-Optical Instrumentation Engineers (International Society for Optical Engineering), Bellingham, WA, pp.244-266

[166] Ameduri S., Pagano A., Altmikus A., Cokonaj V., Prachar A., Zachariadis Z., Drikakis D., 2009, "*Helicopter Blade Twist Control through SMA Technology: Optimal Shape Prediction, Twist Actuator Realisation and Main Rotor Enhanced Performance Computation*" – 35th European Rotorcraft Forum, Hamburg, Germany, September 22-25, article 1297

[167] Mabe J.H., Gravatt L., Bushnell G., Gutmark E., DiMiccio R.G., Harris C., 2008, "*Shape Memory Alloy Actuators for Deployable Rotor Blade Aerodynamic Devices*" – 46th AIAA Aerospace Sciences Meeting and Exhibit, January 7-10, Reno, Nevada, AIAA J. 2008-1451

[168] Daynes S., Nall S.J., Weaver P.M., Potter K.D., Margaris P., Mellor P.H., 2009, "*On a Bistable Flap for an Airfoil*" – 50th AIAA/ASME/ASCE/AHS/ASC Structures, Structural Dynamics, and Materials Conference, May 4-7, Palm Springs, California, AIAA J. 2009-2103

[169] Bell L., 2009, "*Deployable Soft Space Structures: Concepts and Application Requirements*" – 50th AIAA/ASME/ASCE/AHS/ASC Structures, Structural Dynamics, and Materials Conference, May 4-7, Palm Springs, California, AIAA J. 2009-2168

[170] Owens J.J., Cobb R.G., Black J.T., 2009, "*Design and Flight Qualification of the Rigidizable Inflatable Get-Away-Special Experiment*" – 50th AIAA/ASME/ASCE/AHS/ASC Structures, Structural Dynamics, and Materials Conference, May 4-7, Palm Springs, California, AIAA J. 2009-2155

[171] Sofla A.Y.N., Elzey D.M., Wadley H.N.G., 2007, "*A rotational joint for shape morphing space truss structures*" – Smart Materials and Structures, vol.16, pp.1277-1284

[172] You Z., "*Overview: Morphing Activities in the USA*" – Advanced Course on Morphing Aircraft Materials, Mechanisms and Systems, November 17-20, Lisbon, Portugal, invited lecturer

[173] Ramrakhyani D.S., 2005, "*Morphing Aircraft Structures using Tendon Actuated Compliant Cellular Truss*" – Ph.D. thesis, The Pennsylvania State University, August 2005

[174] Lesieutre G.A., Frecker M., Mehta V., 2008, "*Compliant Frame: A New Paradigm to Enable Reconfigurable Aircraft Structures*" – Air Force Office of Scientific Research, 28 February 2008

[175] Lin J, Knoll C.F., Willey C.E., 2006, "*Shape Memory Rigidizable Inflatable (RI) Structures for Large Space Systems Applications*" – 47th AIAA/ASME/ASCE/AHS/ASC Structures, Structural Dynamics, and Materials Conference, May 1-4, Newport, Rhode Island, AIAA Journal 2006-1896

[176] Sokolowski W.M., Tan S.C., "*Advanced Self-Deployable Structures for Space Applications*" – Journal of Spacecraft and Rockets, vol.44, no.4, pp.750-754

[177] Pollard E.L., Jenkins C.H.M., 2007, "*Shape Memory Alloy Deployment of Membrane Mirrors for Spaceborne Telescopes*" – Journal of Spacecraft and Rockets, vol.44, no.1, pp.109-120

[178] Kwok K., Pellegrino S., 2009, "*Structural Concepts for Variable Geometry Decelerators*" – 50th AIAA/ASME/ASCE/AHS/ASC Structures, Structural Dynamics, and Materials Conference, May 4-7, Palm Springs, California, AIAA J. 2009-2100

[179] Lafleur J.M., Olds J.R., Braun R.D., 2005, "*Daedalon: A Revolutionary Morphing Spacecraft Design for Planetary Exploration*" – 1st Space Exploration Conference: Continuing the Voyage of Discovery, Orlando, Florida, AIAA Journal 2005-2771

[180] Callister W.D.J., 2006, "*Materials Science and Engineering: An Introduction*" – Seventh edition, Wiley

[181] Keihl M.M., Bortolin R.S., Sanders B., Joshi S., Tidwell Z., 2005, "*Mechanical properties of shape memory polymers for morphing aircraft applications*" – International Society for Optical Engineering

[182] Yokozeki T., Takeda S.-I., Ogasawara T., Ishikawa T., 2006, "*Mechanical properties of corrugated composites for candidate materials of flexible wing structures*" – Composites Part A: Applied Science and Manufacturing, vol.37, no.10, pp.1578-1586

[183] Kudva J.N., 2004, "*Overview of the DARPA smart wing project*" – Journal of Intelligent Material Systems and Structures, vol.15, no.4, pp.261-267

[184] Bornengo D., Scarpa F., Remillat C., 2005, "*Evaluation of hexagonal chiral structure for morphine airfoil concept*" – Journal of Aerospace Engineering, vol.219, no.3, pp.185-192, Proceedings of the Institution of Mechanical Engineers, Part G

[185] Wei G., Edwards S.F., 1998, "*Auxeticity windows for composites*" – Physica A, vol.258, no.1-2, pp.5-10

[186] Olympio K.R., Gandhi F., 2007, "*Zero-v cellular honeycomb flexible skins for one-dimensional wing morphing*" – 48th AIAA/ASME/ ASCE/AHS/ASC Structures, Structural Dynamics and Materials Conference, April 23-26, Honolulu, Hawaii, AIAA J. 2007-1735

[187] Gandhi F., Anusonti-Inthra P., 2004, "*On the Design of Flexible Skins for Morphing Aircraft Structures*" – Proceedings of the 15th International Conference on Adaptive Structures and Technologies (ICAST), October 24-27, Bar Harbor, Maine

[188] Murray G., Gandhi F., Bakis C., 2007, "*Flexible Matrix Composite Skins for One-Dimensional Wing Morphing*" – 48th AIAA/ASME/ ASCE/AHS/ASC Structures, Structural Dynamics and Materials Conference, April 23-26, Honolulu, Hawaii, AIAA J. 2007-1737

[189] Gandhi F., Anusonti-Inthra P., 2008, "*Skin Design Studies for Variable Camber Morphing Airfoils*" – Smart Materials and Structures, vol.17, 015025, 8pp

[190] Lira C., Scarpa F., Olszewska M., Celuch M., 2009, "*The SILICOMB cellular structure: Mechanical and dielectric properties*" – Phys. Status Solidi B, vol.246, no.9, pp.2055-2062, doi: 10.1002/pssb.200982036

[191] Hyer M.W., 1981, "*Calculations of the room-temperature shapes of unsymmetric laminates*" – Journal of Composite Materials, vol.15, pp 296-310

[192] Hyer M.W., 1982, "*The room-temperature shapes of 4-layer unsymmetric cross-ply laminates*" – Journal of Composite Materials, vol16, pp.318-340

[193] Kebadze E., Guest S.D., Pellegrino S., 2004, "*Bistable prestressed shell structures*" – International Journal of Solids and Structures, vol.41, no.11-12, pp.2801-2820

[194] Hufenbach W., Gude M., Kroll L., 2002, "*Design of multistable composites for application in adaptive structures*" – Composites Science and Technology, vol.62, no.16, pp.2201-2207

[195] Iqbal K., Pellegrino S., 2000, "*Bi-stable composite shells*" – American Inst Aeronautics and Astronautics

[196] Weaver P.M., 2002, "On beneficial anisotropic effects in composite structures" – 43rd AIAA/ASME/ASCE/AHS/ASC Structures, Structural Dynamics, and Materials Conference, Denver, CO

[197] Potter K., Weaver P., Seman A.A., Shah S., 2007, "Phenomena in the bifurcation of unsymmetric composite plates" – Composites Part A: Applied Science and Manufacturing, vol.38, no.1, pp. 100-106

[198] Mattioni F., Weaver P.M., Friswell M.I., Potter K.D., 2007, "*Modelling and applications of thermally induced multistable composites with piecewise variation of lay-up in the planform*" – 48th AIAA/ASME/ASCE/AHS/ASC Structures, Structural Dynamics, and Materials Conference, April 23-26, Honolulu, Hawaii, AIAA J. 2007-2262

[199] Norman A.D., Guest S.D., Seffen K.A., 2007, "*Novel Multistable Corrugated Structures*" – 48th AIAA/ASME/ASCE/AHS/ASC Structures, Structural Dynamics, and Materials Conference, April 23-26, Honolulu, Hawaii, AIAA J. 2007-2228

[200] Otsuka K., Wayman C.M., 1999, "*Shape memory materials*" – Cambridge University Press

[201] Zheng Y.J., Cui L.S., Schrooten J., 2005, "*Basic design guidelines for SMA/epoxy smart composites*" – Materials Science and Engineering a Structural Materials Properties Microstructure and Processing, vol.390, no.1-2, pp.139-143

[202] Dano M.L., Hyer M.W., 2003, "*SMA-induced snap-through of unsymmetric fiber-reinforced composite laminates*" – International Journal of Solids and Structures, vol.40, no.22, pp.5949-5972

[203] Barrett R., Gross R.S., 1996, "Super-active shape-memory alloy composites" – Smart Materials and Structures, vol.5, no.3, pp.255-260

[204] Shaw J.A., Churchill C., Triantafyllidis N., Michailidis P., Grummon D., Folts J., 2007, "*Shape memory alloy honeycombs: experiments & simulation*" – 48th AIAA/ASME/ASCE/AHS/ASC Structures, Structural Dynamics, and Materials Conference, April 23-26, Honolulu, Hawaii, AIAA J. 2007-1739

[205] Hu J., 2007, "*Shape memory polymers and textiles*" – Woodhead publishing limited

[206] Bellin I., Kelch S., Langer R., Lendlein A., 2006, "*Polymeric triple-shape materials*" – Proceedings of the National Academy of Sciences of the United States of America, vol.103, no.48, pp.18043-18047

[207] Lendlein A., Kelch S., 2002, "*Shape-memory polymers*" – Angewandte Chemie - International Edition, vol.41, no.12, pp.2035-2057

[208] Perkins D.A., Reed J.L., Havens E., 2004, "*Morphing wing structures for loitering air vehicles*" – American Institute Aeronautics and Astronautics

[209] Perkins D.A., Reed J.L., Havens E., 2004, "*Adaptive wing structures*" – Proceeding of the Smart Structures and Materials and Nondestructive Evaluation for Health Monitoring and Diagnostics Conference, San Diego, CA, International Society for Optical Engineering

[210] Cornerstone Research Group, website: http://www.crgrp.net

[211] Henry C., McKnight G., 2006, "*Cellular variable stiffness materials for ultra-large reversible deformations in reconfigurable structures*" – International Society for Optical Engineering

[212] McKnight G., Henry C., 2005, "*Variable stiffness materials for reconfigurable surface applications*" – International Society for Optical Engineering

[213] The Intelligent Material DIAPLEX, Mitsubishi Heavy Industries, website: http://www.diaplex.com

[214] Tupper M., Munshi N., Beavers F., Gall K., Mikuls M., Meink T., 2001, "*Developments in elastic memory composite materials for spacecraft deployable structures*" – IEEE

[215] Lake M.S., Campbell D., 2004, "*The fundamentals of designing deployable structures with elastic memory composites*" – IEEE

[216] Composite Technology Development, website: http://www.ctd-materials.com

[217] Bubert E.A., Woods B.K.S., Kothera C.S., Wereley N.M., 2008, "*Design and Fabrication of a Passive 1-D Morphing Aircraft Skin*" – 49th

AIAA/ASME/ASCE/AHS/ASC Structures, Structural Dynamics, and Materials Conference, April 7-10, Schaumburg, IL, AIAA J. 2008-2045

[218] Nanosonic, Inc., webiste: http://www.nanosonic.com/

[219] Potter K.D., Wisnom M.R., 2002, "*Composites of extreme anisotropy initial experiments*" – Plastics, Rubber and Composites, vol.31, no.5, pp.226-234

[220] Butler G., 2007, "*Investigation of corrugated composite laminates for use in morphing wing skin applications*" – Department of Aerospace, University of Bristol

[221] Ramrakhyani D.S., Lesieutre G.A., Frecker M., Bharti S., 2005, "*Aircraft structural morphing using tendon-actuated compliant cellular trusses*" – Journal of Aircraft, vol.42, no.6, pp.1615-1621

[222] Long J.H., Hale M.E., Mchenry M.J., Westneat M.W., 1996, "*Functions of fish skin: Flexural stiffness and steady swimming of longnose gar Lepisosteus osseus*" – Journal of Experimental Biology, vol.199, no.10, pp.2139-2151

[223] Varma K.B.R., 1990, "*Morphology and dielectric properties of fish scales*" – Current Science, vol.59, no.8, pp.420-422

[224] Bechert D.W., Bruse M., Hage W., 2000, "*Experiments with threedimensional riblets as an idealized model of shark skin*" – Experiments in Fluids, vol.28, no.5, pp.403-412

- Chapter 3 -

Shape Memory Alloys:
State of the Art

1 HISTORY

Shape memory alloys (SMA) have an interesting property for which the metal "remembers" its original shape and size, and returns to it at certain characteristic temperatures: this property is known as the Shape Memory effect (SME).

The first documented observation of the shape memory transformations was in 1932 due to Chang & Read [1]: they noticed the reversibility of the transformation of the Cadmium-Gold alloy (Cd-Au) on the basis of metallurgical observations and resistivity changes; in 1951 they also acknowledged the "shape memory" effect. In 1938, similar changes were observed in brass (Cu-Zn).

However, only in 1962 there was a dramatic surge in research applied to Shape Memory Alloys, after William J. Buehler & al. [2] found that Nickel-Titanium (Ni-Ti) equi-atomic alloys exhibited the Shape Memory too. Like many important discoveries, this was due to chance and deductive abilities of researchers, as reported by Kauffman & Mayo [3].

Buehler was performing research activities at the Naval Ordnance Laboratory (NOL) of U.S. Navy at White Oak (Maryland) on inter-metallic compounds: his aim was to find a metal with high melting temperature and high impact resistance properties for the nose cone of the SUBROC missile. Among sixty compounds, Buehler chose only twelve to be tested: the Nickel-Titanium alloy exhibited the desired properties, and so it was called NiTiNOL, including the acronym of the laboratory where he worked. Table 1 shows some characteristics of this alloy.

One day in 1959, while studying the NiTi alloy with varying percentages of the two components, Buehler made a remark that was behind the discovery of an interesting property: the NiTi rods used for experimental testing, if dropped, produced different

sounds according to their temperature, which was indicative of different damping properties and, at a microscopic level, of different atomic arrangements; in addition, it was possible to change this behaviour simply by heating or cooling the samples.

NiTiNOL Properties		
Density	6.45 gm/cm^3	0.23 lb/in^3
Thermal Conductivity	10 W/mK	5.78 Btu/hr ft^{o}F
Specific Heat	322 j/kgK	0.08 Btu/lb^{o}F
Latent Heat	24,200 J/kg	10.4 Btu/lb
Ultimate Tensile Strength	750-960 MPa	110-140 ksi
Elongation to Failure	15.5%	15.5 %
Yield Strength (Austenite)	560 MPa	80 ksi
Young's Modulus (Austenite)	75 GPa	11 mpsi
Yield Strength (Martensite)	100 MPa	15 ksi
Young's Modulus (Martensite)	28 GPa	4 Mpsi

Table 1: NiTiNOL properties. [4]

But the Shape Memory effect was discovered only in 1960, when Buehler was joined by Raymond Wiley to perform some fatigue resistance tests. During a meeting with management organized by Wiley in order to show the obtained results, one of the technical directors, David Muzzey, decided to assess the behaviour of a NiTiNOL wires under cyclic bending and heating: to the astonishment of those present, when Muzzey heated the deformed wire with his pipe, it returned to its initial non-deformed status.

Immediately they realized the potential of such alloys and their study continued briskly, attracting an increasing number of researchers and producers in the ranks of those who are devoted to experimentation and modeling of these materials.

In 1965, a patent was given to metallurgists Buehler and Wiley [5] for their development of the NiTi alloy series: 55-Nitinol was the name given to the alloy (the 55 refers to the nickel percentage composition in the alloy). Typical Nickel-Titanium alloy contains 49 to 57 percent Nickel. The composition of Nitinol, as illustrated on the nickel-titanium phase diagram in Figure 1, has a titanium composition varying from 0 to 50%, but the ideal composition of Nitinol can only vary between 38% and 50% titanium by weight: only this composition of Nitinol possesses the shape memory characteristics.
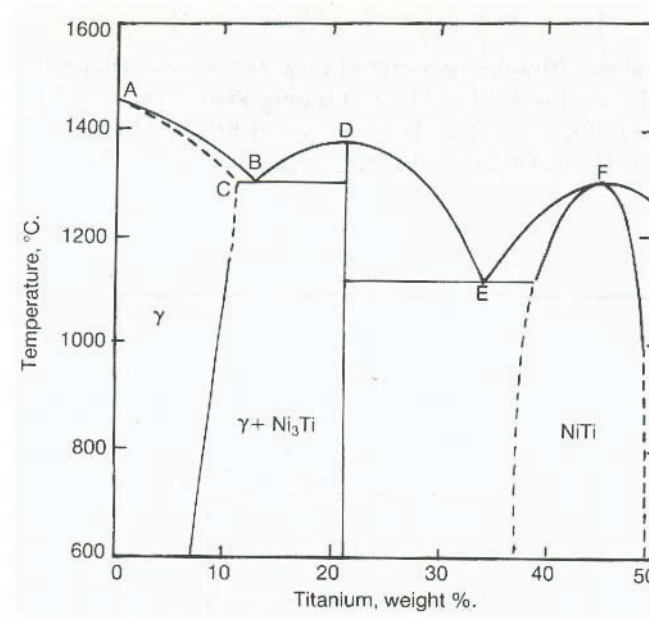
Figure 1: Nickel-Titanium phase diagram. [6]

Table 2 is a list of some of these alloys and associated properties.

Alloy	Composition	Transformation Range (°C)	Transformation Hysteresis (°C)
Ag-Cd	44-49% Cd	-190 to -50	15
Au-Cd	46.5-50% Cd	30 to 100	15
Cu-Al-Ni	14-41.5% Al; 3-4.5% Ni	-140 to 100	35
Cu-Sn	15 at.% Sn	-120 to 30	/
Cu-Zn	38.5-41.5% Zn	-180 to -10	10
Cu-Zn-X (X=Si,Sn,Al)	5-10% X	-180 to 200	10
In-Ti	18-23% Ti	60 to 100	4
Ni-Al	36-38% Al	-180 to 100	10
Ni-Ti	49-51% Ni	-50 to 110	30
Fe-Pt	25% Pt	-130	4
Mn-Cu	5-35% Cu	-250 to 180	25
Fe-Mn-Si	32% Mn; 6% Si	-200 to 150	100

Table 2: Alloys exhibiting a Shape Memory effect. [7]

The most interesting and useful alloys, from a practical point of view, proved to be those of the Nickel-Titanium group and some based on Copper (Cu). Today, the most studied Shape Memory Alloys are the Copper-Aluminum-Nickel, Copper-Zinc-

Aluminum and Iron-Manganese-Silicon. Table 3 shows some characteristics of these alloys.

Properties	Ni-Ti	Cu-Zn-Al	Cu-Al-Ni
Max temperature for shape recovery	100 °C	120 °C	200 °C
Max recoverable strain	8 %	6%	5%
Thermal Hysteresis	12-50 °C	10-25 °C	15-20 °C
Yielding Strength in Austenitic phase	415 Mpa ($41.5 \, Kg/mm^2$)	350 Mpa ($35 \, Kg/mm^2$)	400 Mpa ($40 \, Kg/mm^2$)
Yielding Strength in Martensitic phase	70 Mpa ($7 \, Kg/mm^2$)	80 Mpa ($8 \, Kg/mm^2$)	130 Mpa ($13 \, Kg/mm^2$)
Failure Strength	700 Mpa ($70 \, Kg/mm^2$)	600 Mpa ($60 \, Kg/mm^2$)	500-800 Mpa ($50-80 \, Kg/mm^2$)
Density (g/cm^3)	6.5	7.6-8.0	7.2
Resistivity (micro-ohm-cm)	80-90	8.5-9.7	11-13
Thermal Capacity (J/Kg °K)	837	400	373-574
Thermal Conductibility (J/m*sec*°K)	18	120	30-43

Table 3: Characteristics of some Shape Memory Alloys. [7]

The remarkable complexity of the SMAs metallurgical system has been a hindrance to their diffusion in the industry for many years. Starting from the mid-80s and especially since 1991, one could observe a gradual penetration of these materials into high value-added fields (aerospace, biomedical), traditionally more willing to accept innovative materials, being able to more easily absorb related high costs.

In recent years, the availability of materials with better characteristics and improving quality, together with reduced production costs, allowed the development of an increasing number of products, thus determining the preconditions for the spread of these materials in different technology areas; the existence of new business opportunities, in turn, stimulated research, triggering a synergetic process that makes this industry in rapid evolution.

2 SHAPE MEMORY ALLOYS GENERAL CHARACTERISTICS

Shape Memory Alloys can be found today in an ever increasing number of applications in the aerospace, civil, mechanical, medical field and others.

They represent a class of metallic materials by the unusual mechanical properties: in particular, their main characteristic is to be able to recover (hence the special "memory" feature) a preset macroscopic form (stretched or bent) by a mere change in temperature or applied stress field.

An example of Shape Memory effect is illustrated in the sequence of Figure 2 [8]. By means of an appropriate heat treatment, the shape of a Christmas tree with the inscription CNR was etched in a Ni-Ti wire. Once cooled, the little gadget has been distorted so that the initial form is no longer recognizable. Despite this, however, there has been no damage to nuclear provisions and, simply by heating the wire (in this case with a very ordinary hot-air dryer), a progressive recovery of the initial "pre-set" form is possible.
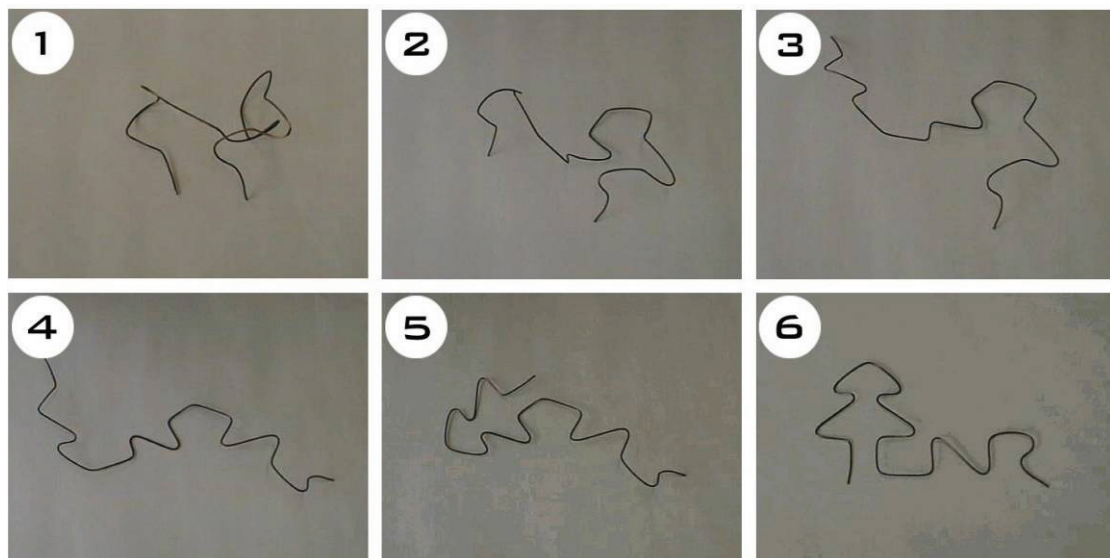
Figure 2: Example of Shape Memory effect. In a NiTi wire a suitable shape has been etched by means of an appropriate heat treatment. After cooling and manual distortion, it can recover its initial "pre-set" shape simply by heating the wire to 60°C. [8]

As previously mentioned, Buehler & al. in 1962 discovered that Nickel-Titanium alloys showed a greater capacity than other alloys to store a given "shape".

Indeed, this alloy shows a resilience to stretching of 100%, provided that the imposed strain does not exceed 8% of the initial extension: this makes it attractive for use as an actuator at low frequency (less than 1 Hz). This shape recovery is associated with the

possibility of the alloy to exist in two different solid phases, each stable at a "high" or "low" temperature; the temperatures at which the alloy "remembers" its shape when heated can also be modified by small changes in composition of material and through heat treatments. For instance, the phase transition temperature for equi-atomic Ni-Ti alloy is at about 100 °C, but the addition of an extra amount of Nickel allows to lower this value to about 0 °C: so, it is possible to modify the behaviour of the alloy according to the application requirements.

Another interesting feature is the variation of Young's modulus (E) between 2 and 4 times when the alloy undergoes the phase change, to which is also associated a large variation in resistivity and release (or absorption) of latent heat.

What makes Shape Memory Alloys very interesting as actuators is their ability, during the pre-strain recovery (phase transition on heating), to dispatch an high recovery strength (many times the initial stress required to pre-strain the alloy at the "low" temperature).

The shape that an SMA alloy stores may be assigned through a process of annealing, at temperatures, for instance, larger than 500 °C for the Ni-Ti alloy.

There are multiple ways to produce a Shape Memory Alloy: generally these involve melting techniques (using electric arc, electron beam, etc.) in a vacuum [9, 10]. The molten alloy (at temperatures between 700 °C and 900 °C) is then shaped in rods by rotation or casting, and eventually in wires. There is also a process of cold production of these alloys, in which case the procedure is similar to the production of titanium: however, this process leads to different physical and mechanical properties for the alloy; Jackson & al. [11] have addressed these issues in great detail.

Properties of Shape Memory Alloys and how they change with the production process can be of great interest: for example, Mahmud et al. [12] showed that it is possible to create Ni-Ti materials with enlarged transformation intervals, either in stress or in temperature: their study investigated a novel concept of partial annealing cold-worked near-equiatomic NiTi alloys in a temperature gradient so to create structurally graded matrices of varying transformation and deformation characteristics, with the purpose of achieving a structural gradient for continuously varying properties.

3 SMA THERMO-MECHANICAL BEHAVIOUR

Shape Memory Alloys are characterized by a solid state phase transformation, that is where both the starting phase (or parent phase, called austenite, named after the English scientist William C. Austen) and the final one (or product phase, called martensite, named after the German scientist Adolf Martens who first observed it) are solid structures, although with different crystallographic arrangements [3]: this transformation is called "martensitic thermo-plastic transformation" (Figure 3).
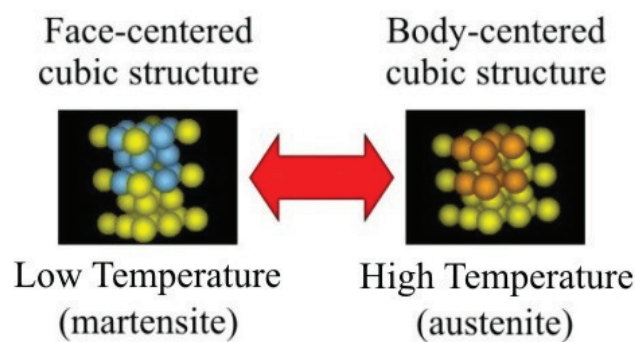
Figure 3: Martensitic thermo-plastic transformation of SMAs.

The different crystalline structure makes the austenite behaves like many metals, while the martensite behave more like an elastomer, in which there is a "plateau" stress: Figure 4 helps to understand this different behaviour by means of stress-strain curves for both phases.
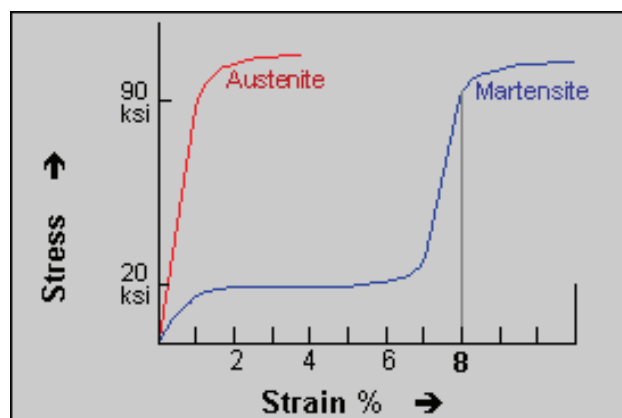
Figure 4: Stress-Strain behaviour of both the austenite and martensite phases.

The thermo-mechanical behaviour of SMA materials is due to such a transformation between two different solid phases: it depends on the temperature, the applied mechanical loads and the history of the material.

The crystal structure of martensite is obtained from austenite following the application of a mechanical load or a decrease in temperature; by heating or reducing the applied load, the austenite phase is recovered [1, 13]. In absence of applied loads, phase transformation temperatures (also called "critical temperatures") are referred to as M_s, M_f, A_s, A_f (M=martensite, A=austenite, s =start, f=final); for many SMAs, it also results that $M_f < M_s < A_s < A_f$.

Figure 5 shows temperature dependence in the composition of the material. By varying the SMA temperature in absence of applied loads, the status of the material will change, whose composition is generally defined in literature as a function of the volume fraction (ξ) of martensite. In particular, during the transition the material will go through several stages, starting from one phase of 100% austenite (temperature equal to or greater than A_f and $\xi = 0$) to a point where both martensite and austenite co-exist in different proportions, and finally a 100% martensite phase (temperatures at or below M_f and $\xi = 1$); the opposite happens when heating the alloy. These transition temperature, also known as "critical temperatures", vary with the applied load, in particular increase with the load (as it requires more energy to deform the crystal structure): details will be discussed later in this work.
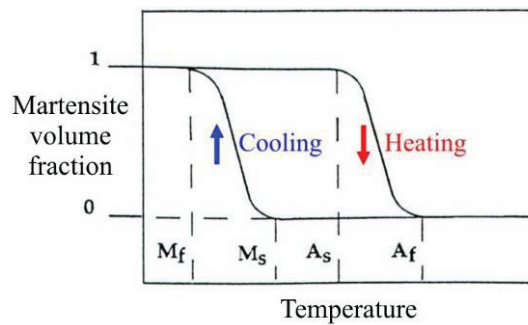
Figure 5: SMA phase transformation with temperature.

As a result of this transformation, the observable macroscopic mechanical behaviour of SMA materials can be separated in 2 categories (Figure 6):

1) the "Shape Memory" effect (SME) (Figure 6(a)), in which an SMA specimen exhibits a large residual strain (apparently plastic) after being subjected to a load and then unloaded, with this deformation that can be completely recovered by raising the temperature of the material;

2) the "pseudo-elastic" effect (Figure 6(b)), in which an SMA specimen exhibits a very large deformation (apparently plastic) after being subjected to a load, which can then be completely recovered by means of a hysteretic loop when unloading.

Let's describe more in detail the two effects [7].
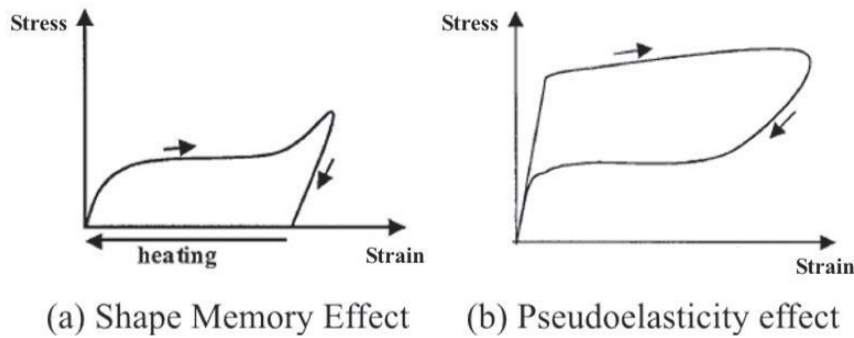
Figure 6: SMA Stress-Strain behaviour: (a) the Shape Memory effect; (b) the Pseudo-elastic effect. [14]

The first property (SME) is particularly useful and is due to the specific crystalline structure of the martensite phase (the typical phase for an SMA at room temperature (or low temperature)). It consists of a dense arrangement of crystal planes placed with an opposite orientation and with very high relative mobility (hence the low Young's modulus and damping characteristics). So, when the material, in martensite phase, is strained from an external stress higher than the yield point, instead of breaking the crystallographic ties and damage its structure, the crystal planes gradually unfolds the lattice (this phenomenon is called "detwinning"), accommodating the strain without achieving significant atomic displacements. Figure 7 summarizes this phenomenon at the microscopic level [14].
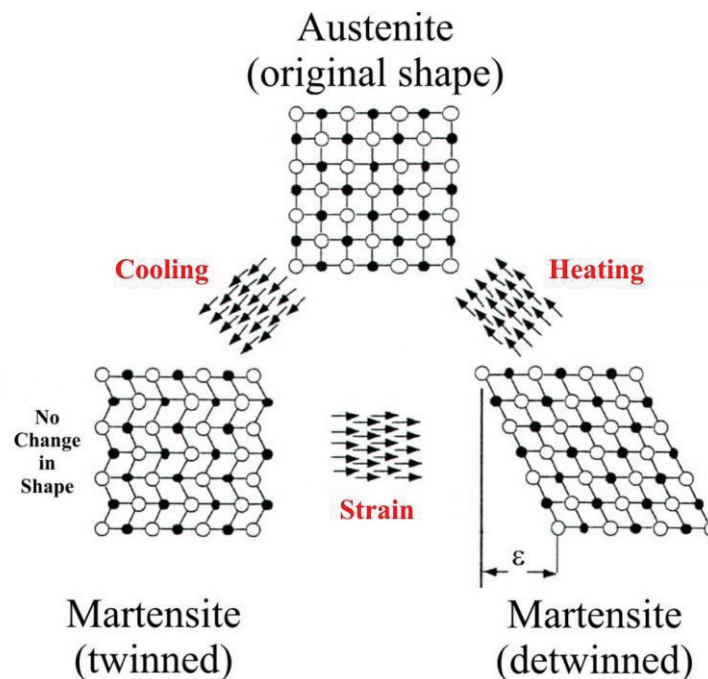
Figure 7: Microscopic phenomenology associated with the Shape Memory Effect.

To better understand this, one can imagine an accordion bellows: when stretching an accordion, the single fold of the bellows moves a little, but the whole structure unfolds to a length much greater. Because of this mechanism, the individual atoms are displaced only slightly from their original locations during this straining; as a result of an imposed heating, they can recover easily their initial configuration and thus promote the recovery of the initial macroscopic shape (this also involves the recovery of the strain), and restore the starting crystal structure (austenite, the high temperature phase) which by its nature is characterized by a rigid crystal structure (this explains the higher Young's modulus and damping of the material in this phase).

Figure 8 focuses on the macroscopic effects, considering hypothetical rods of SMA material [15].

If the Shape Memory alloy upon activation (heating) can not freely return to the original shape due to, for example, the presence of constraints, then a large recovery stress occurs; conversely, if the alloy is in no way restricted, there is no recovery stress (free recovery).

| Austenite | Martensite (twinned) | Martensite (detwinned) | Martensite (detwinned) | Austenite |

COOL Load Unload HEAT

| $T > A_f$ | $T < M_f$ | | | $T > A_f$ |
| $\sigma = 0$ | $\sigma = 0$ | $\sigma > \sigma_{crit}$ | $\sigma = 0$ | $\sigma = 0$ |
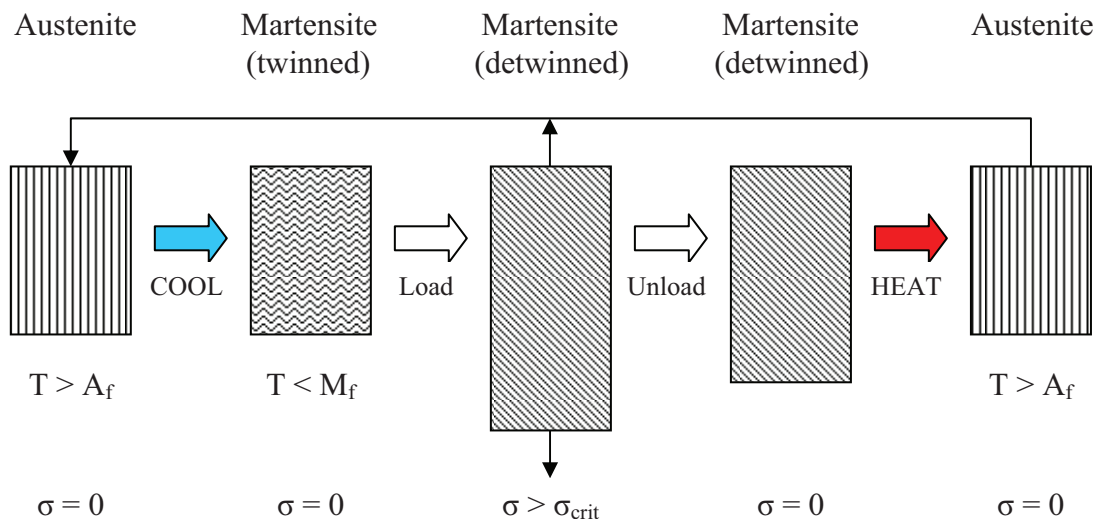
Figure 8: Macroscopic phenomenology associated with the Shape Memory Effect.

The second property (pseudo-elasticity) of the thermo-elastic martensitic transformation is related to the possibility of phase transformation to occur not only by varying the alloy temperature, but also by applying a suitable stress state under appropriate temperature conditions ($T > A_f$, that is the alloy is in austenite phase). In practice it is possible to gain the same "accordion" highly deformable crystalline structure within the material during the application of an external force, directly going from the austenite phase to the strained martensite one. During the straining imposed by means of the

external force, the material gradually forms the martensite structure that instantly deforms, without permanently damaging the crystal structure of the material: compared to the previous case, there is no twinned martensite phase.

Figure 9 and Figure 10 respectively summarize the pseudo-elastic effect on the microscopic and macroscopic level.

However, since this procedure is conducted in a temperature range where the martensite phase could not exist (because at that temperature the stable phase should be the high temperature one, ie austenite), when the external force is removed the alloy is in a state of thermodynamic instability and tends to revert instantly, promoting an immediate shape recovery: from a phenomenological point of view, the material immediately recover its original shape thus giving the idea of a remarkable resilience.
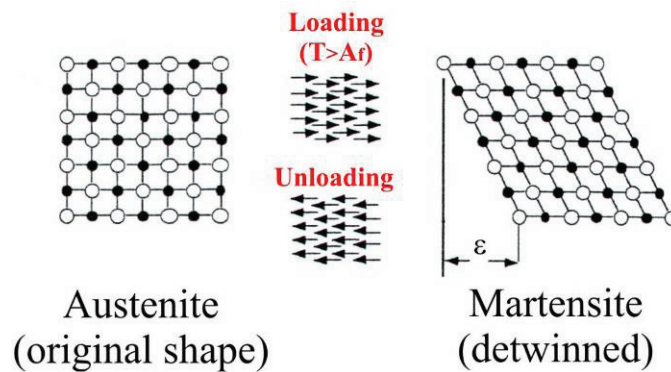
Figure 9: Microscopic phenomenology associated with the Pseudo-elastic Effect.
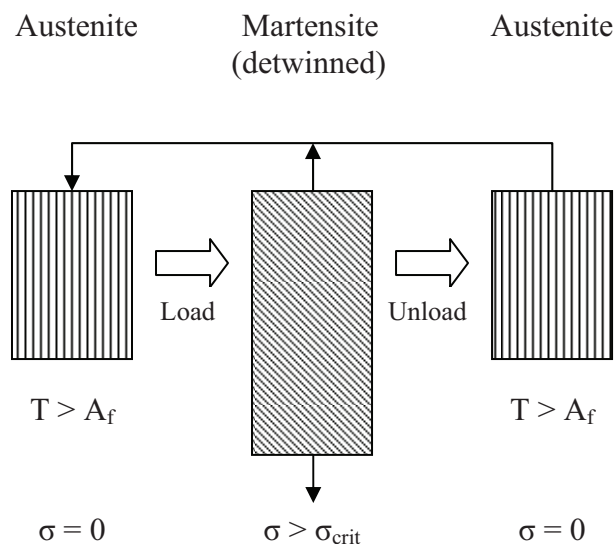
Figure 10: Macroscopic phenomenology associated with the Pseudo-elastic Effect.

This second property of Shape Memory Alloys has found multiple applications also due to its ease of use (obviate the need for heating and cooling the material). An example is

presented in Figure 11: a pair of eye glasses with metal parts in SMA adopting the pseudo-elastic effect, which can be locked inside one hand and highly deformed and, then, immediately return to its original shape by simply removing the straining action.
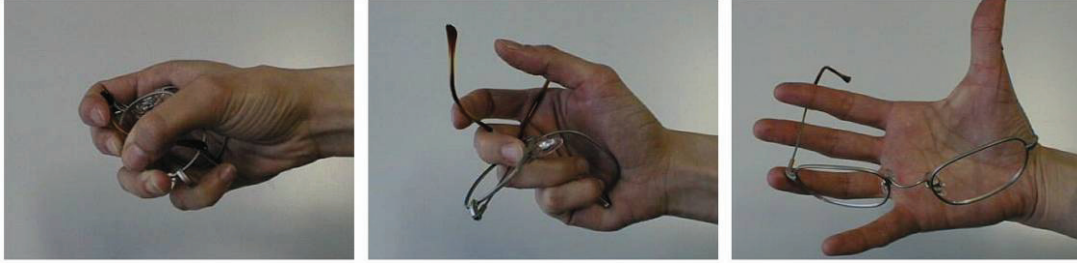
Figure 11: Pseudo-elasticity example for a Ni-Ti alloy. A pair of eye glasses made with SMA is severely deformed and can recover its initial shape when left free. [8]

Both effects (SME and Pseudo-elasticity) can be summarized in a single stress-strain diagram (Figure 12). A solid line represents the behaviour of a SMA tested at a temperature T> A_f, that is the Pseudo-elastic effect.
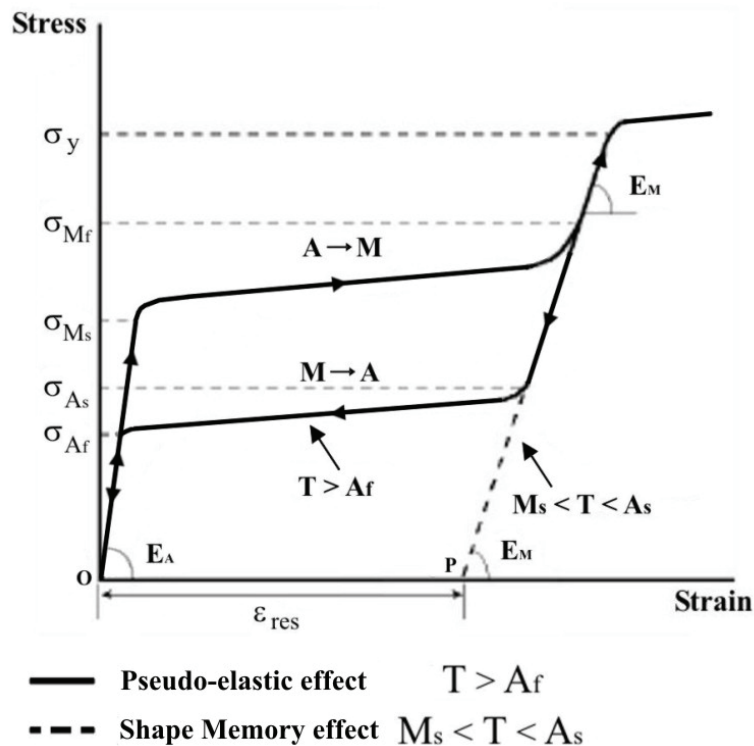
Figure 12: Typical SMA Stress-Strain diagram.

Starting from a zero stress condition, the alloy is subjected to an applied load: the trend is linear in the beginning as associated with the elastic behaviour of the 100% austenite phase (Young modulus E_A), up till the beginning of the phase transition (from austenite to martensite) at the martensite start stress (σ_{Ms}); after the transition finishes, when the

alloy is 100% martensite at the martensite finish stress (σ_{Mf}), the trend is linear again in the elastic range of the new phase (Young modulus E_M) and stops at the yielding limit (σ_y).

During the application of the load is typically reached a point between σ_y and σ_{Mf}; then unloading begins (always considering a constant temperature $T > A_f$). The unloading path initially follows a linear behaviour associated with elastic unloading of martensite, until the austenite start stress (σ_{As}) is reached; continuing to decrease the applied stress load, the phase transition occurs and the alloy again attains a 100% austenite phase at the austenite finish stress (σ_{Af}); the further reduction of stress brings back to the initial condition in a linear elastic fashion.

If the loading-unloading process is conducted at a constant temperature $M_s < T < A_s$, the Shape Memory effect is taken into consideration: the trend followed by the SMA during loading is exactly the same as for the Pseudo-elastic effect, while the dotted line shows its behaviour upon unloading. In this case, the zero stress condition is reached leaving a residual strain in the alloy (ε_{res}): when heated at a temperature $T > A_f$, the material will recover its original shape again, reaching the initial condition (zero stress and strain). So, it can be noticed the need for the Shape Memory effect of having to raise the temperature to recover the austenitic phase (and thus the original form), which instead is not necessary for the Pseudo-elastic effect.

Another way to look at both effects, considering also the temperature variable, is shown in Figure 13.
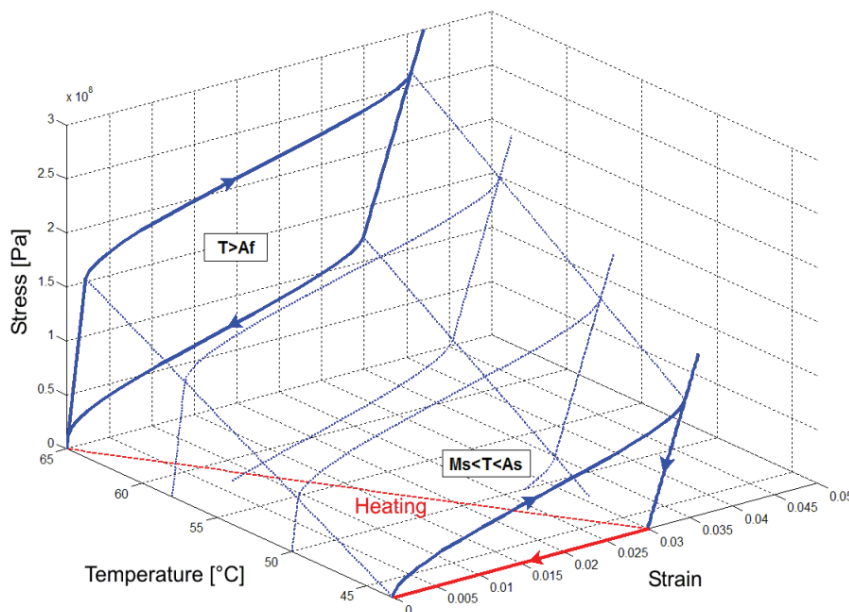
Figure 13: Typical SMA Stress-Strain-Temperature diagram.

Moreover, the Shape Memory effect can be of two different types:

1) **One-Way Shape Memory** (Figure 14(a));

2) **Two-Way Shape Memory** (Figure 14(b)).

The first category refers to SMA materials as hitherto discussed, for which a deformed shape must be imposed and upon thermal activation the initial configuration is attained; the second category, instead, relates to those materials that can "remember" two shapes, each of which can be retrieved at different temperatures, without requiring an imposed deformation. The Two-Way Shape Memory effect is usually attained with particular types of SMAs (which usually exhibit lower mechanical properties) and after extensive "training" (loading-unloading); moreover, they have lower performance as actuators (lower recovery stress when constrained). Some works focused on Two-Way SMAs can be found in [16-18].
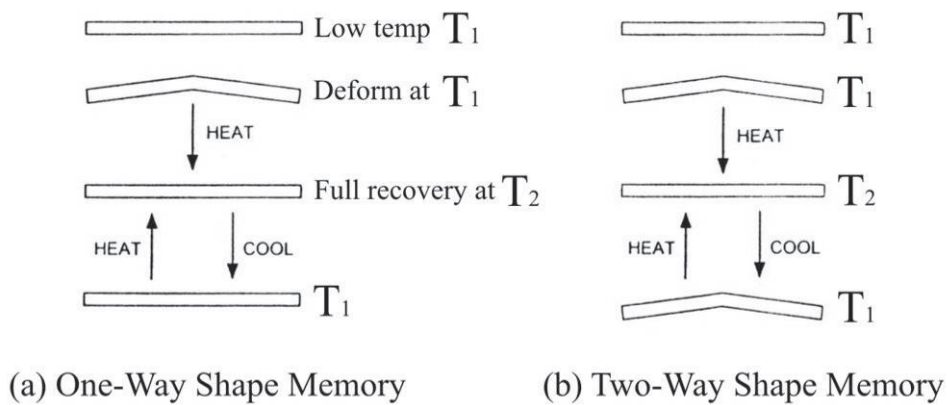
Figure 14: Shape Memory effect: (a) One-Way; (b) Two-Way.
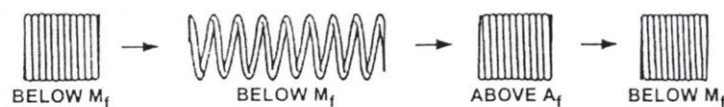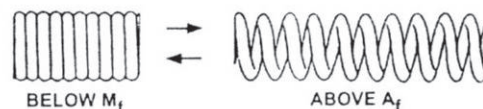
Figure 15: Example of Shape Memory effect: (a) One-Way; (b) Two-Way.

However, there exist another way to look at the martensitic phase transformation, and to understand the reason for which one phase (martensite or austenite) is stable in certain conditions of temperature and stress field.

Depending on its shear deformation ε and temperature T, the lattice layers have a determined free energy. Every layer can be considered as an ensemble of lattice particles being in the same phase. The governing potential for the thermo-mechanical behavior of such an ensemble is the Helmholtz free energy $\Psi = U - T\,S$ consisting of the internal energy U and the entropy S.

Figure 16 (left) shows a schematic sketch of a typical free energy at a fixed temperature and without the action of an external load, where all three phases are stable. It consists of a chain of parabolae: three of them are convex and two concave. The convex parabolae belong to the three phase, whereas the two concave ones are energy barriers separating them. Figure 16 (right) illustrates the action of an external load σ: its work $-\sigma\varepsilon$ needs to be added to the free energy.
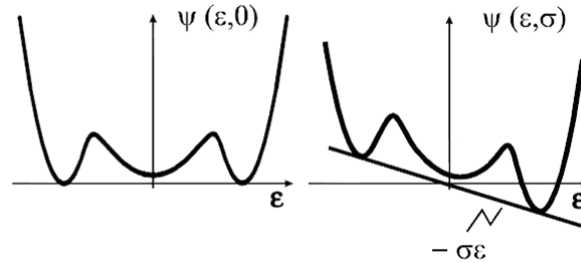
Figure 16: Free energy of a lattice layer for a fixed temperature without (left) and with external load (right).

The Helmholtz free energy Ψ can be derived with arguments from statistical mechanics: the interested reader can refer to [19] for details. Since the free energy is a function of the temperature, its influence can be discussed using Figure 17 for a specimen made of NiTi for four different temperatures [20]. At the lowest temperature of T = 293K there are only the two martensite phases M+ and M− stable; the free energy has two minima. An increase in temperature to T = 300K yields to the creation of a third minimum, which belongs to the austenite phase. Upon further heating to T = 305K the center minimum represents already a lower energy than the ones belonging to the martensite phases, but the remaining energy barrier between the phases prevents a transformation from happening. This occurred already at T = 328K since the austenite is the only stable phase at this temperature, and the energy barriers were eliminated. One identifies this process as entropic stabilization of the austenite; the reversal is the formation of the so-called temperature induced martensite.

Under the action of an external load σ, the Gibbs free energy becomes the governing thermodynamic potential for a lattice layer. The effect of an increasing load is discussed

using Figure 18 for a fixed temperature T = 328K. The illustration at the top left shows the load-free state, where the Helmholtz and Gibbs free energy are identical, and, thus, is the same plot as the last one in Figure 17.
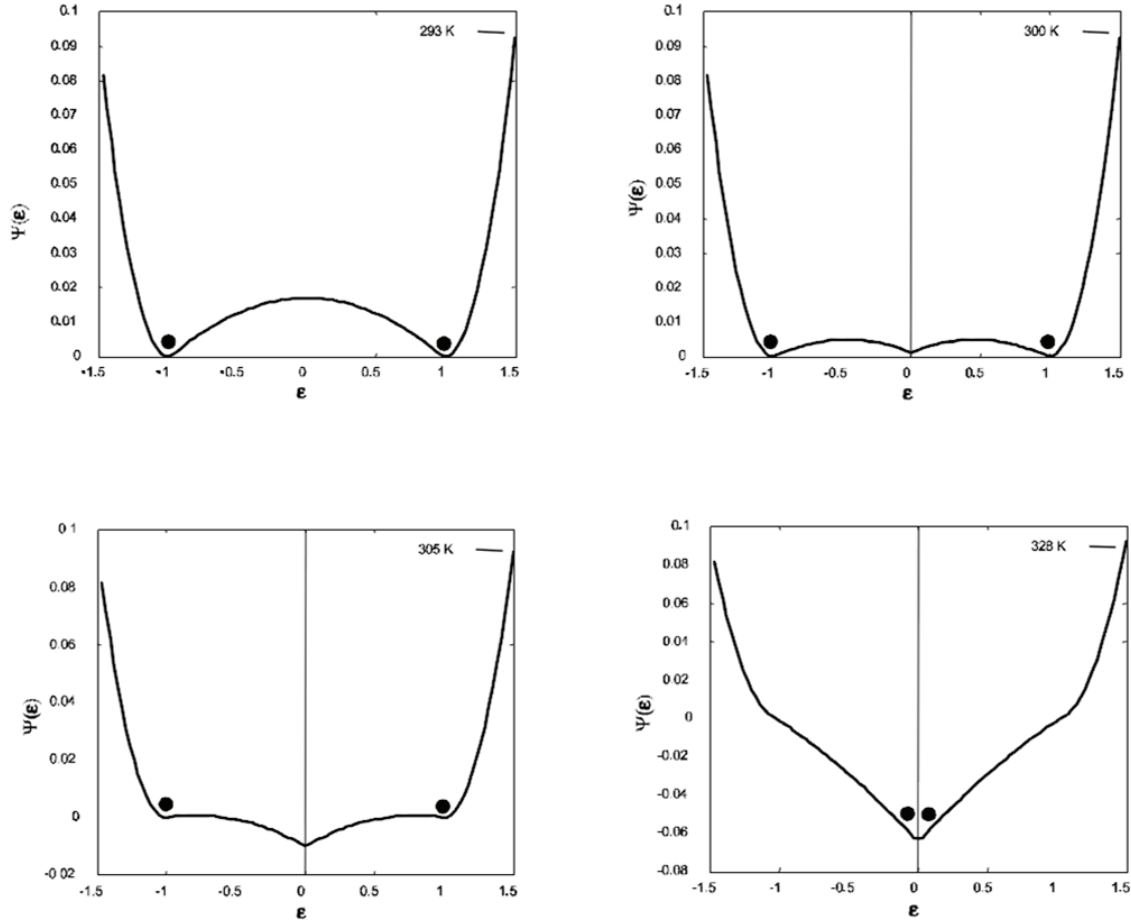
Figure 17: Free energy of a lattice layer for different temperatures. [20]

An increasing load to σ = 50MPa lowers the minimum for M+ and raises the one for M−. It may be observed that the austenite is still stable with the lowest energy minimum. This changes for σ = 150MPa, where the austenite remains stable, although the martensite M+ the same energy. Since both minima are still separated by an energy well, no phase transformation is occurring. At σ = 250MPa the barrier was eliminated, the martensite M+ has the lowest energy and the specimen transformed into the so-called load-induced martensitic phase.

Along with this phase transformation goes a significant increase in the specimen's strain. Subsequent unloading of the specimen to σ = 150MPa does not result in a phase transformation, since Figure 18 shows a present energy barrier for this load. The reverse transformation to the martensite phase will occur at lower load, restoring the transformation strain and, thus, creating a typical stress vs. strain hysteresis. This can be

identified as the pseudoelastic material behaviour of the shape memory alloy typically occurring at high temperatures.
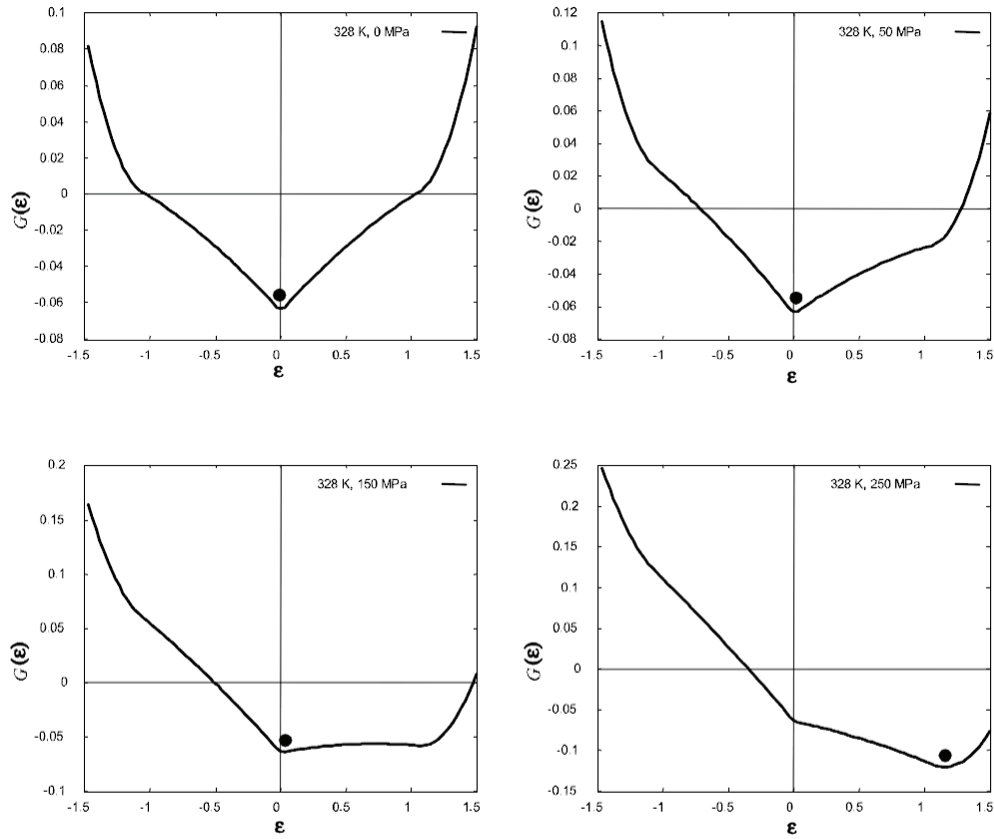
Figure 18: Free energy for a lattice layer for T = 328K and different loads. [20]

4 CONSTITUTIVE MODELS

Many constitutive models have been developed to describe the thermo-mechanical behaviour of SMA materials. Some are based primarily on micro-mechanics, others on a combination of micro and macro-mechanics (SMA phenomenology), statistical mechanics or kinetic methods. The development of numerical methods such as the Finite Element Analysis (F.E.A.) has led to a preference for constitutive models based on the description of the continuum (related to phenomenology, on the macro scale); moreover, these models can also use the typical engineering constants as parameters rather than quantities which are difficult to measure. Most of these macro models have been developed for quasi-static loads only.

One of the first and most popular one-dimensional models is due to Tanaka [21] and is based on thermo-mechanics: in this model, the second law of thermodynamics is written in terms of Helmholtz free energy in the variational form. It is assumed that the mono-axial deformation, temperature and volume fraction of martensite (ξ) are the only state variables; furthermore, the volume fraction of martensite is dependent on stress and temperature by means of an appropriate exponential expression. Liang & Rogers [22] also presented a model based on Tanaka constitutive equation: however, in their model a cosine function of temperature and stress was used to describe the volume fraction of martensite.

One of the major limitations of these models is that they only describe the stress-induced martensitic transformation (Pseudo-elastic effect) and do not consider the transformation induced by the strain (Shape Memory effect): therefore, they can not be applied to model the detwinning of martensite which is responsible for the SME at low temperature.

To overcome this limitation, Brinson [23] developed a constitutive model that separates the volume fraction of martensite in two parts: the one stress induced (often referred to in literature as stress-induced martensite, S.I.M.) and the one induced by temperature. The first part characterizes the amount of detwinned martensite present in the alloy (stress induced), while the second is the fraction of twinned martensite, present after the reversible phase transformation from austenite.

To consider both the Shape Memory and Pseudo-elastic effects, the coefficients of the constitutive equation are considered to be not constant.

Another constitutive model is the thermodynamic model of Boyd & Lagoudas [24, 25], which is based on free energy and the dissipation potential. This model is derived from Gibbs free energy instead of Helmholtz free energy, as used in the Tanaka model. This model can handle three-dimensional effects and not proportional loads.

A thermodynamic formulation is also used in the model developed by Ivshin & Pence [26] and Chang et al. [27]; other models have been conceived in recent years as expansion of previous ones or an adaptation to Finite Element procedures [28-30].

However, there are also models not based on these two types of approach. For example, Grasser & Cozzarelli [31] have developed a three-dimensional model based on developmental plasticity; then, Ren et al. [32] proposed a further improvement. Peng et al. [33] proposed a two-phase mixture model incorporating the conventional theory of plasticity. Similarly Juhasz & al. [34] have proposed evolutionary equations based on the analogy with visco-plasticity, assuming that the phase transformation takes place with a fixed finite speed, so that the relaxation process occurs: these evolutionary equations provide the possibility to calculate the time-dependent effects; this model is able to predict the SMA behaviour under combined loading conditions, both mechanical and thermal. Sun & Hwang [35] have derived a micro-mechanical model taking into account the thermodynamics, the microstructure, the micro-mechanics and dealing with both the Shape Memory effect and Pseudo-plasticity. Matsuzakiet & al. [36] have developed a general one-dimensional thermo-mechanical model taking into account the effects of energy dissipation, latent heat and heat transfer during the phase transformation. They have introduced a general form for the energy function related to interaction of phase, which can be derived from experimental data at different load conditions. Barrett [37] has developed a one-dimensional constitutive model for SMAs which includes the effects of consolidation due to phase change, the hysteresis due to partial conversion and tension-compression transformations; however, the model makes no difference between the volume fractions of martensite induced by stress or by temperature. Heintze [20] developed a computationally efficient free energy model: a first implementation was based on a stochastic homogenization procedure and provided a very accurate description of the observed phenomena, but also required very high computation times; a reformulation of the underlying concept led to a parameterization method, which preserved the advantages of the original method, but dramatically reduced the computation times. He showed that the material behavior prediction of both models were identical, and the parameterization method was compared extensively to

data from tensile experiments with a pseudoelastic SMA wire. Remarkably, the model was able to capture all facets of the material behavior including rate-dependence and minor loops; the versatility of the model also allowed for the simulation of SMA actuator behaviour including the electrical resistance. Auricchio et al. [38-41] addressed some three-dimensional models, considering the isothermal stress-induced transformation in shape-memory polycrystalline materials and presence of permanent inelasticity. They treated the problem within the framework of the energetic formulation of rate-independent processes and investigated existence and continuous dependence issues at both the constitutive relation and quasi-static evolution level. Moreover, they focused on time and space approximation as well as on regularization and parameter asymptotics.

Let's take a look more in detail to some of these models.

<u>Tanaka</u> [21] assumes as state variables the strain ε, the temperature T and the volume fraction of martensite ξ, which can describe the one-dimensional behaviour of Shape Memory Alloys.

The constitutive equation is as follows:

$$(\sigma - \sigma_0) = E(\xi)(\varepsilon - \varepsilon_0) + \Theta(T - T_0) + \Omega(\xi)(\xi - \xi_0)$$

where the subscript 0 represents the initial condition. This equation shows that the stress is made of three quotes (in order):

➢ the mechanical stress,
➢ the thermo-plastic stress,
➢ the stress induced by the phase transformation.

Moreover, the Young's modulus E and the phase transformation coefficient Ω are function of the martensite volume fraction ξ; these are usually expressed as:

$$E(\xi) = E_A + \xi(E_M - E_A) \qquad\qquad \Omega(\xi) = -\varepsilon_L E(\xi)$$

where ε_L is the maximum recoverable strain, while E_A and E_M represent the Young moduli for the austenitic and martensitic phases respectively.

For the martensite volume fraction, Tanaka develops an evolutionary equation, determined by the dissipation potential, which depends on stress and temperature in an exponential fashion; in particular:

$$\xi = \Xi(\sigma, T)$$

➢ A → M transformation (cooling) $\xi = 1 - \exp[a_M(M_S - T) + b_M\sigma]$

➢ M → A transformation (heating) $\xi = \exp[a_A(A_S - T) + b_A\sigma]$

with the material constants defined as:

$$a_A = \frac{\ln(0.01)}{(A_S - A_F)} \qquad\qquad b_A = \frac{a_A}{C_A}$$

$$a_M = \frac{\ln(0.01)}{(M_S - M_F)} \qquad\qquad b_M = \frac{a_M}{C_M}$$

The applied stress is represented by σ, temperature by T. The adopted coefficients E, Θ and Ω, together with the parameters M_S, M_F, A_S, A_F, C_A and C_M are usually experimentally determined [14]: some typical values are reported in Table 4.

Coefficient	Unit measure	Value
Transformation start critical stress for martensitic phase σ_{cr}^{S} (Brinson model)	Pa	1.38e+6
Transformation finish critical stress for martensitic phase σ_{cr}^{F} (Brinson model)	Pa	1.72e+6
Slope of the critical stress-temperature plots for the austenite transformation boundaries C_A	Pa/°C	8e+6
Slope of the critical stress-temperature plots for the martensite transformation boundaries C_M	Pa/°C	12e+6
Austenite Young modulus E_A	Pa	45e+9
Martensite Young modulus E_M	Pa	20.3e+9
Austenite start temperature A_S	°C	52
Austenite finish temperature A_F	°C	65
Martensite start temperature M_S (Tanaka model)	°C	43.5
Martensite finish temperature M_F (Tanaka model)	°C	40.7
Martensite start temperature M_S (Brinson model)	°C	55
Martensite finish temperature M_F (Brinson model)	°C	42

Table 4: Thermo-mechanical properties of SMA wires (Dynalloy 15 mil Ni-Ti binary alloy). [42]

Some of these parameters will be discussed more in detail in the next paragraphs, as for the transformation start (σ_{cr}^{S}) and finish (σ_{cr}^{F}) critical stresses and the slope coefficients (on the stress-temperature diagrams) for austenite (C_A) and martensite (C_M). Let's note that the transformation temperature M_S, M_F, A_S and A_F are measured for a zero stress condition: in particular, M_S and M_F can have different definitions and meanings according to the selected model.

Liang & Rogers [22] utilized the same constitutive relation as Tanaka model, but developed a new form of the evolutionary equation for the martensite volume fraction as a cosine function. The justification for this can be found by a simple graphical observation on the diagram of the phase transformation cycle with temperature (Figure 19): it can be noticed as a cosine function well describes the phenomenon in question, provided its coefficients are properly fixed.
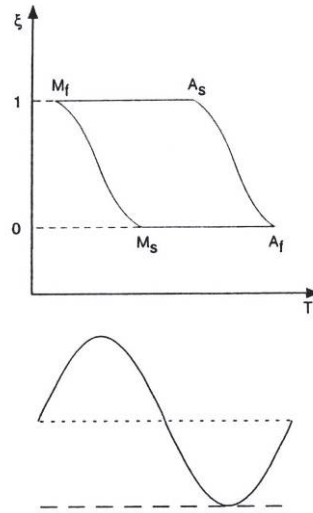
Figure 19: Phase transformation cycle with temperature and martensite volume fraction evolution. [1]

So, the martensite volume fraction function has been expressed as:

➤ A → M transformation (cooling)

$$\xi = \frac{1-\xi_0}{2}\cos\left[\alpha_M(T-M_F)+b_M\sigma\right]+\frac{1+\xi_0}{2}$$

➤ M → A transformation (heating)

$$\xi = \frac{\xi_0}{2}\cos\left[\alpha_A(T-A_S)+b_A\sigma\right]+\frac{\xi_0}{2}$$

where the constants are as follows:

$$\alpha_M = \frac{\pi}{M_S - M_F} \qquad\qquad \alpha_A = \frac{\pi}{A_F - A_S}$$

$$b_M = -\frac{\alpha_M}{C_M} \qquad\qquad b_A = -\frac{\alpha_A}{C_A}$$

and ξ_0 represents the initial martensitic fraction.

The cosine function argument can only assume a value between 0 and π: this implies that phase transformation only occurs if temperature is in an appropriate transformation range (or, similarly, the stress is in a suitable stress range):

➢ A → M transformation (cooling)

$$M_F \leq T \leq M_S \qquad\qquad C_M(T - M_F) - \frac{\pi}{|b_M|} \leq \sigma \leq C_M(T - M_F)$$

➢ M → A transformation (heating)

$$A_S \leq T \leq A_F \qquad\qquad C_A(T - A_S) - \frac{\pi}{|b_A|} \leq \sigma \leq C_A(T - A_S)$$

Both models however lack proper representation of Shape Memory effect (detwinning at room temperature); both models describe transformation from martensite to austenite and vice versa; they are, however, valid only for fully detwinned martensite state (single martensite variant).

Unlike the preceding two models, **<u>Brinson</u>** [23] model represents the transformation from the detwinned martensite to the stress preferred variant, which leads to a description of Shape Memory effect below A_S. This model uses a similar representation for constitutive equation with some modifications (subscript 0 refers to initial conditions as usual):

$$\sigma - \sigma_0 = E(\xi)\varepsilon - E(\xi_0)\varepsilon_0 + \Omega(\xi)\xi_S - \Omega(\xi_0)\xi_{S0} + \Theta(T - T_0)$$

where the martensite volume fraction is now divided into two parts:

$$\xi = \xi_S + \xi_T$$

with ξ_S the portion of the detwinned (or stress preferred) martensite present at low temperature and ξ_T the portion of twinned martensite twinned (or randomly oriented) that comes from reversible thermal phase transformation from austenite.

Also, a modified cosine representation for the martensite volume fraction is used:

➢ Martensite detwinned transformation

$$\bullet T > M_S \quad \begin{cases} \xi_S = \dfrac{1-\xi_{S0}}{2}\cos\left\{\dfrac{\pi}{\sigma_{cr}^S - \sigma_{cr}^F}\left[\sigma - \sigma_{cr}^F - C_M(T - M_S)\right]\right\} + \dfrac{1+\xi_{S0}}{2} \\[4mm] \xi_T = \xi_{T0} - \dfrac{\xi_{T0}}{1-\xi_{S0}}(\xi_S - \xi_{S0}) \end{cases}$$

$$\bullet T < M_S \quad \begin{cases} \xi_S = \dfrac{1-\xi_{S0}}{2}\cos\left[\dfrac{\pi}{\sigma_{cr}^S - \sigma_{cr}^F}(\sigma - \sigma_{cr}^F)\right] + \dfrac{1+\xi_{S0}}{2} \\[4mm] \xi_T = \xi_{T0} - \dfrac{\xi_{T0}}{1-\xi_{S0}}(\xi_S - \xi_{S0}) + \Delta_{T\xi} \end{cases}$$

with $\quad \Delta_{T\xi} = \dfrac{1-\xi_{T0}}{2}\{\cos[\alpha_M(T - M_F)] + 1\} \quad$ if $\quad M_F \leq T \leq M_S \quad$ and $\quad T < T_0$,

otherwise $\quad \Delta_{T\xi} = 0$

➢ Austenite transformation

$$\bullet T > A_S \quad \begin{cases} \xi = \dfrac{\xi_0}{2}\left\{\cos\left[\alpha_A(T - A_S - \dfrac{\sigma}{C_A}\right] + 1\right\} \\[4mm] \xi_S = \xi_{S0} - \dfrac{\xi_{S0}}{\xi_0}(\xi_0 - \xi) \\[4mm] \xi_T = \xi_{T0} - \dfrac{\xi_{T0}}{\xi_0}(\xi_0 - \xi) \end{cases}$$

The fourth model by **Boyd & Logoudas** [24, 25] is a more general three-dimensional model. In this model the total specific Gibbs free energy is determined by summing the free energy of each phase of shape memory materials plus the free energy of mixing.

A constitutive relation satisfying the second law of thermodynamics is then developed. The total strain consists of two parts: the mechanical strain ε_{ij} and the transformation strain ε_{ij}^{tr}, which is a function of the martensite volume fraction:

$$\sigma_{ij} = C_{ijkl}[\varepsilon_{kl} - \varepsilon_{kl}^{tr} - \alpha_{kl}(T - T_0)]$$

An evolutionary equation for the martensite volume fraction is derived from the dissipation potential:

$$\sigma_{ij}^{eff} + d^1 T - \rho b_1 \xi = Y^{**} + d_{ijkl}^3 \sigma_{ij}\sigma_{kl} + d_{ij}^4 \sigma_{ij}\Delta T$$

where Y^{**} is the threshold stress value, d^1T is related to the entropy reference state, d^3_{ijkl} and d^4_{ij} are parameters that are related to changing elastic moduli, ρ is the mass density, b_1 is a material constant, and ΔT is the temperature difference. Brinson and Huang [43] showed that this model reduced to one-dimensional format becomes identical to Tanaka's model. There is, however, one exception, that unlike Tanaka's model this one is applicable to represent the martensite transformation from twinned to detwinned state at a low temperature.

Another model developed by **Ivshin & Pence** [26] was derived from a thermodynamic consideration of the kinetic relations for the hysteresis of the phase fraction. Instead of using the martensite volume fraction ξ as the primary variable, they used the austenite volume fraction α with:

$$\alpha = 1 - \xi$$

So, total strain is:

$$\varepsilon = (1-\alpha)\varepsilon_M + \alpha\varepsilon_A$$

where ε_M and ε_A are strains in martensite and austenite regions.

Since the formulation of the original Tanaka model [21], it has been updated to cover the influence of the Shape Memory effect [44-49]. The primary update of the model has been carried out through the introduction of new effect called the rhombohedral-phase transformation (**R.P.T.**) or R-phase transformation.

The R.P.T. is a thermally reversible transformation that takes place at low strains and low temperatures, much like martensite detwinning; what makes it so interesting is the low thermal hysteresis and cyclic stability, so that it allows to approximate the stress-strain characteristic curve during unloading with the one during loading; the main disadvantage is the low attainable strain.

At low temperatures (below A_S) R.P.T. takes place, followed by regular martensite transformation. In repeated stress-strain cycling at room temperature (strain > 1%), the R.P.T. is noticeable only in the first cycle and disappears thereafter: this is attributed to two-way shape memory effect observed through heating and cooling of the specimen.

At high temperatures (between A_S and A_F) the R.P.T. is noticeable in the form of small non-linearity of the linear region of the pseudo-elastic curve. The RPT or R-phase effect is represented by a volume fraction coefficient η. Assuming the first cycle under zero stress/strain condition ($\eta=0$, $\xi=0$), an application of strain below 1% results in R-phase transformation ($\eta=1$, $\xi=0$). On heat activation the R-phase is recovered. In all other cases this does not happens. Using this concept, the authors were able to correlate

predictions with test data especially at low temperatures. **Naito et al.** [49] and **Sittner et al.** [48] represented the R.P.T. and martensite transformation in a unified way using energy function, with appropriate "switching functions" to handle different transformations.

Using the constitutive models in conjunction with the models for the martensite volume fraction develops stress-strain curves. Because ξ is a function of stress in all models, an iterative process such as the Newton–Raphson method is used to solve the mathematical problem for the stress. In this regard it should be noted that the Tanaka model uses an exponential representation of the martensite volume fraction and this may lead to convergence problems during the solution of the iterative process.

Recent works have highlighted some limitations of phenomenological models. **Elahinia & Ahmadian** [29, 30] have noted that in certain circumstances, combining contemporary variation of the applied stress and temperature (which may be a result of the physics of the problem), the model predictions do not correlate with experimental data: this is due to the dependence of critical temperatures with the applied stress (see next paragraph) and the assumption, made in the models, that the phase transformation is only possible between appropriate critical temperatures in the direction of the thermal cycle (and not otherwise).

However, other than constitutive models, also different approaches have been adopted in the scientific community: in particular, artificial intelligence algorithm known as "**Reinforcement Learning**" received quite a bit of interest [50-53]. This is a form of machine learning that utilizes the interaction with multiple situations many times in order to discover the optimal path that must be taken to reach the pre-determined goal.

By mapping the behaviour in real-time, both major and minor hysteresis loops of SMAs can be experimentally determined through this method, while simultaneously learning the policy required for control.

The SMA phase transformation is not a thermodynamically reversible process: this leaves uncertainty in the model due to the highly non-linear behaviour of the SMA. This model needs to be determined by use of the RL algorithm in conjunction with the experimental setup, so that a "black box" control policy can be determined for the use of the SMA.

A variety of implementations of some of these models can be found in literature, taking advantage of different commercial Finite Element solvers: ABAQUS [54-57], FEMLAB (now COMSOL Multi-physics) [58-62], Ansys [63-66].

5 CRITICAL TRANSFORMATION REGIONS

The modelling of Shape Memory Alloys starts from the constitutive models, which require some constants that can be obtained from the critical stress-temperature diagrams. Also if experimental results show some slightly non-linearity at the beginning and the end of the phase transformation, is it still possible to represent the critical stresses trend as a linear function of temperature.

Figure 20 is a plot that delineates the transformation regions [14].
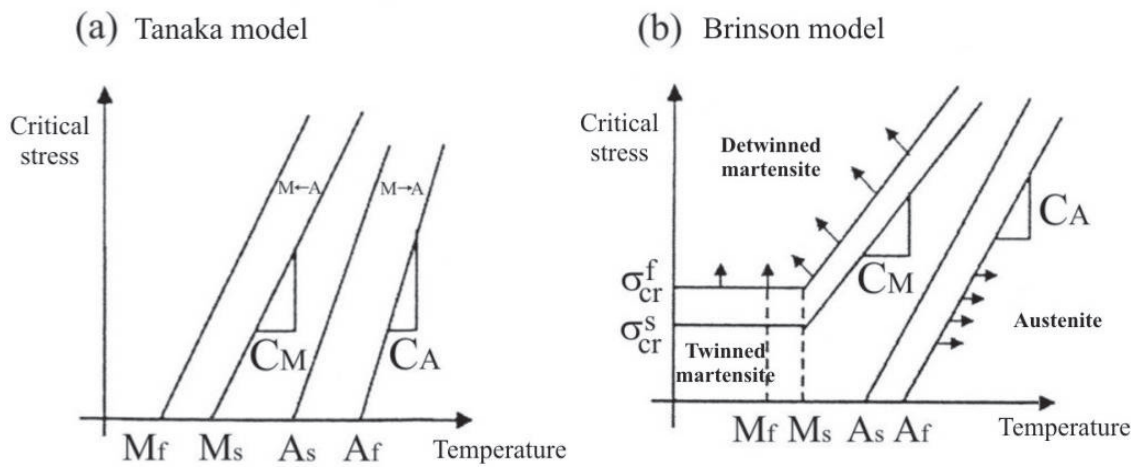
Figure 20: Critical stress-temperature profiles in constitutive models: (a) Tanaka; (b) Brinson. [14]

It can be interesting to observe how the martensitic phase transformation takes place in the stress-temperature diagram, for both the Shape Memory and Pseudo-elastic effect (Figure 21).
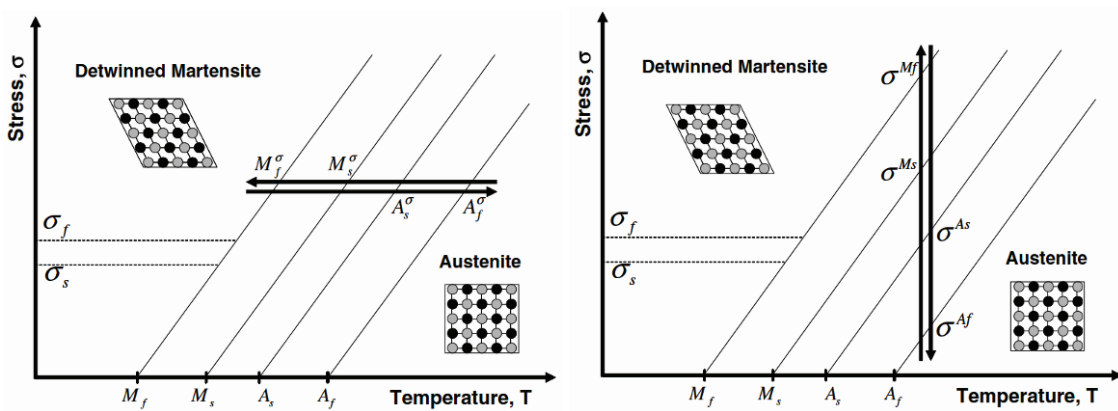
Figure 21: SMA phase transformation in the stress-temperature diagram for both the Shape Memory Effect (left) and the Pseudo-elastic effect (right).

The regions marked with arrows are those in which the material exists in pure form. All other regions could have a mixture of phases, and the exact content of the mixture depends on the thermo-mechanical history of the material. There are, however, differences in the definition of the material constants in different models. Both the **Tanaka** [21] and **Liang & Rogers** [22] models assume a straight-line stress-temperature relationship, and M_s, M_f, A_s and A_f correspond to zero stress condition; assuming non zero stress condition, the critical temperatures will raise in a linear fashion, to make the phase transition happen. On converse, when temperature is above M_s, the necessary stress to induce the martensite phase from austenite will be higher. Usually these models also assume $C_A = C_M$ (curve slopes), with a constant value along all the temperature range.

The stress-temperature relationship is somewhat different for **Brinson**'s model [23]: a new region is present representing the martensite twinned phase, which allows for the modelling of the Shape Memory effect at low temperature. The M_s and M_f are defined as the temperature above which the application of stress does not cause a pure transformation from twinned to detwinned martensite.

The critical stress σ^s_{cr} is the stress at which the transformation from twinned to detwinned martensite starts, and the critical stress σ^f_{cr} represents the stress where this transformation is nearly complete: these critical stresses are determined for a temperature below M_s and are considered indipendend with temperature. Strain at which detwinning gets completed is referred to as ε_L (limit strain).

Because of these differences, the interpretation of the transformation temperatures in the two types of models differs from each other. In Brinson's model the parameters M_s and M_f are defined as the temperature above which the martensite transformation stresses are a linear function of temperature, as shown in the Figure 20(b). In the Tanaka and Liang & Rogers models, however, these parameters are defined at zero stress, and are the temperatures for martensite start and finish obtained by cooling from austenite without the application of stress (Figure 20(a)).

Therefore, when calculating these constants from the experimental critical points, the numerical values used for Tanaka and Liang & Rogers model for M_s and M_f are obtained from extrapolating the martensite start and finish lines to zero stress, whereas those used by Brinson model are obtained at the critical stresses σ^s_{cr} and σ^f_{cr}. These different values for the models must be used in order to obtain a fair comparison between these models and to match them to experimental observations.

Prahlad & Chopra [67] presented critical stress-temperature data from different tests on the same curve and demonstrated the linear variation of the critical stresses with temperature that is assumed in all of the models (Figure 22).
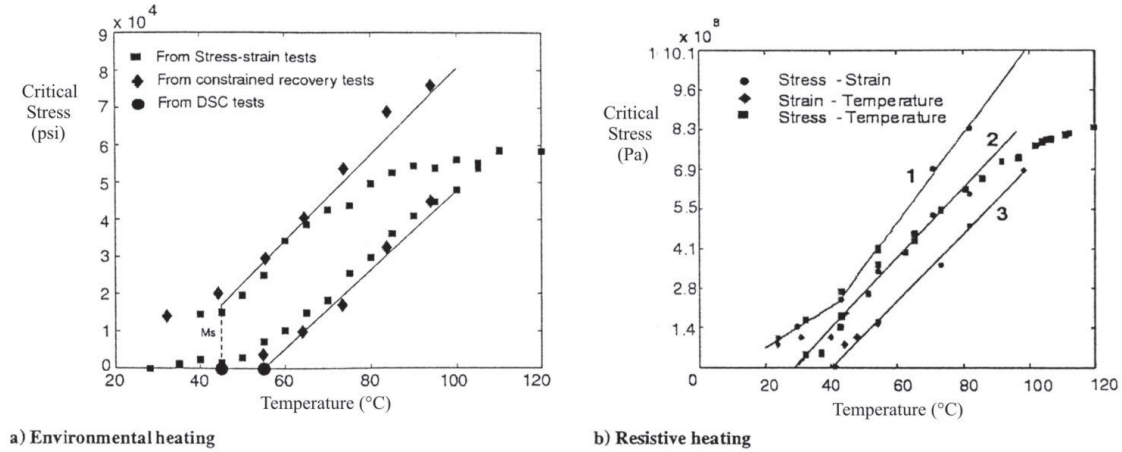
Figure 22: Experimental critical stress-temperature plots. [67]

Data corresponded to three different tests that, respectively, used heat flow measurements with differential scanning calorimeter (D.S.C.), constant temperature, and constant strain (constrained recovery) conditions. All of these tests were carried out at a very low heat rate and as such represented quasi-static conditions.

The recovery stress data points lie in the transformation region between the austenite start and finish states for heating phase, and martensite start and finish states for cooling phase. Thus the two straight lines represent martensite and austenite start condition, and help determining M_s and A_s; similarly the martensite and austenite finish follow nearly the same slopes and help determine M_f and A_f.

It is evident that if the coefficients are correctly identified from the experimental tests, all the considered models can predict the stress-strain behaviour of the SMA in an acceptable way at high temperature (above A_s) [42]: the Tanaka and the Liang & Rogers models are not valid for temperatures below A_s, whereas the Brinson model is applicable.

To determine the transformation temperatures (M_s, M_f, A_s and A_f) of the SMA under no stress condition, Perkin–Elmer DSC is normally used (Figure 23). This instrument uses the change in heat capacity of the material to determine the start and finish transformation temperatures. When the material undergoes phase transformation, it absorbs (or emits) large amount of heat with a relatively small change of temperature, and the DSC captures such a change. Two different temperature control methods are

used; the first involves the use of a thermal chamber (environmental heating), and the second involves internal heating (resistive heating).
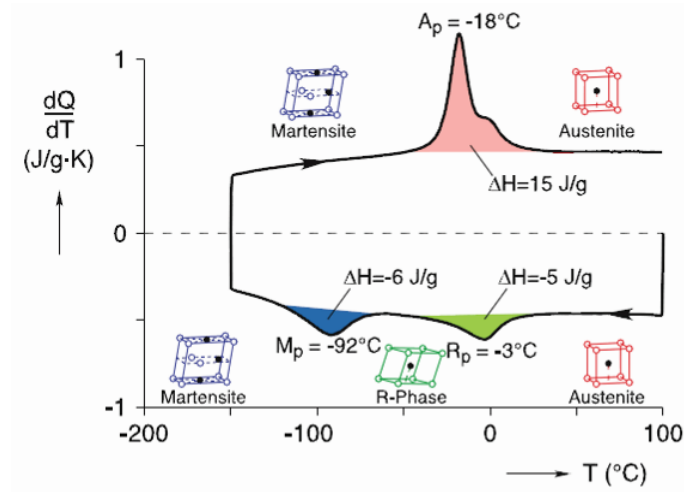
Figure 23: Example of transition temperatures measured for an SMA wire by means of a Differential Scanning Calorimeter. [27]

Even though similar trends are observed with both methods of heating, transformation stresses differ as a result of small variations in temperature (the plot is translated towards lower temperatures for the resistive heating, but slopes do not change).

Since during the phase transformation there is great variation in the internal resistance of the material [68], associated with the different crystalline nature of the two involved phases, it is quite difficult to maintain a constant temperature by the resistive heating technique, especially during the transition; it is still possible to get a control in the order of 2 -3 °C if the heating is very slow.

To stabilize the SMA for a repeatable behaviour, it becomes necessary to "cycle" the material mechanically (in the order of 20-30 cycles [69, 70]). One approach is to stretch the sample at a constant temperature (above A_f) and then release to zero stress condition. In the second approach the SMA is mechanically strained at room temperature (in martensite phase) followed by a thermal cycle under no stress condition by heating the material above A_f and then cooling down below M_f. Both methods are equally effective to stabilize the material, except the first method is simple because it does not require thermal cycling.

6 CONSTRAINED RECOVERY BEHAVIOUR

Large recovery stresses are developed when the SMA sample is constrained during the heating process and can not freely recover its strain. Figure 24 [67] shows the complete constrained stresses developed at different temperatures for different pre-strains.
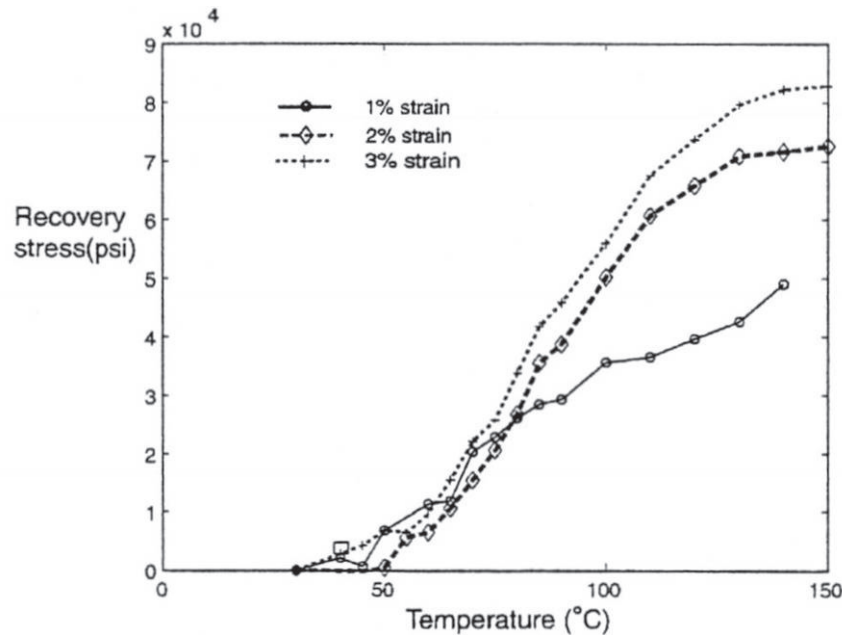
Figure 24: Restrained recovery behaviour with pre-strain. [67]

The final constrained stress is independent of pre-strain as long as it is above a threshold value of 2%; below this value, the stress path followed, and the final stresses are dependent on pre-strain. Most of the models satisfactorily predict the constrained recovery stress, as long as the values are low (less than plastic yield stress). Lower pre-strains offer the advantage of less permanent plastic deformation and fatigue with repeated cycles (Figure 25 and Figure 26) [69-71].

In general, while testing an SMA sample in repetitive cycles, the material behaviour gets stabilized after three cycles [67]: this clearly shows that the SMAs can be used as active force generators under repetitive loading.

However, fatigue life of SMA can be difficult to forecast: **Hornbogen** [72] studied how a modification of microstructure by thermo-mechanical treatments affects fatigue resistance.
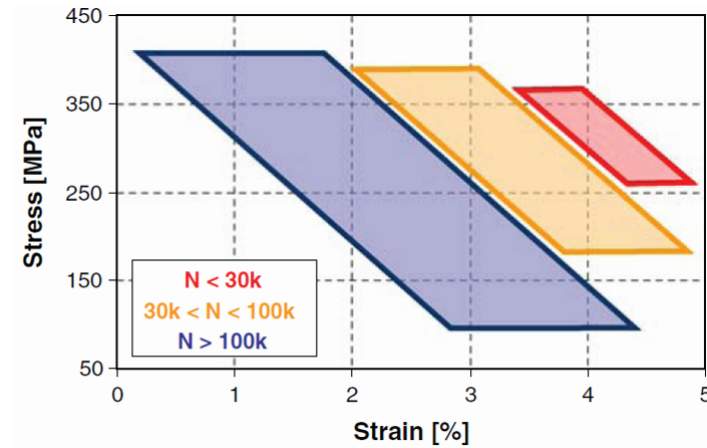
Figure 25: Fatigue lifetime for Smartflex 76 under different stress-strain conditions. [71]
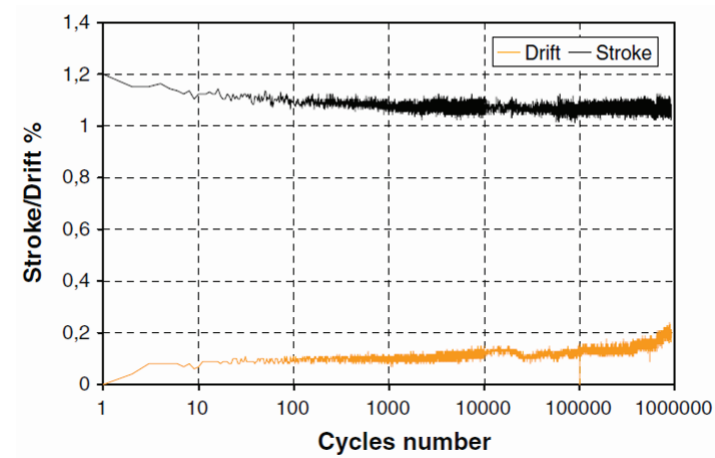
Figure 26: Fatigue lifetime output (stroke and drift) for Smartflex 76. [71]

7 NONQUASISTATIC LOADING

The mechanical behaviour of a material is usually studied in quasi-static conditions, that is, for a slow applied load or strain. If the material is strained at a faster rate, the material does not have time to relax, and as a result attains a higher stress value. In the case of Shape Memory Alloys, the rise in stresses might be a result of local temperature changes that occur immediately if the sample undergoes nonquasistatic loading. After a high strain rate, if the material is relaxed it returns to its quasistatic stress value (local temperatures might settle down to equilibrium values).

This is called stress relaxation phenomenon [68, 73-75].

Shaw [76] pointed out that some of the self-heating effect arises from the origination of local nucleation sites with temperature differences along the sample. It has been shown that the transformation stresses increase significantly as a function of strain rates (Figure 27).
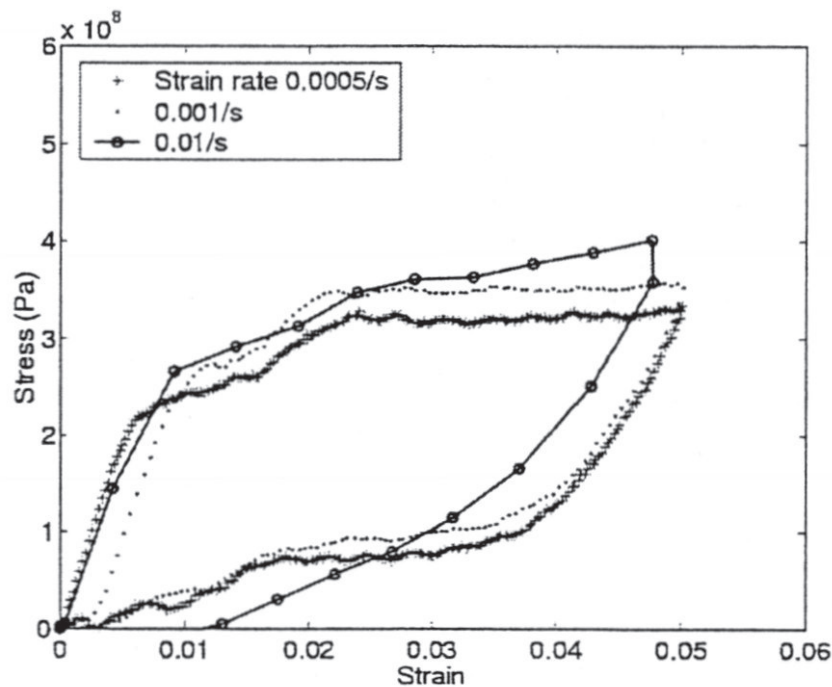
Figure 27: Effect of loading rates on stress-strain loading pattern on stress-strain behavior. [67]

If the loading is non-continuous, the SMA appears to fall back into its thermodynamic equilibrium state (stress relaxation). This phenomenon also manifests itself as a dependence of the material behaviour on the loading pattern (Figure 28).

For dynamic loading it is necessary to develop suitable constitutive models.
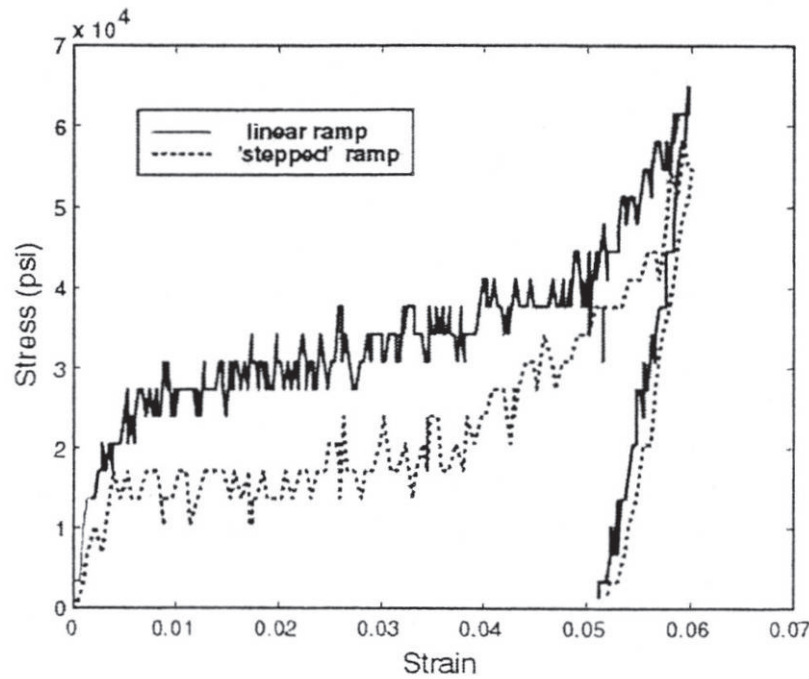
Figure 28: Effect of loading pattern on stress-strain behavior. [67]

Lexcellent & Rejzner [77] determined the change in temperature caused by strain rate through the integration of heat equation. Predicted results agreed satisfactorily with test data.

Prahlad & Chopra [75] used the rate form of the Brinson equation coupled with an energy equilibrium analysis to obtain simultaneously both temperature and stress as a function of strain for a given strain rate. The predictions showed good qualitative agreement for both stress and temperature evolution under loading involving an instantaneous change in the strain rate during the loading cycle (Figure 29). However, more careful temperature measurements are required to validate the model quantitatively.

Potapov & Silva [78] developed a simple time response model of Ni-Ti alloys, which takes into account latent heat and thermal hysteresis of transformation under conditions of free and forced air convection.

The actuation frequency of shape memory actuators was seen to be controlled primarily by the cooling time while increasing the input power can reduce the heating time. The calculated time response showed good agreement with test data.

Stress profiles

Temperature profiles
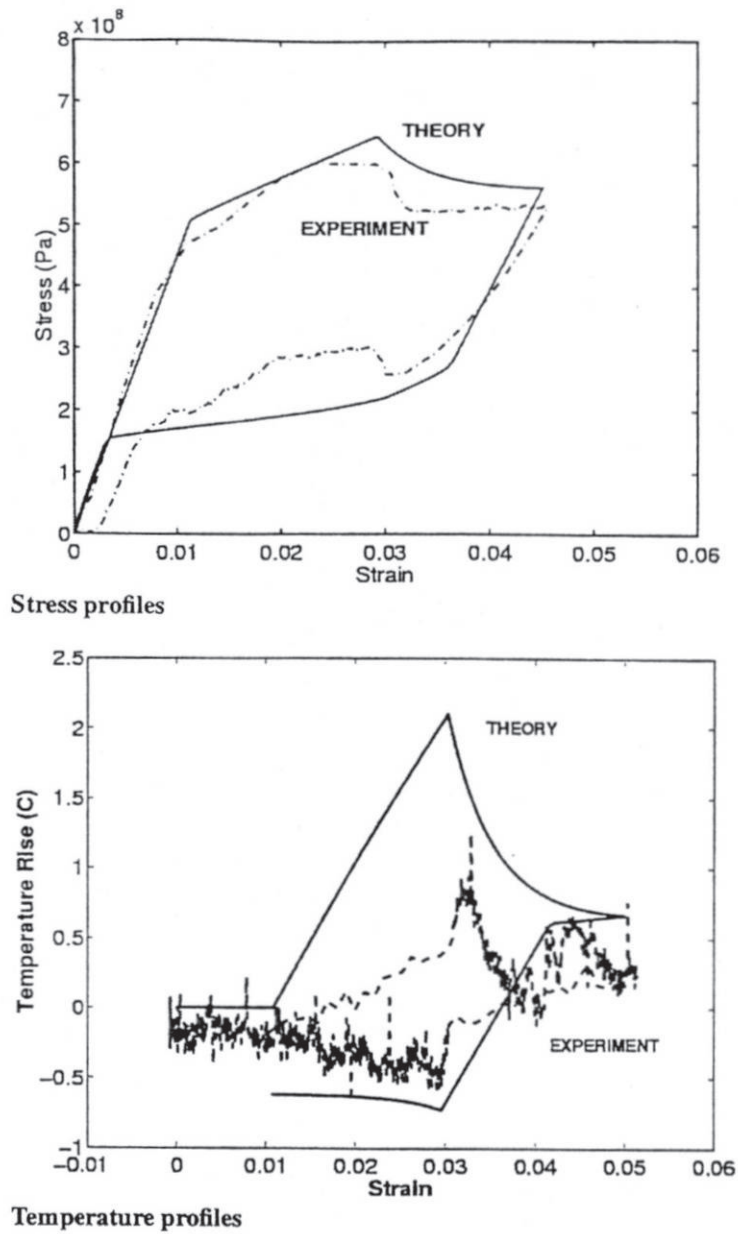
Figure 29: Comparison of nonquasisteady model prediction with experimental data (strain stepped from 0.01/s to 0.0005/s at 3% strain). [75]

- 165 -

8 TORSIONAL CHARACTERISTICS OF SMA RODS AND TUBES

In addition to the use of SMA wires under uniaxial loading as actuation elements, SMA rods and tubes have also been used for twist actuation. The principle of operation is the same as in the case of SMA wires: the rod (or tube) is first pre-twisted and then tends to recover its original, untwisted state when heat activated.

One of the first torsional models was proposed by **Davidson et al.** [79]: it uses the Liang & Rogers [22] constitutive model in conjunction with standard relationships for pure shear deformations for the torsional actuation of SMA rods. The model parameters were obtained by curve fitting the parameters required for Liang & Rogers model to the torsional experimental data.

Keefe & Carman [80] proposed an exponential model for the relationship between shear stresses and strains in the SMA alloy. However, this relies more on fitting the model parameters to torsional data over a prescribed range of thermo-mechanical data and does not include the modelling of the SMA phenomenology over the entire thermo-mechanical range.

Prahlad & Chopra [81] and **Atulasimha & Chopra** [82] proposed a torsional model based on the Brinson model for the SMA constitutive behaviour. The model parameters were obtained in extensional testing and then applied to the torsional case. Good overall agreement was obtained both in the constant temperature (Figure 30(a)) case and while actuating a torsional spring (Figure 30(b)).

a) Constant temperature predictions   b) Actuation against torsional springs
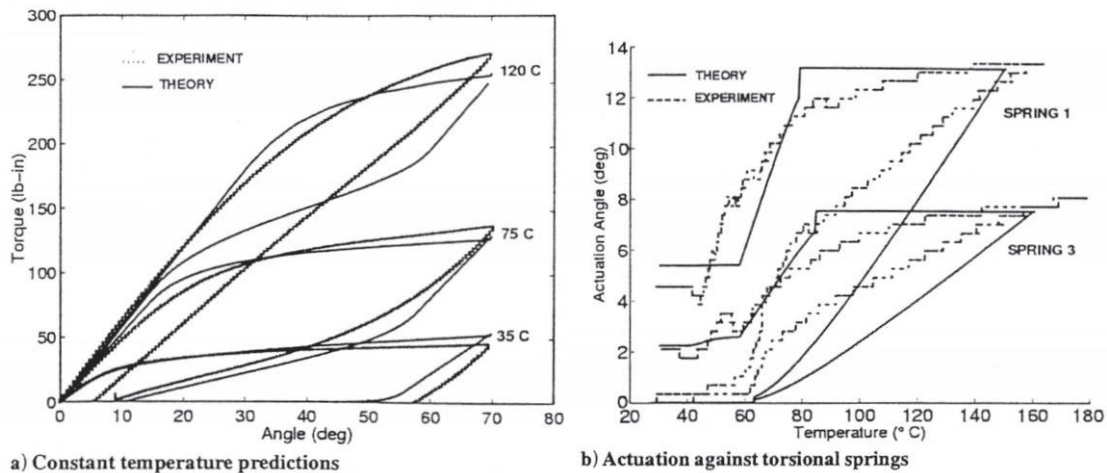
Figure 30: Comparison of torsional model prediction with experimental data. [75]

In contrast to these models that only describe shear deformations of the SMA, there are several models that are fully three-dimensional and therefore theoretically capable of

handling loading in any arbitrary direction (including combined tension-torsion loading). An example of these models is the **Boyd & Lagoudas** [24, 25] model. Also the 3-D model developed by **Auricchio et al.** [41] is capable of a good prediction of the pure torsion behaviour (Figure 31) and the combined tension-torsion case (Figure 32). However, the identification of model parameters and implementation for these models are not usually simple (fine tuning is required on experimental data).
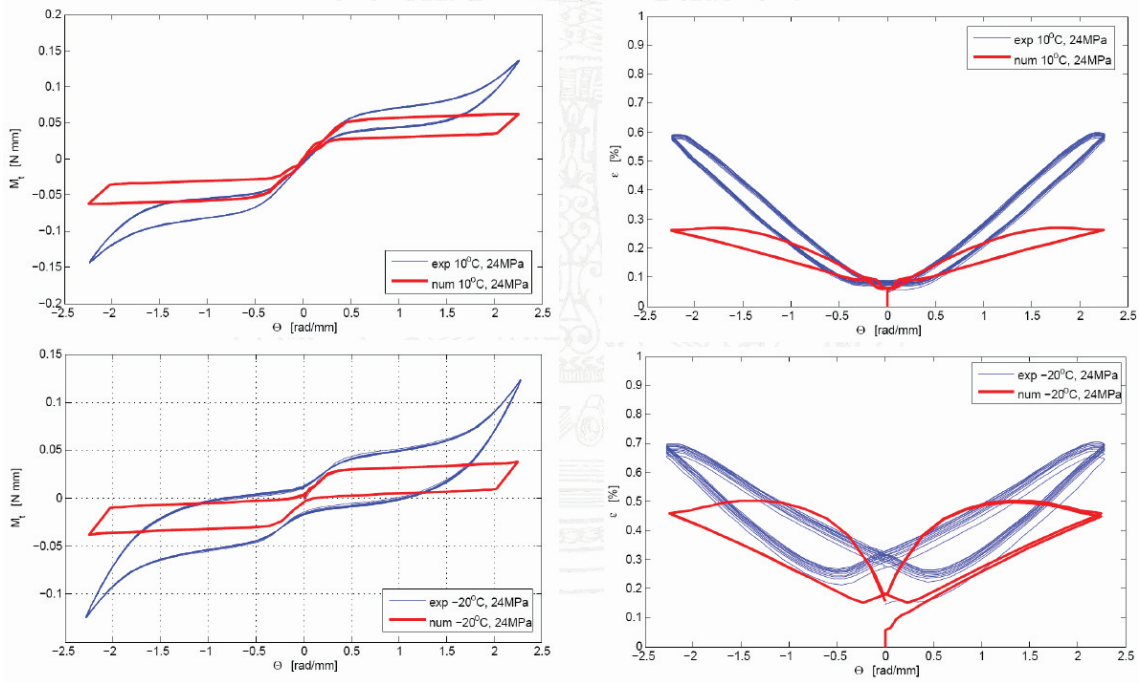
Figure 31: Auricchio's model predictions vs experiments for torsional round-robin tests. [41]
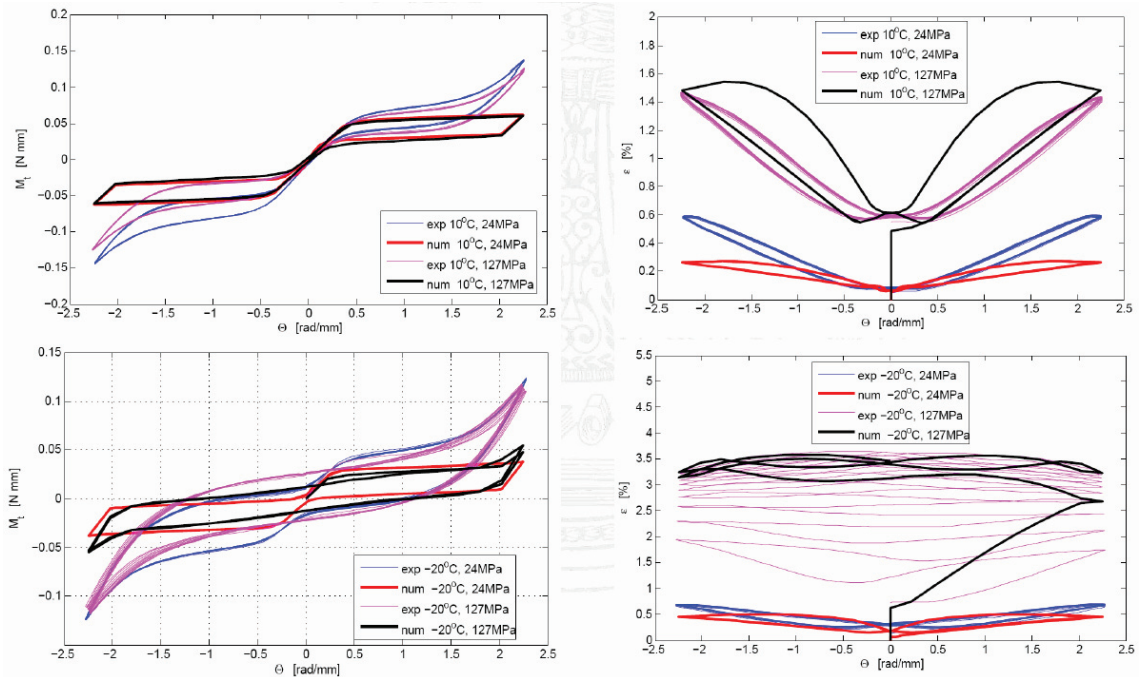
Figure 32: Auricchio's model predictions vs experiments for tension-torsion round-robin tests. [41]

9 DAMPING CHARACTERISTICS

As described in previous paragraphs, above a critical temperature the Shape Memory Alloys exhibit pseudo-elastic stress-strain hysteresis over a large range of strain (6–8%). Cyclic variation in stress and strain can result in a large dissipation of strain energy, that translates into damping augmentation [83, 84].

Wolons et al. [85] carried out experimental investigation to determine damping characteristics of NiTi alloy wires under uniaxial loading and systematically examined the effects of cycling, frequency of oscillation, strain amplitude, temperature, and static-strain offset on damping. It was shown that the shape of the hysteresis loop changes significantly with frequency; the energy dissipation decreases with frequency and reaches a saturation value at about 10Hz. Also, the energy dissipation decreases with higher temperatures and increases with lower static strain offset [86].

Fosdick & Ketema [87] also studied the thermal effects on damping properties of SMAs, with particular reference to the control of amplitude of steady state motions in the case of impulsively initiated motions. Other related studies have been presented by [88-91]. Also, **Lammering & Schmidt** [92] examined damping capacity of NiTi in the pseudo-elastic range and showed that the area of hysteresis loop decreases with increasing strain rate.

Ju & Shimamoto [93] developed composite beam with embedded SMA fibres to augment its damping, which was shown to be a function of both temperature and electric current.
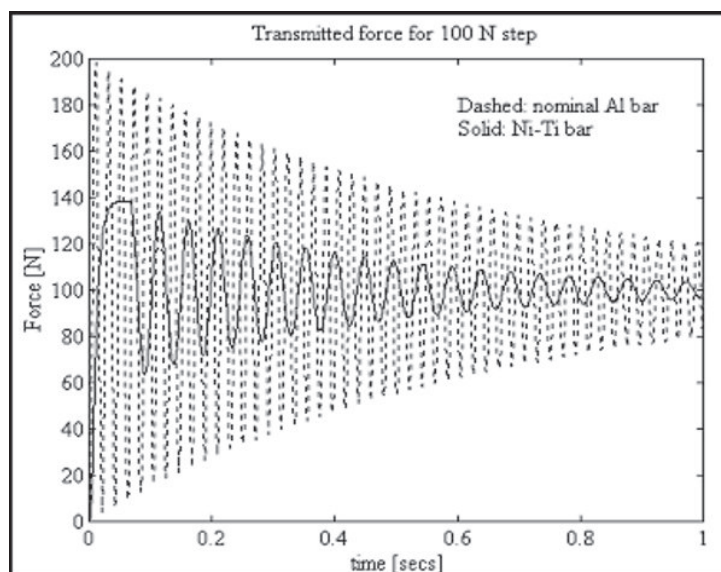
Figure 33: Transmitted force for a NiTiNOL bar as compared to a similar aluminium bar. [94]

Similarly, **<u>Tuissi et al.</u>** [95] integrated Ni-Ti alloy yarns as "smart fibers", embedded in a conventional laminated composite material, in order to make new horns with increased damping capacity for flexural modes of the collectors of the railway pantograph for the italian high-speed train.

Finally, in literature some devices can be found, usually referred to as Adaptive Tuned Vibration Absorbers (ATVAs), capable of vibration control: some of these adopt SMAs, where upon heating or cooling the effective stiffness and tuned frequency of the ATVA can change [96, 97].

10 FATIGUE IN SHAPE MEMORY ALLOYS

Since SMAs are widely preferred for actuation and sensing applications that require multiple cycles, it is important to understand the fatigue behaviour, which depends on the material processing (fabrication process, heat treatment, etc.), the type of loading conditions (applied stress, strain, temperature variations, environment, etc.), and transformation induced microstructural modifications (e.g., defects on grain boundaries due to strain incompatibilities) [98].

In most SMA applications, a large number of transformation cycles are induced by repeating a loading path that exhibits either pseudo-elasticity or thermally induced phase transformation under applied load. Repeated loading along a thermo-mechanical path causes gradual microstructural changes. These changes cause the degradation of the SMA behavior leading to low cycle fatigue as opposed to high cycle fatigue most commonly observed in loading paths operating in a purely elastic regime of a material. This section will provide a brief review of mechanically and thermally induced transformation fatigue behaviour of SMAs.

Mechanically induced fatigue behavior of SMAs is typically examined by performing rotating bending tests or by mechanically cycling the material on the load frame between two stress or strain levels along a given loading path [99, 100]. Such mechanical cycling can be performed to induce a complete transformation (i.e., cycled between complete austenite and martensite phase) or partial transformation (cycling between states where one or both end limits are not purely martensite or austenite but a mixture). If the deformation or stress level applied to the SMA specimen remains within the elastic regime, this can lead to fatigue life as high as $\sim 10^7$ cycles. However, in some cases, the material can be taken through detwinning or stress induced martensitic transformation by applying sufficiently high load levels. In such cases, the material fails considerably earlier in what is termed "transformation-induced low cycle fatigue," with a fatigue life of the order of thousands of cycles [101, 102].

Similar to mechanically induced transformation fatigue, thermally-induced transformation fatigue behavior of SMAs is extremely important to study for actuation applications. Fatigue life for SMAs undergoing thermally-induced transformation cycles under applied load is dictated by the amount of transformation strain allowed to occur (partial or complete transformation) as well as the stress level under which the material is cycled. The amount of cyclic transformation strain allowed in the material can

significantly affect the number of cycles to failure [103]. Under conditions of partial transformation, SMAs can exhibit much higher fatigue lives. A partial transformation limits the generation of martensite and the associated transformation strain, which causes a significant improvement in the fatigue life of the alloy [104-106].

Typical fatigue test data for complete and partial transformation in a NiTiCu material under a fixed stress level of 200MPa is shown in Figure 34.

(a) Complete transformation   (b) Partial transformation
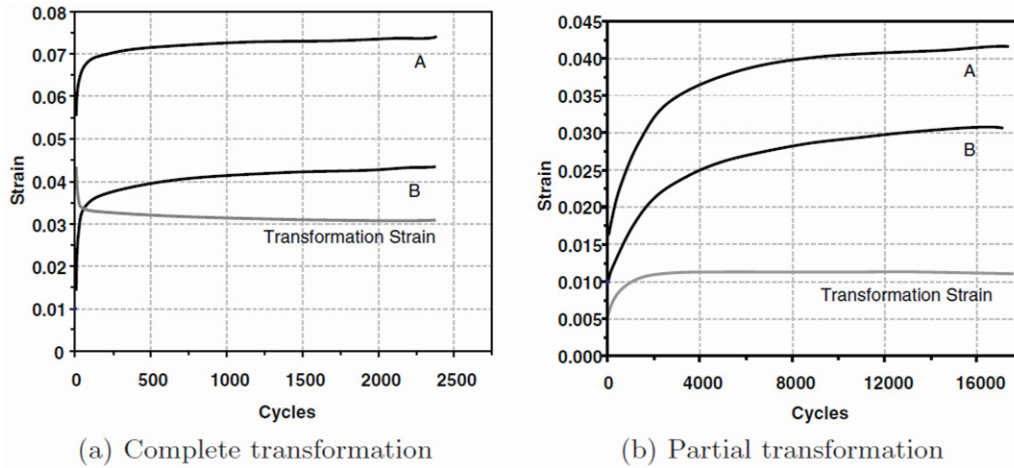
Figure 34: Thermally-induced transformation fatigue results for 200MPa applied stress level. Curves indicate strain levels in martensite (A) and complete or partial austenite (B), in addition to recoverable transformation strain. [98]

In the figures, the line A represents the strain in the SMA wire specimen at the end of each cycle after cooling to a certain level. Similarly, line B represents the strain in the SMA after heating to a certain level. In the complete transformation case, Figure 34(a), these levels pertain to complete martensitic transformation. In Figure 34(b), lines A and B represent strains generated during partial martensitic transformation. Taking the difference between these strain values at a given cycle and accounting for the effects of elastic moduli, one can obtain the transformation strain for the complete and partial transformations as shown in Figure 34(a) and Figure 34(b) respectively. The fatigue life is improved by approximately a factor of seven for a partial transformation and the amount of stable maximum transformation strain is reduced by a factor of three.

Other microstructural characteristics such as precipitate size and crystallographic orientation can also have a significant impact on the fatigue life of SMAs [107]. Heat treating the material under optimal conditions can also improve the fatigue behavior of SMAs. However, high annealing temperatures or chemically active environments can result in oxidation and corrosion, leading to crack nucleation and growth, thus reducing the fatigue life of SMAs [102, 106, 108, 109].

11 COMPOSITE BEAMS AND PANELS WITH EMBEDDED SMA WIRES

The idea of integrating SMA actuators in a composite element to gain an active structural control was first introduced by **Rogers & Robertshaw** [110]: such structure was called SMAH.C., that is shape memory alloy hybrid composite.

To realize composite structures integrating SMA wires is a demanding task. Wires surface requires to be cured to obtain good binding capacity with the composite matrix; moreover, it must prevent pre-strain loss in the SMA wires during the curing process of the composite (which usually needs high temperatures and can bring to SMA activation).

To resolve this problem there are three possible approaches. The first regards the use of special composites that may be packed at environmental temperature, keeping the SMA wires far from critical temperatures. The second approach consists in fixing each SMA wire separately from the composite during production autoclaving (by means of external constraints). The third method regards the use, during the fabrication process, of appropriate silicone tubules silicone filled with provisional steel wires in place of the SMA ones: once the curing process ends, steel wires are replaced with pre-strained shape memory wires; to ensure good airtightness, a adhesive film may be used between the silicone tubes and the graphite-epoxy resin composite.

SMA wires have been used to alter the natural frequencies of composite beams, to obtain the removal of a resonance by shifting the natural frequency from the harmonic or periodic forcing, or the creation of a frequency range with no resonance (with no natural frequencies).

Rogers & Barker [111] showed an increase in the natural frequencies of a composite beam because of the activation of SMA wires embedded directly in the structure. In this experimental study, the beam and SMA wires were independently clamped. When the SMA wires were heated, the beam was subjected to an axial force caused by the Shape Memory effect. They demonstrated a 200% increase in the natural frequency of graphite-epoxy beams by using a 15% volume fraction of SMA wires.

Baz et al. [112] conducted a study on the active vibration control of flexible beams. Experiments were conducted on flexible beams with SMA wires mechanically constrained on the exterior of the structure. The recovery force caused by mechanically constrained, pre-strained SMA wires at higher temperatures was used to demonstrate

active vibration control of flexible beams. In such an application, external access to the substructure becomes essential in order to clamp SMA wires to an independent support. For many aerospace structures like rotor blades or airplane wings, it might not be possible to follow this scheme. In another study, **Baz et al.** [113] inserted SMA wires into flexible beams with sleeves to control their buckling and vibration behaviour. They used a finite element method to correlate with their experimental results. Overall, predictions correlated satisfactorily with test data. They showed that the buckling load of a flexible fiberglass composite beam could be increased three times when compared to the buckling load of an uncontrolled beam.

Brinson et al. [114] investigated active control of beam deflection with temperature activation using a single surface-attached SMA wire. Also, predictions were successfully compared with test data. The potential of shape control with SMA wires was pointed out.

Lagoudas et al. [115] used a layer-wise shear deformation theory to show the shape control of plate structures with embedded SMA strips using thermal activation.

Turner [116] developed a finite element formulation for predicting the thermo-mechanical response of SMA hybrid composite structures with constrained or free boundary conditions. The model captures the material nonlinearity with temperature for composites with embedded SMA actuators.

Epps & Chandra [117] tested graphite-epoxy solid beams with sleeve-inserted SMA wires for their bending frequencies under clamped boundary conditions. The natural frequencies of this composite beam depend not only on the beam properties but also on SMA characteristics. An important SMA-related characteristic is the recovery force in wires, which in turn depends on pre-strain, mechanical properties of SMA and temperature. Figure 35 shows the first bending frequency of a graphite-epoxy composite beam activated by one 20mm diameter SMA wire. It shows a 22% increase in the first bending frequency with an SMA volume fraction of 2%.

For analysis, the SMA wires were treated as an elastic foundation for the composite beam, and the stiffness of foundation depended on the constraint recovery force: good correlation between theory and experiment was achieved.

A similar work was carried out at C.I.R.A. by **Diodati et al.** [118], developing a numerical model suitable for simulating the behaviour of a $[\pm45_3{}^G]_s$ composite with fiberglass and epoxy matrix laminate, having SMA wires integrated by ducts in the median laminate. It was then examined the variation of the natural frequencies of the

composite panel depending on the number of SMA wires and their temperature (Figure 36).
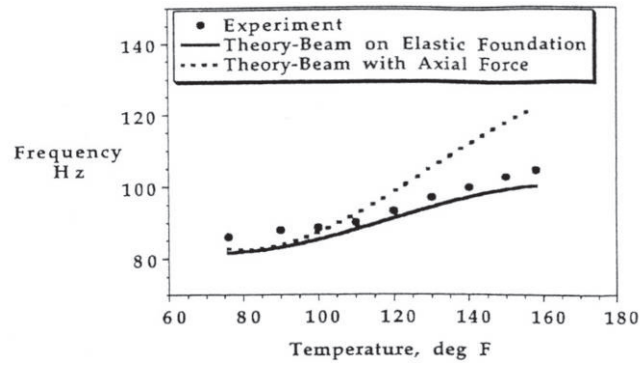
Figure 35: Fundamental frequency of clamped-clamped graphite-epoxy beam activated by one 20mm diameter SMA wire. Beam dimensions: length =18 in. (45.72cm), width = 0.25 in. (6.35mm), thickness = 0.068in. (0.173mm). [117]
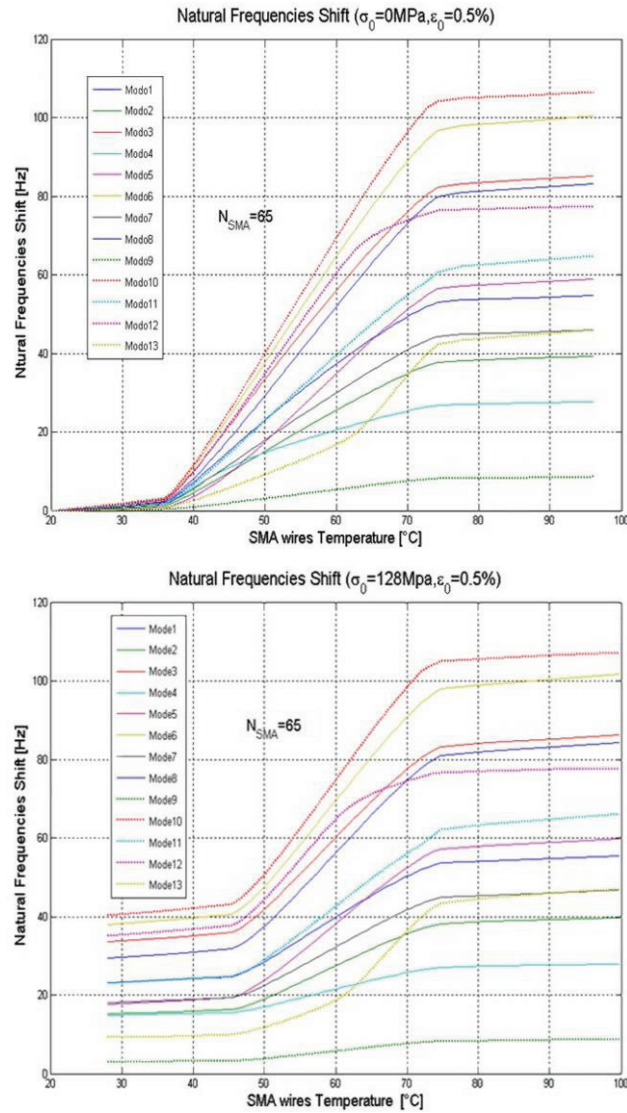
Figure 36: Variation of natural frequencies with the SMA wires activation temperature. [118]

Furuya [119] discussed design and material evaluation for the development of shape memory composites. Two types of concepts were proposed: TiNi fiber/aluminum matrix and TiNi fibers and particles/plaster matrix. The first composite showed increase of tensile strength (yield stress) and fatigue resistance, and the second showed increase of fracture resistance and vibration damping.

Birman [120] presented a micromechanics analysis of composite structure with embedded SMA wires.

Bisagni & Sala [121] evaluated the effects of the presence of SMA wires in composites by means of the microscope and thermal analysis (thermal damage due to activation of the wires, reduction in the ability to transfer stress between fibers and matrix), focussing particularly on composite laminates with epoxy matrix and carbon or aramid fibers. The results showed no adverse effects or deterioration of the mechanical behaviour of the composite.

They also assessed the behaviour of the composite panel actuated by the SMA wires under free condition and compression buckling, showing in the latter case only small changes compared to the original (in absence of SMA wires) composite panel behaviour.

Balta et al. [122] produced an adaptive composite by embedding thin pre-strained shape memory alloy actuators into a Kevlar-epoxy host material. In order to combine the activation and sensing capabilities, fibre Bragg grating sensors were also embedded into the specimens, and the strain measured in situ during activation. Finally, a pilot experiment was carried out to provide an example of how a strain-stabilizing feedback mechanism can be implemented in the smart structure.

Gao et al. [123], instead, proposed to use the SMA wires embedded in a metal matrix composite panel to repair any cracks in the matrix created as a result of applying a tensile load (Figure 37): it is possible to create in this manner a panel that is "self-healing" for activation of the SMA wires.

They also evaluated the different behaviour of the wires when subjected to a pre-existing strain or induced by the tensile load. A similar concept has been investigated by **Wang** [124], in which the SMA embedded wires produces an active closure stress in presence of a cracked structure.

Finally, some applications can be found in literature which adopts composites with embedded SMA elements to improve impact damage resistance [125, 126].
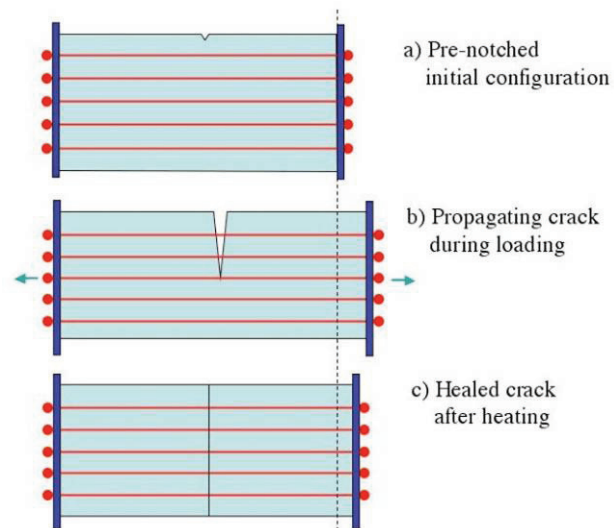
Figure 37: Composite panel with metal matrix reinforced by SMA wires. [123]

12 JOINING TECHNIQUES FOR SMA

Many applications that use shape memory materials require that the SMA elements should be combined with other SMA elements or with parts made of different materials. The possibility of such aggregation is not always so obvious, and therefore the joining technique should be chosen appropriately.

There are four main joining methods for the SMA (Ni-Ti alloys).

➢ *Fusion welding without binding metal*

To bind an element in Ni-Ti alloy with himself it is possible to use one of the many proven methods of **fusion welding**: by means of laser [127], plasma, electron beam, electric arc, etc.; welding can be done simply by contact or by subjecting the samples to bind to compression during cooling, so as to eliminate any cracks due to impurities (typical in commercial alloys). However, these techniques are not acceptable to join a Ni-Ti alloy with other materials such as steel, as inter-metallic alloys (TiFe) would be created locally (where the welding took place) which are very fragile [128].

To obtain a weld without oxides or other substances that could damage the alloy, it is necessary to carry out this in an inert, clean atmosphere or in vacuum, due to the titanium high reactivity.

In some cases, after the junction, the Ni-Ti alloys may require heat treatment to reduce stresses in the bonding area: it should be noted that the area affected by the heat treatment (H.A.Z.) in most cases is not able to produce the expected pseudo-elastic of shape memory alloys.

Another technique is based on the junction **by diffusion** of metals in the solid state without melting: in this case, to prevent the formation of inter-metallic alloys, an intermediate layer of a suitable metal is used [129].

Other joining techniques were also tested between titanium alloys and steel, based on the use of **explosives** [130] so to generate a shock wave and consolidate the material at the interface (the choice and quantity of explosives determines the detonation velocity and collision, changing substantially the quality of the bonding), or **by rubbing** [131], which generates heat and promotes a plastic flow of materials at interface.

➢ *Soldering with binding metal*

Soldering can be an effective technique in joining the Ni-Ti alloy with steels and other materials. This method is preferred because it prevents the thermal degradation on the

pseudo-elasticity effect. When the Ni-Ti alloys are heated to 500 °C (as in the case of welding), they locally lose their pseudo-elasticity, requiring heat treatment to recover it [130]; since the soldering takes place at about 426 °C, this presents no particular problems.

However, it is necessary to inhibit the formation of surface oxides (which impact on the anti-corrosive abilities of the alloy, but also makes it extremely difficult to solder). Some manufacturers have found it extremely effective to use soldering techniques similar to those used for the aluminium alloys, *halogen*-based: however, in 1993 this method was patented by Cook Industries [132]. Following the growing market demand for an effective soldering technique for Ni-Ti alloys, SMA Inc. has developed a proprietary blend (sold under license), known as Nitinol Flux 400 (tm).

One way to circumvent the problem of the low soldering capacity of Ni-Ti alloys can be to proceed with the *plating* of the SMA by other metals which are more easily solderable: experiences in this regard have been successful in coating Ni-Ti alloys with Nickel through electrolysis; to further increase the possibility of soldering, it is also possible to have a second layer of another metal such as silver. The main drawback associated with this technique is its complexity: it is indeed necessary an appropriate preparation of the alloy to be coated, especially in order to remove surface oxides; often, the coating is done for several steps, making it an expensive process; also, there are issues associated with conservation and use of chemicals involved in the processing.

To avoid the formation oxides also the ultrasonic soldering was experienced, with excellent results [133]. The ultrasonic soldering did not receive much attention so long as it has been used successfully for the construction of aluminium-based heat exchangers. It is based on the same principle of ultrasonic cleaning: high-frequency vibrations (in the 20kHz order) are introduced in the molten metal used for soldering, which causes the cavitation phenomenon thus resulting in severe erosion of the surface to be soldered (Figure 38), so as to disperse the surface oxides. The strength of the joints thus realized is comparable to that of traditional welds, eliminating the need for cleaning the residues.

Also brazing with the use of pure niobium as a melting-point depressant that can induce contact melting with NiTi at tractable temperatures has been studied in [134]. A strong, ductile, corrosion-resistant, biocompatible braze joint can then be achieved without the use of fluxes and allows processing in normal industrial vacuum conditions.
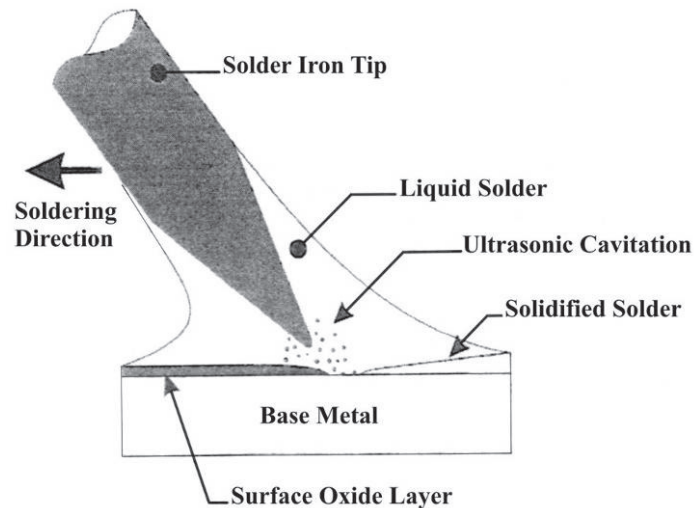
Figure 38: Ultrasonic cavitation removing surface oxide and wetting solder. [133]

➤ *Adhesives and epoxy resins*

Many epoxy resins and adhesives have been used successfully in many applications to bind the Ni-Ti alloys with themselves and with other materials: however the choice must take into account the compatibility with the production technique of the device, and the environment in which it will operate.

➤ *Mechanical joining*

The mechanical crimping is perhaps one of the most common techniques: however, the Ni-Ti alloys have a very limited ductility, so it is necessary to be careful not to excessively strain the material or cause cracks in it.

Another method is based on mechanical interference or clamping between components: here much attention should be paid to the strain state of the alloy and dimensional tolerances.

Because of difficulties in handling those alloys, the possibility of working Ni-Ti materials by means of filature and beating must be carefully considered.

13 SMA PROPERTIES AND OTHER SMART MATERIALS

In this section some of the main characteristics on Shape Memory materials are summarized. The following tables represent a deeper view in the main features of SMAs: however, it should be considered that these properties can have a wide variability, according to the different possible chemical compositions and heat treatments to which the alloy has been subjected to.

Table 5 reports a comparison among some different alloys, including SMAs [1].

Metal	Specific Damping Capacity (%)	Yield Strength (10^3 psi)	Density (g/cm^3)
Magnesium (wrought)	49	26	1,74
Cu-Mn alloys (Incramute, Sonoston)	40	45	7,5
Ni-Ti alloy (NiTiNOL)	40	25	6,45
Fe-Cr-Al alloy (Silentalloy)	40	40	7,4
High-C gray iron	19	25	7,7
Nickel (pure)	18	9	8,9
Iron (pure)	16	10	7,86
Martensitic strainless steel	8	85	7,7
Gray cast iron	6	25	7,8
SAP (aluminum powder)	5	20	2,55
Low-carbon steel	4	50	7,86
Ferritic stainless steel	3	45	7,75
Malleable, nodular cast irons	2	50	7,8
Medium-carbon steel	1	60	7,86
Austenitic stainless steel	1	35	7,8
1100 Aluminum	0,3	5	2,71
Aluminum alloy 2024-T4	< 0,2	47	2,77
Nickel-base superalloys	< 0,2	Range	8,5
Titanium alloys	< 0,2	Range	4,5
Brasses, bronzes	< 0,2	Range	8,5

Table 5: Comparison among several alloys. [1]

Table 6 summarizes some properties for the most spread Shape Memory Alloys, such as Ni-Ti, Cu-Zn-Al and Cu-Al-Ni alloys [1].

	Ni-Ti	Cu-Zn-Al	Cu-Al-Ni
Physical Properties			
Density (g/ m^3)	6,4	6,45	7,64
Resistivity (μΩ cm)	80 ÷ 100	8,5 ÷ 9,7	11 ÷ 13
Thermal Conductivity (W/m K)	10	120	30 ÷ 43
Heat Capacity (J/kg K)	390	400	373 ÷ 574
Mechanical Properties			
Young's modulus (GPa) (parent phase)	83	72	85
Young's modulus (GPa) (martensite)	34	70	80
Yield Strength (MPa) (parent phase)	690	350	400
Yield Strength (MPa) (martensite)	70 ÷ 150	80	130
Ultimate Tensile Strength (MPa)	900	600	500 ÷ 800
Transformation Properties			
Heat of Transformation (J/mole) (martensite)	295	160 ÷ 440	310 ÷ 470
Heat of Transformation (J/mole) (R-phase)	55	-	-
Hysteresis (K) (martensite)	30 ÷ 40	10 ÷ 25	15 ÷ 20
Hysteresis (K) (R-phase)	2 ÷ 5	-	-
Recoverable Strain (%) (One-Way martensite)	8	4	4
Recoverable Strain (%) (One-Way R-phase)	0,5 ÷ 1	-	-
Recoverable Strain (%) (Two-Way martensite)	3	2	2

Table 6: Most spread SMAs main properties. [1]

Among all the Shape Memory Alloys, Ni-Ti alloys deserve a special consideration: ever since their discovery, these materials have received particular attention for their higher thermo-mechanical properties and lower production costs (when compared, for instance, to the first Ag-Cd alloy) and, to date, are among the most popular ever.

Table 7 shows the typical properties of engineering interest for a Ni-Ti alloy [135]: it should be reiterated that these properties are still rough, as they change from producer to producer for the reasons outlined above.

Transformation temperatures and strains	
Transformation temperature range	-200* ÷ +110 °C
Transformation enthalpy	0,47 ÷ 0,62 kJ/Kg K
Transformation strains: up to 1 cycle	up to 8 %
" up to 100 cycles	up to 5 %
" up to 100.000 cycles	up to 3 %
" above 100.000 cycles	ca. 2 %
Thermal hysteresis**	30 ÷ 80 °C
Latent Heat of Transformation	5,78 cal/g
Physical properties	
Melting point	ca. 1310 °C
Density	6,45 kg/dm^3
Thermal conductivity of the Martensite	ca. 9 W/m K
Thermal conductivity of the Austenite	ca. 18 W/m K
Electrical resistivity	50 ÷ 110 μΩ cm
Linear thermal expansion factor α of the Martensite	ca. 6,7 e-6 1/K
Linear thermal expansion factor α of the Austenite	10 ÷ 11 e-6 1/K
Corrosion properties and biocompatibility	excellent
Specific Heat	0,20 cal/g °C
Magnetic permeability	< 1,002
Magnetic susceptibility	3,0 e+6 emu/g
Mechanical Properties	
Young's modulus of the Austenite	ca. 70 ÷ 80 GPa
Young's modulus of the Martensite	ca. 23 ÷ 41 GPa
Ultimate tensile strength (cold worked condition)	up to 1.900 MPa
Ultimate tensile strength (fully annealed condition)	ca. 900 MPa
Elongation to fracture	15,5 %
Plateau stress Martensite	70 ÷ 200 MPa
Plateau stress Austenite	200 ÷ 650 MPa
Yield stress Austenite	550 ÷ 700 MPa
Yield stress Martensite	~ 100 Mpa
Transversal contraction factor (Poisson's ratio)	0,33
Tensile strain (fully annealed)	20 ÷ 60 %
Tensile strain (cold worked)	5 ÷ 20 %
Hot workability	reasonable
Cold workability	difficult (work hardening)
Machinability	very poor

Table 7: Typical properties for Ni-Ti alloys. [135]

*: Too low transformation temperatures can be easily attained by increasing the amount of Nickel; however, this makes the material extremely brittle.

**: The hysteresis is evaluated on complete load-unload cycles; it reduces for partial cycles.

Shape Memory Alloys fall in the SMART materials family, that is, all those materials that can change their mechanical behaviour in response to external demands.

In addition to SMAs, in literature can be found also ferromagnetic (or magnetic) shape memory alloys, referred to with the acronym **F.SMA** or M.SMA, that will be extensively discussed in the next paragraphs. These are characterized by the presence of ferromagnetic metals, which allow the actuation of the alloy by means of the magnetic fields (other than temperature): the main advantage compared to the SMAs is the higher actuation frequency; however, the first practical applications are still under study.

Equally popular and widely used are **piezoelectrics**. These materials undergo a suitable strain when an electric field is applied and, conversely, produce a voltage if strained: therefore, they can be used either as actuators or as sensors. What distinguishes piezoelectrics from SMAs is the wider range of actuation frequencies together with very low strains.

Piezoelectric materials are relatively linear (for low values of the electric field) and bipolar, but exhibit hysteresis. The most popular piezoelectric material is definitely the PZT (lead zirconate titanate) and is commercially available in the form of thin platelets that can be attached or integrated into the structure to be controlled, or grouped to create discrete actuators (capable of greater forces, but with small shifts). These platelets generate isotropic strain: however it is possible to induce directional deformations using special techniques (piezoelectrics with special shapes, etc.). Very popular is also the piezoelectric polymeric film PVDF (Polyvinylidenefluoride).

There are also **electro-strictive** materials, similar to piezoceramics, with roughly the same ability to generate deformations. They are activated by an electric field, but are very sensitive to temperature, exhibit a negligible hysteresis and a nonlinear relationship between the applied field and the induced strain. A ceramic electro-strictive material is the common P.M.N. (lead magnesium niobate).

Magneto-strictive materials, finally, change shape when exposed to a magnetic field. They are mono-polar, non-linear materials and exhibit hysteresis; they allows the generation of forces and strains of moderate intensity over a wide range of frequencies. The most widely diffused is the Terfenol-D (the name itself contains the elements (terbium, dysprosium and iron) and the laboratory that discovered it (Naval Ordnance Laboratory, NOL)).

Table 8 summarizes the main differences among the discussed "SMART" materials [14]: the different properties of each material allow for preferential use in different applications.

Actuator	**PZT-5H**	**PVDF**	**PMN**	**TerFeNOL-D**	**NiTiNOL**	**NiMnGa**
Type	Piezoceramic	Piezofilm	Electrostrictive	Magnetostrictive	SMA	M.SMA
Free strain (μ strain)	1.000	700	1.000	2.000	60.000	40.000
Young's modulus (10^6 psi)	10	0,3	17	7	$4 \div 13$	4
Band width	High	High	High	Moderate	Low	Moderate
ε_{MAX} for aluminum beam (t_{BEAM}/t_{ACT}=10)	350	10	500	580	8.500	/
Behaviour	Linear	Linear	Non-linear	Non-linear	Non-linear	Non-linear

Table 8: SMART materials comparison. [14]

Figure 39 shows similar data as obtained from an SMA manufacturer website [94]; similar considerations and comparisons are shown in Figure 40 and Figure 41.

	PZT 5H	PVDF	PMN	Terfenol D	Nitinol	PowerAct™
Actuation Mechanism	Piezo-ceramic (31)	piezo film	electro-strictive	magneto-strictive	shape mem. alloy	Conformable piezo-electric composite
Max Strain	0.13%	0.07%	0.1%	0.2%	2%-8%	Call
Modulus, GPA	60.6%	2	64.5	29.7	28 m, 90 a	Call
Density, kg/m3	7500	1780	7800	9250	7100	Call
Actuation Energy Dens	6.83	0.275	4.13	6.42	252-4032	Call
Hysteresis	10%	>10%	<1%	2%	High	Call
Temp Range	-20 to 200C	-70 to 70C	0 to 40C	-20 to 180C	-100 to 200C	0 to 200C
Bandwidth	100 kHz	100 kHz	100 kHz	<10 kHz	<5 Hz	>10 kHz

Figure 39: SMART materials performance comparison. [94]
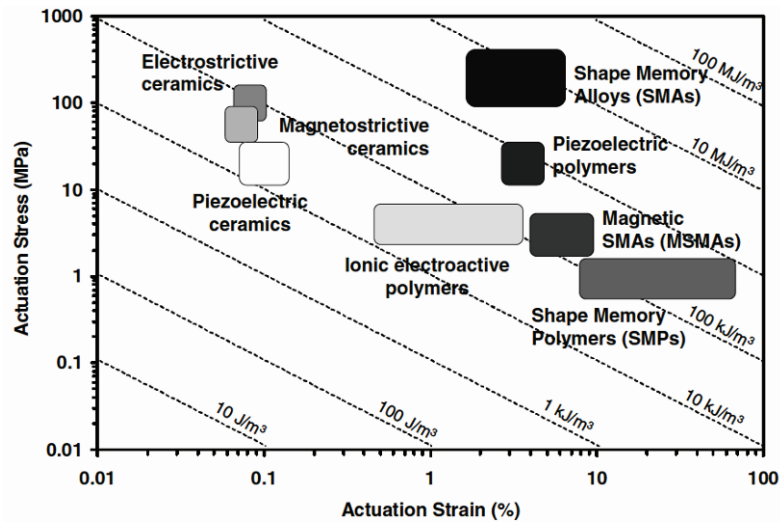
Figure 40: Actuation energy density diagram indicating typical ranges of actuation stress, actuation strain, and the actuation energy densities of different active materials that exhibit direct coupling.
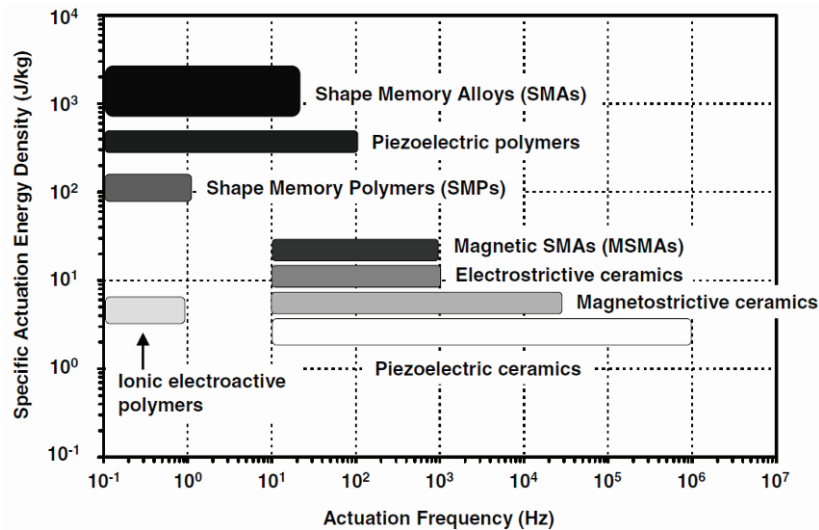
Figure 41: Actuation frequency diagram comparing the actuation frequency ranges of different active materials that exhibit direct coupling.

- 185 -

14 SMA APPLICATIONS

This paragraph will briefly outline some of the applications currently available on the market or being tested, involving the use of Shape Memory materials (excluding aerospace applications).

The use of these alloys is spreading very quickly, even if production costs are rather high. SMAs are available commercially in various forms, typically wires or plates, also with very small dimensions (30 μm diameter wires and 50 μm thick plates).

Having the SMA materials two distinct behaviours, the Shape Memory effect and the Pseudo-elastic one, applications have been divided into two categories.

➢ *Applications using the Pseudo-elastic effect*

It regards all applications requiring high flexibility: Ni-Ti alloys, having a (pseudo-) elasticity 10 times that of steel, are ideal.

In the previous paragraphs it has been already presented an application in the field of optical frames. In the past, much of the mobile phones antennas were made with SMA wires. But one area where SMA materials led to a revolution is the biomedical field, with applications ranging from orthodontic wires to aortic stents for support in angioplasty interventions, or spacers to correct defects of the cervical spine.

In all cases, the particular mechanical response of Shape Memory wires is exploited, for which during the loading phase a region appears (due to the phase transformation) that with increasing strain does not show an increase in stress; something similar then happens during unloading. These pseudo-elastic "plateaux" make it possible to strongly strain the material (up to 6-8%) without needing a significant increase in the applied force. Hence the possibility of applying **orthodontic wires** to recover large deformations without causing dental pain, capable of applying a slow and progressive force, clinically more effective than the intense response from old steel wires [135] (Figure 42).

Figure 42: SMA application in the orthodontic field. [135]

Similarly in a wide range of ***surgical instruments***, especially in the field of minimally invasive surgical items (f.i., endoscopes, catheters [135], etc. [137]), SMA can be used so not to develop high forces and retain permanent strain despite undergoing severe deformations, such as those required to travel on small vessels (Figure 43).

In the case of ***aortic stents*** (a kind of cylindrical mantles that are responsible for preventing the narrowing of arteries), these must be restricted to a smaller diameter without breaking so to be placed in the arteries and, once in position, to dilate the artery walls. [138] (Figure 44).

Figure 43: SMA-based surgical instrument. [137]

Figure 44: Aortic stents made in SMA [138]

Biomedical applications also cover ***spinal fixtures*** (Figure 45) and ***cambers*** (Figure 46); other examples of biomedical applications for SMAs can be found in [139].
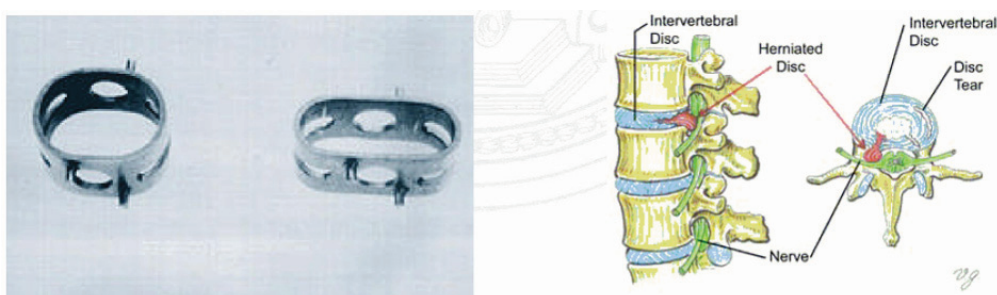
Figure 45: Spinal fixtures made in SMA for the treatment of herniated disks.
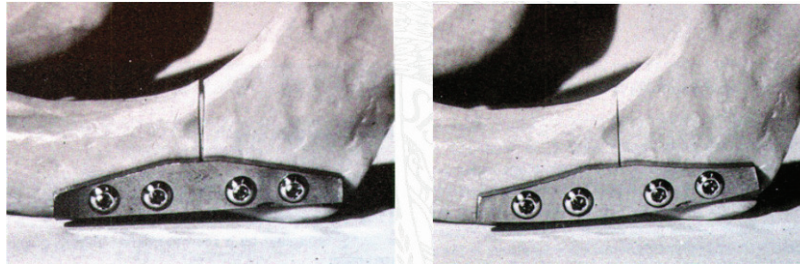
Figure 46: Cambers made in SMA to help bone healing.

Moreover, many applications that use the pseudo-elastic effect take advantage of the phase transformation induced by applied stress at a constant temperature for ***damping*** purposes: some studies in this field have already been presented in the previous paragraphs, and consider traditional materials or structural elements integrated or coupled with SMA wires as dampers. An example is shown in Figure 47, which represents a coupling device for damping within a drive train [140].
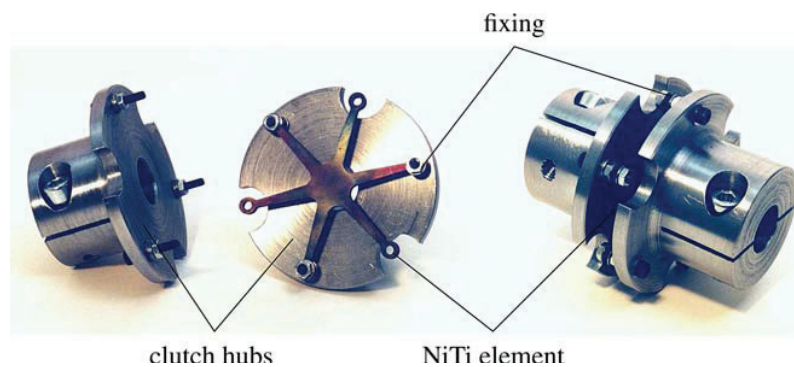
Figure 47: Drive train device coupled with SMA damping elements. [140]

Studies can be found in literature also regarding the development of oil-free metal ***mesh dampers*** weaved from several different types of materials (Figure 48) [141], among which also SMA are considered: in particular, the authors pointed out that the damping behavior generated by the NiTi material responds opposite to vibration amplitude when compared to the other materials.
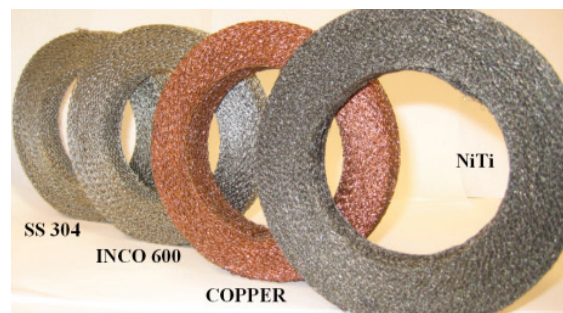
Figure 48: Wire mesh dampers. [141]

➢ *Applications using the Shape Memory effect*

In this case, different modalities of shape recovery must be considered.

Free Recovery: absence of constraints.

Main applications are in the "***gadgets***" field (Figure 49) and in the development of logos or small devices that remind some intended shape, usually by simple heating at temperatures slightly above the environmental one. Another typical application is related to **thermostats**.

Figure 49: Electric moving butterflies gadgets using Flexinol. [142]

SMA free recovery capability has been used in the aerospace field for the realization of "***hinges***" for the deployment of solar panels (Figure 50) in the L.F.S.A. project (Lightweight Flexible Solar Array) carried out by A.F.R.L. (Air Force Research Laboratory) [143]. The adoption of SMAs allows for low-shock controlled deployment, fewer parts, lighter weight, higher reliability, and ease of production and assembly. The SMA hinges were demonstrated on STS-93 in July 1999 on the space shuttle Columbia: this experiment tested 6 SMA hinges for overall performance and deployment rate characteristics (Figure 51). A second flight consisted of a subscale two-panel solar array that was demonstrated on NASA's Earth Observation 1 (EO-1) spacecraft in November 2000, commanded by SMA hinges.
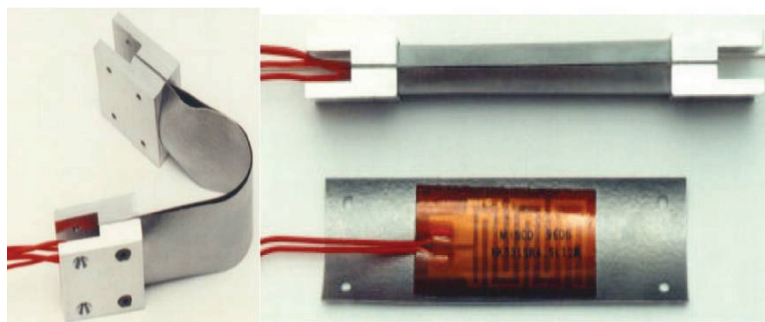
Figure 50: SMA hinge for solar panels deployment on NASA EO-1 satellite. [143]

S93E5085 1999:09:01 09:03:00
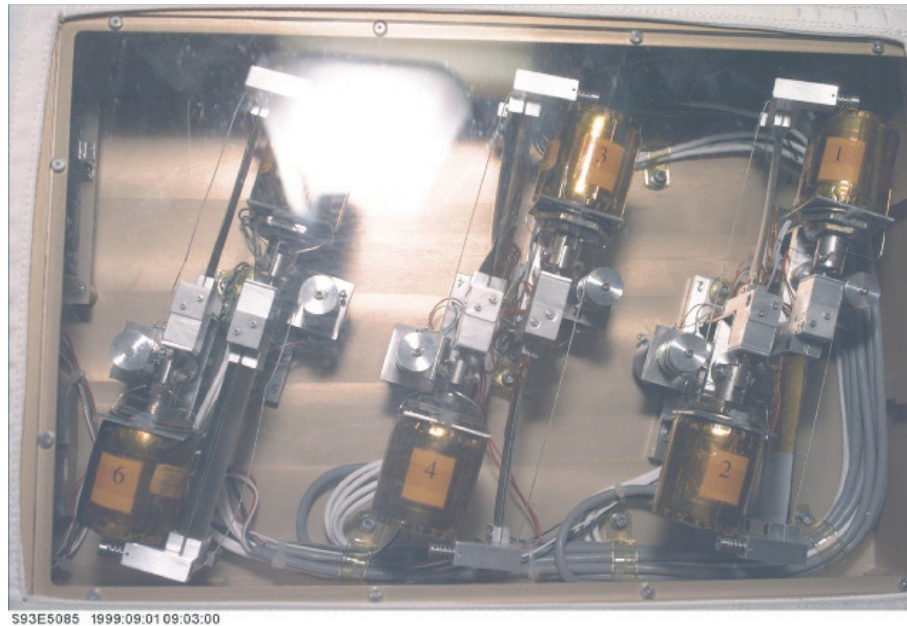
Figure 51: STS-93 Shuttle flight experiment on SMA hinges. [143]

Constrained Recovery: the recovery is prevented due to the presence of constraints.

This gas been one of the first areas where the Shape Memory materials have been used with success both technically and commercially. SMA metal rings have been used to make joining which may replace brazing or ***mechanical clamping*** in all those applications where they are difficult to achieve (heterogeneous materials, confined spaces, small objects) [144]. The mode of use is very simple: first the Shape Memory element is "formed" with a smaller geometry than that of the system to be tightened; so, at low temperature, it is expanded so that it is easy to assembly. Once mounted the Shape Memory element is simply heated and recovers the initial shape (the presence of the element to be tightened will prevent the full recovery of the initial geometry, thus enabling the generation of an applied stress) (Figure 52).
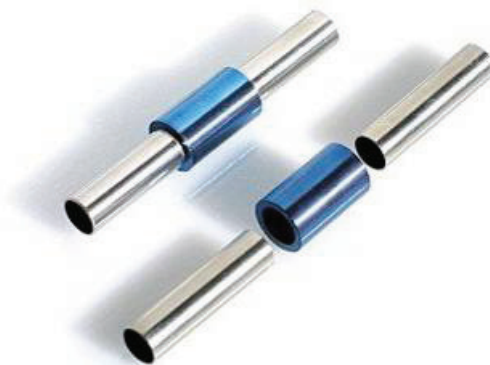
Figure 52: Mechanical camping of hydraulic lines by means of SMA junctions. [144]

- 190 -

This method has been mainly implemented in the tightening of hydraulic lines on board of aircrafts (F-14) since 1960 [145]. Another similar application is related to the self-loosening of bolted joints, in which SMAs can be used to restore tension in the loose bolt [146] (Figure 53).

Other implementations relate to the tightening of electronic cards (Z.I.F. connectors (Zero Insertion Force), Figure 54) or electrical connections of wires.
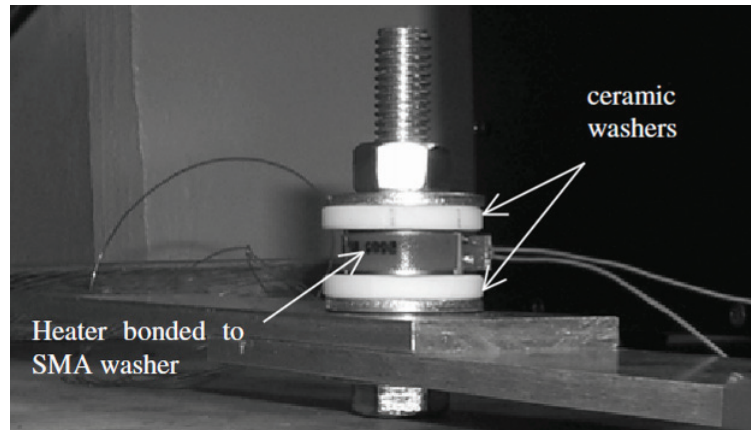
Figure 53: Loose bolt tension restoration by means of an SMA washer. [146]
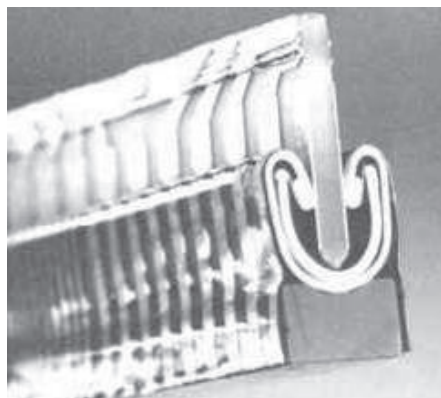
Figure 54: Z.I.F. connectors for electronic cards.

Partial Recovery: recovery limited due to a constraint that yields according to a specific law, related to the effort exhibited by the material during the shape recovery; the law may be sufficient to restore the initial conditions at the end of recovery, making cyclic applications feasible (actuators): in this case the SMA can do work.

The main reason researchers are interested in developing SMA based actuators is summarized in Figure 55 [71]: for certain power/weight ratios, shape memory actuators can be lighter and smaller than traditional ones.
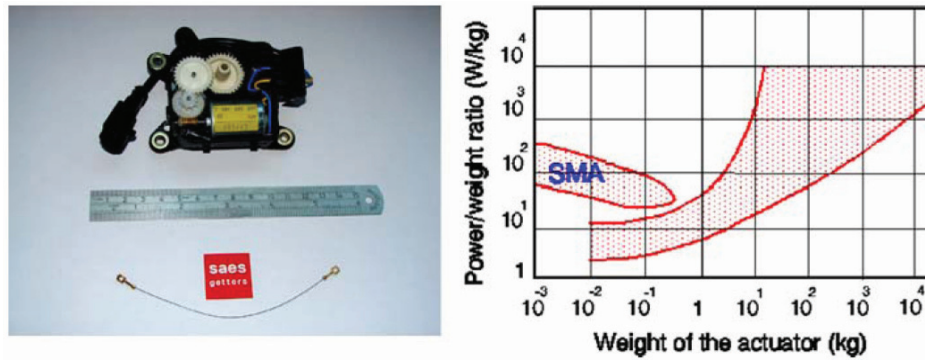
Figure 55: Comparison between traditional and shape memory actuators. [71]

The best known scheme is represented in Figure 56, where a Shape Memory spring works as an antagonist of a traditional steel spring. It exploits the different elasticity modulus that the shape memory material exhibits at high and low temperature: at low temperature the steel spring can overcome the SMA spring force, keeping it in a compressed position; by increasing the temperature of the SMA, transformation occurs and the Shape Memory spring can win the antagonistic steel one, thus creating a movement of the cursor to the opposite end. Upon cooling the device will return to the initial configuration, ready to repeat this actuation again.

Based on this simple design concept, several solutions have been engineered that provide automated systems which are small, compact, silent and without the presence of motors, able to control several parameters temperature dependent. A direct application of this scheme is a common ***water faucet*** (Figure 57) that can automatically adjust the temperature of outflow with a much higher efficiency (in terms of response time) when compared to traditional systems with wax. A similar idea can be applied also to automatically control the flap orientation of an air conditioning system (Figure 58): when air is cold, it is directed upwards; vice versa for hot air.
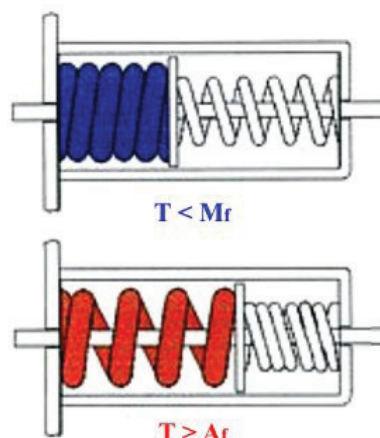
Figure 56: SMA actuator based on antagonistic springs.
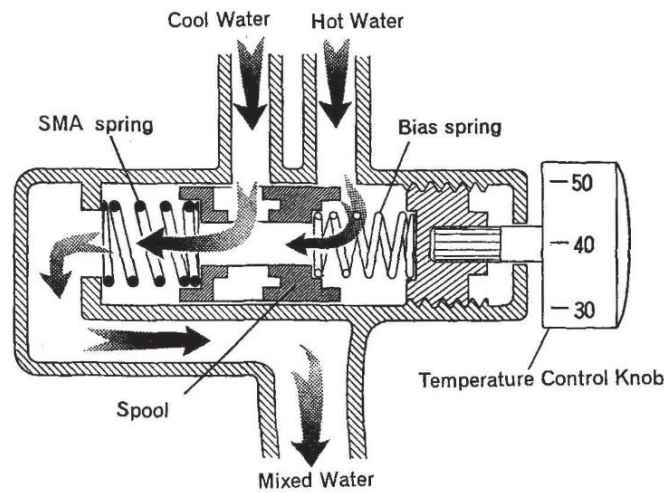
Figure 57: SMA based water faucet.
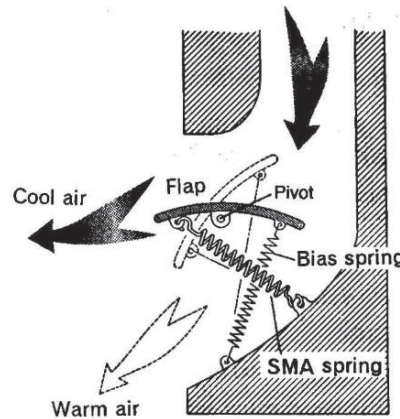
Figure 58: SMA based control of flap orientation for air conditioning systems.

Then, this general concept has been applied to several actuators, for different purposes: for instance, to create a lifter actuator (Figure 59) by means of a central SMA element and two springs [147].
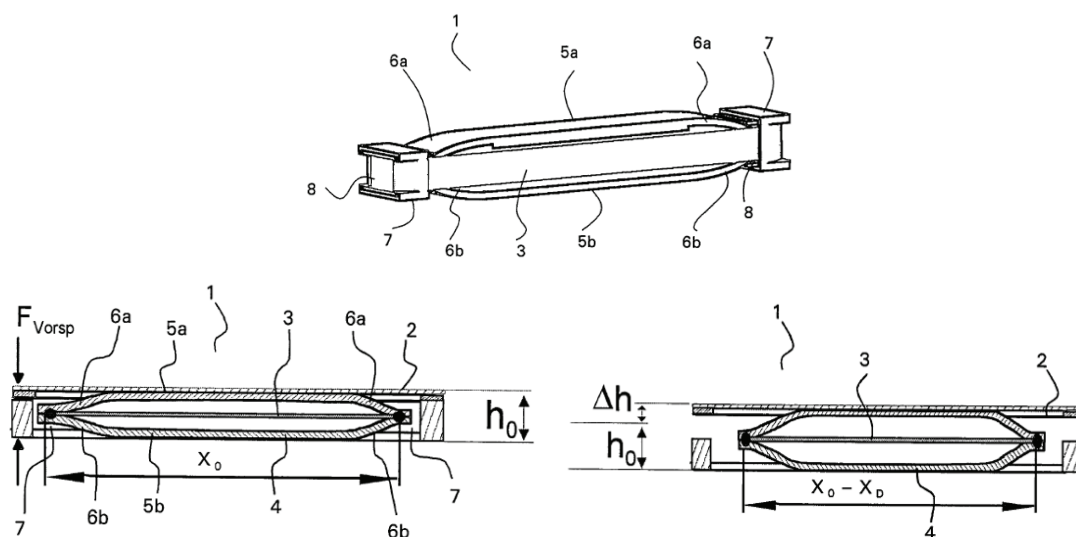
Figure 59: Patented SMA based lifter actuator. [147]

Many other examples of actuators based on SMA can be found in [148] (Figure 60 and Figure 61): here many examples of possible implementation of SMA within actuators are shown.
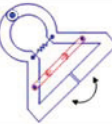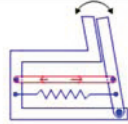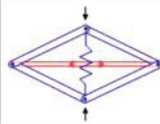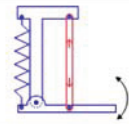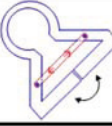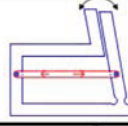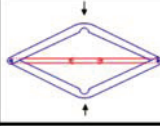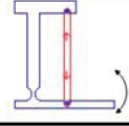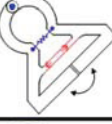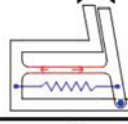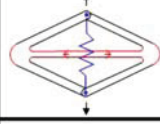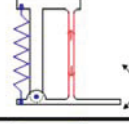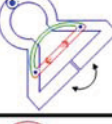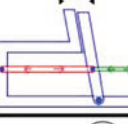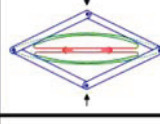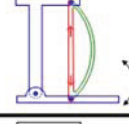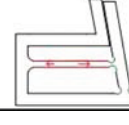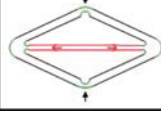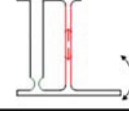
partial activatable SMA-structures (return spring design)							
design	parts	material SMA	material no SMA	integrated parts	gripper-structures 1	gripper-structures 2	actuator-structures 1 / 2
differential	carrier		X	-			
	return spring		X	-			
	SMA-component	X		-			
partial integrated	carrier		X	X			
	return spring		X	X			
	SMA-component	X		-			
	carrier	X		X			
	return spring		X	-			
	SMA-component	X		X			
	carrier		X	-			
	return spring	X		X			
	SMA-component	X		X			
integrated	carrier	X		X			
	return spring	X		X			
	SMA-component	X		X			

Figure 60: Systematic development of partially activatable actuator structures (return spring design). [148]
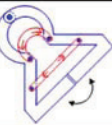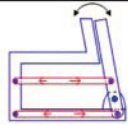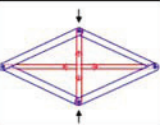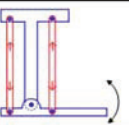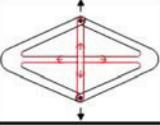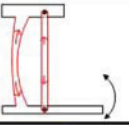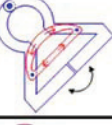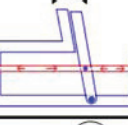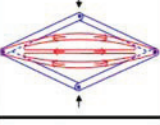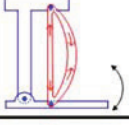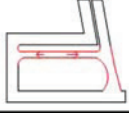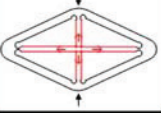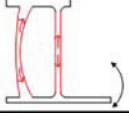
partial activatable SMA-structures (agonist-antagonist design)							
design	parts	material SMA	material no SMA	integrated parts	gripper-structures 1	gripper-structures 2	actuator-structures 1 / 2
differential	carrier		X	-			
	SMA-component1	X		-			
	SMA-component2	X		-			
partial integrated	carrier	X		X			
	SMA-component1	X		X			
	SMA-component2	X		-			
	carrier		X	-			
	SMA-component1	X		X			
	SMA-component2	X		X			
integrated	carrier	X		X			
	SMA-component1	X		X			
	SMA-component2	X		X			

Figure 61: Systematic development of partially activatable actuator structures (agonist-antagonist design). [148]

Also an application for a rotary servo, using a Nitinol wire wound on a threaded non-conductive rotor, can be found in [149] or as a similar commercial device [150].

Other applications concern the field of ***robotics***, where it is possible to simulate the movement of human muscles simply by controlling the force that the SMAs can explicit upon heating (Figure 62) [151-153]; similarly, the movement of snakes, fishes [154], etc. can be reproduced with a certain naturalness.
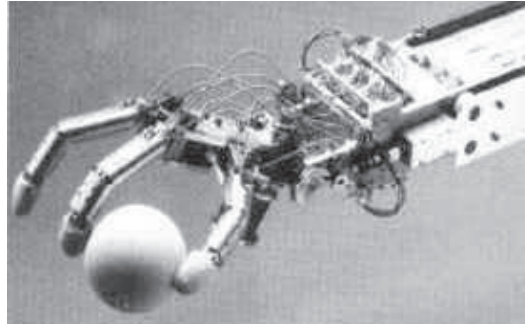
Figure 62: Robotic applications for SMAs. [152]

In this same field, a miniature gripper has been developed [155], suitable for laparoscopic operations, taking advantage of SMAs to keep volume small (Figure 63); similarly, a micro gripper has been studied in [38] (Figure 64).
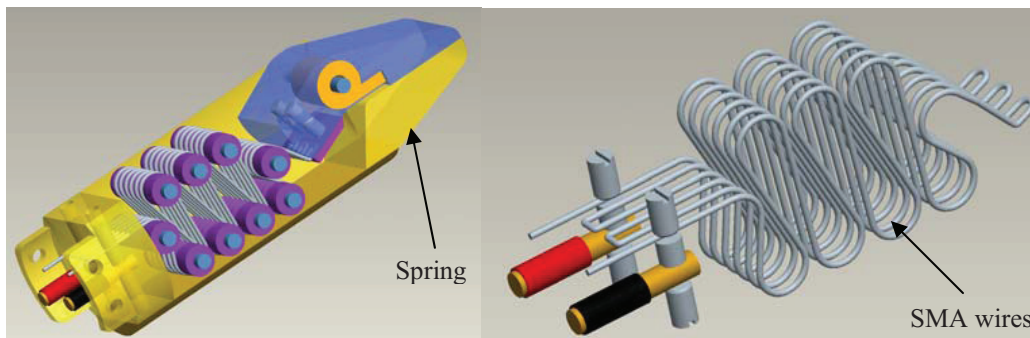
Figure 63: Miniature gripper with SMA wires. [155]
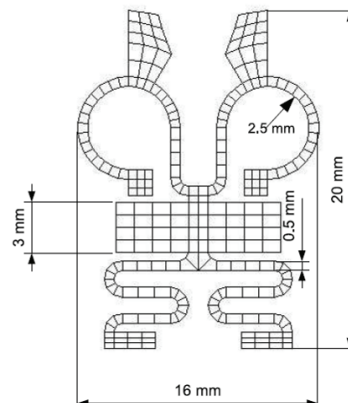
Figure 64: Micro gripper made of SMA. [38]

- 195 -

The favourable force/volume ratio of SMAs also allows for the building of micro-robots, trying to emulate already existing insects or small invertebrates (Figure 65) [156].

Figure 65: Artificial earthworm prototype based on SMAs: single module (left) and assembly (right). [156]

In electronics, some studies have been developed towards the use of SMAs for computer hard disk suspensions systems [157], in order to prevent friction between the head (slider) and disk (Figure 66).

Other more traditional suspension-like systems adopting SMAs have been developed too (Figure 67), and are commercially available [158].
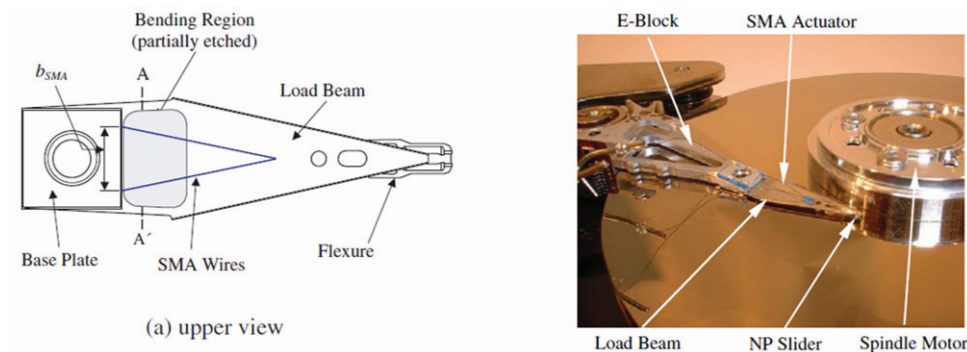
Figure 66: Hard disk suspension adopting an SMA wire as actuator. [157]
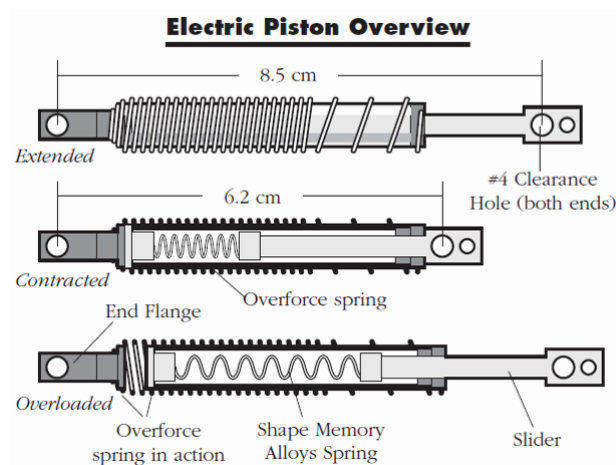
Figure 67: Electric piston sold by Mondo-tronics Inc. [158]

SMAs can be found also in some civil applications, especially as regards *fire safety systems*: it is possible to achieve thermal actuators for the automation of smoke and heat evacuators (Figure 68) and fire doors, able to ensure reliability of operation and complete reversibility of actuation [159].

Figure 68: Smoke Evacuator based on SMAs. [159]

There are also few applications about concrete reinforcement by means of pre-stressed SMA wires [160], to increase tensional strength, or seismic vibration absorption systems (Figure 69) taking advantage of super-elastic and energy dissipating properties of Shape Memory Alloys [161]. A similar idea is also applied for retrofitting of bridges [162].
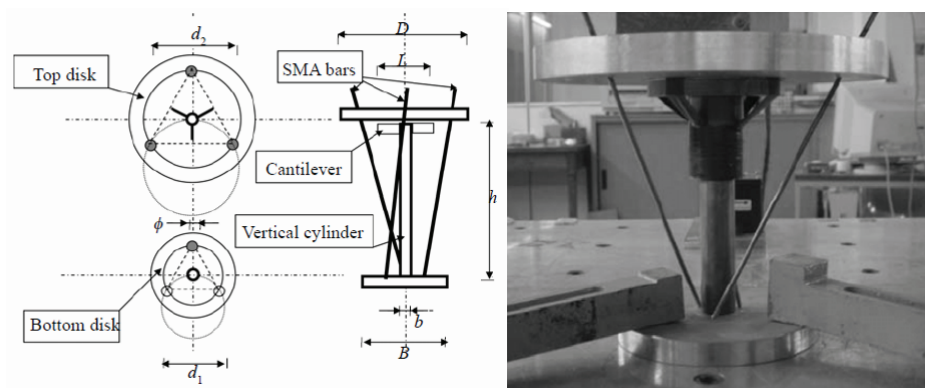
Figure 69: Base isolator prototype adopting SMAs for seismic applications. [161]

Some interesting works can be found in literature regarding the development of *SMA heat engines*. Ridgway M. Banks invented the first continuously operating heat engine that uses SMAs, at the Lawrence Berkely Laboratory of the University of California, in 1973 [163]: he filled half of a small circular cylinder, about the size of a cookie tin, with hot water; then constructed a flywheel, holding 20 nitinol-wire loops suspended from

the spokes of the wheel, and set it into the cylinder (Figure 70). The wheel-hub is on an offset axis: the eccentric position of the hub causes the SMAs to stretch more on one side of the wheel than on the other. Because the nitinol loops contracted powerfully and straightened out as they went through the hot water, with a force of somewhere around 67,000 pounds per square inch, they were able to turn the flywheel, and then because they quickly assumed their original shape in the cold water bath they were able to exert their force again when they hit the hot-water side. The wheel thus could run continually providing energy of up to about 70 rpm and capable of generating about half a watt of electricity. This device operated to more than 23 million cycles with the original wires, but it had inherently inefficient use of SMA wires, because the system did not employ uniaxial deformation, which provides larger power densities.
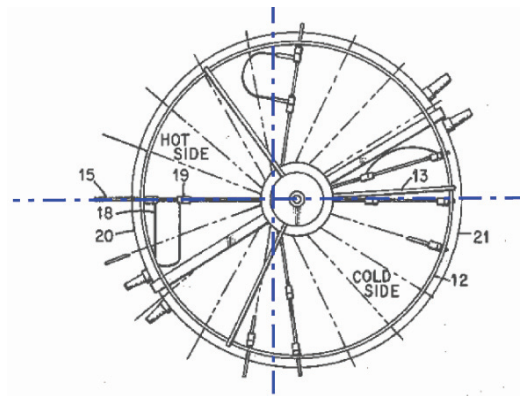
Figure 70: Plain view of Banks' SMA based heat engine. [163]

For this reason, many other heat engines based on SMA wires have been developed [164-166], trying to overcame these limitations: among these, some crank engines (which convert the reciprocating linear motion of an SMA actuator into continuous rotary motion) have been studied too (Figure 71) [167].
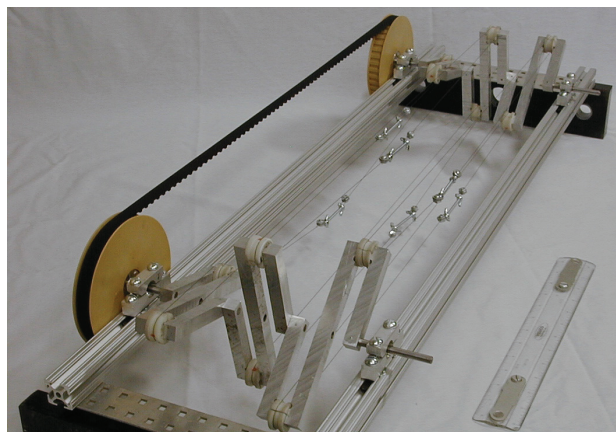
Figure 71: Isometric view of Schiller's crank engine based on SMA. [167]

In the automotive field, SMAs are being considered for door locks, turn signal oscillators, environmental controls, mirror controls, gear changing, triggers, pneumatic valve, remote releases, alarm devices, light fiber gates, etc.: Figure 72 and Figure 73 show two implementations made by FIAT automotive manufacturer.

Figure 72: Trunk lock commanded by an SMA actuator with mechanical back-up.

Figure 73: Internal mirror anti-glare actuator based on SMA.

In the space field, SMA actuators mainly used to **replace traditional pyrotechnic actuators** for the release of satellite parts or the opening of solar panels, radiators, etc.. The obvious advantage of such a system is reusability, in addition to minor stresses exerted during actuation. An example is the actuator developed by NASA Lewis Research Center (Figure 74) [168].
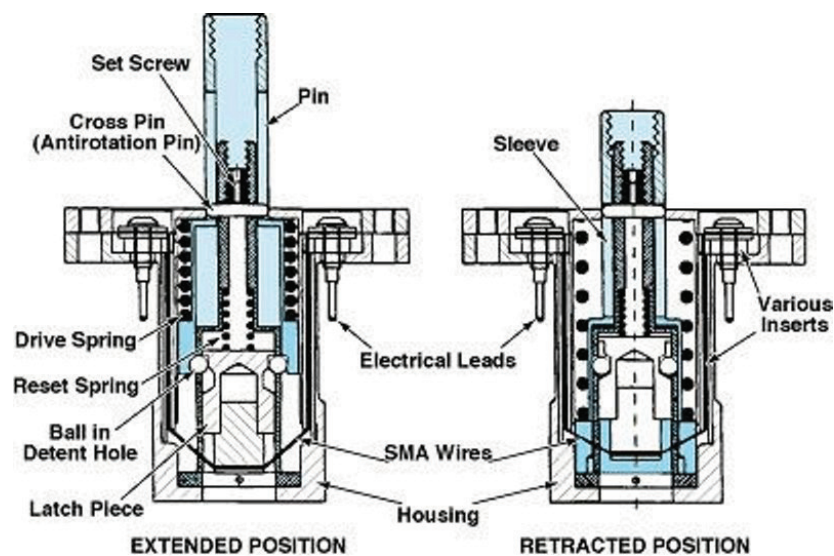
Figure 74: Space actuator based on SMAs developed by NASA. [168]

Furthermore, one of the experiments on board NASA's Mars Pathfinder mission adopted Shape Memory Alloys for a multi-cycle, electrically activated actuator [169], as shown in Figure 75.
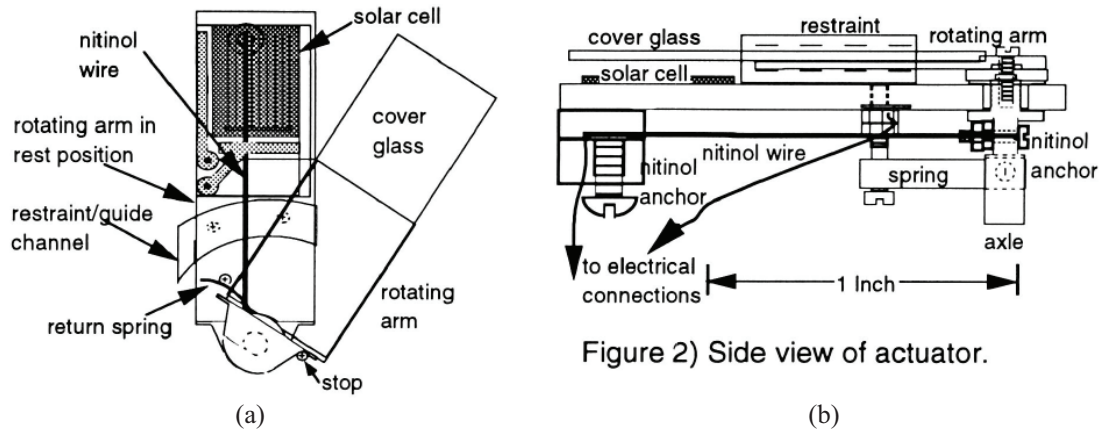
Figure 75: Mars Pathfinder SMA-based actuator: (a) top view and (b) side view of actuator. [169]

Other recent space applications engaged SMAs in the ***active monitoring of mirrors for telescopes*** (to increase the pointing precision) [170, 171] and ***antennas pointing***, or actuation of ***robotic arms*** [4]; some concern was also directed towards the control of large space systems vibrations. Also an actuation has been conceived for a ***hopping robot*** prototype destined to the exploration of planets with a low gravitational environment (Mars for instance): this robot uses diurnal variations of temperature at Mars' surface as a source of power for the SMA actuator; an "innovating" cylindrical mechanism with scissors used to transfer the energy needed by the robot's jump was designed and tested [172] (Figure 76).
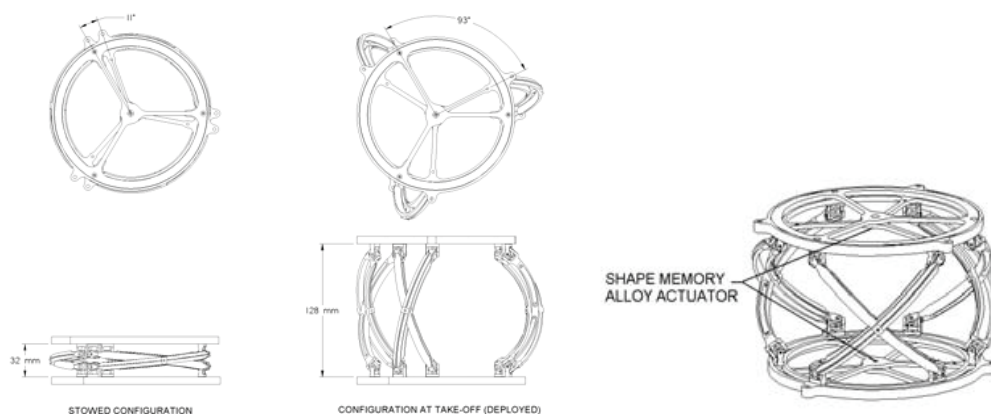
Figure 76: Hopping robot prototype based on a SMA actuator. [172]

Moreover, great interest is nowadays focused on the development of ***deployable structures*** for launch-packaged space vehicle programs and structural reconfiguration

in-service due to SMAs [173]: a prototype of a deployable elastic composite SMA reinforced (DECSMAR) structure is shown in Figure 77.
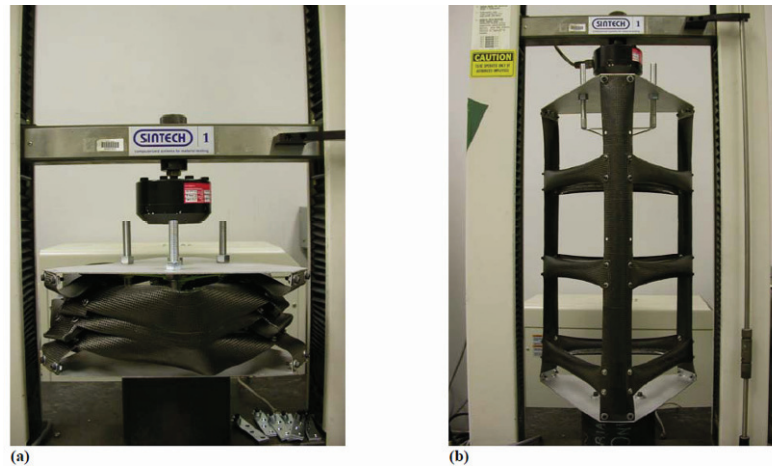
Figure 77: Three-bay DECSMAR prototype: (a) stowed configuration; (b) deployed architecture. [173]

There is no lack of studies on SMA actuators in other fields such as shipbuilding, especially for the actuation of **submarine rudders** [174] or **directional ducted propellers**, using SMA to increase manoeuvre capabilities [175].

In general in the aeronautical, helicopter and rocket science fields, Shape Memory Alloys are mainly used in active vibration control (using the different damping characteristics of the SMA two phases or their ability to stiffen the structural elements), the improvement of the aerodynamic characteristics of a fixed wing or rotary-wing aircraft (by means of the control of flutter [176-181], shape and inclination variation of load-bearing surfaces or parts thereof, variation in the lift distribution, the optimization of transonic regime [182] or the control of aero-elastic effects [183, 184]), the increase in manoeuvrability [185], landing gear for lightweight aircrafts [186], de-icing systems, etc..

Given the great complexity of helicopters, they seem to offer nowadays a greater potential for development and performance improvement through Shape Memory Alloys, and through the adoption of "SMART" materials in general: studies in this field are focused on the optimization of the main rotor blades shape at different operating conditions [187, 188], since it is the source of high vibrations [189], noise [190] and poor aerodynamic performance [191-196] .

15 SMA EVOLUTION: FSMA / MSMA

Traditional Shape Memory Alloys can be "activated" by means of thermal heating, in order to induce the martensitic thermo-plastic transformation: as previously shown, this implies a strong restriction on the actuation frequency, below 1Hz, due to the thermal inertia of the alloy.

There exists Shape Memory materials whose composition includes ferromagnetic metals, and therefore their activation can also be referred to an external magnetic field, allowing for a faster phase transformations.

These materials, known as FSMA (Ferromagnetic SMA) or MSMA (Magnetic SMA), combine the typical properties of ferromagnetism with those of the martensitic transformation (reversible and without dissemination).

Ferromagnetic SMAs have attracted much attention since the discovery of the high strains induced by the magnetic field in the Ni-Mn-Ga alloy [197-199]: this strain is due to the ability of martensitic phase to deform (as already happens for traditional SMAs) and thus differs from the magneto-striction phenomenon already observed by Joule in 1842 in ferromagnets. In traditional ferromagnets, indeed, such as Fe or Ni (with uniform crystalline structure), the strain associated with the magnetic-striction is in the $10^{-4}\%$ order, while materials that exhibit a large magneto- striction, such as Tb-Dy-Fe alloys (Terfenol-D), can achieve values of 0.1% [200]; in contrast, the FSMA show induced strains in the order of 10% [201], because the magnetic activity occurs in the martensitic phase, whose microstructure can deform easily.

Considering the *Ni_2MnGa* alloy, it has a cubic ordered $L2_1$ crystal structure (also known as the Heusler structure) in the austenitic phase (high temperature) which is modified as a result of the martensitic transformation in a tetragonal structure (low temperature, in martensite phase) (Figure 78).

Similarly to what has been described for SMAs, since the crystal lattice straining (twinning) from the high symmetry austenitic structure can be achieved in many equivalent ways, there will be several strain "orientations" of the lattice in different regions of the material (in the case of Ni_2MnGa alloys, there are three different martensite variants): so, there will be well-defined domains, each with its martensite variant (it is the extreme mobility of these domains to ensure the extreme strain ability of martensite); a typical martensitic microstructure is characterized by a mixture of different variants. But what distinguishes the FSMAs from traditional SMAs is being

characterized by spontaneous magnetic moments, which are present even in the absence of an external magnetic field: since there are different domains, differently oriented, each will have its direction of magnetization.
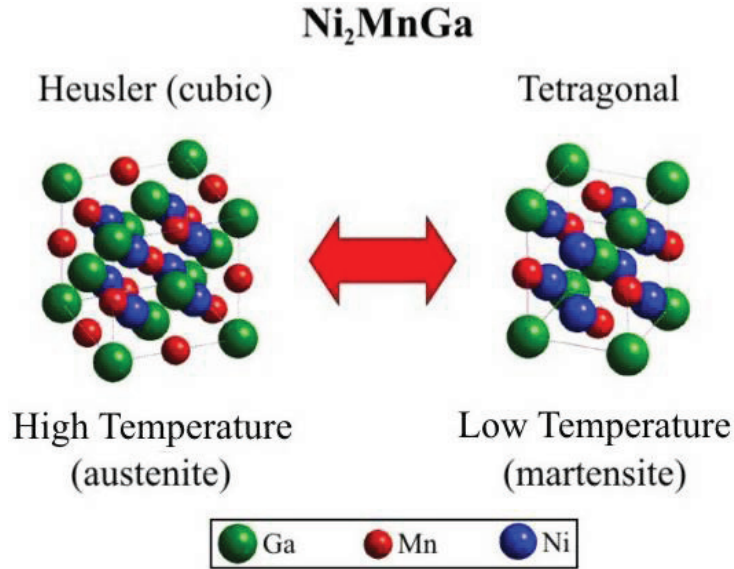
Figure 78: Crystal structure transformation for a FSMA.

Following the application of an external magnetic field, the magnetic moments try to align with the field: if the energy necessary to "rotate" the magnetization of each domain is high enough, then it will be more favourable from an energy standpoint to move (reorient) the entire domain (given their extreme mobility); so, there will be an increase in the number of domains whose orientation is precisely that of the external magnetic field (and this also leads to a single martensite variant), resulting in great shape change.

So, for the magnetic activation of an FSMA to take place, it is necessary a low temperature (ie, the alloy is in martensite phase) and the intensity of the required external magnetic field depends on the local magnetic moment of the material, which should be high (the magnetic anisotropy energy should be greater than the energy needed to rotate the domains) [202].

Currently, the Shape Memory effect due to magnetic activity was observed in alloys such as Fe-Pd [199] (even with the addition of Co and Pt [203]), Co-Ni-Ga [204], La-Sr -CuO_4 [205] and Ni-Mn-Ga [198, 201, 206, 207]: however, these alloys are expensive and generally weak for the required applications. The La-Sr-CuO_4 alloy is interesting because it is not a ferromagnetic material, but anti-ferromagnetic: this confirms that the

magnetic anisotropy is more important in these alloys of the macroscopic magnetic moment.

For practical applications, the most promising alloy is the Ni-Mn-Ga. This alloy has a relatively high Curie temperature ($\sim$ 90 °C) and the martensitic transformation temperature can be controlled, as for SMAs, by changing the percentage composition of different metals in the alloy (Guo & al. [208] experimentally tested variations introduced by the addition of small amounts of Fe, Co, Tb). Some features of this alloy are collected in Table 9 [209].

Ni-Mn-Ga alloy	
Composition	Ni:51.3 Mn:24.0 Ga:24.7
Transformation Temperature M_s	$\sim$ -10°C
Transformation Hysteresis M_s - M_f	< 3°C
Curie Temperature T_c	$\sim$ 85°C
Austenite Saturation Magnetization a_s (a 20°C)	485 emu/cm^3
Martensite Saturation Magnetization m_s (a -17°C)	602 emu/cm^3
Density ρ	8.02 g/cm^3

Table 9: Ni-Mn-Ga alloy main properties. [209]

FSMAs are very promising materials: they combine the unique features of SMAs (high strain rates, up to 10%) with the possibility of a more rapid actuation rate (in the millisecond order). However, their behaviour is still under experimentation and modeling, in order to assess the influence of the external magnetic field and temperature on phase transition [210-214].

There are some applications still in prototype phase, such as the two actuators developed by Tellinen & al. [215]. Some very promising works are geared towards the use of FSMAs for the development of advanced helicopter rotors, in order to improve performance [216].

16 A LOOK TO THE FUTURE: SHAPE MEMORY POLYMERS (SMP)

Shape Memory Polymers (SMPs) are a class of polymers which can undergo deformation at high temperatures, retain the deformed shape when cooled, and return to its original, unaltered configuration upon heating above the glass transition temperature. Advanced polymers could have two or more different shapes that would be reached at different target temperatures.

Materials capable of undergoing thermal shape-recovery are a division of smart or intelligent materials. In contrast to SMAs, SMPs possess a much lower density, have a lower cost, and recover strains up to a reported 400%, an order of magnitude greater than their metal counterparts [217-219]. Conversely, SMPs present a design challenge due to their material weakness.

First introduced in Japan and then the United States in 1984, Shape Memory Polymers are polymers whose qualities have been altered to give them dynamic shape "memory" properties. Using thermal stimuli, Shape Memory Polymers can exhibit a radical change from a rigid polymer to a very elastic state, then return back to a rigid state again. In the elastic state, a shape memory polymer will recover its "memory" shape if left unrestrained. However, while in this pliable state it can be stretched, folded or otherwise conformed to other shapes, tolerating up to 500% elongation. While manipulated, the shape memory polymer can be cooled and therefore returned to a rigid state, maintaining its manipulated shape indefinitely. This manipulation process can be repeated many times without degradation.

Unlike Shape Memory Alloys, a SMP exhibits a radical change from a normal rigid polymer to a very stretchy elastic and back on command, a change which can be repeated without degradation of the material. The "memory" (or recovery) quality comes from the stored mechanical energy attained during the reconfiguration and cooling of the material. The secret behind these clever materials lies in their molecular network structure, which contains meltable "switching segments".

Shape Memory Polymers, like all polymers, possess two material phases. The two phases – the glass and the rubber phases – are separated by the glass-transition temperature T_g. In the glass phase, the material is rigid and cannot be easily deformed. On the other hand, when the temperature is greater than T_g, the material enters the soft rubber phase and becomes easily deformable. In this phase, the SMP can be strained to

large values, which can be recovered through a specific cooling and heating procedure to be discussed later.

Modern variations on the classic turn-of-the millennium Shape Memory Polymers react to other stimuli than heat – one of the most important is a photonic reaction [220, 221] which allowed for the creation of quick and affordable fibre-optic switching units. Other developments include exposure (or lack of exposure) to oxygen – these polymers are now in use in many orbital applications where they can instantly seal small breaches in vehicle and station hulls as well as personal protective equipment.

Finally, piezo-stimulus Shape Memory Polymers react to different electrical currents by taking on different shapes. Some become pliable under a specific current, others remain pliable until a current is established, and the more elaborate designs have multiple states, and can switch from one hardened state to another through the intermediary pliable state simply by changing the current applied to the plastic [222]. Some other varieties include magnetic field-triggered polymers [223] and acid-base reaction polymers used in some scientific applications.

To date, the most common usage for Shape Memory Polymers is in the production of other plastics. SMP moulds can be made of a hard and high-temperature material for high precision injection moulding, and then with the application of electrical current, the moulds seem to melt away from the final product, then reform into the mould format again when the current is turned off. In addition, modern SMP foamed polystyrene allows for convenient shipping of products in large polystyrene shipping units to protect against jostling and abuse, then the polystyrene packing containers can be compressed, releasing the air within the structure and reducing the container down to a plastic block less than 3% of the normal volume of the polystyrene. These are shipped back to the original sender where they are heated and "fluffed" to be returned to their normal size and shape.

However, many industries are already underway for the adoption of a Shape Memory Polymers, such as CRG Inc. which produces the Veriflex (Figure 79) [224].

The ability of SMPs to recover large strains combined with its low weight and low cost advantages has produced much interest in design applications. For instance, Lockheed Martin and Hypercomp/NextGen are developing and testing morphing wings, with portions of the testing set to occur at NASA Langley Research Center. These wings are expected to adjust the surface area based on the flying conditions, with possible surface area increases of 300%. In this project, funded by the Defense Advanced Research

Projects Agency (DARPA), Toensmeir [225] reports that SMPs are being considered as a possible choice for the skin of the wing.
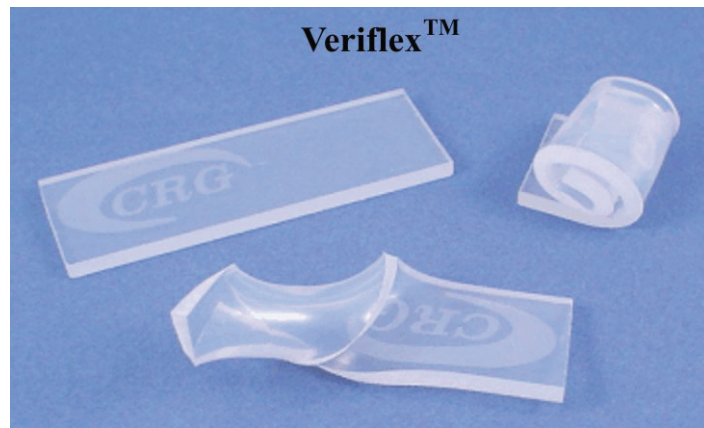
Figure 79: Veriflex sample: it is elastic when heated over transition temperatures and keeps the imposed shape when cooled down. [224]

Other possible applications for shape memory polymers are biodegradable sutures and other biomedical applications [226-228], repairable automobile skins, satellites and other space vehicles. In order to better and more efficiently investigate application possibilities, it is necessary to accurately model the thermo-mechanical behaviour of the Shape Memory Polymers. Consequently, to develop the necessary constitutive model, a thorough set of experiments must be performed to fully characterize the material: today, many avenues exist for such investigation [229-231].

By the late 2020's, it is expected that SMP characteristics can be engineered into almost all polymers, allowing for automobile fenders to be bent back into shape with the application of the right amount of heat; the creation of multiform solid-state furniture that shifts to accommodate different users with the press of a button; and a million other household uses. Some low-rent apartment buildings could even use piezo-activated SMPs for the doors on their units so the door can be quickly "melted" with the application of a simple stun-gun-like device.

17 CONCLUSIONS

Shape Memory Alloys such as NiTiNOL have the ability to express great strengths and recover large strains, and thus have enormous potential for low frequency applications (quasi-stationary).

Today, these alloys are commercially available in the form of wires, strips, rods and plates; there exist different chemical combinations, although the Ni-Ti alloys are by far the most used: however, also fixing the chemical elements constituting the alloy, their properties strongly depend on the percentage composition and the manufacture process. Nowadays three-component alloys are widely spread, whose properties can be better adapted to the specific application.

These materials have an highly nonlinear behaviour that is function of temperature, stress, strain history, and therefore require an accurate "tuning" to obtain the desired state: this represents a barrier to their deployment in many applications.

Many numerical models developed to estimate the SMA behaviour are valid for quasi-static loading, and should be extended to the dynamic case of low frequency. In general, these models succeeded in validating constitutive models for SMA wires under an extensional load with the experimental data: these should now be extended to other conditions, such as a torsional loading.

Next step could be important to validate the predictive models with experimental data even in the case of composite beams and plates with embedded SMA wires. For these structures, the local distribution of stress / strain, obtained with a Finite Element analysis or an accurate shear strain theory of the higher-order type, could reveal the actuation mechanism as well as helping to determine the integrity of the structure.

In most commercial applications, Shape Memory Alloys are not used "directly", but as actuation elements for actuators, able to carry mechanical work after the phase transformation of the SMA during heating: in this way, the SMA actuation, in terms of force and displacement, may be dispensed basing on the geometry and design of the actuator. Large capacity for cyclic repetition of SMA also make them particularly suited for several types of actuators.

A limitation of SMAs is the low actuation frequency: but on this characteristic FSMAs prove to be a valuable alternative, combining the large recoverable strain (up to 10%) with increased actuation speed (in the order of milliseconds).

18 REFERENCES

[1]   Srinivasan A.V., McFarland D.M., 1995, "*Smart Structures: Analysis and Design*" – Cambridge University Press, ISBN 0-521-65977-9

[2]   Buehler W.J., Gilfrich J.V., Wiley R.C., 1963, "*Effect of low-temperature phase changes on the mechanical properties of alloys near composition TiNi*" – Journal of Applied Physics, vol.34, pp.1475

[3]   Kauffman G.B., Mayo I., 1993, "*The metal with a memory*" – Invention & Tecnology, vol.9, no.2, pp.18-23

[4]   TiNi Aerospace Inc., website: http://www.tiniaerospace.com/

[5]   Buehler W.J., Wiley R.C., Wang F.E., 1965, "*Nickel-based Alloys*" – U.S. Patent 3,174,851,23

[6]   Betteridge W., 1984, "*Nickel and its alloys*" – Halsted Press, ISBN 0-853-12729-8

[7]   Shimizu K., Tadaki T., 1987, "*Shape Memory Alloys*" – Funakubo H. Ed., Gordon and Breach Science Publishers, New York, pp.1-60

[8]   Stefano Besseghini, 2000, CNR – TEMPE – Lecco, website: http://www.tempe.mi.cnr.it/tempelc/index.htm (in italian)

[9]   Stoeckel D., Yu W., "*Superelastic Nickel- Titanium Wires*" – Available at Raychem Corporation, Menlo Park, CA, website: http://www.raychem.com

[10]   Lin R., 1996, "*Shape Memory Alloys and Their Applications*" – Website: http://www.stanford.edu/~richlin1/sma/sma.html

[11]   Jackson C.M., Wagner H.J., Wasilewski R.J., 1972, "*55-Nitinol-The Alloy With a Memory: Its Physical Metallurgy, Properties, and Applications: A Report*" – NASA SP-5110, Washington DC

[12]   Mahmud A.S., Liu Y., Nam T., 2008, "*Gradient anneal of functionally graded NiTi*" – Smart Materials and Structures, vol.17, 015031 (5pp)

[13]   Brocca M., Brinson L.C., Bazant Z.P., 2002, "*Three Dimensional Constitutive Model for Shape Memory Alloys Based on Microplane Model*" – Journal of the Mechanics and Physics of Solids, vol.50, pp.1051-1077

[14]   Chopra I., 2002, "*Review of State of Art of Smart Structures and Integrated Systems*" – 42nd AIAA/ASME/ASCE/AHS/ASC Structures, Structural Dynamics, and Materials Conference, Seattle, WA, AIAA Journal, vol.40, no.11

[15] Brinson L.C., 1993, "*One-Dimensional Constitutive Behaviour of Shape Memory Alloys: Thermomechanical Derivation with Non-Constant Material Functions and Redefined Martensite Internal Variable*" – Journal of Intelligent Material Systems and Structures, vol.4, no.2, pp.229-242

[16] Yu H.J., Wang Z.G., Zu X.T., Yang S.Z., Wang L.M., 2006, "*Temperature memory effect in two-way shape memory TiNi and TiNiCu springs*" – J. Mater. Sci., vol.41, pp.3435-3439

[17] Huang W., Toh W., 2000, "*Training two-way shape memory alloy by reheat treatment*" – Journal of Materials Science Letters, vol.19, pp.1549-1550

[18] Wada K., Liu Y., 2006, "*Some factors affecting the shape recovery properties of NiTi SMA*" – 47th AIAA/ASME/ASCE/AHS/ASC Structures, Structural Dynamics, and Materials Conference, May 1-4, Newport, Rhode Island, AIAA Journal 2006-1969

[19] Seelecke S., 1996, "*Zur Thermodynamik von Formgedächtnislegierungen*" – Number 433 in Fortschr.-Ber. VDI Reihe 5. VDI Verlag Düsseldorf

[20] Heintze O., 2004, "*A Computationally Efficient Free Energy Model for Shape Memory Alloys - Experiments and Theory*" – Ph.D. thesis, University of North Carolina

[21] Tanaka K., 1986, "*A Thermomechanical Sketch of Shape Memory Effect: One-Dimensional Tensile Behaviour*" – Res. Mechanica, vol.18, no.3, pp.251-263

[22] Liang C., Rogers C.A., 1990, "*One-Dimensional Thermomechanical Constitutive Relations for Shape Memory Material*" – Journal of Intelligent Material Systems and Structures, vol.1, no.2, pp.207-234

[23] Brinson L.C., 1990, "*One-Dimensional Constitutive Behaviour of Shape Memory Alloy Constitutive Models*" – Journal of Intelligent Material Systems and Structures, vol.1, no.2, pp.207-234

[24] Boyd J.G., Lagoudas D.C., 1996, "*A Thermodynamical Constitutive Model for Shape Memory Materials. Part. I. The Monolithic Shape Memory Alloys*" – International Journal of Plasticity, vol.12, no.6, pp.805-842

[25] Boyd J.G., Lagoudas D.C., 1996, "*A Thermodynamical Constitutive Model for Shape Memory Materials. Part. II. The Monolithic Shape Memory Alloys*" – International Journal of Plasticity, vol.12, no.7, pp.843-873

[26] Ivshin Y., Pence T.J., 1994, "*A Thermo Mechanical Model for One variant Shape Memory Material*" – Journal of Intelligent Material Systems and Structures, vol.5, no.4, pp.455-473

[27] Chang B.-C., Shaw J.A., Iadicola M.A., 2006, "*Thermodynamics of shape memory alloy wire: modeling, experiments, and application*" – Continuum Mech. Thermodyn., vol.18, pp.83-118

[28] Jaber M.B., Smaoui H., Terriault P., 2008, "*Finite element analysis of a shape memory alloy three-dimensional beam based on a finite strain description*" – Smart Materials and Structures, vol.17, 045005 (11pp)

[29] Elahinia M.H., Ahmadian M., 2005, "*An Enhanced SMA phenomenological model: I. The Shortcomings of the existing models*" – Smart Materials and Structures, vol.14, pp.1297-1308

[30] Elahinia M.H., Ahmadian M., 2005, "*An enhanced SMA phenomenological model: II. The experimental study*" – Smart Materials and Structures, vol.14, pp. 1309-1319

[31] Graesser E.J., Cozzarelli F.A., 1994, "*A Proposed Three-Dimensional Model Constitutive Model for Shape Memory Material*" – Journal of Intelligent Material Systems and Structures, vol.5, no.1, pp.78-89

[32] Ren W., Li H., Song G., 2007, "*A one-dimensional strain-rate-dependent constitutive model for superelastic shape memory alloys*" – Smart Materials and Structures, vol.16, pp.191-197

[33] Peng X., Li H., Chen W., 2005, "*A comprehensive description for shape memory alloys with a two-phase mixture model incorporating the conventional theory of plasticity*" – Smart Materials and Structures, vol.14, pp. 425-433

[34] Juhàsz L., Andrä H., Hesebeck O., 2000, "*A Constitutive Model of Shape Memory Alloys Based on Viscoplastic Like Evolution Equations*" – Periodica Polytechnica Ser. Mech. Eng., vol.44, no.1, pp.59-69

[35] Sun Q.P., Hwang K.C., 1993, "*Micromechanics Modeling for the Constitutive Behaviour of Polycrystalline Shape Memory Alloys-1. Derivation of General Relations*" – Journal of Mechanical Physics Solids, vol.41, no.1, pp.1-17

[36] Matsuzaki Y., Naito H., Ikeda T., Funami K., 2001, "*Thermo-Mechanical Behaviour Associated with Pseudoelastic Transformation of Shape Memory Alloys*" – Smart Materials and Structures, vol.10, no.5, pp.884-892

[37] Barrett D.J., 1995, "*A One-Dimensional Constitutive Model for Shape Memory Alloys*" – Journal of intelligent Material Systems and Structures, vol.6, no.3, pp.329-337

[38] Auricchio F., Reali A., 2008, "*Shape Memory Alloys: Material Modeling and Device Finite Element Simulations*" – Materials Science Forum, vol.583, pp.257-275

[39] Auricchio F., Mielke A., Stefanelli U., 2008, "*A Rate-Independent Model for the Isothermal Quasi-Static Evolution of Shape-Memory Materials*" – Mathematical Models and Methods in Applied Sciences, vol.18, no.1, pp.125-164

[40] Auricchio F., Reali A., Stefanelli U., 2007, "*A three-dimensional model describing stress-induced solid phase transformation with permanent inelasticity*" – International Journal of Plasticity, vol.23, pp.207-226

[41] Auricchio F., Coda A., Reali A., Urbano M., 2009, "*SMA Numerical Modeling Versus Experimental Results: Parameter Identification and Model Prediction Capabilities*" – Journal of Materials Engineering and Performance, vol.18, no.5-6, pp.649-654

[42] Prahlad H., Chopra I., 2001, "*Comparative Evaluation of Shape Memory Alloy Constitutive Models with Experimental Data*" – Journal of Intelligent Material Systems and Structures, vol.12, no.6, pp.386-396

[43] Brinson L.C., Huang M., 1996, "*Simplification and Comparisons of Shape Memory Alloy Constitutive Models*" – Journal of Intelligent Material Systems and Structures, vol.7, no.1, pp.108-114

[44] Tobushi H., Lin P.H., Tanaka K., Lexcellent C., Ikai A., 1995, "*Deformation Properties of TiNi Shape Memory Alloy*" – Journal of Physique IV, vol.5, C2, pp.409-410

[45] Lin P.H., Tobushi H., Ikai A., Tanaka K., 1995, "*Deformation Properties Associated with the Martensitic and R-Phase Transformations in TiNi Shape Memory Alloy*" – Journal of Applied Biomechanics, vol.10, no.2, pp.1-11

[46] Tanaka K., Nishimura F., Matsui H., Tobushi H., Lin P.H., 1996, "*Phenomenological Analysis of Plateaus on Stress-Strain Hysteresis in TiNi Shape Memory Alloy Wires*" – Mechanics of Materials, An International Journal, vol.24, no.1, pp.19-30

[47] Tobushi H., Yamada S., Hachisuka T., Ikai A., Tanaka K., 1996, "*Thermomechanical Properties due Martensitic and R-Phase Transformations of*

TiNi Shape Memory Alloy Subjected to Cyclic Loadings" – Smart Materials and Structures, vol.5, no.6, pp.788-795

[48] Sittner P., Stalmans R., Tokuda M., 2000, "*An Algorithm for Prediction of the Hysteresis Responses of Shape Memory Alloys*" – Smart Materials and Structures, vol.9, no.4, pp.452-465

[49] Naito H., Matsuzaki Y., Ikeda T., 2001, "*A Unified Model of Thermo-mechanical Behaviour of Shape Memory Alloys*" – Society of Photo-Optical Instrumentation Engineers, vol.4333, Society of Photo-Optical Instrumentation Engineers (International Society for Optical Engineering), Bellingham, WA, pp.291-313

[50] Haag C., Tandale M., Valasek J., 2005, "*Characterization of Shape Memory Alloy Behavior and Position Control Using Reinforcement Learning*" – Proceedings of the AIAA Infotech@Aerospace Conference, Arlington, VA, September 26-29, AIAA Journal 2005-7160

[51] Valasek J., Tandale M., Rong J., 2005, "*A Reinforcement Learning - Adaptive Control Architecture for Morphing*" – Journal of Aerospace Computing, Information, and Communication, vol.2, no.5, pp.174-195

[52] Valasek J., Doebbler J., Tandale M., Meade A.J., 2008, "*Improved Adaptive-Reinforcement Learning Control for Morphing Unmanned Air Vehicles*" – IEEE Transactions on Systems, Man, and Cybernetics: Part B, vol.38, no.4, pp.1014-1020

[53] Kirkpatrick K., Valasek J., 2008, "*Reinforcement Learning for Active Length Control of Shape Memory Alloys*" – AIAA Guidance, Navigation and Control Conference and Exhibit, August 18-21, Honolulu, Hawaii, AIAA Journal 2008-7280

[54] Han L.H., Lu T.J., 2006, "*3D Finite Element Simulation for Shape Memory Alloys*" – IUTAM Symposium on Mechanics and Reliability of Actuating Materials, ed. by Yang W., ISBN 1-402-04130-6, pp.227-236

[55] Richter F., Kastner O., Eggeler G., 2009, "*Implementation of the Müller-Achenbach-Seelecke Model for Shape Memory Alloys in ABAQUS*" – Journal of Materials Engineering and Performance, vol.18, no.5-6, pp.626-630

[56] Chemisky Y., Duval A., Piotrowski B., Ben-Zineb T., Patoor E., 2008, "*Numerical Tool Based on Finite Element Method for SMA Structures Design*" – Proceedings of ASME 2008 Conference on Smart Materials, Adaptative

Structures & Intelligent Systems (SMASIS), October 28-30, Turf Valley Resort, Ellicott City, MD, USA, SMASIS08-485 (9pp)

[57] Gong X.-Y., Pelton A.R., Duerig T.W., Rebelo N., Perry K., 2004, "*Finite Element Analysis and Experimental Evaluation of Superleastic Nitinol Stent*" – Proceedings of the International Conference on Shape Memory and Superleastic Technologies (SMST-03), May 5-8, Pacific Grove, California, CA, eds. by Pelton A.R. and Duerig T.W., pp.443-451

[58] Li Q., Seelecke S., 2007, "*Thermo-Mechanically Coupled Analysis of Shape Memory Actuators*" – Proceedings of the COMSOL Users Conference 2007, Boston, MA

[59] Shrivastava S., 2006, "*Simulation for Thermomechanical Behavior of Shape Memory Alloy (SMA) using COMSOL Multiphysics*" – Proceedings of the COMSOL Users Conference 2006, Bangalore, India

[60] Collet M., 2008, "*Modeling Implementation of Smart Materials such as Shape Memory Alloys and Electro-Active Metamaterials*" – Proceedings of the COMSOL Conference 2008, Hannover, Germany

[61] Thiebaud F., Collet M., Foltete E., Lexcellent C., 2005, "*Implementation of a multi-axial pseudoelastic model in FEMLAB to predict dynamical behaviour of Shape Memory Alloys*" – Proceedings of the COMSOL Conference 2005, Paris, France

[62] Yang S., Seelecke S., 2008, "Modeling and Analysis of SMA-Based Adaptive Structures" – Proceedings of the COMSOL Conference 2008, Boston, MA

[63] Barrett P.R., Fridline D., "*User Implemented Nitinol Material Model in ANSYS*", website: http://www.caeai.com/all-downloads.php

[64] Barrett P.R., Cunningham P., "*Super Elastic Alloy Eyeglass Frame Design Using the ANSYS Workbench Environment*", website: http://www.caeai.com/all-downloads.php

[65] Terriault P., Viens F., Brailovski V., 2006, "*Non-isothermal finite element modeling of a shape memory alloy actuator using ANSYS*" – Computational Materials Science, vol.36, no.4, pp.397-410

[66] Sreekumar M., Nagarajan T., Singaperumal M., 2008, "*Modelling and simulation of a novel shape memory alloy actuated compliant parallel manipulator*" – Journal of Mechanical Engineering Science, vol.222, no.6, pp.1049-1059

[67]   Prahlad H., Chopra I., 2000, "*Experimental Characterization of NiTi Shape Memory Alloy Wires Under Uniaxial Loading Conditions*" – Journal of Intelligent Material Systems and Structures, vol.11, no.4, pp.272-282

[68]   Faulkner M.G., Amairaj J.J., Battaacharyya A., 2000, "*Experimental Determination of Thermal and Electrical Properties of Ni-Ti Shape Memory Wires*" – Smart Materials and Structures, vol.9, no.5, pp.632-639

[69]   Epps J., Chopra I., 1997, "*Comparative Evaluation of Shape Memory Alloy Constitutive Models with Experimental Test Data*" – 38th AIAA/ASME/ASCE/AHS/ASC Structures, Structural Dynamics, and Materials Conference and Adaptive Structures Forum, Reston, VA, AIAA 1997-1194

[70]   Bo Z., Lagoudas D.C., 1994, "*Comparison of Different Thermo Mechanical Models for Shape Memory Alloys*" – Adaptive Structures and Composite Materials: Analysis and Applications: American Society of Mechanical Engineers Symposium, vol.54, pp.9-19

[71]   Fumagalli L., Butera F., Coda A., 2009, "*SmartFlex NiTi Wires for Shape Memory Actuators*" – Journal of Materials Engineering and Performance, vol.18, no.5-6, pp.691-695

[72]   Hornbogen E., 2004, "*Review Thermo-mechanical fatigue of shape memory alloys*" – Journal of Material Science, vol.39, pp.385-399

[73]   Mikuriya S., Nakahara T., Tobushi H., Watanabe H., 2000, "*The Estimation of Temperature Rise in Low-Cycle Fatigue of TiNi Shape-Memory Alloy*" – JSME International Journal, Series A, vol.43, no.2, pp.166-172

[74]   Tobushi H., Nakahara T., Shimeno Y., Hashimoto T., 2000, "*Low-Cycle Fatigue of TiNi Shape Memory Alloy and Formulation of Fatigue Life*" – Journal of Engineering Materials and Technology, vol.122, no.2, pp.186-191

[75]   Prahlad H., Chopra I., 2001, "*Development of a Strain-Rate Dependant Model for Uniaxial Loading of SMA Wires*" – 12th International Conference on Adaptive Structures and Technologies, CRC Press, Boca Raton, FL

[76]   Shaw J.A., 2002, "*Thermo-Mechanical Model for 1-D Shape Memory Alloys Wire with Propagating Instabilities*" – International Journal of Solids and Structures, vol.139, no.5, pp.1275-1305

[77]   Lexcellent C., Rejzner J., 2000, "*Modeling of the Strain Rate Effect, Creep and Relaxation of a Ni-Ti Shape Memory Alloy Under Tension (Compression)-*

Torsional Proportional Loading in the Pseudoelastic Range" – Smart Materials and Structures, vol.9, no.5, pp.613-621

[78] Potapov P.L., Silva P.D., 2000, "*Time Response of Shape Memory Alloy Actuators*" – Journal of Intelligent Material Systems and Structures, vol.11, no.2, pp.125-134

[79] Davidson F.M., Liang C., Lobitz D., 1996, "*Investigation of Torsional Shape Memory Alloy Actuators*" – Society of Photo-Optical Instrumentation Engineers' Symposium on Smart Structures and Materials, Smart Structures and Integrated Systems, vol.2717, Society of Photo-Optical Instrumentation Engineers (International Society for Optical Engineering), Bellingham, WA, pp.672-682

[80] Keefe A.C., Carman G.P., 2000, "*Thermo-Mechanical Characterization of Shape Memory Alloy Torque Tube Actuators*" – Smart Materials and Structures, vol.9, no.5, pp.665-672

[81] Prahlad H., Chopra I., 2002, "*Characterization of SMA Torsional Actuators for Variable Twist Tilt Rotor (VTTR) Blades*" – 43rd AIAA/ASME/ASCE/AHS/ASC Structures, Structural Dynamics, and Materials Conference and 10th Adaptive Structures Forum, Reston, VA, AIAA 2002-1445

[82] Atulasimha J., Chopra I., 2003, "*Behavior of Torsional Shape Memory Alloy Actuators*" – 44th AIAA/ASME/ASCE/AHS Structures, Structural Dynamics, and Materials Conference, April 7-10, Norfolk, Virginia, AIAA Journal 2003-1558

[83] Thomson P., Balas G.J., Leo P.H., 1993, "*Pseudoelastic Hysteresis of Shape Memory Wires for Passive Structural Damping: Theory and Experiments*" – Society of Photo-Optical Instrumentation Engineers, vol.1917, Society of Photo-Optical Instrumentation Engineers (International Society for Optical Engineering), Bellingham, WA

[84] Van Humbeeck J., Kustov S., 2005, "*Active and passive damping of noise and vibrations through shape memory alloys: applications and mechanisms*" – Smart Materials and Structures, vol.14, pp.S171-S185

[85] Wolons D., Gandhi F., Malovrh B., 1998, "*Experimental Investigation of the Pseudoelastic Hysteresis Damping Characteristics of Shape Memory Alloy Wires*" – Journal of Intelligent Material Systems and Structures, vol.9, no.2, pp.116-126

[86] Malovrh B., Gandhi F., 2001, "*Mechanism-Based Phenomenological Models for the Pseudoelastic Hysteresis Behaviour of Shape Memory Alloys*" – Journal of Intelligent Material Systems and structures, vol.12, no.1, pp.21-30

[87] Fosdick R., Ketema Y., 2009, "*Thermal Effects on the Vibration Damping Properties of Shape Memory Alloys*" – Journal of Intelligent Material Systems and Structures, vol.20, pp.1587-1601

[88] Gandhi F., Wolons D., 1999, "*Characterization of the Pseudoelastic Damping Behavior of Shape Memory Alloy Wires Using Complex Modulus*" – Smart Materials and Structures, vol.8, pp.49-56

[89] Gandhi F., Chapuis G., 2002, "*Passive Damping Augmentation of a Vibrating Beam using Pseudoelastic Shape Memory Alloy Wires*" – Journal of Sound and Vibration, vol.250, no.3, pp.519-539

[90] Gandhi F., 2005, "*Maximizing the Effectiveness of Pseudoelastic Shape Memory Alloy Wires for Structural Damping Augmentation*" – Invited paper at the Workshop on Damping in Shape Memory Alloys, Composites and Foams, May 10-11, Metz, France

[91] Pappadà S., Gren P., Tatar K., Gustafson T., Rametta R., Rossini E., Maffezzoli A., 2009, "*Mechanical and Vibration Characteristics of Laminated Composite Plates Embedding Shape Memory Alloy Superelastic Wires*" – Journal of Materials Engineering and Performance, vol.18, no.5-6, pp.531-537

[92] Lammering R., Schmidt I., 2001, "*Experimental Investigations on the Damping Capacity of NiTi Components*" – Smart Materials and Structures, vol.10, no.5, pp.853-859

[93] Ju D.Y., Shimamoto A., 1999, "*Damping Property of Epoxy Matrix Composite Beams with Embedded Shape Memory Alloy Fibers*" – Journal of Intelligent Material Systems and Structures, vol.10, no.7, pp.514-520

[94] Midè Technology Corporation, Smart Materials, website: http://www.mide.com/index.php

[95] Tuissi A., Bassani P., Casati R., Bocciolone M., Collina A., Carnevale M., Lo Conte A., Previtali B., 2009, "*Application of SMA Composites in the Collectors of the Railway Pantograph for the Italian High-Speed Train*" – Journal of Materials Engineering and Performance, vol.18, no.5-6, pp.612-619

[96] Williams K.A., Chiu G.T., Bernhard R.J., 2002, "*Adaptive-passive absorber using shape-memory alloys*" – J. Sound Vib., vol.249, pp.835-848

[97] Rustighi E., Brennan M.J., Mace B.R., 2005, "*Real-time control of a shape memory alloy adaptive tuned vibration absorber*" – Smart Materials and Structures, vol.14, pp.1184-1195

[98] Kumar P.K., Lagoudas D.C., 2008, "*Shape Memory Alloys: Modeling and Engineering Applications*" – Springer, ed. by Lagoudas D.C., ISBN 0-387-47684-1

[99] Miller D.A., Lagoudas D.C., 2000, "*Thermo-mechanical characterization of NiTiCu and NiTi SMA actuators: Influence of plastic strains*" – Smart Materials and Structures, vol.9, no.5, pp.640-652

[100] Miller D.A., Lagoudas D.C., 2001, "*Influence of cold work and heat treatment on the shape memory effect and plastic strain development of NiTi*" – Material Science & Engineering A, vol.308, pp.161-175

[101] Melton K.N., Mercier O., 1979, "*Fatigue of NiTi thermoelastic martensites*" – Acta Metallurgica, vol.27, pp.137-144

[102] Tobushi H., Hachisuka T., Yamada S., Lin P.H., 1997, "*Rotating-bending fatigue of a TiNi shape-memory alloy wire*" – Mechanics of Materials, vol.26, pp.35-42

[103] McNichols J.L., Brooks P.C., 1981, "*NiTi fatigue behaviour*" – Journal of Applied Physics, vol.52, pp.7442-7444

[104] Tobushi H., Hachisuka T., Hashimoto T., Yamada S., 1998, "*Cyclic deformation and fatigue of a TiNi shape memory alloy wire subjected to rotating bending*" – Journal of Engineering Materials and Technology, vol.120, pp.64-70

[105] Miller D., 2000, "*Thermomechanical characterization of plastic deformation and transformation fatigue in shape memory alloys*" – PhD thesis, Texas A&M University

[106] Bertacchini O., Lagoudas D., Patoor E., 2003, "*Fatigue life characterization of shape memory alloys undergoing thermomechanical cyclic loading*" – Proceedings of SPIE, Smart Structures and Materials, pp.612-624

[107] Gall K., Maier H., 2002, "*Cyclic deformation mechanisms in precipitated NiTi shape memory alloys*" – Acta Materialia, vol.50, pp.4643-4657

[108] Eggeler G., Hornbogen E., Yawny A., Heckmann A., Wagner M., 2004, "*Structural and functional fatigue of NiTi shape memory alloys*" – Materials Science and Engineering A, vol.378, pp.24-33

[109] Predki W., Klonne M., Knopik A., 2006, "*Cyclic torsional loading of pseudoelastic NiTi shape memory alloys: Damping and fatigue failure*" – Materials Science and Engineering A, vol.417, pp.182-189

[110] Rogers C.A., Robertshaw H.H., 1988, "*Shape Memory Alloy Reinforced Composite*" – Engineering Science Preprints 25, Society of Engineering Science Inc., ESP25.8027

[111] Rogers C.A., Barker D.K., 1990, "*Experimental Studies of Active Strain Energy Tuning of Adaptive Composites*" – 31st AIAA/ASME/ASCE/AHS/ASC Structures, Structural Dynamics, and Materials Conference, Washington, DC, AIAA 1990-1086

[112] Baz A., Imam K., McCoy J., 1990, "*Active Vibration Control of Flexible Beams Using Shape Memory Actuators*" – Journal of Sound and Vibration, vol.140, no.3, pp.437-456

[113] Baz A., Ro J., Mutua M., Gilheany J., 1991, "*Active Buckling Control of Nitinol-Reinforced Composite Beams*" – Conference on Active Material and Adaptive Structures, Society of Photo-Optical Instrumentation Engineers (International Society for Optical Engineering), Bellingham, WA, pp.167-176

[114] Brinson L.C., Bekker A., Huang M., 1996, "*Deformation of Shape Memory Alloys due to Thermo-Induced Transformation*" – Journal of Intelligent Material Systems and Structures, vol.7, no.1, pp.97-107

[115] Lagoudas D., Moorthy D., Quidwai M.A., Reddy J.N., 1997, "*Modeling of Thermomechanical Response of Active Laminates with SMA Strips Using Layerwise Finite Element Method*" – Journal of Intelligent Material Systems and Structures, vol.8, no.6, pp.476-488

[116] Turner T.L., 2000, "*A New Thermoelastic Model for Analysis of Shape Memory Alloy Hybrid Composites*" – Journal of Intelligent Material Systems and Structures, vol.11, no.5, pp.382-394

[117] Epps J., Chandra R., 1995, "*Shape Memory Actuation for Active Tuning of Composite Beams*" – Society of Photo-Optical Instrumentation Engineers (International Society for Optical Engineering), Bellingham, WA

[118] Diodati G., Ameduri S., Concilio A., 2005, "*A SMA Embedded Anisotropic Panel Aimed at Controlling Vibration due to Variable Regimes Sources*" – 8th Conference on Dynamical Systems Theory and Applications, Lódź, Poland

[119] Furuya Y., 1996, "*Design and Material Evaluation of Shape Memory Composites*" – Journal of Intelligent Material Systems and Structures, vol.7, no.2, pp.321-330

[120] Birman V., 1996, "*Micromechanics of Composites with Shape memory Alloy Fibers in Uniform Thermal Fields*" – AIAA Journal, vol.34, no.9, pp.1905-1912

[121] Bisagni C., Sala G., 2004, "*Buckling and Shape Control of Composite Laminates Using Embedded Shape Memory Alloys Wires*" – 45th AIAA/ASME/ASCE/ AHS/ASC Structures, Structural Dynamics, and Materials Conference, Palm Springs, California, AIAA 2004-1648

[122] Balta J.A., Bosia F., Michaud V., Dunkel G., Botsis J., Manson J.-A., 2005, "*Smart composites with embedded shape memory alloy actuators and fibre Bragg grating sensors: activation and control*" – Smart Materials and Structures, vol.14, pp.457-465

[123] Gao X., Burton D.S., Brinson L.C., 2004, "*Finite Element Simulation of a Self-Healing Shape Memory Alloy Composite*" – Mechanics of Materials, An International Journal

[124] Wang X., 2002, "*Shape memory alloy volume fraction of pre-stretched shape memory alloy wire-reinforced composites for structural damage repair*" – Smart Materials and Structures, vol.11, pp.590-595

[125] Jia H., 1998, "*Impact Damage Resistance of Shape Memory Alloy Hybrid Composite Structures*" – PhD thesis, University of Virginia, Blacksburg, VA

[126] Roh J.-H., Kim E.-H., Lee I., 2008, "*Low Velocity Impact Behaviors of Composite Structures with Embedded Shape Memory Alloy Films*" – 49th AIAA/ASME/ASCE/AHS/ASC Structures, Structural Dynamics, and Materials Conference, April 7-10, Schaumburg, IL, AIAA Journal 2008-2206

[127] Schloßmacher P., Haas T., Schüßler A., 1997, "*Laser Welding of a Ni-Rich TiNi Shape Memory Alloy: Pseudoelastic Properties*" – 2nd International Conference on Shape Memory and Superelastic Technologies, ed. by Pelton A. et al., SMST-97, pp. 137-142

[128] Wang G., 1995, "*Weldability of Nitinol to Stainless Steel*" – 2nd International Conference on Shape Memory and Superelastic Technologies, ed. by Pelton A. et al., SMST-97, pp.131-136

[129] Wisbey A., Ward-Close C.M., 1994, Materials Letters, vol.21, pp.47-53

[130] Nishida M., Chiba A., Honda Y., Hirazumi J., Horikiri K., 1995, ISIJ International, vol.35, pp.217-219

[131] Fuji A., North T.H., Ameyama K., Futamata M., 1992, Materials Sci. Technol., vol.3, p.219

[132] Hall T.A., 1993, "*Joint, a Laminate and a Method of Preparing a Nickel-Titanium Alloy Member Surface for Bonding to Another Layer of Metal*", U.S. Patent 5,242,759

[133] Hall P.C., 1997, "*Methods of Promoting Solder Wetting on Nitinol*" – 2nd International Conference on Shape Memory and Superelastic Technologies, ed. Pelton A. & al., SMST-97, pp.125-130

[134] Grummon D.S., Low K.-B., Foltz J., Shaw J.A., 2007, "*A New Method for Brazing Nitinol Based on the Quasibinary TiNi-Nb System*" – 48th AIAA/ASME/ASCE/AHS/ASC Structures, Structural Dynamics, and Materials Conference, April 23-26, Honolulu, Hawaii, AIAA Journal 2007-1741

[135] Johnson Matthey Inc., website: http://www.jmmedical.com/

[136] Langelaar M., Van Keulen F., 2007, "*Gradient-based Design Optimization of Shape Memory Alloy Active Catheters*" – 48th AIAA/ASME/ASCE/AHS/ASC Structures, Structural Dynamics, and Materials Conference, April 23-26, Honolulu, Hawaii, AIAA Journal 2007-1744

[137] Langelaar M., Van Keulen F., 2004, "*Modeling of a Shape Memory Alloy Active Catheter*" – 45th AIAA/ASME/ASCE/AHS/ASC Structures, Structural Dynamics, and Materials Conference, Palm Springs, California, AIAA 2004-1653

[138] Memory-Metalle GmbH, website: http://www.memory-metalle.de/

[139] Mantovani D., 2000, "*Shape Memory Alloys: Properties and Biomedical Applications*" – JOM, vol.52, no.10, pp.36-44

[140] Luig P., Knopik A., Oberste-Brandenburg C., Grabe C., Bruhns O.T., Predki W., 2006, "*Damping couplings with elements of pseudoelastic NiTi shape memory alloys*" – Arch. Appl. Mech., vol.76, pp.75-87

[141] Ertas B., Luo H., Hallman D., 2009, "*Dynamic Characteristics of Shape Memory Alloy Metal Mesh Dampers*" – 50th AIAA/ASME/ASCE/AHS/ASC Structures, Structural Dynamics, and Materials Conference, May 4-7, Palm Springs, California, AIAA Journal 2009-2521

[142] Elegant Aliforms, website: http://www.innovativeanimation.com/default.html

[143] Fosness E., Maji A., Guerrero J., Carpenter B., Tupper M., 2003, "*Development of Low Shock Deployment Devices for Aerospace Applications Using Shape Memory and Elastic Memory Materials*" – Space 2003, September 23-25, Long Beach, California, AIAA J. 2003-6246

[144] Raychem Corporation, Tyco Electronics, website: http://www.raychem.com/

[145] Kauffman G.B., Mayo I., 1993, "*Memory Metal*" – Chem Matters, vol.11, no.3, pp.4-7

[146] Peairs D.M., Park G., Inman D.J., 2004, "*Practical issues of activating self-repairing bolted joints*" – Smart Materials and Structures, vol.13, pp. 1414-1423

[147] Campanile L.F., Melz T., Keimer R., Wadehn W., 2003 – Patent DE10155119A1

[148] Langbein S., Welp E.G., 2009, "*One-Module Actuators Based on Partial Activation of Shape Memory Components*" – Journal of Material Engineering and Performance, vol.18, no.5-6, pp.711-716

[149] Song G., 2007, "*Design and control of a Nitinol wire actuated rotary servo*" – Smart Materials and Structures, vol.16, pp.1796-1801

[150] BM Smart Servo TK-B10, Toki Corporation, website: http://www.toki.co.jp

[151] Rogers C., 1995, "*Intelligent Materials*" – Scientific American, September 1995, pp.154-157

[152] University of Alberta, Canada, website: http://www.cs.ualberta.ca/~database/MEMS/sma_mems/sma.html

[153] Cocaud C., Price A., Jnifene A., Naguib H., 2007, "*Position control of an experimental robotic arm driven by artificial muscles based on shape memory alloys*" – Int. J. Mech. Mater. Des., vol.3, pp.223-236

[154] Wang Z., Hang G., Wang Y., Li J., Du W., 2008, "*Embedded SMA wire actuated biomimetic fin: a module for biomimetic underwater propulsion*" – Smart Materials and Structures, vol.17, 025039 (11pp)

[155] Morra F., Molfino R., Cepolina F., 2004, "*Miniature gripping device*" – Proceedings of IEEE International Conference on Intelligent Manipulation and Grasping IMG 04, July 1-2, Genova, Italy

[156] Menciassi A., Gorini S., Pernorio G., Dario P., 2004, "*A SMA Actuated Artificial Earthworm*" – Proceedings of ICRA '04, IEEE International Conference on Robotics and Automation, vol.4, pp.3282-3287, ISBN 0-7803-8232-3

[157] Lim S.-C., Park J.-S., Choi S.-B., Park Y.-P., 2001, "*Non-contact start/stop motion control of HDD suspension using shape memory alloy actuators*" – Smart Materials and Structures, vol.10, pp. 1069-1077

[158] Electric Piston, Mondo-tronics Inc., website: http://www.robotstore.com

[159] Gambardella V., Cavanna G., Bravin E., 2003, "*I materiali a memoria di forma - Una nuova applicazione nel campo della previsione incendi*" – L'Edilizia-

Speciale ITC, Istituto per le Tecnologie delle Costruzione, C.N.R., website: http://www.itc.cnr.it/default.asp (in italian, available also in english)

[160] Freed Y., Aboudi J., 2008, "*Micromechanical investigation of plasticity–damage coupling of concrete reinforced by shape memory alloy fibers*" – Smart Materials and Structures, vol.17, 015046 (14pp)

[161] Casciati F., Favarelli L., Hamdaoui K., 2007, "*Performance of a base isolator with shape memory alloy bars*" – Earthquake Engineering and Engineering Vibration, vol.6, no.4, article ID: 1671-3664(2007)04-0401-08

[162] Johnson R., Padgett J.E., Emmanuel Maragakis M.E., DesRoches R., Saiidi M.S., 2008, "*Large scale testing of nitinol shape memory alloy devices for retrofitting of bridges*" – Smart Materials and Structures, vol.17, 035018 (10pp)

[163] Banks R.M., 1975, "*Energy Conversion Systems*" – Patent US03913326

[164] Johnson A.D., 1977, "*Memory alloy heat engine and method of operation*" – Patent US4055955

[165] Pachter J.J., 1979, "*Engine*" – Patent US4150544

[166] Wakjira J.F., 2001, "*The VT1 Shape Memory Alloy Heat Engine Design*" – Master's thesis, University of Virginia, Blacksburg, VA

[167] Schiller E.H., 2002, "*Heat Engine Driven by Shape Memory Alloys: Prototyping and Design*" – Master's thesis, University of Virginia, Blacksburg, VA

[168] Bokaie M. of TiNi Alloy Co. for NASA Lewis Research Center, February 1998, LEW-16511, website: http://www.nasatech.com/Briefs/Feb98/LEW16511.html

[169] Jenkins P.P., Geoffrey A.L., 1995, "*A Rotating Arm Using Shape Memory Alloy*" – Proceedings of the 29th Aerospace Mechanisms Symposium, May 17-19, Houston, Texas, pp.167-171

[170] Wada B.K., Fanson J.L., Crawley E.F., 1990, "*Adaptive Structures*" – Journal of Intelligent Material Systems and Structures, vol.1, no.2, pp.157-174

[171] Pollard E.L., Jenkins C., 2005, "*Shape Memory Alloy Deployment of Membrane Mirrors for Spaceborne Telescopes*" – 46th AIAA/ASME/ASCE/AHS/ASC Structures, Structural Dynamics, and Materials Conference, Austin, Texas, AIAA 2005-2196

[172] Montminy S., Dupuis E., Champliaud H., 2008, "*Mechanical Design of a Hopper Robot for Planetary Exploration using SMA as a Unique Source of Power*" – Acta Astronautica, vol.62, no.6-7, pp.438-452

[173] Pollard E.L., Murphey T.W., 2006, "*Development of Deployable Elastic Composite Shape Memory Alloy Reinforced (DECSMAR) Structures*" – 47th AIAA/ASME/ASCE/AHS/ASC Structures, Structural Dynamics, and Materials Conference, May 1-4, Newport, Rhode Island, AIAA Journal 2006-1681

[174] Gowing S., Carpenter B., Lee Y., Atsavapranee P., Hess D., 2004, "*Flextac: An Advanced Submarine Control Surface and Actuation System*" – 42nd AIAA Aerospace Sciences Meeting and Exhibit, Reno, Nevada, AIAA 2004-902

[175] Quackenbush T.R., Carpenter B.F., Gowing S., 2005, "*Design and Testing of a Variable Geometry Ducted Propulsor Using Shape Memory Alloy Actuation*" – 43rd AIAA Aerospace Sciences Meeting and Exhibit, Reno, Nevada, AIAA 2005-1077

[176] Lin C.Y., Crawley E.F., Heeg J., 1996, "*Open- and Closed-Loop Results of a Strain-Actuated Active Aeroelastic Wing*" – Journal of Aircraft, vol.33, no.5, pp.987-994

[177] Kudva J., Appa K., Martin C., Jardine P., Sendeckji G., 1997, "*Design, Fabrication and Testing of the DARPA/WL 'Smart Wing' Wind Tunnel Model*" – AIAA Paper 97-1198

[178] Kudva J., Martin C.A., Scherer L.B., Jardine A.P., McGowan A.R., Lake R.C., Sendeckji G., Sanders B., 1999, "*Overview of the DARPA/AFRL/NASA Smart Wing Program*" – Society of Photo-Optical Instrumentation Engineers' North American Symposium on Smart Structures and Materials, vol.3674, Society of Photo-Optical Instrumentation Engineers (International Society for Optical Engineering), Bellingham, WA, pp.230-248

[179] Becker J., Schroeder W., 1999, "*Advanced Aircraft Structures Program: An Overview*" – Society of Photo-Optical Instrumentation Engineers' North American Symposium on Smart Structures and Materials, vol.3674, Society of Photo-Optical Instrumentation Engineers (International Society for Optical Engineering), Bellingham, WA, pp.2-12

[180] Duan B., Abdel-Motagaly K., Guo X., Mei C., 2003, "*Suppression of Supersonic Panel Flutter and Thermal Deflection Using Shape Memory Alloy*" – 44th AIAA/ASME/ASCE/AHS Structures, Structural Dynamics, and Materials Conference, Norfolk, Virginia, AIAA 2003-1513

[181] Guo X., Lee Y.-Y., Mei C., 2007, "*Supersonic Nonlinear Panel Flutter Suppression Using Shape Memory Alloys*" – Journal of Aircraft, vol.44, no.4

[182] Bein T., Hanselka H., Breitbach E., 2000, "*An Adaptive Spoiler to Control the Transonic Shock*" – Smart Materials and Structures, vol.9, no.2, pp.141-148

[183] Ehlers S.M., Weisshaar T.A., 1993, "*Static Aeroelastic Control of an Adaptive Lifting Surface*" – Journal of Aircraft, vol.30, no.4, pp.534-540

[184] Lazarus K.B., Crawley E.F., Bohlmann J.D., 1991, "*Static Aeroelastic Control Using Strain Actuated Adaptive Structures*" – Journal of Intelligent Material Systems and Structures, vol.12, no.3, pp.386-410

[185] Wong F.C., Boissonneault O., Lechevin N., Rabbath C.A., 2007, "*Development of a Shape Memory Alloy-based Micro-Flow Effector for Missile Side Force Control*" – 48th AIAA/ASME/ASCE/AHS/ASC Structures, Structural Dynamics, and Materials Conference, April 23-26, Honolulu, Hawaii, AIAA Journal 2007-1701

[186] Dayananda G.N., Varughese B., Subba Rao M., 2007, "*Shape Memory Alloy Based Smart Landing Gear for an Airship*" – Journal of Aircraft, vol.44, no.5

[187] Testa C., Leone S., Ameduri S., Concilio A., 2005, "*Feasibility study on rotorcraft blade morphing in hovering*" – Proceedings of SPIE, Smart Structures and Materials, vol.5764, San Diego, CA, pp.171-182

[188] Prahlad H., Chopra I., 2001, "*Design of a variable twist tilt-rotor blade using shape memory alloy (SMA) actuators*" – Proceedings of SPIE, Smart Structures and Materials, vol.4327, Newport Beach, CA, pp.46-59

[189] Konstanzer P., Grohmann B., Kroplin B., 2001, "*Decentralized Vibration Control and Coupled Aeroservoelastic Simulation of Helicopter Rotor Blades with Adaptive Airfoils*" – Journal of Intelligent Material Systems and Structures, vol.12, no.4, pp.209-214

[190] Chen P.C., Baeder J.D., Evans R.A.D., Niemczuk J., 2001, "*Blade-Vortex Interaction Noise Reduction with Active Twist Smart Rotor Technology*" – Smart Materials and Structures, vol.10, no.1, pp.77-85

[191] Koratkar N.A., Chopra I., 2001, "*Wind Tunnel Testing of a Mach-Scaled Rotor Model with Trailing-Edge Flaps*" – Smart Materials and Structures, vol.10, no.1, pp.1-14

[192] Bernhard A.P.F., Chopra I., 2001, "*Analysis of a Bending-Torsion Coupled Actuator for a Smart Rotor with Active Blade Tips*" – Smart Materials and Structures, vol.10, no.1, pp.35-52

[193] Cesnik C.E.S., Shin S.J., Wilbur M.L., 2001, "*Dynamic Response of Active Twist Rotor Blades*" – Smart Materials and Structures, vol.35, no.1, pp.6-16

[194] Shin S.J., Cesnik C.E.S., Hall S.R., 2002, "*Control of Integral Twist-Actuated Helicopter Blades for Vibration Reduction*" – 58th American Helicopter Society Annual Forum, American Helicopter Society, Alexandria, VA, vol.2, pp.328-343

[195] Epps J.J., Chopra I., 2000, "*In-Flight Tracking of Helicopter Rotor Blades Using Shape Memory Alloy Actuators*" – Smart Materials and Structures, vol.10, no.1, pp.104-111

[196] Singh K., Chopra I., 2002, "*Design of an Improved Shape Memory Alloy Actuator for Rotor Blade Tracking*" – Society of Photo-Optical Instrumentation Engineers' North American Symposium on Smart Structures and Materials, vol.4701, Society of Photo-Optical Instrumentation Engineers (International Society for Optical Engineering), Bellingham, WA, pp.244-266

[197] Ullakko K., Huang J.K., Kantner C., O'Handley C., Kokorin V.V., 1996, "*Large Magnetic-Field-Induced Strains in Ni_2MnGa single Crystals*" – Journal of Applied Physics Letters, vol.69, pp.1966-1968

[198] James R.D., Tickles R., Wuttig M., 1999, "*Large Field-Induced Strains in Ferromagetic Shape Memory Materials*" – Materials Science and Engineering, A273-275, pp.320-325

[199] James R.D., Wuttig M., 1998, "*Magnetostriction of Martensite*" – Philosophical Magazine, vol.77A, pp.1273-1299

[200] Clark A.E., 1980, "*Ferromagnetic Materials*" – Wohlfarth E.P., North Holland, Amsterdam, vol.1, p.531

[201] Sozinov A., Likhachev A.A., Lanska N., Ullakko K., 2002, – Journal of Applied Physics Letters, vol.80, p.1746

[202] Enkovaara J., 2003, "*Atomistic Simulations of Magnetic Shape Memory Alloys*" – Dissertations of Laboratory of Physics, Helsinki University of Technology, Espoo, Finlandia, ISBN 951-22-6313-0

[203] Vokoun D., Wang Y.W., Goryczka T., Hu C.T., 2005, "*Magnetostrictive and Shape Memory Properties of Fe-Pd alloys with Co e Pt additions*" – Smart Materials and Structures, vol.14, pp.261-265

[204] Wuttig M., Li J., Craciunescu C., 2001, "*A New Ferromagnetic Shape Memory Alloy System*" – Scripta Materialia, vol.44, pp.2393-2397

[205] Lavrov A.N., Komiya S., Ando Y., 2002 – Nature, vol.418, p.385

[206] Murray S.J., Marioni M., Allen S.M., O'Handley R.C., Lograsso T.A., 2000, "*6% magnetic-field-induced strain by twin-boundary motion in ferromagnetic Ni–Mn–Ga*" – Journal of Applied Physics Letters, vol.77, p.886

[207] Söderberg O., Ge Y., Sozinov A., Hannula S.-P., Lindroos V.K., 2005, "*Recent Breakthrough Development of the Magnetic Shape Memory Effect in Ni-Mn-Ga Alloys*" – Smart Materials and Structures, vol.14, pp.223-235

[208] Guo S., Zhang Y., Quan B., Li J., Qi Y., Wang X., 2005, "*The Effect of Doped Elements on the Martensitic Transformation in Ni-Mn-Ga Magnetic Shape Memory Alloy*" – Smart Materials and Structures, vol.14, pp.236-238

[209] Tickle R., Aerospace Engineering and Mechanics, University of Minnesota, website: http://www.aem.umn.edu/people/others/tickle/

[210] Vasil'ev N., Bozhko A.D., Khovailo V.V. et al., 1999, "*Structural and magnetic phase transitions in shape-memory alloys $Ni_{2+x}Mn_{1-x}Ga$*" – Phys. Rev., vol.59, pp.1113-1120

[211] Chu S.-Y., Cramb A., De Graef M., Laughlin D.E., McHenry M.E., 2000, "*The Effect of Field Cooling and Field Orientation on The Martensitic Phase Transformation in a Ni_2MnGa Single Crystal*" – Journal of Applied Physics Letters, vol.87, p.5777

[212] Kiselev N.S., Dragunov I.E., Onisan A.T., Roßler U.K., Bogdanov A.N., 2008, "*Theory of stripe domains in magnetic shape memory alloys*" – Eur. Phys. J. (Special Topics), vol.158, pp.119-124

[213] Scoby S., Chen Y., 2006, "*Dynamic behavior of ferromagnetic shape memory alloys*" – 47th AIAA/ASME/ASCE/AHS/ASC Structures, Structural Dynamics, and Materials Conference, May 1-4, Newport, Rhode Island, AIAA Journal 2006-1768

[214] Couch R.N., Chopra I., 2007, "*A quasi-static model for NiMnGa magnetic shape memory alloy*" – Smart Materials and Structures, vol.16, pp.S11-S21

[215] Tellinen J., Suorsa I., Jääskeläinen A., Aaltio I., Ullakko K., 2002, "*Basic Properties of Magnetic Shape Memory Actuators*" – 8th International Conference ACTUATOR 2002, Bremen, Germany

[216] Couch R.N., 2005, "*Development of a Swashplateless Rotor Using Magnetic Shape Memory Alloys*" – Storming Media, Report no. A918234, website: http://www.stormingmedia.us/91/9182/A918234.html

[217] Liang C., Rogers C.A., Melafeew E., 1997, "*Investigation of Shape Memory Polymers and Their Hybrid Composites*" – Journal of Intelligent Material Systems and Structures, vol.8, no.4, pp.380-386

[218] Gall K., Mikulas M., Munshi N.A., Beavers F., Tupper M., 2000, "*Carbon Fiber Reinforced Shape Memory Polymer Composites*" – Journal of Intelligent Material Systems and Structures, vol.11, no.11, pp.877-886

[219] Abrahamson E.R., Lake M.S., Munshi N.A., Gall K., 2003, "*Shape Memory Mechanics of an Elastic Memory Composite Resin*" – Journal of Intelligent Material Systems and Structures, vol.14, no.10, pp.623-632

[220] Erine H., Emily A.S., Tat H.T., 2005, "*Light-Activated Shape Memory Polymers and Associated Applications*" – Proceedings of SPIE, Bellingham, WA., vol. 5762, pp.48-55

[221] Andreas L., Honyan J., Oliver J., Robert L., 2005, "*Light-Induced Shape-Memory Polymers*" – Nature, vol.434, pp.879-882

[222] Leng J., Lu H., Du S., 2008, "*Conductive Shape Memory Polymer Composite Technology and Its Applications in Aerospace*" – 49th AIAA/ASME/ASCE/AHS/ASC Structures, Structural Dynamics, and Materials Conference, April 7-10, Schaumburg, IL, AIAA Journal 2008-2203

[223] Schmidt A.M., 2006, "*Electromagnetic Activation of Shape Memory Polymer Networks Containing Magnetic Nanoparticles*" – Macromol. Rapid Commun., vol.27, pp.1168-1172

[224] Cornerstone Research Group Inc., website: http://www.crgrp.net/veriflex.htm

[225] Toensmeir P.A., 2005, "*Radical Departure*" – Aviation Week & Space Technology, May 23, pp.72-73

[226] Wache H.M., Tartakowska D.J., Hentrich A., Wagner M.H., 2003, "*Development of a polymer stent with shape memory effect as a drug delivery system*" – J. Mater. Sci. Mater. Med., vol.14, pp.109-12

[227] Small W. IV, Buckley P.R., Wilson T.S., Benett W.J., Hartman J., Saloner D., Maitland D.J., 2007, "*Shape memory polymer stent with expandable foam: a new concept for endovascular embolization of fusiform aneurysms*" – IEEE Trans. Biomed. Eng., vol.54, pp.1157-1160

[228] Lendlein A., Langer R., 2002, "*Biodegradable, elastic shape-memory polymers for potential biomedical applications*" – Science, vol.296, pp.1673-1676

[229] Beblo R., MauckWeiland L., 2008, "*Strain Induced Anisotropic Properties of Shape Memory Polymer*" – Smart Materials and Structures, vol.17, 055021 (7pp)

[230] Huang W.M., Lee C.W., Teo H.P., 2006, "*Thermomechanical Behavior of Polyurethane Shape Memory Polymer Foam*" – Journal of Intelligent Material Systems and Structures, vol. 17, no.8-9, pp. 753-760

[231] Atli B., Gandhi F., Krast G., 2007, "*Thermomechanical Characterization of Shape Memory Polymers*" – Proceedings of 2007 SPIE Conference on Smart Structures and Materials, March 18-22, San Diego, California

- *Chapter 4* -

Former Application:

Transonic Bump

1 INTRODUCTION

In this chapter, a study regarding the formation of an airfoil upper bump is presented (*).

It is among the first experiences in the morphing field done by the author and researchers at CIRA: it represents one of the less invasive possible morphing techniques, not affecting the wing primary load-bearing structure, and capable of introducing some benefits in transonic regime (according to wind tunnel tests conducted by DLR).

A simple and lightweight device has been conceived, actuated by a Shape Memory Alloy, capable of inducing the bump formation on a metal plate: numerical simulations and experimental tests on a scaled down prototype demonstrated pro and cons of such a solution.

Further investigations have been carried out at CIRA on a full scale demonstrator, adopting similar architectures: results have been published only in internal reports.

PAPER

"Wing Shape Control through an SMA-Based Device"

S. Barbarino, S. Ameduri, L. Lecce, A. Concilio

Wing Shape Control through an SMA-Based Device

S. Barbarino,[1] S. Ameduri,[2] L. Lecce[1] and A. Concilio[2],*

[1]Department of Aerospace Engineering (DIAS), Engineering Faculty,
University "Federico II" of Napoli (NA), Italy

[2]The Italian Aerospace Research Centre (CIRA) Capua (CE), Italy

ABSTRACT: Based on numerical and experimental analyses, this article proposes an application of the smart structure concept aimed at realizing a bump on an airfoil profile, finalized to reduce transonic drag, through the use of shape memory alloys (SMAs). The ability of morphing the wing profile is functional to maximize the aerodynamic efficiency in different mission conditions. The use of the so-called smart materials allows a favorable actuation performance per weight ratio, also leading to simple and integrated devices. Currently, to model their mechanical behavior is still an open issue and this work presents some original ideas about this. Numerical results and experimental tests herein presented, demonstrate the efficacy of the developed concept device, calling for further studies on real structures; their correlation also validate the implemented simulation procedure.

Key Words: morphing, wing shape control, transonic bump, SMA.

INTRODUCTION

T HE current generation of aircraft is characterized by fixed airfoil geometry, optimized for a single or a few operational conditions (through mobile surfaces, such as flaps and slats) of a typical mission profile.

Such a solution leads to a non-complete exploitation of the aerodynamic potential, which means, for instance, higher costs per flight (Martins and Catalano, 1998) or lower performances.

The controlled modification of the wing shape can increase the aerodynamic efficiency of a wing, allowing its profile to fit to the external free-stream conditions; besides, it can be used to fulfil aircraft maneuvers necessities, with a consequent relief of control surfaces requirements (Szodruch, 1985; Smith and Nelson, 1990; Thornton, 1993; Siclari et al., 1996; Stanewsky, 2001; Browman et al., 2002).

Shape modification may be attained by changing different parameters, as reported in the literature: for instance, the local or global curvature (DeCamp and Hardy, 1984; Bonnema and Smith, 1988; Smith and Nelson, 1990; Spillman, 1992; Monner et al., 1998; Poonsong, 2004; European project 3AS), the wing span (Gevers Aircraft Inc., 1997; AeroVisions Inc.; Blondeau and Pines, 2004) or the twist angle (Pendleton, 2000; Wilson, 2002).

Some solutions have been found since the 1970s (Frost et al., 1978; Statkus, 1980) and have also led inflatable surfaces to be considered (Lin et al., 2002; Murray et al., 2002; Cadogan et al., 2003; Allred et al., 2004; Simpson and Jacob, 2005; Simpson et al., 2005a,b). Unfortunately, they have always brought higher costs, weight, architectural complexity and more severe maintenance requirements, de facto restricting such solutions only to military aircrafts (e.g., Northrop-Grumman F-14 'Tomcat'), where higher performances fully justify also very higher expenses.

Since the late 1980s, the development of 'intelligent' materials (usually referred in literature as 'smart') has shown major benefits for auto-deforming structures, eliminating some major drawbacks of previous morphing solutions and resulting into highly integrated and actuation-capable structures (Austin et al., 1997; Geissler et al., 2000; Inman, 2001; Munday and Jacob, 2001; Kikuta, 2003; Perkins et al., 2004; Cornerstone Research Group Inc.).

Among the several smart materials, shape memory alloys (SMAs) are playing a more and more determining role. They were first discovered (Kauffman and Mayo, 1993) in 1932 by Chang and Read as a Cd–Au alloy. However, only since 1962, when Buehler et al. (1963), at the Naval Ordnance Laboratory (NOL) of US Navy, observed the shape memory effect for the Ni–Ti equiatomic alloy, have they received increasingly more attention and study: in fact, such an alloy was cheaper to manufacture, and exhibited interesting mechanical properties.

SMAs are metal alloys (commonly nickel–titanium, gold–cadmium, copper–zinc–aluminum) that exhibit both the unique characteristics of large recoverable strains and large induced internal forces under temperature change (Brinson et al., 1996).

Aforementioned thermomechanical properties of SMAs are due to a crystallographic phase transformation from a body-centered cubic structure (austenite/parent phase, present at high temperatures) to a face-centered cubic structure (martensite/product phase, present at low temperatures), or vice versa. These transformations can also be induced by changes in the internal stress state. If the austenite temperature is lower than the environmental temperature, the so-called superelastic effect is shown; otherwise, the high residual strain may be recovered by a temperature change and the proper shape memory effect takes place (Figure 1). The phase changes arise between the respective start and finish temperatures of the austenite and martensite phases: the transition temperatures are supposed to vary with the applied stress, commonly with a pretty linear relationship (Figure 2) (Chopra, 2002).

Recent studies about smart materials applied to morphing-wing concepts demonstrated the advantages of using SMAs (usually in the form of wires or ribbons, thermally activated) above all for their capability in producing relevant amount of force levels, being characterized by a favorable performance per weight ratio (Kudva et al., 1996a,b; Kudva, 2001; Benavides and Correa, 2002; Alasty et al., 2004; Lecce, 2004; Lemme and Caruso, 2004). Nevertheless, these solutions have been applied only to small prototypes or UAVs, focusing on maneuvering aspects more than flight control capabilities because of their characteristic response times, usually measured in units of seconds.

In this study, a morphing wing concept has been exploited, aiming at achieving aerodynamic efficiency

gain, by means of thickness adaptive control (local bumps on the upper wing surface) for transonic drag reduction (Bein et al., 1998; Bannasch, 2000; Stanewsky, 2001). SMAs were herein used as actuation devices to produce a local bump by means of a simple, light, and compact actuation device.

THE AERODYNAMIC PROBLEM AND SOME PROPOSED SOLUTIONS

In transonic regime, the aerodynamic field around an airfoil (Figure 3) is very complex, because of the presence of an extended supersonic region which ends with a shock wave (Anderson, 2001). The development of the boundary layer and its interaction with the shock wave at the wing upper-surface essentially establish the flight performance of transonic transport aircraft at cruise. As shock wave develops, it produces additional drag contributions. Viscous drag strongly increases too, because of the subsequent thickening of
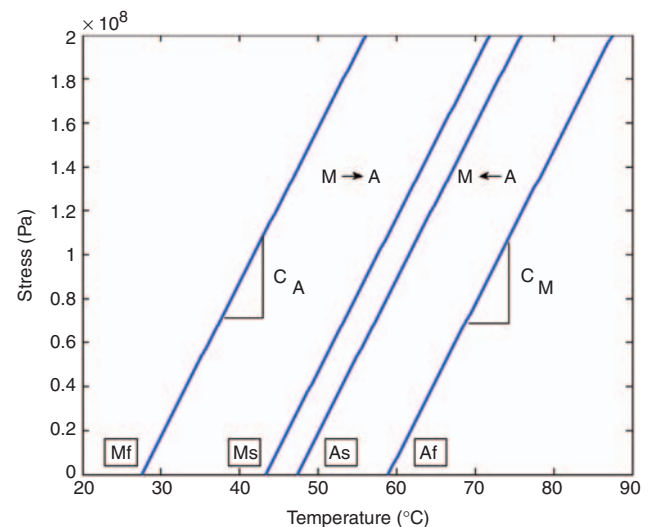
Figure 2. Stress–temperature behavior of SMAs (Chopra, 2002).

Figure 1. Stress–strain behavior of SMAs (Chopra, 2002).
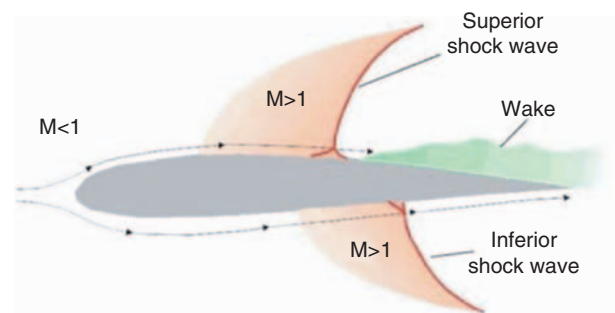
Figure 3. Schematics of typical aerodynamic conditions around an airfoil in transonic regime (the picture is not in scale, the boundary layer thickness is intentionally emphasized)(Ameduri, 2003).

the boundary layer. At higher speeds, flow separation occurs, finally leading to buffet and buffeting (Stanewsky and Krogmann, 1985).

Recent studies, conducted by DLR in collaboration with EADS-Airbus (Richter and Rosemann, 1999) in the frame of the European projects EUROSHOCK I and II (drag reduction by shock and boundary layer control), have proved the feasibility of reducing the airfoil drag generated during transonic flight conditions because of the shock wave onset, through simple shape modifications (positive or negative bumps) or other active devices (Stanewsky et al., 1997,1999).

Many different solutions were tested, from discrete slot suctions to cavity ventilations, pulsing jets, etc. (Figure 4). Among those, a contour bump, jointly with a variable rear camber, proved to be the most effective solution, bringing up to a 24% of aerodynamic efficiency increase (Richter and Rosemann, 1999; Stanewsky, 2001). However, to take advantage of such a solution, the use of an adaptive bump is mandatory: in normal flight conditions, a contour bump is counterproductive, causing an aerodynamic drag increase; on the other hand, during transonic flight, the position, length and height of the bump should be optimized with respect to free-stream conditions (Figure 5).

The adoption of shock wave and boundary layer control exhibits a large potential for improving flight performance, for instance in terms of cruise drag, fuel consumption or speed increase. Considering the great economical growth of the aeronautical transportation in the last decades (Bencke, 2000; Gal-Or, 2000) both in terms of passengers and goods, the efficiency increase of the next generation aircraft would help to allow the aeronautic industry to remain competitive with respect to the emerging means of transport, and increase economical gains.

Aiming at increasing aerodynamic efficiency in transonic conditions, at least two ways of controlling the shock and the shock-associated boundary layer development can be recognized: by trying to weaken the shock strength, by spreading the pressure rise over a larger span, or by supplying energy to the boundary layer, making it able to counteract adverse pressure gradients. Contour bump generation belongs to the first method, and also locally reduces the boundary layer thickness, increasing its stability and delaying its separation.

The bump effectiveness largely depends on the Mach number and the drag reduction increases for high lift coefficients (Stanewsky, 2001). The effectiveness of a bump strongly depends on free-stream conditions, i.e., shock location and shock strength: the first parameters determines the optimal bump position (centered at the shock); the second establishes the optimal bump height. Regarding the shape, it should allow the conversion of the shock into an isentropic compression
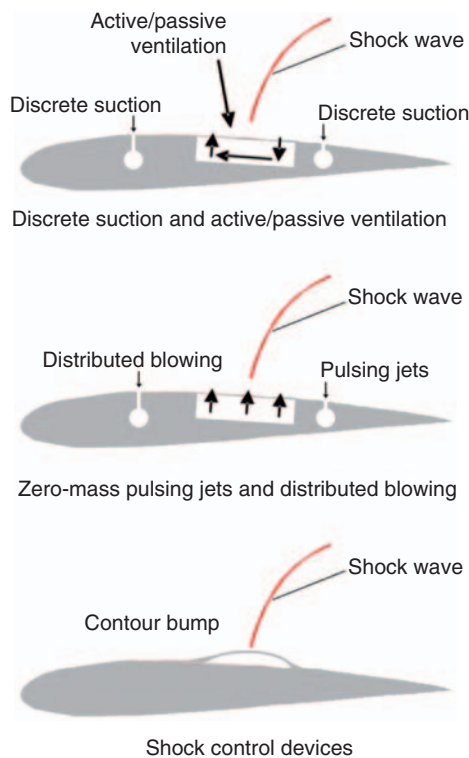
Figure 4. Examples of boundary layer and flow control devices (Stanewsky, 2001).
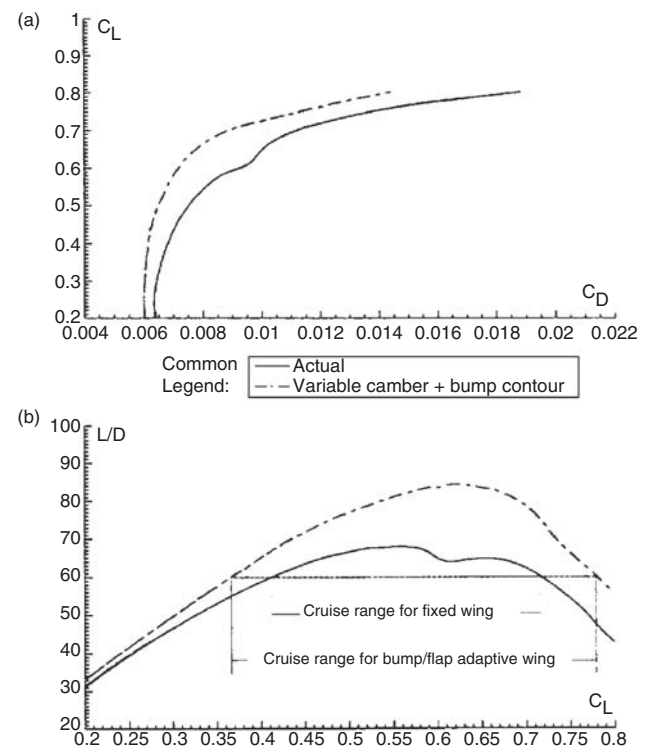
Figure 5. Effect of local contour optimizations on drag (a) and L/D ratio (b) (Richter and Rosemann, 1999).

followed by a weak shock (Stanewsky, 2001). For optimal performance over a given range of free-stream conditions, these geometric features should be adaptive. In order to permit dynamic control, time response should be as short as possible.

SMA MODELS

Among the actuation systems that can lead to adaptive bumps realization (mechanical kinematic chains, air pressure, etc.), smart materials-based devices are preferred because of the basic simplicity of their architectures.

SMAs are ideal for their favorable actuation performance per weight ratio: one of the major current drawbacks in engineering applications is the difficulty of fully characterizing their behavior which is highly nonlinear and load history dependent.

In 1986, Tanaka, presented a unified one-dimensional martensitic phase transformation model. His study was restricted to the stress-induced martensite phase transformation. The basic assumption of his theory was that the thermomechanical process of the material is fully described by three state variables: strain, temperature, and martensite (austenite) volume fraction (ξ), intended as a measure of the phase transformation. Using the classical Helmholtz free energy expression and the Clausius–Duhem inequality, Tanaka developed the constitutive equation in the rate form:

$$(\sigma - \sigma_0) = E(\xi)(\varepsilon - \varepsilon_0) + \Theta(T - T_0) + \Omega(\xi - \xi_0)$$

where the subscript 0 represents the initial condition. This equation shows that the stress consists of three parts (in the order): mechanical, thermal, and induced by phase transformation.

The martensite fraction was assumed an exponential function of the applied stress and temperature, following studies of the phase transformation.

In 1990, Liang and Rogers developed a new phenomenological model based on Tanaka's one: they adopted his constitutive equation but, for the phase kinetics, they assumed a simpler cosine relationship to describe the martensite fraction as a function of stress and temperature. They also assumed the material properties to be constant during the transformation.

The heating phase transformation kinetics equation is:

$$\xi = \frac{\xi_M}{2} \cos[a_A(T - A_S) + b_A \sigma] + \frac{\xi_M}{2},$$

while, the cooling one is:

$$\xi = \frac{1 - \xi_A}{2} \cos[a_M(T - M_F) + b_M \sigma] + \frac{1 + \xi_A}{2}$$

where $a_A = \pi/A_F - A_S$ and $a_M = \pi/M_S - M_F$ are combinations of material constants: A_F, A_S, M_F, M_S are

material characteristic temperatures, respectively known as austenite final, austenite start, martensite final, and martensite start. They refer to phase transformations of the material and define when a particular crystal structure appears or the conversion is complete. Two other combination of the material constants are defined as $b_A = -a_A/C_A$ and $b_M = -a_M/C_M$. C_A and C_M are the angular coefficients of the straight lines approximating the functions relating the four temperatures to the acting stress (Figure 2). Finally, ξ_M and ξ_A are the martensite volume fractions present in the alloy before heating and cooling, respectively. The aforesaid cosine function takes into account that transformation may occur only when the temperature is in the transformation range:

$$A_S \leq T \leq A_F \quad \text{or} \quad M_F \leq T \leq M_S.$$

Many other constitutive models have been developed since then, (Brinson, 1990; Sun and Hwang, 1993; Graesser and Cozzarelli, 1994; Ivshin and Pence, 1994; Barrett, 1995; Boyd and Lagoudas, 1996a,b; Juhàsz et al., 2000; Matsuzaki et al., 2001; Prahlad and Chopra, 2001) and are capable of explaining the complex behavior of SMAs in specific load situations or extending the model validity to three-dimensional cases; anyway, engineering applications have paid attention to phenomenological models, which avoid difficult-to-measure parameters, such as free energy and use only clearly defined engineering material constants; in particular, Tanaka's and Liang and Rogers' models can be easily implemented in FE analysis.

In this study, the latter was used to simulate the SMA's behavior. The necessary material constants were experimentally computed and refer to a Ni–Ti–Cu alloy (Table 1).

SMA-BASED DEVICE

In this study, the interest was focused on the SMA structural actuation capabilities, directed to reach the expected increase in airfoil thickness, leaving to future investigations the estimation of the aerodynamic and

Table 1. Thermomechanical properties of Ni–Ti–Cu SMA ribbons used in experimental tests.

Martensite start temperature M_S 43°C	Martensite finish temperature M_F 27°C
Stress–temperature curve's slope in martensite phase C_M 7 MPa/°C	Stress–temperature curve's slope in austenite phase C_A 7 MPa/°C
Austenite start temperature A_S 47°C	Austenite finish temperature A_F 59°C
Martensite Young's modulus E_M 25 GPa	Austenite Young's modulus E_A 70 GPa

structural coupling effects. Accordingly, this work was aimed at simulating and realizing a preliminary device, considering only a reduced portion of the airfoil surface; particular attention was devoted to avoid the issue of permanent deformations (cyclic actuation).

Based on the already mentioned conclusions reached by DLR (Stanewsky et al., 1997; Thiede and Dargel, 1997; Knauer, 1998; Richter and Rosemann, 1999) and taking into consideration the application to transport aircraft, a reference bump may be generally estimated around 20% wing chord long, and about 0.5% high. Reducing the surface panel dimensions by a suitable ratio for testing purposes, the bump length was set to 130 mm, then having as reference target a 3 mm vertical displacement (Figure 6). In this first study, in fact, aerodynamic requirements were only geometrically scaled, also because of the limited size variation.

The wing span is not herein considered (2D study), but it is not expected to have a great relevance in the practical application. The device was then limited only to a panel strip, 50 mm wide, actuated by a single SMA ribbon. It has been conceived since the beginning to minimize costs and complexity but preserving its capabilities, lightness, and reliability.

The basic idea is to constrain an SMA ribbon ($250 \times 10 \times 1$ mm^3 – commercial size), with a given deformation previously imposed, to the panel (298×50 mm^2) that will make the bump. When the SMA ribbon is heated, it shrinks, deforming the panel surface; when it is cooled down, the structural elasticity forces the SMA ribbon to recover its initial length. This process could also be accelerated by adding concentrated stiffness elements (by inserting a number of springs, for instance), paying the penalty of higher activation temperatures.

The plate is constrained on both the smaller edges, representing the connections to the remaining airfoil structure). The SMA ribbon is instead connected through a hinge-system to the panel, preserving the active device from bending actions (Figures 7 and 8). These constraints are placed symmetrically at one-fourth of the total strip length, offset with respect to the plate, in order to generate the desired momentum. This solution also permits to shun any soldering (Fuji et al., 1992; Hall, 1993, 1997; Wisbey and Ward-Close, 1994; Nishida et al., 1995; Wang, 1995; Schloßmacher et al., 1997).
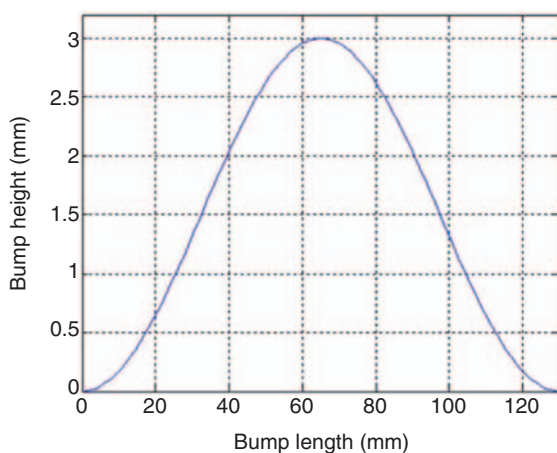
The lab solutions did not take into account problems like the necessity of having the device architecture only on one side, for the sake of simplicity, being this configuration easily modifiable in later stages of the research. For instance, screws were preferred to rivets, to facilitate assembly and disassembly activities.

Several versions of the upper panel, featuring the upper wing surface, were realized with typical aeronautic materials and different thicknesses. Basically, 7075 T6 aluminum alloy was considered; however, also 2024 T4 aluminum alloy and 17-7 stainless steel were allowed for, because of the lower yield strength of the former and the more ductile behavior of the latter. Considered thicknesses were constant and equal to 1.0, 1.5, and 2.0 mm; however, some combinations of material/thickness were not considered in simulations and experimental tests.

The deformation induced in the SMA ribbon before construction (recovered after activation) was imposed to 1.0 and 1.5% of the ribbon total length; for higher values (3%, experimentally tested), the plastic limit was exceeded also for the 2.0 mm thick 17-7 stainless steel panel (generally not used in aeronautic structures because of its weight), proving the SMA actuation potential.
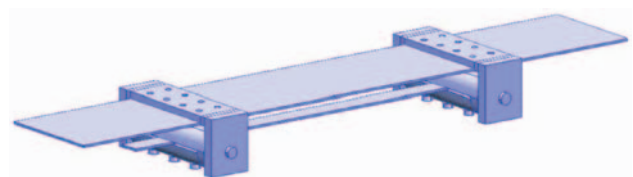
Figure 7. *CAD model of the SMA actuated bump device.*

Figure 6. *Expected chordwise bump profile.*
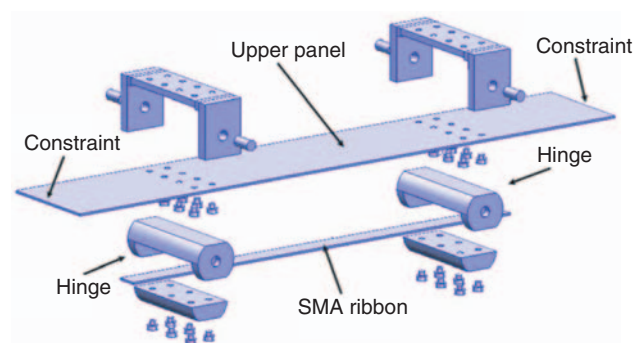
Figure 8. *Exploded CAD model of the SMA actuated bump device.*

NUMERICAL SIMULATIONS AND SOME CONSIDERATIONS

Numerical simulations were used to estimate the device actuation effectiveness and to verify the structural strain was under the plastic limit. Von Mises criterion was applied. Different configurations were considered, varying both the SMA imposed deformation and the panel material. Furthermore, the activation temperature, intended as the one necessary to attain the complete phase transformation (essentially a function of the stress field), and the achievable length recovery, were estimated.

Numerical simulations were carried out with FEA software COMSOL Multiphysics®. In detail, for this specific study, the structural mechanics module was used whether for 3D (bump device) or 2D (SMA ribbon) problems.

Because of the device model complexity (even though opportunely simplified for FE analysis), mainly due to the SMA behavior, the numerical simulation process was split into two parts:

1. a structural static simulation of the bump without the SMA ribbon (related action was introduced by means of concentrated forces);
2. a thermal nonlinear simulation of the SMA ribbon itself, with an applied equivalent rigidity attained by the previous simulation and taking into account the stiffness of the remaining part of the actuator.

For each combination, the results of both simulations were unified using the congruency principle: comparing forces and translations in both the simulations, the common 'working point' was individuated as the common value of SMA applied force and length recovery. Additionally, this approach made possible to reduce the computational times.

First, the bump device simulation was done on a simplified representation (Figure 9), where hinges were modeled as rigid, non-deformable blocks and a perfect moment transmission to the panel was considered (in this way, the hinges rotations were completely transmitted to the above structure).

Moreover, attention was paid to some aspects and, in particular: SMA actuators were placed in the center of the rigid blocks, where the real hinges rotate However, the hinge translation was evaluated on the internal edges
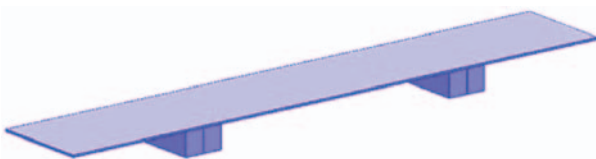
of the blocks, because the SMA ribbon can recover only its length between the hinges.

Many available models are able to precisely describe the mechanical behavior of the SMAs but they may give rise to serious difficulties in the implementation; in general, simpler phenomenological models are preferred in engineering applications, in conjunction with FE approaches (Chopra, 2002). The adopted Liang and Rogers' model (Liang and Rogers, 1990) was implemented within an original MATLAB® routine, parameterizing the stress–strain curve with respect to temperature (Figure 10) in the 0–120°C range.

The model uses the Ni–Ti–Cu alloy material constants, reported in Table 1. The stress–strain–temperature curves were passed to the FE software as functions, and used to determine, in the 2D ribbon simulation, at each iteration of the thermal nonlinear analysis (due to the phase changes inside the SMAs), the resulting SMAs deformation (ribbon length recovery), given the predicted stress and the temperature condition. Because of the iterative process, the SMA curves were interpolated in the temperature range, so to solve the analysis for any temperature value.

The structural effects due to the other part of the structure were simulated through an equivalent stiffness, introduced in series to the SMA element, as a function of the longitudinal movement of the hinge with respect to the SMA applied force. In this way, the opposition of the device to the deformation was considered.

By applying the congruency principle, the activation temperatures range was individuated, together with the SMA ribbon recoverable strain.

NUMERICAL RESULTS

Before starting the numerical campaign, preliminary simulations were performed, to compare the behavior of the panel strip with a larger panel and verify the results of the actuation in the two cases.

Figure 9. Simplified FEM model of the SMA actuated bump device.
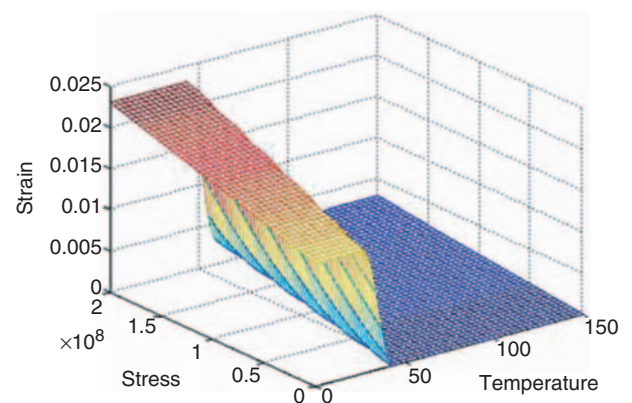
Figure 10. Stress–strain–temperature curve of implemented SMA model.

A 1.0 m wide panel was taken into account, equivalent to 20 strips (one by one actuated), and constrained on the edges (to reproduce the typical panel installation on a real aircraft wing). Near the constraints, the desired bump shape cannot be created: anyway, no remarkable boundary effects were observed at a distance higher than 20% panel span from the lateral constraints.

Fifteen numerical simulations were performed (see summary in Table 2), to study different combinations of the considered values of the three project parameters: the panel material, the thickness, and the SMA ribbon imposed deformation. In the case of the 2024 T4 alloy, the SMA initial deformation was not forced to values of 1.5%, because it brought to exceed the material limit yield stress.

In this study, only the most relevant results are shown, with respect to aeronautical applications. In particular, the configuration considering a panel strip made of 7075 T6 alloy, 1.5 mm thick and SMA ribbons with a 1.0 and 1.5% initial deformation (Figures 11–17). Concerning the remaining test cases, only the attained bump maximum height is reported (Table 2).

Table 2. Summary of performed numerical simulations and maximum bump height (mm).

T (mm)	2024 T4	7075 T6	17-7
SMA ribbon deformation: 1.0%			
1.0	2.752	2.756	2.644
1.5	2.982	2.989	2.788
2.0	3.108	3.096	2.802
SMA ribbon deformation: 1.5%			
1.0	N A	3.465	3.257
1.5	N A	3.753	3.458
2.0	N A	3.980	3.545

Numerical simulations demonstrated the ability of the SMA ribbons to properly actuate the bump device; moreover, an initial deformation of 1.5% of the total length proved to be sufficient to reach the expected
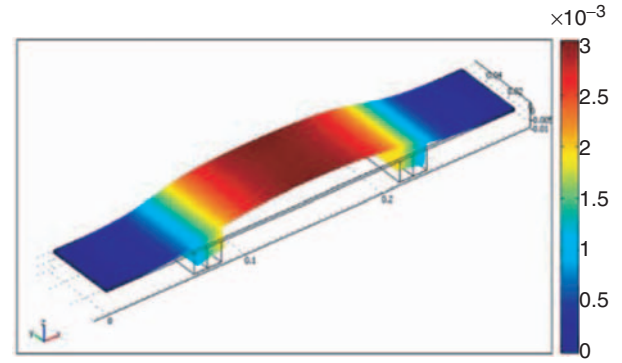
Figure 12. *Bump profile for SMA ribbon with a 1.0% initial deformation: maximum bump height of 2.98 mm.*
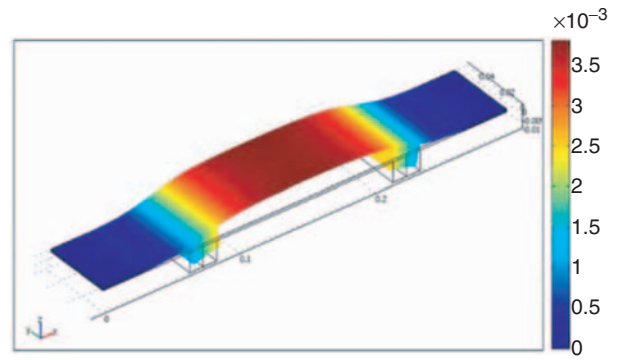
Figure 13. *Bump profile for SMA ribbon with a 1.5% initial deformation: maximum bump height of 3.75 mm.*
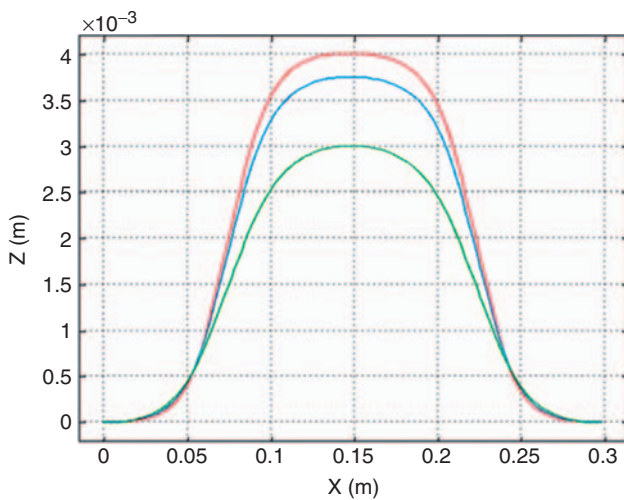
Figure 11. *Bump profile for different actuation schemes: lowest curve for 1.0% SMA ribbon; middle curve for 1.5% SMA ribbon; highest curve for plastic limit.*
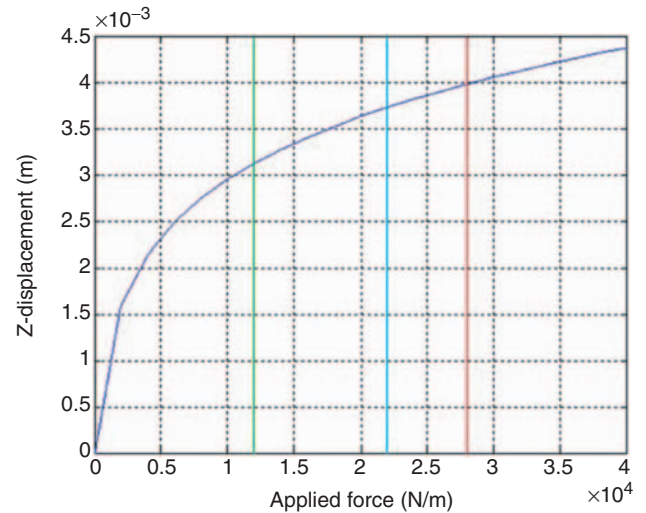
Figure 14. *Bump attained height versus SMA applied force: from left, first curve for 1.0% imposed strain, second curve for 1.5% imposed strain and third curve for plastic limit.*
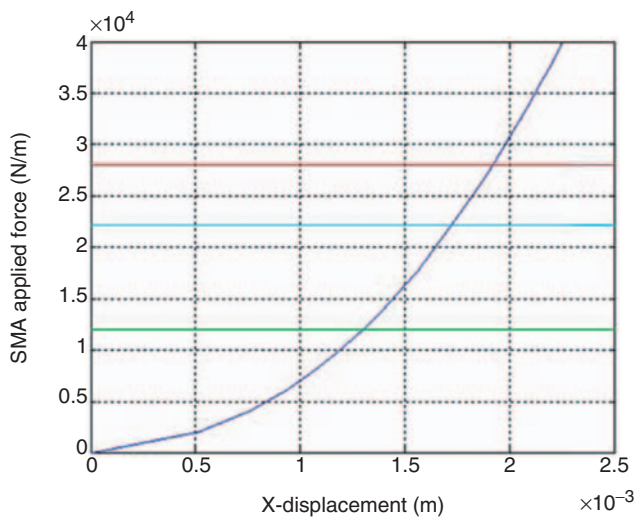
Figure 15. *SMA applied force versus hinges displacement: from bottom, first curve for 1.0% imposed strain; second curve for 1.5% imposed strain; and third curve for plastic limit.*

Figure 17. *SMA ribbon 1.74 mm length change as temperature increases, for a 1.5% initial deformation.*

In conclusion, the configuration made of the 7075T6 panel strip 1.5 mm thick, and the SMA ribbon with 1.0% initial deformation, showed to be sufficient to get the desired bump profile and seems to be suitable for aeronautic applications.

EXPERIMENT SCHEME AND TEST RESULTS

Based on the results coming from the numerical simulations, an experimental prototype of the bump device (Figure 18) was manufactured.

The bump device was fixed to a basic structure, reproducing the remaining part of the wing: the panel strip had then to be longer than the reference measures, to assure a perfect clamp.

The experimental setup was prepared according to the scheme illustrated in Figure 19.

Figure 16. *SMA ribbon 1.20 mm length change as temperature increases, for a 1.0% initial deformation.*

bump height and brought the panel stress level quite near the plastic limit in many arrangements. In addition, the use of the shape memory effect with low initial strains allowed several actuation cycles (up to 100.000 as reported in the literature (Johnson Matthey Inc.)) without appreciable losses of performance levels.

As expected, as the panel thickness increased, the SMA was called to apply larger recovery forces. However, the required stress level remained within the range of its capabilities. In the end, higher thickness values caused a benefit because of the better attained strain actuation quality.

When the SMA ribbon has to apply a larger force, the necessary temperature to achieve a complete activation increases: in any case, it remained well below 70°C for the selected material.

To activate the SMA element, a DC power source was required to produce a 10 A continuous current at 1.5 V, directly transmitted to the ribbon in between the two hinges, producing a temperature increase by Joule's effect: active control of power generation was not herein implemented. The electrical power affects the time the SMA ribbon takes to heat up, but allows always reaching the complete transformation temperature. Letting constant the current level makes simpler the test setup and permits evidencing the transition temperatures of the SMA ribbon.

A digital comparator was used to measure the bump contour (maximum actuated height and profile), a chronometer recorded the activation time, and a thermocouple system traced the temperature history.

The SMA element was thermally and electrically isolated from the structure and was, after the experiment, refrigerated in few seconds by a convective cooling (Figure 20).
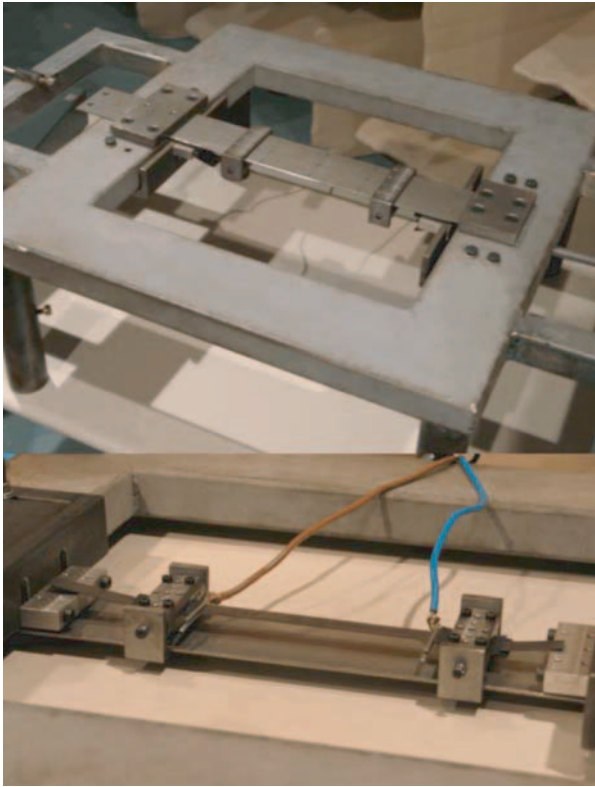
Figure 18. Bump device prototype.
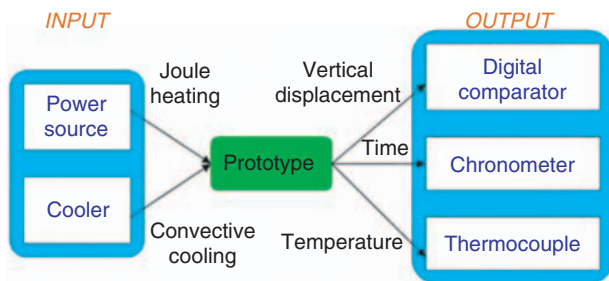
Figure 19. Setup schematic.
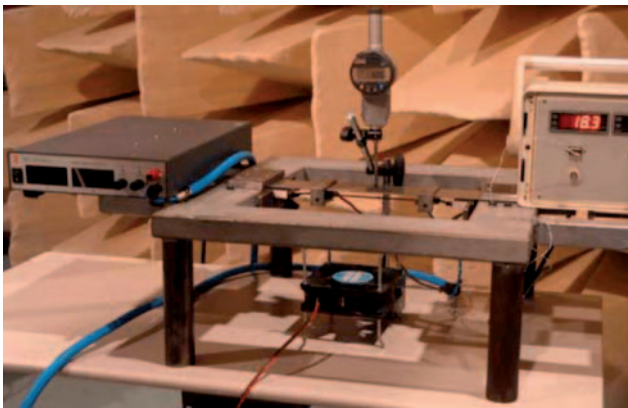
Figure 20. Experimental setup.

Table 3. Summary of performed experimental tests and achieved maximum bump height (mm).

SMA ribbon deformation: 1.0%		
Thickness (mm)	Al 7075T6	17-7 stainless steel
1.5	2.71	2.36
2.0	2.80	2.29
SMA ribbon deformation: 1.5%		
1.5	3.21	3.27
2.0	3.42	3.98

The chosen Ni–Ti–Cu alloy, whose characteristics are reported in Table 1, presents a limited value for the austenite finish temperature. It can then be easily heated and cooled without the need of expensive power devices or particular shrewdness. The thermal transition range can be adjusted by slightly changing its composition.

The bump device was assembled several times to test all the considered combinations (Table 3).

The SMA strip must be assembled with a pre-strain it can recover when activated; this deformation is achieved using a tensile machine. Before the use, it must be trained with some load/unload cycles, to stabilize its mechanical behavior at a given deformation (Bo and Lagoudas, 1994). Another care about SMA system assembly regards the correct joining of the ribbon to the hinges, in order to assure electrical and thermal insulation together with a solid link with the structure; in addition, the SMA ribbon must appear stiff after assembly.

The experimental results reported in this study have been measured at the third activation cycle of each configuration, because a structural assessment was observed in the first two activation cycles.

As for numerical simulations, only results of the most relevant configurations, relating to future aeronautical applications, are reported. Particularly, the panel belt made of 7075 T6 alloy, 1.5 mm thick, activated by an SMA ribbon with an initial deformation of 1.0 and 1.5%, was considered (Figures 21–24).

Figure 23 shows that almost the 90% of the maximum bump height is reached after 3–4 min, while the complete actuation is achieved some time after: this behavior is due to the limited amount of the used electrical power (15W) and can be easily improved.

Figure 24, instead, shows the thermal profile of SMA activation with respect to time, allowing to detect the phase change and the transition temperatures.

NUMERICAL-EXPERIMENTAL COMPARISON

As from Table 3, the experimental tests confirmed the device effectiveness, also if lab results are in most cases lower if compared to numerical ones (Table 4).
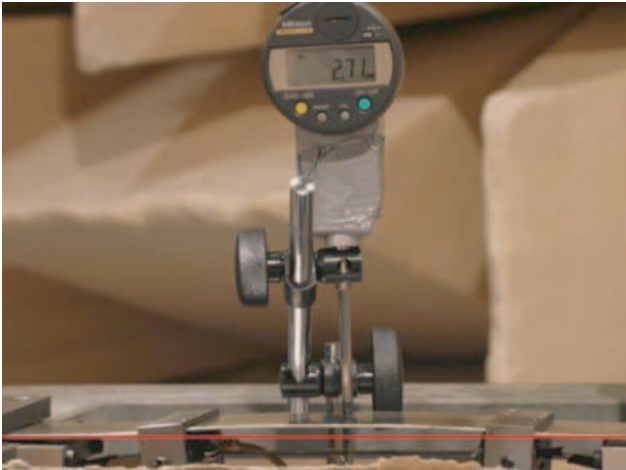
Figure 21. *Bump profile for SMA ribbon with a 1.0% initial deformation: maximum bump height of 2.71 mm.*

Figure 22. *Bump profile for SMA ribbon with a 1.5% initial deformation: maximum bump height of 3.21 mm.*
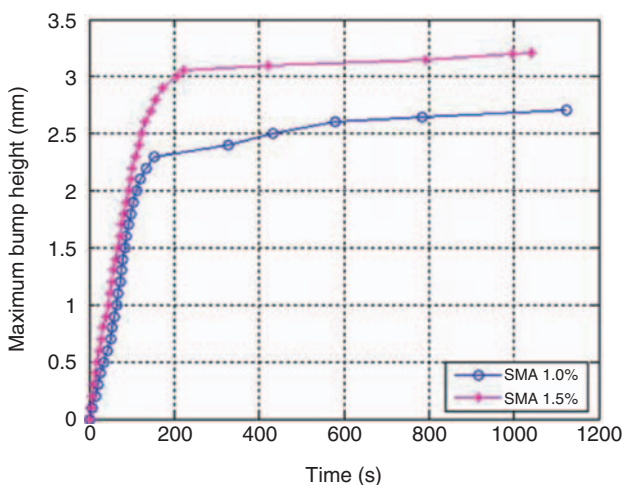
Figure 23. *Temporal bump actuation for SMA ribbon with a 1.0 and 1.5% initial deformation.*
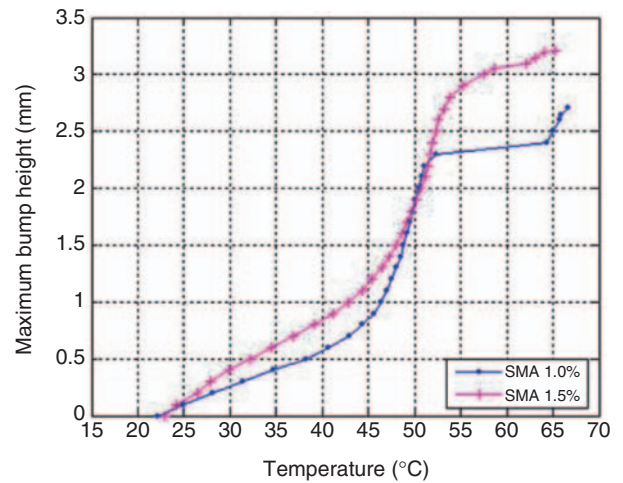
Figure 24. *Thermal bump actuation for SMA ribbon with a 1.0 and 1.5% initial deformation.*

Table 4. Numerical versus experimental results comparison: difference on maximum bump height (mm).

Thickness (mm)	Al 7075T6	17-7 stainless steel
SMA ribbon deformation: 1.0%		
1.5	+0.279 (9.33%)	+0.428 (15.35%)
2.0	+0.296 (9.56%)	+0.512 (18.28%)
SMA ribbon deformation: 1.5%		
1.5	+0.543 (14.47%)	+0.188 (5.44%)
2.0	+0.560 (14.07%)	−0.435 (10.94%)

This can be explained as follows: the used power source generated 15 W for heating the SMA ribbon, allowing a maximum temperature of 65°C, hardly sufficient to attain a complete phase transformation in some cases. The available power also affects activation times. Furthermore, a proper implementation of the active element, respecting the necessity to provide it with a minimum pre-stress, was quite a challenge, due to the presence of the hinges. It was estimated that the found numerical-experimental gap can be explained with just a 0.1 mm assembly error.

The configuration considering the 17-7 steel panel strip, 2.0 mm thick also deserves attention: in this case, in fact, with a 1.0% SMA imposed initial deformation, it was shown the maximum error between numerical and experimental results; instead, when 1.5% deformation was applied, a larger height than what revealed during numerical simulations was appraised.

Referring to the Al 7075 T6 configuration, comparing the numerical and experimental bump profile center lines, a good correlation between the collected results was achieved (Figures 25 and 26). Results herein largely reported regard this arrangement, with the panel strip 1.5 mm thick and an SMA ribbon with an initial deformation of 1.0 and 1.5% (Figures 27–30).
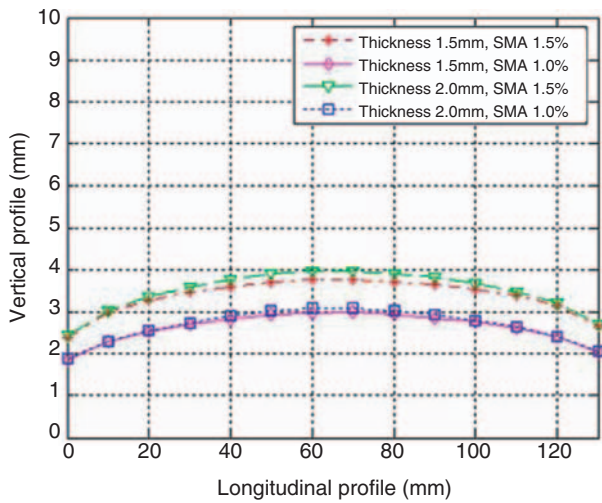
Figure 25. *Numerical bump profile center line for a 7075 T6 panel strip in various configurations.*
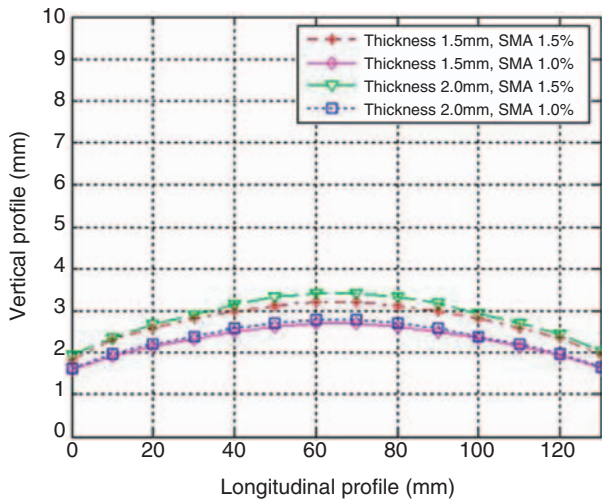
Figure 26. *Experimental bump profile center line for a 7075 T6 panel strip in various configurations.*
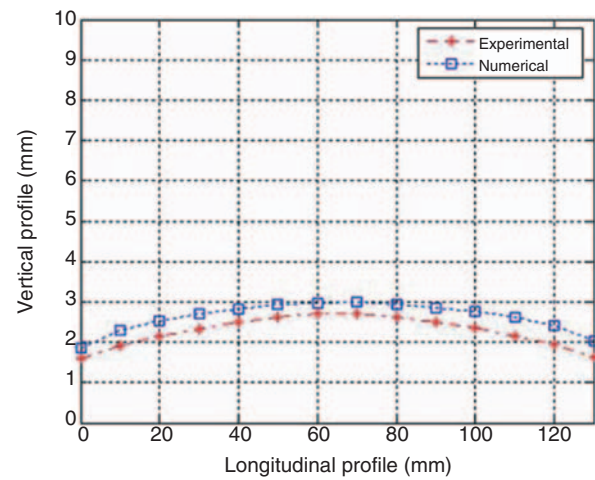
Figure 27. *Comparison of bump profile center line for Al7075T6 1.5 mm thick and SMA ribbon at 1.0%.*
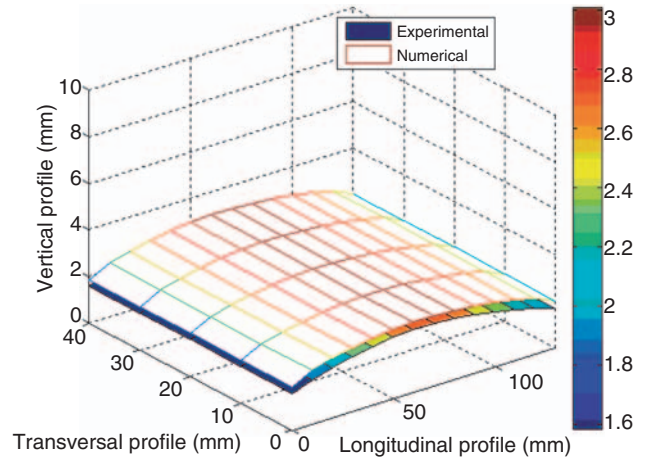
Figure 28. *Comparison of 3D bump profile for Al7075T6 1.5 mm thick and SMA ribbon at 1.0%.*
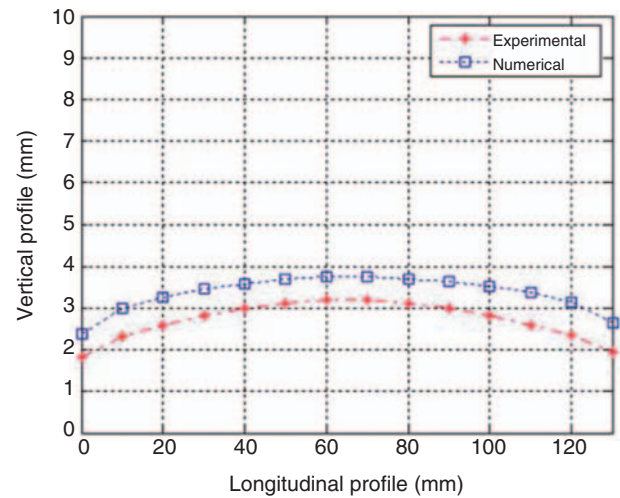
Figure 29. *Comparison of bump profile center line for Al7075T6 1.5mm thick and SMA ribbon at 1.5%.*
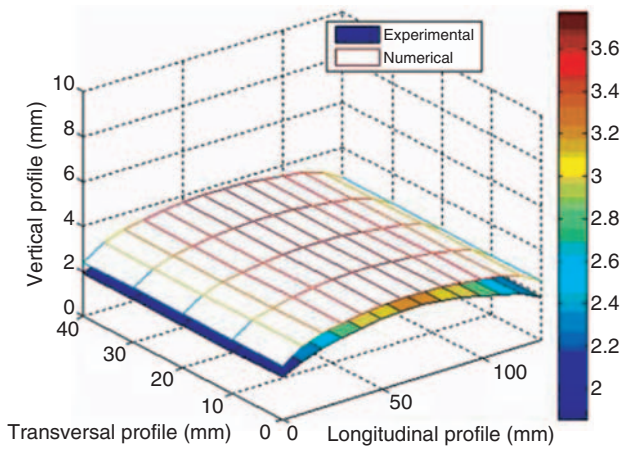
Figure 30. *Comparison of 3D bump profile for Al7075T6 1.5 mm thick and SMA ribbon at 1.5%.*

As expected, in transversal direction the panel actuation could be considered uniform, validating the initial assumption of reducing the study to a panel strip without loosing in generality.

CONCLUSIONS AND FUTURE DEVELOPMENTS

The presented study was focused on the creation of an actuation device for a bump creation upon an airfoil profile, aimed at producing an increase in aerodynamic efficiency in transonic regime through a reduction of the shock-wave induced drag; moreover, to simplify the actuation mechanism and minimize costs and weight, SMA materials (shape memory alloys, belonging to the so-called smart materials family) were used.

Numerical simulations showed the effectiveness of the device in producing a bump on the airfoil upper surface with respect to different configurations, proving the capabilities of SMA as smart actuator elements and producing the desired result, to attain a 3.0 mm high bump. Experimental test results, then, displayed good correlation with FE simulations, validating the adopted models and theoretical procedures, and demonstrating the device capabilities.

Anyway, deviations limited to 18% have been noticed: this difference may be simply explained by considering that small assembling inaccuracy on the SMA ribbon clamping operation may lead to relevant discrepancies: f.i. an imprecision <0.3 mm on the ribbon length may lead to changes of the 15% in the bump height. However, as the SMA imposed pre-strain augments, this zero-shift effect vanishes, because the SMA recovered length increases with respect to the aforesaid inaccuracy. This consideration is verified to be coherent with the attained results. In fact, if this error is added as a constant all over the attained measurements, the values are practically coincident with the numerical prediction and the deviations fall to the 1–2%.

Among the others, the configuration referring to a typical aeronautic material (Al 7075 T6, with typical thicknesses values), turned out to be the best performing.

SMA revealed effective but exposed one of the possible drawbacks of such a solution, mainly linked to the slow time response. A possibility to accelerate SMA warm up can be the use of complementary hot sources, as the exhaust gases coming from engines or alternative driving elements, like the Peltier's cells. In the same way, the cooling down can be shortened by exposing the alloy to the exterior air. Regarding transition temperatures: it is opportune to remind these can be properly adjusted by changing the alloy composition, so to fit different requirements.

The presence of constraints around the panel proved to be not a problem. Indeed, they help the elastic return of the structure to its original shape and, in turn, of the SMA ribbon to its initial deformation.

The concept demonstrator, presented in this study, is very simple and leaves wide margin of improvements with respect to its final configuration. It is important once more to remark that the simplicity of its architecture is one of the most important strength point.

The work showed itself, moreover, as a useful basis for further studies, currently ongoing, related to the application of this concept to a real wing, with a more sophisticated activation system aimed at reducing the response times and improving the control capabilities.

REFERENCES

AeroVisions Inc., web site: http://www.canosoarus.com/05UMAAV/UMAAV01.htm

Alasty, A., Alemohammad, S.H., Khiabani, R.H. and Khalighi, Y. 2004. "Manoeuvrability Improvement for an Ultra Light Airplane Model Using Variable Shape Wing," *AIAA Atmospheric Flight Mechanics Conference and Exhibit*, Providence, Rhode Island, *AIAA J.*, pp. 2004–4831.

Allred, R., Hoyt, A., Harrah, L., McElroy, P., Scarborough, S. and Cadogan, D. 2004. "Light Curing Rigidizable Inflatable Wing," *45th AIAA/ASME/ASCE/AHS/ASC Structures, Structural Dynamics and Materials Conference*, Palm Springs, CA, *AIAA J.*, 2004–1809.

Ameduri, S. 2003. "Sistemi Integrati di Attuazione per il Miglioramento delle Prestazioni Aerodinamiche di un Profilo Alare in Campo Transonico," *Philosophy Doctor's Thesis*, Dept. of Aeronautical Design (D.P.A.), University of Napoli "Federico II", Napoli, Italy.

Anderson Jr, D.J. 2001. *Fundamentals of Aerodynamics*, McGraw-Hill International Editions, 2nd edn, pp. 48–54.

Austin, F., Siclari, M.J., Van Nostrand, W., Weisensel, G.N., Kottamasu, V. and Volpe, G. 1997. "Comparison of Smart Wing Concepts for Transonic Cruise Drag Reduction," Smart Structures and Materials 1997: Industrial and Commercial Applications of Smart Structures Technologies, May 23, Proceedings of SPIE, 3044:33–40.

Bannasch, R. 2000. "Innovative Fuselage, Wing and Propeller Constructions Derived from Bionic Research on Bird Flight," *International Conference Aerospace Technologies of the 21st Century*, New Technologies Research and Simulation, Session II, 8–9 June, Berlin, Germany, pp. 94–115.

Barrett, D.J. 1995. "A One-Dimensional Constitutive Model for Shape Memory Alloys," *Journal of Intelligent Material Systems and Structures*, 6(3):329–337.

Bein, Th., Hanselka, H. and Breitbatch, E. 1998. "The Adaptive Spoiler – Mechanical Aspects of a Local Spoiler Thickening to Control the Transonic Shock," *9th International Conference on Adaptive Structures and Techniques*, 14–16 October, Cambridge, USA, pp. 225–237.

Benavides, J.C. and Correa, G. 2002. "*Morphing Wing Design Using Nitinol Wire*," University of Missouri-Rolla (UMR), Intelligent System Centre, web site: http://www.isc.umr.edu/index.htm

Bencke, M. 2000. "Boeing International Cooperative Programs," *International Conference Aerospace Technologies of the 21st Century*. New Technologies Research and Simulation, Session II, 8–9 June, Berlin, Germany, pp. 89–92.

Blondeau, J. and Pines, D. 2004. "Pneumatic Morphing Aspect Ratio Wing," *45th AIAA/ASME/ASCE/AHS/ASC Structures, Structural Dynamics and Materials Conference*, Palm Springs, California, *AIAA J.*, April 19–22, 2004–1808.

Bo, Z. and Lagoudas, D.C. 1994. "Comparison of Different Thermo Mechanical Models for Shape Memory Alloys," *Adaptive Structures and Composite Materials:Analysis and Applications*: *American Society of Mechanical Engineers Symposium*, 54:9–19.

Bonnema, K.L. and Smith, S.B. 1988. AFTI/F-111 Mission Adaptive Wing Flight Research Program, San Diego, California, May 18–20, pp. 155–161.

Boyd, J.G. and Lagoudas, D.C. 1996a. "A Thermodynamical Constitutive Model for Shape Memory Materials. Part. I. The Monolithic Shape Memory Alloys," *International Journal of Plasticity*, 12(6):805–842.

Boyd, J.G. and Lagoudas, D.C. 1996b. "A Thermodynamical Constitutive Model for Shape Memory Materials. Part. II. The Monolithic Shape Memory Alloys," *International Journal of Plasticity*, 12(7):843–873.

Brinson, L.C. 1990. "One-Dimensional Constitutive Behaviour of Shape Memory Alloy Constitutive Models," *Journal of Intelligent Material Systems and Structures*, 1(2):207–234.

Brinson, L.C., Bekker, A. and Huang, M. 1996. "Deformation of Shape Memory Alloys due to Thermo-Induced Transformation," *Journal of Intelligent Material Systems and Structures*, 7(1):97–107.

Browman, J., Sanders, B. and Weisshaar, T. 2002. "Evaluating the Impact of Morphing Technologies on Aircraft Performance," *AIAA J.*, 2002–1631.

Buehler, W.J., Gilfrich, J.V. and Wiley, R.C. 1963. "Effect of Low-temperature Phase Changes on the Mechanical Properties of Alloys near Composition TiNi," *Journal of Applied Physics*, 34:1475.

Cadogan, D., Smith, T., Lee, R., Scarborough, S. and Graziosi, D. 2003. "Inflatable and Rigidizable Wing Components for Unmanned Aerial Vehicles," *44th AIAA/ASME/ASCE/AHS/ASC Structures*, Structural Dynamics and Materials Conference, Norfolk, VA, *AIAA J.*, 2003–6630.

Chopra, I. 2002. "Review of State of Art of Smart Structures and Integrated Systems," *42nd AIAA/ASME/ASCE/AHS/ASC Structures, Structural Dynamics, and Materials Conference*, Seattle, WA, *AIAA Journal*, 40(11).

Cornerstone Research Group Inc., web site: http://www.crgrp.net/veriflex.htm

DeCamp, R.W. and Hardy, R. 1984. "Mission Adaptive Wing Advanced Research Concepts," *AIAA J.*, 19: 84–2088.

European project 3AS (Active Aeroelastic Aircraft Structures), web site: http://3as.ist.utl.pt/index.html

Frost et al. 1978. "*Airfoil Variable Cambering Device and Method*," U.S. Patent no.4,247,066, General Dynamics Corporation, Fort Worth, TX.

Fuji, A., North, T.H., Ameyama, K. and Futamata, M. 1992. *Materials Sci. Technol.*, 3:219.

Gal-Or, B. 2000. "The New Era of Flight Control & Safety," *International Conference Aerospace Technologies of the 21st Century*. New Technologies Research and Simulation, Session I, 8–9 June, Berlin, Germany, pp. 59–66.

Geissler, W., Sobieczky, H. and Trenker, M. 2000. "New Rotor Airfoil Design Procedure for Unsteady Flow Control," *26th European Rotorcraft Forum*, The Hague, Holland, Paper No. 31, September 2000, Vol. 1, pp. 31.1–31.9.

Gevers Aircraft Inc. 1997. "*Multi-Purpose Aircraft*," United States Patents Office, Patent Number 5,645, 250.

Graesser, E.J. and Cozzarelli, F.A. 1994. "A Proposed Three-Dimensional Model Constitutive Model for Shape Memory Material," *Journal of Intelligent Material Systems and Structures*, 5(1):78–89.

Hall, T.A. 1993. "*Joint, a Laminate and a Method of Preparing a Nickel-Titanium Alloy Member Surface for Bonding to Another Layer of Metal*," U.S. Patent 5,242,759.

Hall, P.C. 1997. "Methods of Promoting Solder Wetting on Nitinol," In: da Pelton, A. et al. (ed.), *2nd International Conference on Shape Memory and Superelastic Technologies*, SMST-97, Pacific Grove, CA, 2–6 March, pp. 125–130.

Inman, D.J. 2001. "Wings: Out of the Box. Determining Actuator Requirements for Controlled Morphing Air Vehicles – Aerodynamic Loads," *DARPA Technology Interchange Meeting*, Wright Patterson Air Force Base, Dayton, Ohio, Nov. 4–8.

Ivshin, Y. and Pence, T.J. 1994. "A Thermo Mechanical Model for One variant Shape Memory Material," *Journal of Intelligent Material Systems and Structures*, 5(4):455–473.

Johnson Matthey Inc., web site: http://www.jmmedical.com

Juhàsz, L., Andrä, H. and Hesebeck, O. 2000. "A Constitutive Model of Shape Memory Alloys Based on Viscoplastic Like Evolution Equations," *Periodica Polytechnica Ser. Mech. Eng.*, 44(1):59–69.

Kauffman, G.B. and Mayo, I. 1993. "The Metal with a Memory," *Invent. & Tech.*, 9(2):18–23.

Kikuta, M.T. 2003. "*Mechanical Properties of Candidate Materials for Morphing Wings*," *Master's Thesis*, University of Virginia, Blacksburg, Dec. 11.

Knauer, A. 1998. "Performance Improvement of Transonic Airfoils through Contour Modifications in the Shock Region," DLR Research Report 98–03.

Kudva, J.N. 2001. "Overview of the DARPA/AFRL/NASA Smart Wing Phase II Program," *Smart Structures and Materials Conference*, USA, *SPIE*, 4332:383–389.

Kudva, J.N. and Carpenter, B. 2000. "Smart Wing Program," *DARPA Technology Interchange Meeting*, June.

Kudva, J.N., Lockyer, A.J. and Appa, K. 1996a. "Adaptive Aircraft Wing," AGARD SMP Lecture Series 205, *Smart Structures and Materials:Implications for Military Aircraft of New Generation*, AGARD-LS-205.

Kudva, J.N., Jardine, P., Martin, C. and Appa, K. 1996b. "Overview of the ARPA/WL "Smart Structures and Material Development – Smart Wing Contract," *SPIE*, 2721: 10–16.

Lecce, L. 2004. "Deliverable 4 - Relazione di progetto del dimostratore bidimensionale," Dept. report no.04/64, Dept. of Aeronautical Design (D.P.A.), University of Napoli "Federico II", Napoli, Italy.

Lemme, M. and Caruso, A. 2004. "Deliverable 3 - Modellazione FEM del dimostratore bidimensionale di un bordo d'attacco deformabile con attuazione tramite fili di SMA," Dept. report no.04/72, Dept. of Aeronautical Design (D.P.A.), University of Napoli "Federico II", Napoli, Italy.

Liang, C. and Rogers, C.A. 1990. "One-Dimensional Thermomechanical Constitutive Relations for Shape Memory Material," *Journal of Intelligent Material Systems and Structures*, 1(2):207–234.

Lin, J.K., Sapna, G.H., Cadogan, D.P. and Scarborough, S.E. 2002. "Inflatable Rigidizable Isogrid Boom Development," *43rd AIAA/ASME/ASCE/AHS/ASC Structures, Structural Dynamics, and Materials Conference and Exhibit*, AIAA Gossamer Spacecraft Forum, Denver, CO, *AIAA J.*, pp. 2002–1297.

Martins, A.L. and Catalano, F.M. 1998. "Viscous Drag Optimization for a Transport Aircraft Mission Adaptive Wing," *21st ICAS Congress*, Melbourne, Australia, Sep. 13–18, Paper A98–31499.

Matsuzaki, Y., Naito, H., Ikeda, T. and Funami, K. 2001. "Thermo-Mechanical Behaviour Associated with Pseudoelastic Transformation of Shape Memory Alloys," *Smart Materials and Structures*, 10(5):884–892.

Monner, H.P., Bein, T., Hanselka, H. and Breitbach, E. 1998. "*Design Aspects of the Adaptive Wing –The Elastic Trailing*

Edge and the Local Spoiler Bump," Royal Aeronautical Society, Multidisciplinary Design and Optimization, London, October 26–27.

Munday, D. and Jacob, J. 2001. "Active Control of Separation on a Wing with Conformal Camber," *AIAA J.*, 2001–0293.

Murray, J.E., Pahle, J.W., Thornton, S.V., Vogus, S., Frackowiak, T., Mello, J.D. and Norton, B. 2002. "Ground and Flight Evaluation of a Small-Scale Inflatable-Winged Aircraft," *40th Aerospace Sciences Meeting & Exhibit*, Reno, NV, *AIAA J.*, 2002–0820.

Nishida, M., Chiba, A., Honda, Y., Hirazumi, J. and Horikiri, K. 1995. *ISIJ International*, 35(2):217–219.

Pendleton, E. 2000. "Active Aeroelastic Wing," *AFRL Technology Horizons*, 1(2):27–28.

Perkins, D.A., Reed, J.L. and Havens, E. 2004. "Morphing Wing Structures for Loitering Air Vehicles," *45th AIAA/ASME/ASCE/AHS/ASC Structures, Structural Dynamics & Materials Conference*, Palm Springs, California, *AIAA J.*, pp. 2004–1888.

Poonsong, P. 2004. "Design and Analysis of a Multi-Section Variable Camber Wing," *Master's Thesis*, University of Maryland.

Prahlad, H. and Chopra, I. 2001. "Comparative Evaluation of Shape Memory Alloy Constitutive Models with Experimental Data," *Journal of Intelligent Material Systems and Structures*, 12(6):386–396.

Richter, K. and Rosemann, H. 1999 "Numerical Investigation of Transonic Airfoil Drag Reduction by the Combined Application of a Contour Bump and Variable Rear Camber," *DLR Internal Report IB 223–1999 A 31*.

Schloßmacher, P., Haas, T. and Schüßler, A. 1997. "Laser Welding of a Ni-Rich TiNi Shape Memory Alloy: Pseudoelastic Properties," In: da Pelton, A. et al. (ed.), *2nd Int.l Conf. on Shape Memory and Superelastic Technologies*, SMST-97, Mar. 2–6, pp. 137–142.

Siclari, M.J., Van Nostrand, W. and Austin, F. 1996. "The Design of Transonic Airfoil Sections for an Adaptive Wing Concept Using a Stochastic Optimization Method," *34th Aerospace Sciences Meeting and Exhibit*, Reno, NV, *AIAA J.*, pp. 1996–0329.

Simpson, A. and Jacob, J. 2005. "Aerodynamic Control of an Inflatable Wing Using Wing Warping," *35th AIAA Fluid Dynamics Conference and Exhibit*, Toronto, Ontario, Canada, *AIAA J.*, pp. 2005–5133.

Simpson, A., Coulombe, N., Jacob, J. and Smith, S. 2005a. "Morphing of Inflatable Wings," *46th AIAA/ASME/ASCE/AHS/ASC Structures, Structural Dynamics and Materials Conference*, Austin, Texas, *AIAA J.*, pp. 2005–2110.

Simpson, A., Jacob, J. and Smith S. 2005b. "Inflatable and Warpable Wings for Meso-scale UAVs," *AIAA J.*, 2005–7161.

Smith, S.B. and Nelson, D.W. 1989. "Determination of the Aerodynamic Characteristics of the Mission Adaptive Wing," *6th Applied Aerodynamics Conference*, Williamsburg, VA, *AIAA J.*, pp. 88–2556.

Smith, S.B. and Nelson, D.W. 1990. "Determination of the Aerodynamic Characteristics of the Mission Adaptive Wing," *AIAA J.*, 27(11).

Spillman, J. 1992. "The Use of Variable Camber to Reduce Drag, Weight and Costs of Transport Aircraft," *Aeronaut. J.*, 96:1–8.

Stanewsky, E. 2001. "*Adaptive Wing and Flow Control Technology*," *Progress in Aerospace Sciences*, Elsevier Science Ltd., Vol. 37, pp. 583–667.

Stanewsky, E. and Krogmann, P. 1985. "Transonic Drag Rise and Drag Reduction by Active/Passive Boundary Layer Control," *AGARD Report No.723*, Lecture Series Aircraft Drag Prediction and Reduction.

Stanewsky, E., Délery, J., Fulker, J. and Geissler, W. 1997. "EUROSHOCK – Drag Reduction by Passive Shock Control," *Notes on Numerical Fluid Mechanics*, Vol. 56, Friedr. Vieweg and Sohn Verlagsgesellschaft mbH, Braunschweig, Wiesbaden.

Stanewsky, E., Délery, J., de Matteis, P.P., Fulker, J. and Doe, R. 1999. "EUROSHOCK II – Drag Reduction by Shock and Boundary Layer Control," *EUROSHOCK II Final Technical Report*, TR BRPR-95-76/1.

Statkus, F.D. 1980. "*Continuous Skin Variable Camber Airfoil Edge Actuating Mechanism*," United States Patent No. 4,351,502, The Boeing Company, Seattle, WA.

Sun, Q.P. and Hwang, K.C. 1993. "Micromechanics Modeling for the Constitutive Behaviour of Polycrystalline Shape Memory Alloys-1. Derivation of General Relations," *Journal of Mechanical Physics Solids*, 41(1):1–17.

Szodruch, J. 1985. "The Influence of Camber Variation on the Aerodynamics of Civil Transport Aircraft," *23rd Aerospace Sciences Meeting*, Reno, NV, *AIAA J.*, 85–0353.

Tanaka, K. 1986. "A Thermomechanical Sketch of Shape Memory Effect: One-Dimensional Tensile Behaviour," *Res. Mech.*, 18(3):251–263.

Thiede, P. and Dargel, G. 1997. "Design and Manufacture of the Cryogenic Laminar-type Airfoil Model DA LVA-1A with Passive Shock Control," In: Prahlad, H. and Chopra, I. 2001. "Comparative Evaluation of Shape Memory Alloy Constitutive Models with Experimental Data," *Journal of Intelligent Material Systems and Structures*, 12(6):386–396.

Thornton, S.V. 1993. "Reduction of Structural Loads Using Manoeuvre Load Control on the Advanced Fighter Technology Integration (AFTI)/F-111 Mission Adaptive Wing," *NASA TM* 4526.

Wang, G. 1995. "Weldability of Nitinol to Stainless Steel," In: Pelton, A. et al. (ed.), *2nd International Conference on Shape Memory and Superelastic Technologies*, SMST-97, Mar. 2–6, pp. 131–136.

Wilson, J.R. 2002. "Active Aeroelastic Wing: A New/Old Twist on Flight," *Aerospace America*, 40(99):34–37.

Wisbey, A. and Ward-Close, C.M. 1994. *Materials Letters*, 21:47–53.

- Chapter 5 -

Variable Camber Morphing Flap:

Preliminary Research

1 INTRODUCTION

In this chapter, several conceived solutions regarding variable camber for skin panels (morphing panels) and for wing trailing edge (morphing flap) are presented.

Literature showed a dearth of real scale applications of morphing technologies with smart materials to civil transportation class aircrafts. Basing on the funding of Alenia Aeronautica Spa industry, innovative concepts for a morphing flap have been designed and tested.

At first, an English translation of two papers [1, 2] presented at a national congress on morphing panels will be presented.

Then, other two papers [3, 4] regarding some numerical studies on preliminary morphing flaps solutions will be discussed: these architectures have been evaluated in presence of aerodynamic loads but lack the possibility of cyclic actuation.

[1] R. Pecora, L. Lecce, M. Riccio, A. Concilio, "Numerical Optimization of Wing Skin Panels Actuation Based-On S.M.A.", XIX AIDAA National Congress, September 17-20 2007, Forlì (FC), Italy, Conference proceedings on CD, article N.232, 10pp.

[2] S. Barbarino, L. Lecce, E. Calvi, S. Ameduri, "Numerical and Experimental Investigation on S.M.A. Actuated Wing Skin Panels", XIX AIDAA National Congress, September 17-20 2007, Forlì (FC), Italy, Conference proceedings on CD, article N.231, 10pp.

[3] S. Barbarino, S. Ameduri, R. Pecora, "Wing Camber Control Architectures based on SMA: Numerical Investigation", International Conference on Smart Materials and Nanotechnology in Engineering (SMN2007), July 1-4 2007, Harbin, China, Proceedings of SPIE vol. 6423, 64231E-1, (2007), 8pp., doi: 10.1117/12.779397

[4] S. Barbarino, S. Ameduri, R. Pecora, L. Lecce, A. Concilio, "Design of an Actuation Architecture based on SMA Technology for Wing Shape Control", Actuator 2008 Conference, June 9-11 2008, Bremen, Germany, Conference proceedings and on CD, poster P144, pp.961-964

Thus, among them conceived architectures, the best performing one has been selected for further investigations to improve its performance and take into account the possibility of cyclic working: the final two papers here reported [5, 6] describe these studies in great detail.

Finally, starting from the last presented (best performing) architecture, characterized by the elastic hinges, a further study can be found in literature developed by De Rosa & al. [7] which extends the rib design to a 3D flap bay: from a first comparison with a traditional flap mechanism, the actual solution, integrating SMAs as actuators, can lead to weight savings in the order of 27%.

[5] S. Barbarino, R. Pecora, L. Lecce, A. Concilio, S. Ameduri, E. Calvi, "A Novel SMA-Based Concept for Airfoil Structural Morphing", Published online the 02/13/2009 and printed the 08/01/2009 on J. of Materials Engineering and Performance (JMEP), vol.18, issue 5, pp.696-705 (2009), doi: 10.1007/s11665-009-9356-3

[6] S. Barbarino, S. Ameduri, R. Pecora, L. Lecce, A. Concilio, "Airfoil Morphing Architecture Based on Shape Memory Alloys", Conference on Smart Materials, Adaptive Structures & Intelligent Systems (SMASIS08), October 28-30 2008, Ellicott City, Maryland, USA, Conference proceedings on CD, paper SMASIS2008-480, 9pp.

[7] De Rosa L., Lecce L., Nappi E., "*Prototype Shape Memory Alloy Morphing Trailing Edge*", XX AIDAA National Congress, June 29 - July 3, 2009, Milan, Italy, 15pp.

PAPER

ENGLISH TRANSLATION OF AIDAA 2007 PAPERS

"Numerical Optimization of Wing Skin Panels Actuation Based-On S.M.A."

R. Pecora, L. Lecce, M. Riccio, A. Concilio

article no.232

"Numerical and Experimental Investigation on S.M.A. Actuated Wing Skin Panels"

S. Barbarino, L. Lecce, E. Calvi, S. Ameduri

article no.231

XIX AIDAA National Congress, September 17-20 2007, Forlì (FC), Italy

2 ENGLISH TRANSLATION OF AIDAA 2007 PAPERS

Introduction

This chapter is focused on numerical investigations and experimental testing of smart structure concepts, developed through the integration of Smart Materials within a wing skin structure, in order to achieve prescribed surface deformation with simple and integrated devices.

Among the large family of Smart Materials, Shape Memory Alloys (SMAs) are considered a suitable solution for many static applications, because of their capability to transmit very large forces. The phase transformation, which drives the SMAs' shape memory effect, can be controlled through Joule effect by a very limited amount of electrical supply, and can manage the structure activation state. This, in conjunction with other peculiarities like performance per weight ratio, justifies the increasing interest for aerospace applications.

Explored architectures are aimed at controlling the camber of a generic airfoil skin structure (panels with stringers) through the insertion of SMA ribbons; performance was evaluated in terms of maximum displacement and rotation of the free panel trailing edge, estimated by a FE approach. SMA behaviour was modelled through a dedicated routine for evaluating the activation temperature and internal stress state.

Several configurations were simulated, corresponding to different actuation strategies; the presence of different sets of smart ribbons also entitles for a multi-stable configuration, able to assume multiple actuation shapes; the most efficient architectures were optimized using a genetic algorithm for further actuation improvements.

Finally, two prototypes have been built and tested, demonstrating the efficacy of the developed concepts and validating the SMA model implementation strategy.

Modelling strategy and SMA Integration within the FE Approach

A FE approach has been adopted to predict the performance of the architectures described in the following paragraphs. As solver the MSC/Nastran tool has been used. Since no SMA model is implemented within MSC/Nastran, an external routine in Matlab code has been written to simulate the behaviour of the alloy; a suitable procedure has been realized in order to simulate the action of the SMA elements integrated within the several architectures. Due to the expected large deformations, a nonlinear analysis has been implemented. Finally, after achieving an overall estimate of

the performance for each specific configuration, a genetic optimization process has been carried out on the best performing configurations, in order to further maximize the performance.

CQUAD elements have been used to represent a F.E. model of the panels, while SMA elements have been simulated through CBEAM.

In this study, due to related implementation easiness within a F.E. analysis, Liang & Rogers model [1] has been used to simulate SMAs' behaviour: a detailed description of this model has been already presented in Chapter 3. The necessary material constants were experimentally computed and refer to a Ni-Ti-Cu alloy commercially available (NiTiCu10 produced by the C.N.R. of Bologna, IT). Table 1 shows some characteristics of the alloy used for the experimental prototypes: this is a One-Way alloy, which stores the recovered shape after cooling in absence of external loads.

Martensite start temperature Ms	Martensite finish temperature Mf	Austenite start temperature As	Austenite finish temperature Af
43°C	27°C	47°C	59°C
Martensite Young modulus Em	Stress-temperature slope for martensite Cm	Austenite Young modulus Ea	Stress-temperature slope for austenite Ca
25 Gpa	7 Mpa/°C	70 Gpa	7 Mpa/°C

Table 1: Thermo-mechanical properties of the adopted SMA ribbons.

The SMA actions have been simulated by an external home-made Matlab routine, able to find the working point of the structure activated by an SMA based-on actuator. The F.E. approach used to simulate the structure behavior is based on the assumption that the SMA, working as actuator, generates large displacements, recovering an assigned deformation without undergoing bending actions, coherently with the 1D model described in the previous paragraph.

According to these assumptions, a non-linear analysis has been implemented and the SMA elements imposed deformations have been simulated by assigning to the material a suitable thermal contraction coefficient (able to assure under a unitary temperature increase the desired recovery strain); moreover, to avoid bending solicitations, the SMA actuators have been connected to the surrounding structure through hinges.

In Figure 1, the logical scheme adopted for simulations is illustrated: at first, a non linear analysis on the structure for different values of the equivalent thermal coefficient is carried out, in order to relate the forces to be provided by the SMA actuator with the displacements transmitted to the structure (a maximum strain recovery of 3% of the initial length of the SMA ribbons is considered); then, the corresponding curve is

compared with the SMA force-displacement curves, estimated by the Liang & Rogers model for several temperatures values; among the different curves, the Matlab routine finds out the one corresponding to the minimum activation temperature, whose intersection with the structure curve gives the effectively recoverable strain (Figure 2); finally, the equivalent thermal expansion coefficient in the F.E. simulation is updated to meet the solution found out by the afore described procedure.
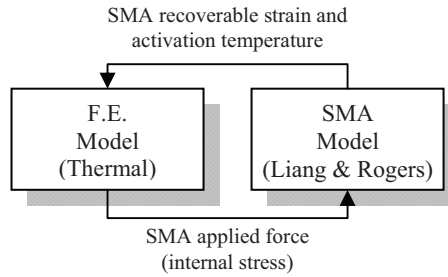
Figure 1: SMA model integration within the F.E. approach.
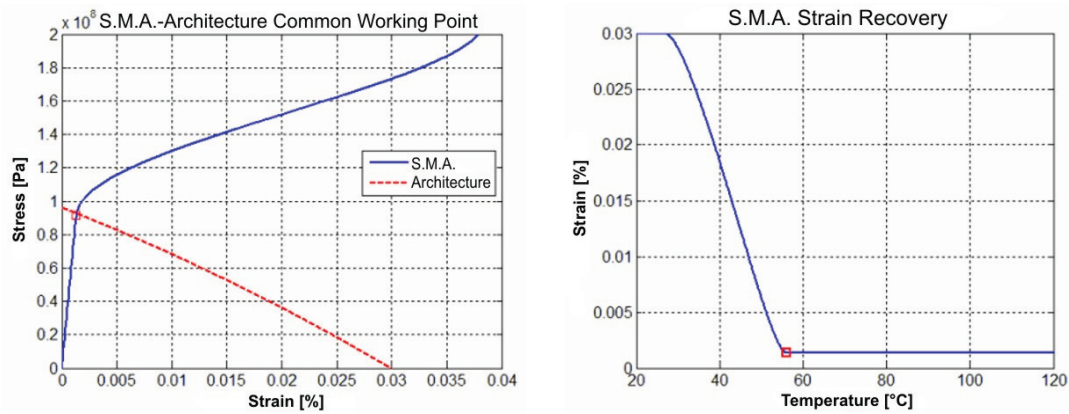
Figure 2: SMA behaviour estimated by the Liang & Rogers model implemented in Matlab.

Investigated architectures

The architectures described below are all based on an Al 7075T6 panel having dimensions 500x300x1 mm. The panel is constrained at one edge (along a 300mm side) and free to the others.

The proposed architectures differ in the technique with which SMA actuators are arranged; the curvature has been studied along the largest dimension, evaluating the maximum vertical displacement and rotation obtained for the free edge of the panel.

The SMA elements have been considered with the sole function of actuators, chosen in the shape of wires or ribbons to minimize the weight increase resulting from their

presence: in the case of wires, they have a 1 mm diameter, while the ribbons have a 10x1 mm section; the length varies with the architecture in question.

For the correct evaluation of their performance, parameters and constants to be implemented in the simulation model for the S.M.A have been taken from experimental tests, as shown in Table 1. The considered Ni-Ti-Cu alloy is "One-Way", that is it can retain the recovered shape after cooling in absence of applied load: so, the cyclic use of SMA is not possible without an antagonistic elastic element (absent in the considered architectures), able to restore the initial condition.

The SMA maximum recoverable strain has been assumed to the value of 3% of the wire/ribbon initial length: this value is compatible with the structure, without inducing excessive stresses in the panel or close to yielding; moreover, they represent a good compromise between actuation performance and cyclic fatigue life [2].

Architecture 1 is constituted by three pairs of SMA ribbons arranged longitudinally, along the panel biggest dimension; for a more uniform panel actuation, each strip is located at ¼ of the panel width (300 mm) from the panel edges (Figure 3, left). Three stringers are equi-spaced in the longitudinal direction, with the final one at the free panel: the ribbons are considered hinged to the stringers. The stringers are solid blocks (section: 10x5 mm) to ensure the complete transmission of the SMA actuation to the panel. The presence of multiple stringers and pairs of ribbons allows to obtain multiple stable configurations, as a function of the possible combinations of activated SMA pairs.
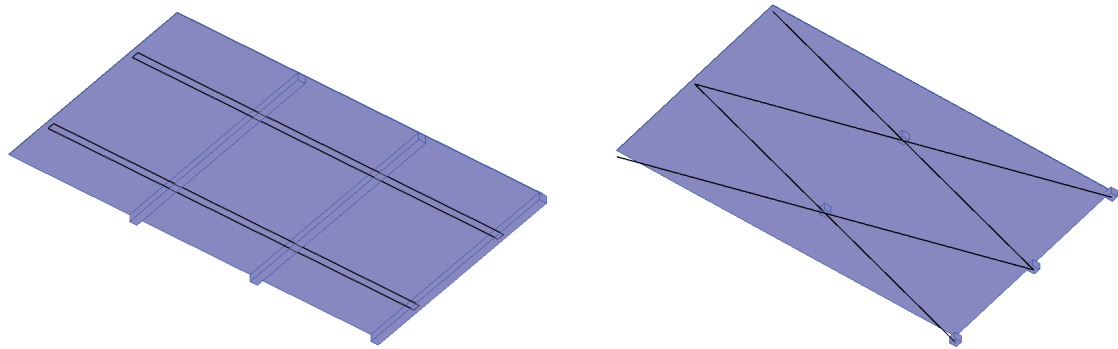
Figure 3: CAD model for Architecture 1 (left) and Architecture 2 (right).

Architecture 2, instead, is characterized by eight SMA wires arranged to form "diamonds" and are bound to some stringer portions (of course, one could consider full stringers current that cross the entire width of the panel with a weight increase), respectively positioned in the middle and the free end of the panel; the arrangement is

symmetrical in both directions (Figure 3, right).

Compared with the previous architecture, the "slanted" scheme of wires allows for an higher total length; in addition, the recovery strength undertaken by SMA now does not act in the longitudinal direction.

This architecture also allows for separate activation of different SMA wires; therefore many different actuation configurations of the panel are possible: however, in this study only symmetric configurations have been considered.

Architecture 3 also uses SMA wires: two of them are arranged transversely to the panel and equi-spaced in the longitudinal direction; upon activation, they transfer their action to two steel wires (diameter 1 mm) that extend longitudinally throughout the panel, ending attached to the stringer positioned on the free edge (the stringer has a solid section of 10x5 mm) (Figure 4, left).

This arrangement does not allow for multiple configurations on actuation: it has been chosen because it minimizes the stress field within the SMA elements and, therefore, their activation temperature. The idea behind this architecture is the three hinge arch principle: each SMA wire can be assumed as a tie-beam which, on strain recovery, induces a displacement in the steel cable connected to it, approaching the extremes and moving the panel free edge.
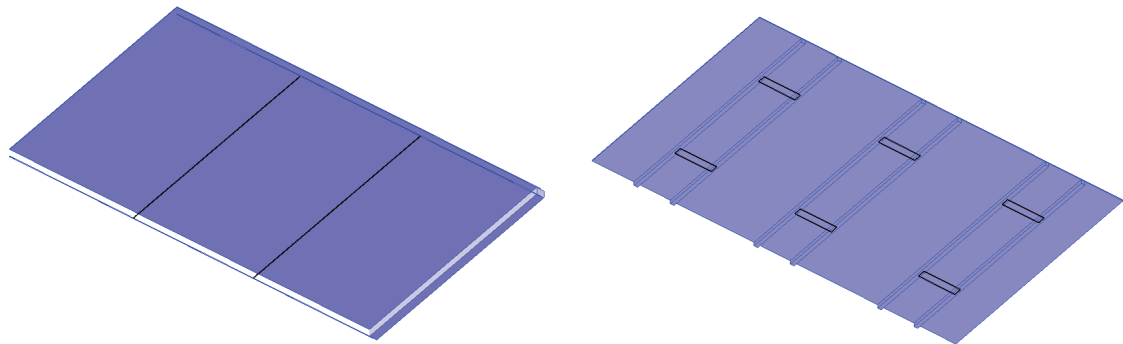
Figure 4: CAD model for Architecture 3 (left) and Architecture 4 (right).

The last investigated solution, Architecture 4, stems from the consideration that panels used for aircraft structures generally have multiple stiffeners, distributed across the surface, which are well placed to be used to constrain the SMA ribbons. Each SMA ribbon is 50 mm long and is hinged at both ends to the stringers (having a solid section of 5x5 mm), which are equi-spaced in the longitudinal direction (Figure 4, right).

Given the smaller total length of the SMA ribbons when compared to the first architecture, it is expected the actuation performance to be lower: the study of such a solution allows an evaluation of the effect of the ribbon length on performance. As with the first architecture, also Architecture 4 offers the possibility of multiple activation configurations.

Numerical results

The actuation performance of each architecture have been evaluated considering the maximum vertical displacement and rotation of the panel free edge; at same time, the SMA minimum complete activation temperature has been estimated.

A summary of the performance achieved by each architecture is shown in Table 2: let's observe that in this preliminary comparison, for architectures capable of multiple activation configurations, only the maximum performance case has been considered (that is, with all the SMA wires or ribbon activated).

Architecture 1 shows to have the best performance; Architecture 3, instead, was the least performing mainly because of the transverse arrangement of SMA wires and their reduced length, so not justifying the expected amplification effect.

Architecture	Free edge rotation [deg]	Free edge vertical displacement [m]	Max activation temperature [°C]
1	67,55	0,2492	45,5
2	49,13	0,2171	52,2
3	0,64	0,0028	42,7
4	47,53	0,1937	56,0

Table 2: Summary of actuation performance for all the investigated architectures.

After these preliminary results, Architectures 1 and 4 have been selected for a more in depth study: not only they resulted to have good performance, but they also are more similar to a traditional stiffened aeronautical panel; in addition, both architectures provide multiple possible activation configurations. A detail of the performance for both these solution is reported in Table 3, showing the displacement and rotation of the free panel edge for several combinations of activated SMA elements; Figure 5 shows the same results in a graphical form which allows for a direct comparison between the two architectures.

In all cases, the stress field induced in the aluminium panel has been below 200MPa.

Architecture 4 clearly shows lower performance due to lower total length of the SMA ribbons. Furthermore, it should be emphasized that the stress field within the SMA

ribbons is considerably higher than in Architecture 1: this is essentially due to the shorter distance (stringer height) of the ribbons from the panel. This has a negative effect on the activation temperature required for the phase transition to occur in the SMA, which is higher.

Architecture	Thermally activated S.M.A. ribbons	Free edge rotation [deg]	Free edge vertical displacement [m]	Max activation temperature [°C]
1	All S.M.A. pairs	67,55	0,2492	45,5
	1° pair (constraint)	18,65	0,1360	
	2° pair (middle)	24,45	0,1033	
	3° pair (free edge)	24,49	0,0350	
	1° and 2° pairs	43,08	0,2273	
	2° and 3° pairs	48,91	0,1329	
4	All S.M.A. pairs	47,53	0,1937	56,0
	1° pair (constraint)	15,81	0,1131	
	2° pair (middle)	15,84	0,0683	
	3° pair (free edge)	15,82	0,0219	
	1° and 2° pairs	31,68	0,1764	
	2° and 3° pairs	31,69	0,0887	

Table 3: Detailed summary of actuation performance for Architecture 1 and 4.
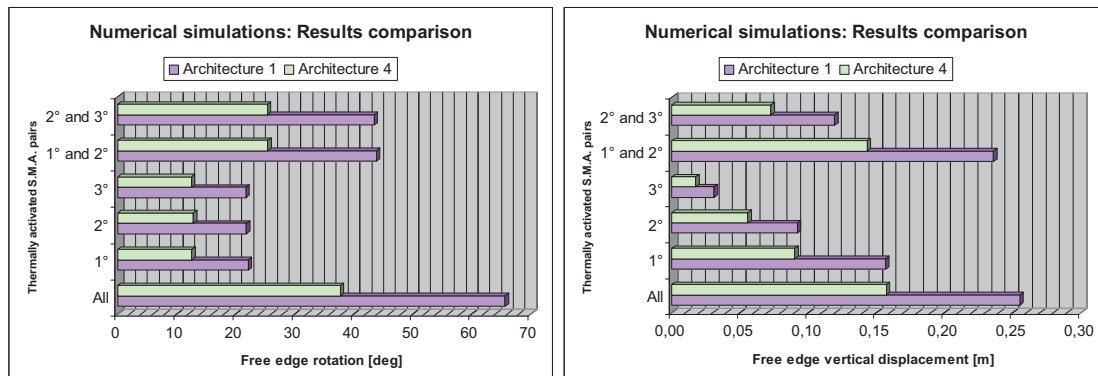
Figure 5: Graphical comparison of actuation performance for both Architecture 1 and 4 for several combinations of activated SMA elements.

These two architectures have been further optimized by adopting a home-made genetic algorithm [3] implemented in MATLAB. The optimization had as its objective function (or fitness function) the maximization of performance in terms of vertical displacement of the panel free edge: using an appropriate simplified F.E. model for each architecture, the Matlab routine was able to interface with the MSC/NASTRAN solver to evaluate the actuation performance and change the optimization parameters accordingly. For both architectures, the variables used during the optimization process included the location and height of the stringers (to which SMA elements can be bound); the optimization has been performed on each architecture considering all the SMA pairs activated. The genetic evolution, performed with 50 populations consisting of 60 individuals each, showed a rapid convergence to the optimal solution in both cases.

Figure 6 shows the final genetically optimized architectures; Table 4 summarizes the new actuation performance; Figures 7 shows these performance in a graphical way.
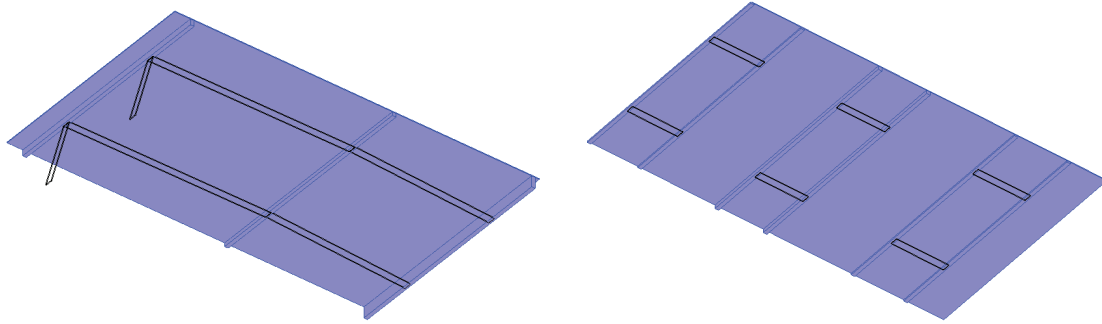
Figure 6: CAD models for the genetically optimized Architecture 1 (left) and Architecture 4 (right).

Architecture	Thermally activated S.M.A. ribbons	Free edge rotation [deg]	Free edge vertical displacement [m]	Max activation temperature [°C]
1	All S.M.A. pairs	63,58	0,2736	50,2
	1° pair (constraint)	9,24	0,0785	
	2° pair (middle)	31,77	0,1809	
	3° pair (free edge)	22,95	0,0376	
	1° and 2° pairs	40,86	0,2493	
	2° and 3° pairs	54,53	0,2095	
4	All S.M.A. pairs	68,88	0,2992	56,1
	1° pair (constraint)	26,34	0,2063	
	2° pair (middle)	17,03	0,0838	
	3° pair (free edge)	25,52	0,0390	
	1° and 2° pairs	43,40	0,2761	
	2° and 3° pairs	42,51	0,1187	

Table 4: Performance summary for the genetically optimized architectures.
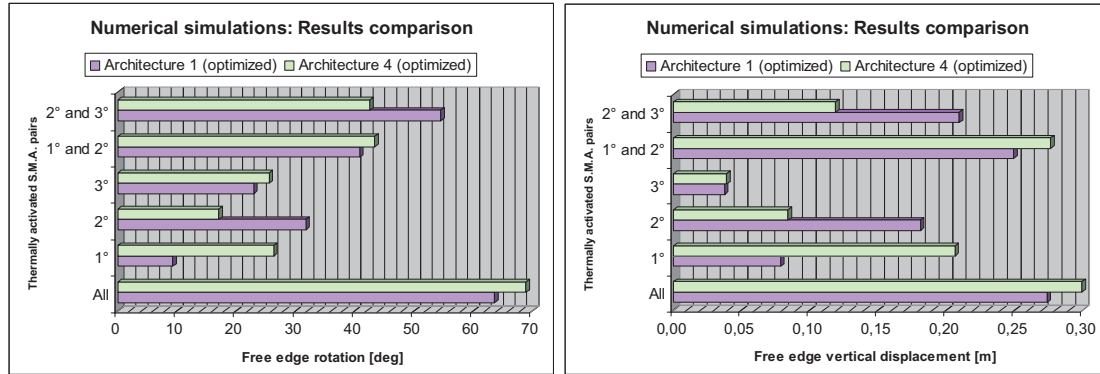
Figure 7: Graphical comparison of actuation performance for both the genetically optimized Architecture 1 and 4 for several combinations of activated SMA elements.

Observing the results for Architecture 1, it can be noticed that the optimization process allowed an increased displacement (about 7%) of the panel free edge of the panel; however, performance in terms of rotation are decreased by 3%. This is mainly due to the fact that the genetic algorithm detected a configuration optimized in terms of displacement (as required), which did not result in improved rotations.

The optimization was more profitable for Architecture 4, with a performance increase of 90% for the vertical displacement and 83% for rotations (given the considered greater length for the ribbons): this way Architecture 4 also surpassed Architecture 1 in most cases.

In any case, the optimization process led to really "original" architectures that can hardly find a real application; then, one should not overlook the significant increase in the SMA stress state, which increases the activation temperature for both architectures.

Experimental campaign: prototypes, setup and test results

Architecture 1 and 4 (the initial, not genetically optimized one) have been selected for the experimental campaign. The prototypes have been manufactured by Alenia Aeronautica Spa (Pomigliano d'Arco (NA) plant) and are showed in Figure 8.
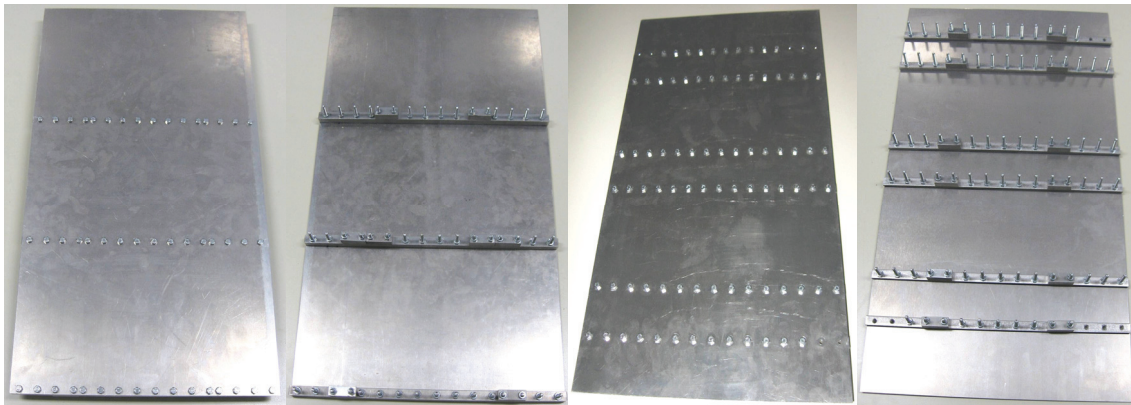
Figure 8: Experimental prototypes manufactured by Alenia Aeronautica Spa according to Architecture 1 (left) and Architecture 4 (right) schemes.

The stringers to be connected to the panel, different in size and arrangement for each architecture, are made of Al 7075T6 alloy too: a common thickness of 10 mm has been chosen for all of them (note that the stringers are intended as solid blocks, in order to convey to the panel the SMA actuation without any loss). Then, stringers have been attached to the panel by means of bolts (screw diameter of 4 mm and a length of 35 mm) so as to have a reversible method of anchoring, facilitating the installation of the SMA ribbons during tests.

A suitable mechanical clamping method has been developed to easily assembly the SMA ribbons, taking advantage of the already present bolts (the one used to attach the stringers to the panel) and guarantee the thermal and electrical insulation from the rest of the panel.

As for the SMA ribbons, they were subjected to some training cycles (5 stretch / recovery cycles) by means of a mechanical testing machine and subsequent heating at CIRA facilities, to impose the recoverable deformation (equal to 3.3% of its initial length) and stabilize their behaviour [4]: in this regard, it must be observed that the ribbons are assembled already having the pre-strain that they will recover during heating. Their length was determined during assembly, cutting them properly: it is also apparent that only the portion of ribbon between two stringers is thermally activated and participates in the strain recovery (and, thus, the panel actuation).

Experiments were performed by placing the prototypes on an optical bench, with the bolts heads downwards: this way the two demonstrators had to work against gravity, putting the SMA ribbons in a more burdensome condition and avoiding any bending due to the weight of the demonstrators themselves. Displacement and rotation of the panel free edge was measured by means of a ruled panel (Figure 9): a camera and a camcorder recorded each experiment, allowing also to determine the activation time.
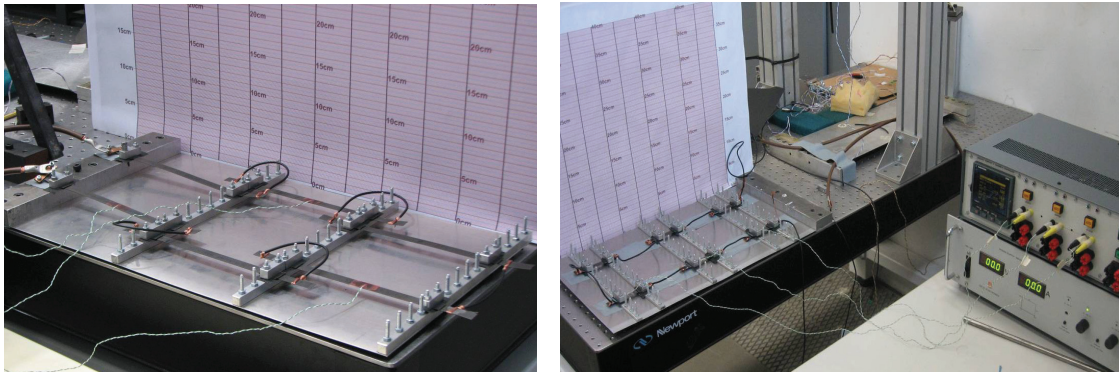
Figure 9: Experimental setup for the two prototypes.

The SMA ribbons activation (heating) has been carried out by means of Joule effect, using a DC power supply capable of delivering 20 Amperes at 8-9 Volts: this allowed to easily reach the estimated activation temperatures, measured by thermocouples. It has to be noticed that the ribbon heating could have occurred also with a lower electrical current, but this would have required a longer activation time because of the convective cooling still present. All the ribbons have been connected in a single circuit by means of "bridges" built with adequate electrical wires: the different activation conditions, to study all the multiple stable configurations, were obtained by changing the electrical connections from time to time.

Between a test and the subsequent one, SMA ribbons (once cooled) have not been dismantled: the prototypes have been manually retrieved to the initial conditions via an

appropriate mechanism for tensioning the ribbons again and bring back the panel to its original un-deformed shape.

Table 5 illustrates the experimental measures for several activation conditions and Figure 10 shows the complete actuation condition (all pairs of SMA ribbons activated) for both prototypes.

Architecture	Thermally activated S.M.A. ribbons	Free edge rotation [deg]	Free edge vertical displacement [m]
1	All S.M.A. pairs	57,00	0,2150
	1° pair (constraint)	16,00	0,0790
	2° pair (middle)	21,50	0,0800
	3° pair (free edge)	21,00	0,0320
	1° and 2° pairs	38,50	0,1800
	2° and 3° pairs	40,50	0,1020
4	All S.M.A. pairs	29,50	0,1200
	1° pair (constraint)	12,00	0,0820
	2° pair (middle)	13,50	0,0480
	3° pair (free edge)	15,50	0,0250
	1° and 2° pairs	22,00	0,1100
	2° and 3° pairs	25,50	0,0570

Table 5: Detailed summary of actuation performance experimentally measured for Architecture 1 and 4.
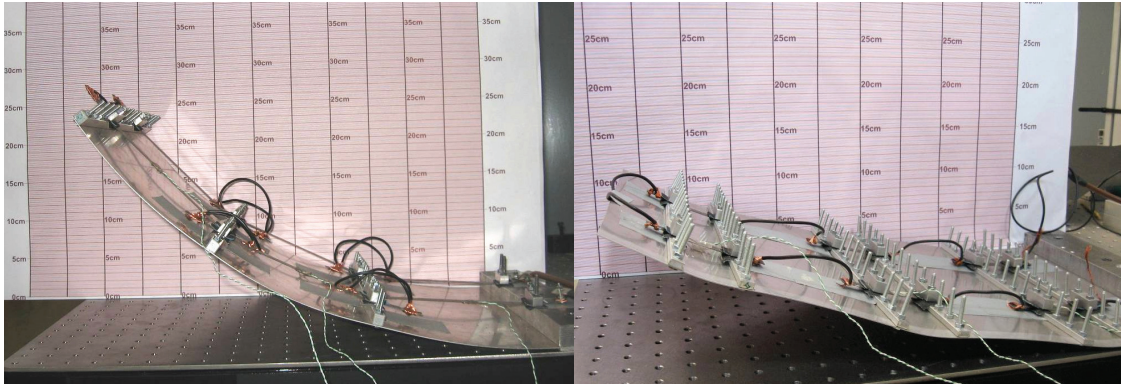
Figure 10: Complete actuation condition for both the experimental prototypes.

The environmental temperature has been always around 20 °C; during the activation by Joule effect, the SMA ribbons temperature always exceeded the threshold of 55-60 °C (due to the high electrical input), sufficient to attain a complete activation in all cases and in a short time (maximum 25 seconds).

As it can be noticed, experimental performance for both architectures are generally lower than the numerical estimate: more details will be discussed in the next section.

Numerical-experimental correlation

Figure 11 and Figure 12 show a comparison of the experimental measured performance with the numerical estimate, respectively for Architecture 1 and Architecture 4.

About Architecture 1, considering only the condition with all SMA pairs activated, during the experimental tests has been detected an actuation loss of approximately 15%

for rotations and nearly 14% for displacements of the panel free edge when compared to the numerical results. Similarly, for Architecture 4, these percentages become equal to about 38% for both rotations and displacements.
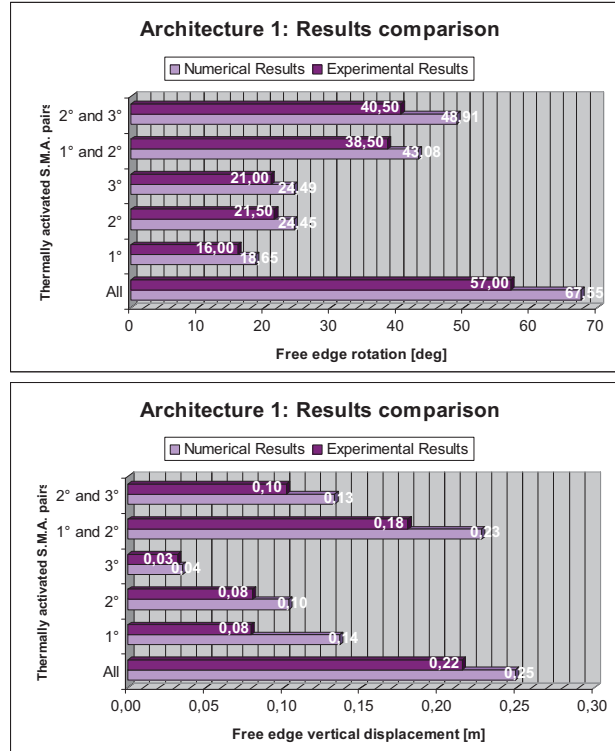
Figure 11: Numerical-Experimental performance comparison for Architecture 1.
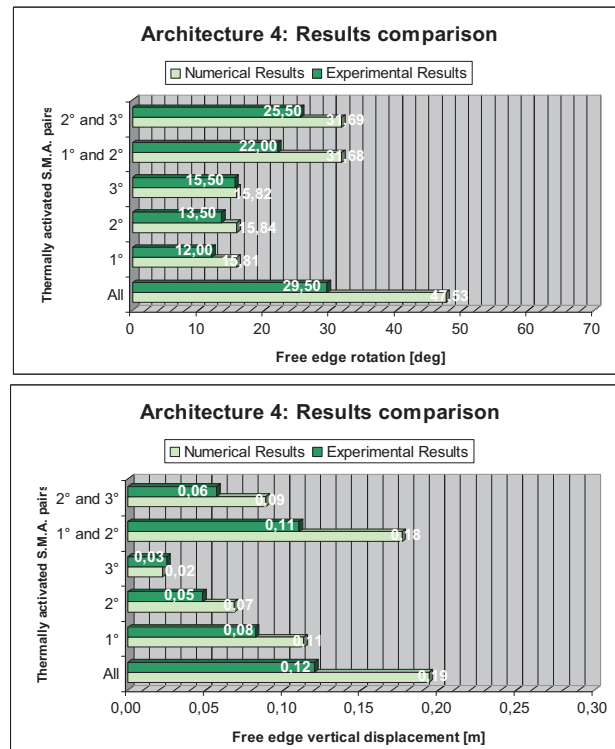
Figure 12: Numerical-Experimental performance comparison for Architecture 4.

These differences between numerical and experimental performance can be explained with the following considerations. First, one must not overlook the lack of weight force in numerical simulations, however present in the experimental stage: this inevitably leads to an increased stress state in the SMA ribbons, slightly reducing the effective recoverable strain as opposed to the originally imposed one (this loss is limited, as shown in Table 6). This behaviour leads to having to update the numerical simulations in order to take into account the SMA actuation loss, resulting in decreased performance.

Another effect to consider, found predominantly in the emergence of marked differences in performance, is related to possible assembly errors in the experimental stage: such errors are believed to be due to imperfect manual assembly and tensioning of the SMA ribbons in their place, which produces a loss of recoverable strain (because during activation the ribbons do not actuate the prototype but recover these errors), and any failures / shifts that have occurred in correspondence to the stringer clamping mechanisms.

Table 6 evaluates the percentage of performance change due to errors in assembly or failure, which can be estimated to fluctuate between 13% and 15% for Architecture 1 and about 35% for Architecture 4: in both cases, this is almost all of the discrepancy found between numerical results and experimental measures.

Considering that for Architecture 1 the length of each SMA ribbon is 16.5cm (for the pair near the constrained edge) and 15.5cm (for all the others), the discrepancy percentage between numerical and experimental actuation translates into an error of 0.93 mm on the length; for Architecture 4 (which shows greater percentage errors but has shorter ribbons), this length is equal to 0.62 mm.

These values define the amount of average length of each SMA ribbon that has not been activated or, similarly, underwent slippage at the clamping, or is the result of an imperfect assembly of the demonstrators: these values are very small, unlikely to be removed or unavoidable during experimental manual assembly, and can reasonably explain the difference in performance.

These percentages show that Architecture 4, having a shorter individual (and total) length of SMA ribbons as opposed to Architecture 1, is trivially more sensitive to assembly errors or slippage: as a matter of fact, an hypothesized failure for each single ribbon of 0.62 mm leads to a performance loss of 35%, a lot greater than 0.93 mm for each ribbon in Architecture 1 which leads to a 15% loss.

Architecture	Thermally activated S.M.A. pairs	Numerical Results		Updated Results		Experimetal Results	
		Free edge rotation [deg]	Free edge vertical displacement [m]	Free edge rotation [deg]	Free edge vertical displacement [m]	Free edge rotation [deg]	Free edge vertical displacement [m]
1	All	67,55	0,2492	67,04	0,2477	57,00	0,2150
		Percentage difference when compared to Numerical Results		**0,75%**	**0,60%**	**15,62%**	**13,72%**
				Percentage difference when compared to Updated Results		**14,98%**	**13,20%**

Architecture	Thermally activated S.M.A. pairs	Numerical Results		Updated Results		Experimetal Results	
		Free edge rotation [deg]	Free edge vertical displacement [m]	Free edge rotation [deg]	Free edge vertical displacement [m]	Free edge rotation [deg]	Free edge vertical displacement [m]
4	All	47,53	0,1937	45,64	0,1869	29,50	0,1200
		Percentage difference when compared to Numerical Results		**3,98%**	**3,51%**	**37,93%**	**38,05%**
				Percentage difference when compared to Updated Results		**35,36%**	**35,79%**

Table 6: Evaluation of the numerical-experimental error for both architectures.

Conclusions and further steps

This study presents some architectures able to change the curvature of typical stiffened panels for use in the aeronautical field. Through the integration of SMA elements (wires or ribbons) as actuators (wire or strip), the devised solutions can alter the geometry with a minimum increment in weight; their design also allows to generate large curvatures without loss of structural integrity.

In particular, two architectures can be easily implemented in real life applications due to the high similarity with traditional structures: their optimization, using genetic algorithm, showed a further increase in performance, however leading to solutions not always practical, as well as requiring higher activation temperatures.

Having adopted commercially available "One-Way" Shape Memory Alloys and in the absence of elements for elastic recovery, the proposed architectures are not able of cyclic actuation.

The total length of SMA actuators (having fixed the recoverable strain to 3% in length) is decisive in determining the performance of different architectures; moreover, different arrangements induce different stress states in the SMA elements, and thus different activation temperatures needed for the complete phase transition. However, temperatures around 50 °C are easily obtained by Joule heating in the considered SMA elements and with relatively low electrical power; as an alternative, other options for heating could involve Peltier cells or the use of exhaust engine gas.

During experimental test, temperatures in the order of 55-60 °C have been easily obtained by Joule heating with a 20 ampere electrical current, and 25 seconds for full

activation: lower electrical powers can in the same way achieve the SMA activation, but in a longer time range.

The two architectures selected for experimental investigations have provided satisfactory results, showing a good numerical-experimental correlation, within the limits of the uncertainties of the experimental stage, validating the adopted modelling technique. The performance reduction measured in the experiments are also unlikely to be removed, since they are caused by tolerances of the order of tenths of a millimetre.

Future developments could regard the evaluation of aerodynamic loads and their effects on actuation performance; the necessity of cyclic actuation is also mandatory for a real application, calling for the introduction of suitably designed elastic elements or "Two-Way" SMA elements.

References

[1]   Liang C., Rogers C.A., 1990, "*One-Dimensional Thermomechanical Constitutive Relations for Shape Memory Material*" – Journal of Intelligent Material Systems and Structures, vol.1, no.2, pp.207-234

[2]   Shimizu K., Tadaki T., 1987, "*Shape Memory Alloys*" – Funakubo H. Ed., Gordon and Breach Science Publishers, New York, pp.1-60

[3]   Goldberg D.E., "*Genetic Algorithms in Search, Optimization & Machine Learning*", Addison-Wesley Publishing Company Inc., ISBN: 0-201-15767-5, 1989

[4]   Srinivasan A.V., McFarland D.M., 1995, "*Smart Structures: Analysis and Design*" – Cambridge University Press, ISBN 0-521-65977-9

PAPER

"Wing Camber Control Architectures based on SMA: Numerical Investigation"

S. Barbarino, S. Ameduri, R. Pecora

Wing chamber control architectures based on SMA: numerical investigations

Silvestro Barbarino*[a], Salvatore Ameduri[b], Rosario Pecora[a]
[a]Dept. of Aerospace Engineering, Univ. of Naples "Federico II", Via Claudio 21, Naples, Italy 80100;
[b]Smart Structures Lab., Italian Aerospace Research Centre (CIRA), Via Maiorise, Capua (CE), Italy 81043

ABSTRACT

Benefits in terms of aerodynamic efficiency, aeroelastic behaviour, stability and manoeuvrability performance coming from the adaptive variation of wing geometric (e.g. thickness and chamber) and mechanical (e.g. rigidity) parameters were widely proved. In this scenario, more and more efficient architectures based on innovative materials like shape memory alloys, piezoelectrics, magneto-rheologic fluids were ideated and related morphing ability was tested. Due to the large transmitted forces and deformations, for static applications, SMA based-on architectures were implemented. The essential idea of all these architectures is to integrate a SMA actuator, lacking of remarkable structural value, within a classical wing structure or within a suitably designed one. The main disadvantage of such architectures derives by the necessity of deforming a classical structure, not designed for reaching large displacements. In order to avoid these problems, in this work, the idea of integrating compliant structures by SMA elements, was considered. Some deformation strategies, focused on the wing aft part morphing, were ideated; related performance in terms of vertical displacement and rotation of the trailing edge was estimated by a FE approach. Each architecture is characterised by SMA rod elements able to guarantee large deformations and shape control under aerodynamic loads.

Keywords: SMA, Wing morphing, Hingeless flap, Shape control

1. INTRODUCTION

Generally, the aerodynamic surfaces of a typical aircraft are characterized by a fixed geometry, optimized for a single or few working conditions (cruise regime, take-off, landing, specific manoeuvres). This design approach implies a non-complete exploitation of the aerodynamic performance, being the geometry not optimized for all the flight regimes [1].

The wing shape control, as proved by several numerical and experimental investigations [2-3], can strongly improve the aerodynamic efficiency of a wing, by assuring an optimal adaptive behavior with respect to the external free-stream conditions. As reported in literature, geometry modifications may be attained by affecting different parameters: the local or global chamber [4-5], the wing span [6-7], the twist angle [8].

Some morphing solutions have been ideated since 1970s: unfortunately, due to related higher costs, weight, architectural complexity and more severe maintenance requirements, such solutions were only implemented for military aircrafts (f.i., Northrop-Grumman F-14 "Tomcat").

The development of "intelligent" materials (or "Smart" materials) has shown major benefits for auto-deforming structures, resulting into highly integrated and actuation-capable structures [9-10]. Among the others, Shape Memory Alloys are playing a more and more determining role. Discovered in 1932 by Chang & Read as a Cd-Au alloy, only since 1962, when Buehler et alii observed the shape memory effect for the Ni-Ti equi-atomic alloy [11], they have received increasingly more attention. SMAs are metal alloys that exhibit both the unique characteristics of large recoverable strains and large induced internal forces under temperature change [12]. Recent investigations about Smart materials focused on morphing-wing concepts demonstrated the advantages of using SMAs, for their ability in producing relevant amount of force levels, being characterized by a favourable performance per weight ratio [13-14]: nevertheless, these solutions have been applied only to small prototypes or UAVs, focusing on maneuvering aspects more than flight control capabilities, because of their characteristic response times, usually measured in unit of seconds.

*postadisilvio@gmail.com; phone 0039 081 824 8810

In this paper, several morphing wing concepts have been exploited, aiming at achieving aerodynamic efficiency gain, by means of chamber adaptive control. More in details, the design of the aft part of a rib, corresponding to the flap zone, is presented, by taking into account different strategies of actuation, designed to produce remarkable chamber variations, in any case, compatible with the structural integrity under aerodynamic.

In the following table, a short description of the selected architectures with related Id is provided.

Table 1. Architecture description and Ids.

Id	Architecture description
A1	Monolithic aluminum rib, suitably shaped to allow large chamber variations (Figure 4a)
A2	Multi-body rib, whose components rotate each other, around hinges (Figure 4b)
A3	Multi-body rib, whose components rotate each other, through elastic hinges (Figure 4c)
A4	Multi-body rib, based on amplification mechanic chains (Figure 4d)

2. MODELLING STRATEGY

A FE approach has been adopted to predict the performance of the architectures described in the following paragraphs. As solver the MSC/Nastran tool has been used. Since no SMA model is implemented within MSC/Nastran, an external routine in Matlab code has been written to simulate the behaviour of the alloy; a suitable procedure has been realized in order to simulate the action of the SMA element, integrated within the rib structure. The effect of the shape memory actuator has been estimated for all the architectures with and without the aerodynamic loads. Due to the expected large deformations, a nonlinear analysis has been implemented. Finally, after achieving an overall estimate of the performance of the specific configuration, a genetic optimization process has been carried out, in order to maximize the trailing edge vertical displacement.

2.1 Shape memory alloy model

Thermomechanical properties of SMAs are due to a crystallographic phase transformation from a body-centred cubic structure (austenite / parent phase, present at high temperatures) to a face-centered cubic structure (martensite / product phase, present at low temperatures), or vice versa: this allows controlling the phase transformation of the alloy through, f.i., Joule heating. These transformations can also be induced by changes in the internal stress state. If the austenite temperature is lower than the environmental temperature, the so-called "super-elastic" effect is shown; otherwise, the high residual strain may be recovered by a temperature change and the proper "shape memory" effect takes place (Figure 1, a and b). The phase changes arise between the respective start and finish temperatures of the austenite and martensite phases: the transition temperatures are supposed to vary with the applied stress, commonly with a pretty linear relationship (Figure 1c), [13].

In 1986, Tanaka, [15], presented a unified one-dimensional martensitic phase transformation model. His study was restricted to the stress-induced martensite phase transformation. His theory was based on the assumption that the thermomechanical phase transformation of the material is fully described by three state variables: strain, temperature and martensite (austenite) volume fraction (ξ), which represents a measure of the phase evolution. Using the classical Helmholtz free energy relation and the Clausius-Duhem inequality, Tanaka developed the constitutive equation in the rate form:

$$(\sigma - \sigma_0) = E(\xi)(\varepsilon - \varepsilon_0) + \Theta(T - T_0) + \Omega(\xi - \xi_0) \tag{1}$$

where the subscript $_0$ represents the initial condition. As from this equation, the stress consists in three parts: mechanical, thermal and induced by phase transformation. The martensite fraction was assumed an exponential function of the applied stress and temperature.

In 1990, Liang and Rogers, [16], developed a new phenomenological model based on the Tanaka's one: they adopted his constitutive equation but, for the phase kinetics, they assumed a simpler cosine relationship to describe the martensite fraction as a function of stress and temperature. They also assumed the material properties to be constant during the transformation. The equations describing the martensite concentration during heating and cooling phases are:

$$\xi = \frac{\xi_M}{2}\cos[a_A(T - A_S) + b_A\sigma] + \frac{\xi_M}{2} \quad \text{and} \quad \xi = \frac{1 - \xi_A}{2}\cos[a_M(T - M_F) + b_M\sigma] + \frac{1 + \xi_A}{2} \tag{2}$$

where $a_A = \pi/(A_F - A_S)$ and $a_M = \pi/(M_S - M_F)$ are combinations of material constants: A_F, A_S, M_F, M_S are material characteristic temperatures, respectively known as austenite final, austenite start, martensite final and martensite start. They refer to phase transformations of the material and define when a particular crystal structure appears or the conversion is complete. Two other combinations of the material constants are $b_A = -a_A/C_A$ and $b_M = -a_M/C_M$, being C_A and C_M the slopes of the straight lines approximating the functions relating the four temperatures to the acting stress. Finally, ξ_M and ξ_A are the martensite and austenite volume fractions present in the alloy before heating and cooling, respectively. Many other constitutive models have been developed since then, [17-19], able of explain the complex behaviour of SMAs in specific load situations or extending the model validity to three-dimensional cases; anyway, engineering applications have paid attention to phenomenological models, which avoid difficult-to-measure parameters such as free energy and use only clearly defined engineering material constants. One of the major drawbacks of SMA in engineering applications is the difficulty of fully characterising their behaviour, highly non linear and load history dependent.

In this study, due to related implementation easiness within a FE analysis, Liang and Rogers model has been used to simulate SMAs' behaviour; the necessary material constants were experimentally computed and refer to a Ni-Ti-Cu alloy commercially available.

| (a) | (b) | (c) |
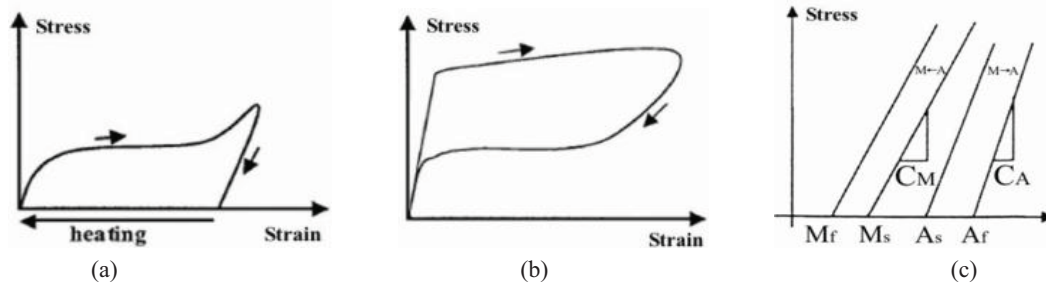
Figure 1. Shape memory effect (a), Superelastic effect (b), Stress-Temperature behaviour of SMAs (c), Chopra [13]

2.2 SMA model integration within a FE approach

Due to the complexity of the geometries taken into account, a FE approach has been adopted to estimate related performance. As FE solver, the MSC/Nastran code has been selected. Since no specific model of SMA materials are implemented within this code, the structural behavior of such an alloy has been simulated by an external Matlab routine, able to find the working point of the structure activated by an SMA based on actuator. The FE approach used to simulate structure behavior is based on the assumption that the SMA, working as actuator, generates large displacements, recovering an assigned deformation without undergoing bending actions, coherently with the 1D model described in the previous paragraph.

According to these assumptions, a non-linear analysis has been implemented and the SMA elements imposed deformations have been simulated by assigning to the material a suitable thermal expansion coefficient (able to assure under a unitary temperature increase the desired recovery strain); moreover, to avoid bending solicitations, the SMA actuators have been connected to the surrounding structure through hinges.

Figure 2. SMA model integration within a FE approach.

In Figure 2, the logical scheme adopted for simulations is illustrated: at first, a non linear analysis on the structure for different values of the equivalent thermal coefficient is carried out, in order to relate the forces to be provided by the

SMA actuator with the displacements transmitted to the structure (a maximum strain recovery of 3% in length is considered); then, the corresponding curve is compared with the SMA force-displacement curves, estimated by the Liang and Rogers [16] model for several temperatures values; among the different curves, the Matlab routine finds out the one corresponding to the minimum activation temperature, whose intersection with the structure curve gives the effectively recoverable strain; finally, the equivalent thermal expansion coefficient in the FE simulation is updated to meet the solution found out by the afore described procedure.

2.3 Aerodynamic loads evaluation and integration

The considered airfoil is a RA 18-43NIL1 provided with a split flap whose hinge axis is located at 70% of mean aerodynamic chord; aerodynamic loads have been evaluated on a wing portion whose span has been imposed equal to 300 mm. The distribution of pressure coefficient (c_p) along wing airfoil has been evaluated by means of bi-dimensional vortex lattice method (VLM); no 3-D effects have been taken in account for loads evaluation (the wing sections delimiting the investigated portion have been considered characterized by the same c_p distribution). Once the c_p distribution has been evaluated, the global airfoil lift coefficient (C_l) has been obtained: this has been done for several flap deflection angles (δ), from 2° up to 24°, and in correspondence of attitude parameters typical of take-off and landing conditions (at sea level, with dynamic pressure of 1531.25N/mm^2 and a 5° angle of incidence). The obtained results in terms of C_l have been reported in Table 2.

Be given a bi-dimensional Cartesian reference system S_0 defined as follows: origin located at airfoil leading edge; X-axis directed along unflapped airfoil chord and oriented towards airfoil trailing edge; Z-axis in the airfoil plane and upwards oriented. In correspondence of a flap deflection δi around the hinge point A [0.7·c;Z_A] the airfoil trailing edge moves from the position individuated in S_0 by point P [c;0] to the position individuated by point P' whose coordinates in S_0 are: $X_{P'} = 0.7 \cdot c + \overline{AP} \cdot \cos(\alpha + \delta_i)$, $Y_{P'} = \overline{AP} \cdot \sin(\alpha + \delta_i) - Z_A$ where c stands for the airfoil chord length, and $\alpha = \sin^{-1}(0.3 \cdot c / \overline{AP})$.

In order to reach the same trailing edge position due to a δ_i flap deflection, a morphing law has been imposed to flap chamber-line. The motion of point P to point P' has been then obtained by means of flap chamber line morphing into a parabolic arch connecting point A to P' and tangent in A to flap chamber line (see Figure 3a). Adopting the above described morphing law, for each airfoil flapped shape obtained by a δ_i flap deflection, it has been defined a morphed airfoil shape leading to same trailing edge displacement: C_l related to morphed shapes associated to deflection angles have been reported in Table 2. It can be noticed that, for a given deflection angle, the morphed flap leads to higher C_l values with respect to conventionally rotated flap (Figure 3b). The morphed flap configuration leading to airfoil C_l equal to 2.09 has been considered the most satisfactory from aerodynamic performance point of view, and has been chosen as this work target: it corresponds to a deflection angle of 12° and a vertical displacement of 160 mm. Be said s_i the generic aerodynamic strip, delimited by two homologue panels p_i located respectively on right and left section of wing portion, the normal aerodynamic load $F_{n,i}$ acting on s_i has been evaluated as $F_{n,i}=q \cdot A_i \cdot c_{p,i}$, where q is the dynamic pressure, A_i the strip area and $c_{p,i}$ the pressure coefficient on panels p_i. Such load distribution has been used for a proper sizing of the ribs to be located at the end of the investigated wing portion. In Figure 3c, the evaluated normal load distribution has been reported; the symbol '+' has been adopted for the positive orientation of normal loads' vectors.
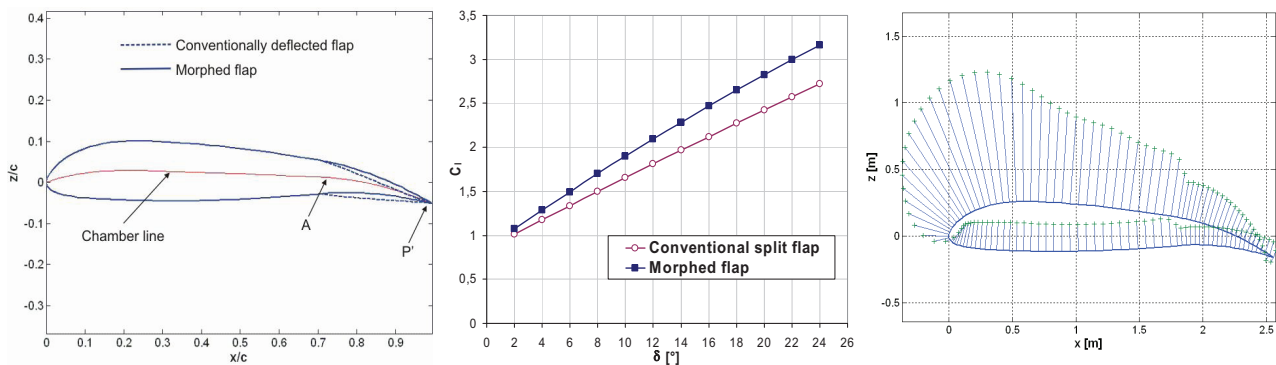
Figure 3. Conventionally deflected flap/morphed flap shapes (a); Airfoil Cl comparison (b); Normal load distribution on wing rib for the selected morphed flap shape (c)

Table 2. Airfoil C_1 for several flap deflection angles

δ [°]	2	4	6	8	10	12	14	16	18	20	22	24
C_1 (conventional)	1.0155	1.1760	1.3359	1.4950	1.6532	1.8103	1.9663	2.1209	2.2740	2.4253	2.5749	2.7224
C_1 (morphed)	1.0760	1.2866	1.4944	1.6990	1.8996	2.0956	2.2868	2.4727	2.6530	2.8275	2.9962	3.1589

2.4 Structural optimization

In order to maximize the chamber variations achievable through the SMA activation, due to the large amount of involved parameters, a genetic optimization has been implemented for the architectures described in the following. Even though the architectures are generally very different each others, some common parameters have been identified and optimized: for A2 and A3, the location of the multi-body hinges along the rib thickness; for A3, the geometric features of the hinges; for all the architectures, the SMA elements length and location on the rib.

3. ARCHITECTURES WORKING PRINCIPLE

The architectures described in the following paragraphs have been designed to meet the requirements of a flap of a traditional, short range commercial aircraft. The chord of this flap is 0.77m (30% of the wing shape chord), while the maximum thickness is of 0.21m. The flap cross section in the evaluations presented has been supposed constant. Due to the large required deformations and to the specific features of the materials involved, a non conventional design approach has been considered. The architectures taken into account represent a compromise between the typical high rigidity of a traditional flap (whose geometry has not to be remarkably affected by external loads) and a large flexibility, as a consequence of the required large scale deformations. According to this trend, the SMA elements have been exploited not only as actuators, but also as structural components, able to undergo even large deformations. SMA rod elements (with a 5mm diameter) have been picked up for all the architectures, currently with the structural required role and the 1D nature of the Liang and Rogers simulation model; as recoverable strain, a typical value of 3% has been assumed. In order to get a recovery strain as large as possible and also for availability problems, the "One-way" typology of SMA has been picked up: that is, the alloy retains the recovered shape even after cooling. As a consequence, a cyclic use of the SMA is not possible without an elastic antagonistic element, able to restore the initial condition.

3.1 A1 architecture: monolithic aluminum rib

This architecture, as shown in Figure 4a, is constituted by a single aluminum plate element (1mm thick), suitably shaped to exhibit required flexibility under SMA actuation, without reaching stress failure. The monolithic feature in some way makes this architecture similar to a traditional one. A smoothed geometry (based on elliptic shapes) has been privileged to prevent as much as possible critical stress increases. The SMA rods have been placed in order to maximize the transmitted displacements. Their contraction, due to the large flexibility of the structure, in absence of aerodynamic loads leads to remarkable chamber variations, as it will be shown in the next section.

3.2 A2 architecture: multi-body rib, with rigid hinge connections

The rib has been divided into different aluminum plate elements, sequentially connected by rigid hinges, allowing relative rotation (see Figure 4b). The intrinsic structural compliance is compensated by the presence of the SMA rods, playing also the role of actuators. Structure-SMA rods connections have been chosen to maximize the recoverable displacements. The hinges position on the flap mid line assures large cinematic vertical deflections, without inducing excessive tensile stress on an eventual upper skin.

3.3 A3 architecture: multi-body rib, with elastic hinge connections

As for the previous case, the rib has been divided into different aluminum plate elements; however, in this architecture, relative rotations are assured by elastic hinges, constituted by high flexibility steel plate elements, as shown in Figure 4c. Elastic hinges, when compared to rigid ones, show a vertical movement of the center of rotation during actuation, amplifying the rotation itself.

3.4 A4 architecture: multi-body rib, based on amplification mechanic chains

The different plates which constitute the rib (arc elements in Figure 4d) are connected by amplification chains. The main advantage is represented by the ability of transmitting large forces to the structure without high loads on the SMA wire.
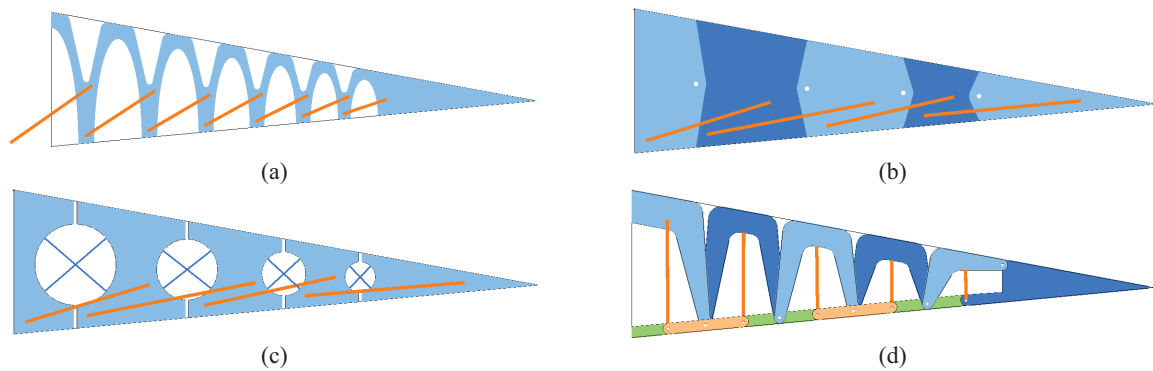
Figure 4. Summary of the investigated architectures

4. NUMERICAL RESULTS

Actuation capability of each architecture has been evaluated, in presence of SMA activation, considering the maximum vertical displacement and rotation of the trailing edge of the flap; nonetheless, the performance estimate has been carried with and without aerodynamic loads, calculated as illustrated in paragraph 2.3 (see Figure 5, from a to h). For each configuration, two separate simulations have been done, considering aerodynamic loads for non-actuated flap and actuated flap (at a certain angle, depending of the selected architecture): the former has not been reported in this paper, being all the architectures able to keep their integrity under external loads (weight and aerodynamic.

4.1 Results for A1 architecture

A strong deviation has been found between achievable displacements with and without aerodynamic loads, 96mm and 198mm, Figure 5, b and a, respectively. Related rotations resulted 23.3° and 12.4°. The initial target (160 mm of vertical displacement under external loads) has not been accomplished: this appears imputable to the large flexibility of the rib structure. Larger displacements would be possible through an SMA displacement oriented design; anyway, the real constraint is represented by the stress arise in some points (486 MPa for a 1mm thick aluminium alloy rib).

4.2 Results for A2 architecture

Differently from the previous one, performance of the second architecture does not remarkably depend on the external aerodynamic loads; vertical displacements resulted to be 277mm and 261mm (Figure 5, c and d, respectively), meeting and exceeding vertical displacement target. Related rotations are 41.9° and 39.5°. The structure exhibits higher shape rigidity than the first one, mainly due to the fixed position of the hinges and to a different ability of absorbing shear stress; also SMA elements benefit from this configuration, with a lower internal stress, allowing a larger recovery.

4.3 Results for A3 architecture

This architecture also exceeds the proposed target performance (Figure 5, e and f, respectively with a vertical displacement of 289mm and 267mm, and associated rotations of 44.5° and 40.7°), showing similar results to the A2 architecture, from which differs only for the elastic hinges. This configuration is a compromise between a rigid rib and allowable deformations, concentrated into suitably designed elastic elements, eliminating the presence of kinematics.

4.4 Results for A4 architecture

This last architecture showed a strong deviation between performance with and without aerodynamic loads, 125mm and 232mm, Figure 5, g and h, respectively. Related rotations resulted 13.7°and 25.1°. The actuation target has not been accomplished (under loads): this appears imputable to the large mobility of the rib, due to the kinematics.

4.5 Comparison of actuation capabilities

Table 3 shows a summary of the performance of the investigated architectures. Architecture A3 shows the best performance among the other solutions: it extends the good performance of the A2 configuration thanks to the elastic hinges, which, on SMA activation, undergoes a displacement of the centre of rotation, with a consequent amplification of the actuation. Given the stress level estimated within SMA rods, the temperature necessary to the complete activation of the shape memory effect is well under the 60°C for every architecture (for the considered Ni-Ti-Cu alloy).
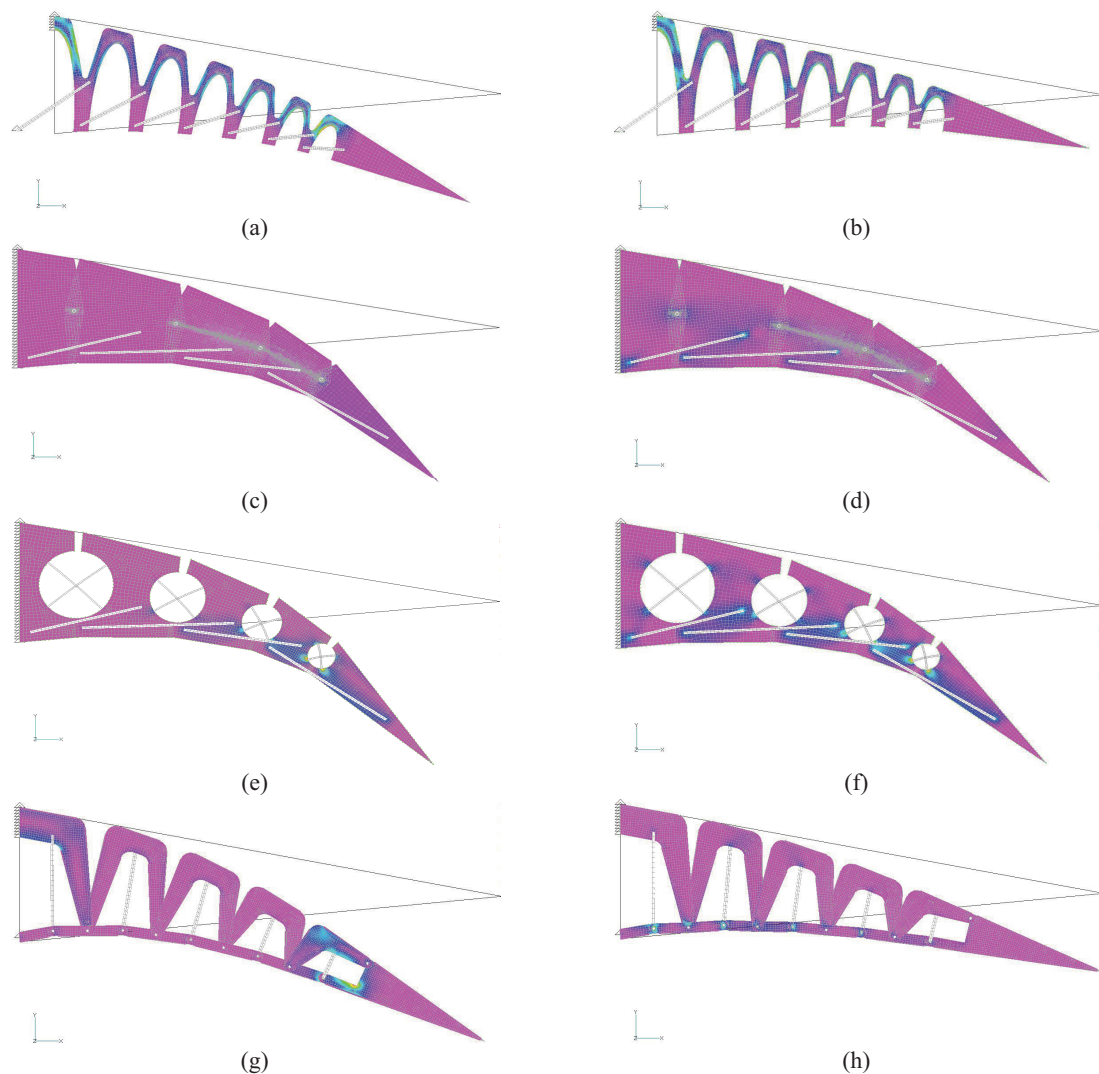
Figure 5. Summary of numerical displacement and stress evaluated for each architecture. Simulations carried out without applied loads are reported on the left (a, c, e, g); on the right (b, d, f, h), the same architectures are actuated in presence of aerodynamic load.

Table 3. Summary of performance of investigated architectures

	SMA actuation without Aerodynamic Loads		SMA actuation with Aerodynamic Loads	
	Vertical displacement	Rotation	Vertical displacement	Rotation
A1	198mm	23.3°	96mm	12.4°
A2	277mm	41.9°	261mm	39.5°
A3	289mm	44.5°	267mm	40.7°
A4	232mm	25.1°	125mm	13.7°

5. CONCLUSIONS AND FURTHER STEPS

This paper presents some original architectures focused on the chamber control of the aft part of a wing; related aerodynamic benefits are illustrated in paragraph 2.3. These solutions highly integrate SMA rods as structural and actuation elements, allowing for a weight reduction when compared to traditional counterparts. Their design allows accommodating remarkable chamber variations, under aerodynamic loads, without affecting structural continuity. As shown in this paper, the SMA total length plays an important role to maximize actuation performance; anyway, configurations limiting the SMA internal stress also result into larger recoverable strains. Among the others, architecture

A3 based on elastic hinges has proved the best performance in terms of max trailing edge displacements and rotations; also its ability to maintain its shape under aerodynamic loads makes this solution preferable with respect to the others. Abovementioned architectures do not include systems able to restore initial conditions; this represents a critical point of the design of an actuation architecture based on "one-way" SMA. Further investigations will be focused on the definition of such restore systems. One of the problems deriving from hingeless morphing solutions is the stress field induced within skin elements. To overcome this problem some strategies may be adopted: multi-panel skin (whose ability of sliding each other would reduce stress accumulation) and panel partially made of elastomeric material. Investigation presented in this paper deal with static applications; problems related with dynamic excitation will be object of future works. Moreover, due to the frequency working range limitations of the SMA, faster and more efficient activation systems will be taken into account (f.i., Peltier cell technology).

ACKNOWLEDGEMENTS

REFERENCES

1. A.L. Martins and F.M. Catalano, "Viscous Drag Optimization for a Transport Aircraft Mission Adaptive Wing", *21st ICAS Congress, Melbourne, Australia* Paper A98-31499 (1998)
2. E. Stanewsky, "Adaptive Wing and Flow Control Technology", *Progress in Aerospace Sciences, Elsevier Science Ltd.*, 37, 583-667 (2001)
3. J. Browman, B. Sanders, T. Weisshaar, "Evaluating the Impact of Morphing Technologies on Aircraft Performance", *AIAA J.* 2002-1631 (2002)
4. J. Spillman, "The Use of Variable Chamber to Reduce Drag, Weight and Costs of Transport Aircraft", *Aeronaut. J.* 96, 1-8 (1992)
5. H.P. Monner, T. Bein, H. Hanselka, E. Breitbach, "*Design Aspects of the Adaptive Wing – The Elastic Trailing Edge and the Local Spoiler Bump*", Royal Aeronautical Society, Multidisciplinary Design and Optimization, London, 1998
6. Gevers Aircraft Inc., "*Multi-Purpose Aircraft*", U. S. Patents No. 5,645,250 (1997)
7. J. Blondeau and D. Pines, "Pneumatic Morphing Aspect Ratio Wing", *45th AIAA/ASME/ASCE/AHS/ASC Structures, Structural Dynamics and Materials Conference, Palm Springs, California, AIAA J.* 2004-1808 (2004)
8. J.R. Wilson, "Active Aeroelastic Wing: A New/Old Twist On Flight", *Aerospace America* 40(99), 34–37 (2002)
9. D. Munday and J. Jacob, "Active Control of Separation on a Wing with Conformal Camber", *AIAA J.* 2001-0293
10. D.A. Perkins, J.L. Reed, E. Havens, "Morphing Wing Structures for Loitering Air Vehicles", *45th AIAA Structures, Structural Dynamics & Materials Conf., Palm Springs, California, AIAA J.* 2004-1888 (2004)
11. W.J. Buehler, J.V. Gilfrich, R.C. Wiley, 1963, "Effect of low-temperature phase changes on the mechanical properties of alloys near composition TiNi", *Journal of Applied Physics* 34, 1475 (1963)
12. L.C. Brinson, A. Bekker, M. Huang, "Deformation of Shape Memory Alloys due to Thermo-Induced Transformation", *J. of Intelligent Material Systems and Structures* 7(1), 97-107 (1996)
13. I. Chopra, "Review of State of Art of Smart Structures and Integrated Systems", *42nd AIAA/ ASME/ASCE/AHS/ASC Structures, Structural Dynamics, and Materials Conference, Seattle, WA, AIAA Journal* 40(11), (2002)
14. J.N. Kudva, "Overview of the DARPA/AFRL/NASA Smart Wing Phase II Program", *Smart Structures and Materials Conference, SPIE* 4332(48), 383-389 (2001)
15. K. Tanaka, "A Thermomechanical Sketch of Shape Memory Effect: One-Dimensional Tensile Behaviour", *Res. Mech.* 18(3), 251-263 (1986)
16. C. Liang and C.A. Rogers, "One-Dimensional Thermomechanical Constitutive Relations for Shape Memory Material", *J. of Intelligent Material Systems and Structures* 1(2), 207-234 (1990)
17. L.C. Brinson, "One-Dimensional Constitutive Behaviour of Shape Memory Alloy Constitutive Models", *J. of Intelligent Material Systems and Structures* 1(2), 207-234 (1990)
18. J.G. Boyd and D.C. Lagoudas, "A Thermodynamical Constitutive Model for Shape Memory Materials. Part. I. The Monolithic Shape Memory Alloys", *International Journal of Plasticity* 12(6), 805-842 (1996)
19. H. Prahlad and I. Chopra, "Comparative Evaluation of Shape Memory Alloy Constitutive Models with Experimental Data", *J. of Intelligent Material Systems and Structures* 12(6), 386-396 (2001)

PAPER

"Design of an Actuation Architecture based on SMA Technology for Wing Shape Control"

S. Barbarino, S. Ameduri, R. Pecora, L. Lecce, A. Concilio

Design of an Actuation Architecture Based on SMA Technology for Wing Shape Control

S. Barbarino[a], A. Concilio[b], R. Pecora[a], L. Lecce[a], S. Ameduri[b]
[a]Dept. of Aerospace Engineering, Univ. of Naples "Federico II", Naples, Italy
[b]Smart Structures Lab., Italian Aerospace Research Centre (CIRA), Capua (CE), Italy

Abstract:
The development of new structural aeronautics architectures together with the implementation of innovative materials is mandatory for succeeding in critical tasks, as aircraft efficiency improvement. For this reason, the Smart Structure concepts are taken into account for more and more aerospace applications and for the one here discussed.
In this work, an application for a morphing wing trailing edge for a CS-25 category (regional transport) aircraft is presented. Attention has been paid to the design of a compliant rib structure, based on SMA technology, able to sustain the external aerodynamic loads and simultaneously allow controlled wing shape modification. The numerical results, achieved through a FE approach, have been presented in terms of trailing edge induced displacement and flap zone morphed shape.

Keywords: SMA, morphing, shape control, aerodynamic surfaces

Introduction

The possibility of controlling the geometry of aerodynamic surfaces (ailerons, flaps, horizontal and vertical tails, etc.) represents a challenging target, that justifies the more and more research activities carried out on the morphing concept.

The adoption of this kind of approach proved to lead to benefits in terms of aerodynamic efficiency, structural weight, stability and manoeuvrability performance [1-2].

Shape modification may be attained by changing different parameters, as reported in literature: for instance, the local or global curvature, [3-4]; the wing span, [5]; the twist angle, [6].

To this aim, traditional design approaches have been adopted to realise some actuation architectures; anyway, despite of the effective ability of reaching desired deformations, related disadvantages in terms of weight and complexity, led to consider novel strategies, concerning with the "Smart Structure and Material" concept [7-8]. Among the several Smart materials, Shape Memory Alloys (SMA) are playing a more and more determining role, due to the favourable performance per weight ratio measured for instance in terms of mechanical energy.

In the work at hand, the working principle, design, optimisation and predicted performance of an original SMA based on architecture, is presented.

More in detail, such an architecture assures the trailing edge chamber modification for a CS-25 category (regional transport) aircraft, by catching a target shape, under typical take-off and landing aerodynamic loads.

A FE approach has been adopted to simulate the behaviour of the architecture for different working conditions; a Matlab routine has been realised to take into account the non linear constitutive law of the SMA actuator; finally, after identifying the main design parameters, a genetic optimisation has been carried out both to maximise trailing edge displacement performance and to fit the best required geometry.

SMAs main features and simulation

Firstly discovered by Chang & Read [9] in 1932 as a Cd-Au alloy, they received increasing attention and study only since 1962, when Buehler et alii, [10], at the Naval Ordnance Laboratory (NOL) of US Navy, observed the shape memory effect for the Ni-Ti equi-atomic alloy. SMAs are metal alloys exhibiting both the unique characteristics of large recoverable strains and large induced internal forces under temperature change.

Aforementioned thermo-mechanical properties of SMAs are due to a crystallographic phase transformation from a body-centred cubic structure (austenite / parent phase, present at high temperatures) to a face-centered cubic structure (martensite / product phase, present at low temperatures), or vice versa. These transformations can be induced by changes in the internal stress state: if the austenite temperature is lower than the environmental temperature, the so-called super-elastic effect is shown; otherwise, the high residual

strain may be recovered by a temperature change and the proper shape memory effect takes place, [11] (Fig. 1).
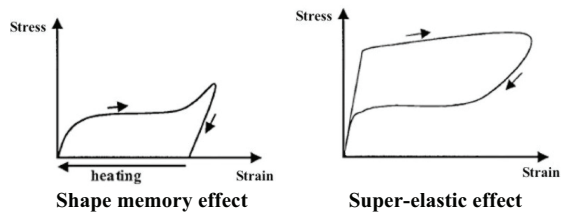
Fig. 1: *Stress-Strain behaviour of SMAs.*

Among the different SMA descriptive schemes, the Liang and Rogers' model [12] has been adopted in this work, being a valid compromise between implementation simplicity and prediction accuracy. The SMA constitutive law has been implemented within a Matlab routine, capable of predicting the effective recovery strain and actuation temperature for a given stress level. Since the adopted FE solver, MSC/Nastran, does not contain dedicated elements for SMA simulation, an iterative process aimed at matching structural and SMA deformation (congruency condition) has been carried out.

Aerodynamic loads estimate

The considered airfoil is a RA 18-43NIL1 provided with a split flap whose hinge axis is located at 70% of the chord; aerodynamic loads have been evaluated on a not-tapered wing portion whose span has been imposed equal to 0.3 m. The distribution of pressure coefficient (c_p) along wing airfoil has been evaluated by means of bi-dimensional vortex lattice method (VLM); no 3-D effects have been taken in account for c_p evaluation (the wing sections delimiting the investigated portion have been considered characterized by the same c_p distribution). Once the c_p distribution has been evaluated, the global airfoil lift coefficient (C_l) has been obtained: this has been done for several flap deflection angles (δ), from 2° up to 24°, and in correspondence of attitude parameters typical of take-off and landing conditions; the obtained results have been plotted in Fig. 2 (*curve 1*). For each airfoil flapped shape obtained by a δ rotation of flap around hinge point, it has been defined a correspondent morphed-trailing-edge airfoil shape leading to the same trailing edge displacement; morphed airfoil shape has been obtained by modifying the chamber-line related to flap zone into a parabolic arch linking the hinge point projection on chamber-line with deflected trailing edge position.
C_l related to each morphed shape have been evaluated and plotted in Fig. 2 (*curve 2*). It can be noticed that, for a given deflection angle, the morphed-trailing-edge configuration leads to higher

C_l values with respect to the conventionally flapped one. The morphed trailing edge configuration leading to airfoil C_l equal to 2.09 has been considered as the most satisfactory from aerodynamic performance point of view, and has been chosen as this work target: it corresponds to a deflection angle of 12° and to a vertical displacement of trailing edge equal to 160 mm. In correspondence of the selected morphed configuration, aerodynamic loads distribution on considered span-wise wing portion have been evaluated. Such load distribution has been then used for a proper sizing of the compliant ribs delimiting morphing trailing edge.
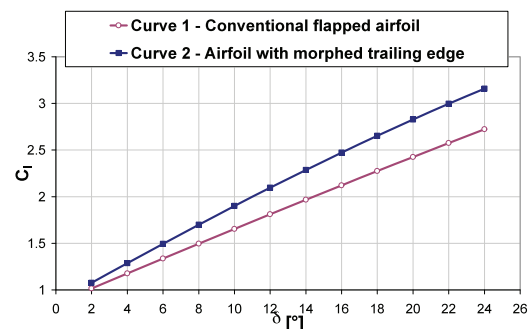
Fig. 2: *Airfoil C_l comparison.*

Selected morphing architecture

The proposed architecture (constituting the aft part of a rib) is sketched in Fig. 3. It represents a compromise between two opposite needs: the achievement of a desired deflection and the ability of sustaining external loads: SMA elements play an important role in fulfilling these goals. The rib frame is constituted by three rod elements made of SMA (bold lines): the actuation is obtained by heating SMA rods, causing their contraction; also aerodynamic loads are sustained by the SMA rods.
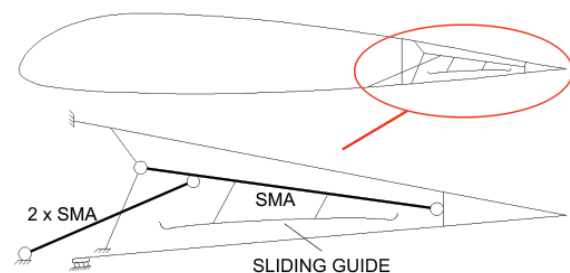
Fig. 3: *Architecture scheme.*

The lower part of the rib structure is capable of sliding into the wing box: this allows for a smooth skin deformation during actuation. However, in order to match the upper and lower skin target curves related to the parabolic-chambered airfoil, a guide element connected with the central SMA rod has been necessary: this constrains the lower skin to

follow an established geometry on activation, also in presence of external loads.

Moreover, two pendulums (not sketched in Fig. 3) have been used to connect upper and lower skins, to assure the correct fitting to the desired shape.

The achievable performance has been evaluated by a FE approach, both in presence and absence of external loads; SMA behaviour has been integrated as previously exposed; also the rib shape smoothness has been taken into account.

Given the expected large deformation and SMA behaviour, a thermal nonlinear analysis has been carried out and the SMA elements imposed deformations have been simulated by assigning to the material a suitable thermal expansion coefficient. In Fig. 4 the FE model of the aft part of the rib is illustrated. Related main features are summarised in Tab.1.

For simplicity, the guide element has been modelled with multiple independent beams, so that changing the length of each of them (within an optimisation process) would result in the required airfoil shape.
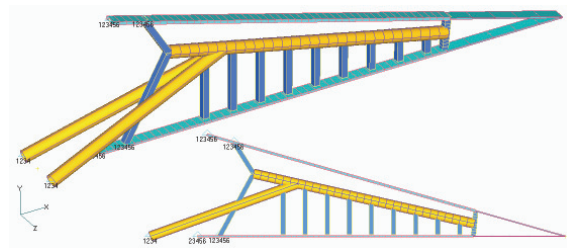
Fig. 4: *Architecture FE model.*

Total nodes	162
Total elements	165
SMA features	
Activation Temperature [°C]	75
Austenite Young mod. [GPa]	30
Martensite Young mod. [GPa]	25
FE typology	CBEAM
Cross section area [m^2]	$3.14*10^{-4}$
Rib features	
Material	Al 7075T6
Upper skin cross section [m^2]	$1*10^{-4}$
Lower skin cross section [m^2]	$6*10^{-5}$
Rod cross section [m^2]	$1*10^{-2}$

Tab. 1: *FE model main parameters.*

Genetic optimization

In order to maximize the trailing edge displacement performance and to achieve an optimised shape (capable of maximizing the aerodynamic benefits), a home made optimisation algorithm has been used; due to the large amount of involved parameters, a genetic approach has been adopted.

The following parameters have been chosen for the optimisation: position of SMA rods' hinges (and consequently the rods length); shape of the guide for the lower panel (changing the length of the vertical beams connected to the central SMA element); connections of the two pendulums between the upper and lower skins.

According with the above-mentioned target, a suitable fitness function has been defined:

$$fitness = \frac{\left\| v_{a,TE} \right\|}{\max\left(\left\| \vec{v}_a - \vec{v}_d \right\|\right)} \qquad (1)$$

being

- $v_{a,TE}$ the actual displacement of the rib trailing edge;

- $\vec{v}_a$ and $\vec{v}_d$ respectively the actual and desired displacement vectors;

where the desired displacement vectors are the ones leading to the airfoil parabolic-chambered target shape. The evolution of the mean and the max fitness during the optimisation has been plotted in Fig. 5.
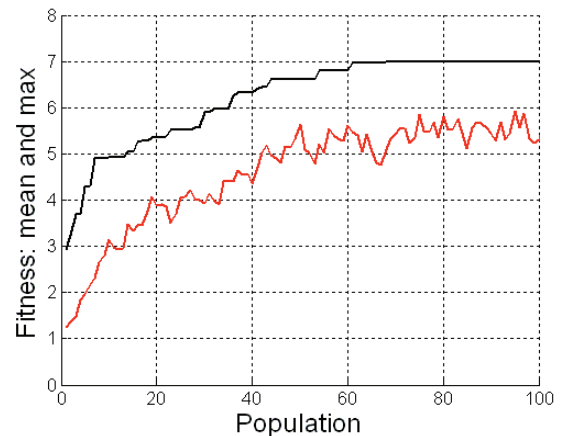
Fig. 5: *Fitness evolution vs. iterative step.*

Numerical results

Fig. 6 shows the final configuration obtained through the genetic optimisation process: the position of the SMA elements' hinges (light grey) allows to maximize the actuation performance, while each of the independent beams constituting the guide element (dark grey) has been set with a specific length, in order to assure rib morphing in compliance with final target shape.

Actuation capability of the developed architecture has been evaluated, in presence of SMA activation, considering the maximum vertical displacement and rotation of the trailing edge of the rib, under aerodynamic loads (Fig. 7).

Fig. 6: Final optimised architecture FE model.
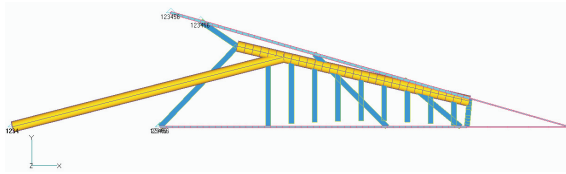
A vertical displacement of 180 mm has been reached, superior to the target for the desired C_l, with a final rotation of 25.3° (with respect to the initial lower skin slope). Also required shape continuity and smoothness have been achieved.

Fig. 7: Architecture FE simulation.

Conclusions

A novel approach has been adopted in this study by highly integrating the SMAs' elements within the architecture: they have both a structural and actuation role, working as principal actuators of the global structure, whose integrity depends on SMAs' structural capability of sustaining external of loads.
In order to assure the complete return to the un-morphed initial condition (no SMA activation), elastic elements have been foreseen. More in detail, traditional spring elements can be easily integrated within the architecture, so that they could act axially with respect to the SMA components.
Benefits of the exposed architecture, when compared to other morphing solutions, also cover some not negligible aspects as wing skin integrity: the architecture presented in this study allows for wing trailing edge commanded shape change without inducing skin discontinuities, which could reduce aerodynamic efficiency.
Performance has been evaluated in terms of maximum displacement and rotation of the rib structure trailing edge, estimated by a FE approach. SMA behaviour has been modelled through a dedicated routine for evaluating the activation temperature and internal stress state.
Numerical results herein presented demonstrate the efficacy of the developed concept device also in presence of aerodynamic loads, calling for further studies on full scale real prototypes; other solutions are also under investigation for the guide element, to prevent from load concentration on SMA element.

References

[1] Stanewsky E., 2001, "Adaptive Wing and Flow Control Technology" – Progress in Aerospace Sciences, Elsevier Science Ltd., vol.37, pp.583-667

[2] Browman J., Sanders B., Weisshaar T., 2002, "Evaluating the Impact of Morphing Technologies on Aircraft Performance" – AIAA J. 2002-1631

[3] Poonsong P., 2004, "Design and Analysis of a Multi-Section Variable Camber Wing" – Master's thesis, University of Maryland

[4] Monner H.P., Bein T., Hanselka H., Breitbach E., 1998, "Design Aspects of the Adaptive Wing – The Elastic Trailing Edge and the Local Spoiler Bump" – Royal Aeronautical Society, Multidisciplinary Design and Optimization, London, October 1998

[5] Gevers Aircraft Inc., 1997, "Multi-Purpose Aircraft", United States Patents Office, Patent Number 5,645, 250

[6] Pendleton E., 2000, "Active Aeroelastic Wing" – AFRL Technology Horizons, vol.1, no.2, June 2000, pp.27-28

[7] Statkus F.D., 1980, "Continuous Skin Variable Camber Airfoil Edge Actuating Mechanism" – United States Patent No. 4,351,502, The Boeing Company, Seattle, WA

[8] Inman D.J., 2001, "Wings: Out of the Box. Determining Actuator Requirements for Controlled Morphing Air Vehicles – Aerodynamic Loads" – DARPA Technology Interchange Meeting, Wright Patterson Air Force Base, Dayton, Ohio, Nov. 2001

[9] Kauffman G.B., Mayo I., 1993, "The metal with a memory" – Invent. & Tech. vol.9, no.2, pp.18-23

[10] Buehler W.J., Gilfrich J.V., Wiley R.C., 1963, "Effect of low-temperature phase changes on the mechanical properties of alloys near composition TiNi" – Journal of Applied Physics, vol.34, pp.1475

[11] Chopra I., 2002, "Review of State of Art of Smart Structures and Integrated Systems" – 42nd AIAA/ ASME/ASCE/AHS/ASC Structures, Structural Dynamics, and Materials Conference, Seattle, WA, AIAA Journal, vol.40, no.11

[12] Liang C., Rogers C.A., 1990, "One-Dimensional Thermomechanical Constitutive Relations for Shape Memory Material" – Journal of Intelligent Material Systems and Structures, vol.1, no.2, pp.207-234

PAPER

"A Novel SMA-Based Concept for Airfoil Structural Morphing"

S. Barbarino, R. Pecora, L. Lecce, A. Concilio, S. Ameduri, E. Calvi

A Novel SMA-based Concept for Airfoil Structural Morphing

S. Barbarino, R. Pecora, L. Lecce, A. Concilio, S. Ameduri, and E. Calvi

(Submitted September 16, 2008; in revised form November 28, 2008)

The adaptive structures concept is of great interest in the aerospace field because of the several benefits which can be accomplished in the fields including noise reduction, load alleviation, weight reduction, etc., at a level in which they can be considered as compulsory in the design of future aircraft. Improvements in terms of the aerodynamic efficiency, aeroelastic behavior, stability, and manoeuvrability performance have already been proved through many international studies in the past. In the family of the Smart Materials, Shape Memory Alloys (SMA) seem to be a suitable solution for many static applications. Their high structural integrability in conjunction with actuation capabilities and a favorable performance per weight ratio, allows the development of original architectures. In this study, a morphing wing trailing edge concept is presented; morphing ability was introduced with the aim of replacing a conventional flap device. A compliant rib structure was designed, based on SMA actuators exhibiting structural potential (bearing external aerodynamic loads). Numerical results, achieved through a FE approach, are presented in terms of trailing edge induced displacement and morphed shape.

1. Introduction

Because several flight regimes occur during a typical aircraft mission, it is practically impossible to define a single configuration able to maximize aerodynamic efficiency, manoeuvrability, stability, fuel consumption and so on in any circumstance.

Currently, a common design strategy is to identify few dominant flight regimes within a typical mission and define a specific set of parameters like wing body geometry and control surfaces attitude, with respect to which the aircraft performance is maximized. In this way, drawbacks within conditions that fall outside the design range are unavoidable. Solutions characterized by a certain adaptivity level can lead to overcome these limits. Components like ailerons, flaps, equilibrators, together with the related actuation strategies, correspond somehow to

the necessity of facing very different states, even dramatically far from the nominal design ones (e.g., take-off and landing) (Ref 1).

To simplify the actuation chain and deform a limited part of the structure, these movable devices are confined to limited regions of the wing; this causes, however, sharp shape modifications, badly affecting the aerodynamic field and, due to the concentration of the external loads around the hinges zone, a significant increase of the structural weight. Classical actuator systems generally lead to a 50% increase in weight relative to a naked wing.

To avoid such problems, different design strategies have been taken into account. An interesting one was implemented within the 3AS (Active Aeroelastic Aircraft Structures) European Project, (Ref 2, 3). By controlling the rigidity of some parts of a wing, the suitable displacement field corresponding to the said optimal configuration for a specific flight regime was attained. This strategy, recalling the classical aeroelastic tailoring philosophy, was applied to an all-movable vertical tail (AMVT), and led to an integrated shaft with a variable stiffness. Instead of using the external loads to deform the aerodynamic surfaces, the so-called 'morphing' strategy may be pursued. In this case, large and distributed deformation of specific parts of the wing body are achieved by generating proper internal forces (Ref 4-6). In order to reach this objective, leading and trailing edges have to be designed to withstand the external loads and undertake dramatic deformations, following the selected flight regime requirements (Ref 7, 8). Large displacement capabilities associated with load bearing capacities is the paradox which the smart or adaptive structure systems have to overcome in order to provide a reliable alternative to classical devices. In this article, the proposed solution to eliminate the above paradox is to refer to actuators that play a structural role, also.

The use of smart materials has a crucial role in this challenging approach. What the authors use in the research

S. Barbarino, R. Pecora, and **L. Lecce**, Department of Aerospace Engineering, University of Naples "Federico II", Via Claudio 21, Naples 80125, Italy; **A. Concilio** and **S. Ameduri**, Smart Structures Lab., The Italian Aerospace Research Centre (CIRA), Via Maiorise, Capua, 81043 CE, Italy; and **E. Calvi**, ALENIA AERONAUTICA S.p.a., Viale dell'Aeronautica snc, Pomigliano d'Arco, 80038 NA, Italy. Contact e-mail: silvestro.barbarino@gmail.com.

herein presented, are the Shape Memory Alloys, SMA. Their Super Elastic and Shape Memory properties, jointly with their capacity to transmit large loads, make them a privileged material for applications that require both large strains and high actuation forces (hundreds to thousands of Newton for classical commercial elements) (Ref 9).

In this article, the design of an adaptive flap, driven by SMA-based actuators, is illustrated (Ref 10, 11). More in detail, by taking advantage of a FE approach and implementing an SMA descriptive model (Ref 12), the concept of an original rib is dealt with. This structural element is made of different plates that are connected to each other through crossed spring laminas. These are in charge of providing a certain amount of rigidity to the structure, assuring the required preload for the SMA elements and allowing for large relative rotations. SMA elements are wires, located under the springs, which connect two consecutive plates. When they are activated, their contraction leads to a rotation of the rib parts, with consequent camber variations. External aerodynamic loads are considered when the system performance is evaluated; in detail the configuration corresponding to a traditional rotated flap is referred to.

On this architecture, an optimization study is carried out, over certain selected architecture parameters such as the springs, length, their angular position, and location. SMA mechanical properties and geometry are also considered. Results are presented in terms of achievable camber variations and trailing edge displacements.

2. Architecture Working Principle and Modeling Strategy

The considered structure is sketched in Fig. 1. It is made of five bulkily shaped panels, connected in couples by crossed laminas, working as spring elements. The single panel may be assumed to be rigid in the performed study; the set of five constitutes the skeleton of the rib.

The connecting thin plates (beams in a 2D representation, shown in the same figure) exhibit the necessary elastic properties to allow the architecture undergo suitable deflections. Their rigidity is tuned so that deflections related to the external loads are restricted into small fractions of the ones associated with the driving commands.

The proposed actuator system is composed of the union of the active SMA wires and the spring elements. They are thought to show cyclic behavior and to carry out the prescribed external load, i.e., to have a structural purpose that is a function of their characteristic elasticity. These components can be referred to as "bearing actuators." The activation of SMA generates a contraction of the wires that in turn causes, because of the eccentricity with respect to the spring subsystem center of rotation, a relative angular movement of the bulk plates.
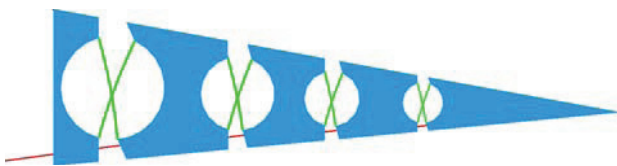
Fig. 1 Rib architecture

SMA ribbons and rods are also considered in the following discussion.

The used springs show a nonlinear behavior, because of the translation of the rotation pivot during deflection. This property goes into the direction of achieving in principle higher preloads for SMA wires recovery and larger relative rotations, while assuring the desired rigidity levels. These properties are strongly dependent on some geometric parameters, as shown in the next paragraph; then, by properly adjusting those values, the performance may be improved or optimized.

MSC/Nastran FE models were set up to investigate the behavior of the described structural system, integrated with an external proprietary Matlab routine aimed at simulating the behavior of the SMA elements, implementing the Liang and Rogers' 1D model (Ref 12). The assumptions, this model is based on, are coherent with the working modality of the actuators: no bending actions (the wires are hinged with the rib panels) and 1D behavior of the material (strain recovery is thought to occur only along the axial direction). Liang and Rogers' is an approximation of the former Tanaka's model (Ref 13), substituting exponential with sinusoidal expression in the description of the material composition (austenite versus martensite fraction, ξ_M and ξ_A), function of the temperature, T, and the stress field, σ:

$$\xi = \frac{\xi_M}{2}\cos[a_A(T - A_S) + b_A\sigma] + \frac{\xi_M}{2} \quad \text{Austenite} \rightarrow \text{Marteniste}$$

(Eq 1)

and

$$\xi = \frac{1 - \xi_A}{2}\cos[a_M(T - M_F) + b_M\sigma] + \frac{1 + \xi_A}{2}$$

Marteniste → Austenite

The values $a_A = \pi/(A_F - A_S)$ and $a_M = \pi/(M_S - M_F)$ are combinations of the material characteristic constants, A_F, A_S, M_F, M_S, namely, austenite final, austenite start, martensite final, and martensite start temperature, respectively. They refer to the beginning or the completion of phase transformation and define when a particular crystal structure appears or when the conversion is complete. Two other parameters appearing in the above formulas are $b_A = -a_A/C_A$ and $b_M = -a_M/C_M$, C_A and C_M being the slopes of the linear relationship between stress and temperature characteristic transformation.

Non-linearity assumption is necessary in order to properly consider the large strains, the characteristic of an SMA application. SMA-active elements are simulated through thermal 1D elements characterized by a negative expansion coefficient (SMA contracts as the temperature increases). Following activation, the structure deforms under the action of the wires. They both undergo a stressed condition. The attained displacement is associated with the computed SMA material stress. This operation is repeated for increasing values of the activation temperature, so that the dot-line curve in Fig. 2 may be sketched. As the force increases, the strain also does and because of the large strains attained, the classical non-linear behavior is shown (smaller strains for an equal increase of the forces). The initial configuration is assumed to have an offset of a roughly 5% strain, while the starting point of the operative function is at 3%, corresponding to the imposed recoverable strain for repeated cyclic applications (Ref 14, 15). In reality, the SMA wires will exhibit growing contractions until it

transforms completely into austenite. This is represented by the intersection point of the dot-line curve with the dotted curve that is the graphical representation of the constitutive material law for a generic SMA. The intersection point determines then the working condition of the proposed actuator. This kind of procedure allows reaching the "maximum" recoverable strain. The process may instead be stopped at a certain point, not letting the material undergo the complete phase transformation (partial recovery).

The process herein described is a simplification of the followed strategy. In fact, in order than the process may be cyclic, the activation point shall be moved at a prestressed configuration and, particularly, fixed at the complete martensite state. This assures the capability of recovering the maximum value of strain (complete transformation martensite-austenite is thus accessible). As the activation takes place (austenite start), the working point moves toward higher stress values. The final point is established when the desired strain recovery percentage is attained that is a function of the cycles number to be faced (Ref 14, 15).

From a figurative point of view, increasing temperature makes the SMA material curve to move up in the 2D stress-strain material plane and the working point to shift towards left, over the lower boundary of the SMA material curve (austenite transformation). On cooling the wire, the process is reversed under the action of a recalling force that makes the SMA to transform again into the martensite phase. The working point in this case runs over the upper part of the SMA material curve (martensite transformation). Thus, in the loading phase, the

transformation may be said to be temperature driven; and in the recovery phase, stress driven.

3. Aerodynamic Loads

The aerodynamic load computation has been addressed by assuming the RA 18-43NIL1 as wing airfoil; the RA 18-43NIL1 is a typical wing airfoil used in regional transport aircraft. In Fig. 3 the RA 18-43NIL1 geometry is plotted and some related parameters are indicated.

Points O and P are, respectively, called *leading* and *trailing edge* while the segment OP is referred to as the airfoil chord c. The chord divides the airfoil boundary curve in two parts: the *upper camber* (represented by the curve connecting O to P in a clockwise orientation) and the *lower camber* (represented by the curve connecting P to O in a clockwise orientation). The airfoil *mean camber line*, or more synthetically, the airfoil *camber line* is defined as the locus of the centers of circles tangent both to upper and to lower cambers.

Referring to the coordinate system of Fig. 3, the function $z_C = z_C(x)$ describing the camber line is given by $z_C(x) = [z_U(x) + z_L(x)]/2$, where $z_U = z_U(x)$ and $z_L = z_L(x)$ are the functions describing the upper and lower cambers. An airflow characterized by a velocity vector V induces a pressure distribution on the airfoil, along the upper and the lower camber, essentially related to: the shape of the airfoil, the magnitude of V, the air density, ρ, and the airfoil *angle of attack* defined as the angle between the airfoil chord and the direction of V.

Approximating the upper and the lower camber by means of n linear segments delimited by points A_i and A_{i+1} ($i = 1 \ldots n$ 1), the pressure p_i arising on each segment A_iA_{i+1}, can be expressed according to the following equation:

$$p_i = \frac{1}{2}\rho V^2 C_{p,i} = qC_{p,i} \qquad \text{(Eq 2)}$$

where $q = \rho V^2/2$ is called the *dynamic pressure* and $C_{p,i}$ the *local pressure coefficient*. The local pressure coefficient $C_{p,i}$ is a non-dimensional parameter whose value depends on the orientation of the segment A_iA_{i+1} in the airflow and therefore by the airfoil shape and angle of attack. The evaluation of the local pressure coefficients is usually performed by means of specific numerical methods of computational aerodynamics. In this study, they were evaluated by means of a two-dimensional vortex lattice method (VLM) (Ref 16).

A split-flap was considered, hinged at a distance of $0.7c$ from the airfoil leading edge; the wing airfoil portion between $0.7c$ and c was assumed to be representative of a flap airfoil and rotated around the hinge point in order to simulate the split-flap down deflection. Deflection angles δ between 2 and 24 deg
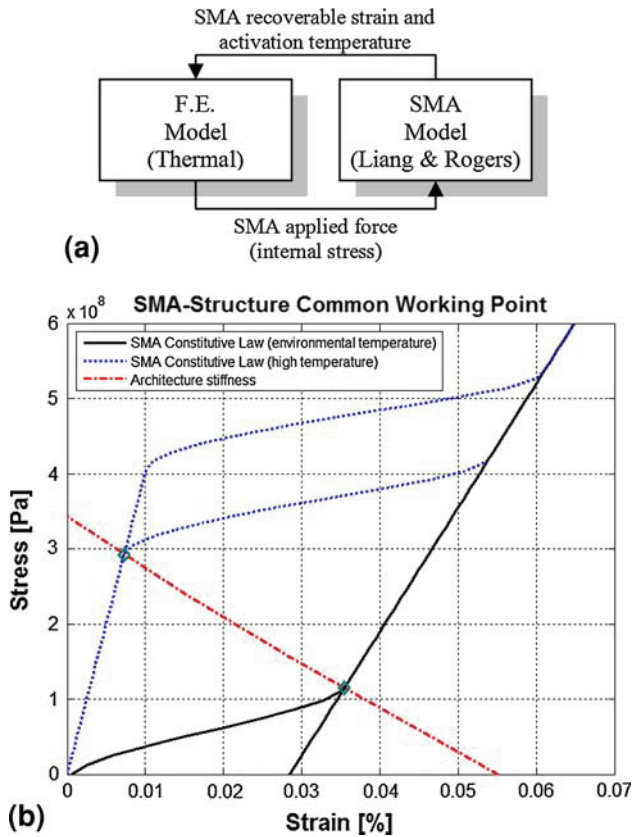
Fig. 2 Simulation scheme adopted for SMA integration within the FE approach
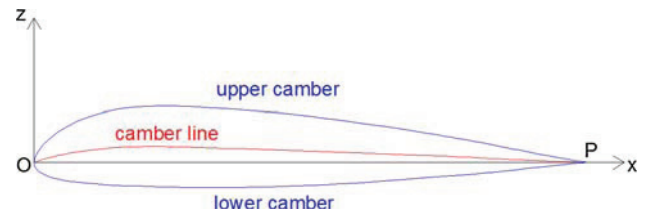
Fig. 3 RA 18-43NIL1 airfoil

were considered; for each step the C_p distribution and the wing airfoil lift coefficient, C_l, were evaluated in correspondence of a 5-deg angle of incidence (angle of attack). The airfoil lift coefficient C_l is defined by the following equation:

$$C_l = \sum_{i=1}^{n} C_{p,i} \left(\underline{n_i} \cdot \underline{\zeta} \right) \qquad \text{(Eq 3)}$$

where n is the number of linear segments used to approximate the upper and the lower camber, $C_{p,i}$ is the pressure coefficient related to the i-th segment, n_i is the normal unit vector of the segment contained in the airfoil plane and positively oriented outwards of the airfoil surface, and ζ is the normal unit vector to the airflow velocity vector V. The airfoil lift coefficient, C_l, is a non-dimensional parameter used to characterize the lifting performance of airfoils or, in other terms, the airfoil's capability to generate a force orthogonal to the airflow velocity direction. Such a force, called *lift*, is responsible of aircraft sustentation and is proportional to C_l; higher C_l leads to higher lift. The obtained C_l values for each examined flap deflection are reported in Table 1 ($C_{l\text{(conventional)}}$).

Let us consider a two-dimensional Cartesian reference system S_0, defined as follows: origin located at the airfoil leading edge; X-axis directed along the non-flapped chord and oriented towards the trailing edge; Z-axis in the airfoil plane and oriented upward. In correspondence of a flap rotation δ_i, around the hinge point A [$0.7 \cdot c$; Z_A], the trailing edge moves from the point P [c; 0] to the point P', defined by the coordinates: $X_{P'} = 0.7 \cdot c + \overline{AP} \cdot \cos(\alpha + \delta_i)$, $Y_{P'} = \overline{AP} \cdot \sin(\alpha + \delta_i) - Z_A$ where $\alpha = \sin^{-1}\left(0.3 \cdot c / \overline{AP} \right)$. Fixed by the same trailing edge position due to a δ_i flap deflection, a quadratic morphing law was imposed to the camber line related to the flapped airfoil. In detail, the motion of point P to point P' was obtained by morphing the flapped airfoil camber line according to a parabolic arch connecting the point A to the point P', and the tangent in A to the wing airfoil camber line (Fig. 4). Camber line morphing was obviously obtained by means of a congruent morphing of the upper and lower cambers of the flapped airfoil.

According to this procedure, for each of the previously investigated hinged flap rotations, a corresponding morphed flap shape was found and the related global C_l was evaluated. The obtained results are reported in Table 1 ($C_{l\text{(morphed)}}$). In Fig. 5, the wing airfoil C_ls related to conventional split and morphed flap are compared for each δ_i. For a given trailing edge down-deflection, the morphed flap solution leads to higher wing airfoil C_l than the conventional split solution.

The morphed flap configuration leading to a wing airfoil $C_l = 2.09$ was considered the most satisfactory from an aerodynamic performance point of view, and was chosen as the target of this. It corresponds to a 12-deg deflection angle and a 160-mm vertical trailing edge displacement.

A morphed flap portion of span b = 300 mm was then considered for aerodynamic load evaluation purpose. Let us call, MS_a and MS_b, the two morphed flap airfoil shapes which delimit the flap portion. Considering the generic aerodynamic

strip s_i, delimited by two homologues segments A_i,A_{i+1} and B_i,B_{i+1} lying, respectively, on MS_a and MS_b boundaries, according to (2), the aerodynamic load acting normally to s_i was evaluated as

$$F_{n,i} = q S_i C_{p,i} \qquad \text{(Eq 4)}$$

where q is the dynamic pressure, S_i is the strip area, given by the product of the span, b, between the segments A_i,A_{i+1} and B_i,B_{i+1}, and length d_i; $C_{p,i}$ is the pressure coefficient, assumed equal for both segments A_i,A_{i+1} and B_i,B_{i+1}. A dynamic pressure of around 1500.00 N/mm^2 was considered, typical for take-off and landing of a regional transport aircraft. Using Eq 4, the aerodynamic load distribution acting on the flap portion was evaluated; this load distribution was then used for a proper sizing of the ribs to be located at the end of the investigated wing portion.
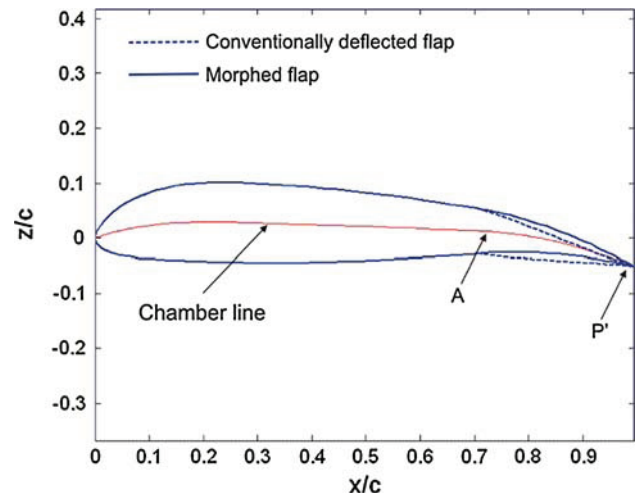
Fig. 4 Wing airfoil shapes corresponding to conventionally deflected flap and morphed flap
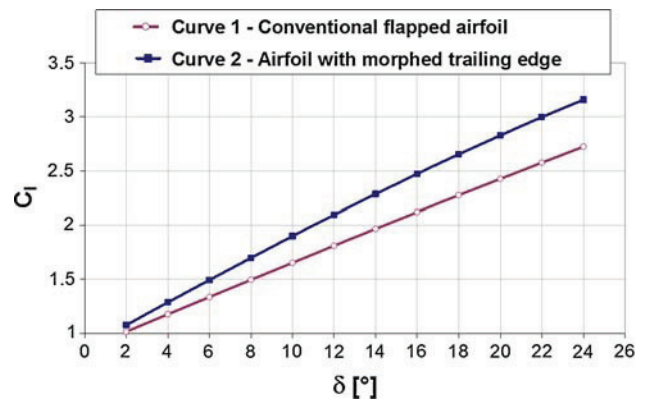
Fig. 5 Wing airfoil C_l comparison

Table 1 Wing airfoil C_l for several flap deflection angles

δ, °	2	4	6	8	10	12	14	16	18	20	22	24
C_l (conventional)	1.0155	1.1760	1.3359	1.4950	1.6532	1.8103	1.9663	2.1209	2.2740	2.4253	2.5749	2.7224
C_l (morphed)	1.0760	1.2866	1.4944	1.6990	1.8996	2.0956	2.2868	2.4727	2.6530	2.8275	2.9962	3.1589

4. Design Criteria of the Elastic Hinge

A parametric study was carried out on the aforementioned architecture. Since the elastic hinges play a fundamental role, the first efforts were focused on the identification of their optimal configuration. Through a FE approach, a single element was studied: its performance was estimated with respect to the cross plates length, d, and their relative angle, γ (Fig. 6). Discrete values for both parameters were assumed: 100, 120, and 140 mm for d; 60, 90, 120, and 150 deg for γ. A total of 12 runs were carried out to exploit all the possible combinations. Values higher than 150 deg were not considered, because of practical integration problems. The spring thin plates were assumed to be made of titanium, to meet both typical aeronautic lightness requirements and high allowable stresses, within the elastic range of the material.

The first phase was aimed at evaluating the performance dependence on the hinge geometry. Laminas, rectangular cross section was considered constant and set to 3×8 mm^2. Dimensions were defined according to design considerations based on the required flexibility and rigidity of the structure, together with the necessity of attaining a sufficient SMA preload and the capability of sustaining sufficient stress levels during actuation. SMA element features were fixed as follows: a wire 280-mm long, with a 0.5-mm diameter, called to recover a max strain of 3% (Ref 14, 15) with respect to its original length (martensite phase); further details can be found in Table 3.
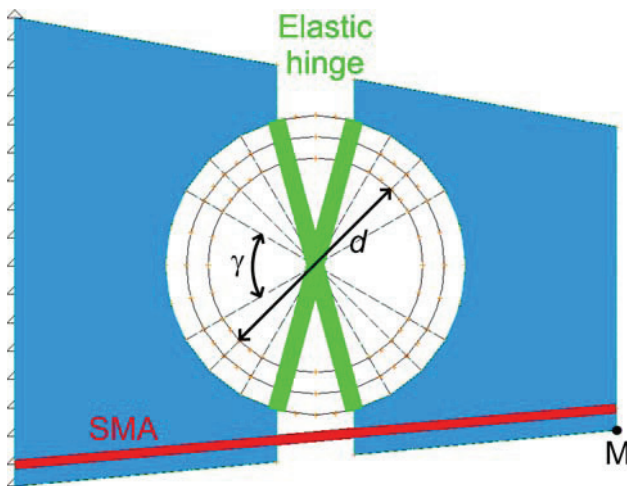
Fig. 6 Single elastic hinge scheme adopted for the parametric study

The results obtained are expressed in terms of hinge rotation and vertical displacement of the trailing edge. They are normalized and presented as histograms in Fig. 7, while actual values are reported in Table 2.

As a result of this first study, the max performance is achieved by maximising both d and γ: in this case, a displacement of 16.48 mm and a rotation of 5.91 deg is obtained ($d = 140$ mm; $\gamma = 150$ deg).

Assuming then the above parameters as the optimal configuration, further investigations were carried out by changing the SMA element characteristics and dimensioning the plate's cross section to withstand SMA preload and actuation requirements.

The active component properties were not made to change as a parametric variation but for modifying its nature, instead. Ribbon and rod forms were tested. The architecture of the actuators was maintained the same in each of the three cited cases, as well as the mechanism by which the load is transferred to the structure (two hinges). In Table 3, the features of the different SMA elements taken into account are reported, basing on experimental tests of material characterization carried out in our laboratory (Ref 17-19); length was set as the original, at 280 mm.

For the sake of clarity, it is useful to explain the exact meaning of the martensite and austenite Young moduli. The behavior of an SMA material is generally nonlinear, having to consider transformation between a phase and another and, contemporaneously having to take into account both the phases. However, when the transformation fully occurs (in a sense or the other), the material behaves as a classical linear one with distinct elastic moduli for the austenite and martensite status, respectively, E_A and E_M. Typically, E_M is one-third of E_A. Given the maximum recoverable strain ε_{max} for a given SMA, maximum recoverable force may be attained as:

$$F_{max} = E_A A \varepsilon_{max} \qquad \text{(Eq 5)}$$

SMA commercial products were considered in the comparison. The use of different SMA materials for the different forms (wires, ribbons, rods) does not allow for an immediate comparison of the results but gives an idea of what can be expected in the different cases.

As already mentioned, preload is necessary to guarantee a full cyclic behavior inside the boundaries of the environmental and the austenite finish temperature (A_f), i.e., to guarantee the working point to run a complete loop over its martensite-austenite-martensite transformation. Because of this necessity, preload requires stiffer elastic elements for stiffer active elements: Table 3 shows the necessary preload for the diverse material typology and cross section. Furthermore, max stress
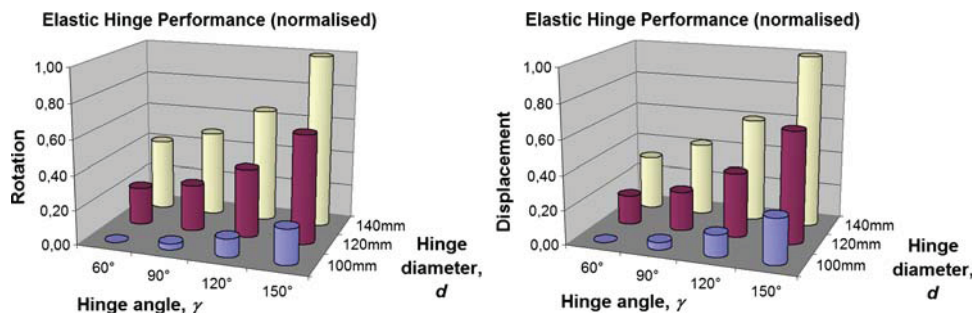
Fig. 7 Normalized performance of the elastic hinge vs. length, d, vs. relative angle

Table 2 Performance of the elastic hinge vs. length, *d*, vs. relative angle, γ

	Rotations				Displacements			
d/γ, mm	60°	90°	120°	150°	60°	90°	120°	150°
100	5.7452	5.7509	5.7624	5.7778	0.01615	0.01617	0.01619	0.01624
120	5.7807	5.7887	5.8094	5.8466	0.01621	0.01623	0.01627	0.01636
140	5.8122	5.8248	5.8512	5.9068	0.01626	0.01629	0.01635	0.01648

Table 3 SMA actuators features (Ref 17-19)

	Wire	Ribbon	Rod
Cross section dimensions	0.5 mm diameter	1.0×10 mm	5.0 mm diameter
Cross section area	0.196 mm^2	10 mm^2	19.63 mm^2
Young's Modulus of Austenite E_A	24.67 GPa	40.18 GPa	28.16 GPa
Young's Modulus of Martensite E_M	18.27 GPa	16.5 GPa	8.78 GPa
Martensite start temperature	35 °C	43.3 °C	10 °C
Martensite finish temperature	12.6 °C	27.5 °C	−20 °C
Austenite start temperature	59.3 °C	47.3 °C	39 °C
Austenite finish temperature	85.9 °C	58.9 °C	82 °C
Stress necessary to achieve 3% strain (preload)	175 MPa	155 MPa	165 MPa
Force necessary to achieve preload	35 N	1550 N	3239 N
Maximum recoverable force (actuation)	∼550 N	∼8000 N	∼15000 N

Table 4 Results summary of the plate cross section dimensioning

	Wire	Ribbon	Rod
Elastic hinge cross section dimensions	3.0×8.0 mm	8.0×20 mm	8.5×32 mm
Elastic hinge cross section area	24 mm^2	160 mm^2	272 mm^2
Elastic hinge material	Titanium	Titanium	Titanium
Elastic hinge estimated weight	29.75 g	198.37 g	337.23 g
SMA preload			
SMA force level	35.65 N	1550.08 N	3238.69 N
Elastic hinge max stress	128 MPa	317 MPa	366 MPa
SMA actuation			
SMA force level	79.43 N	3426.84 N	6686.59 N
Elastic hinge max stress	289 MPa	715 MPa	769 MPa
Hinge performance			
Net displacement	13.217 mm	12.788 mm	12.495 mm
Net rotation	5.89 deg	5.67 deg	5.55 deg

following actuation shall be kept inside the titanium elastic range. The elastic hinges were then dimensioned according to a trial and error procedure: an arbitrary cross section was preliminarily assumed and stress conditions were evaluated at preload and activation phases. According to the preliminary outcomes, the cross sections were modified, taking into consideration the inertia moment and aiming at minimizing the total weight and bulk. The final results are summarized in Table 4, for the three configurations. The actuation performance in terms of hinge rotation and trailing edge displacement are finally shown in Fig. 8.

Elastic hinge resulting stress field presents the classical composed normal-bending shape, being caused by an eccentric normal force. Its maximum value is reported in the table and an example of the stress state into the plate components is shown in Fig. 9, where normal stress is shown.

From these results the wire architecture appears to lead to the best actuator performance. This trend is also confirmed when comparing the three configurations in terms of weight and SMA activation temperature (which in turn influences the required energy), estimated through the Liang & Rogers' model-based Matlab routine (Fig. 10).

Although the SMA represents a small amount of the overall weight, related preload and working constraints heavily condition the elastic hinge size. The SMA choice demonstrates once more to be a critical design aspect: an excessive powerful actuator may not lead to better performance while increasing total weight.

5. Design Criteria of the Rib Structure

The higher hinge performance, measured in terms of trailing edge vertical displacement and rotation is thus obtained for the highest values of *d* and γ in the considered interval and for a configuration wire-based SMA. By following these results, the design of the rib was accomplished.

In order to maximize the architecture features, it is necessary to accommodate the largest number of elastic hinges, each
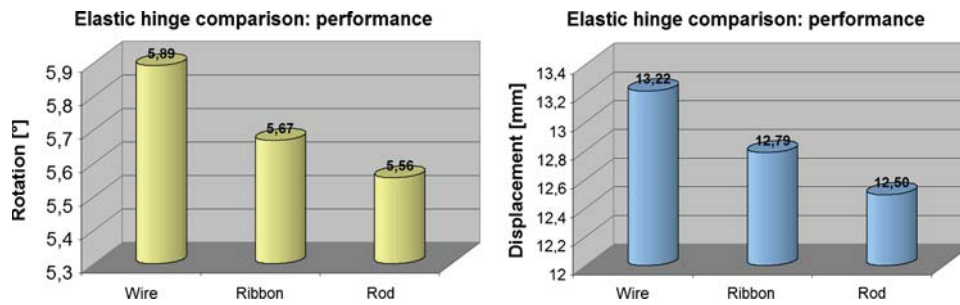
Fig. 8 Performance of the elastic hinge vs. SMA element typology
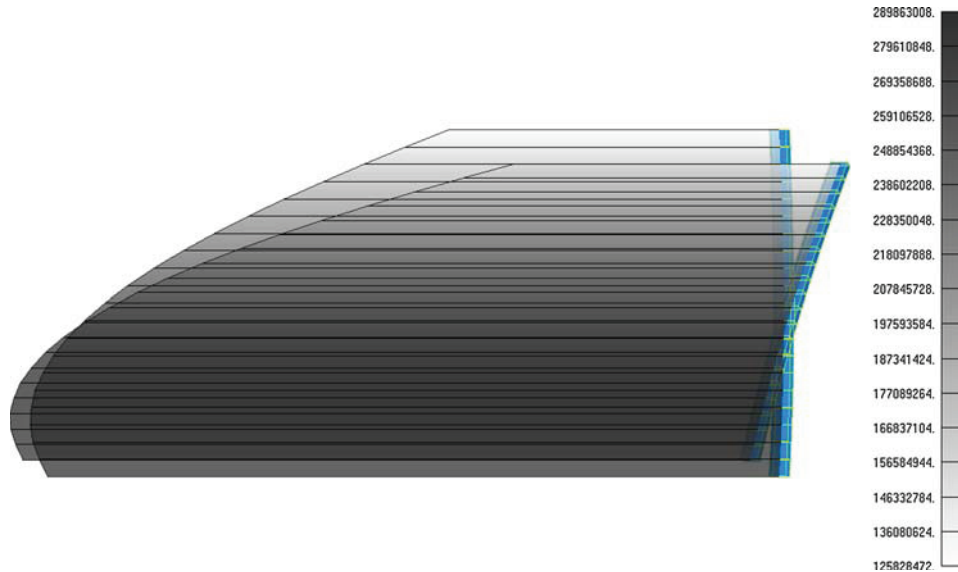
Fig. 9 Stress field distribution into the component plates of a reference hinge (wire solution)
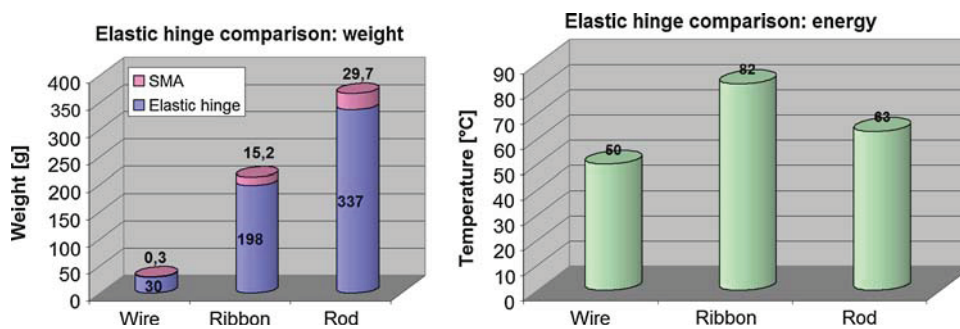
Fig. 10 Weight and SMA activation temperature comparison

characterized by the largest *d* parameter (of course, compatible with the local airfoil thickness) and the defined relative angle γ, in the considered section.

Finally, the actuator length also affects the attainable figures in a direct way (the longer the wire, the higher the performance). In Fig. 11, a sketch of the final rib arrangement is reported, while the design parameters are reported in Table 5.
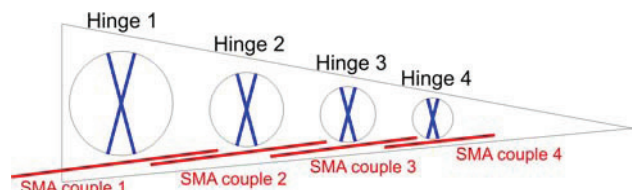
Fig. 11 Elastic hinges disposition within the rib

Table 5 Design parameters for each elastic hinge of the rib

	Hinge 1	Hinge 2	Hinge 3	Hinge 4
Elastic plates length, d	140 mm	100 mm	75 mm	55 mm
Elastic plates cross section	3.0 × 8.0 mm	3.0 × 6.0 mm	2.5 × 6.0 mm	2.0 × 7.0 mm
Elastic plates angle, γ	150 deg	150 deg	150 deg	150 deg
SMA wires length	280 mm	240 mm	200 mm	150 mm

Two SMA wires were considered for each elastic hinge, in order to properly counteract the aerodynamic loads, also being compatible with typical fail-safe design criteria, because of being associated with a certain redundancy level. SMA element splitting together with the geometrical variation of the d parameter, limited by the local airfoil thickness, led to a new sizing of the plate cross sections. Final results are reported in Table 5.

6. Numerical Simulation and Results

Once the final configuration was defined, a FE model was realized; analysis was carried out through MSC/Nastran. 7075 T6 aluminium alloy, 2-mm thick plates were considered for the rib panels. SMA wires were simulated through beam elements with a suitable thermal expansion coefficient (negative). This allowed for simulating the SMA contraction following the activation input; however, the nonlinear numerical analysis was performed by step, until reaching the equilibrium value, shown in Fig. 2(b). SMA beams were hinged at the rib panels in order to avoid any bending stress. In the same way, the titanium elastic hinges were simulated through beam elements.

In order to meet the necessity of attaining cyclic behavior and accessing the maximum recoverable strain, the configuration shall undergo prestress. In the real case, this can be attained by deforming the structure downward and then installing the SMA element. The elastic force tries to restore the initial configuration, deforming the SMA that, in turn, resists this recovery. Now, both the structural elements (elastic hinge) and the SMA wires go through a prestress condition.

The designer's ability is crucial to individualize the structural deformed configuration that is able to generate the stress in the SMA wire that assures equilibrium with the "residual" elastic force at the required "neutral" position (Fig. 12b).

In the numerical simulation, to replay the physical process is difficult enough. Instead the following alternative process may be followed. A non-deformed structure is realized according to the schematic shown in Fig. 12(a). Numerically, this configuration is not loaded (no internal stress) at the level of the crossed laminas or the SMA wires. Starting from this configuration, the rib is brought to the "neutral" condition (Fig. 12b), by activating the SMA via a fictitious negative thermal load. In this condition, both the structure and the wires experience a stress field. In spite of the different theoretical paths, followed to reach this condition, the numerical and the real configuration are conceptually the same. The numerical approach may be said to properly imitate the reality. Finally, a further activation of the SMA wires simulate the action of the active devices aimed at deflecting the proposed flap.
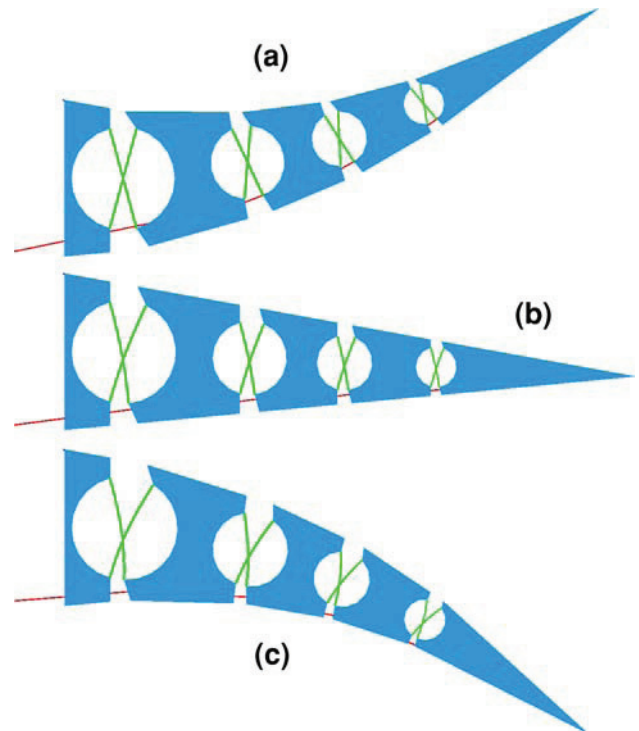
Fig. 12 Adaptive rib reference layouts: unloaded configuration (a); "neutral" position (b); activated rib (c)

Table 6 Preload condition details

	Hinge 1	Hinge 2	Hinge 3	Hinge 4
SMA force level[a]	82.6 N	81.94 N	81.65 N	79.91 N
Elastic hinge max stress	250 MPa	252 MPa	278 MPa	263 MPa
Hinge pre-load angle	10.17 deg	7.32 deg	7.42 deg	6.58 deg

[a]Each hinge has 2 SMA wires as actuator, doubling the necessary preload

Due to the modularity of the referred architecture, intermediate configurations are possible, between neutral and totally extended outline, according to the couples of SMA wires that are activated.

In Table 6, preload details are reported for both the laminas and SMA elements. It can be remarked that the maximum stress level reached in the elastic hinges under activation is always under 700 MPa.

Trailing edge vertical displacement and rotation, with and without aerodynamic loads, are reported in Table 7 for different activation conditions. Figure 13 shows finally the morphed

Table 7 Morphed flap performance: trailing edge displacement and rotation

	Performance without aerodynamic loads		Performance with aerodynamic loads	
	Vertical displacement, mm	Rotation, °	Vertical displacement, mm	Rotation, °
All SMA couples activated	246.7	32.24	223.9 (−9.24%)	29.84 (−7.44%)
Only first couple	84.83	7.01	71.24 (−16.20%)	5.71 (−18.54%)
Only second couple	72.31	7.95	61.2 (−15.30%)	6.83 (−14.08%)
Only third couple	58.33	8.51	49.53 (−15.08%)	7.62 (−10.45%)
Only forth	41.23	8.77	32.37 (−21.48%)	7.88 (−10.15%)
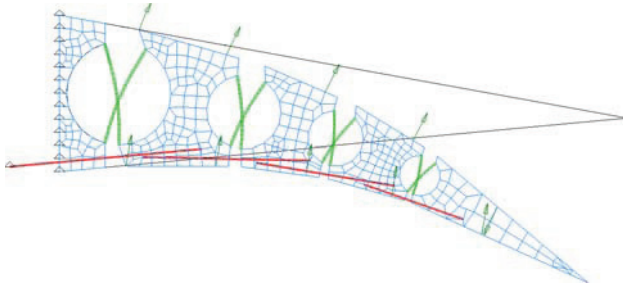
Fig. 13 Rib morphed shape for all SMA wires activated under aerodynamic loads

Table 8 Load conditions for the SMA wires during actuation

	Axial force[a] during actuation (without aerodynamic loads), N	Axial force[a] during actuation (with aerodynamic loads), N
SMA wires for hinge 1	153.27	651.73
SMA wires for hinge 2	183.28	446.09
SMA wires for hinge 3	186.65	310.01
SMA wires for hinge 4	199.21	238.77

[a]Force levels must be divided for the SMA actuators (2 wires for each hinge)

shape of the rib in presence of aerodynamic loads when all the SMA wires are activated.

The rib performance is well over the target of 160-mm trailing edge vertical displacement, estimated to lead to a lift coefficient of 2. Aerodynamic loads affect this result by 9.24% (a 7.44% difference is instead evaluated for rotation). This effect can be easily attributed to the flexibility introduced by the crossed laminas and the major stress level the SMA wires are subjected to (Table 8), however, compatible with their actuation capabilities.

When activating a single couple of SMA wires, vertical displacement and rotation show an opposite behavior; the more the "active" hinge is backward, the more the rotation increases while the vertical displacement reduces.

7. Conclusions and Further Steps

In this article, the design and the optimization of an SMA-based architecture, aimed at producing a morphing flap, have been presented.

The main innovation proposed by this study consists of the specific features of the rib architecture, following the principles of a "smart structure" (integrated, light, compact actuators), which is able both to largely deform itself (morphing) as well as to withstand external loads (bearing actuators).

A multi-body rib is referred to, whose components are linked to each other through elastic hinges made of crossed thin plates. In spite of the large forces produced, all the involved materials work inside the linear range. Geometrically, the configuration has intrinsic nonlinearities, caused by the pivots' translations. This effect has two main consequences: it decreases the effective carried load and increases the net rotation.

In order to maximize the adaptive flap performance in terms of max achievable rotations and vertical displacements, evaluated at the trailing edge, a parametric study was carried out, involving crossed laminas length and their relative angle. The best configuration was found to correspond at the higher values for thin plates length and angle, within the considered intervals.

Another study was then accomplished, by considering three different SMA element typologies: wires, ribbons, and rods. The optimal choice, when performance, compactness, and lightness are considered, was proved to be the wire-based one.

The problem of integrating the optimized elastic hinges within the rib was then faced. In order to obtain the max vertical displacement of the trailing edge, the largest number of these devices was integrated in the spar, considering the compatibility with the local airfoil thickness. Thus, four hinges suitably scaled and characterized by a 150-deg plate's relative angle were figuratively installed in the rib. Each of them presented peculiar characteristics, following the different geometric features, selected in order to guarantee the linear working of the involved materials.

Nonlinear numerical simulations were finally carried out, which can take into account a large number of expected displacements. A dedicated FE model of the rib architecture and the surrounding structure (i.e., skin elements and stiffeners) was realized. MSC/Nastran code was selected for simulations, integrated with an external Matlab routine for replicating the SMA elements behavior. A dedicated procedure was also set up in order to integrate the two programs. External aerodynamic loads were estimated by using a panel method on the morphing airfoil.

The structure behavior with and without aerodynamic loads, under the action of the designed device, was estimated and compared indicating the performance reduction following the presence of the external pressure field. Max displacement proved, however, to stand well above the target of 160 mm, corresponding to a C_L (lift coefficient) of 2.

The sophisticated numerical implementation of the morphing trailing edge herein presented would deserve a wider use. For example, to answer questions linked to the real use of these systems, such as the influence of the SMA actuator geometry

on the cooling time, max achievable actuation frequency etc. This would provide new and interesting details in evaluating the active devices performance in view of the integration on actual elements and will be the subject of future investigations.

In the same way, the active rib design and functionality could be further improved. Attention should be paid to the skin elements: sliding panels or more performing aerodynamic solutions like "elastomeric" skins, which can absorb cyclically large deformations could be examined.

Moreover, the possibility of expanding the proposed device working envelop, as its implementation like an aileron (able to undergo both positive and negative camber variations) shall be considered. Such architecture would require for instance SMA wires working in an antagonistic way, i.e., mounted, respectively, over and under the hinges' location. One of the most important additions to the complexity of the implemented model should be the one of pondering over whether to opt for the SMA Shape Memory or the Super Elastic Effect.

References

1. E. Stanewsky, Adaptive Wing and Flow Control Technology, *Prog. Aerospace Sci.*, 2001, **37**, p 583–667 (Elsevier Science Ltd.)
2. S. Kuzmina, G. Amiryants, J. Schweiger, J. Cooper, M. Amprikidis, and O. Sensberg, Review and Outlook on Active and Passive Aeroelastic Design Concept for Future Aircraft, *ICAS 2002 Congress*, September 8-13, Toronto, Canada, ICAS Vol. 432, 2002, p 1–10
3. J. Schweiger, A. Suleman, S. Kuzmina, and V. Chedrik, MDO Concepts for an European Research Project on Active Aeroelastic Structures, *9th AIAA/NASA/ISSMO Symposium on Multidisciplinary Analysis and Optimisation*, CP Atlanta, GA, 2002
4. J. Spillman, The Use of Variable Chamber to Reduce Drag, Weight and Costs of Transport Aircraft, *Aeronaut. J.*, 1992, **96**, p 1–8
5. H.P. Monner, T. Bein, H. Hanselka, and E. Breitbach, *Design Aspects of the Adaptive Wing—The Elastic Trailing Edge and the Local Spoiler Bump*, Royal Aeronautical Society, Multidisciplinary Design and Optimization, London, 1998
6. J.R. Wilson, Active Aeroelastic Wing: A New/Old Twist on Flight, *Aerospace Am.*, 2002, **40**(99), p 34–37
7. I. Chopra, Review of State of Art of Smart Structures and Integrated Systems, *42nd AIAA/ASME/ASCE/AHS/ASC Structures, Structural Dynamics, and Materials Conference*, Seattle, WA, *AIAA J.*, **40**(11), 2002
8. J. Browman, B. Sanders, and T. Weisshaar, Evaluating the Impact of Morphing Technologies on Aircraft Performance, *43rd AIAA/ASME/ASCE/AHS/ASC Structures, Structural Dynamics, and Materials Conference*, Denver, CO, USA, AIAA Paper 2002-1631, 22-25 April 2002
9. W.J. Buehler, J.V. Gilfrich, and R.C. Wiley, Effect of Low-temperature Phase Changes on the Mechanical Properties of Alloys Near Composition TiNi, *J. Appl. Phys.*, 1963, **34**, p 1475
10. S. Barbarino, S. Ameduri, and R. Pecora, Wing Chamber Control Architectures based on SMA: Numerical Investigation, *International Conference on Smart Materials and Nanotechnology in Engineering (SMN2007)*, 1-4 July 2007, Harbin, China, SPIE No. 6423-077
11. S. Barbarino, R. Pecora, L. Lecce, S. Ameduri, and A. Concilio, Airfoil Morphing Architecture Based on Shape Memory Alloys, *2008 ASME International Conference on Smart Materials, Adaptive Structures & Intelligent Systems (SMASIS08)*, October 28-30, Ellicot City, MD, USA, SMASIS08-480
12. C. Liang and C.A. Rogers, One-Dimensional Thermomechanical Constitutive Relations for Shape Memory Material, *J. Intel. Mater. Syst. Struct.*, 1990, **1**(2), p 207–234
13. K. Tanaka, A Thermomechanical Sketch of Shape Memory Effect: One-Dimensional Tensile Behaviour, *Res. Mechanica*, 1986, **18**(3), p 251–263
14. A.V. Srinivasan and D.M. McFarland, *Smart Structures: Analysis and Design*, Cambridge University Press, ISBN 0-521-65977-9, 1995
15. K. Shimizu and T. Tadaki, *Shape Memory Alloys*, H. Funakubo, Ed., Gordon and Breach Science Publishers, New York, ISSN 0889-860X, 1987, p 1–60
16. A.M. Kuethe and C.Y. Chow, *Foundations of Aerodynamics*, 4th ed., Wiley and Sons, 1986
17. S. Ameduri, P. Caramuta, and F. Lenzi, Experimental Characterisation of an SMA Rod Element for Helicopter Blade Morphing, *Internal Report*, CIRA-CF-08-0185, 2008
18. S. Ameduri, Test report di accettazione per nastri di SMA, *Internal Report* (in Italian), CIRA-TR-06-0215, 2006
19. A. Vigliotti and L. Lecce, Prove su campioni di SMA, *Internal Report* (in Italian), CIRA-TR-06-0346, 2006

PAPER

"Airfoil Morphing Architecture Based on Shape Memory Alloys"

S. Barbarino, S. Ameduri, R. Pecora, L. Lecce, A. Concilio

SMASIS2008-480

AIRFOIL MORPHING ARCHITECTURE BASED ON SHAPE MEMORY ALLOYS

Silvestro Barbarino   **Rosario Pecora**   **Leonardo Lecce**
Aerospace Engineering Dept., Univ. of Naples "Federico II", Naples, Italy

Antonio Concilio   **Salvatore Ameduri**
Smart Structures Lab., Italian Aerospace Research Centre, Capua (CE), Italy

ABSTRACT

The adaptive structures concept is of great interest in the aeronautical field because of the several benefits which can be accomplished in the design of future aircraft. Improvements in terms of aerodynamic efficiency, aero-elastic behaviour and manoeuvrability were proved by many international studies. The development of new structural architectures implementing and integrating innovative materials is mandatory for succeeding in these critical tasks. The so-called Smart Structure idea is more and more taken into account in aerospace applications Among the family of Smart Materials, Shape Memory Alloys (SMAs) certainly represents a convenient solution for many static applications.

In this work, an application for a morphing wing trailing edge is presented as alternative for conventional flap devices. A compliant rib structure has been designed, based on SMA components working both as actuators, controlling wing chamber, and as structural elements, sustaining external aerodynamic loads. Achievable performance has been estimated by a FE approach; SMA behaviour has been modelled through a dedicated routine implementing the Liang & Rogers' model for evaluating the internal stress and the minimum temperature necessary for activation. The numerical results have been presented in terms of induced displacements and morphed shape.

INTRODUCTION

Because of the large variety of flight regimes occurring during a mission, to achieve an omni comprehensive optimized design is practically impossible; in practice, only some mission profiles, the most common and temporally extended, are taken into account and considered as constraints during the design phase.

Among the different aircraft components, the geometry of aerodynamic surfaces (camber, thickness and attitude) is strongly influenced by the flight regimes. they are assumed to prevalently work in; without any alternative technical solution, this approach usually results in a strong penalisation, even for crucial regimes, like take off and landing.

Thus, the idea of adaptive aerodynamic surfaces, [1], i.e. able to change some features to fit the best optimal shape for a specific regime, promises interesting developments. According to this trend, a large amount of investigations [2-6] have been addressed on components like flaps, slats, by pointing out related benefits and drawbacks. More challenging strategies (e.g. variable sweep wings) have been taken into account, remaining, at least for the moment, confined to military applications.

Classical geometry-variation devices, like flaps, exhibit some advantages: they are easy to be integrated within the surrounding structure and do not compromise the wing structural integrity. Moreover, they interest a limited zone of the wing; this simplifies the actuation system architecture that can be practically concentrated close to the hinge zone. However, due to their concentrated nature, they produce discontinuities, sharpening of the geometry and worsening the aerodynamic efficiency. Moreover, connecting zones shall support the transmitted loads with inevitable structural and weight rise.

To avoid these problems, novel strategies are being considered. Among the others, the idea of producing smooth variations of the geometry (i.e. morphing) [7, 8], even in presence of large displacements, is well doing for itself. Of course, extending and distributing the zones whose geometry may vary, means to interest a wider part of the structure. It also gives rise to an interesting paradox: the same structure that has to endure to external aerodynamic loads without suffering

appreciable deformations, has to dramatically change its shape to fit the best current flight condition.

One solution to solve this contradiction is represented by self-deforming materials, playing the twofold role of structural and actuator elements. An example of these materials is constituted by SMA's [9, 10], whose ability of recovering large deformations (Shape Memory Effect), tolerating large extensions (Super Elastic Effect) and providing high transmitted forces, makes them a privileged tool for morphing applications.

The objective of this work is represented by an SMA based on rib architecture, aimed at controlling the airfoil camber on the wing trailing edge by producing a smoothed morphed flap. This architecture has been conceived to be integrated within an RA-18-43NIL1 airfoil, originally provided with a split flap whose hinge axis is located at 70% of mean aerodynamic chord.

The main innovation of the architecture herein presented is constituted by the role played by the SMA elements, no more used only as actuators, but also assigned with a structural function.

The proposed rib is a multi-body panel, whose parts are connected each others by elastic springs. They are called to assure whether the necessary structural bending rigidity or the initial SMA pre-load, to restore the initial shape after activation. The relative rotation of the different parts is controlled by SMA rod elements, able to act both as struts and tie-beams.

The design and the simulation of the architecture take advantage of a combined numerical approach: a commercial FE code (MSC Nastran) is exploited to predict structural deformations under the joint action of external loads and SMA elements; the specific SMA behaviour is instead predicted through a dedicated code, implementing the Liang & Rogers' model, [11].

The numerical predictions are addressed by considering external aerodynamic loads, computed on the deformed shape Achieved results have been expressed in terms of trailing edge vertical displacements, rotations, and attained airfoil shape. A comparison with a traditional flapped architecture concludes the work.

ARCHITECTURE WORKING PRINCIPLE

The architecture has been designed to meet the requirements of a flap of a traditional, short range commercial aircraft: hence, the chord of this flap is 0.77m (30% of the wing shape chord), while the maximum thickness is of 0.21m; the flap cross section in the evaluations presented has been supposed constant.

The architecture investigated in the following is constituted by a rib split into five panels connected each others by spring plates disposed to form "X" structural elements (see Fig. 1). This latter design choice, despite of its evident complication (the plates cannot lay on the rib plane, to avoid overlapping problems) exhibits interesting advantages.

First: the angular pivot is not fixed, but moves itself during rotations, by conferring a non linear behaviour to the springs; as a consequence, even in presence of wide angular deformations, related stress field remains limited, preventing from structural collapses. Second: due to aforementioned non-linear nature, it is possible to pre-strain the springs and mount SMA rods, so that desired pre-load may be achieved. Third: jointly with the SMA rod,, acting prevalently (under expected aerodynamic loads) as tie beam, they assure necessary bending rigidity. Due to the necessity of exploiting the best such peculiarities, many efforts has been focused on the dimensioning of the springs, as it will shown in the next paragraphs.
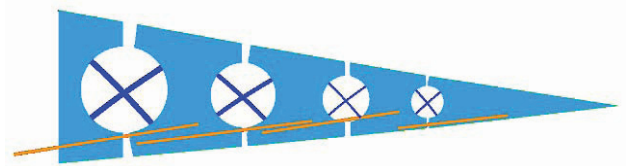
Fig.1 . Architecture main components.

The rotation of the different components is commanded by SMA rods acting as external "by pass" with respect to the springs. Their plane disposition has been chosen to maximise recoverable deformations (i.e. recoverable angles). Also the decision of splitting the rib into five parts is the result of a compromise between the necessity of achieving a final morphed geometry as smooth as possible and reducing the structural complexity of the architecture.

To have an idea of the effective integration of the rib within the wing structure, a 3D sketch has been illustrated in Fig. 2.

Each rib plate is linked through upper and lower aluminium skin elements to the corresponding one along the span; this multi-body solution has been preferred to the global one constituted by a unique classical skin panel, because structurally incompatible with the large expected deformations.
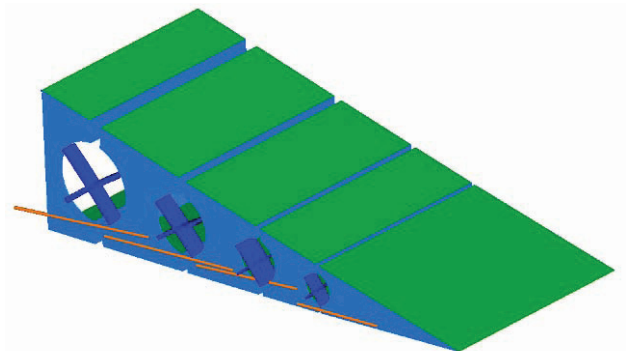
Fig.2 . 3D scheme of the rib architecture.

To increase the ability of the flap to endure external (aerodynamic) and internal (SMAs) loads, lateral folding of the skins have been performed.

2   Copyright © 2008 by ASME

Finally, it is possible to identify three different flap configurations (see Fig. 3).

The first one (Fig.3 (a)) corresponds to no activated neither preloaded SMA rods; the flap is in this condition before mounting the SMA rods; then, starting from this configuration, the flap is mechanically brought to the "neutral" condition (Fig.3 (b)), in which SMA are integrated: SMA elements are subjected to the pre-load due to elastic reaction of the structure, but no activated; finally (Fig.3 (c)), the configuration of the flap totally extended is achieved, by heating SMA rods.
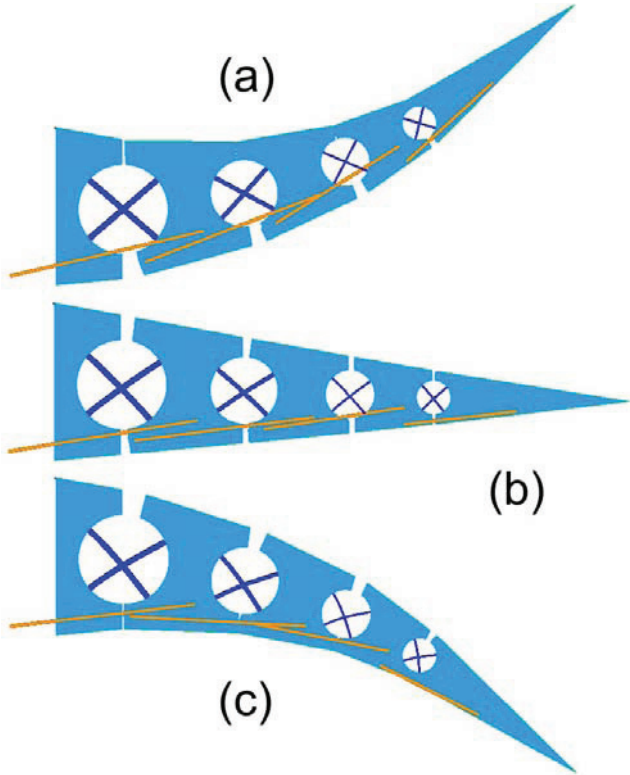
Fig.3 . Flap main configurations: no active neither pre-l oaded SMA (a), "neutral" position (b), flap completely exte nded (c).

Of course, due to the modular nature of the flap, intermediate attitudes, between neutral and totally extended configurations, are possible, according to the number of SMA rods activated.

SIMULATION STRATEGY

To predict the performance of the morphed flap, a FE approach has been adopted. Since no SMA model has been implemented within MSC/Nastran FE code, an external routine in Matlab has been written to simulate the behavior of the alloy; a suitable procedure has been realized in order to simulate the action of the SMA element, integrated within the rib structure. Due to the expected large deformations, a nonlinear analysis has been implemented. Concerning with SMA modelling problem, the Liang and Rogers 1D model [11] has been implemented. This model was developed in 1990,

basing on Tanaka phenomenological approach [12]; however, even adopting the same constitutive law of Tanaka, Liang and Rogers assumed, for the phase kinetics, a simpler cosine relationship to describe the martensite fraction as a function of stress and temperature:

$$\xi = \frac{\xi_M}{2}\cos\left[a_A(T - A_S) + b_A\sigma\right] + \frac{\xi_M}{2}$$

and $\quad$ (1)

$$\xi = \frac{1 - \xi_A}{2}\cos\left[a_M(T - M_F) + b_M\sigma\right] + \frac{1 + \xi_A}{2}$$

where $\quad a_A = \pi/(A_F - A_S) \quad$ and $\quad a_M = \pi/(M_S - M_F) \quad$ are combinations of material constants: A_F, A_S, M_F, M_S are material characteristic temperatures, respectively known as austenite final, austenite start, martensite final and martensite start. They refer to phase transformations of the material and define when a particular crystal structure appears or the conversion is complete. Two other combinations of the material constants are $b_A = -a_A/C_A$ and $b_M = -a_M/C_M$, being C_A and C_M the slopes of the straight lines approximating the functions relating the four temperatures to the acting stress. Finally, ξ_M and ξ_A are the martensite and austenite volume fractions present in the alloy before heating and cooling, respectively.

The FE approach used to simulate structure behavior is based on the assumption that the SMA, working as actuator, generates large displacements, recovering an assigned deformation without undergoing bending actions, coherently with the adopted 1D model. Furthermore, the hinge connection of the SMA with the surrounding structure avoids any bending stress.

In Fig. 4, the logical scheme adopted for simulations is illustrated.

(a)

Copyright © 2008 by ASME
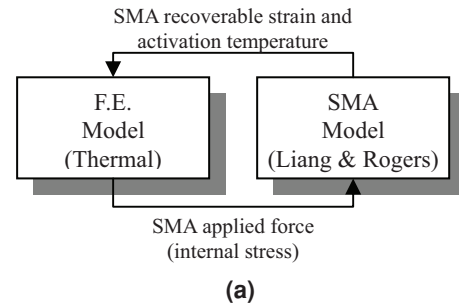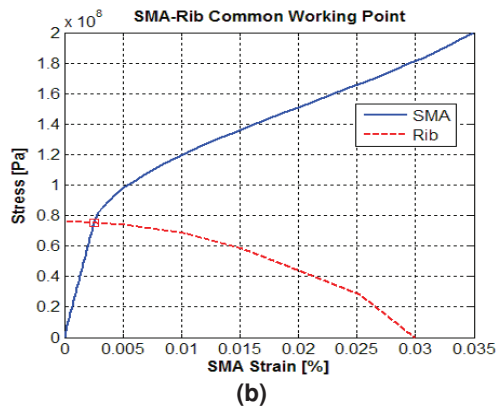
(b)
Fig.4 . SMA model integration within a FE approach.

At first, a non linear analysis on the structure for different values of the equivalent thermal coefficient is carried out, in order to relate the forces to be provided by the SMA actuator with the displacements transmitted to the structure (a maximum strain recovery of 3% in length is considered); then, the corresponding curve is compared with the SMA force-displacement curves, estimated by the Liang and Rogers model for several temperatures values; among the different curves, the Matlab routine finds out the one corresponding to the minimum activation temperature, whose intersection with the structure curve gives the effectively recoverable strain; finally, the equivalent thermal expansion coefficient in the FE simulation is updated to meet the solution found out by the afore described procedure.

AERODYNAMIC LOADS

The considered airfoil is a RA 18-43NIL1 provided with a split flap whose hinge axis is located at 70% of mean aerodynamic chord; aerodynamic loads have been evaluated on a wing portion whose span has been imposed equal to 300 mm. The distribution of pressure coefficient (c_p) along wing airfoil has been evaluated by means of bi-dimensional vortex lattice method (VLM); no 3-D effects have been taken in account for loads evaluation (the wing sections delimiting the investigated portion have been considered characterized by the same c_p distribution). Once the c_p distribution has been evaluated, the global airfoil lift coefficient (C_l) has been obtained: this has been done for several flap deflection angles (δ), from 2° up to 24°, and in correspondence of attitude parameters typical of take-off and landing conditions (at sea level, with dynamic pressure of 1531.25N/mm^2 and a 5° angle of incidence). The obtained results in terms of C_l have been reported in Tab. 1.

δ [°]	2	4	6	8
C_l (conventional)	1.0155	1.1760	1.3359	1.4950
C_l (morphed)	1.0760	1.2866	1.4944	1.6990

δ [°]	10	12	14	16
C_l (conventional)	1.6532	1.8103	1.9663	2.1209
C_l (morphed)	1.8996	2.0956	2.2868	2.4727

δ [°]	18	20	22	24
C_l (conventional)	2.2740	2.4253	2.5749	2.7224
C_l (morphed)	2.6530	2.8275	2.9962	3.1589

Tab.1 . Airfoil C_l for several flap deflection angles.

Be given a bi-dimensional Cartesian reference system S_0 defined as follows: origin located at airfoil leading edge; X-axis directed along unflapped airfoil chord and oriented towards airfoil trailing edge; Z-axis in the airfoil plane and upwards oriented. In correspondence of a flap deflection δi around the hinge point A [0.7·c;Z_A] the airfoil trailing edge moves from the position individuated in S_0 by point P [c;0] to the position individuated by point P' whose coordinates in S_0 are: $X_{P'} = 0.7 \cdot c + \overline{AP} \cdot \cos(\alpha + \delta_i)$, $Y_{P'} = \overline{AP} \cdot \sin(\alpha + \delta_i) - Z_A$ where c stands for the airfoil chord length, and $\alpha = \sin^{-1}\left(0.3 \cdot c / \overline{AP}\right)$.

In order to reach the same trailing edge position due to a δ_i flap deflection, a morphing law has been imposed to flap chamber-line. The motion of point P to point P' has been then obtained by means of flap chamber line morphing into a parabolic arch connecting point A to P' and tangent in A to flap chamber line (see Fig. 5).

Fig.5 . Conventionally deflected flap/morphed flap shapes.

Adopting the above described morphing law, for each airfoil flapped shape obtained by a δ_i flap deflection , it has been defined a morphed airfoil shape leading to same trailing edge displacement: C_l related to morphed shapes associated to deflection angles have been reported in Tab. 1. It can be noticed that, for a given deflection angle, the morphed flap leads to higher C_l values with respect to conventionally rotated flap (Fig. 6).

4
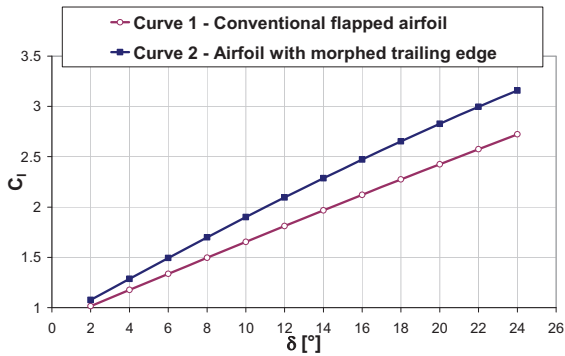
Fig.6 . Airfoil C_l comparison.

The morphed flap configuration leading to airfoil C_l equal to 2.09 has been considered the most satisfactory from aerodynamic performance point of view, and has been chosen as this work target: it corresponds to a deflection angle of 12° and a vertical displacement of 160 mm. Be said s_i the generic aerodynamic strip, delimited by two homologue panels p_i located respectively on right and left section of wing portion, the normal aerodynamic load $F_{n,i}$ acting on s_i has been evaluated as $F_{n,i}=q \cdot A_i \cdot c_{p,i}$, where q is the dynamic pressure, A_i the strip area and $c_{p,i}$ the pressure coefficient on panels p_i.

Such load distribution has been used for a proper sizing of the ribs to be located at the end of the investigated wing portion.

NUMERICAL MODEL

The numerical model adopted for simulations (Fig. 7) comprehends two flap ribs at a distance of 300 mm each others, connected by skin panels.
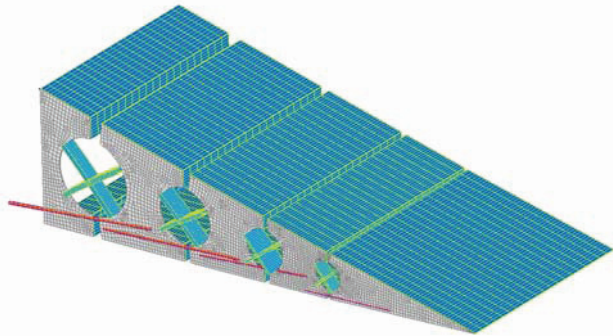
Fig.7 . The FE model of the flap.

2 mm thick plate elements made of 7075 T6 aluminum alloy have been used to simulate the rib panels. The SMA components have been simulated through beam elements with suitable thermal expansion coefficient, defined according with afore illustrated procedure. To avoid any bending stress, all rotational dofs of the contact nodes with the rib plates, have been released. The connecting springs have been realized through beam elements made of titanium alloy, for enduring large deflections; related cross section dimensions have been defined to meet both SMA pre-load requirements (pre-stress higher than 130 MPa) and structural integrity specifications

(max stress for complete deflection lower than 800 MPa). In Tab.2 the main features of the model are summarized.

Number of elements	13816
Number of nodes	14287
Rib plate element type	CQUAD
Rib material	7075 T6 aluminum alloy
Spring plate element type	CBEAM (rectangular cross section)
Spring plate material	Titanium alloy
SMA rod element type	CBEAM (circular cross section)
SMA rod material	NiTiNol, A_s=43°C

Tab.2 . Main features of the FE model.

For the pre-load computation, each rib plate has been assumed to be rotated of 10 deg with respect to the previous one (pre-load configuration, Fig. 3 (a)); fictitious expansion coefficients have been assigned to each SMA rod, so that, under the action of a unitary thermal load, the neutral configuration (see Fig. 3 (b)) could be reached. In this condition, the stress within the rods has been estimated and compared with the minimum required, 130 MPa; by playing on the cross section dimensions of the springs, the desired configuration has been found. After assessing the neutral position, the complete activation (Fig.3 (c)) has been computed: to this aim, each fictitious thermal coeff. has been increased of the SMA recoverable strain (more or less 3%) and structural integrity verified. In Tab. 3-6. the parameters used for simulating flap in pre-load, neutral and extended configuration are reported, referring to the four connecting springs.

SMA length (m)	0.27
SMA radius (mm)	2.5
Plate spring length (m)	0.12
Plate spring cross section (mm x mm)	8.0 x 20.0
Pre-load conditions	
Pre-stress angle (deg)	10.0
SMA pre-stress (MPa)	136
Plate pre-stress (MPa)	395
Imposed recovery *	0.039
Actuation conditions	
Actuation angle (deg)	17.4
Delta angle (deg)	7.4
SMA stress (MPa)	221
Plate pre-stress (MPa)	617
Imposed recovery	0.039+0.030
* strain necessary for achieving neutral condition (pre-load)	

Tab.3 . Simulation parameters for the first spring.

SMA length (m)	0.25
SMA radius (mm)	2.5
Plate spring length (m)	0.12
Plate spring cross section (mm x mm)	6.0 x 25.0
Pre-load conditions	
Pre-stress angle (deg)	10.0
SMA pre-stress (MPa)	133
Plate pre-stress (MPa)	375
Imposed recovery *	0.030

Actuation conditions	
Actuation angle (deg)	28.36
Delta angle (deg)	11.0
SMA stress (MPa)	275
Plate pre-stress (MPa)	780
Imposed recovery	0.030+0.030
* strain necessary for achieving neutral condition (pre-load)	

Tab.4 . Simulation parameters for the second spring.

SMA length (m)	0.19
SMA radius (mm)	2.0
Plate spring length (m)	0.065
Plate spring cross section (mm x mm)	3.0 x 35.0
Pre-load conditions	
Pre-stress angle (deg)	10.0
SMA pre-stress (MPa)	110
Plate pre-stress (MPa)	378
Imposed recovery *	0.022
Actuation conditions	
Actuation angle (deg)	41.0
Delta angle (deg)	11.0
SMA stress (MPa)	190
Plate pre-stress (MPa)	683
Imposed recovery	0.022+0.030
* strain necessary for achieving neutral condition (pre-load)	

Tab.5 . Simulation parameters for the third spring.

SMA length (m)	0.158
SMA radius (mm)	1.5
Plate spring length (m)	0.045
Plate spring cross section (mm x mm)	3 x 20
Pre-load conditions	
Pre-stress angle (deg)	10
SMA pre-stress (MPa)	127
Plate pre-stress (MPa)	495
Imposed recovery *	0.030
Actuation conditions	
Actuation angle (deg)	47
Delta angle (deg)	7.0
SMA stress (MPa)	218
Plate pre-stress (MPa)	800
Imposed recovery	0.030+0.030
* strain necessary for achieving neutral condition (pre-load)	

Tab.6 . Simulation parameters for the fourth spring.

NUMERICAL RESULTS

The numerical results have been expressed in terms of vertical displacement and rotations of the trailing edge and morphed shape, with and without aerodynamic loads.

In Fig. 8 the morphed configuration obtained by activating the upward hinge only is illustrated.
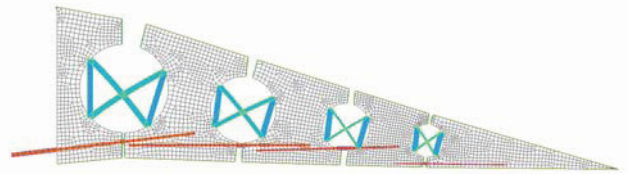
Fig.8 . Flap deflection by activating the first hinge.

In Fig. 9-11, the single contributions of remaining hinges are illustrated. The contribution of all the hinges in presence of aerodynamic loads is illustrated in Fig. 12.
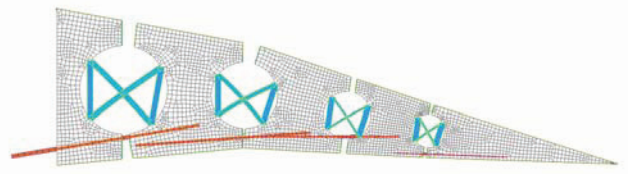
Fig.9 . Flap deflection by activating the second hinge.
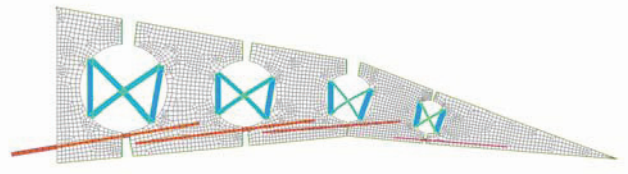
Fig.10 . Flap deflection by activating the third hinge.
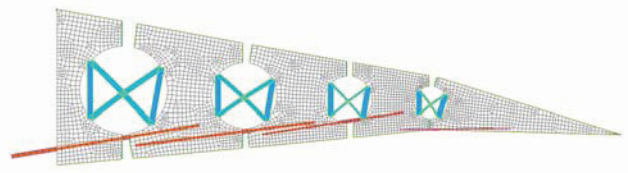
Fig.11 . Flap deflection by activating the fourth hinge.

Copyright © 2008 by ASME
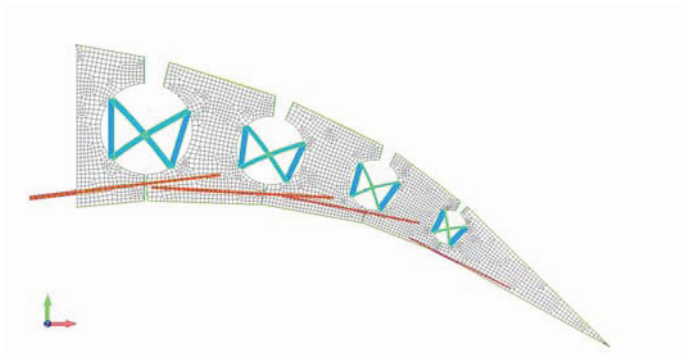
Fig.12 . Flap deflection by activating all the hinges.

In Fig. 13-19, the other actuation combinations are presented.

Fig.13 . Flap deflection by activating 1st and 2nd hinges.
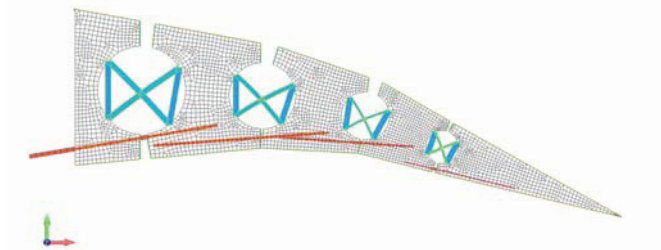
Fig.14 . Flap deflection by activating 2nd and 3rd hinges.
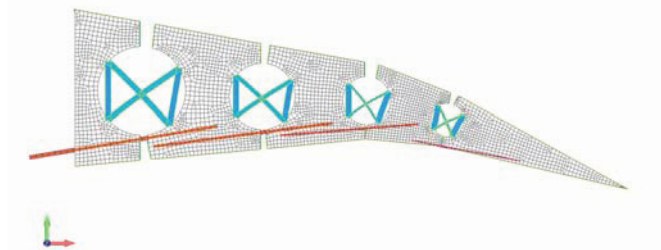
Fig.15 . Flap deflection by activating 3rd and 4rt hinges.

Fig.16 . Flap deflection by activating 1st and 3rd hinges.
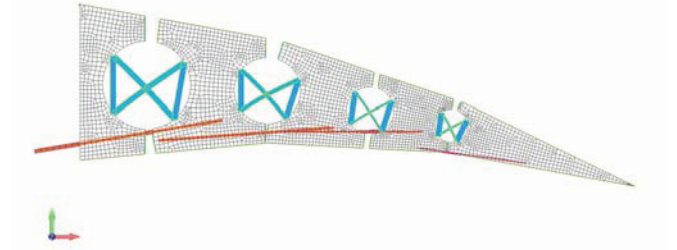
Fig.17 . Flap deflection by activating 2nd and 4rt hinges.

The same investigations have been addressed in presence of aerodynamic loads: achieved results have been reported in Tab. 7. It has to be observed that deviation of performance in presence and absence of aerodynamic loads is always well below 1%, given the SMA capability of sustaining external loads. The multiple SMA actuators also allow for multi-stable configurations, with several morphing shapes characterized by different actuation performance.
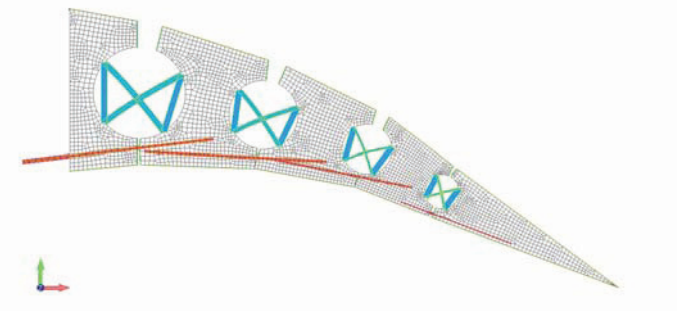
Fig.18 . Flap deflection by activating the 1st, 2nd and 3rd hinges.
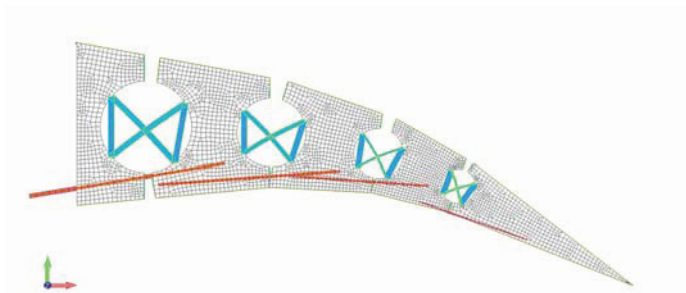
Fig.19 . Flap deflection by activating the 2nd, 3rd and 4rt hi nges.

Activated hinges	TE vertical displacement [m]	TE rotation [°]
1st hinge active	0.08705	7.32
2nd hinge active	0.07815	8.67
3rd hinge active	0.07407	11.37
4th hinge active	0.03826	8.36
1st and 2nd hinges	0.16366	15.99
2nd and 3rd hinges	0.15016	20.04
3rd and 4th hinges	0.11096	19.72
1st and 3rd hinges	0.15945	18.69
2nd and 4th hinges	0.11550	17.02
1st, 2nd and 3rd hinges	0.23261	27.37
2nd, 3rd and 4th hinges	0.18504	28.40
All hinges active	0.26374	35.57

Tab.7 . Morphed flap performance: trailing edge vertical dis placement and rotation.

CONCLUSIONS AND FURTHER STEPS

In the paper at hand the design and the optimisation of a SMA based architecture, aimed at producing morphing of the aft part of an airfoil, has been presented.

The innovation of the work is mainly represented by the high integration of the SMA elements within the flap structure, playing the twofold role of actuator and structural components, being able to endure external loads.

The architecture is constituted by a multi-body rib, whose components are linked each others through spring plate elastic elements (i.e. elastic hinges), to guarantee the achievement of large deflections; their non linear behaviour, due to the translation of the pivot during rotation, guarantees the possibility of pre-loading the springs so that required pre-strain for SMA recovery may be achieved. Many efforts have been focused on the dimensioning of the elastic elements, in order to achieve both required preload and bending rigidity under external aerodynamic loads, avoiding structural collapse.

Rib components relative rotations are commanded by SMA rods, linked to them through hinges, to avoid any bending transmission on the SMAs.

Two ribs, at a span distance of 300mm, have been connected by using upper and lower skin panels; due to the large expected deflections and to guarantee the structural integrity without worsening actuation performance of SMA elements, also the skin has been conceived according to a multi-body philosophy.

A suitable FE model of the rib architecture and the surrounding structure (i.e. skin elements and stiffeners) has been realised. Since no SMA dedicated finite element is implemented within the MSC\Nastran solver, a suitable procedure, made in Matlab environment and able to interact with the FE solvers, has been ideated to predict the thermodynamic state of SMA material integrated with the structural rib element.

Due to the large expected deformations, a non linear approach has been followed; architecture performance has been estimated in terms of vertical displacements of the trailing edge and global rotations. The contribution of external aerodynamic loads has been taken into account in order to appreciate the effective ability of the structure of changing its shape under realistic operative conditions.

Numerical investigations have proved the effective ability of the SMA based on structure to produce morphing and achieve remarkable chamber variations: required max vertical displacement of the trailing edge (i.e. 160mm to achieve a C_l of 2) has been exceeded even in presence of the most restrictive load conditions (aerodynamic loads estimate for landing conditions). Moreover, the presence of multiple SMA actuators allows for multi-stable configurations, able to reproduce different morphing shapes.

Further investigations will be carried out to appreciate the effective power supply necessary to activate the structure under operative load conditions. Dedicated optimisation processes will be addressed to improve structural performance, costs, weight and durability.

The realization and experimental testing of a suitable demonstrator will be valuable to validate the architecture herein presented and estimated actuation performance.

Also the challenging problem of the skin continuity needs to be further investigated, with the development of new solutions.

REFERENCES

1. E. Stanewsky, "Adaptive Wing and Flow Control Technology", *Progress in Aerospace Sciences, Elsevier Science Ltd.*, 37, 583-667 (2001)
2. J. Spillman, "The Use of Variable Chamber to Reduce Drag, Weight and Costs of Transport Aircraft", *Aeronaut. J.* 96, 1-8 (1992)
3. H.P. Monner, T. Bein, H. Hanselka, E. Breitbach, "*Design Aspects of the Adaptive Wing – The Elastic Trailing Edge and the Local Spoiler Bump*", Royal Aeronautical Society, Multidisciplinary Design and Optimization, London, 1998
4. Gevers Aircraft Inc., "*Multi-Purpose Aircraft*", U. S. Patents No. 5,645,250 (1997)
5. J. Blondeau and D. Pines, "Pneumatic Morphing Aspect Ratio Wing", *45th AIAA/ASME/ASCE/AHS/ASC Structures, Structural Dynamics and Materials Conference, Palm Springs, California, AIAA J.* 2004-1808 (2004)

6. J.R. Wilson, "Active Aeroelastic Wing: A New/Old Twist On Flight", *Aerospace America* 40(99), 34–37 (2002)

7. I. Chopra, "Review of State of Art of Smart Structures and Integrated Systems", *42nd AIAA/ ASME/ASCE/AHS/ASC Structures, Structural Dynamics, and Materials Conference, Seattle, WA, AIAA Journal* 40(11), (2002)

8. J. Browman, B. Sanders, T. Weisshaar, "Evaluating the Impact of Morphing Technologies on Aircraft Performance", *AIAA J.* 2002-1631 (2002)

9. W.J. Buehler, J.V. Gilfrich, R.C. Wiley, 1963, "Effect of low-temperature phase changes on the mechanical properties of alloys near composition TiNi", *Journal of Applied Physics* 34, 1475 (1963)

10. L.C. Brinson, A. Bekker, M. Huang, "Deformation of Shape Memory Alloys due to Thermo-Induced Transformation", *J. of Intelligent Material Systems and Structures* 7(1), 97-107 (1996)

11. C. Liang and C.A. Rogers, "One-Dimensional Thermomechanical Constitutive Relations for Shape Memory Material", *J. of Intelligent Material Systems and Structures* 1(2), 207-234 (1990)

12. K. Tanaka, "A Thermomechanical Sketch of Shape Memory Effect: One-Dimensional Tensile Behaviour", *Res. Mech.* 18(3), 251-263 (1986)

- *Chapter 6* -

Variable Camber Morphing Flap:
SMA Actuator Development

1 INTRODUCTION

A SMA-based actuator, suitable for morphing applications, has been conceived by the author and is illustrated in this chapter: two papers have been recently submitted on the topic (***) and are herein presented.

Details about its design features, numerical simulations and optimizations which brought to the final configuration are discussed. The manufactured prototype has been experimentally tested, and a discrete correlation with the numerical estimate has been achieved: in general, good actuation performance have been reached.

These research activities have raised great interest in the industrial partner (Alenia): a EU patent is pending on the device (see Appendix) and further studies and collaborations are currently starting for improving the design and attainable performance.

***

S. Barbarino, L. Lecce, A. Concilio, S. Ameduri, S. Russo, "A Novel Smart Actuator for Airfoil Structural Morphing: Design and Optimization", submitted to the Journal of Intelligent Material Systems and Structures (JIMSS)

S. Barbarino, L. Lecce, A. Concilio, S. Ameduri, L. De Rosa, "A Novel Smart Actuator for Airfoil Structural Morphing: Test Campaign and Numerical Correlation", submitted to the Journal of Intelligent Material Systems and Structures (JIMSS)

PAPER

"A Novel Smart Actuator for Airfoil Structural Morphing: Design and Optimization"

S. Barbarino, L. Lecce, A. Concilio, S. Ameduri, S. Russo

A Novel Smart Actuator for Airfoil Structural Morphing: Design and Optimization

S. Barbarino[a], L. Lecce[a]
A. Concilio[b], S. Ameduri[b]
S. Russo[c]

[a]Dept. of Aerospace Engineering, Univ. of Naples "Federico II", Via Claudio 21, Naples, Italy
[b]Smart Structures Lab., The Italian Aerospace Research Centre (CIRA), Via Maiorise, Capua (CE), Italy
[c]ALENIA AERONAUTICA S.p.a., Viale dell'Aeronautica snc, Pomigliano d'Arco (NA), Italy

Abstract

Nowadays, aircraft morphing is a relevant research area. The idea of realising an adaptive structural wing is a promising objective, leading to large advantages in terms of weight, general performance, architectural complexity and so on. Antithetic structural needs of a sufficient stiffness and required deformation generates a sort of paradox the smart structures are called to overcome. The authors chose to refer to load-bearing actuators, that means, actuator systems able to sustain external forces. Shape Memory Alloys were selected as smart elements, able to express high forces and strains. After having experienced several solutions, an arc-shaped metallic actuator was conceived. Its design is the essence of this paper. The paper starts by introducing the structural concepts backward and presenting the selected smart material characteristics. A survey on the adopted tools takes then place, involving Genetic Algorithms-based routines and FE-based simulation procedures. The final simulation of the assembled system completes this work. Information on its performance, cyclic activation capability and structural resistance are derived. A EU patent is pending for the shown device. The designed arc allows reaching the required displacement field still demonstrating an adequate stiffness, addressed to face the external loads. Selected SMA element produces the required internal forces. A simulation procedure is available, addressing both the non-linear behaviour of the structure and the peculiar SMA constitutive law. Analytical and numerical models and procedures confirmed their reliability after experimental test campaigns allowed their tuning.

Keywords: SMA, Actuator, Morphing, Optimization

1 – Introduction.

In the recent years, aircraft morphing has become more and more popular among the scientific and technological community. Since the start of DARPA technological program, Smart Wing [1], and the successes attained by the Northrop Grumman team, led by Jay Kudva [2], the concepts were investigated by more and more researchers, spread all over the world. Among the others, the idea of realising an adaptive structural wing was a promising objective, leading to large advantages in terms of weight, general performance, architectural complexity and so on. It was like coming back to the architectures of the first powered aircraft, where mobile surfaces did not yet exist and

the manoeuvres were performed through modification of the wing shapes, [3]. The increased flight velocities and the consequent growth of the aerodynamic loads, forced the designers to use rigid wing sections. Only lately, after the discover of the so-called smart materials, the possibility of shaping the structure in order to face different flight conditions came back to the attention of the engineers. Really, prototypic appearance of this kind of architectures dates back to the seventies of last century, mounted on-board of the De Havilland Buffalo, where a rubber LE modified the airfoil shape at landing or take-off; other applications were adopted on the F14, confined to in-plane wing geometry variations, or for inflatable wing configurations, such as the Stingray, etc. [4-7].

Afterwards in the nineties, the introduction of the piezoelectric ceramics in the world scientific community, moved the attention towards structural dynamics control. F18 vertical tail buffeting attenuation by piezoelectric ceramics was studied [8], being one of the first attempt of lift surface control by smart materials. Inside EREA group, the Adaptive Airfoil project started in 1997, concerning the realisation of a morphing bump over an airfoil surface, aimed at reducing shock wave-induced drag, [9].

However, it was the cited DARPA program to set a turning point in the aircraft structural control. Jay Kudva started by using Shape Memory Alloys (SMA) to morph an UCAV wing, to come to refer to some more traditional eccentric actuators in the last frame of his first research, [2]. Other authors looked at the possibility of modifying different parts of the wing structure to achieve certain shape modifications by means of normal, bending or torsion actuators, [10-16].

One of the main challenges of morphing applications is related to the antithetic necessities of structural stiffness and required deformation. In order to attain large displacements, the system should be somehow compliant with the control forces. On the other side, the structure should ensure a certain rigidity to counteract the external loads and maintain a reference shape. These two aspects are in clear conflict, generating a paradox the smart structures are called to overcome, [17]. Different strategies may be followed in order to overcome this difficulty. The authors chose to refer to "load-bearing" actuators, that means, actuator systems able to sustain external forces, [18]. Such actuators shall be integrated with proper structural elements, in order to ensure the desired stiffness and mobility.

Different configurations may be generally thought of, being the focus devoted to pointing out at that architecture, able to deflect when commanded but still ensuring a

certain shape under the action of the external loads. As smart elements, the authors selected the SMA, already tested before. This choice was mainly due to both their capability of expressing relatively high actuation forces and the absolute characteristic of exhibit namely the same strain recovery, irrespectively of the acting force (within a suitable range). The effects are however not independent on the external loads because they produce an initial deformation that, having to be recovered, subtracts effectiveness to the SMA action.

In literature, Shape Memory Alloys have been selected as "active" elements for the development of several innovative actuators [19-23] due to their compactness and better power/weight ratio in certain circumstances when compared to traditional ones: usually, the SMA element is joined by a spring system to allow for cycles. The novelty of the herein presented work is the design of the adopted elastic element also as highly integrated structural element of a morphing rib that will be presented in a successive paper.

After having experienced several solutions, a summary of which was reported in [18], the authors came to an arc-shaped metallic actuator, the design of which is the main topic of this paper. It shall withstand to the external load, the SMA action and shall enable the reconfiguration towards the original position once the control signal is off. The selected SMA element is not capable of bringing the structure to the non-deformed position, unless the structural elasticity itself does not drive the system to the original state.

The paper starts by introducing the structural concept backward (the arc) and presenting the selected smart material characteristics (SMA constitutive law, characteristic behaviour, etc.). A survey on the adopted tools, simulating the whole system made of the structural part, the SMA active element, the different devices mounted on it to optimise its behaviour, takes then place. In synthesis, they refer to GA-based optimisation tools and FE-based simulation procedures, integrating commercial codes (MSC/Nastran) and advanced languages (Matlab). The final simulation of the assembled actuator system completes this work, providing information on its performance, the cyclic activation capability and the structural resistance. In this phase, the external loads are not taken into account and together with the experimental test campaign are remanded to a successive paper. A patent is pending on the presented actuator assembly [24].

2 – Actuator Design.

Different considerations drove actuator identification and design. Being an aerospace-oriented product, weight, costs and performance played a fundamental role. Attention was also devoted to materials selection, manufacturing possibilities and power consumption. In addition, the device had to respect geometrical constraints related to the opportunity of being integrated within flap available space. Beyond abovementioned criteria, whose validity is common to several aeronautic products, other requirements drove the actuator choice and design. To allow large structural deformations, still guaranteeing the necessary structural rigidity, the actuator was designed to be able to cooperate in absorbing external loads. SMA cyclic actuation made more severe the exigency of improving fatigue behaviour. Structural solutions able both to withstand cyclic loads and to reduce internal stress were then preferred and achieved through large-flexibility configurations. Because a "One-way" SMA material was selected (that is, after the material is activated, only a suitable stress may restore the initial conditions), actuator architecture was pre-loaded, to prepare the SMA elements to the next activation cycle: this last requirement particularly restricts and conditions available design solutions

Actuator configuration

The actuator is made of an active smart and a passive elastic element, able to exhibit the required levels of rigidity and flexibility to withstand external loads and to allow operative deformations, respectively. The solution referring to a ribbon-shaped SMA integrated into a metallic arch seemed to meet the just mentioned requirements at the best. A schematic of the actuator is illustrated in Figure 1(a). When the smart ribbon is activated, it contracts; the arch undergoes a rotation, while its edges approach, Figure 1(b).

The structure is assembled as follows. Arch is compressed, so that the edges approach and the ribbon can be installed. When the arch is released, the elastic reaction stretches the SMA element. The actuator is then pre-loaded, before operation. By varying the early compression force and then the edges distance, the internal stress may be regulated to a desired value.

Summarising, the arch is called to provide the system with the needed elastic properties: rigid as necessary (external loads) and flexible as required (specifications). SMA ribbon

cooperates with the arch, structurally: it strongly hinders upward deflections, being itself an elongation constraint. From a simulation point of view, being only normal stresses involved, widely validated one-dimensional models may be adopted, [25], for predicting SMA material behaviour, with great simplifications of computational schemes. The adopted arrangement also eases the pre-load process.
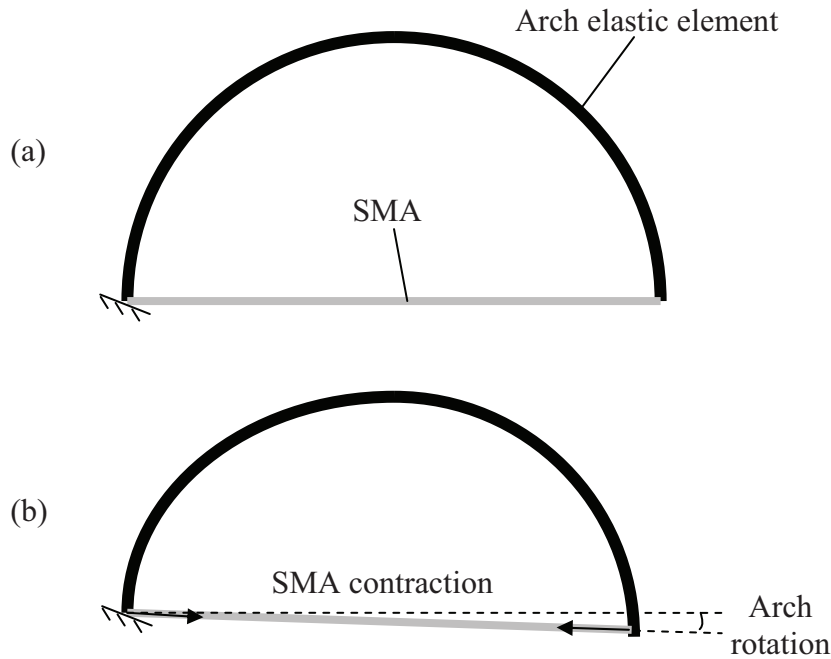
Figure 1. Actuator conceptual scheme and working modality: (a) initial and (b) actuated configuration.

SMA characterisation

Shape Memory Alloy characterisation played a fundamental role in the design assessment. A commercially available NiTiCu ribbon, having a 10 x 1 mm cross section, was opted for because of previous experiences with the selected material, which proved suitable, due to its properties, for the selected application. A characterisation campaign was carried out in order to find the parameters required by the reference model [25]. At first, an ultimate stress test at room temperature was performed to appreciate max available elongation and martensite Young modulus. Resulting stress-strain curve is illustrated in Figure 2. The martensite Young modulus was computed as the slope of the upper straight part of the reported curve (highlighted by a box in the cited figure).
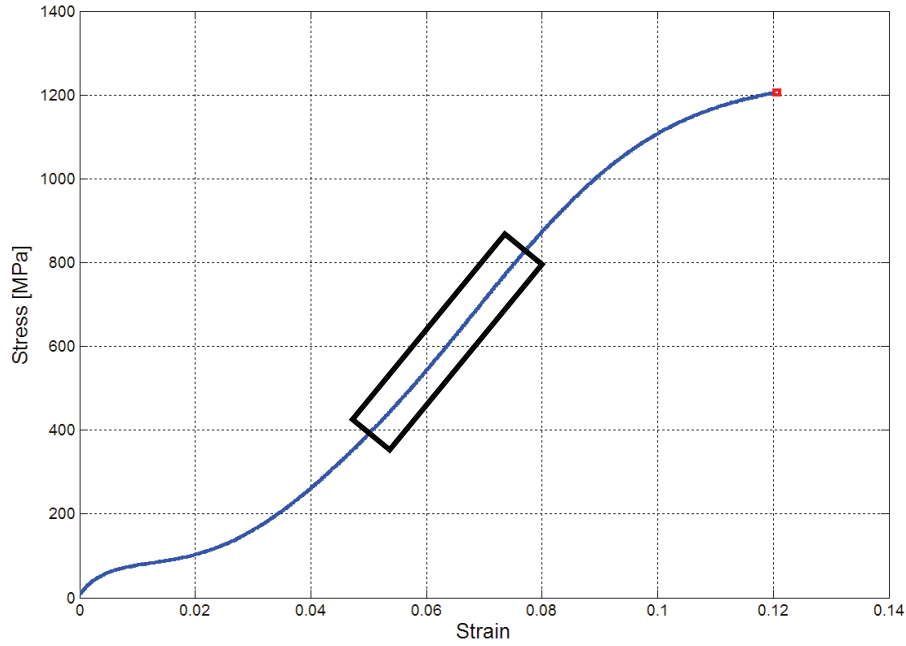
Figure 2. Ultimate stress test on selected SMA specimen.

Then, a tensile test at 100 °C was accomplished, to measure austenite Young modulus. However, because the machine clamps could not be integrated in the climatic chamber, only the non-constrained part of the ribbon was controlled in temperature. This gave rise to the stress-strain curve reported in Figure 3, exhibiting different straight parts as a result of the coexistence of the austenite and martensite phase, the latter prevailing for high stress values. The highest slope, highlighted by a box in Figure 3, was assumed as the austenite Young modulus.
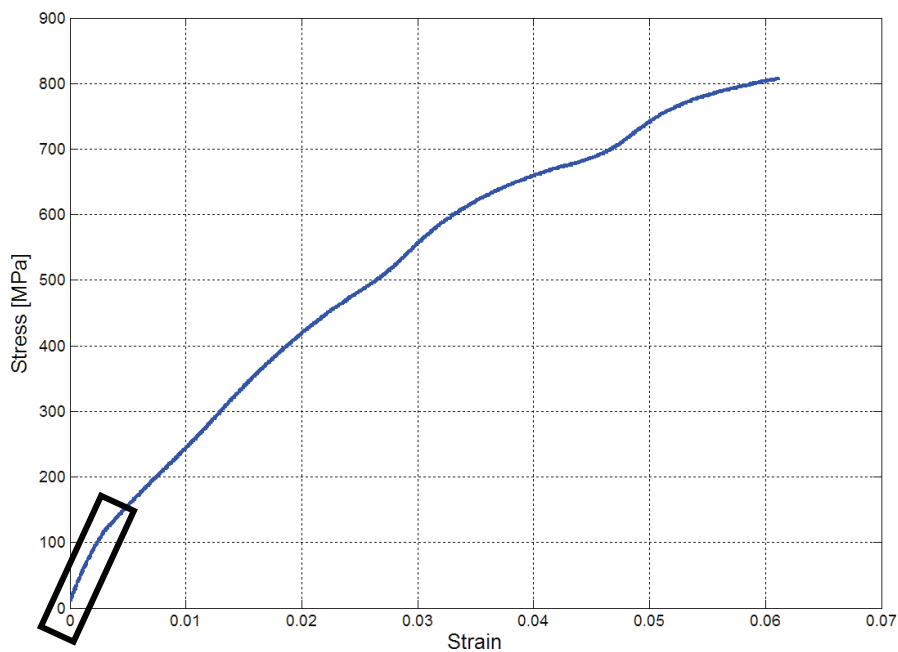
Figure 3. Tensile stress on selected SMA specimen at a temperature of 100°C.

Some training cycles were finally performed to have a preliminary measure of the test repeatability, Figure 4. The specimen underwent a normal stress up to a target recoverable strain and, then, restored by heating. The force, used to produce such a deformation, was assumed as the needed pre-load to restore the initial conditions during operative life. This value is the martensite finish stress and resulted as one of the main drivers in the actual design of the elastic arch. In Table 1, the main results of the mentioned test campaign are finally reported, together with the material activation temperatures, as provided by the manufacturer.
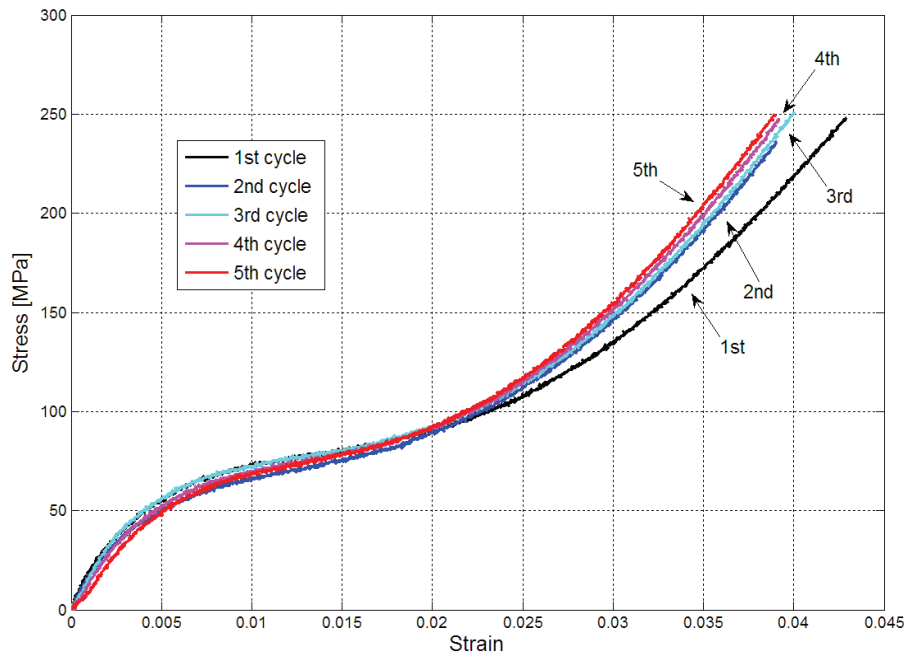
Figure 4. SMA training cycles.

Martensite Young modulus, E_M [GPa]	16.5
Austenite Young modulus, E_A [GPa]	40.2
Ultimate elongation [%]	12.0
Target recoverable strain [%]	3.0
Min necessary pre-load [MPa]	155.0
Martensite start temperature, M_S (C°)	*43.3*
Martensite finish temperature, M_F (C°)	*27.5*
Austenite start temperature, M_S (C°)	*47.3*
Austenite finish temperature, M_F (C°)	*58.9*

Table 1. Selected SMA material properties.

Arch design

The actuator was aimed at producing rotations in the active rib for a flap device: this ability was targeted as the main design feature, constrained to the lowest force generation effort and weight penalty. The efficacy in inducing certain pre-load within

the SMA element and withstanding further stresses during activation were other project drivers.

Different parameters proved to affect the mentioned attributes as the kind of material, the arch mean plane radius, the thickness and depth vs. tangential coordinates. The definition of the related geometric laws in turn introduces further parameters whose amount discourages the use of the so-called exact optimisation methods, in favour of heuristic ones like genetic algorithms [26].

To reduce computational efforts, considering small transversal cross section with respect to the axis curvature radius, an analytical model was realised, based on the curved beam theory, [27]: arch deformations may be then expressed as a function of the local rotation, φ, Figure 5, as:

$$\varphi(\vartheta) = \left(\frac{F\rho_G}{K(E,b,t,\rho_n)} \right)(1+\cos\vartheta) \qquad (1)$$

In the above formula, θ, F, ρ_n, ρ_G, t, b, E are the angular coordinate of the arch, the SMA-generated force (Figure), the neutral axis and barycentre curvatures radii, the thickness, the depth and the material Young modulus, respectively. K represents a function of the four parameters (E, β, t, ρ_n):

$$K = b \cdot E \cdot \left(\rho_n^2 \cdot \log\left(\frac{2\rho_n + t}{2\rho_n - t} \right) - \rho_n \cdot t \right) \qquad (2)$$

An original MATLAB routine computed arch deformed configuration and stress field under the action of the assigned force F. In Figure 6 and Figure 7 the un-deformed and deformed shapes and related induced stress are reported, relative to a stainless steel arch (40 mm mean line radius, 7.0 mm depth; 6.0 mm thickness) loaded with a 800 N force. Results were validated through a FE non-linear analysis on the arch itself. A comparison of numerical and analytical results showed a deviation not higher than 2%.
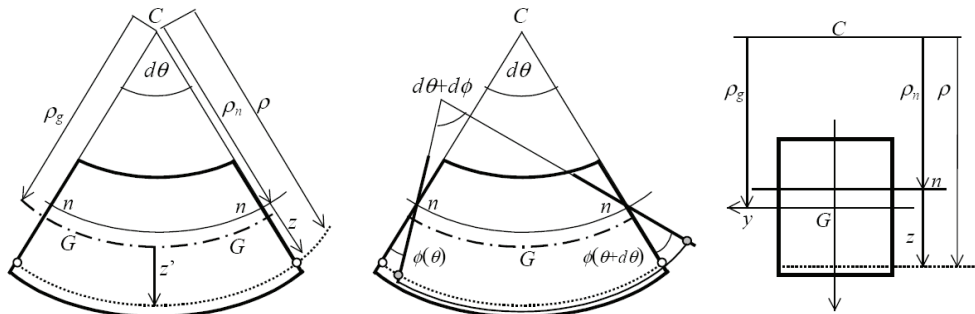
Figure 5. Curved beam scheme.
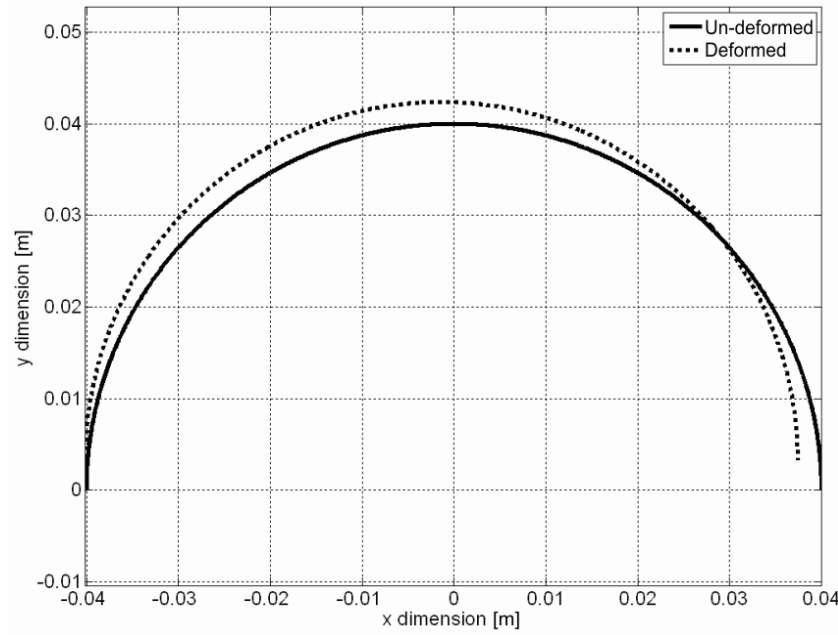
Figure 6. Arch mean line deformation.
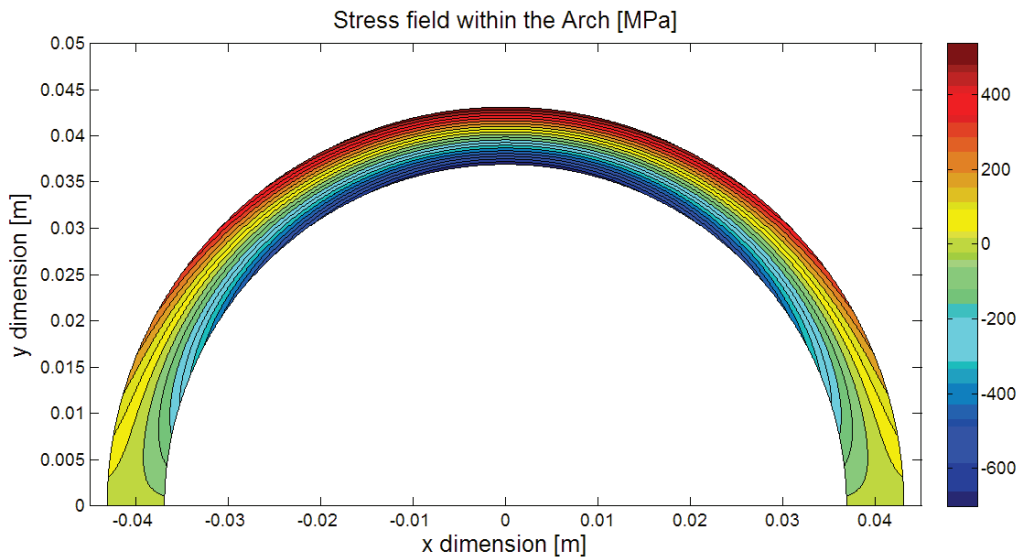
Figure 7. Arch stress field.

A preliminary optimisation process was then performed by minimising a multi-objective function, taking into account both actual stress and applied force ratios as a function of thickness, depth and mean radius, constant along the angular coordinate. This choice addresses the intention of minimising the operative tension level and reducing the forces, produced by the SMA element. In the investigated domain, defined as in Table 2, the solution goes towards flexible structures. Figure 8 reports the evolution of the mean and max values of the fitness function during the optimization process, carried out by an own genetic algorithm. Convergence is reached after 300 generations, corresponding to a global number of 15000 investigated configurations.

Thickness [mm]	1 ÷ 10
Mean radius [mm]	50 ÷ 100
Depth [mm]	2 ÷ 20
Material	Steel
σ_{alw} [MPa]	1700
F_{alw} [N]	1600

Table 2. Optimisation parameters variation ranges and constraints.
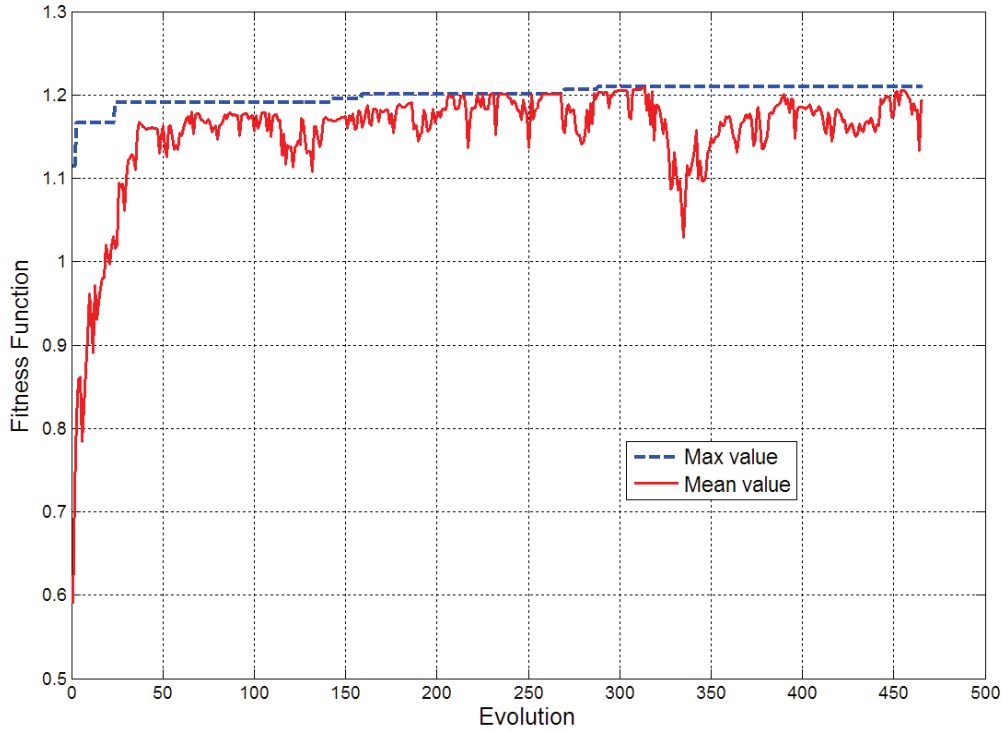
Figure 8. Optimization algorithm results: mean and max value of the fitness function.

Following the optimised geometry definition, results in terms of preload and attained activated deformation are illustrated in Figure 9 and summarised in Table 3.

Further optimisations were carried out: among the others the possibility of elliptic arches was investigated to drop as much as possible rotation centre, thus maximising rotary motion. Nevertheless, the algorithm privileged solutions characterised by almost similar axes, corresponding to a more uniform stress distribution. Even linear tapered thickness effects were investigated: both envisaged performance, very close to the constant thickness ones, and ensuing manufacturing complications discouraged the adoption of this latter solution typology.

Transmitted strain strongly depends on SMA length. It can be extended through tailored extensions of the arch edges and the introduction of a vertical rod, mounted on the middle of the arch and working as an SMA lead. This configuration was numerically tested (FE analysis, Figure 10).

Mean radius:	55 mm	SMA pre-load force:	1550 N
Thickness:	5 mm	SMA actuation (operative) force:	2009 N
Depth:	18 mm	Overall rotation:	2.66°
Material:	Steel	Max stress:	1541 N/mm^2

Table 3. Preliminary optimisation results (analytical model).
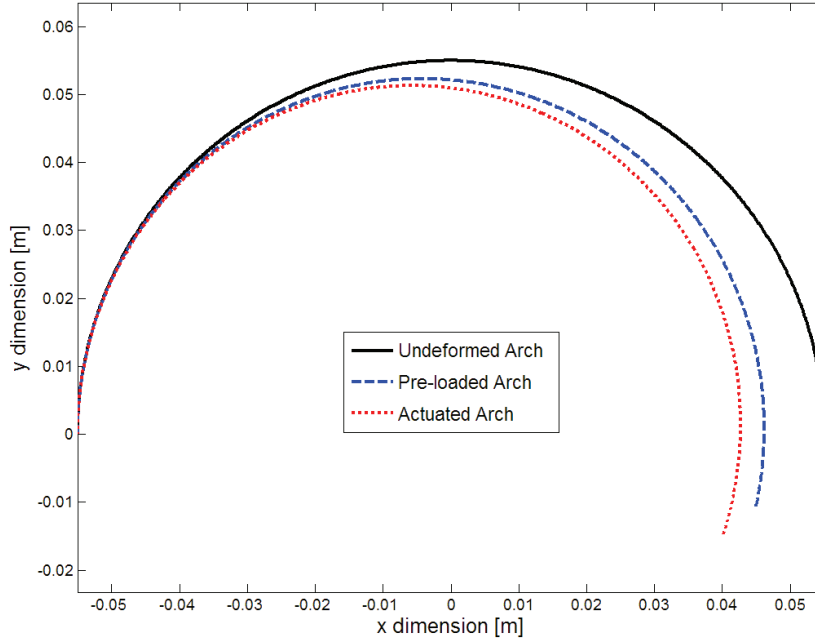
Figure 9. Preliminary optimisation results (analytical model).
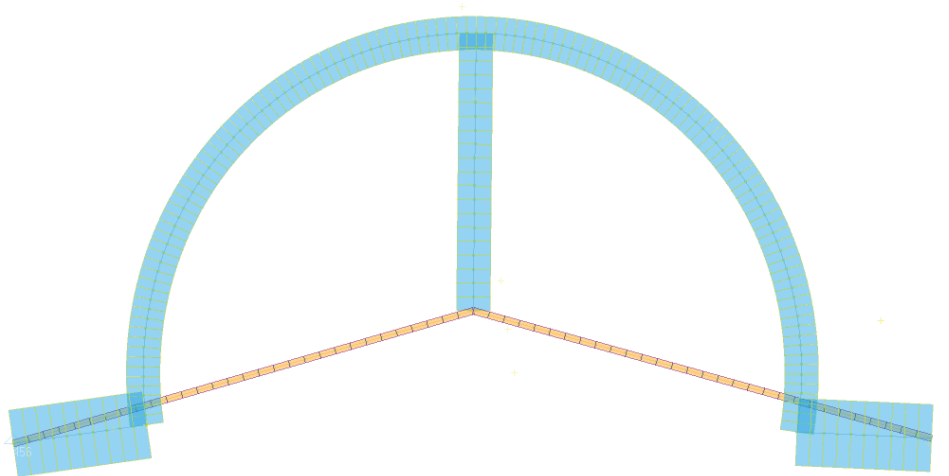
Figure 10. Arch FE model, complete of an SMA centred lead.

Arch performance was computed for different position of the vertical constraint: 13, 25, 50, 75 and 100% of the mean radius. Results are reported in Table 4. The shortest the rod, the highest is the overall rotation (reaching 19.36 deg when the middle constraint lays on the arch). Strong stress levels increase within the active element led to consider solutions with lower heights: 25% seemed a good compromise between actuation efficiency, structural integrity and energy expense.

	SMA lead height (radius %)					
	0	13	25	50	75	100
Overall rotation [deg]	4.83	5.82	6.73	8.6	12.07	19.36
SMA force [N]	2021	2297	2534	3332	5411	13003
Vertical rod tension [N]	0	822	1373	2831	6010	Absent
Max stress [MPa]	1673	1503	1425	1341	1475	2357

Table 4. Performance of the arch instrumented with different vertical rod lengths.

Actuator assembly

On the base of aforementioned consideration and investigation outcomes, the design of the actuator was finally defined. A customised FE model (MSC/Nastran) of the system integrating the arch and the SMA device was realised, Figure 11. Among the peculiarities, rigid elements were used to describe the interface between the smart ribbon and the vertical rod. In addition, the SMA ends were figured as hinged in correspondence of the lateral extension blocks and then, not cooperating to arch deflection. Achieved performance is summarised in Table 5.
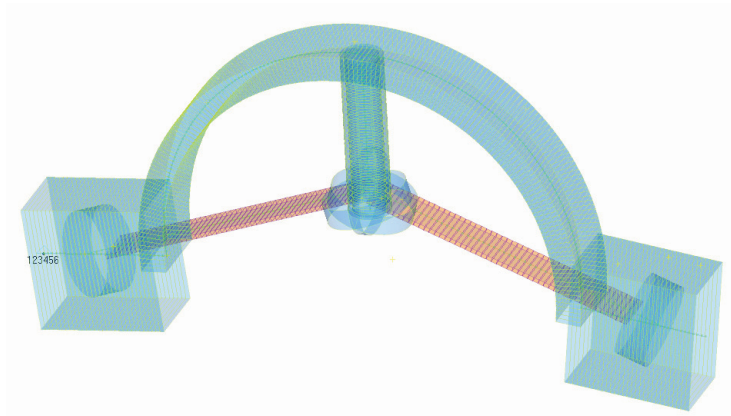
Figure 11. Arch FE model – Final design.

Actuation force, by the SMA ribbon [N]	2799
Max stress, within the arch [MPa]	1347
Overall rotation [deg]	7.30

Table 5. Actuator predicted performance.

The considered model does not take into account mechanical interference problems: the SMA element and the central support rod cannot permeate each others in reality. Two architectures were then proposed and investigated to overcome this numerical abstraction and envisage possible problems linked to non-symmetric configurations.

The first architecture is shown in Figure 12, very simple from a manufacturing point of view: SMA ribbon, clamps and vertical constraint are mounted on a single side of the arch. In the second architecture, the SMA element is placed into the middle of the arch construction and splits the structure in two parts, Figure 13. Both architectures performances are reported in Table 6. Out of plane deformation of the asymmetric configuration is plotted in Figure 14.
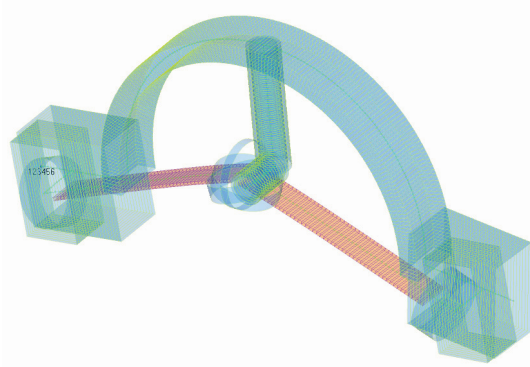
Figure 12. Asymmetric arch: FE model.   **Figure 13. Symmetric arch: FE model.**
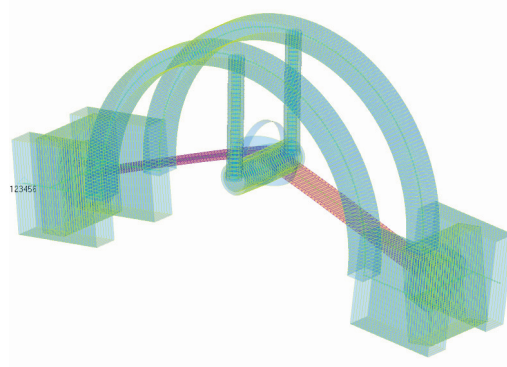
Asymmetric actuation	
SMA actuation force, [N]	2725
Max stress within the arch, [MPa]	1284
Net rotation of the free basement, [deg]	6.82
Out-of-plane deformation,[mm]	3.15
Symmetric actuation	
SMA actuation force, [N]	2852
Max stress within the arch, [MPa]	1303
Net rotation of the free basement, [deg]	7.15

Table 6. Symmetric and asymmetric configuration performance.
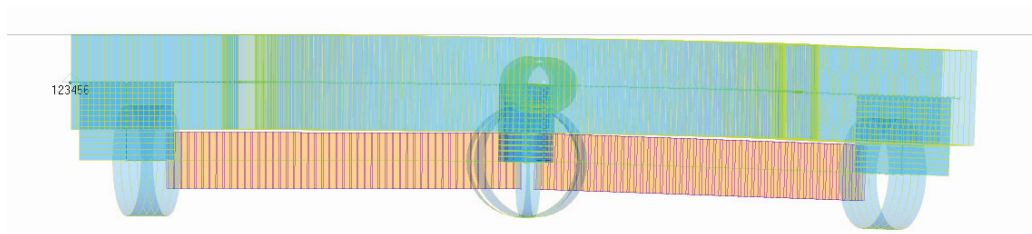
Figure 14. Out of plane deformation of the asymmetric architecture.

Mechanical simplicity, small out-of-plane effects further hindered through a suitable 3D integration scheme, weight savings and smaller dimensions led to select the asymmetric solution. In order to better point out the architectures features, CAD drawings were prepared, Figure 15 and Figure 16, considering also details not reported in the FE models (components connections).
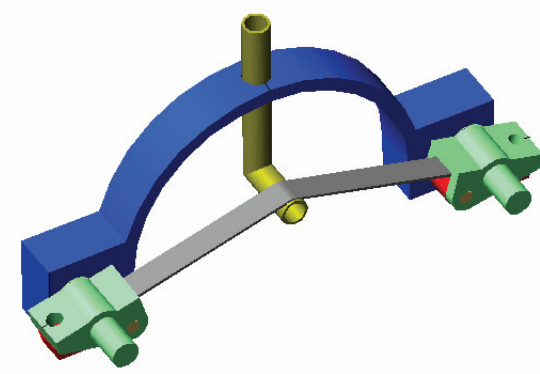
Figure 15. Asymmetric configuration: CAD drawing.
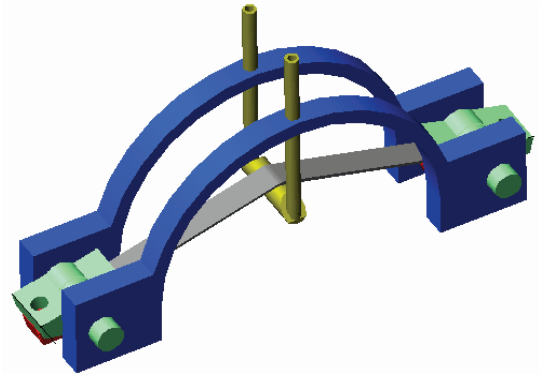
Figure 16. Symmetric configuration: CAD drawing.

The chosen configuration leads to high structural stress values. This fact suggested to consider the use of other material typologies, possibly able to operate in the linear range of the stress-strain curve. A titanium-based alloy material was then selected, namely TI-6AL-4V AMS 4911 ANNEALED, whose mechanical features are reported in Table 7. It exhibits a large allowable stress level and a relative low specific density. Design tasks were then repeated with the new data. Tension limit was set at 700 MPa, corresponding to the material linear elastic behaviour.

Other slight modifications were implemented in the final arrangement: the top of the arch was made wider and thicker to limit interference problem and out of plane deformations, as well as to take into account the presence of a hole for the vertical rod mounting. Characteristics of this final lay-out are summarised in Table 8, and sketched in Figure 17. The arch basements is specifically drawn to host a tailored pre-loader.

Titanium TI-6AL-4V AMS 4911 ANNEALED	
Young modulus, E [GPa]	110
Shear modulus, G [GPa]	42.75
Poisson modulus, ν [-]	0.31
Density, ρ [kg/m^3]	4428
Ultimate stress, σ_u [MPa]	896.3 ÷ 1103
Yield stress, σ_y [MPa]	827.4 ÷ 999.74

Table 7. Mechanical features of the arch material.

Mean radius, [mm]	55
Thickness, [mm]	5
Depth, [mm]	18 / 33 / 41
Length, [mm]	170
Volume, [cm^3]	60.478
Weight, [g]	268

Table 8. Mechanical features of the arch.
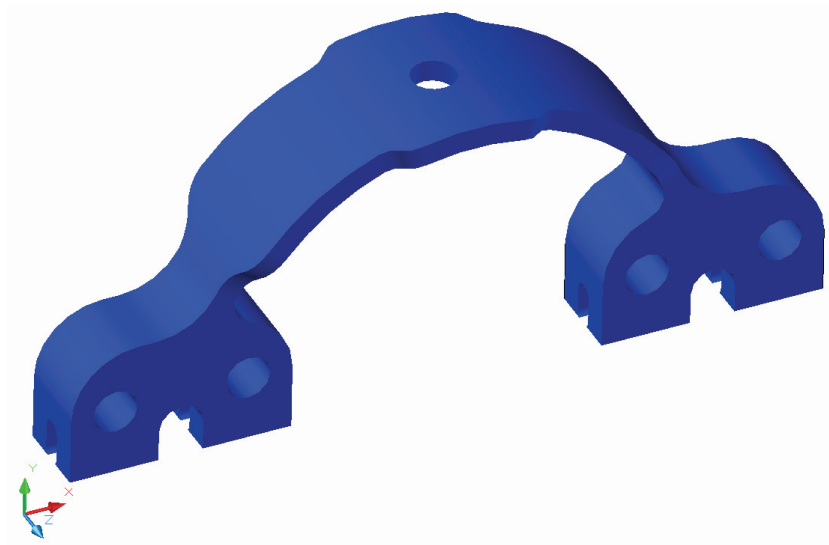
Figure 17. CAD drawing of the tapered arch.

Special attention was devoted to the design of the SMA clamp: it is in charge of constraining the ribbon and insuring electric insulation. The adopted solution resulted into a compromise between the requirements and the ease of manufacture, Figure 18.
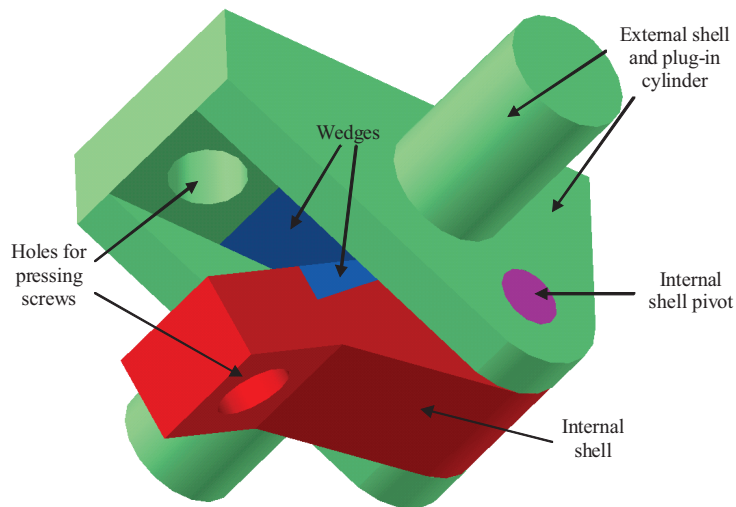
Figure 18. SMA clamp CAD drawing.

The device consists basically of an external and an internal component. The former hosts two lateral cylinders, conceived as plugs within the arch holes. The latter is connected to the external element through a pivot. By rotating, the parts approach until the contact occurs along prepared rough wedges, inserted in their body, Figure 18. A suitable clamping level is then guaranteed to the SMA ribbon, compressed between the two aforementioned components, tighten together by the action of a screw, not shown in Figure 18, passing through appropriate holes. The clamp is made of 15-5PH AMS5659 steel. Since SMA heating is attained by an electrical current circulating inside it (Joule

effect), shunt circuit is avoided by interposing nylon bushes between plug in cylinders and arch holes. An "L" shaped, threaded component is the vertical support for the SMA ribbon, made of the same material as the clamps and allowing height adjustment by dies. The complete arch system is illustrated in Figure 19.
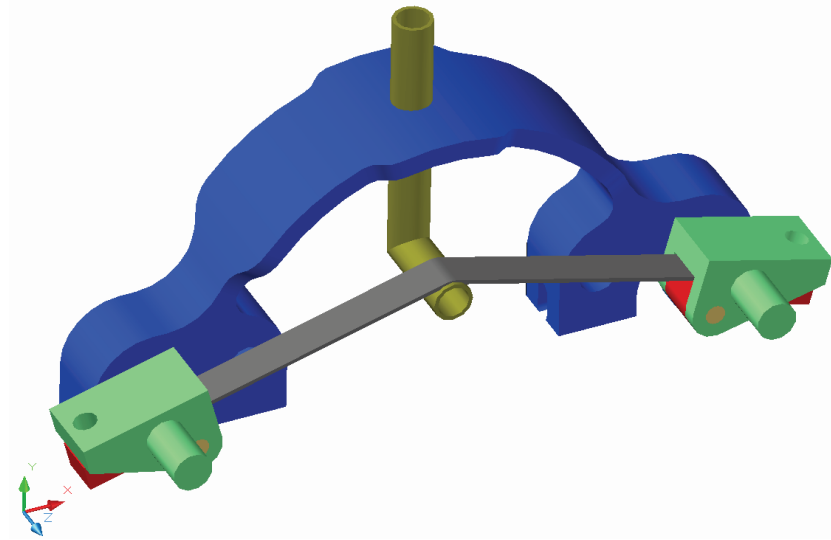
Figure 19. Arch element integrated with clamps, ribbon and vertical stem.

3 – FE Analysis.

Herein, the results of a numerical analysis, carried out on a FE representation of the developed actuator are reported. A classical Finite Element approach was followed; MSC/Nastran solver and UGS/Femap pre/post-processor were used in the job. First, a static non-linear analysis was done: actuator performance was evaluated in terms of the attained rotation and vertical displacement of the free basement. An estimation of the SMA behaviour, complete activation temperature and the stress/strain levels within the arch are also illustrated.

Actuator model

CAD design of the genetically optimized elastic arch was used to develop the initial geometry for the Finite Element analysis, by taking advantage of the import functionalities of UGS/Femap. The numerical model is made of 3D CTETRA elements, Figure 20.
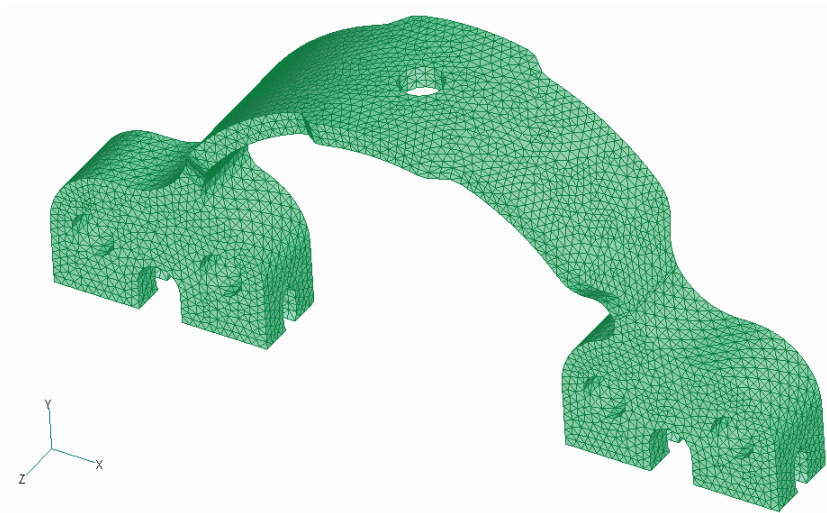
Figure 20. FE model of the titanium elastic arch.

The SMA ribbon and the vertical support rod were simulated by CBEAM elements, Figure 21. Rigid elements were used to reproduce the appropriate constraint conditions between the different components of the actuator system. To avoid stress concentrations at the connections, multiple rigid links were used (not shown in figure for the sake of clarity), to spread the ribbon action to the real connecting arch holes surface.
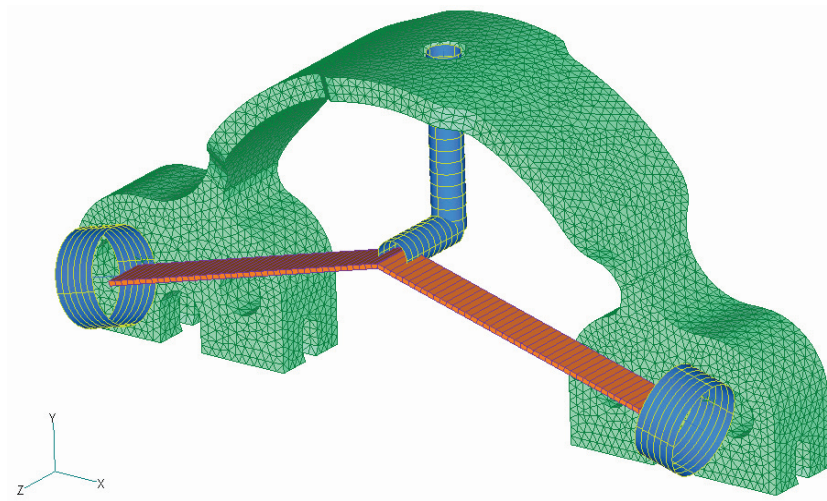
Figure 21. FE model of the proposed actuator.

The ribbon was segmented in two parts hinged at both the ends (at the vertical rod support and the arch connections) to circumvent bending actions, not supposed to be present. In particular, at the joints with the L-shaped rod, the two ribbon pieces were both attached to the central node of the vertical beam, greatly simplifying the connection scheme: to alleviate this approximation, the support beam was shortened to a proper length, resulted to be about 32 mm and consisting of the sum of half the rod radius and half the ribbon thickness.

It should be noted that at the joining between the active element and the central node of the arch connection holes there is an offset, suitable to solve interference problems. Moreover, these ties were achieved by the use of quasi-rigid elements at both the ends, 10 mm long, taking into account the retention mechanism: the ribbon portion being mechanically constrained does not ideally participate to the activation process (in the sense of transmitting forces). The left basement of the arch was perfectly constrained, while the other was left completely free to move. The current model is made of 34155 elements and 61093 nodes.

Actuator operation

Shape memory alloy ribbon action was simulated via FEM by a non-linear thermal analysis, owing to the necessity of taking into account large displacements. The titanium arch is supposed to work within the elastic range of the material. In this simulation, the SMA material model is not directly integrated; details are illustrated further. The elements reproducing the ribbon were then assigned with a proper (negative) thermal contraction coefficient and loaded with a unit thermal gradient. To guarantee the complete activation of the SMA, a large Young modulus was considered (a magnitude larger than other materials involved in the simulation). This procedure ensures the expected effects to occur onto the structure.

To investigate the behaviour of the smart alloy, instead, a separate Matlab routine was developed and implemented. The total non-deformed geometrical length of the SMA ribbon, resulted to be around 136.7 mm. To estimate the herein presented smart actuator performance, its two main working conditions should be considered, namely:

- the "pre-load" condition, corresponding to a 1550 N normal force in the SMA, producing a first 3% normal strain; that force is generated by the elastic arch after it is compressed, instrumented with the active element and successively released to achieve the new equilibrium position;
- the "actuation" condition, when the ribbon recovers the above strain, further deforming the elastic arch.

The net performance of the smart actuator is then obtained as difference between the actuated state (max ribbon contraction with respect to the pre-tensioned configuration and correlated max arch deformation) and the pre-load condition (max ribbon extension at the target deformation – here set at 3% – and arch deformed at the corresponding equilibrium point).

From a numerical point of view, the actuator is firstly brought into the pre-load state (set to a 1550N axial force in the SMA ribbon and equivalent to the martensite finish stress) from the unloaded, geometrical configuration. Under different hypotheses concerning physical and geometrical characteristics, a fictional negative thermal contraction coefficient is attributed to the SMA ribbon for producing the desired inner normal force (found to be 3.88 $^{o}C^{-1}$): this process allows simulating the operational pre-loads occurring into the ribbon, the vertical rod and the arch, otherwise neglected.

At that state, the ribbon results about 131.4 mm long. This value is equal to the effective length of the ribbon once it is connected to the elastic arch and 3% strained (elongated). When it will be heated further, an extra contraction will occur, setting the ribbon length at around 127.6 (= 131.4 / 1.03) mm, that is the full recovery state.

From a practical point of view, the SMA ribbon is originally 127.6 mm long (unloaded). Then, the elastic arch is contracted with a puller, and the ribbon is installed. When released, an equilibrium condition is reached, that can be tuned at the desired pre-load condition (131.4 mm). Upon thermal activation, SMA recovers that deformation, gaining its initial length. Operationally, it can be concluded that:

- the pre-load condition is reached by imposing a thermal load following a thermal coefficient set to 3.88 $^{o}C^{-1}$ under the condition of reaching the desired axial force level into the SMA;

- the actuated condition is reached through a total thermal contraction coefficient of 3.88 + 2.80 = 6.68 $^{o}C^{-1}$ (attained by scaling the 3% set recovery to the real geometrical length).

These two steps are performed into the FE simulations. A summary of the obtained results is reported in Table 9, while the actuator un-deformed and deformed shapes (step 1 and step 2) are illustrated in Figure 22. It must be remarked that this procedures does not implement the physical behaviour of the Shape Memory Alloy, but it is a way to estimate the physical occurrences. Liang & Rogers' model implementation and results are instead presented in the next paragraph, giving rise to prediction updates.

SMA pre-load [N]	1556
SMA actuation force [N]	2641
Force applied to the vertical rod [N]	1979
Net rotation [deg]	6.66
Max stress reached in the elastic arch [N/mm^2]	758
Out-of-plane displacement, arch free basement [mm]	2.82

Table 9. Summary of the estimated numerical performance.
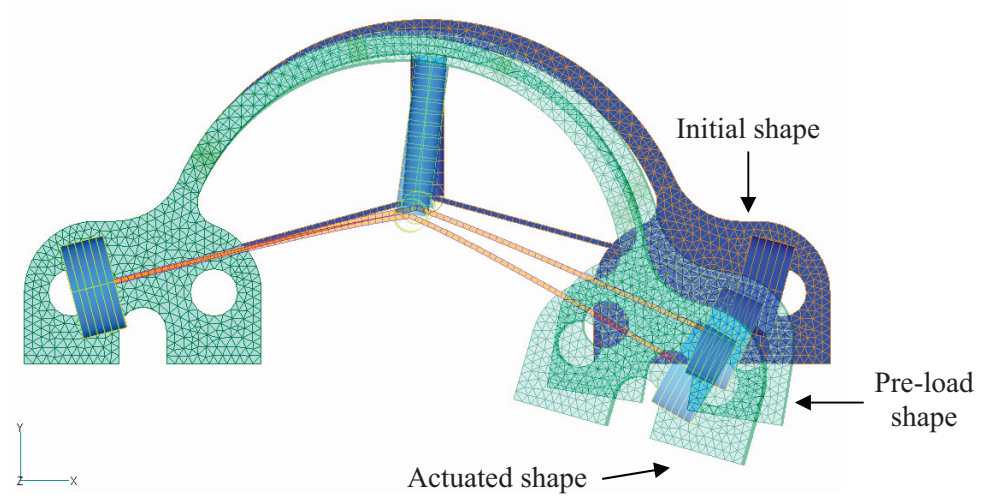
Figure 22. Smart actuator: initial, pre-load and deformed shape.

SMA constitutive equation and behaviour as an actuator

The FE model was integrated with an external proprietary Matlab routine implementing Liang and Rogers' 1D analytical model, [25] to simulate the behaviour of the SMA material. The model assumptions are coherent with the ribbon operation, exhibiting only axial forces. It is derived from a former model, [28], by substituting exponential with sinusoidal expressions in the description of the material composition (austenite vs. martensite fraction, ξ_A and ξ_M), as a function of the temperature, T, and the stress field, σ:

$$\xi = \frac{\xi_M}{2}\cos\left[a_A\left(T - A_S\right) + b_A\sigma\right] + \frac{\xi_M}{2} \qquad \text{Austenite} \rightarrow \text{Marteniste}$$

$$\xi = \frac{1-\xi_A}{2}\cos\left[a_M\left(T - M_F\right) + b_M\sigma\right] + \frac{1+\xi_A}{2} \quad \text{Marteniste} \rightarrow \text{Austenite}$$

(3)

Values a_A and a_M are combinations of material constants A_F, A_S, M_F, M_S, namely austenite finish and start, martensite finish and start temperature: $a_A = \pi/\left(A_F - A_S\right)$ and $a_M = \pi/\left(M_S - M_F\right)$. They are associated to phase transformation onset or completion for both the possible crystalline structures. The other two parameters appearing in the above formulas are $b_A = -a_A/C_A$ and $b_M = -a_M/C_M$, being C_A and C_M the slopes of the linear relationship between the transformation characteristic stress and temperature, [25].

Non-linearity assumption is necessary in order to properly manage the large strains, typical of an SMA application. SMA active components are simulated through beam elements, characterised by a negative expansion coefficient (SMA contracts as the temperature grows). Following activation, the structure deforms under the action of the

alloy; the attained displacement is related to the internal SMA stress. This operation is repeated for growing values of the thermal coefficient, so that the structural stiffness curve may be obtained: in Figure 23b a qualitative trend is shown. For growing absolute thermal coefficients, the structure deforms accordingly and the required actuation force increases. SMA wires will exhibit growing contractions only until the complete transformation into austenite is attained. This point is represented by the intersection of the dot-line with the dotted curve, a graphical representation of the constitutive material law for a generic SMA (high temperature, super-elastic behaviour). This point is the working condition of the proposed actuator. This way of proceeding allows reaching the maximum recoverable strain for the specific configuration (initial stress equal or larger than the martensite finish stress; final stress equal to austenite finish stress for the related temperature).
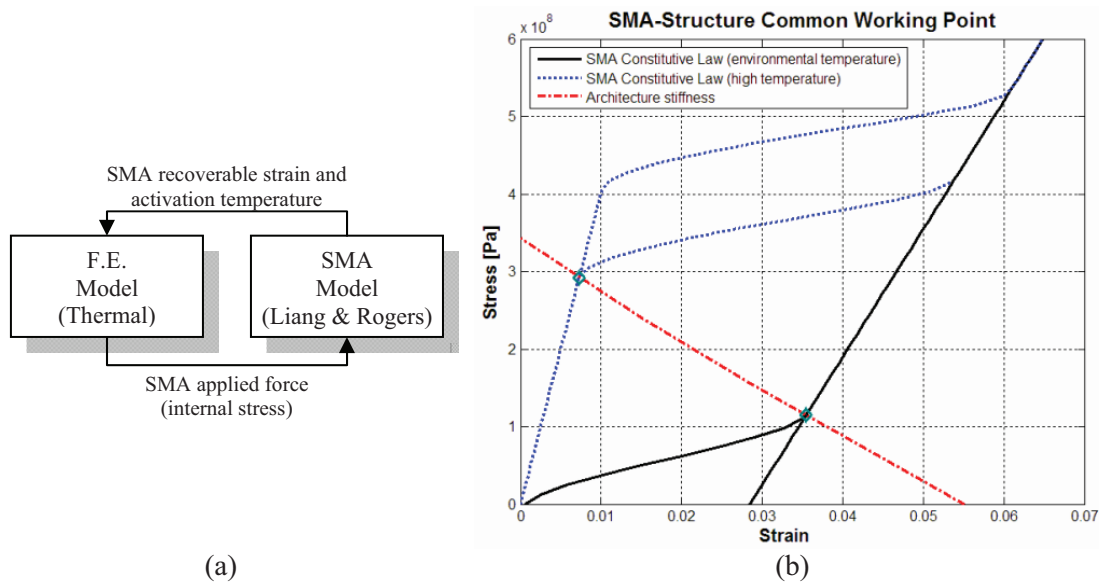
Figure 23. Simulation scheme adopted for SMA integration within the FE approach:
(a) iterative procedure and (b) graphical representation.

The process herein described represents the followed strategy. In order the process to be cyclic, the activation point shall be moved at a pre-stressed configuration featuring a complete martensite state. This assures the capability of recovering the maximum value of strain for the referred architecture (a complete transformation martensite-austenite is accessible). As the SMA is activated, (austenite start), the working point moves towards higher stress values. The final point is met when the desired strain recovery percentage is attained, that can be expressed as a function of the cycles number to be faced, [29, 30]. Apart the assumed 3% recovery strain, an additional pre-strain is numerically

required to attain the necessary SMA pre-load levels (roughly 5% in Figure 23b), as already illustrated in the previous paragraphs.

From a graphical point of view, growing temperature makes the SMA material curve to move up in the stress-strain material plane and the working point shifts towards left, over the lower boundary of the SMA material curve (austenite transformation). By cooling the alloy, the process is reversed under the action of the structural recalling force, and the SMA transforms again into martensite. In this case the working point runs over the higher part of material curve (martensite transformation). In the loading or recovery phase, the transformation may be then said to be temperature- or stress-driven, respectively.

SMA integration and FE model update

According to these considerations, the previously described simulations need to be updated to take into account the SMA behaviour, following Liang & Rogers' model. This step will lead to estimate the effective recoverable strain for the selected SMA ribbon and configuration and, thus, the ultimate thermal contraction coefficient to be used in the final F.E. analysis. The stress-strain curve of the system made of the structural body (arch) and the active element (SMA) is reported in Figure 24. The graph was obtained for growing values of the thermal coefficient and, then, of the SMA strain recovery and actuation. The associated numerical values are reported in Table 10.
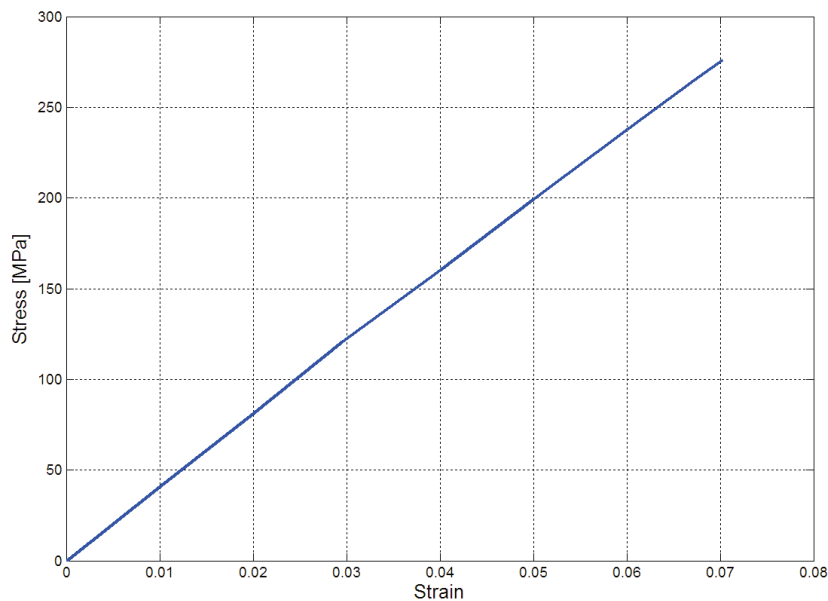
Figure 24. Actuator system stress-strain curve: stress applied vs. strain recovery.

Strain [%]	Stress [MPa]
0	0
0.00996	40.5
0.01996	80.9
0.02955	120.8
0.03882	155.6
0.04003	160.3
0.05009	199.5
0.06018	238.1
0.06725	264.9
0.07028	276.3

Table 10. Stress-strain curve of the structure: numerical values.

The arch elastic behaviour shows then a linear trend for all the considered coefficient values for the ribbon strain recovery. The expected max recoverable strain for the SMA selected material was then evaluated by means of an own Matlab routine, implementing the procedure previously presented. This process also allows estimating the min required activation temperature for the complete phase transformation (recovery) to take place. The input parameters, needed by the adopted model, following Liang & Rogers' formulation, were experimentally measured and are reported in Table 1.

The actuator system estimated working point is reported in Figure 25. It can be noted the 3 % strain matches with a stress level exactly equal to the required 155 MPa (experimentally measured).
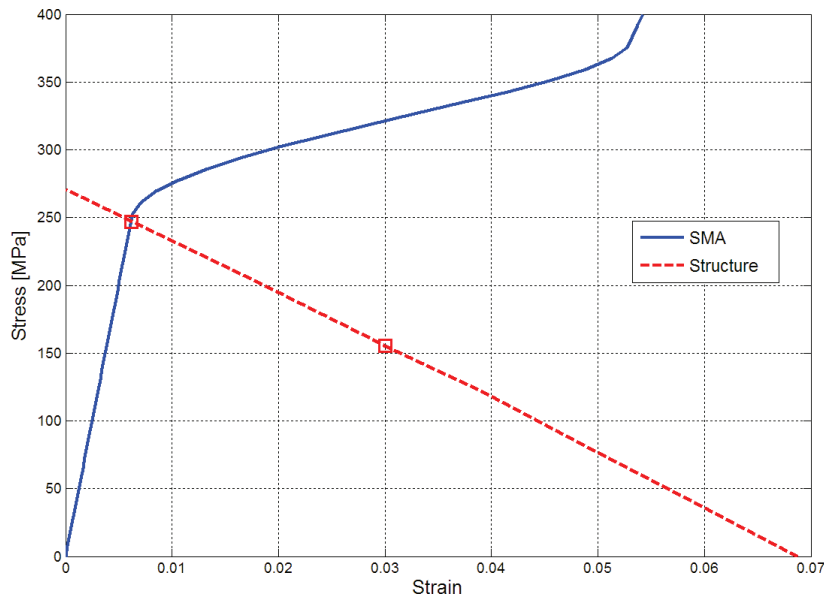
Figure 25. Arch-SMA ribbon assembly working point (congruency principle): stress-strain curve.

Strain recovery as a function of the temperature is instead reported in Figure 26. The min complete activation temperature results into 74.6 °C, corresponding to an effective

2.39 % strain recovery (instead of the theoretical 3%) due to the structural elasticity. According to the illustrated procedure, this quantity is now scaled with respect to the geometrical ribbon length (the one Nastran solver refers to) associated to the very first configuration. In the mentioned case, 2.39 % of the pre-load length equals to 3.05 mm and becomes 2.23 % of the ribbon length (3.05 / 136.7 = 2.23 %).
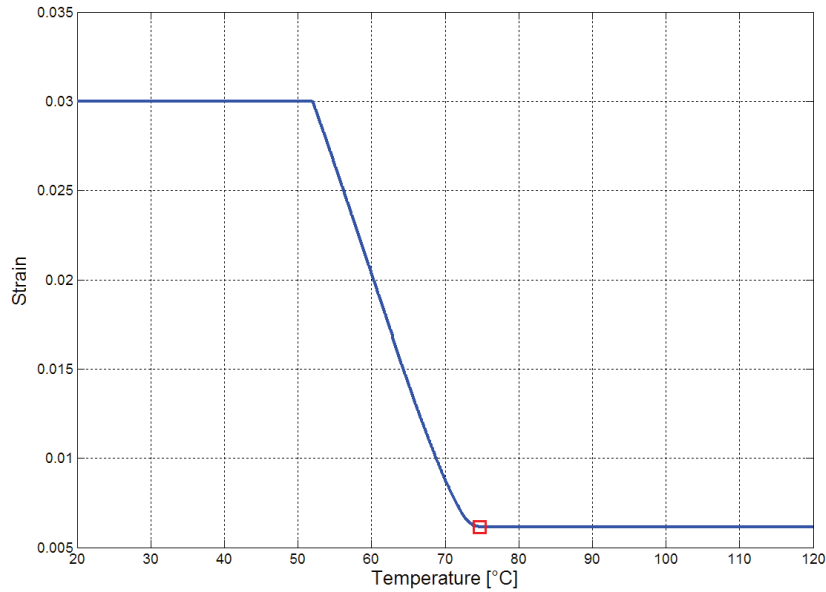
Figure 26. Arch-SMA ribbon assembly working point (congruency principle): strain-temperature curve.

Having determined the effective recoverable strain following the SMA complete activation, the simulation thermal contraction coefficient can be finally updated in the FE model.

In particular, according to the same general scheme previously illustrated, it can be concluded that:

- the pre-load condition is reached by imposing a thermal load associated to a thermal coefficient set to 3.88 $^{\circ}C^{-1}$ under the condition of reaching the desired axial force level into the SMA (this value is the same, given that both the arch geometry and the required pre-load are not changed; it does not depend on the SMA characteristics);

- the actuation condition is instead estimated by a negative thermal coefficient equal to 3.88 + 2.23 = 6.11 % (by scaling the 2.39 % expected recovery to the geometrical length).

The net performance of the smart actuator was then updated and reported in Table 11.

SMA pre-load [N]	1556
SMA actuation force [N]	2424
Force applied to the vertical rod [N]	1776
Net rotation [deg]	5.28 deg
Max stress reached in the elastic arch [N/mm^2]	723
Out-of-plane displacement, arch free basement [mm]	2.60

Table 11. Updated estimated numerical performance by integrating an SMA constitutive model.

4 – Preliminary experimental tests.

The current study presents details about the manufactured titanium arch only, leaving the experimental testing of the complete smart actuator system and the following numerical correlation for future works. In fact, after the arch was manufactured, some further updates were applied to the FE model to better fit the experimental prototype and tune the numerical model, as illustrated in the next paragraphs.

Elastic arch manufacture

The actuator was manufactured on the bases of the final CAD model. The arch was produced by using numerical-controlled machines, milling a solid block of titanium (material references as in Table 7), Figure 27.

Figure 27. Arch manufacture: initial milling of the solid block of titanium.

Additional refinements led to the final shape, reported in Figure 28. The final arch weighs 260 g, in good accordance with the estimated value of 268 g, Table 8.

(a)

(b)
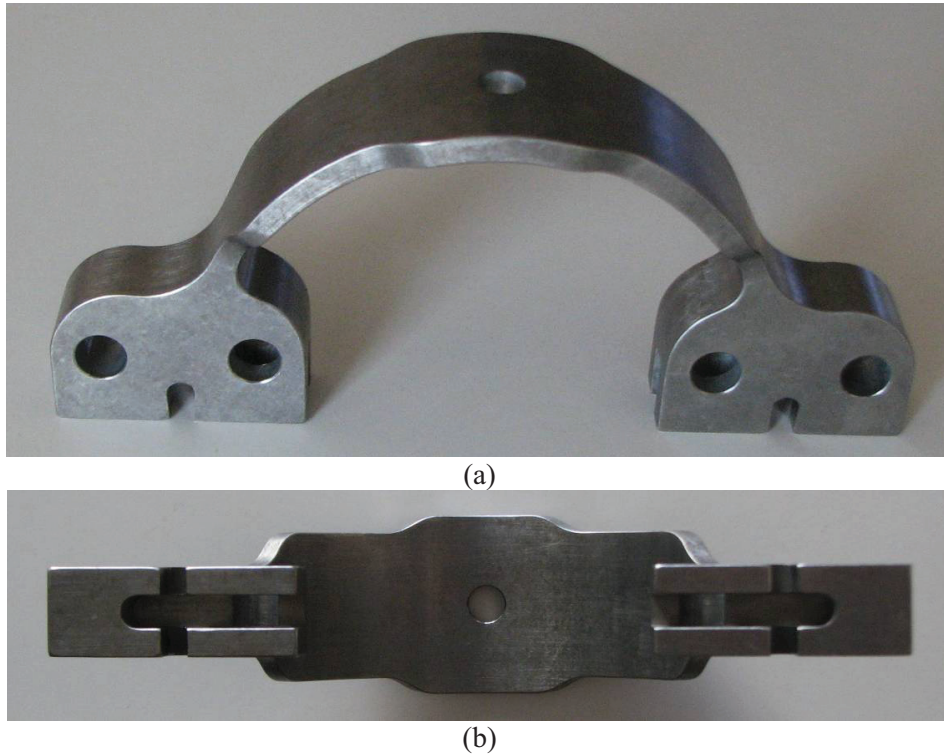
Figure 28. Details of the final manufactured arch: (a) lateral view, (b) bottom view.

Elasticity check of the manufactured arch

The first attempt to check the reliability of the actuator system numerical FE model with respect to its experimental counterpart focused on the titanium arch, the structural core of the device. The tests were carried out to verify the elastic behaviour under different load conditions: variable weights were applied to the free basement and its vertical displacements were measured, Figure 29, at the middle of the most external hole. The configuration, adopted for the equivalent FE analysis, is illustrated in Figure 30. To well correlate the experimental with the numerical results, the angle between the arch basement line and the weight direction, measured in 32 deg, was considered in the model.

Table 12 reports both such numerical and experimental vertical displacements under the same load conditions. The same results are graphically reported in Figure 31. The sound linear elastic behaviour of the titanium arch is evident. According to these outcomes, the numerical model was found to exhibit a softer response than the FE model. A possible

motivation relies on the natural variability of the material Young modulus (set to 110 GPa in the computations), also related to the annealing, after machining the elastic arch.

Load [Kg]	Displacement [mm]	
	Experimental	**Numerical**
1.439	0.39	0.46
3.439	0.95	1.09
6.439	1.82	2.05
12.179	3.43	3.85
38.639	10.2	12.07

Table 12. Experimental and numerical displacements of the free end of the arch, under static loads.
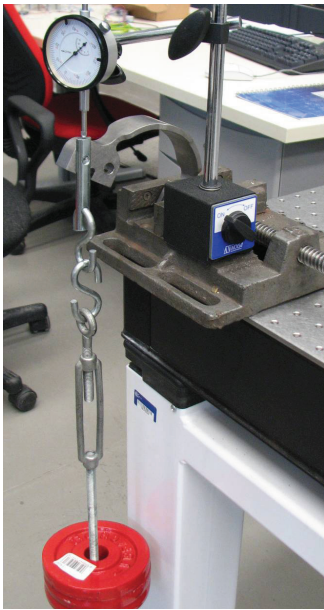
Figure 29: Test set-up – the loaded arch.   **Figure 30: FE model of the loaded titanium arch**
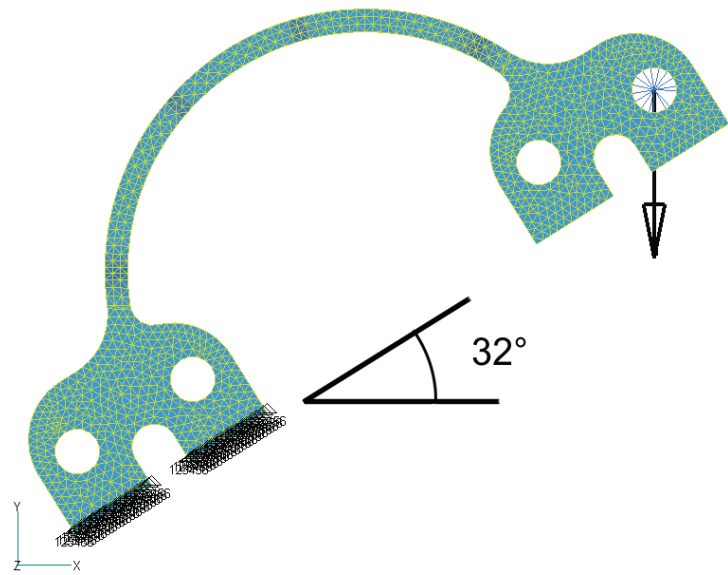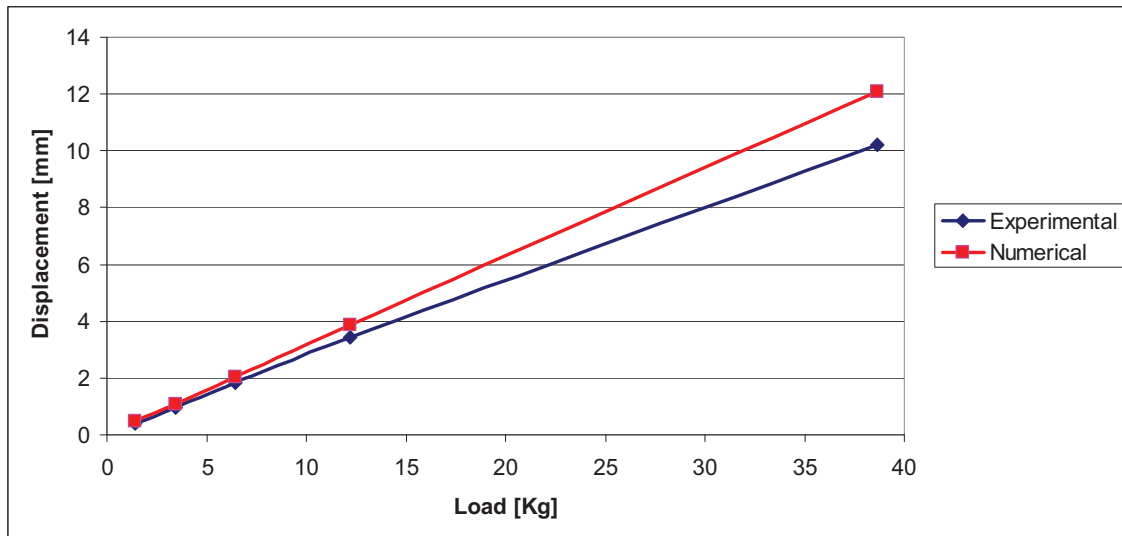
Figure 31. Elastic behaviour comparison between the numerical and experimental titanium arch.

5 – Numerical-Experimental correlation on the elastic arch: F.E. model update.

The experimental prototype resulted stiffer than the numerical prediction. To improve theoretical estimation, titanium Young modulus was increased to 120 GPa, remaining within the classical 10 % engineering uncertainties (reference material: TI-6AL-4V AMS 4911 Annealed).

This update well increased the numerical-experimental correlation, as reported in Table 13 and Figure 32, establishing the basis for a correct simulation of the complete assembly. This change reduced the error in the vertical displacement prediction to about 8.5 % (max deviation).
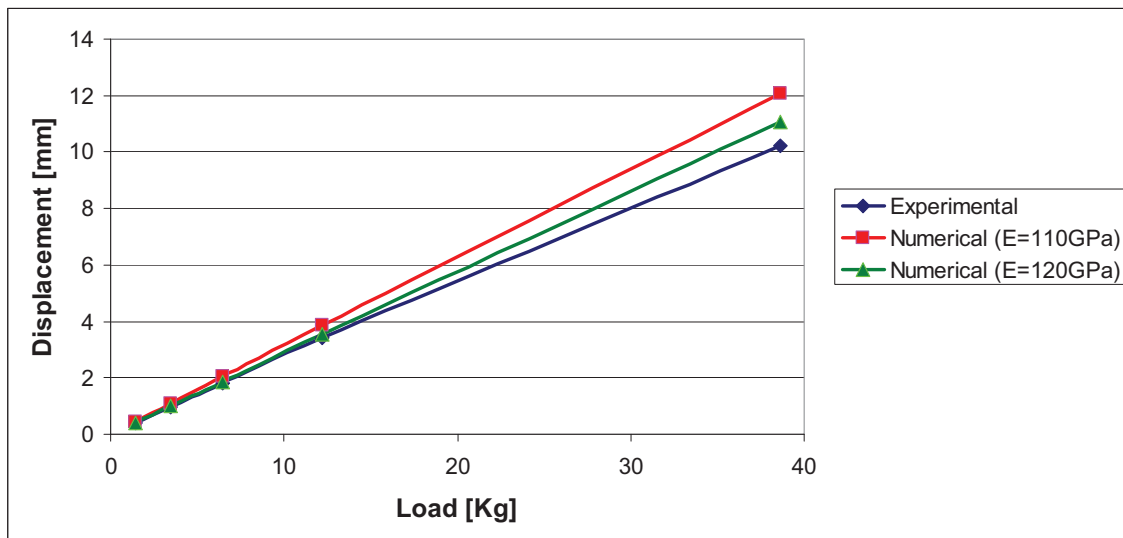
Figure 32. Experimental vs. numerical predictions, for different Young moduli – graphical representation.

Load [Kg]	Displacement [mm]		
	Experimental	Numerical (Ea=110 GPa)	Numerical (Ea=120 GPa)
1.439	0.39	0.46	0.42
3.439	0.95	1.09	0.99
6.439	1.82	2.05	1.86
12.179	3.43	3.85	3.53
38.639	10.2	12.07	11.07

Table 13. Experimental vs. numerical predictions, for different Young moduli – numerical data.

The implemented modification required a complete revision of the former numerical estimation, given the effect on the SMA ribbon pre-load and the following actuation performance. The assessed procedure was again applied. In detail, having assumed a force requisite of 1550N for producing a 3 % pre-strain in the SMA ribbon, the

increased Young modulus modifies the thermal contraction coefficient, necessary to reach the pre-load condition, in the sense of reducing it. A 3.5 % value is estimated, vs the previous 3.88 %: it is evident that an increased stiffness needs lower strain values to exhibit the same forces.

The SMA under pre-load results 131.9 mm long. The un-deformed ribbon length can be then calculated as 131.9 / 1.03 = 128.0 mm. The stress-strain curve of the actuator system, made of the arch and the installed smart element is reported in Figure 33, for growing values of the thermal coefficient; associated numerical values are reported in Table 14.

Strain [%]	Stress [MPa]
0.0	0.0
0.00996	44.0
0.01995	87.6
0.02996	130.9
0.03558	154.9
0.04000	173.7
0.05006	216.1
0.06014	257.9
0.06386	273.2
0.07024	299.2
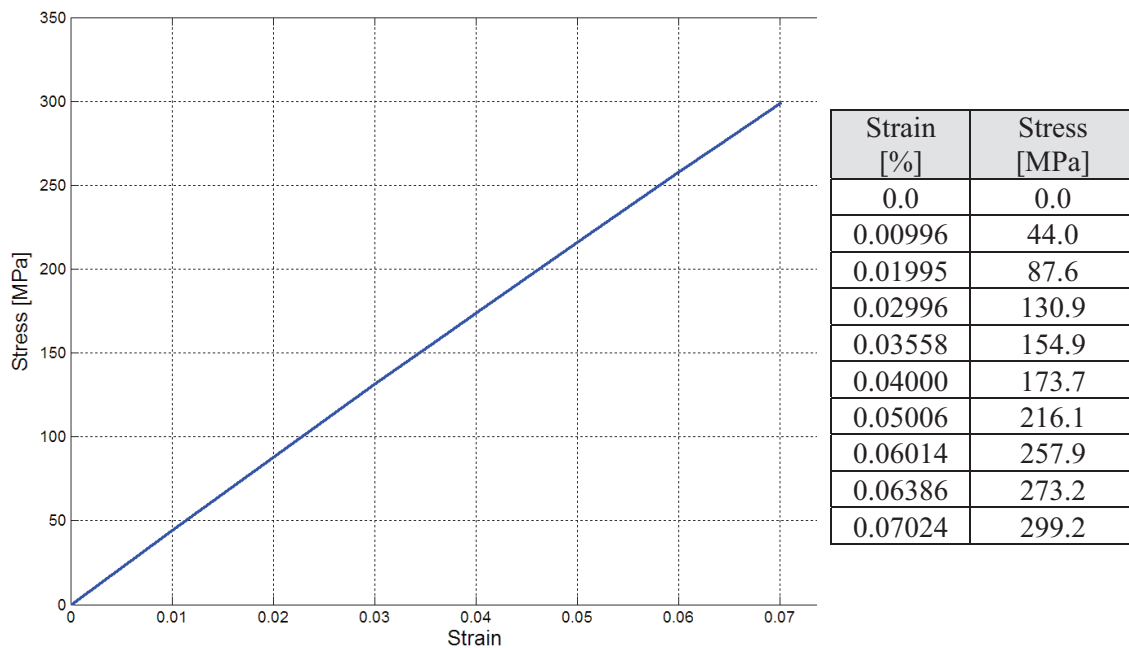
Figure 33. Actuator stress applied – strain recovery – updated model.   **Table 14. Numerical values**

Actuation condition is then defined as the combination of the pre-load and the recovery strain-equivalent thermal coefficient (scaled to the appropriate ribbon length). In Figure 34, the estimated working point for the arch-ribbon assembly is shown: it can be noted once again the simulation steps: 3.56 % pre-strain and the 3 % recovery strain. According to the adopted model, the complete activation temperature results into 75.3 °C, corresponding to an effective strain recovery of 2.37 % for the considered architecture. Higher activation temperature and lower effective recoverable strain is expected, as a consequence of the higher stiffness values. Scaling 2.37 % to the original ribbon length (numerical simulation value), 2.21 % is obtained. The global actuation condition is obtained for a value of 5.77 %.

Summarizing:

- pre-load condition is reached for an imposed 3.56 % strain;

- actuation condition is attained for a 3.56 + 2.21 = 5.77 % strain.

Results about the net performance of the smart actuator are reported in Table 15.
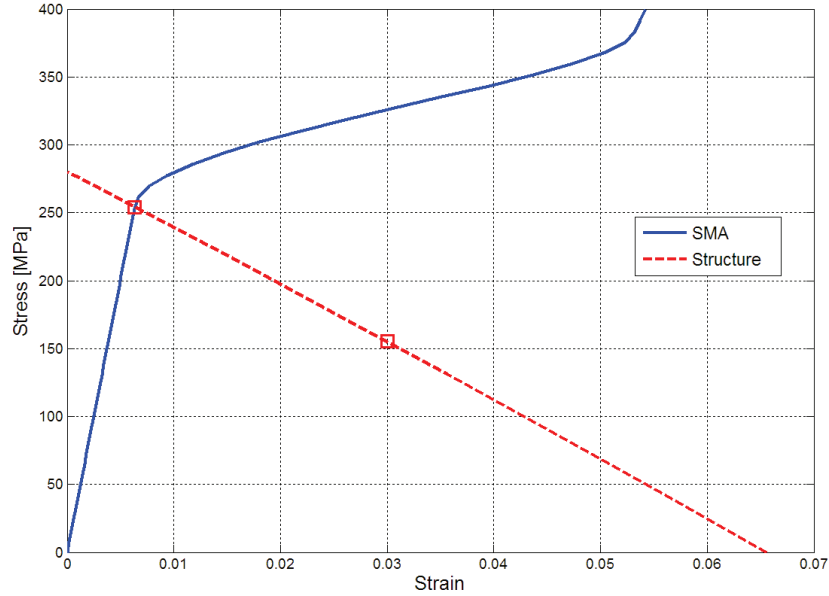
Figure 34. Actuator system working point: congruency principle at the stress-strain curve.
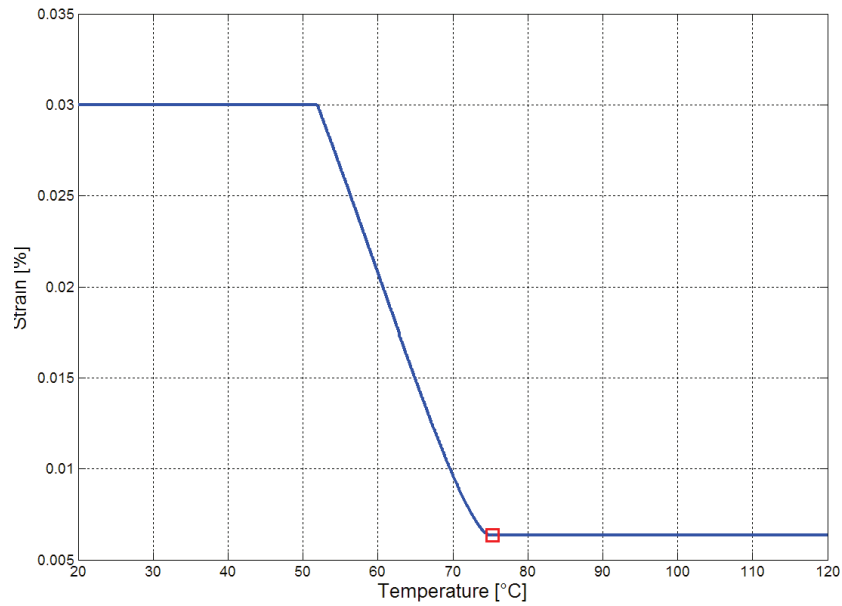
Figure 35. Actuator system working point: strain-temperature curve.

SMA pre-load [N]	1549
SMA actuation force [N]	2487
Force applied to the vertical rod [N]	1790
Net rotation [deg]	5.23
Max stress reached in the elastic arch [N/mm^2]	736
Out-of-plane displacement, arch free basement [mm]	2.52

Table 15. Summary of the estimated numerical performance for the final model.

Strain field on the actuator structure following actuation is reported in Figure 36: max deformation is measured as 0.7 % in some points near the edges; globally, strain is below 0.47 %.
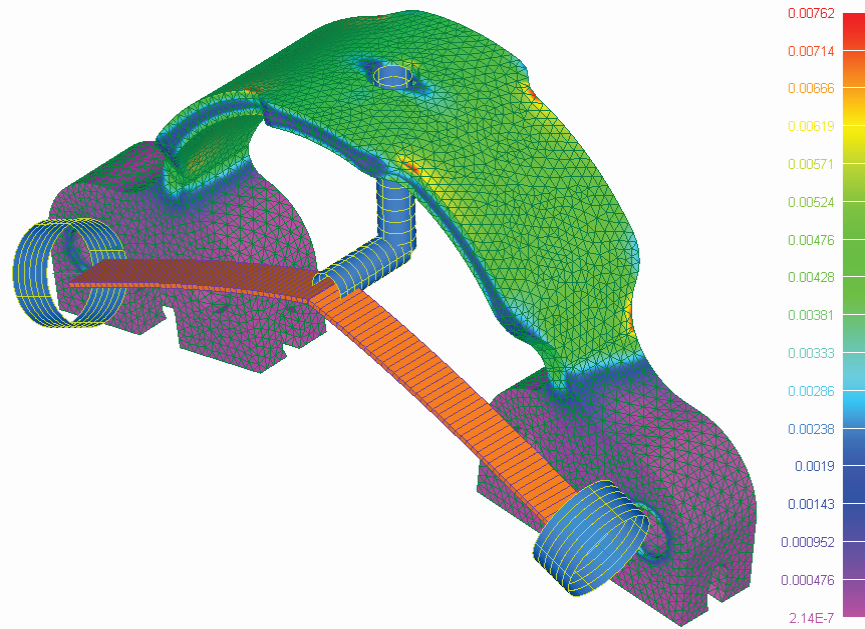
Figure 36. FE model of the smart actuator: contour of the local strains during actuation.

6 – Conclusions.

The paper shows the design process of a structural morphing actuator. In detail, an arc element is referred to and shall provide the necessary robustness with respect to the external loads and an adequate capability in producing deformations. The internal force system, used to generate the required displacements, is originated by the action of an SMA element, fully integrated into the device.

As a starting point, an SMA ribbon is mechanically characterised, so to define the constitutive curve and identify its major parameters, such as austenite and martensite Young moduli, the recovery deformation, activation temperatures and so on. These parameters are implemented in the reference material model, by Liang & Rogers'.

The structural arc is firstly modelled by using a simplified non-linear analytical model (curved beam) in order to address a basic design (thickness, width, radius) capable to guarantee the mechanical stiffness under the expected displacement for SMA pre-loading, and to minimise the required actuation force introduced by the SMA. Then, a suspension device has been found to improve the actuation characteristics, slightly

complicating the actuator architecture; also details of the SMA clamp elements are defined. The final design of the actuator is finally achieved and presented.

The assembled actuator is then meshed in a FE environment: the developed non-linear, iterative approach finds the effective working point of the actuator, where the elastic and the SMA-generated forces are balanced. Numerically estimated performance are reported.

Having completed the design part, the activity is directed towards the manufacturing and testing of the structural component. A description of the real arc is carried out, introducing to the experimental test set-up and the first characterisation campaign. The information acquired during this step are basically aimed at improving the original FE model. Once this step is performed, a full numerical stress analysis is performed, guaranteeing the structural robustness of the realised device.

The designed arc allows reaching the required displacement field still demonstrating an adequate stiffness, addressed to face the external loads. Selected SMA elements demonstrated to produce the required internal forces. Analytical and numerical models and procedures demonstrated their reliability after devoted experimental test campaigns. Specifically, a simulation procedure was set up, addressing both the non-linear behaviour of the structure and the peculiar SMA constitutive law.

Semicircle shape for the elastic element could be substituted by elliptic or other arc-shaped elements in a future design, because of the advantage in lowering the centre of rotation to improve actuation; also other non metallic materials (f.i., composite) could be adopted to reduce weight and size. SMA materials characterised by largest strain recovery or with greater pre-loads could be implemented, in order to improve the actuator performance. Because the energy shall be balanced, of course, larger displacement should produce a penalty in terms of necessary power. On the other side fatigue aspects shall be considered too: a reduction of the utilised strain recovery fraction may improve their behaviour, as reported in literature. Simplifications of the added architecture elements like suspension and clamp devices should be addressed. In the first case, the reference to symmetric scheme should be investigated. In the second one, alternatives like welding should be taken into consideration. Still, the complete arc may be made lighter by a proper optimization analysis of the produced stress field. As a last item, because the arc is supposed to work under a pre-load, tuning mechanical elements should enrich its design to allow fine adjustments, after the SMA is mounted (variation of the structural stiffness).

References

[1] Sater J.M., et alii, 1997, "*DARPA Smart Wing program*" – Engineered Adaptive Structures Conference, United Engineering Foundation, Banff, Canada

[2] Kudva J., 2000, "*DARPA AFRL Northrop-Grumman Smart Materials and Structures Demonstration: Smart Wing Phase 2*" – DARPA Technology Exchange Meeting, June 26

[3] Wright O., 1988, "*How we Invented the Airplane*" – Dover Publications, Mineola (NY-USA)

[4] Stanewsky E., 2001, "*Adaptive Wing and Flow Control Technology*" – Progress in Aerospace Sciences, Elsevier Science Ltd., vol.37, pp.583-667

[5] Frost & al., 1978, "*Airfoil Variable Cambering Device and Method*" – U.S. Patent no.4,247,066, General Dynamics Corporation, Fort Worth, TX

[6] Statkus F.D., 1980, "*Continuous Skin Variable Camber Airfoil Edge Actuating Mechanism*" – United States Patent No. 4,351,502, The Boeing Company, Seattle, WA

[7] Simpson A., Coulombe N., Jacob J., Smith S., 2005, "*Morphing of Inflatable Wings*" – 46th AIAA/ ASME/ASCE/AHS/ASC Structures, Structural Dynamics and Materials Conference, Austin, Texas, AIAA J. 2005-2110

[8] Moses R.W., 1997, "*Active Vertical Tail Buffeting Alleviation on a Twin-Tail Fighter Configuration in a Wind Tunnel*" – International Forum on Aeroelasticity and Structural Dynamics, CEAS, June, pp. 269-276

[9] Ruiz-C. L.P., 2000, "*EREA Adaptive Airfoil Project*" – Exec. Summ., February, INTA, Torrejon de Ardoz, Spain

[10] Monner H.P., Bein T., Hanselka H., Breitbach E., 1998, "*Design Aspects of the Adaptive Wing – The Elastic Trailing Edge and the Local Spoiler Bump*" – Royal Aeronautical Society, Multidisciplinary Design and Optimization, London, October 1998

[11] Gevers Aircraft Inc., 1997, "*Multi-Purpose Aircraft*", United States Patents Office, Patent Number 5,645, 250

[12] Smith S.B., Nelson D.W., 1989, "*Determination of the Aerodynamic Characteristics of the Mission Adaptive Wing*" – 6th Applied Aerodynamics Conference, Williamsburg, VA, AIAA J. 88-2556

[13] Inman D.J., 2001, "*Wings: Out of the Box. Determining Actuator Requirements for Controlled Morphing Air Vehicles – Aerodynamic Loads*" – DARPA

Technology Interchange Meeting, Wright Patterson Air Force Base, Dayton, Ohio, Nov. 2001

[14] Wilson J.R., 2002, "*Active Aeroelastic Wing: A New/Old Twist On Flight*" – Aerospace America, vol.40, no.99, pp.34–37

[15] Austin F., Siclari M.J., Van Nostrand W., Weisensel G.N., Kottamasu V., Volpe G., 1997, "*Comparison of Smart Wing Concepts for Transonic Cruise Drag Reduction*" – SPIE 1997, p.3044

[16] Perkins D.A., Reed J.L., Havens E., 2004, "*Morphing Wing Structures for Loitering Air Vehicles*" – 45th AIAA/ASME/ASCE/AHS/ASC Structures, Structural Dynamics & Materials Conference, Palm Springs, California, AIAA J. 2004-1888

[17] Barbarino S., Ameduri S., Pecora R., 2007, "*Wing Camber Control Architectures based on SMA: Numerical Investigation*" – International Conference on Smart Materials and Nanotechnology in Engineering (SMN2007), July 1-4, Harbin, China, Proceedings of SPIE vol. 6423, 64231E-1, (2007), 8pp., doi: 10.1117/12.779397

[18] Barbarino S., Pecora R., Lecce L., Concilio A., Ameduri S., Calvi E., 2009, "A Novel SMA-Based Concept for Airfoil Structural Morphing" – Journal of Materials Engineering and Performance (JMEP), vol.18, issue 5, pp.696-705 (2009), doi:10.1007/s11665-009-9356-3

[19] Campanile L.F., Melz T., Keimer R., Wadehn W., 2003 – Patent DE10155119A1

[20] Langbein S., Welp E.G., 2009, "*One-Module Actuators Based on Partial Activation of Shape Memory Components*" – Journal of Material Engineering and Performance, vol.18, no.5-6, pp.711-716

[21] Electric Piston, Mondo-tronics Inc., website: http://www.robotstore.com

[22] Banks R.M., 1975, "*Energy Conversion Systems*" – Patent US03913326

[23] Bokaie M. of TiNi Alloy Co. for NASA Lewis Research Center, February 1998, LEW-16511, website: http://www.nasatech.com/Briefs/Feb98/LEW16511.html

[24] Iannuzzo G., Riccio M., Russo S., Calvi E., Pecora R., Lecce L., Barbarino S., Concilio A., Ameduri S., "*An actuator device based on a shape memory alloy, and a wing flap assembly fitted with such an actuator device*" – Filed on July 21, 2009 at the European Patent Office, 2280 HV Rijswijk, Netherland, application/patent no. 09165941-7 - 1254, proprietor Alenia Aeronautica S.p.a., priority IT/23.07.08/ITA TO20080566

[25] Liang C. and Rogers C.A., 1990, "*One-Dimensional Thermomechanical Constitutive Relations for Shape Memory Material*" – J. of Intelligent Material Systems and Structures, vol.1, no.2, pp.207-234

[26] Goldberg D.E., 1989, "*Genetic Algorithms in Search, Optimization & Machine Learning*" – Addison-Wesley Publishing Company Inc., ISBN: 0-201-15767-5

[27] Richards R., 2001, "*Principles of Solid Mechanics*" – CRC Press LLC, ISBN 0-8493-0114-9, pp.162-164

[28] Tanaka K., 1986, "*A Thermomechanical Sketch of Shape Memory Effect: One-Dimensional Tensile Behaviour*" – Res. Mechanica, vol.18, no.3, pp.251-263

[29] Srinivasan A.V., McFarland D.M., 1995, "*Smart Structures: Analysis and Design*" – Cambridge University Press, ISBN 0-521-65977-9

[30] Shimizu K., Tadaki T., 1987, "*Shape Memory Alloys*" – Funakubo H. Ed., Gordon and Breach Science Publishers, New York, pp.1-60

PAPER

"A Novel Smart Actuator for Airfoil Structural Morphing: Test Campaign and Numerical Correlation"

S. Barbarino, L. Lecce, A. Concilio, S. Ameduri, L. De Rosa

A Novel Smart Actuator for Airfoil Structural Morphing: Test Campaign and Numerical Correlation

S. Barbarino[a], L. Lecce[a]
A. Concilio[b], S. Ameduri[b]
L. De Rosa[c]

[a]Dept. of Aerospace Engineering, Univ. of Naples "Federico II", Via Claudio 21, Naples, Italy
[b]Smart Structures Lab., The Italian Aerospace Research Centre (CIRA), Via Maiorise, Capua (CE), Italy
[c]ALENIA AERONAUTICA S.p.a., Viale dell'Aeronautica snc, Pomigliano d'Arco (NA), Italy

Abstract
The concept of aircraft structural morphing refers to systems enabling load-bearing capabilities while allowing sufficient deformations. These devices try to overcome the paradox of guaranteeing a certain robustness but permitting large displacements. An adaptive structural wing promises large advantages in terms of weight, general performance, architectural complexity and so on. The authors chose to refer to stiff actuators, able to sustain external forces. Such actuators can be integrated with proper structural elements, in order to ensure the desired stiffness and mobility. It is the complete actuator system to replace the shape enforcing element, providing at the same time the force-displacements field to achieve the target shape. Shape Memory Alloys were selected as smart elements, mainly because of their peculiar properties of developing high mechanical energy levels. An arc-shaped load-bearing metallic actuator is the object of this paper. A EU patent is pending for this device. After a short recall on the arc components design, the numerical model of the complete system is presented. Then, its manufacture and assembly are described. The experimental characterisation campaign is finally illustrated: the structural part is integrated with the SMA active element and its static response is evaluated and compared with the numerical predictions. The actuator design takes into account the necessity of ensuring a pre-load, aimed at fully recover the original position after activation, as well as the attainment of the prescribed displacement requirements. The device characteristics are time-stable. The experimental prototype behaviour is well represented by the proposed numerical models and procedures.

Keywords: SMA, Actuator, Morphing, Test, Correlation

1 – Introduction.

The concept of aircraft structural morphing refers to systems enabling load-bearing configurations while allowing sufficient deformations, with respect to the issued requirements. These devices try to overcome the evergreen paradox of the adaptive structures in guaranteeing a certain robustness but permitting large displacements, [1]. This necessity is strictly related to integrated apparatuses for substituting wing mobile surfaces (like flaps and ailerons) actuators systems.

The research for integrated devices that could substitute classical rigid movable elements is a sort of flashback to the architectures of the first powered aircrafts, when the manoeuvres were performed through modification of the wing shape, [2]. It was only the increased flight speed and the consequent growth of the aerodynamic loads as well as the onset of static and dynamic instabilities, that forced the designers to use rigid wing sections. A fundamental role was played by the introduction of the smart materials in the scientific community. They allowed thinking to architectures, namely able to shape the structure in order to face different flight conditions, while avoiding any kind of classical cinematic system. They drastically led to visions where the complex devices enabling wing modifications could be substituted by simplest and more compact structures.

Precursors of aircraft morphing devices were the systems mounted on the De Havilland Buffalo, where a rubber LE driven by a standard electrical motor modified the airfoil shape at landing or take-off, the Northrop-Grumman F14, where a standard mechanical system allowed attaining in-plane wing geometry variations, and other applications on inflatable lift devices, like the Stingray, [3-6]. The Concorde itself had a variable fuselage device, aimed at increasing the lift at take-off and landing. In the nineties of the last century, the introduction of the piezoelectric ceramics in the active noise and vibration control field, focused the attention towards structural dynamics control. F18 vertical tail buffeting attenuation by PZT was studied [7], being one of the first attempt of lift surfaces control by smart materials. Inside EREA group, the Adaptive Airfoil project started in 1997, concerning the realisation of a morphing bump over an airfoil surface, aimed at reducing shock wave-induced drag, [8].

However, it was with the DARPA "Smart Materials and Structures" technological program [9], and the successes attained by the Northrop Grumman team, led by Jay Kudva [10], to set a turning point in the aircraft structural control. Jay Kudva started by using Shape Memory Alloys (SMA) to morph an UCAV wing, to come to refer to some more traditional eccentric actuators in the last frame of his first research, [10]. Other authors looked at the possibility of modifying different parts of the wing structure to achieve certain shape modifications by means of normal, bending or torsion actuators, [11-17]. An adaptive structural wing promises in fact to lead large advantages in terms of weight, general performance, architectural complexity and so on. It is not just matter of lightest, but also cleanest systems from the aerodynamic point of view, shunning the use of nacelles and other covers. The devices may be in fact completely integrated in the

structural body. An obvious consequence derives: the architecture implementing smart structural devices shall be different, in principle, than a similar, classical one, aimed at the same objective.

Smart actuators often refers to weakened structure elements, in order to be able to provide the required deformations, [11-17]. However, this kind of solution exposes the structure to external loads action, in the same way. The authors chose instead to refer to stiff actuators, able to sustain external forces, [18]. Such actuators shall be integrated with proper structural elements, in order to ensure the desired stiffness and mobility. It is the complete actuator system to replace the shape enforcing element (rib, for instance), being at the same time the part that provides the force-displacements field to achieve the target shape. In such a way, the wing will appear externally clean.

As smart elements, the authors selected SMA, already tested before. This choice was driven by two peculiar properties of such materials: the capability of developing relatively high mechanical energy levels and the absolute characteristic of exhibiting namely the same contraction, irrespectively of the acting external force (within a suitable range). However, because the external loads produce an initial deformation that has to be equally recovered, they effectively subtracts a certain effectiveness to the SMA action. In literature, Shape Memory Alloys have been selected as "active" elements for the development of several innovative actuators [19-23] due to their compactness and better power/weight ratio in certain circumstances when compared to traditional ones: usually, the SMA element is joined by a spring system to allow for cycles. The novelty of the herein presented work is the design of the adopted elastic element also as highly integrated structural element of a morphing rib that will be presented in a successive paper. After having experienced several solutions, a summary of which was reported in [18], the authors came to an arc-shaped metallic actuator, the design of which was described in a previous paper [24]. Therein, the single components design was presented: the active element, in a shape of an SMA ribbon; the structural elastic part, in the form of a metallic arc; the supporting devices, aimed at realising the necessary constraints and connection components. After a short recall on the arc components design, this work starts with describing the numerical modelling of the complete actuator system and its real manufacturing and assembly. Therefore, the experimental characterisation campaign is illustrated: the structural part is integrated with the SMA active element and its static response is evaluated and, then, compared with the numerical predictions. This fully characterised actuator and its numerical

version are the basic element of the envisaged morphing rib that will be presented in a future paper. A patent is pending on the presented actuator assembly [25].

2 – Actuator design and F.E. simulation.

The device shows two main components: a SMA element combined with an elastic spring, Figure 1.
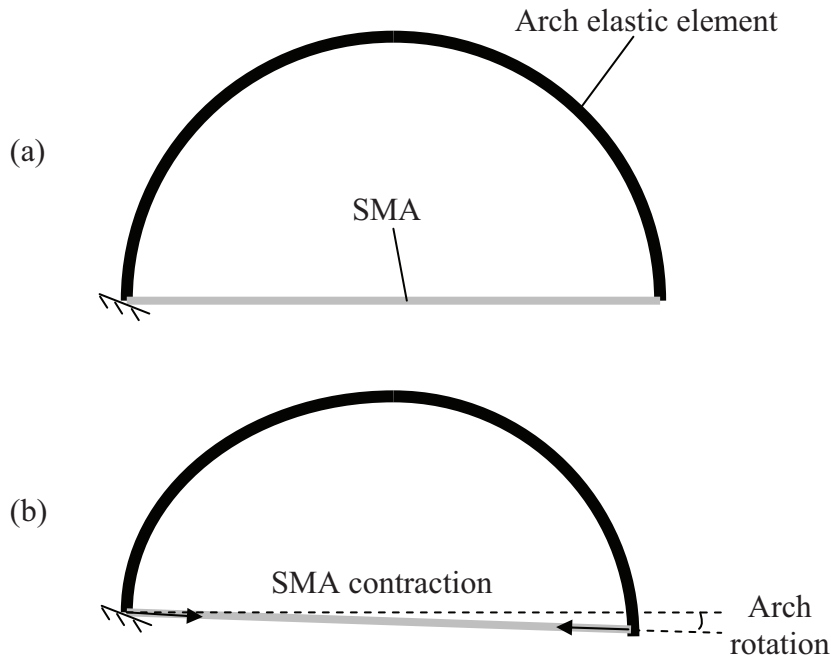
Figure 1. Actuator conceptual scheme and working modality: (a) initial and (b) actuated configuration.

In the referred configuration, "One-way" SMA elements are used: after activation, an external load is then required to come back to the initial state. This is provided by the elastic element (made of Titanium TI-6AL-4V AMS 4911 ANNEALED), opportunely pre-loaded. Among the different spring types, the authors opted for an arch-shaped one, because of intrinsic flexibility and the larger attainable rotations.

Different considerations drove the design phase. Being the device an aerospace-oriented product, parameters like weight and costs, as well as fatigue life, were taken into account. Arch geometry and material choice was directed to limit over-all dimensions (embeddable system) and structural weight. Operative stress field was kept low, to mitigate cyclic loads effects (fatigue). Other issues were linked to the necessity of insuring the cited recovery pre-load to the SMA element and to the opportunity of reducing the necessary activation force.

A dedicated experimental campaign was planned to detect the main features of the adopted SMA material, in the selected shape. In detail, a commercially available NiTiCu ribbon, 10 x 1 mm cross section, was tested in order to get the parameters, required as input by the adopted simulation model [26]. Ultimate stress test at room temperature was performed to appreciate the max available elongation and martensite Young modulus. A tensile test at 100 °C allowed instead measuring austenite Young modulus; in this case, a controlled chamber was used. Main results are reported in Table 1, together with the characteristic activation temperatures (manufacturer's data).

Martensite Young modulus, E_M [GPa]	16.5
Austenite Young modulus, E_A [GPa]	40.2
Ultimate elongation [%]	12.0
Target recoverable strain [%]	3.0
Min necessary pre-load [MPa]	155.0
Martensite start temperature, M_S (C°)	*43.3*
Martensite finish temperature, M_F (C°)	*27.5*
Austenite start temperature, M_S (C°)	*47.3*
Austenite finish temperature, M_F (C°)	*58.9*

Table 1. Selected SMA material properties.

A curved beam theory-based approach [27] was followed to design the arch, coherent with the expected configuration, characterised by a large radius to thickness ratio. A dedicated FE model was then realised, and the different predictions compared, showing a deviation on displacements and stresses smaller than 2%.

A geometric optimisation was finally carried out, through a home-made genetic algorithm [28], referring to the theoretical model. At first, radius, thickness and depth distributions were maintained constant along the tangential coordinate, and assuming values in the ranges reported in Table 2. A multi-objective function was defined, including both allowable stress and produced forces. This choice means reducing contemporarily the arch operative stress level and the SMA-produced force during actuation.

Thickness [mm]	$1 \div 10$
Mean radius [mm]	$50 \div 100$
Depth [mm]	$2 \div 20$
Material	Steel
σ_{alw} [MPa]	1700
F_{alw} [N]	1600

Table 2. Optimisation parameters variation ranges and constraints.

Attained pre-load and other results are illustrated in Figure 2 and summarised in Table 3.
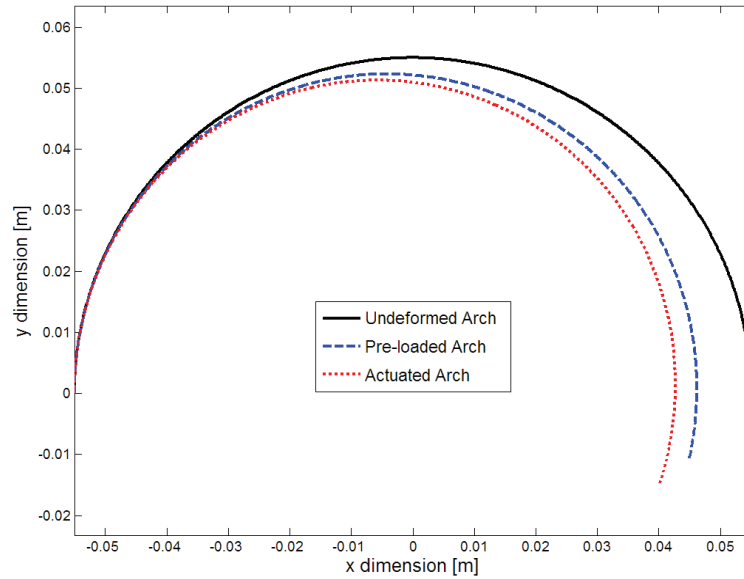
Figure 2. Preliminary optimisation results.

Mean radius, [mm]	55	SMA pre-load, [N]	1550
Thickness, [mm]	5	SMA actuation force, [N]	2009
Depth, [mm]	18	Over-all rotation, [deg]	2.66
Material:	Steel	Max stress, [N/mm^2]	1541

Table 3. Preliminary optimisation results.

Further optimisations were then carried out, considering for instance the possibility of radius-variable arches to push down the rotation centre, maximising downwards motion. The algorithm however privileged solutions characterised by homogeneous radii distribution, corresponding to a uniform stress distribution. Linear tapered thickness were also investigated, but also in this case homogeneous solutions were preferred, avoiding manufacturing penalties associated to limited performance improvements.

In the end, to maximise SMA energy authority, a vertical rod was mounted at the middle of the arch, to enforce a larger action path and a stringer bending action. The effects due to the rod length were explored. The best compromise between actuation efficiency (arch rotations) and structural integrity (stress field level) was found for a 75% radius height rod, Figure 3. Achieved rotation and arch max stress resulted into 6.73 deg and 1425 N/mm^2, respectively.

After having fixed reference parameters, the executive design was defined. To prevent SMA-arch interference at the clamps, the asymmetric configuration, depicted in Figure 4 (FE model), was referred to. Clamps were tailored to assure proper connections between ribbon and the arch edges (allowing relative rotations) yet electrically insulating the actuation element (SMA activation is realized through Joule effect). In the CAD drawing, reported in Figure 5, the connection system is shown.
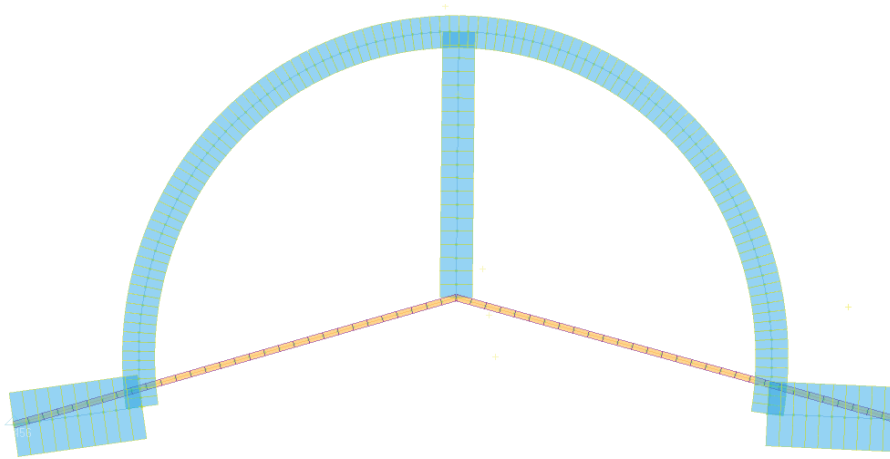
Figure 3. FE model of the arch with the central vertical rod.
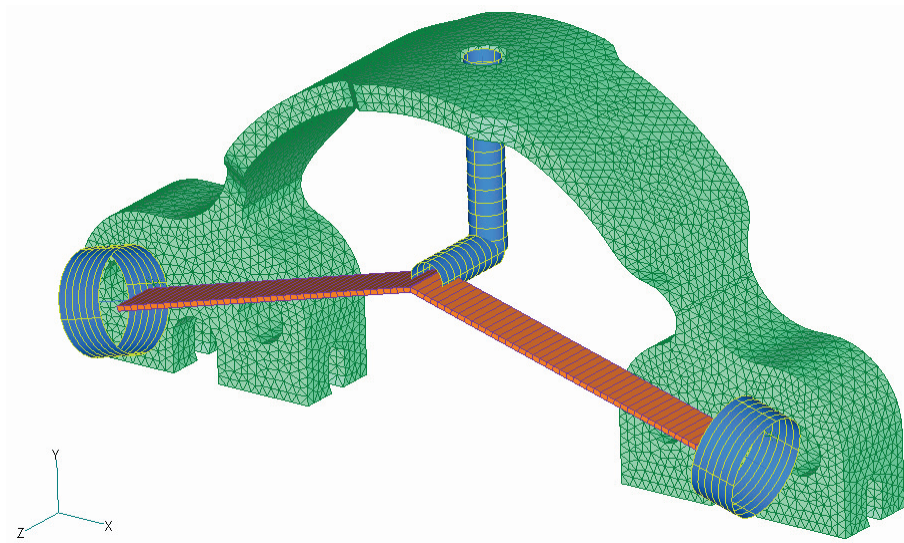
Figure 4. FE model of the arch with asymmetric actuation.
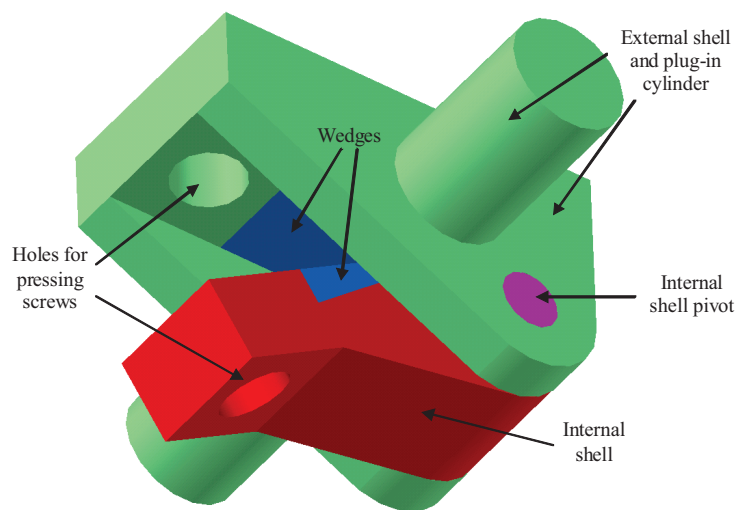
Figure 5. SMA clamp CAD drawing.

It is made of an external shell connected to the arc edge via a plug-in cylinder (hinge) and an internal shell, compressing the ribbon through a passing screw. Shells may

relatively rotate to ease the ribbon installation. Inner wedges are rough enough to magnify friction between clamps and SMA ribbon. A nylon sheet (not shown) is mounted between the plug-in cylinder and the relative installation hole to guarantee desired electrical isolation.

The arch width was dimensioned to counter the effects related to the asymmetric SMA action, then reducing the out-of-plane displacements. SMA activation was simulated by a thermal load, acting to the ribbon elements, associated to a negative contraction coefficient. Ribbon shrinks a given quantity under a unit temperature gradient.

To guarantee the complete contraction to occur, a large Young modulus was assumed for the SMA material (one order of magnitude larger than the other materials involved in the simulation), not affecting the simulation results in terms of structural behaviour prediction. A Matlab-based code implemented Liang & Rogers' model [26] to estimate the intrinsic behaviour of the alloy. Actuator system performance were achieved through a non-linear analysis (large displacements are searched for) and are illustrated in Table 4.

SMA pre-load [N]	1549
SMA actuation force [N]	2487
Force applied to the vertical rod [N]	1790
Net rotation [deg]	5.23
Max stress reached in the elastic arch [N/mm^2]	736
Out-of-plane displacement, arch free basement [mm]	2.52

Table 4. Summary of the estimated numerical performance.

From a numerical point of view, the arc-shaped actuator is firstly brought into a pre-load state (set to 1550 N axial force in the SMA ribbon and equivalent to a 3% strain) from the unloaded, geometrical configuration. When SMA activation is simulated, an extra contraction occur, whose amount is estimated by Liang and Rogers' model. Further details about the smart actuator design and optimization process, F.E. simulation and SMA behaviour integration can be found in a previous work [24].

3 – Experimental prototype.

The actuator was manufactured on the bases of the final CAD model. The arch was produced by using numerical-controlled machines, milling a solid block of titanium (TI-6AL-4V AMS 4911, Annealed), as shown in Figure 6. Additional processing brought to the final shape, Figure 7: details of the manufacturing process will not be discussed

here. Other details are reported in [24]. The final arch weights 260 g, coherently with the numerical estimated value of 268 g (CAD model).

In Figure 7(b), a particular of the basement processing can be observed, needed to accommodate the puller. The assembly of the elastic arch with both the puller and the vertical L-shaped rod is shown in Figure 8. A couple of mechanical clamps was manufactured for connecting the SMA ribbon to the elastic arch, yet allowing rotations; details are visible in Figure 9 and 10.

Figure 6. Arch manufacture: initial milling of the solid block of titanium.
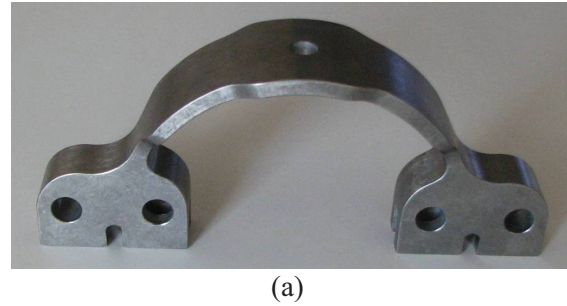
(a)

(b)

Figure 7. Details of the final manufactured arch: (a) lateral view, (b) bottom view.
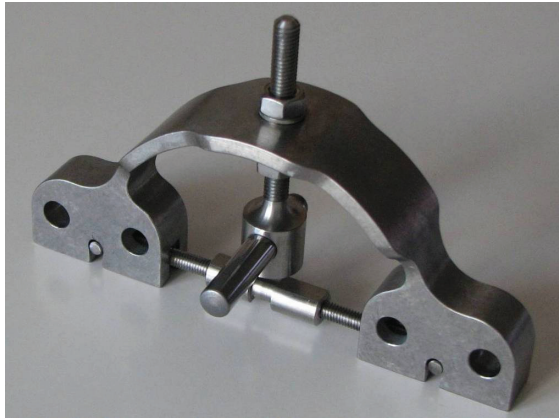
Figure 8. Assembly of the elastic arch together with the puller and vertical L-shaped rod.
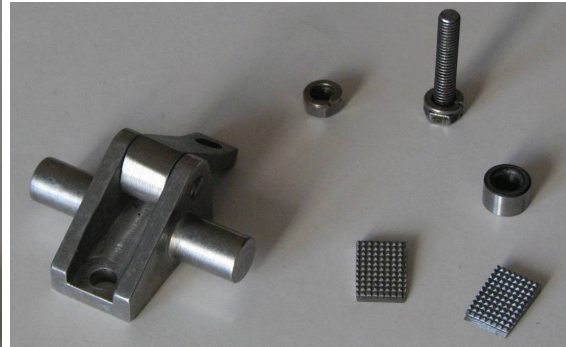
Figure 9. Details and components of the mechanical clamp for the SMA ribbon.

For each clamp, one plug-in cylinder was further processed; this, inserted in the arch holes, makes the hinge system. Because the SMA ribbon was activated through an electrical current (heating by Joule effect), insulation from the rest of the device was necessary. It was realised by means of a nylon ring (1 mm thick; 10 mm external diameter) inserted into the clamp holes, as shown in Figure 11. The vertical rod, supporting the ribbon, was suitably insulated too.
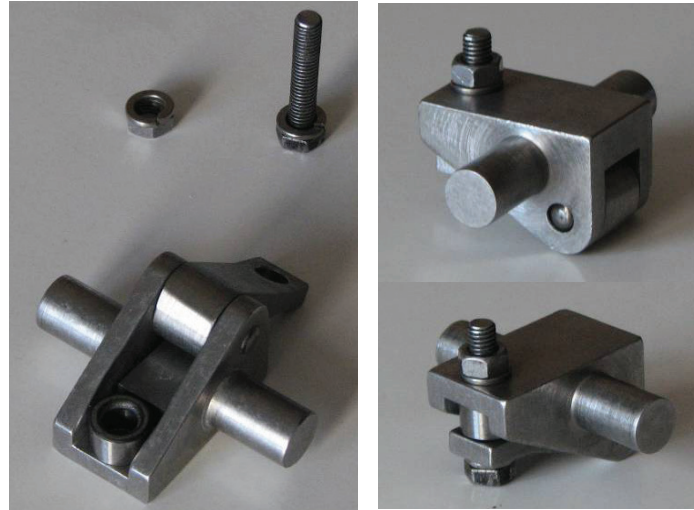
Figure 10. Mechanical clamp: details.

| (a) | (b) |
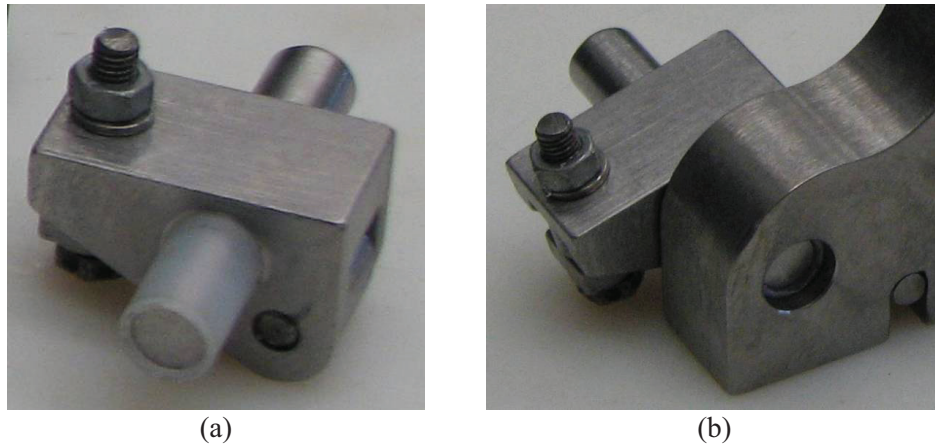
Figure 11. Electrical insulation system details: (a) nylon ring, (b) assembled view.

Figure 12: Experimental prototype: full assembled view (SMA ribbon not installed)

The measured weights for each component are reported in Table 5. A full view of the complete assembled actuator (SMA ribbon not yet installed) is presented in Figure 12.

Item	Weight [g]
Complete Actuator System	630
Titanium arch	260
Single clamp	70
SMA ribbon	30
Vertical L-shaped rod	110
Puller	90

Table 5. Weight details for the smart actuator and its components.

4 – Experimental test campaign.

The actuator system, called smart, is characterized by the presence of an SMA ribbon, capable of large contractions as it undergoes a temperature increase (strain recovery, following the so-called external "activation"). There are several ways this temperature increase can be achieved (radiation, convection, etc.): Joule effect was herein considered.
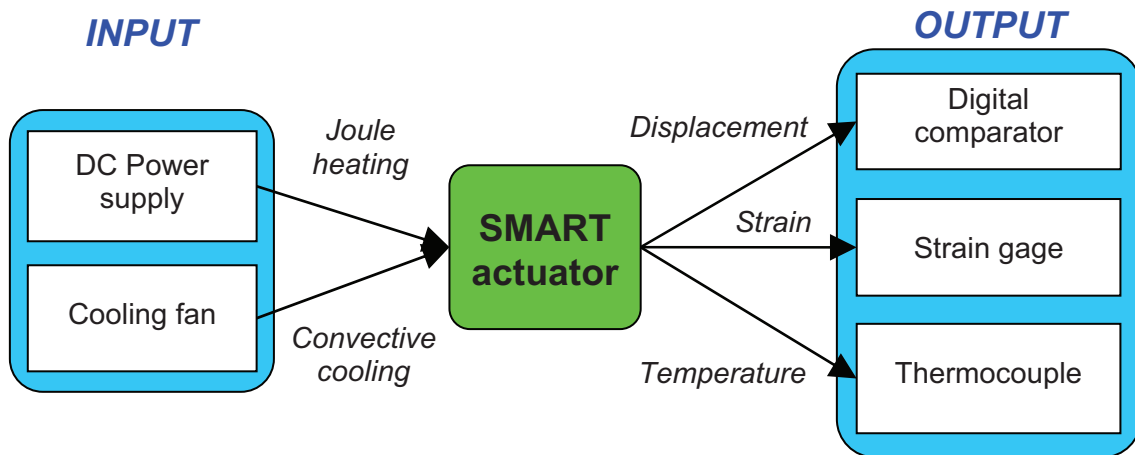
Figure 13. Conceptual scheme and experimental test set-up.

A suitable DC power source was then selected and proper electrical insulation devices were fixed. A nylon ring, placed at the hinge, insulates the elastic arch from the mechanical clamps; the vertical L-shaped support is insulated from the ribbon too. All the actuator system is then insulated from the support desk by a Teflon sheet, for safety reasons.

A small fan was used to speed up the ribbon cooling, after actuation. The SMA ribbon temperature cycles were monitored with thermocouples, placed on the ribbon itself. Strain gages were also installed on the device to monitor strain history. Experimental set-up included a digital mechanical comparator, addressed to detect the arch free

basement vertical displacements together with a reference background, which helped in observing related rotations and displacements, Figure 13.

Assembling sequence

The actuator is bolted on an optical test bench, with an intermediate insulating Teflon sheet, Figure 14.
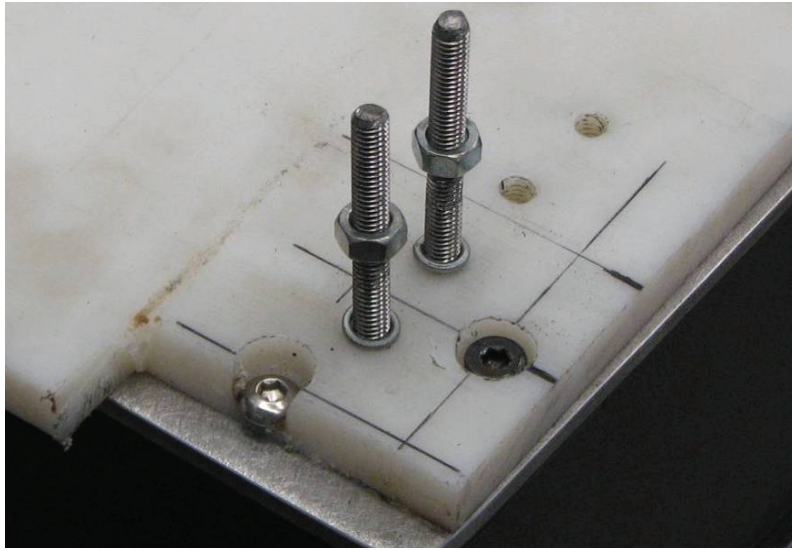
Figure 14. Detail of the Teflon sheet and the mounting bolts on the optical bench.

The support L-shaped rod is then mounted on the titanium arch at a proper height, following the indications coming from the numerical simulations and data elaboration (around 32 mm). A number of nuts and washers helped stiffening and positioning the stick. A rectangular bar, leaning on the arch itself and placed near the inner radius of the arch, helps stiffening the vertical rod with respect to unwanted rotations and moments. The L-bar horizontal element, aimed at supporting the SMA ribbon, is suitably insulated.

Then, the actuator is clamped to the bench and the puller is applied, Figure 15(a). The reference background, the horizontal rod connected to the free basement for angular measures and the linear digital comparator can be clearly observed in Figure 15(b). After having cut the SMA ribbon according to the estimated length (128 mm, unstrained) and clamped both ends to the devices allowing its integration within the elastic arch, Figure 16 and 17, both clamps are electrically insulated on the side that face the remaining part of the structural system.

(a)   (b)
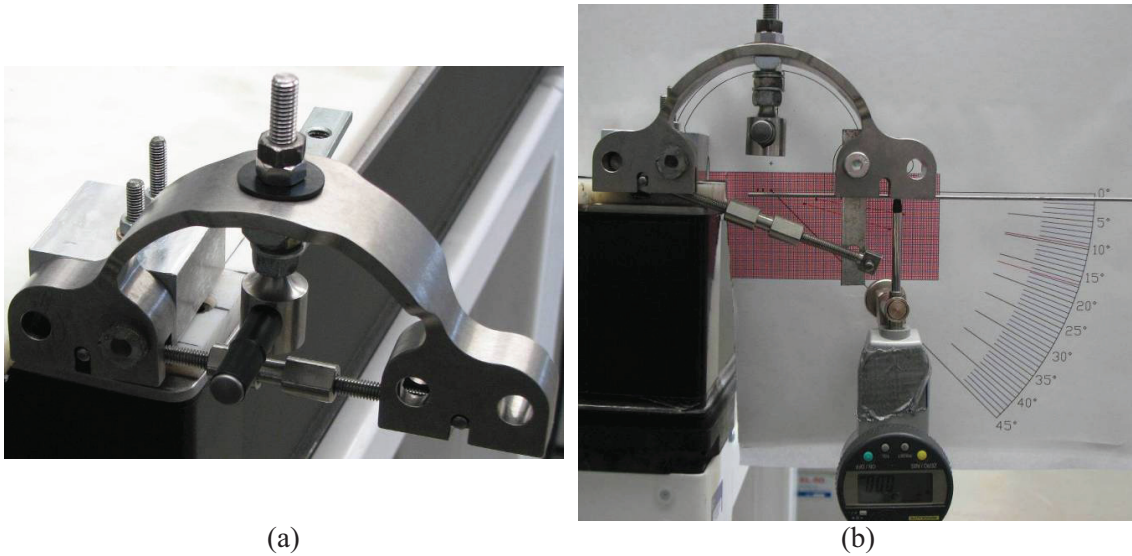
Figure 15. Actuator installation on the optical bench: (a) view of the vertical rod and the puller, (b) view of the reference background and the linear comparator.
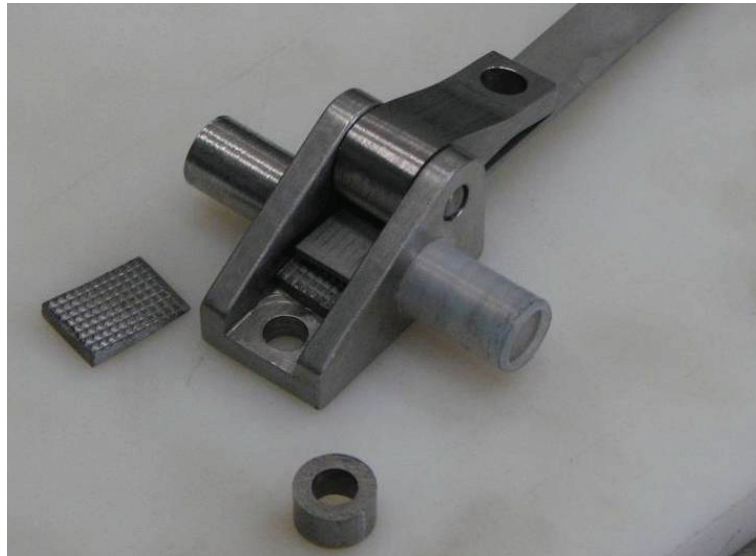
Figure 16. Detail of the mechanism addressed to clamp the SMA ribbon ends.

Figure 17. View of the unstrained SMA ribbon, secured to the clamps, both insulated.

To mount the SMA ribbon-clamps system into the elastic arch, a puller is used: it is necessary in order to bend the arch and approach the mounting holes, so that the plug-in cylinders can be inserted inside them, Figure 18(a). Because the SMA ribbon is unstrained, this configuration corresponds to the max arch deformation.

Finally, electrical connections are applied at the SMA, thermocouples are attached and the puller is relaxed and removed. The system at this point attains a new equilibrium position, determined by the balance between the arch recall elastic force and the SMA ribbon resistance (inner tension). This is the initial, pre-load condition for cyclic actuation.

The strain gages, applied to the elastic arch are not visible. They are instead shown in Figure 19, at the selected locations, chosen as the more representative of the phenomenon under investigation. The complete experimental set-up is shown in Figure 20.

(a)   (b)
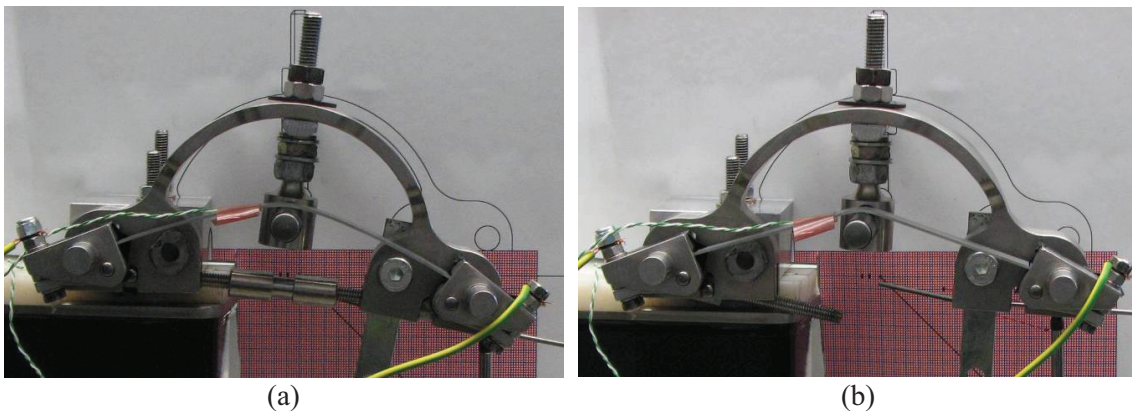
Figure 18. Assembled actuator: (a) SMA mounting by the puller action, (b) Fully assembled prototype.
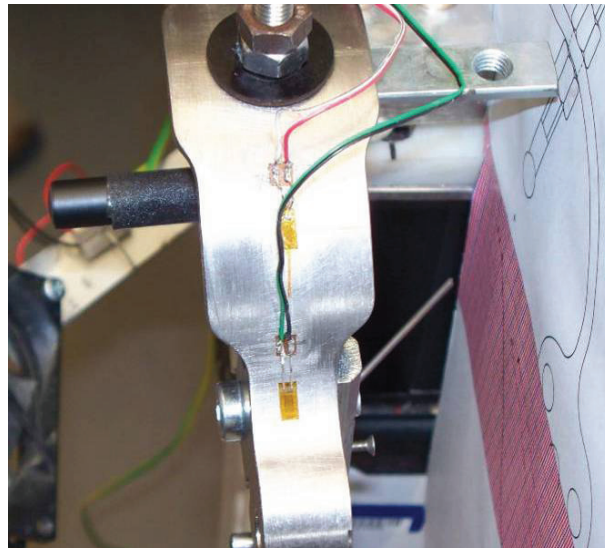
Figure 19. Detail of the installed strain gages.

A further consideration regards the active ribbon initial length and the clamping mechanism. These aspects greatly influences the prototype performance and the correlation levels between numerical and experimental data. During the experimental

tests, a systematic adjustment of the SMA ribbon was observed during the first actuation cycle. A pretty constant 1 mm slip of the SMA ribbon was measured at each clamp: the active strip was marked before the clamped process occurred, to better visualize and somehow quantify this kind of sliding. This phenomenon can be attributed to different causes as: a slight movement of the wedges, internal to each clamp; a proper adjustment of the system made of the ribbon and the clamps; a further contraction of the clamps themselves, that are designed in order to self-lock by a ribbon skidding; and so on.
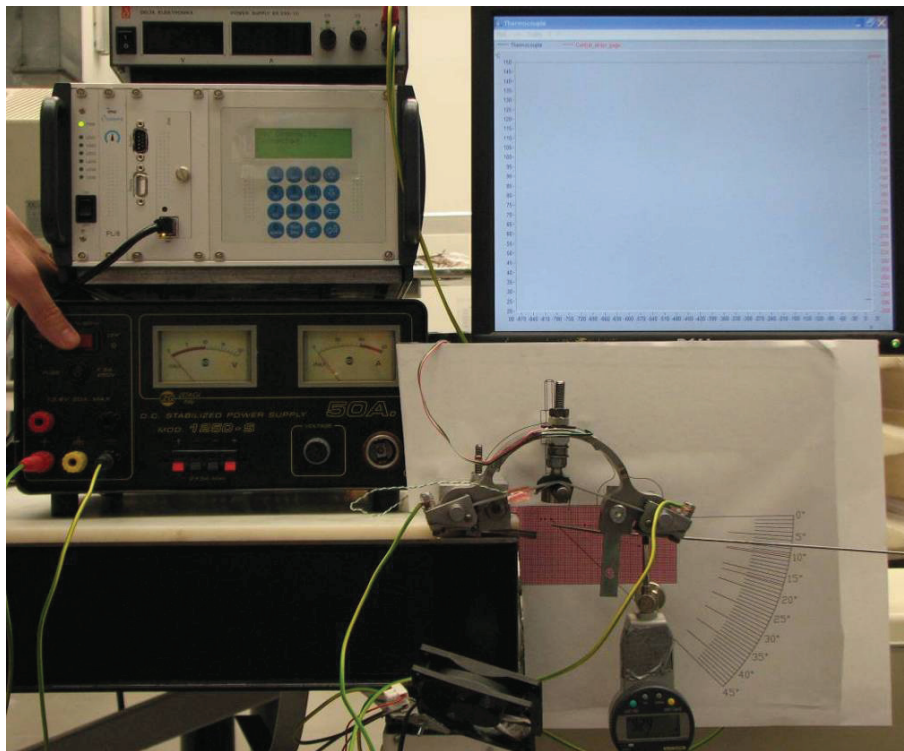
Figure 20. Complete experimental setup.

This effect was compensated by implementing a 2 mm shorter SMA ribbon in the actuator system during its initial assembly. In this way, after the first actuation cycles, the proper net length between the two clamps is shown, as testified by the two blue marks in Figure 21. In the original assembled configuration these marks were covered by the constraining structure and could not be seen.

Experimental tests

In this paragraph, the experimental results are presented, attained on the manufactured, complete prototype. SMA temperature and the arch strain were acquired by proper sensors (thermocouple and strain gages, respectively) and elaborated by a digital

equipment, which allowed to record the relative time histories, during the different actuation cycles (consisting of both heating and cooling). Cross correlation was performed; vertical displacements and rotation angles, measured at the free basement of the elastic arch, were instead acquired manually and reported in table form.
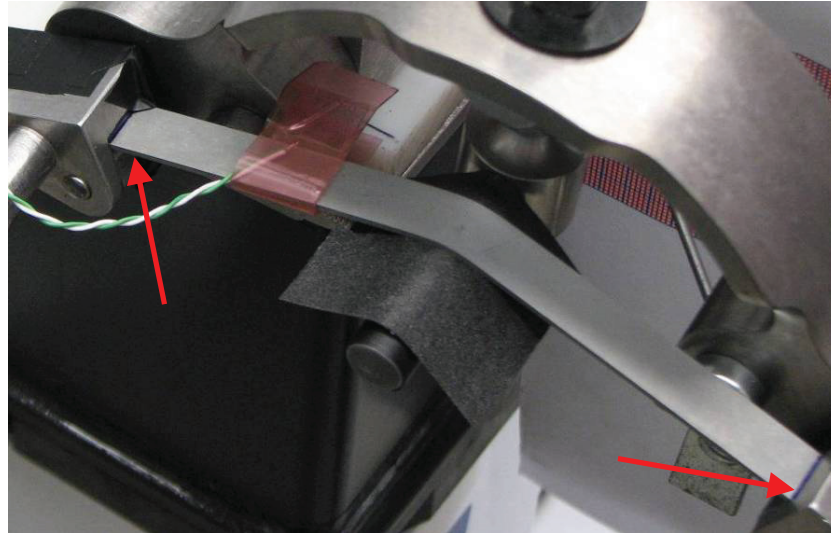
Figure 21. Sliding effect – After the first actuation cycles, ribbon is found to slip at both the ends, homogeneously along the width and repeatable as the ribbon is replaced with others.

After several tests and collected data, vertical displacements, measured by the digital comparator, were correlated with the rotation angles, measured on the background scale, Figure 22. This was used to achieve a better accuracy on the angular evaluations, by exploiting the reliable displacement measures. A linear correlation function was assumed.
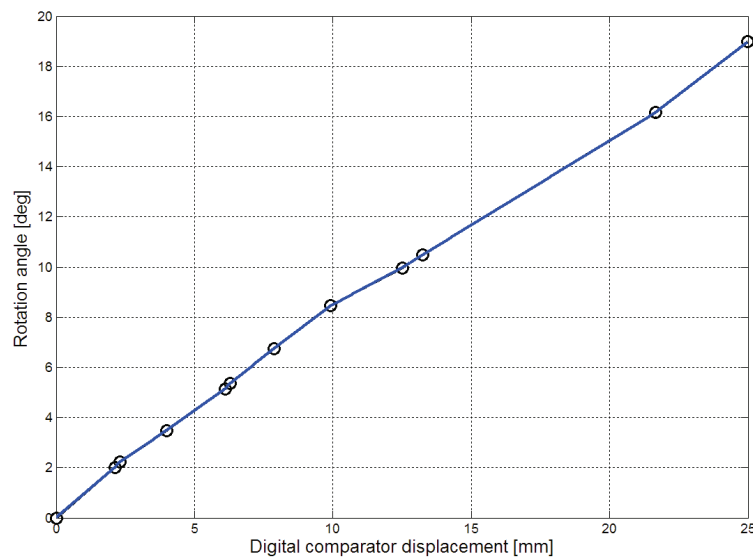
Figure 22. Correlation between vertical displacement and rotation angle.

The experimental campaign was structured into three parts. First of all, a group of 20 cycles was executed, at about 26 °C (environmental temperature) and using a 30 A max – 3 V DC electrical current for Joule effect-heating. This specific choice was considered a good compromise between actuation speed and max attainable SMA temperature. Measured values of temperature, vertical displacements and rotation angles are reported in Table 6 (installation, actuation and recovery).

The first 20 cycles were performed in 4 separate groups; between two phases, the actuator system was completely dismantled and re-assembled. In Table 6, data referred to separate groups are divided by bold lines. Reported temperature are the max values, reached during the heating phase, and the min values, achieved during cooling. Displacements and rotations are reported for both the actuation and the recovery phase in terms of deviation from the reference configuration (pre-loaded system). Displacements and rotations are considered negative when SMA is activated. Normalised angular performance at the same cycles (reference: pre-load condition), is reported in Figure 23. Actuation reliability is evident: those values are in fact attained for different re-assembled systems.

Cyc.	Reference (Pre-load)			Actuation (Heating)			Recovery (Cooling)		
	Temp. [°C]	Disp. [mm]	Rot. [deg]	Temp. [°C]	Disp. [mm]	Rot. [deg]	Temp. [°C]	Disp. [mm]	Rot. [deg]
1	26.5	-6.21	-5.27	147	**-7.04**	**-5.21**	26.5	**-0.04**	**-0.05**
2	26.5	-6.26	-5.33	150	**-6.75**	**-4.99**	26.5	**0.11**	**0.13**
3	26.5	-6.14	-5.19	155	**-6.78**	**-5.07**	26.5	**0.01**	**0.02**
4	25.8	-6.11	-5.15	130	**-6.71**	**-5.04**	25.8	**0.04**	**0.03**
5	26.8	-7.44	-5.27	128	**-5.37**	**-4.91**	26.8	**1.40**	**0.18**
6	26.2	-5.99	-4.98	133	**-6.64**	**-5.08**	26.2	**0.07**	**-0.02**
7	26.0	-5.92	-5.00	114	**-6.60**	**-4.98**	26.4	**0.02**	**0.02**
8	26.4	-5.58	-4.73	132	**-6.96**	**-5.27**	26.4	**-0.31**	**-0.25**
9	26.4	-5.85	-4.94	132	**-6.66**	**-5.04**	26.4	**0.00**	**0.00**
10	24.8	-5.85	-4.94	140	**-6.40**	**-4.88**	24.8	**0.19**	**0.14**
11	24.0	-5.67	-4.80	120	**-6.60**	**-5.04**	24.0	**-0.02**	**-0.02**
12	25.0	-5.69	-4.82	120	**-6.59**	**-5.02**	24.0	**0.01**	**0.01**
13	25.0	-5.68	-4.81	115	**-6.57**	**-5.01**	25.0	**0.01**	**0.01**
14	25.0	-5.67	-4.80	107	**-6.56**	**-5.01**	25.0	**0.03**	**0.02**
15	25.0	-5.64	-4.78	120	**-6.56**	**-5.01**	25.0	**0.01**	**0.01**
16	25.0	-5.63	-4.77	120	**-6.57**	**-5.02**	25.0	**0.01**	**0.01**
17	25.0	-5.62	-4.76	130	**-6.63**	**-5.06**	25.0	**-0.01**	**-0.01**
18	25.0	-5.62	-4.76	130	**-6.63**	**-5.06**	25.0	**-0.01**	**-0.01**
19	25.0	-5.63	-4.77	130	**-6.62**	**-5.05**	25.0	**0.00**	**0.00**
20	26.0	-5.54	-4.70	130	**-6.52**	**-5.02**	26.0	**0.00**	**0.00**

Table 6. Actuator performance for the first group of actuation cycles.
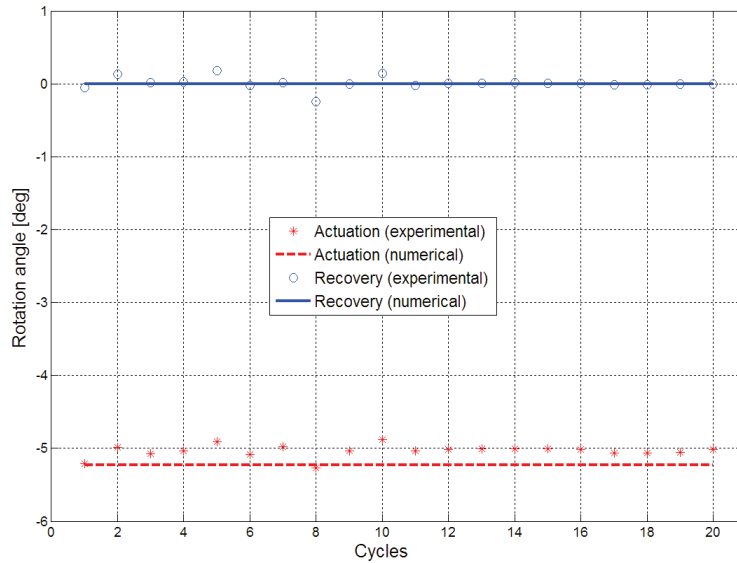
Figure 23. Actuator angular performance: activation and recovery effect for several cycles.

This first test campaign showed a substantial stability of the actuator system performance with cycles, exhibiting a constant net rotation of about 5 deg and the complete recovery of SMA-induced deformation. The difference in the max temperature, following actuation is basically due to errors related to the manual control of the power source. As a remark, it has to be mentioned the cycles had a duration of around 500 seconds, because of the structural thermal inertia in cooling down and the use of the power source itself.

A second group of 15 cycles was then executed with a more sophisticated DC power source (used at 50 A – 1 V); in this case, the device was kept assembled for all the experiment. These tests were executed at 30 °C (environmental temperature). Given the functional dependence on applied stress and temperature of the SMA produced strain, and the characteristic temperatures of the used alloy (martensite finish temperature, M_F = 27.5 °C), lower performance were expected. A mean value of 4.88 deg net rotation was achieved, instead of the previous 5 deg. Practically, the SMA could not completely cool down and, then, could not exhibit the same strain recovery.

In these further tests a still higher stability of the actuator behaviour is noticed, in terms of max activation temperature, max net rotation, attained recovery strain values. Results from all the 15 cycles are reported in Figure 24, for both thermocouple and strain gage output. Similarly, the same information is reported as a single time history in Figure 25, again showing the actuator stability. Actuation time is relatively small, lasting about 30 seconds, while the cooling time is larger (about 4 minutes). In this case, in fact, the cooling was driven by natural convection, only.

Cyc.	Reference (Pre-load)			Actuation (Heating)			Recovery (Cooling)		
	Temp. [°C]	Disp. [mm]	Rot. [deg]	Temp. [°C]	Disp. [mm]	Rot. [deg]	Temp. [°C]	Disp. [mm]	Rot. [deg]
1	29.0	-5.32	-4.53	110	**-6.33**	**-4.94**	30.0	**-0.07**	**-0.05**
2	30.0	-5.39	-4.58	120	**-6.24**	**-4.88**	30.0	**0.19**	**0.00**
3	30.0	-5.39	-4.58	120	**-6.24**	**-4.88**	30.0	**0.00**	**0.00**
4	30.0	-5.39	-4.58	120	**-6.24**	**-4.88**	30.0	**0.02**	**0.01**
5	30.0	-5.37	-4.57	120	**-6.24**	**-4.88**	30.0	**-0.01**	**-0.01**
6	30.0	-5.38	-4.58	120	**-6.22**	**-4.86**	30.0	**0.01**	**0.01**
7	30.0	-5.37	-4.57	120	**-6.23**	**-4.87**	30.0	**0.00**	**0.00**
8	30.0	-5.37	-4.57	120	**-6.24**	**-4.88**	30.0	**0.00**	**0.00**
9	30.0	-5.37	-4.57	120	**-6.21**	**-4.86**	30.0	**0.01**	**0.02**
10	30.0	-5.36	-4.55	120	**-6.21**	**-4.87**	30.0	**0.02**	**0.01**
11	30.0	-5.34	-4.54	120	**-6.22**	**-4.88**	30.0	**0.00**	**0.00**
12	30.0	-5.34	-4.54	120	**-6.21**	**-4.87**	30.0	**0.00**	**0.00**
13	30.0	-5.34	-4.54	120	**-6.21**	**-4.87**	30.0	**0.00**	**0.00**
14	30.0	-5.34	-4.54	120	**-6.21**	**-4.87**	30.0	**0.05**	**0.04**
15	30.0	-5.29	-4.50	120	**-6.25**	**-4.90**	30.0	**-0.02**	**-0.02**

Table 7. Actuator performance for the second group of actuation cycles.
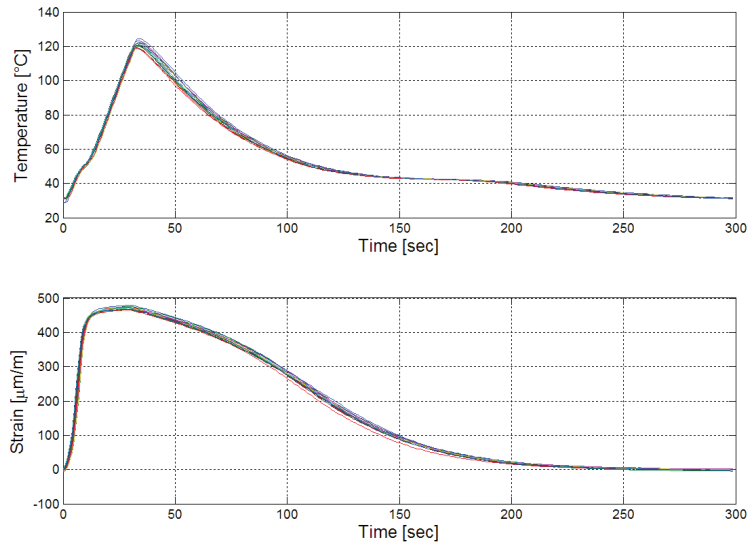
Figure 24. SMA temperature and arch strain measurements during the second group of actuation cycles.

When a single cycle is isolated, Figure 26, a good correlation is found between the thermocouple (SMA temperature on heating or during cooling) and the strain gage (elastic arch deformation) output. In particular, looking at the temperature curve, SMA phase transition point can be observed, occurring in both the directions at different temperature and stress levels (Ms, As). Most of the strain actuation is reached soon after the phase transition during heating, and is almost completely recovered at the phase transition during cooling. In the first transformation, further temperature growth is mainly directed to avoid distribution problems (forced homogeneous transformation)

and produces just a little performance increment. These considerations can be also extracted by Figure 27.
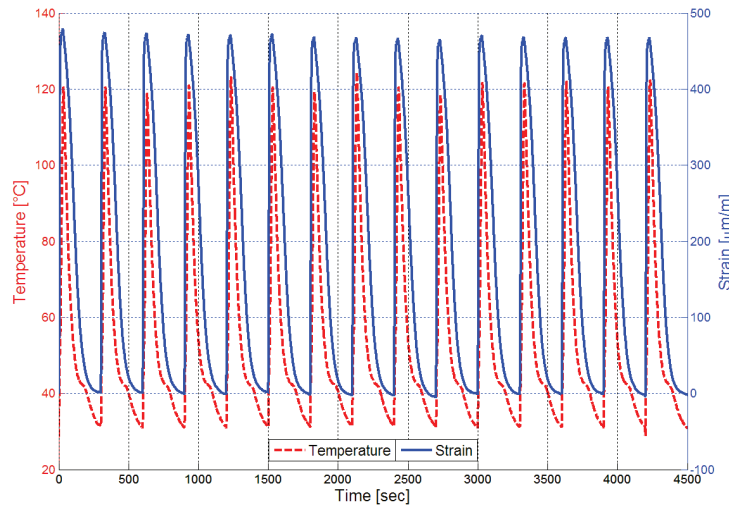
Figure 25. Cycles of figure 24, reported as a continuous time history.
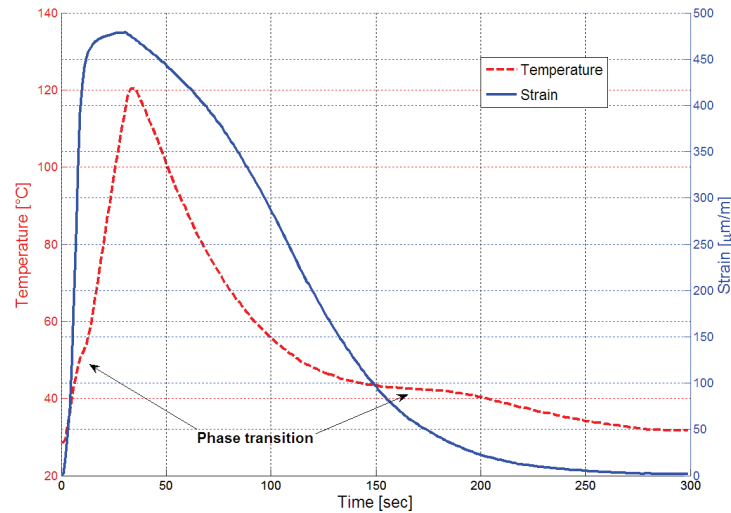
Figure 26. SMA temperature and arch strain measurements correlation for a single cycle.

A third set of experimental tests was finally carried out with the same methodology, to check the performance stability after a higher number of cycles. An automatic control system was set-up to repeat a 300-second cycle for 100 times, using a 40 A – 0.8 V electrical current. It allowed reaching 120 °C within 60 sec. Complete cooling time was instead estimated to occur after 240 sec. Due to the large amount of data, only graphical results will be discussed (Figure 28).

Performance in terms of angular rotations, normalized with respect to the reference condition, presents great time stability. As the actuation cycle number grows,

performance slightly reduces, loosing 0.19 deg (correspondent to 3.75 %), from the initial 5.06 deg @ the 1st cycle to the final 4.87 deg @ the 100th cycle.
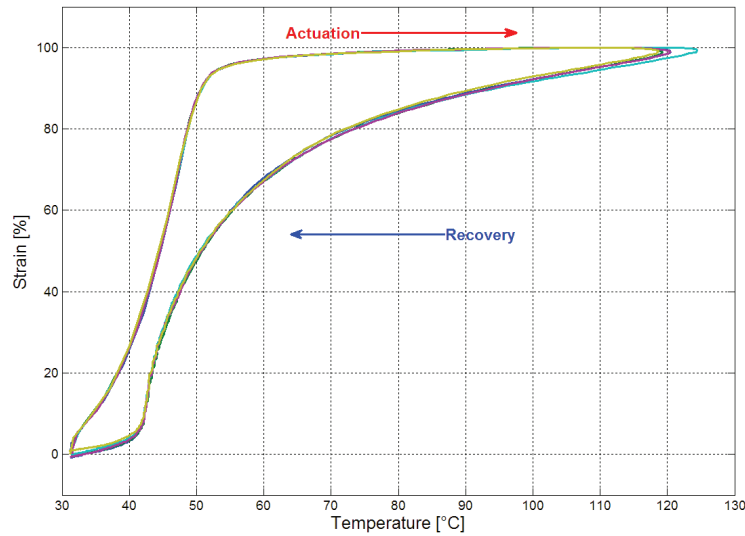
Figure 27. SMA temperature and arch strain percentage correlation.
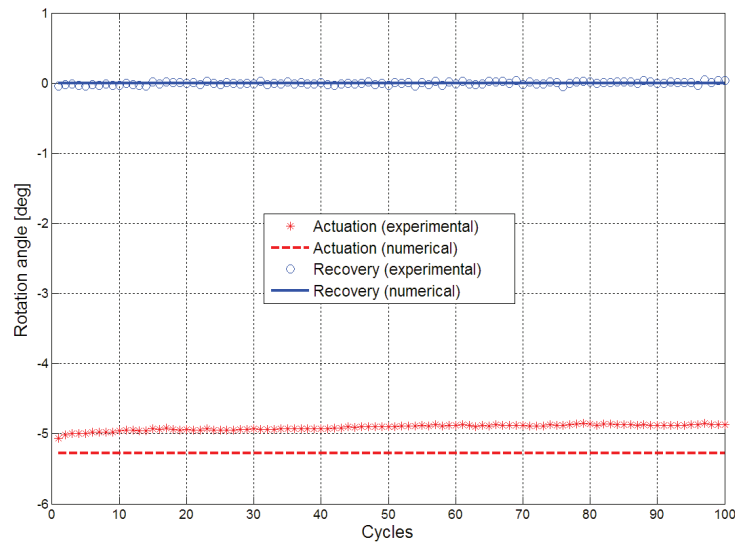
Figure 28. Actuator performance: angular rotations during the third set of cycles.

The same remark can be made by looking at the lower end shift in the strain gage curve, Figure 29. This trend can be explained by considering a fatigue effect into the nylon lining, which deforms as a consequence of the applied load (Figure 30). As a result, clamps are no more parallel with the arch basement: a certain warp is induced. It gives in turn rise to a shift of the pre-load and a consequent actuator performance loss. Pre-loaded and actuated deformations for a single actuation cycle are shown overlapped in Figure 31: the relative displacement is clear.
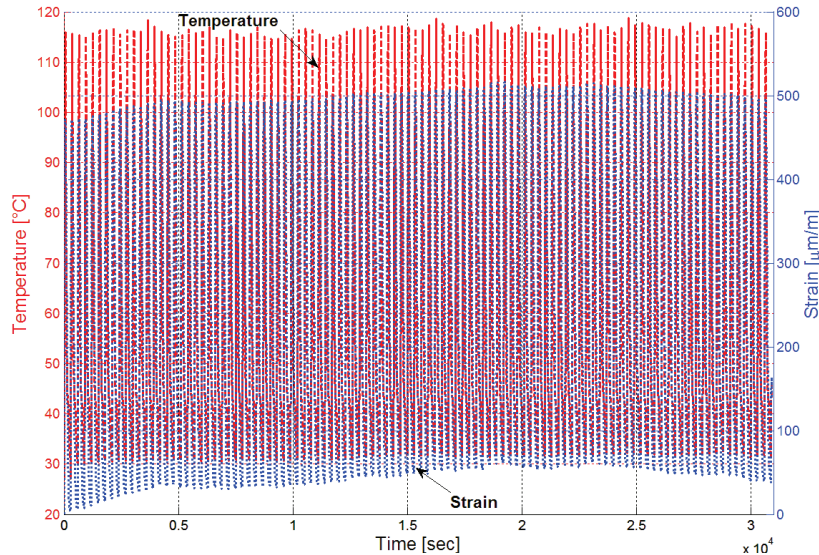
Figure 29. SMA temperature and arch strain time history, detected at the third set of cycles.
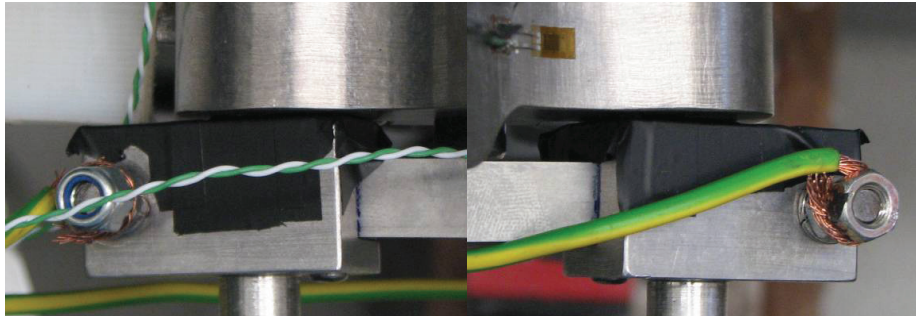
Figure 30. SMA clamps at the end of the third set of cycles: fatigue behaviour.

Nylon lining are deformed and drive the clamps to diverge each other axis; warp is induced.

One of the biggest concern about smart actuator system is related to the long cooling time: quite a lot of techniques can be found to shorten this period, basically connected to the thermal inertia of the SMA material. For instance, some tests were carried out by using a refrigerant spray to accelerate the temperature decay. The required time was largely reduced to less than 20 seconds. This process, moreover, allowed attaining very low values (about -30 °C) that permitted to recover another 1 deg of rotation; of course, pre-load conditions changed, too. Out-of-plane displacements due to the SMA asymmetric position were found to be neglectable and did not affect the actuator performance.

In the end, few considerations should be tracked about the energy (and power) required by the actuator system to work. If the worst case occurring in the cited experimental tests is considered, 50 A – 1 V DC electrical current, a 50 W total power should be grant by the power source. If a time period of 30 sec is considered for attaining a complete activation level, a total energy of 1500 Joule was required.
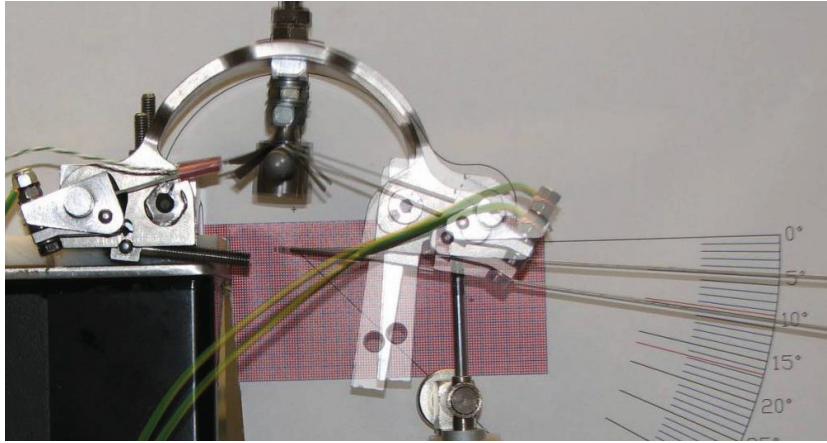
Figure 31. Smart actuator performance: superimpose of the pre-load and actuation condition.

5 – Numerical-Experimental correlation.

Experimental tests proved a great time stability of the tested actuator system. In this paragraph, details about the correlation of these results with the numerical output are presented.

Considering the first group of 20 cycles, when the conceived device was repeatedly dismounted and reassembled, laboratory averages and theoretical results are reported in Table 8, evidencing the percentage differences between ideal and real behaviour.

For each cycle, experimental measures of rotations and vertical displacement are reported for both initial (pre-loaded configuration) and actuated (after SMA activation) state. Numerical simulations, of course, just estimated a single case: however, some corrections were considered for each test according to the real position where the free basement displacement was measured by the digital comparator. As shown in Figure 32, not only this position could change each time the actuator was re-assembled, but also during cyclic actuation the measurement point moves. So, displacement values were selected accordingly from different nodes of the FE model; rotations, of course, were not affected by this phenomenon and could be directly compared.

Taking into account the performance levels, reported in Table 8, it can be concluded that:

- numerically estimated pre-load displacements and rotations are larger than the experimental measures (roughly, about 3.5 mm and 3.5 deg, respectively); this effect was expected, when considering the manufactured arch resulted stiffer than the numerical model, [24], reaching the SMA pre-strain requisite for lower deformations;

- numerical actuation performance are still slightly higher for rotations and displacements (0.2 deg and 0.2 mm, respectively), but substantially equal to the experimental evidence: in fact, in spite of the larger stiffness, SMA theoretical capability assures the attainment of the same deformations; this is an indirect proof of the correct smart alloy modelling.

Cycles	Experimental measures				Numerical estimates				Percentage difference			
	Pre-load		Actuation		Pre-load		Actuation		Pre-load		Actuation	
	Disp.	Rot.	ΔDisp.	ΔRot.	Disp.	Rot.	ΔDisp.	ΔRot.	Disp.	Rot.	ΔDisp.	ΔRot.
	[mm]	[deg]	[mm]	[deg]	[mm]	[deg]	[mm]	[deg]	[%]			
1 to 4	-6.18	-5.24	**-6.82**	**-5.08**	-8.99	8.50	**-7.03**	**5.23**	31.26	38.41	2.99	2.92
5 to 11	-6.04	-4.95	**-6.46**	**-5.03**	-9.53	8.50	**-6.71**	**5.23**	36.59	41.75	3.70	3.85
12 to 19	-5.64	-4.78	**-6.59**	**-5.03**	-9.53	8.50	**-6.71**	**5.23**	40.74	43.72	1.77	3.82
20	-5.54	-4.70	**-6.52**	**-5.02**	-9.53	8.50	**-6.71**	**5.23**	41.87	44.71	2.83	4.02

Table 8. Summary of the experimental averaged measures and numerical results for the first set of cycles.

(a)   (b)
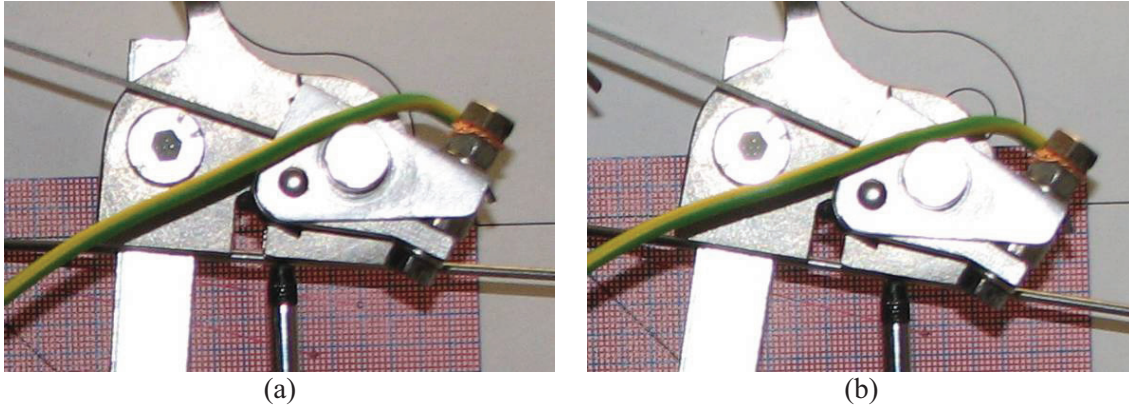
Figure 32. Detailed view of the relative position migration between digital comparator and free basement: (a) during pre-load, (b) during actuation.

Then, the second set of 15 cycles, when the actuator was assembled just at the beginning of the test campaign, can be taken into account. Numerical and experimental performance are reported in Table 9. This second group of tests exhibited a larger stability with cycles. The net performance resulted however lower because of the higher environmental temperature (30°C).

The following conclusions may be drawn:

- predicted pre-load displacements and rotations are larger than the experimental measures (about 4.2 mm and 4.0 deg, respectively);
- predicted performance during actuation are slightly higher for displacement and rotations, also (about 7 % for both).

In these tests, the high environmental temperature (30°) worsened actuator performance: it affected both the pre-load configuration and the actuation levels, by reducing the temperature operative range of the SMA ribbon.

Finally, on the third group of experimental tests, some other general considerations can be made. As shown in Figure 28, at the beginning of the 100-cycle experiment, the net rotation was measured in 5.06 deg (3.25 % lower than the numerical prediction). This value got worse at the end, attaining 4.87 deg (6.88 % lower than the theoretical estimate), equivalent to a performance loss of 0.19 deg, that can be mainly attributed to the nylon rings deformation.

About the correlation between strain actuation and temperature, the smart actuator system attains 98 % of its performance level at around 80 °C (close to the estimated 75.3 °C, well explained with the experimentally evidence of facing with a stiffer arch). Thermal inertia problems, together with uncertainties on the single-point thermocouple detection, led to reach still higher temperature values in order to assure a complete phase transformation on the SMA. These values could be easily reached with the given power source. A better control on the activation temperature could easily bring to benefits in terms of required power and recovery time (over a complete cycle).

The functional link between arch deformation and the activation temperature was found to be fully predicted by the numerical simulations. An average max strain actuation value of 475 με was measured overall the test campaign. Really, in the third phase, a higher value was detected but it is thought to be linked to an initial shift in the strain gage signal, as shown in Figure 29. A larger strain value may be generally explained by the arc higher stiffness pointed out: SMA still recovers its total strain range but moving at higher absolute values.

A final general summary of the smart actuator performance is reported in Tab. 10.

	Experimental measures				Numerical estimates				Percentage difference			
	Pre-load		Actuation		Pre-load		Actuation		Pre-load		Actuation	
Cycles	D[mm]	R[deg]	ΔD	ΔR	D[mm]	R[deg]	ΔD	ΔR	D[mm]	R[deg]	ΔD	ΔR
1 to 15	-5.35	-4.56	**-6.23**	**-4.88**	-9.53	8.50	**-6.71**	**5.23**	43.78	46.40	7.10	6.70

Table 9. Summary of the experimental averaged measures and numerical results for the second set of cycles.

Rotations [deg]	Pre-load	Actuation	Recovery
F.E. analysis	-8.50	-5.23	0.00
Experimental	-4.75 ± 0.20	-5.00 ± 0.10	0.00 ± 0.01

Table 10. Summary of the general actuator performance.

6 – Conclusions.

The paper aims at testing a complete structural actuator for morphing applications. The basic arc architecture choice and its design driving reasons, the optimisation process having determined the structural shape, the lab characterisation of the selected SMA active element are recalled in the first part of this work and refer to a previous publication by the same authors.

Full details of the actuator systems are then dealt with, giving particular emphasis to some peculiar elements as the clamp device and the SMA central support, conceived for maximising the produced displacement. The focus is then moved to the assembly sequence; in this phase the pre-load has to be assigned in order to guarantee the full recovery of the initial position, after activation occurs.

Therefore, the arc device is clamped at one end and activated, heating the SMA element by Joule effect. Both displacement and rotation of its free end are measured and compared with the numerical results. In order to assure the repeatability of the experiment itself and giving a sufficient reliability level to the acquired data, different cycles were imposed.

A full repeatability was shown, evident not only when the maxima attained displacements and rotations were compared but also if the complete phenomenon time history was taken into account. Activation times resulted in the tenth of seconds, while non-forced cooling occurred in hundreds of time unit. This is one of the major concerns of the implemented technique.

The correlation between numerical and experimental data concludes the work. It was carried out at two levels: firstly, comparing actual and estimated pre-loads; secondly, evaluating the effective and the predicted displacements and rotations, after activation. In both the cases an extremely good match was found, ensuring the goodness of the modelling of the complete device.

Just to recall the complexity of the implemented numerical representation, it is important to illustrate the major components: an SMA FE representation, incorporated into a commercial code; a non-linear model of the structural system; an analytical model, defining the details of the smart material behaviour; an integrated overall numerical simulation procedure.

The real actuator behaviour is well represented by the constructed numerical model and procedure. The actuator design takes into account the necessity of ensuring a pre-load, aimed at fully recover the original position after activation, as well as the attainment of

the prescribed requirements. The device behaviour is time-stable, verified all along the test campaign.

The complexity of the implemented architecture should be reduced, at the same time upgrading its general reliability. In particular, three elements should be addressed. At first, the clamp device, by implementing for instance welding techniques. Then, the SMA suspension and the SMA installation devices, by the introduction for instance of tuning tools, aimed at the fine positioning of the actuation system (after pre-load and the early actuation cycles). Activation power is limited: the Joule effect requires in fact low voltage and limited current intensity, being the system a short circuit. Higher voltages may be then attained in order to reduce the activation and relaxation times, referring to wire structures, instead of single, massive SMA elements. Shorter times would correspond to higher implemented power, should the transmitted energy be always the same, for the same configuration. The use of different SMA materials could allow lowering the used recovery strain fraction, increasing the device lifetime (fatigue), according to several authors. Also, the temperature dependence of the apparatus should be improved, above all in view of real applications.

References

[1]   Barbarino S., Ameduri S., Pecora R., 2007, "*Wing Camber Control Architectures based on SMA: Numerical Investigation*" – International Conference on Smart Materials and Nanotechnology in Engineering (SMN2007), July 1-4, Harbin, China, Proceedings of SPIE vol. 6423, 64231E-1, (2007), 8pp., doi: 10.1117/12.779397

[2]   Wright O., 1988, "*How we Invented the Airplan*e" – Dover Publications, Mineola (NY-USA)

[3]   Stanewsky E., 2001, "*Adaptive Wing and Flow Control Technology*" – Progress in Aerospace Sciences, Elsevier Science Ltd., vol.37, pp.583-667

[4]   Frost & al., 1978, "*Airfoil Variable Cambering Device and Method*" – U.S. Patent no.4,247,066, General Dynamics Corporation, Fort Worth, TX

[5]   Statkus F.D., 1980, "*Continuous Skin Variable Camber Airfoil Edge Actuating Mechanism*" – United States Patent No. 4,351,502, The Boeing Company, Seattle, WA

[6]   Simpson A., Coulombe N., Jacob J., Smith S., 2005, "*Morphing of Inflatable Wings*" – 46th AIAA/ ASME/ASCE/AHS/ASC Structures, Structural Dynamics and Materials Conference, Austin, Texas, AIAA J. 2005-2110

[7]   Moses R.W., 1997, "*Active Vertical Tail Buffeting Alleviation on a Twin-Tail Fighter Configuration in a Wind Tunnel*" – International Forum on Aeroelasticity and Structural Dynamics, CEAS, June, pp. 269-276

[8]   Ruiz-C. L.P., 2000, "*EREA Adaptive Airfoil Project*" – Exec. Summ., February, INTA, Torrejon de Ardoz, Spain

[9]   Sater J.M., et alii, 1997, "*DARPA Smart Wing program*" – Engineered Adaptive Structures Conference, United Engineering Foundation, Banff, Canada

[10] Kudva J., 2000, "*DARPA AFRL Northrop-Grumman Smart Materials and Structures Demonstration: Smart Wing Phase 2*" – DARPA Technology Exchange Meeting, June 26

[11] Monner H.P., Bein T., Hanselka H., Breitbach E., 1998, "*Design Aspects of the Adaptive Wing – The Elastic Trailing Edge and the Local Spoiler Bump*" – Royal Aeronautical Society, Multidisciplinary Design and Optimization, London, October 1998

[12] Gevers Aircraft Inc., 1997, "*Multi-Purpose Aircraft*", United States Patents Office, Patent Number 5,645, 250

[13] Smith S.B., Nelson D.W., 1989, "*Determination of the Aerodynamic Characteristics of the Mission Adaptive Wing*" – 6th Applied Aerodynamics Conference, Williamsburg, VA, AIAA J. 88-2556

[14] Inman D.J., 2001, "*Wings: Out of the Box. Determining Actuator Requirements for Controlled Morphing Air Vehicles – Aerodynamic Loads*" – DARPA Technology Interchange Meeting, Wright Patterson Air Force Base, Dayton, Ohio, Nov. 2001

[15] Wilson J.R., 2002, "*Active Aeroelastic Wing: A New/Old Twist On Flight*" – Aerospace America, vol.40, no.99, pp.34-37

[16] Austin F., Siclari M.J., Van Nostrand W., Weisensel G.N., Kottamasu V., Volpe G., 1997, "*Comparison of Smart Wing Concepts for Transonic Cruise Drag Reduction*" – SPIE 1997, p.3044

[17] Perkins D.A., Reed J.L., Havens E., 2004, "*Morphing Wing Structures for Loitering Air Vehicles*" – 45th AIAA/ASME/ASCE/AHS/ASC Structures, Structural Dynamics & Materials Conference, Palm Springs, California, AIAA J. 2004-1888

[18] Barbarino S., Pecora R., Lecce L., Concilio A., Ameduri S., Calvi E., 2009, "*A Novel SMA-Based Concept for Airfoil Structural Morphing*" – Journal of Materials Engineering

and Performance (JMEP), vol.18, issue 5, pp.696-705 (2009), doi:10.1007/s11665-009-9356-3

[19] Campanile L.F., Melz T., Keimer R., Wadehn W., 2003 – Patent DE10155119A1

[20] Langbein S., Welp E.G., 2009, "*One-Module Actuators Based on Partial Activation of Shape Memory Components*" – Journal of Material Engineering and Performance, vol.18, no.5-6, pp.711-716

[21] Electric Piston, Mondo-tronics Inc., website: http://www.robotstore.com

[22] Banks R.M., 1975, "*Energy Conversion Systems*" – Patent US03913326

[23] Bokaie M. of TiNi Alloy Co. for NASA Lewis Research Center, February 1998, LEW-16511, website: http://www.nasatech.com/Briefs/Feb98/LEW16511.html

[24] Barbarino S., Lecce L., Concilio A., Ameduri S., S. Russo, 2009, "*A Novel Smart Actuator for Airfoil Structural Morphing: Design and Optimization*" – Submitted to the Journal of Intelligent Material Systems and Structures (JIMSS)

[25] Iannuzzo G., Riccio M., Russo S., Calvi E., Pecora R., Lecce L., Barbarino S., Concilio A., Ameduri S., "*An actuator device based on a shape memory alloy, and a wing flap assembly fitted with such an actuator device*" – Filed on July 21, 2009 at the European Patent Office, 2280 HV Rijswijk, Netherland, application/patent no. 09165941-7 - 1254, proprietor Alenia Aeronautica S.p.a., priority IT/23.07.08/ITA TO20080566

[26] Liang C. and Rogers C.A., 1990, "*One-Dimensional Thermomechanical Constitutive Relations for Shape Memory Material*" – J. of Intelligent Material Systems and Structures, vol.1, no.2, pp.207-234

[27] Richards R., 2001, "*Principles of Solid Mechanics*" – CRC Press LLC, ISBN 0-8493-0114-9, pp.162-164

[28] Goldberg D.E.,1989, "Genetic *Algorithms in Search, Optimization & Machine Learning*" – Addison-Wesley Publishing Company Inc., ISBN: 0-201-15767-5

- *Chapter 7* -

Variable Camber Morphing Flap:
Smart Flap

1 INTRODUCTION

To be written Several flight regimes occurring during a typical aircraft mission make practically impossible to define a unique optimised configuration able to maximise aerodynamic efficiency, manoeuvrability, stability, fuel consumption etc. in every flight condition (cuise, take-off, landing). Components like ailerons, flaps, equilibrators in some way guarantee a certain level of adaptability, being far from optimal [1].

The wing shape control, as proved by several numerical and experimental investigations [2-3], can strongly improve the aerodynamic efficiency of a wing, by assuring an optimal adaptive behavior with respect to the external free-stream conditions. As reported in literature, by suitably modifying during flight different wing geometrical parameters, such as the local / global chamber [4-6], the wing span [7-8] or the twist angle [9-10], it is possible to achieve a structure that best fits the specific flight regime requirements. Such an approach, in spite of related benefits, presents a critical, challenging problem: the same structure enough rigid to keep its shape under the action of external aerodynamic loads has to largely deform itself without undergoing structural collapses.

The advent of smart materials has proved major benefits in the resolution of such a paradox, allowing for highly integrated and actuation-capable structures. Among the others, Shape Memory Alloys are privileged in many applications due to their Super Elastic and Shape Memory properties, jointly with the large transmitted forces and recoverable strain [11]: for this reason they have been selected for this work too.

In previous studies, the authors investigated several structural solutions [12-13] capable of changing the trailing edge camber (hingeless flap) with SMA actuation, and chose to refer to "load-bearing" actuators, that means, actuator systems able to sustain external forces. In this general frame, also a SMA-based load-bearing actuator was developed (see previous Chapter), which represents the main component of the actual concept herein presented.

In this Chapter, the assessment of the design of an hingeless flap, commanded by the SMA actuator previously presented, is illustrated. The reference geometry is based on a real scale flap for a typical regional transportation aircraft. The developed flap bay is constituted of two morphing ribs, each based on a chord-wise series replication of the elastic SMART actuator, and some rigid blocks, representing the flap shape and its aerodynamic surfaces.

Numerical performance on the FE model and experimental measures on the manufactured prototype have been correlated both in absence and in presence of realistic static loads. Details will be discussed about some design peculiarities and realization issues.

2 AERODYNAMIC LOAD ESTIMATE AND ADVANTAGES

The aerodynamic load computation has been addressed by assuming the RA 18-43NIL1 as wing airfoil and the hypothesis of inviscid flow; the RA 18-43NIL1 is a typical wing airfoil used in regional transport aircraft. In Figure 1 the RA 18-43NIL1 geometry is plotted and some related parameters are pointed out.

Points *O* and *P* are respectively called *leading* and *trailing edge* while the segment *OP* is referred as the airfoil chord *c*. The chord divides the airfoil boundary curve in two parts: the *upper camber* (represented by the curve connecting *O* to *P* in a clockwise orientation) and the *lower camber* (represented by the curve connecting *P* to *O* in a clockwise orientation). The airfoil *mean camber line*, or more synthetically, the airfoil *camber line* is defined as the locus of the centres of circles tangent both to upper and to lower cambers.

Referring to the coordinate system of Figure 1, the function $z_C = z_C(x)$ describing the camber line is given by $z_C(x) = [z_U(x)+z_L(x)]/2$, where $z_U = z_U(x)$ and $z_L = z_L(x)$ are the functions describing the upper and lower cambers. An inviscid airflow characterized by a velocity vector $\underline{V}$ induces a pressure distribution on the airfoil, along the upper and the lower camber, essentially related to: the shape of the airfoil, the magnitude of $\underline{V}$, the air density ρ, and the airfoil *angle of attack* defined as the angle between the airfoil chord and the direction of $\underline{V}$.
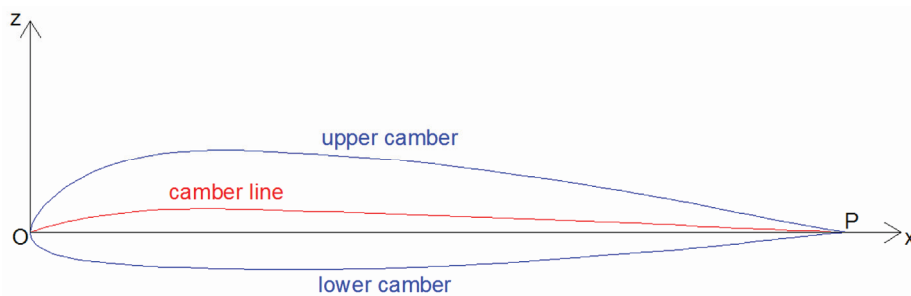
Figure 1: RA 18-43NIL1 airfoil.

Approximating the upper and the lower camber by means of *n* linear segments delimited by points A_i and A_{i+1} (i = 1…n-1), the pressure p_i arising on each segment $\overline{A_i A_{i+1}}$, can be expressed according to the following equation:

$$p_i = \frac{1}{2}\rho V^2 C_{p,i} = q C_{p,i} \tag{1}$$

where $q = \rho V^2/2$ is called *dynamic pressure* and $C_{p,i}$ *local pressure coefficient*. The local pressure coefficient $C_{p,i}$ is a non-dimensional parameter whose value depends on the orientation of the segment A_iA_{i+1} in the airflow and therefore by the airfoil shape and angle of attack. The evaluation of the local pressure coefficients is usually performed by means of specific numerical methods of computational aerodynamics. In this work, they were evaluated by means of a two-dimensional vortex lattice method (VLM), [14].

A split-flap was considered, hinged at a distance of 0.7c from the airfoil leading edge; the wing airfoil portion between *0.7c* and *c* was assumed representative of a flap airfoil and rotated around the hinge point in order to simulate the split-flap down deflection. Deflection angles δ between 2 and 24 deg were considered; for each step the C_p distribution and the wing airfoil lift coefficient C_l were evaluated in correspondence of a 5 deg angle of incidence (angle of attack). The airfoil lift coefficient C_l is defined by the following equation:

$$C_l = \sum_{i=1}^{n} C_{p,i} \left(\underline{n_i} \cdot \underline{\zeta} \right) \qquad (2)$$

where *n* is the number of linear segments used to approximate the upper and the lower camber, $C_{p,i}$ is the pressure coefficient related to the i-th segment, $\underline{n_i}$ is the normal unit vector of the segment contained in the airfoil plane and positively oriented outwards of the airfoil surface and $\underline{\zeta}$ is the normal unit vector to the airflow velocity vector $\underline{V}$. The airfoil C_l is a non-dimensional parameter used to characterise the lifting performance of airfoils or, in other terms, the airfoil capability to generate a force orthogonal to the airflow velocity direction. Such a force, called *lift*, is responsible of aircraft sustentation and is proportional to C_l; higher C_l leads to higher lift. The obtained C_l for each examined flap deflection are reported in Table 1 ($C_{l(conventional)}$).

Be given a two-dimensional Cartesian reference system S_0, defined as follows: origin located at the airfoil leading edge; X-axis directed along the non-flapped chord and oriented towards the trailing edge; Z-axis in the airfoil plane and oriented upwards. In correspondence of a flap rotation δ_i, around the hinge point A $[0.7 \cdot c; Z_A]$, the trailing edge moves from the point P $[c;0]$ to the point P', defined by the coordinates: $X_{P'} = 0.7 \cdot c + \overline{AP} \cdot \cos(\alpha + \delta_i)$, $Y_{P'} = \overline{AP} \cdot \sin(\alpha + \delta_i) - Z_A$ where $\alpha = \sin^{-1}\left(0.3 \cdot c / \overline{AP}\right)$. Fixed the same trailing edge position due to a δ_i flap deflection, a quadratic morphing law was imposed to the camber-line related to the flapped airfoil. In detail, the motion of point P to point P' was obtained by morphing the flapped airfoil camber line

according to a parabolic arch connecting the point *A* to the point *P'* and tangent in *A* to the wing airfoil camber-line (Figure 2). Camber-line morphing was obviously obtained by means of a congruent morphing of the upper and lower cambers of the flapped airfoil.

δ [°]	2	4	6	8
C_l (conventional)	1.0155	1.1760	1.3359	1.4950
C_l (morphed)	1.0760	1.2866	1.4944	1.6990
δ [°]	10	12	14	16
C_l (conventional)	1.6532	1.8103	1.9663	2.1209
C_l (morphed)	1.8996	2.0956	2.2868	2.4727
δ [°]	18	20	22	24
C_l (conventional)	2.2740	2.4253	2.5749	2.7224
C_l (morphed)	2.6530	2.8275	2.9962	3.1589

Table 1: Wing airfoil C_l for several flap deflection angles.
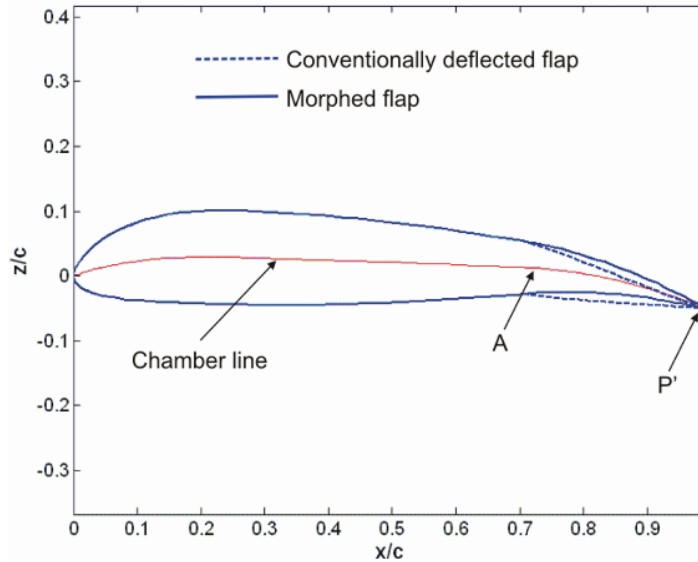
Figure 2: Wing airfoil shapes corresponding to conventionally deflected flap and morphed flap.

According to this procedure, for each of the previously investigated hinged flap rotation, a corresponding morphed flap shape was found and the related global C_l was evaluated. The obtained results are reported in Table 1 ($C_{l(morphed)}$). In Figure 3, the wing airfoil C_l related to conventional split and morphed flap are been compared for each δ_i. For a given trailing edge down-deflection, the morphed flap solution leads to higher wing airfoil C_l then the conventional split solution.

The morphed flap configuration leading to a wing airfoil $C_l = 2.09$ was considered the most satisfactory from an aerodynamic performance point of view, and was chosen as the target of this work. It corresponds to a 12 deg deflection angle and a 160 mm vertical trailing edge displacement.
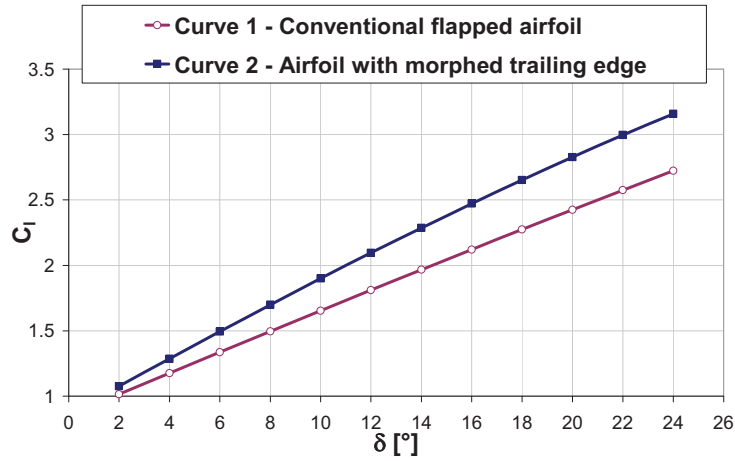
Figure 3: Wing airfoil C$_l$ comparison.

A morphed flap portion of chord c_f=720 mm and span b = 300 mm was then considered for aerodynamic loads evaluation purpose. Referring to Figure 4, let us call MS_a and MS_b the boundaries of the two morphed flap airfoil shapes, delimiting the flap portion along the span. The boundary Ms$_a$ has been approximated by a polygonal line composed by n consecutive segments $\overline{A_i A_{i+1}}$ (i=1..n-1).
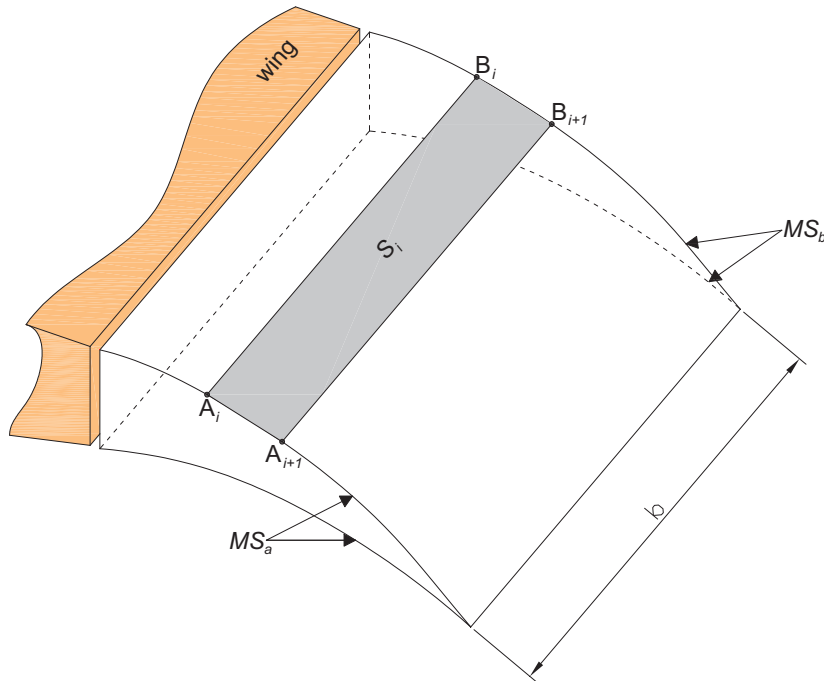
Figure 4: Discretization of morphed flap portion for aerodynamic loads computation.

Same approximation was used for boundary Ms$_b$: the boundary has been considered as a polygonal line composed by n consecutive segments $\overline{B_i B_{i+1}}$ (i=1..n) homologues of the segments $\overline{A_i A_{i+1}}$ lying on the boundary Ms$_a$.

Considering the generic aerodynamic strip s_i, delimited by two homologues segments A_i, A_{i+1} and B_i, B_{i+1}, according to (2), the aerodynamic load acting normally to s_i was evaluated as

$$F_{n,i} = q S_i C_{p,i} \qquad (3)$$

where q is the dynamic pressure, S_i is the strip area, given by the product between the span b and the length d_i of the segments $\overline{A_i A_{i+1}}$ and $\overline{B_i B_{i+1}}$, $C_{p,i}$ is the pressure coefficient, assumed equal for both segments $\overline{A_i A_{i+1}}$ and $\overline{B_i B_{i+1}}$.

The assumption made on C_{pi} is reasonable: due to the limited span of the investigated flap portion, the C_{pi} spanwise variation may be neglected.

A dynamic pressure of around 1500.00 N/mm^2 was considered, typical for take-off and landing of a regional transport aircraft. Using Equation 3, the aerodynamic load distribution acting on the flap portion was evaluated; such load distribution was then used in numerical simulations for proper sizing of the ribs to be located at the end of the investigated wing portion.

In Figure 5, the components F_X, F_Z of obtained load distribution (referred to the X and Z axes of S_0) have been plotted along flap chord.
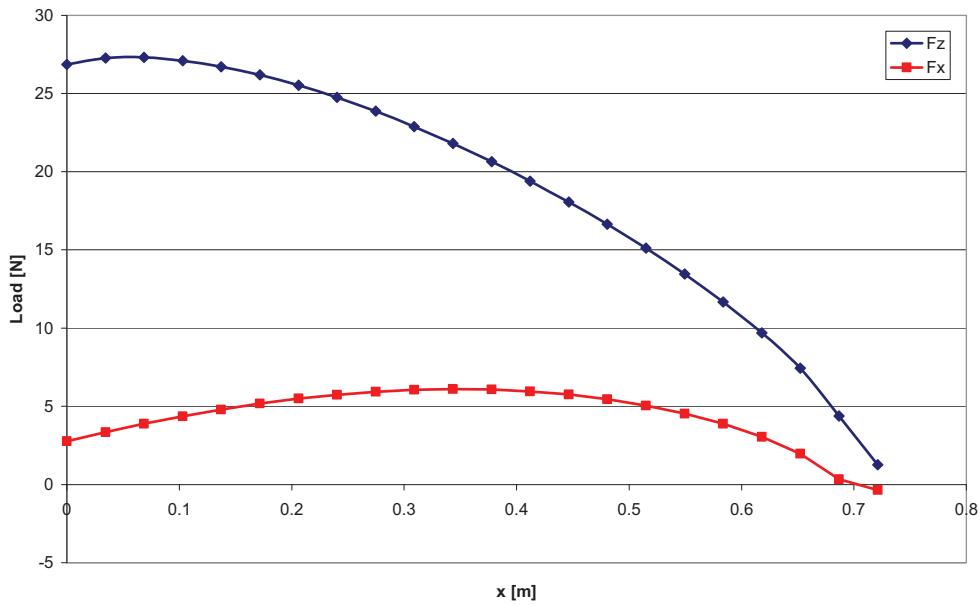
Figure 5: Load distribution along morphed flap.

For static tests purpose only, the following actions have been made:

1. F_X distribution has been neglected;
2. F_Z distribution has been reduced to an equivalent trapezoidal distribution $F_{Z,T}$.

The first actions is reasonable due to the low stress levels induced on rib structure by loads acting along X direction; the second action is compliant with airworthiness standards for static tests on lifting surfaces and is motivated by the necessity of simplifying the experimental procedure aimed to reproduce the actual load set acting on the structure.

The trapezoidal distribution $F_{Z,T}$ has been obtained by imposing the equivalence of its resultant and bending moment at flap rib root respectively to the ones related to the F_Z distribution.

More in detail, referring to Figure 6, the trapezoidal distribution is governed by the following equation:

$$F_{Z,T}(x) = \frac{x}{c_f}\left(\widetilde{F} - F_0\right) + F_0 \tag{4}$$

where c_f is the flap chord while F_0 and $\widetilde{F}$ are unknown parameters.
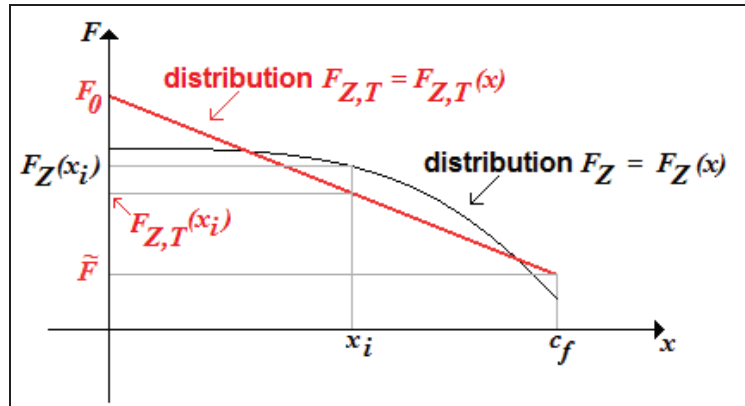
Figure 6: Actual and equivalent trapezoidal load distribution scheme.

By imposing the trapezoidal distribution resultant and the induced bending moment at flap rib root to be respectively equal to the resultant (R_Z) and to the bending moment (M) related to the actual load distribution, it can be obtained:

$$\sum_{x=0}^{x=c_f} F_{Z,T}(x_i) = \sum_{x=0}^{x=c_{fi}} F_Z(x_i)$$

$$\sum_{x=0}^{x=c_f}\left[F_{Z,T}(x_i)\cdot x_i\right] = \sum_{x=0}^{x=c_{fi}}\left[F_Z(x_i)\cdot x_i\right]. \tag{5}$$

By substituting (5) into (6), the following set of equations may be written:

$$\begin{cases} \widetilde{F}\left(\sum_{x=0}^{x=c_f}\frac{x_i}{c_f}\right)+F_0\left[\sum_{x=0}^{x=c_f}\left(1-\frac{x_i}{c_f}\right)\right]=\sum_{x=0}^{x=c_{fi}}F_Z(x_i) \\[4mm] \widetilde{F}\left(\sum_{x=0}^{x=c_f}\frac{x_i^2}{c_f}\right)+F_0\left[\sum_{x=0}^{x=c_f}\left(x_i-\frac{x_i^2}{c_f}\right)\right]=\sum_{x=0}^{x=c_{fi}}\left[F_Z(x_i)\cdot x_i\right] \end{cases} \tag{6}$$

and in a more compact format:

$$\begin{cases} \widetilde{F}\cdot A+F_0\cdot B=R_Z \\ \widetilde{F}\cdot C+F_0\cdot D=M \end{cases} \tag{7}$$

where:

$$A=\sum_{x=0}^{x=c_f}\frac{x_i}{c_f} \quad , \quad B=\sum_{x=0}^{x=c_f}\left(1-\frac{x_i}{c_f}\right) \quad , \quad R_Z=\sum_{x=0}^{x=c_{fi}}F_Z(x_i)$$

$$C=\sum_{x=0}^{x=c_f}\frac{x_i^2}{c_f} \quad , \quad D=\sum_{x=0}^{x=c_f}\left(x_i-\frac{x_i^2}{c_f}\right) \quad , \quad M=\sum_{x=0}^{x=c_{fi}}\left[F_Z(x_i)\cdot x_i\right] \tag{8}$$

Being A,B,C,D, R_Z and M all known parameters, (7) represents a set of two equations by which $\widetilde{F}$ and F_0 may be determined.

In Figure 7 the F_Z distribution of Figure 5 has been plotted together with the obtained equivalent trapezoidal distribution.
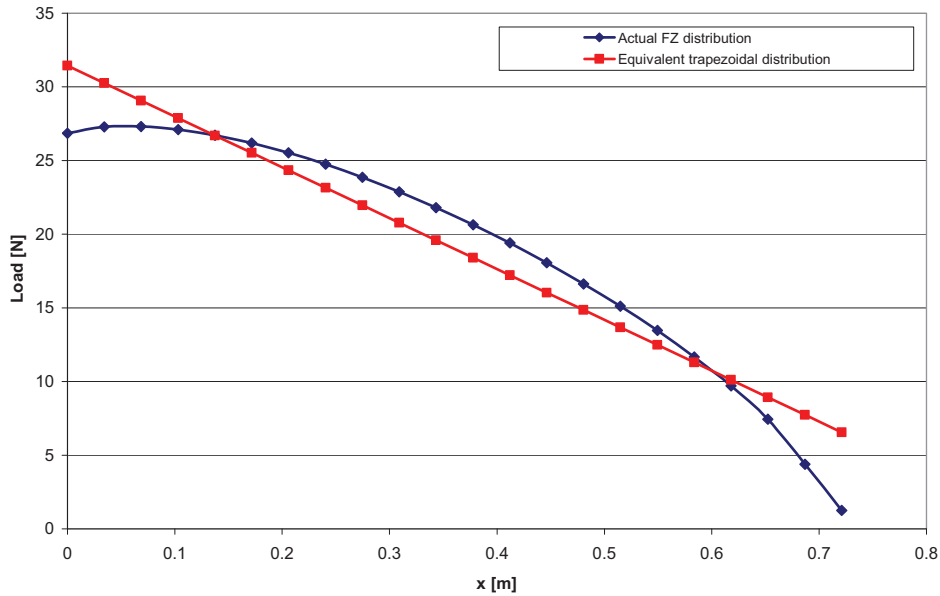
Figure 7: F_Z distribution and obtained equivalent trapezoidal distribution.

3 ARCHITECTURE DESIGN AND SIMULATION

Architecture working principle

In this paragraph the final design of the conceived SMART Flap architecture is presented, based on the adoption of the previously discussed SMA-based actuator. The reference geometry is based on a real scale flap for a typical regional transportation aircraft: a total length of 0.8 m has been considered (equivalent at about 30% of airfoil chord), with a max flap thickness of 0.25 m at root; the considered flap bay portion has a span-wise extension of 0.3 m.

The developed flap bay is constituted of two morphing ribs, each based on a chord-wise series replication of the elastic SMART actuator, and some rigid blocks, representing the flap shape and its aerodynamic surfaces: the disposition of the arc actuators in a series allows for increasing the total achievable displacement and rotation at the trailing edge, thus working as an amplification chain (performance of the single actuator have been discussed in the previous paragraphs). This architecture has an high level of integration of SMART technologies, given that each SMA actuator also defines the rib and, thus, the entire flap rigidity and load-bearing capabilities, by means of the coupled effect of the titanium elastic arc and the SMA ribbon: this way, structural deformability is also demanded to the actuators themselves, which have been suitably designed.

More in detail, the main element of the morphing flap, the rib, is constituted by four actuators in a series: each actuator is very similar to the single one already examined and thus main features will not be recalled at this point; only major changes made to the actuator, needed for a better integration within the rib, will be presented.

The number of integrated actuators within each rib has been chosen as a compromise between the need for higher performance (thus requiring a greater number of actuators) and weight and volume constraints (favouring a lower number of elements): in any case, this solutions can be suitably adapted to several configurations according to the designer needs and flap requirements. Moreover, in this study a simplified approach has been assumed to build the morphing rib, that is to consider all the integrated actuators equals to each other, with particular reference to the previously designed and experimentally tested one: of course, one could scale the actuators dimensions to better fit the flap geometry and increase their number while managing the best possible compromise between the total weight and performance; this has not been done in this work to keep low design complexity and manufacture costs, given that all the actuators are the same.

Furthermore, the presence of multiple actuators which can be individually (or a suitable combination) activated allows for multiple stable configurations for the morphing flap (as for a traditional flap, capable of several selected deflection angles).

The realization of each series of actuators, the morphing rib, required to slightly modify the design of the titanium arc basements, so to allow each titanium arc to connect with its consequent (and create the two series): the joining solution has been attained by means of a male-female mechanical connection between two subsequent basements, keeping in place the holes needed for the SMA ribbon connection to the titanium arc and then united through thorns (to make all the actuators behave like a single block and without interference with the SMA ribbons). This solution also allowed for minimum modifications to the design of the single actuator, which could be produced in a multiplicity of eight to constitute both ribs, while enabled to keep manufacture costs low: details about the final solution will be discussed in the paragraphs related to the prototype manufacture.

Finally, the morphing flap bay also integrates some elements which define the flap shape during the rib actuation, and permits the external load transmission from the surfaces to the ribs: in this solution, four solid blocks with a suitable profile have been considered, attached to each actuator on both sides (one actuator for each rib) and which can rotate and translate according to the ribs actuation (they move together with the element of the series they are connected with): the realization of such elements as rigid boxes interposed between the two ribs also introduces some torsional stiffness in the flap architecture and guarantees a better synchronism between the two ribs during actuation.

Numerical performance estimate

The structural analysis of the morphing flap architecture has been carried out using MSC/Nastran software as Finite Element solver and UGS Femap as pre/post-processor.

Numerical performance for the flap structure have been evaluated by considering a single morphing rib only: due to the expected symmetrical behaviour of the flap bay, reduction to a single rib allows to estimate both displacements and rotations at the trailing edge while cutting down F.E. modelling and solution times; moreover, solid blocks (connected rigidly to each actuator) represents the flap shape only and have no influence on performance, thus they have been excluded from the simulation (with the

exception of the last element, at the trailing edge, necessary to individuate the flap tip and its movement during actuation).

Furthermore, the single rib is constituted by four SMART actuators in a series: starting from the three-dimensional model for the single SMART actuator, based on CTETRA elements for the titanium arc and illustrated in detail in the previous chapter, it has been suitably simplified with a two-dimensional equivalent (Figure 8), completely based on CBEAM elements and tuned on the 3D model, in order to reduce computational time while keeping similar structural behaviour; this simplified model required to calculate again the SMA contribution (effective strain recovery, following exactly the same integration procedure previously illustrated), and has been finally adopted for the simulation of the entire rib.
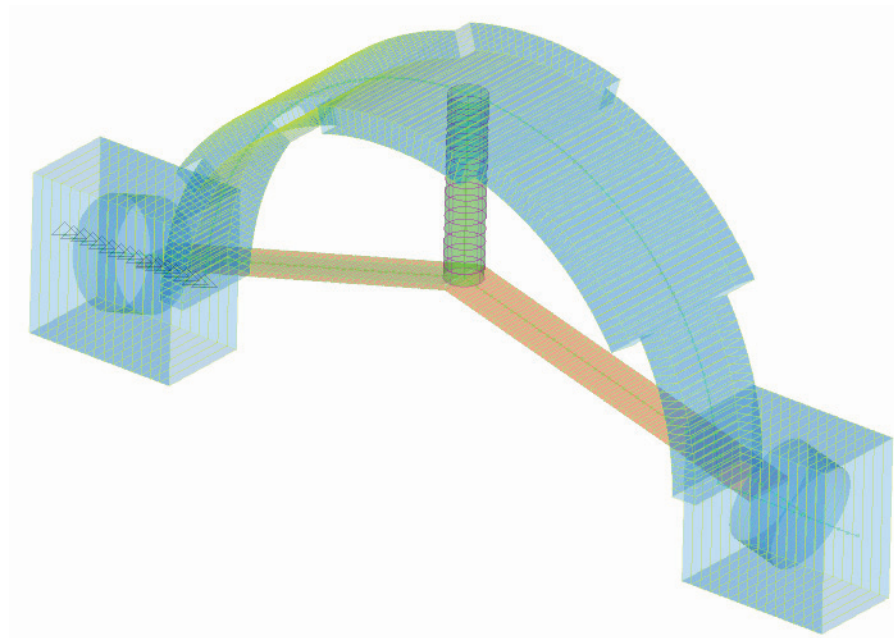
Figure 8: Equivalent simplified 2D model for the single SMART actuator.

Due to the high integration of the SMART actuator in the flap rib, a similar simulation procedure has been applied; more in detail, three conditions are possible for the rib and must be evaluated:

- the initial geometry (Figure 9), that is the shape of the rib when the four elastic arcs are connected in a series in absence of the SMA ribbons: this condition must be carefully evaluated because it is necessary to compensate the rotation (equal to 5 deg, known from the previous work on the single actuator) which each arc undergoes when pre-straining the SMA ribbons (immediately after assembly);

- the pre-load condition (Figure 10), that is the rib shape attained when each titanium arc pre-strains its SMA ribbon (of the selected amount of 3% of its initial length) and reaches the arc-ribbon equilibrium condition, simulating the internal stress state for each complete actuator: this condition is necessary to make possible cyclic actuation (this is the condition reached when cooling the SMA ribbons), and equals to the initial (non actuated) shape of the flap bay;
- the actuation configuration (Figure 11), that is the flap shape reached during the SMART actuators activation: net performance must be estimated as a difference between this condition and the pre-load one.
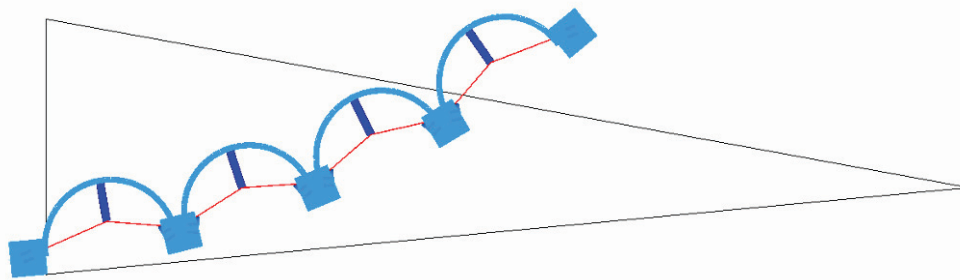
Figure 9: Morphing rib simulation: initial geometry.
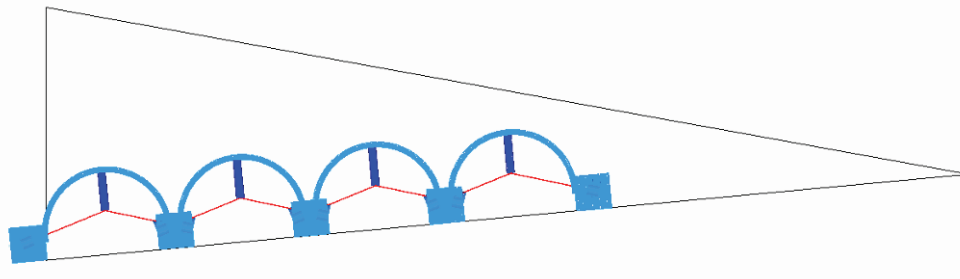
Figure 10: Morphing rib simulation: pre-load condition.
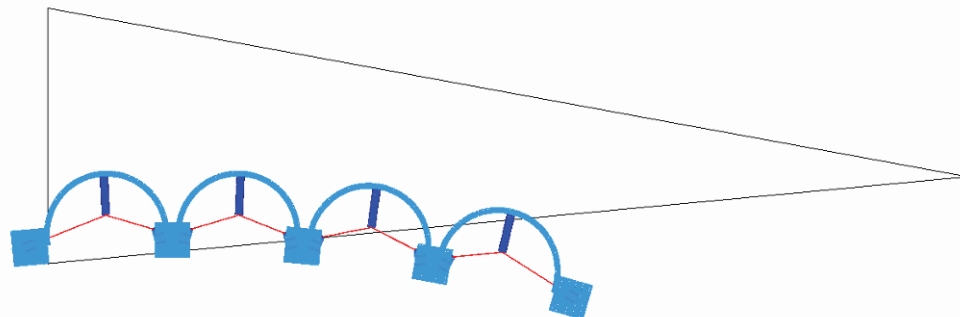
Figure 11: Morphing rib simulation: actuation condition.

The most important aspect of this procedure is the correct evaluation of the initial geometry: in this case, it can be perfectly predicted having already studied in depth the behaviour of the single SMART actuator. These requirements also led to some minor

modifications to the titanium arc basements (compensation of the pre-load rotation by means of a 2.5 deg opposite rotation of each basement, for each arc), as illustrated more in detail in the paragraphs related to the prototype manufacture.

Finally, to estimate numerical performance of the flap bay in terms of vertical displacement and rotation of the trailing edge, a rigid plate has been introduced in the model, connected to the final arc, to reproduce the last solid block which defines the flap shape (Figure 12).

Numerical results are reported in Table 3, evaluated both in absence and in presence of external static loads (Figure 13): in the latter case, the aerodynamic loads have been discretized in 8 equivalent concentrated forces, 4 for each rib (in identical couples for the 2 ribs at the same chord-wise station) and applied. Table 2 shows the equivalent static loads estimated from the aerodynamic study: according to the procedure illustrated in the previous paragraphs, the trapezoidal distribution has been further approximated with four discrete equivalent rectangular load distributions, each acting on the amount of flap surface belonging to the considered rigid box and assuming the mean value of the trapezoidal distribution relative to it; then, this load has been considered applied on top of each SMART actuator, given that they represent also the load-bearing elements of the flap bay.

Net performance have been evaluated as difference between the actuation configuration, both in absence and presence of aerodynamic loads, and the pre-load one, in absence of static loads (external loads only affect the actuated flap).

Equivalent static loads [Kg]	Single Rib	Flap Bay
1st rigid box/actuator (flap root)	15	30
2nd rigid box/actuator	7.5	15
3rd rigid box/actuator	8	16
4th rigid box/actuator (flap tip)	12	24
Total	42.5	85

Table 2: Equivalent rectangular load distribution acting on each rib and the entire flap bay.

Actuation net performance	Without aerodynamic loads	With aerodynamic loads
T.E. vertical displacement [mm]	185	131
T.E. rotation [deg]	18.5	13.8

Table 3: Morphing rib numerical performance estimate in absence and presence of aerodynamic loads.

As it can be noticed, due to the presence of the static loads, net performance decrease of 29% for the vertical displacement and 25% for the rotation of the trailing edge. This can be mainly attributed to the titanium arcs elasticity and not to Shape Memory Alloys: to prove this idea, a reference simulation has been carried out for the pre-load condition

with application of the full static loads (this is a not real load condition), showing that in this case the rib already loses a 22% in terms of vertical displacement (over a total of 29%) and a 18% on rotation (over a total of 25%). Thus, the decay in performance due to static loads which can be attributed to SMA is only about 7%.
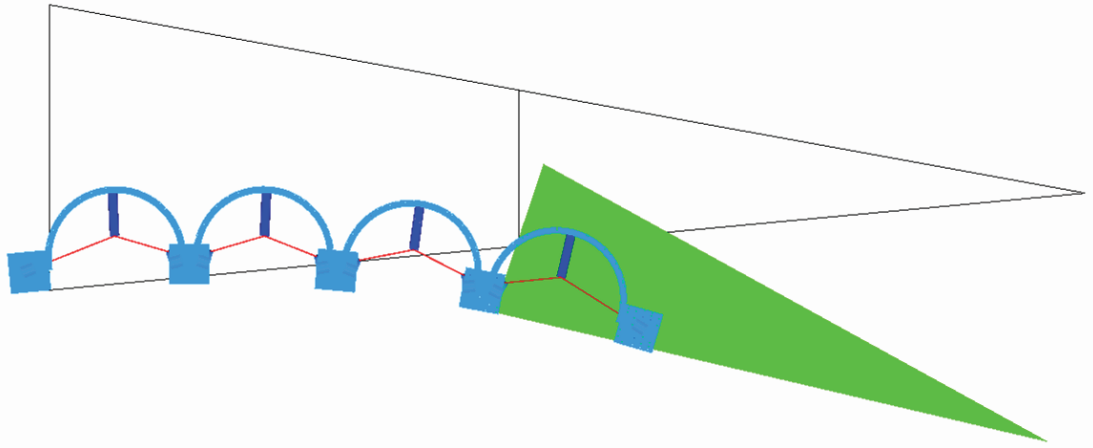
Figure 12: Morphing rib simulation to estimate numerical performance in absence of static loads.
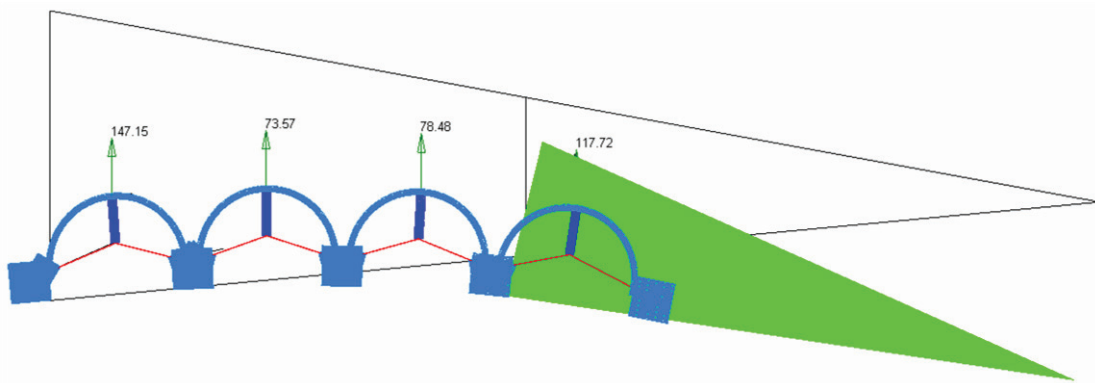
Figure 13: Morphing rib simulation to estimate numerical performance in presence of static loads.

Finally, in presence of static loads also the effective recoverable strain of each SMA ribbon has been updated (with the usual procedure) to take into account the increased stress level: the minimum estimated complete activation temperature for the SMA ribbons increased from 75.3°C to 95.4°C in presence of static loads (due to the increase in the stress field).

4 PROTOTYPE MANUFACTURE AND ASSEMBLY

Prototype design solutions

In this paragraph details will be discussed about difficulties associated with the design and manufacture of the real full scale prototype and the adopted final solutions.

The flap bay, as already illustrated, has been conceived as two morphing ribs to which four solid blocks are connected, defining the flap shape. Each rib is constituted by four SMART actuators, each of them mainly based on the single actuator already presented; minor changes have been applied to take into account:

- the series accommodation of the titanium elastic arcs, with the necessity of connecting them to each other in an unique solid rib: the joining solution has been attained by means of a male-female mechanical connection between two subsequent basements (Figure 14), keeping in place the holes needed for the SMA ribbon connection to the titanium arc and then united through thorns;

- the necessity of tightening each arc of the series during the assembly procedure so to connect the SMA ribbons: both the puller and the arc basement have been modified to take advantage of new holes put in place in the bottom surface of the basement, given that the basement shape has been changed and the previously adopted solution could not be used any more.
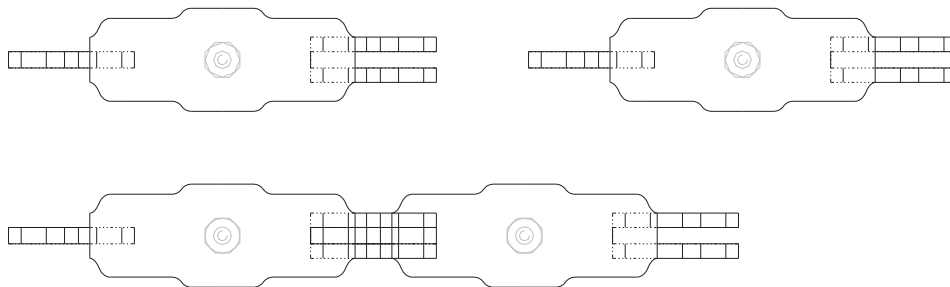
Figure 14: Top view of the adopted joining solution for the arc series.

In any case, the number of modifications has been kept as low as possible to preserve the validity of the results achieved on the single SMART actuator; only the basement has been affected by major changes. In particular, it has been necessary to compensate the 5 deg rotation assumed by each titanium arc during pre-load (to pre-strain the SMA ribbons): thus, both basements of each arc have been tapered towards the external edges of 2.5 deg, allowing to have a unique virtual straight line at the bottom of the flap when

in rest (pre-load) condition; of course, this means that before pre-loading, the series points upward (Figure 15).
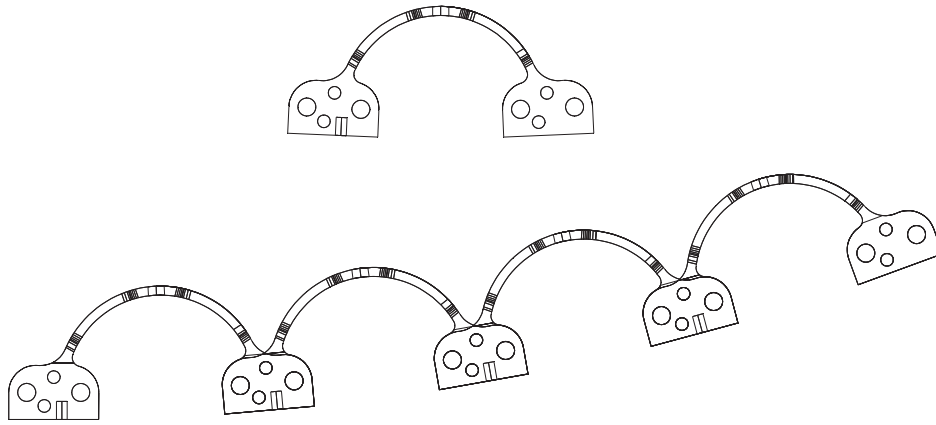
Figure 15: Detail of the rib series with the arc tapering (2.5 deg) and assumed initial geometry.
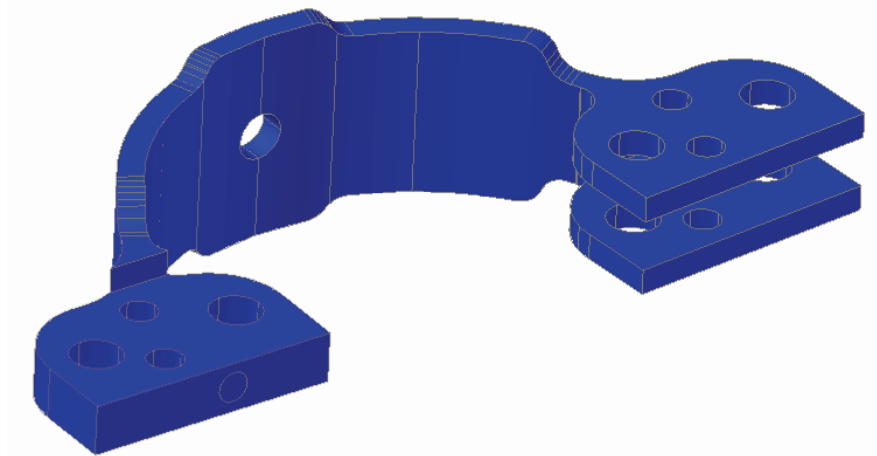
Figure 16: Final CAD model of the titanium arc.

Figure 16, instead, shows a three dimensional CAD model of the final design of the titanium arc: in each basement, other then the usual two bigger holes for the clamping mechanism of the SMA ribbon, two smaller holes can be noticed to host thorns to connect two successive arcs; moreover, on the bottom surface of the left basement another hole is visible which is used, after the series is assembled, to attach the puller (the hole in the left basement of the successive arc represents the right joining for the same puller).

Having chosen this solution for the ribs, some considerations have arisen about the assembly procedure of the SMA ribbons:

- to avoid mechanical interference between ribbons and clamping mechanisms of two successive actuators, they have to be mounted on opposite faces of the same rib;

- to compensate possible out-of-plane displacements of the ribs, due to the alternate assembly of the SMA ribbons, and given the presence of the rigid bars inter-connecting them, a layout taking advantage of axial symmetry has been adopted (the two ribs use a mirrored arrangement for the SMA ribbons.

These considerations can be summarized in the final adopted configuration, shown in Figure 17.
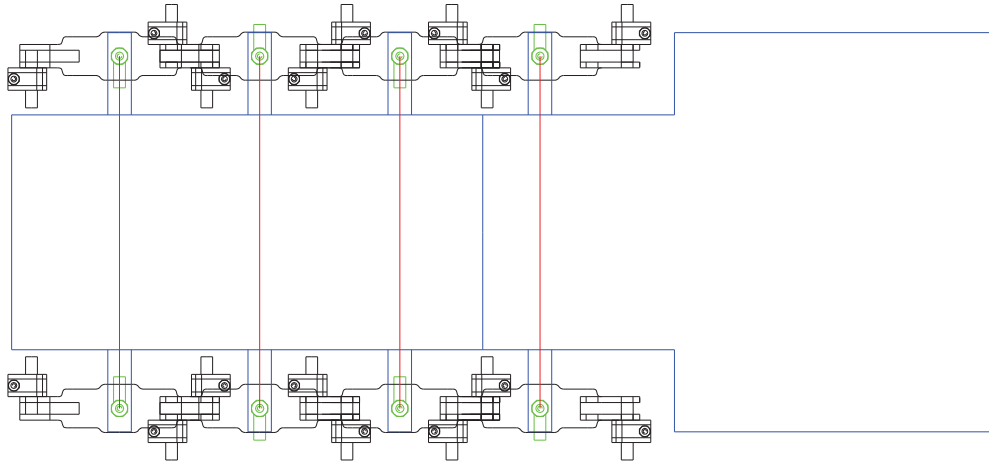
Figure 17: Top view of the adopter solution for the SMA ribbons and camping mechanism disposition; rigid bars used to inter-connect the two rib are also visible, with the filling solid boxes.

Then, after realising two identical morphing ribs, four solid rigid blocks have been added in between to define the flap shape and stiffen the flap bay at torsion: they have been suitably shaped to avoid any interference during the shape change on actuation and keep a smooth aerodynamic surface.
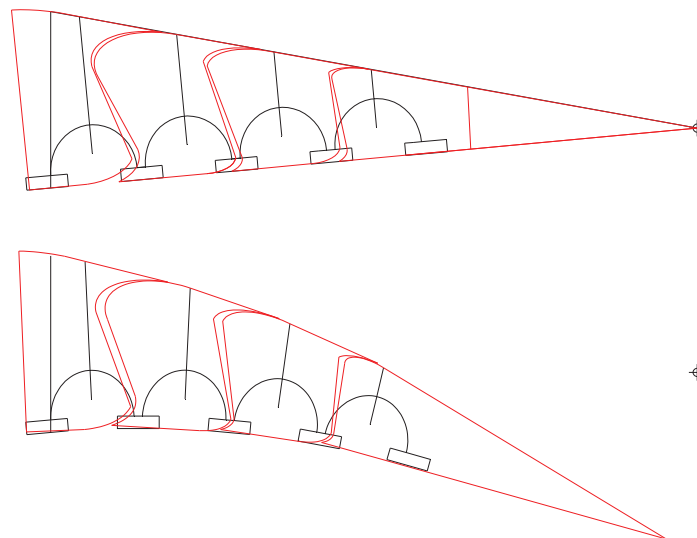
Figure 18: Conceptual layout of the adopted solution for the solid boxes: pre-load (rest) condition (up) and actuation condition (down).

Figure 18 illustrates the final design of these solid boxes, each connected to a SMART actuator of the series. The main difficulty in developing such a solution has been the detection of the correct kinematics of the elastic arcs: as elastic elements, during actuation they undergo a camber variation together with the free (right) basement displacement and rotation.

Each rigid box has been connected to a transverse rigid bar (made in aluminium), which unites the two ribs and connects in the middle of each arc to the vertical rods already present (used to support the SMA ribbons): Figure 19 shows a three dimensional view of the CAD models of the four boxes and rigid bars. The connection between the transverse bars and the rigid boxes can be adjusted by using the provided bushings with screws. Due to the complex shape of rigid boxes, they have been realized with resin and empty to reduce weight; surfaces have been made with 0.5 mm thick aluminium plates, suitably shaped and glued/screwed to the boxes.
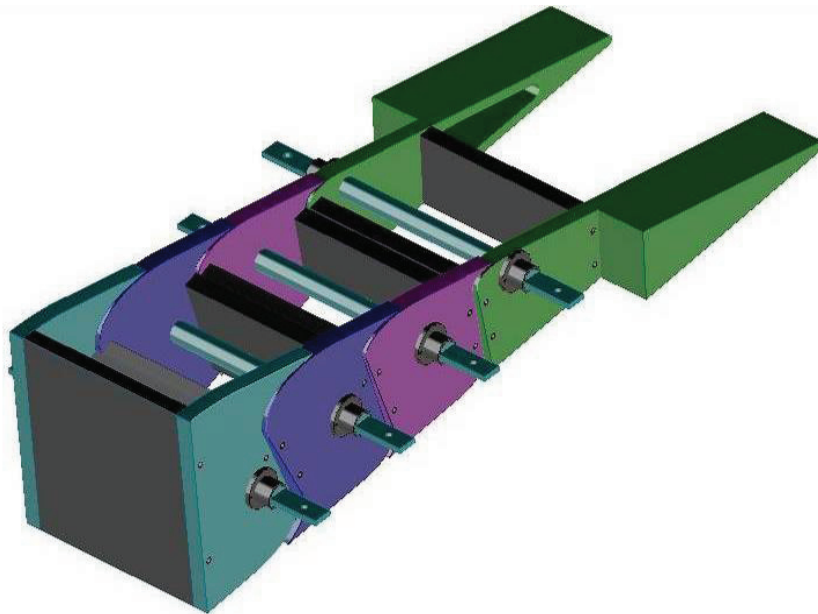
Figure 19: View of the three dimensional CAD models for the four solid boxes (surface panels are not shown).

Manufacture and assembly

The manufacture of the ribs is based on the production of each single SMART actuator, as discussed in Chapter 6 and in previous paragraphs: thus, details will not be presented again; some particulars will be visible in next figures related to the prototype assembly. Figure 20, instead, shows the final realized rigid boxes complete with skin and transverse bars.
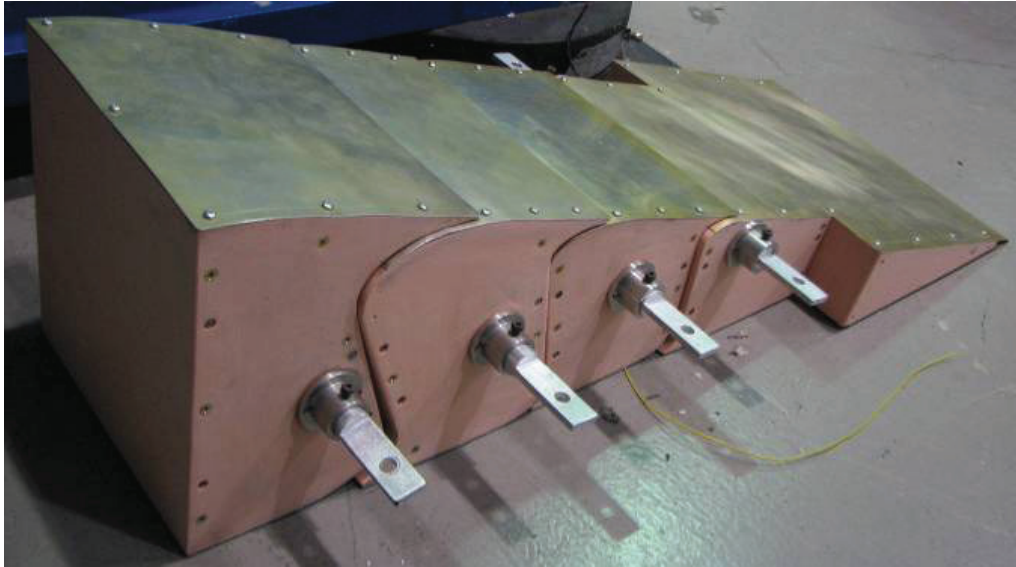
Figure 20: Rigid boxes for the experimental prototype with transverse bars.

In the following, the assembly procedure of the experimental prototype of the flap bay will be discussed. Initially, the several titanium arcs have been assembled to constitute the two ribs by means of the provided thorns, and connected to a support frame (Figure 21): in figure it can be noticed also the presence of two (of the four) transverse bars to show the attach mechanism (they will be assembled only in the end, together with the rigid boxes). It should be observed also that the initial geometry of the ribs (not pre-loaded yet) is as shown in Figure 15.

Figure 21: View of the two arc series (ribs), without SMA ribbons, attached to the support frame.

Once the two ribs are in place, the SMA ribbons can be attached to each titanium arc to obtain the series of SMART actuators: the distance between the two basements of each titanium arc is shortened by means of a puller, which helps in assembling the SMA ribbon (cut at a proper length) together with the two mechanical clamps; then, the puller is detached and used for the successive actuator (Figure 22). During the assembly of all

the SMART actuators, both ribs slowly reach their pre-load condition, which equals to the flap rest position.

Figure 22: Assembly of the SMA ribbon to each titanium arc by means of the puller.

Afterwards, all the SMART actuators of both ribs have been connected in a single electrical series by using some wires as "bridges" between a SMA ribbon and its subsequent (the clamping mechanism insulates the ribbons from the rest of the actuator by means of nylon bushes; the vertical rod is insulated too): due to the high expected electrical currents, to quickly heat the SMA ribbons, wires with big sections have been used (Figure 23).
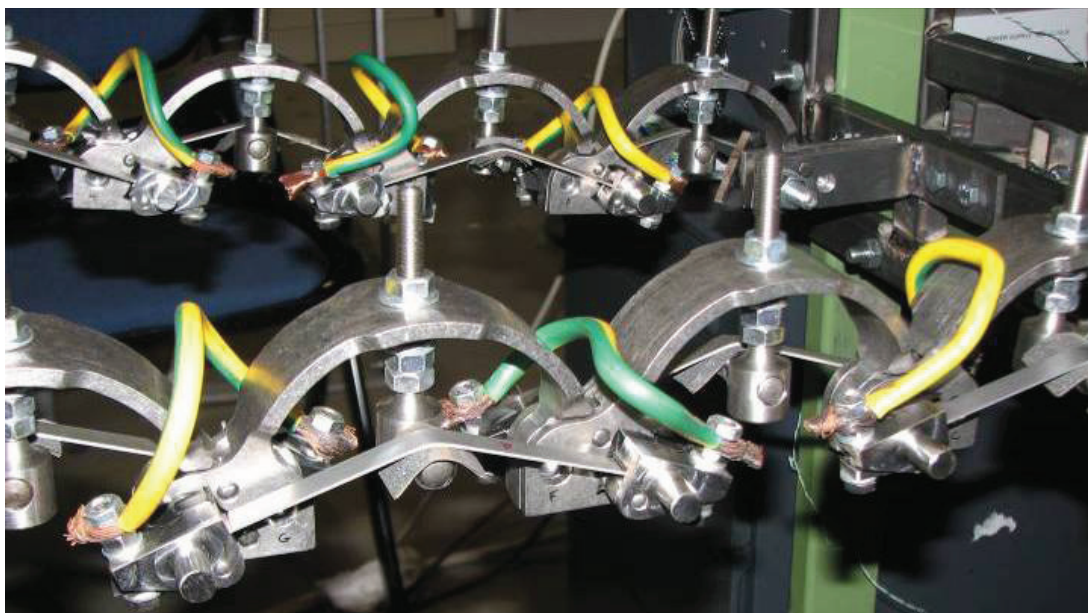
Figure 23: Detail of the electrical wires connecting all the SMA ribbons of both ribs in a common series for full activation.

Finally, all the rigid boxes have been inserted simultaneously (due to space constraints) in between the two ribs and attached to them by means of the transverse bars (Figure 24), which make them move accordingly to the SMART actuator each box is connected with (Figure 25). Finally, also the sliding panel solution for the flap skin can be noticed in the figures.
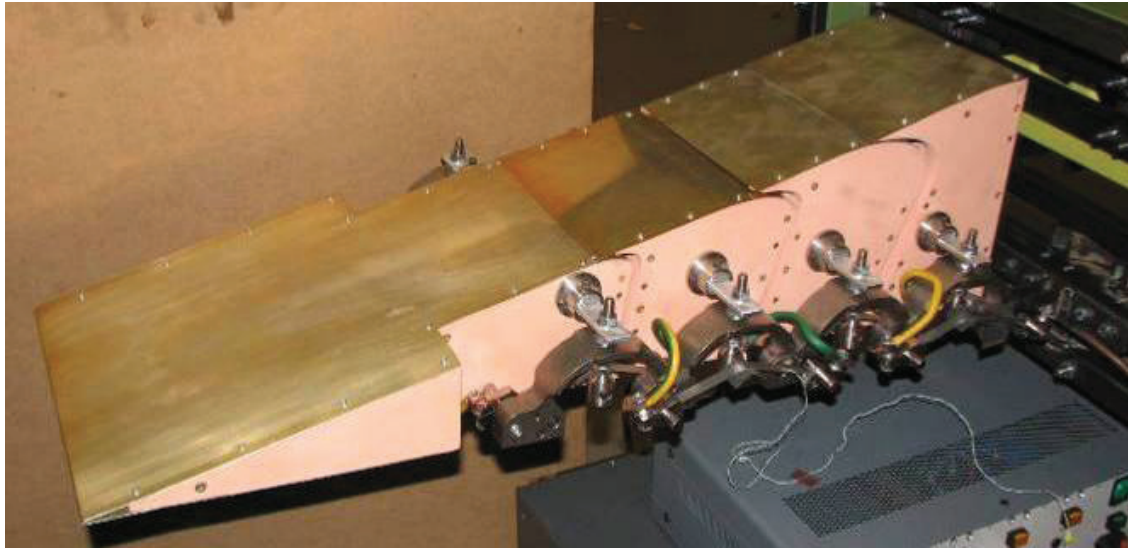
Figure 24: Fully assembled prototype.
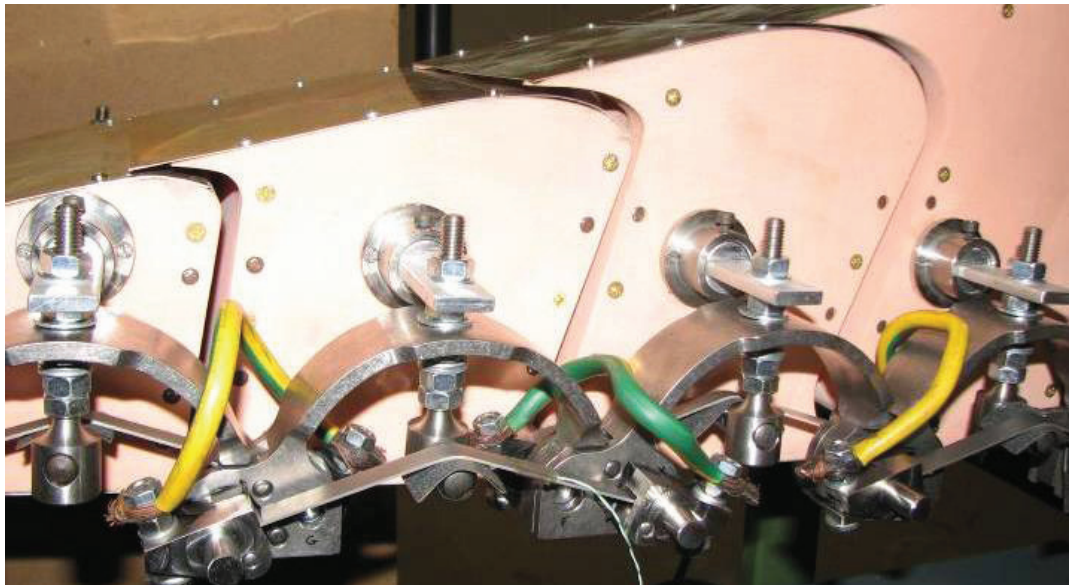
Figure 25: Fully assembled prototype: details of the rib-rigid boxes connections.

5 EXPERIMENTAL CAMPAIGN AND NUMERICAL CORRELATION

Setup and preliminary functional tests

The experimental setup has been constituted by a DC power supply, a thermo-couple reader, a measurement sheet and a timer.

The power supply has been used to heat the SMA ribbons by means of Joule effect: all the SMA elements have been connected in an unique electrical circuit to evaluate the max actuation performance of the flap bay (this way, also the same amount of electrical current is circulating in all the SMAs). A constant supply law has been adopted (On/Off), with 60 Ampere CC and 7.3 Volts for the preliminary functional tests. On this purpose, it can be recalled that:

- Joule effect is only based on current (Ampere): voltage could be set as low as possible, thus reducing the total power, according to the limits of the adopted power supply;

- the amount of electrical current can be changed and only affects the speed of actuation: this value can be lowered (as far as the minimum complete activation temperature of the SMA is reached) to save power, but also increases actuation time.

As a result, the maximum supplied electrical power (for all the SMA ribbons of both ribs) has been of 438 Watts, allowing for a complete actuation in 15 seconds; from an energy perspective, a total of 6570 Joule is absorbed by the flap bay during activation.

The thermo-couple reader has been adopted to verify the max temperature reached by the SMA ribbons: due to the instrument limitations, only three thermo-couples could be attached to as many SMA ribbons. Finally, the measurement sheet and timer allowed to determinate the actuation performance in terms of vertical displacement of the trailing edge with time: both photos and videos have been taken.

The experimental tests were carried out at the CIRA laboratory, with a environmental temperature of 28°C.

Due to the high thermal inertia of SMAs and the adopted natural convective cooling, only activation times will be reported and discussed; possible solutions to lower cooling times can be adopted (as forced convective cooling by means of one or more fans, refrigerating spray, Peltier cells, etc.) but have not been considered in this work.

Figure 26 and 27 show the pre-load and actuation condition respectively for the first actuation cycles of the flap bay: one can notice the smooth surface achieved by the flap in both cases. Table 4 summarizes the results of some preliminary experimental measures oriented to show the functionality of the developed morphing flap, and compares them to the numerical estimate: a good correlation can be assumed.

Actuation performance	Numerical estimate	Experimental measure	Percentage difference
T.E. vertical displacement [mm]	185	180	-2.7 %
T.E. rotation [deg]	18.5 deg	/	/

Table 4: Summary of the actuation performance for the morphing flap: preliminary functionality tests.

Afterwards, during the experimental campaign without and with static loads, a total electrical power of 450 Watts (50 Ampere, 9 Volts, DC) has been used for a complete activation of the SMA ribbons in 37 seconds.

Additionally to the described setup, a suitable method capable of applying the static loads to the prototype has been conceived, based on a pulley-cable-weight system (Figure 28); hooks have been adopted to connect to the SMART actuators on both ribs (Figure 29). As a detail, the operations to add or eliminate the static loads (weights) have been always done symmetrically (acting on both ribs almost on contemporary) and starting from the flap tip towards the root when unloading, and vice versa during application of the load.
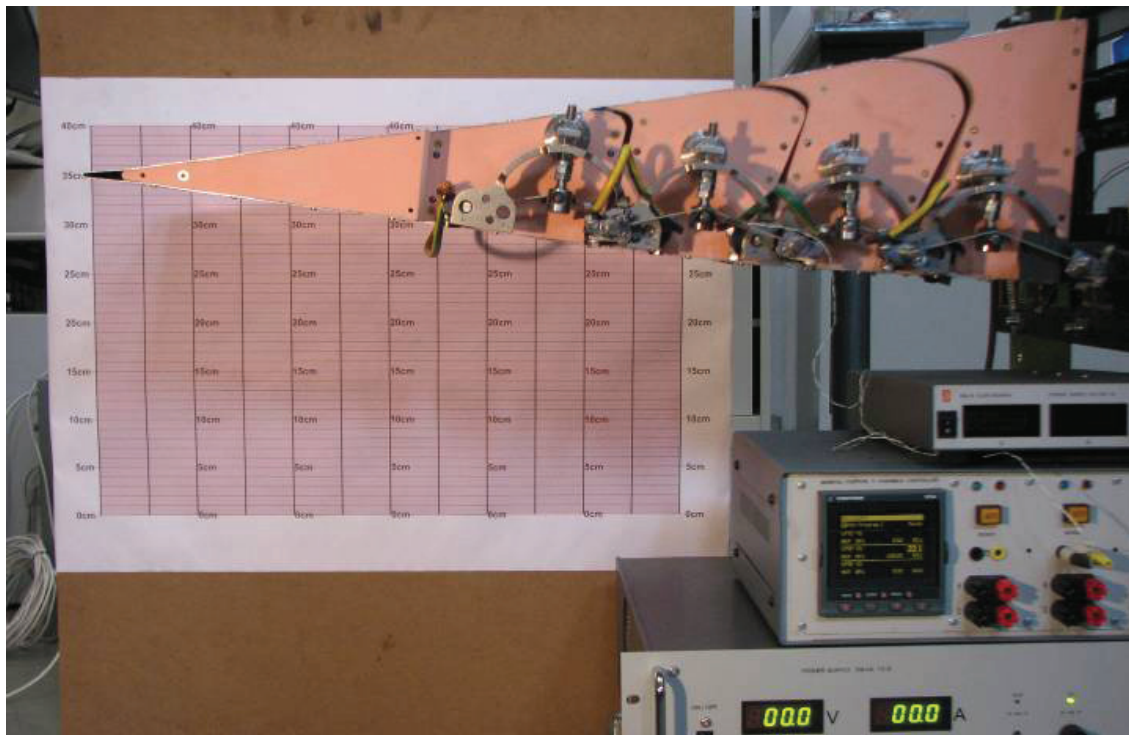
Figure 26: Preliminary functional tests: experimental prototype in pre-load (rest) condition.
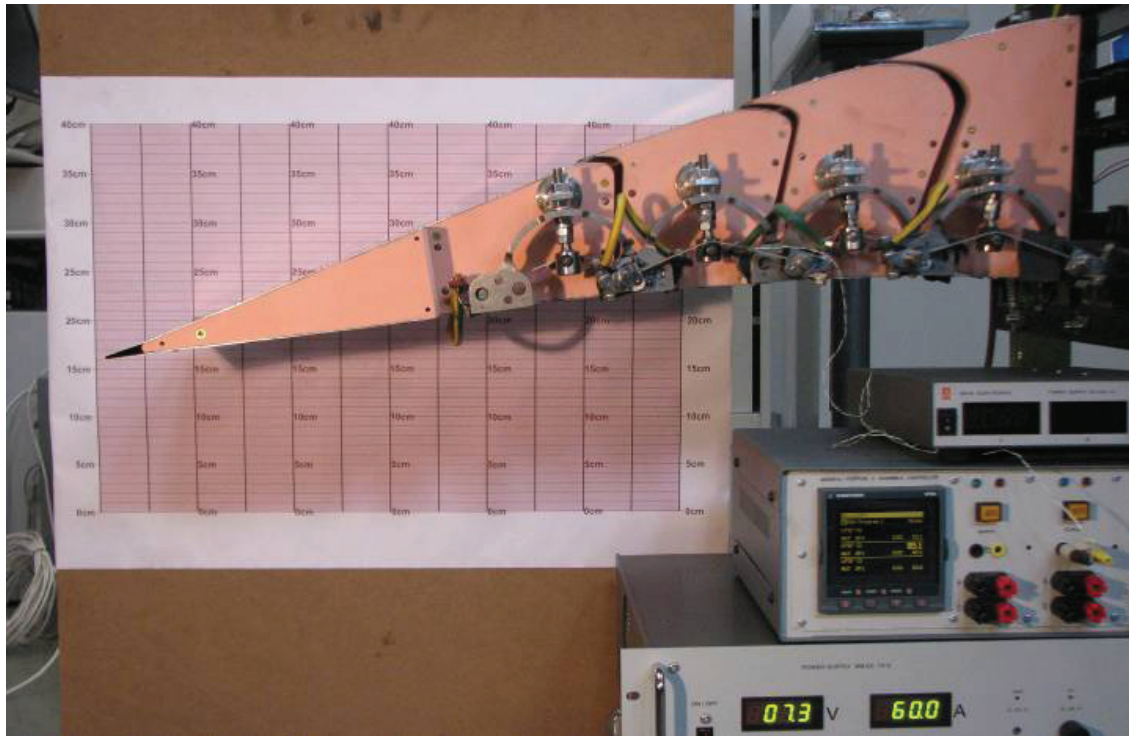
Figure 27: Preliminary functional tests: experimental prototype in actuation condition.

Figure 28: View of the full experimental setup for the test campaign in presence of static loads.

(a)   (b)

Figure 29: Details of the pulley, cables and weights system used to apply static loads to the flap prototype.

Experimental measures without static loads and numerical correlation

The first set of experimental measures has been carried out in absence of static loads: it has been used as a reference for tests with static loads, discussed in the next paragraph.

Several cycles have been executed: results here presented have been obtained after multiple tests which showed a good stability and repeatability. Figure 30 shows typical performance attainable without static loads: a vertical displacement at trailing edge of 123 mm reached in 37 seconds.

It must be noticed that these results are lower than the previously presented one (for the preliminary functional tests, 180 mm of vertical displacement), which were measured experimentally too, on the same prototype, in the first actuation cycles.

Motivations of such a degradation in performance can be explained by considering the following:

- these results have been measured after several actuation cycles for the same unique assembly, both in absence and presence of static loads, the latter affecting the prototype functionality (see next two points);

- SMA ribbons underwent some "yield" at the clamps, losing some strain recovery capability;

- SMA clamps underwent a "warp" at their connection with the titanium arc, due to the nylon bushes.
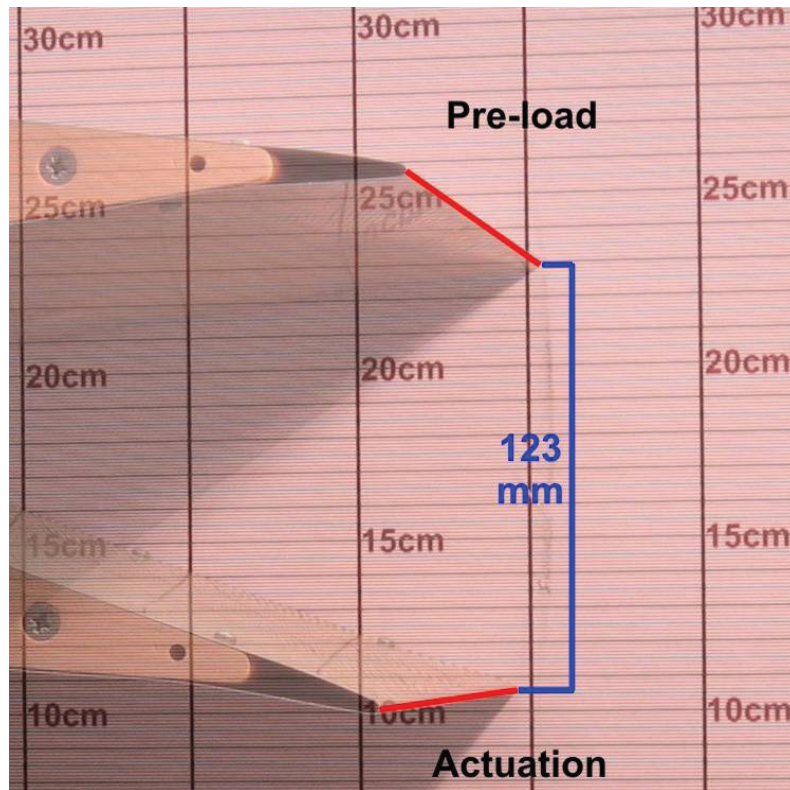
Figure 30: Experimental campaign: trailing edge net performance in absence of static loads.

As shown in Figure 31, SMA clamps are not orthogonal to the titanium arc; moreover, line markers on the SMA ribbons are visible due to some yield at the clamp itself.

The initial performance could be recovered by executing a complete re-assembly of the entire prototype and substituting all the nylon bushes, better if with a more durable material.
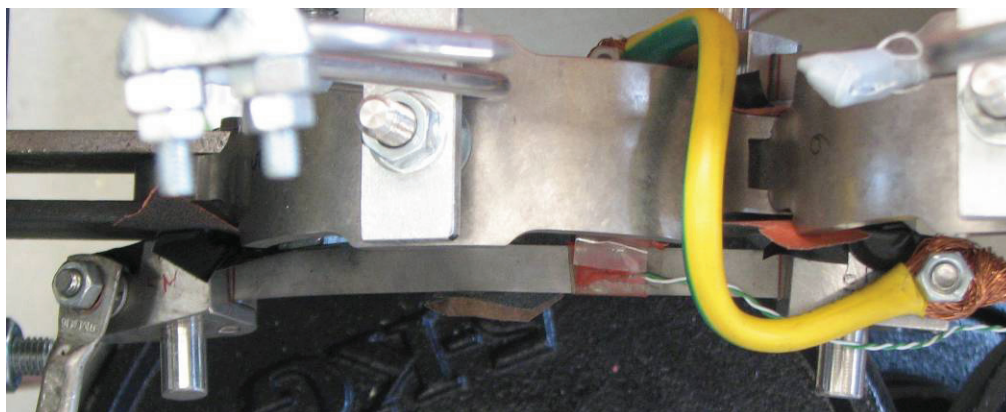
Figure 31: Detail of the SMA ribbon "yield" and clamp "warp" due to a large number of actuation cycles in presence of static loads.

However, keeping in mind this shift in terms of absolute performance, it can be still useful to understand the behaviour of the flap prototype in relative terms, comparing measured performance in absence and presence of static loads, using the former as a reference for comments.

Figures from 32 to 34 illustrate the experimentally measured trend for the vertical displacement, the SMA temperature and time conveniently interrelated: the square marker indicates max performance, with the star marker pointing out performance measured at 95% of max actuation. The same results are summarized in Table 5.
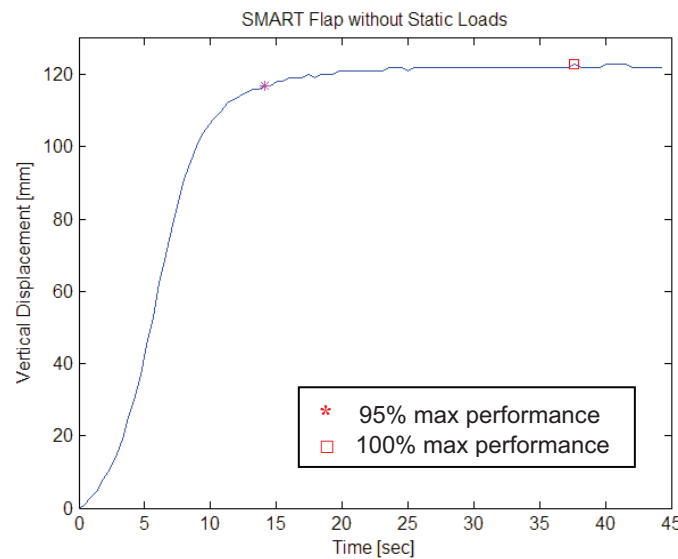
Figure 32: Experimental tests without static loads: vertical displacement vs time.
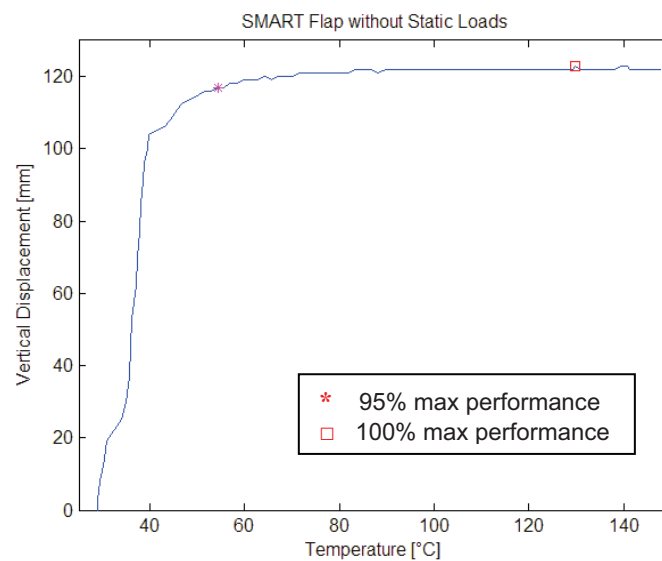
Figure 33: Experimental tests without static loads: vertical displacement vs temperature.
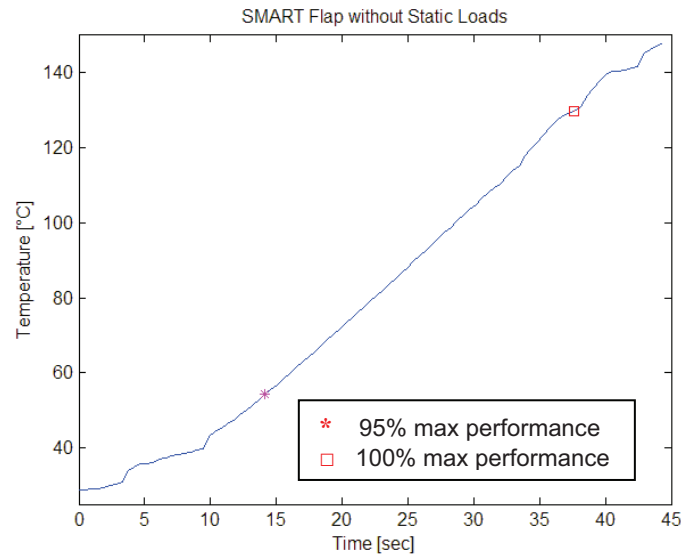
Figure 34: Experimental tests without static loads: temperature vs time.

	95% max performance	Max performance
T.E. vertical displacement [mm]	117	123
Activation time [sec]	14	37
SMA temperature [°C]	54.3	129.7

Table 5: Summary of experimental tests without static loads.

Considering the employed electrical power, activation time is quite speedy (and can be improved, if required) and sufficient to reach the expected activation temperature for SMA ribbons: on this aspect, it must be observed that the numerically estimated temperature of 75.3°C is in between the experimental measured range; the max measured temperature must not be considered as the effective one (it also depends on how much time the power supply has been kept on), since thermal inertia and spot reading by means of thermo-couple may not represent the actual temperature reached by the SMA ribbons uniformly.

Diagrams show that large amount of the expected actuation takes place and completes near the transition temperatures of the considered SMA: in particular, the non-linear behaviour that can be seen in Figure 34 for temperature is due to the phase transition typical for SMAs.

Experimental measures with static loads and numerical correlation

Following the early experimental tests, which demonstrated the functionality of the developed flap bay, further activation cycles have been executed in presence of static loads: as from Table 2, weights have been applied to both ribs and attached on top of each SMART actuator by means of suitable hooks.

The first measured data regards the vertical displacement of the trailing edge induced by the application of the static loads: as shown in Figure 35 and 36, the introduction of static weights, one by one (from the flap root to the trailing edge) to attain the full static load, induces a displacement of the flap bay due to the elasticity of the ribs (mainly, the titanium arcs).
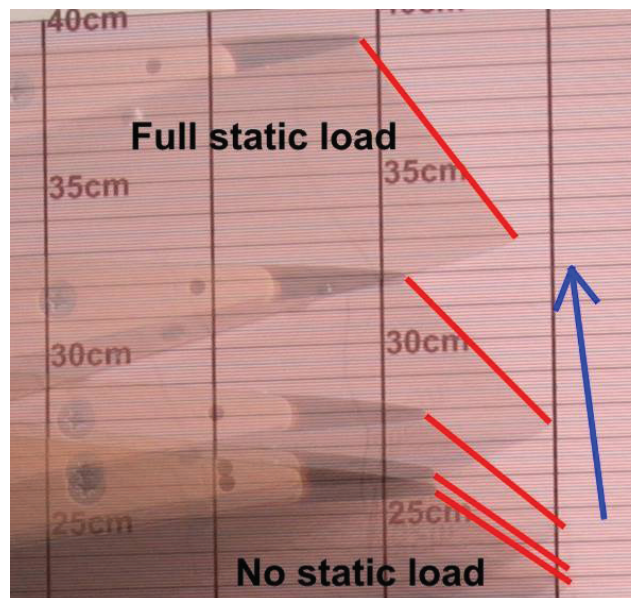
Figure 35: Experimental campaign: trailing edge displacement due to the application of static loads (one by one, from the flap root to the trailing edge).
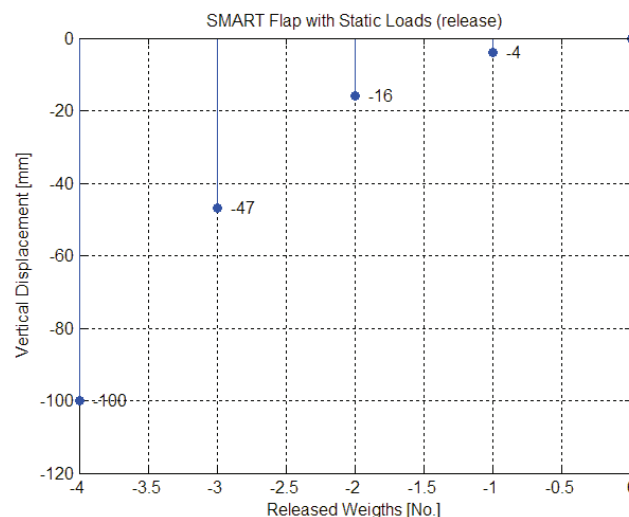
Figure 36: Experimental campaign: trailing edge displacement due to the application of weights (from absence to full static load, adding one weight at a time).

It can be noticed that the application of the first weight, near the flap root, induces a small displacement of the trailing edge also if it is the greater static load (30 Kg), due to the small distance from the root (and, thus, static moment); after, the introduction of

additional loads moving towards the flap tip together with an increased distance from the flap root induces increasing displacements to the flap tip.

Therefore, due to the application of the full static loads, the flap trailing edge undergoes a vertical displacement (upwards) of 100 mm when compared to the same pre-load condition in absence of external loads: Figure 37 shows these two configurations.

(a)

(b)
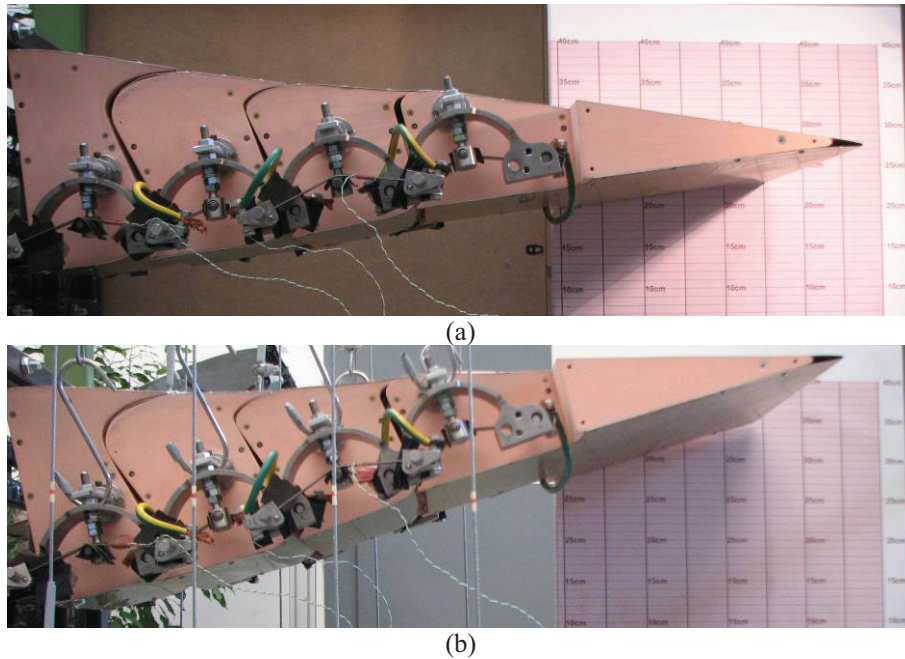
Figure 37: Experimental campaign: pre-load condition for the flap bay (a) in absence and (b) in presence of static loads.

This measured value results to be greater of the numerically expected 41 mm displacement: such a discrepancy can only be attributed to the presence of yokes among the several titanium arcs composing a rib (connected by means of the thorns) and the clamp yield and warp, as already discussed and visible in Figure 31.

Finally, actuation performance in presence of static loads have been measured (Figure 38): a stable vertical displacement of 114 mm has been reached in about 38 seconds with the supplied electrical power.

Again, Figures from 39 to 41 illustrate the experimentally measured trend for the vertical displacement, the SMA temperature and time conveniently interrelated: as always, the square marker indicates max performance, with the star marker pointing out performance measured at 95% of max actuation. The same results, in presence of static loads, are summarized in Table 6.
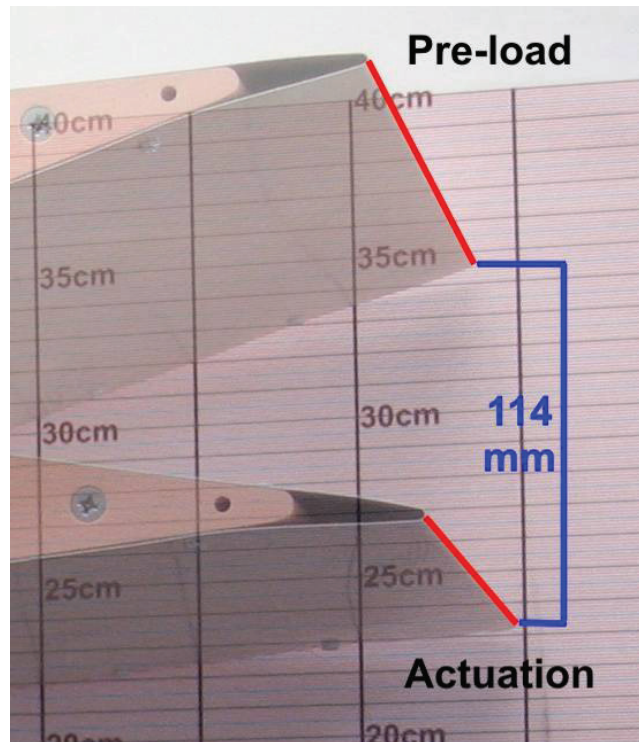
Figure 38: Experimental campaign: trailing edge net performance in presence of static loads.

	95% max performance	Max performance
T.E. vertical displacement [mm]	108	114
Activation time [sec]	18	38
SMA temperature [°C]	65.3	134.2

Table 6: Summary of experimental tests with static loads.
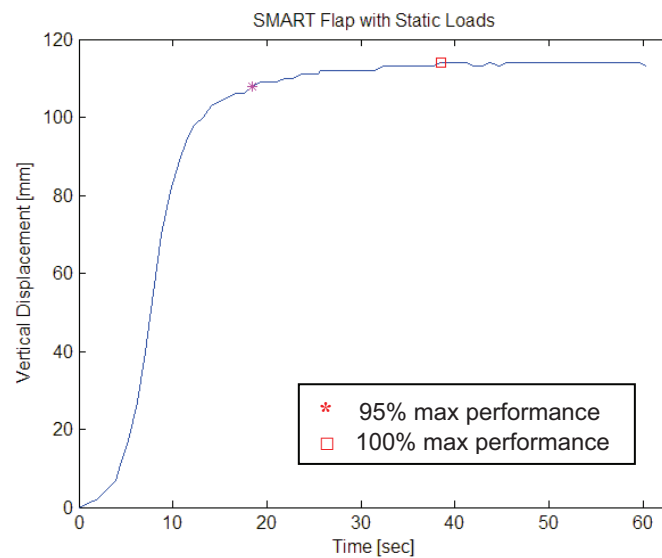
Figure 39: Experimental tests with static loads: vertical displacement vs time.
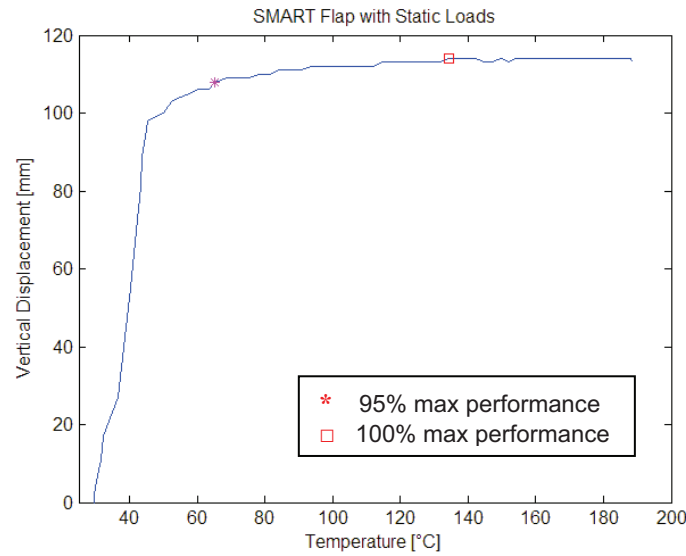
Figure 40: Experimental tests with static loads: vertical displacement vs temperature.
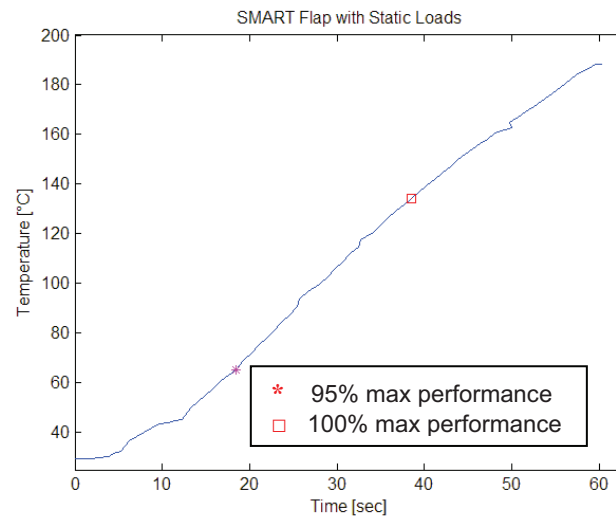
Figure 41: Experimental tests with static loads: temperature vs time.

Also in presence of static loads, the activation time can be considered quite speedy and the power supply sufficient to reach the expected activation temperature for SMA ribbons. In this case the complete activation temperature increased, as numerically expected: however, its increment is lower than the numerical one (from 75.3°c to 95.4°C), thus corroborating the previous considerations about thermal inertia and spot reading, together with the observation that the measured temperature is also affected by the time the power supply is kept on (which leads to a greater than needed Joule heating); in any case, the expected temperature is within the measured range.

The experimental performance in terms of vertical displacement of the flap trailing edge is lower of 9 mm due to static loads, that equals to about 7% of the total displacement, exactly the same percentage difference estimated numerically.

Finally, also the vertical displacement of the cables (to which weights have been attached) has been measured during actuation of the flap bay, which can help in giving an idea of the work executed by the prototype. Figure 42 shows for each cable (from the flap root, left, to the tip, right) the amount of displacement.
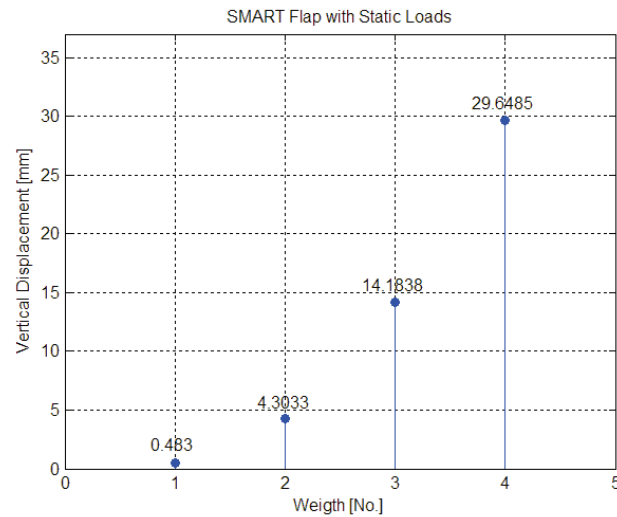
Figure 42: Experimental campaign: vertical displacement of cables to which weights are attached due to the prototype actuation.

6 CONCLUSIONS

This study presents an original architecture focused on the camber control of the aft part of a real scale wing for a typical regional transportation aircraft; related aerodynamic benefits have been illustrated. The flap bay is constituted of two morphing ribs, each based on a chord-wise series replication of the elastic SMA-based actuator, and some rigid blocks, representing the flap shape and its aerodynamic surfaces.

Many of the characteristics of the ribs come from the SMA-based actuator (and same conclusions and considerations apply): the Finite Element model and simulation procedure, also if a suitable 2D reduction of the actuator has been necessary to reduce computational time; its peculiarities and performance, but it has been necessary to apply minor updates to the actuator design to be suitably accommodated in the series. The flap shape, instead, has been realized by means of rigid blocks suitably designed to accommodate the kinematics of the ribs without affecting structural continuity: a multi-panel sliding skin solution has been herein adopted.

The performance of the presented architecture have been numerically estimated in absence of aerodynamic loads, demonstrating the efficacy of the developed solution; in presence of such loads, instead, the flap bay exhibited lower performance, due to the excessive structural elasticity. Similar results have been measured during the experimental campaign, showing full functionality of the proposed architecture and a good correlation with expected estimates. A better aero-elastic design can allow to overcome the highlighted drawbacks; some design aspects (as, f.i, the nylon bushes) need to be revised.

Abovementioned architecture is able to restore its initial condition; however, thermal inertia problems related to the SMA cooling have still to be solved to increase cyclic speed.

Further investigations will be focused on the definition of an active control system capable to control the SMA activation and reduce the cooling time (faster and more efficient activation systems will be taken into account, f.i., Peltier cell technology). Dedicated optimisation processes will be addressed to improve structural performance, costs, weight and durability.

One of the problems deriving from hingeless morphing solutions is the stress field induced within skin elements. To address this challenging problem of the skin continuity and surmount limitations of the adopted multi-panel skin solution, further

investigations need to be taken into account: panels partially made of elastomeric materials can be used; moreover, the implementation of sandwich skins having elastomeric plates and an "accordion" honeycomb (similarly to what will be presented in the next chapter) would represent a brilliant solution to this problem.

Investigation presented in this paper deal with static applications; problems related with dynamic excitation will be object of future works.

The industrial partner (Alenia Aeronautica Spa) funded these activities and showed great interest in their future industrialization: an European patent (see Appendix) has been actually requested for the selected application. Moreover, opportunities to actually deploy these further studies will be taken into account in the "TIAS" project inside Alenia Aeronautica Technological Program for the next generation Jet and Prop Regional Aircraft.

The conceived architecture well integrate with current perspectives on the design of future aircrafts, asking for low weight and noise, capable of wing adaptability to the mission requirements and based on the "all-electric" and "fly-by-wire" paradigm.

7 REFERENCES

[1] Martins A.L., Catalano F.M., 1998, "*Viscous Drag Optimization for a Transport Aircraft Mission Adaptive Wing*" – 21st ICAS Congress, Melbourne, Australia, paper A98-31499

[2] Stanewsky E., 2001, "*Adaptive Wing and Flow Control Technology*" – Progress in Aerospace Sciences, Elsevier Science Ltd., vol.37, pp.583-667

[3] Browman J., Sanders B., Weisshaar T., 2002, "*Evaluating the Impact of Morphing Technologies on Aircraft Performance*" – AIAA J. 2002-1631

[4] Monner H.P., Bein T., Hanselka H., Breitbach E., 1998, "*Design Aspects of the Adaptive Wing – The Elastic Trailing Edge and the Local Spoiler Bump*" – Royal Aeronautical Society, Multidisciplinary Design and Optimization, October 1998, London, UK

[5] Pendleton E., 2000, "*Active Aeroelastic Wing*" – AFRL Technology Horizons, vol.1, no.2, June 2000, pp.27-28

[6] Wildschek A., Grünewald M., Maier R., Steigenberger J., Judas M., Deligiannidis N., Aversa N., 2008, "*Multi-Functional Morphing Trailing Edge Device for Control of All-Composite, All-Electric Flying Wing Aircraft*" – The 26th Congress of International Council of the Aeronautical Sciences (ICAS), September 14-19, Anchorage, Alaska, AIAA J. 2008-8956

[7] Ivanco T.G., Scott R.C., Love M.H., Zink S., Weisshaar T.A., 2007, "*Validation of the Lockheed Martin Morphing Concept with Wind Tunnel Testing*" – 48th AIAA/ASME/ASCE/AHS/ASC Structures, Structural Dynamics, and Materials Conference, April 23-26, Honolulu, Hawaii, AIAA J. 2007-2235

[8] Flanagan J.S., Strutzenberg R.C., Myers R.B., Rodrian J.E., 2007, "*Development and Flight Testing of a Morphing Aircraft, the NextGen MFX-1*" – 48th AIAA/ASME/ASCE/AHS/ASC Structures, Structural Dynamics, and Materials, April 23-26, Honolulu, Hawaii, AIAA J. 2007-1707

[9] Inman D.J., 2001, "*Wings: Out of the Box. Determining Actuator Requirements for Controlled Morphing Air Vehicles – Aerodynamic Loads*" – DARPA Technology Interchange Meeting, Wright Patterson Air Force Base, November 2001, Dayton, Ohio, USA

[10] Kudva J.N., 2001, "*Overview of the DARPA/AFRL/NASA Smart Wing Phase II Program*" – Smart Structures and Materials Conference, SPIE 4332(48), pp.383-389

[11] Chopra I., 2002, "*Review of State of Art of Smart Structures and Integrated Systems*" – 42nd AIAA/ ASME/ASCE/AHS/ASC Structures, Structural Dynamics, and Materials Conference, Seattle, WA, AIAA Journal vol.40, no.11

[12] Barbarino S., Ameduri S., Pecora R., 2007, "*Wing Camber Control Architectures based on SMA: Numerical Investigation*" – International Conference on Smart Materials and Nanotechnology in Engineering (SMN2007), July 1-4, Harbin, China, Proceedings of SPIE vol. 6423, 64231E-1, (2007), 8pp., doi: 10.1117/12.779397

[13] Barbarino S., Pecora R., Lecce L., Concilio A., Ameduri S., Calvi E., 2009, "A Novel SMA-Based Concept for Airfoil Structural Morphing" – Journal of Materials Engineering and Performance (JMEP), vol.18, issue 5, pp.696-705 (2009), doi:10.1007/s11665-009-9356-3

[14] Kuethe A.M. and Chow C.Y., "*Foundations of Aerodynamics*", Fourth edition - WILEY

- *Chapter 8* -

Variable Chord Morphing Blade

1 INTRODUCTION

One of the primary factors limiting the operating envelope of a rotorcraft is the onset of retreating blade stall. Generally occurring at high speed, or even at slightly reduced speeds in the case of high aircraft gross-weight and/or altitude, retreating blade stall leads to a loss in lift, sharp increase in drag and pitching moment, globally reduces blade capabilities and induces high vibration and control loads. Alleviating retreating blade stall is then of much interest when operating close to the flight envelope boundaries, i.e., at high altitude, airspeeds or high gross weight.

Over the past years, many studies have shown the benefits of high-lift devices such as Trailing-Edge Flaps (TEFs) or Gurney Flaps (GFs, also referred to as Miniature Trailing-Edge Effectors or MiTEs) in terms of rotorcraft performance enhancement [1,4]. Such devices aim at increasing the maximum lift coefficient by altering the flow structure around the airfoil and have shown the ability to delay or alleviate stall. However, these approaches have their limitations and challenges including high-frequency actuation requirement (for both TEFs and Gurney flaps), large actuation force (to overcome the hinge moment in the case of TEFs), complexity in implementation, and high drag or limited effectiveness in certain conditions.

Another approach, presented by Liu et al. [5], to generate additional lift near stall is to extend the chord at the trailing edge of the airfoil using a thin splitting plate as illustrated in Figure a. The authors have referred to this concept as a Static Extended Trailing Edge (SETE): the discrete plate can be deployed either at zero angle or at some non-zero inclination angle as depicted in Figure 1 and Figure 2. Figure 3 shows wind-tunnel measurements for the lift coefficient versus angle of attack of a baseline NACA 0012 airfoil, as well as for the cases of the NACA 0012 with a 10% chord SETE deployed at 0 deg and 6 deg [5]. A 6 deg inclination showed a marked improvement in

the lift coefficient, but interestingly, even a 0 deg inclination (essentially a NACA 0012 with a trailing-edge flat-plate tab, a non-optimal airfoil shape) *showed no degradation in lift-coefficient*. Furthermore, the drag penalty of the 0 deg SETE was very low (results not reproduced here), making the SETE a promising trailing-edge lift augmentation device.

Figure 1: Trailing edge devices: (a) Static Extended Trailing Edge (SETE), (b) Trailing Edge Flap (TEF), and (c) Gurney Flap (GF).
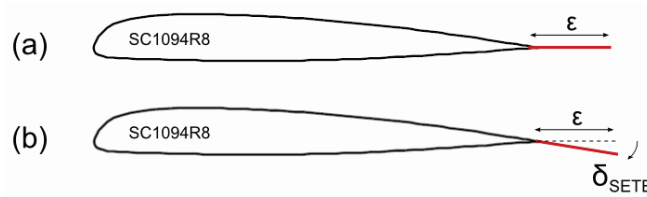
Figure 2: Static Extended Trailing Edge with (a) 0 deg deployment, and (b) non-zero deployment angle, δ_{SETE}.
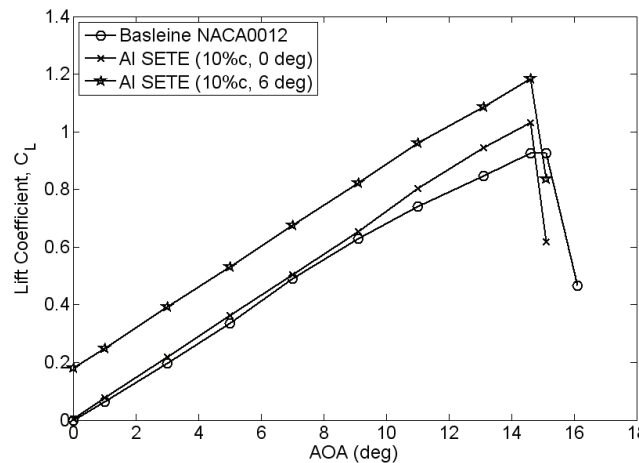
Figure 3: Lift coefficient versus angle of attack wind tunnel data for baseline NACA 0012 airfoil and airfoil with SETE (M < 0.1). [5]

Basing on these results, Léon et al. [6], using CFD, examined the aerodynamic characteristics of the SETE when compared to other high-lift devices such as TEFs and GF. A propulsive trim analysis, based on the UH-60 helicopter, was used to determine

the maximum speeds, altitudes and gross weights attainable with 10%, 20% and 30% chord extensions, showing the flight envelope boundaries expansion as depicted in Figure 4. Possible rotor power reductions with the use of the SETE device near the envelope boundaries were also examined. Finally, for implementation of the concept, a morphing X-truss mechanism was designed and fabricated that allowed the plate to be stowed within the airfoil when contracted, and resulted in a 30% chord increase when extended, as illustrated in Figure 5: the prototype was based on the BO-105 blade chord, ensuring that a SETE with an actuation mechanism fitting within a small dimensions blade would not present any problems when applied to larger rotorcraft (such as the UH-60).
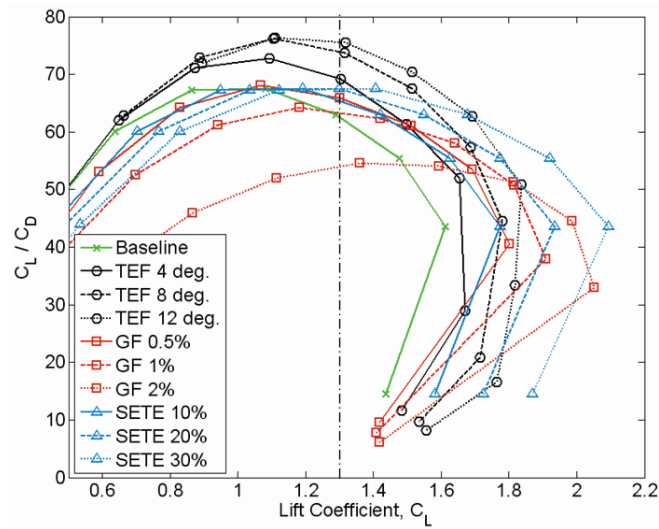
Figure 4: Trailing edge devices on a SC-1094R8 airfoil at Mach 0.3: lift-to-drag coefficient ratio versus lift coefficient. [6]

| (a) | (b) |
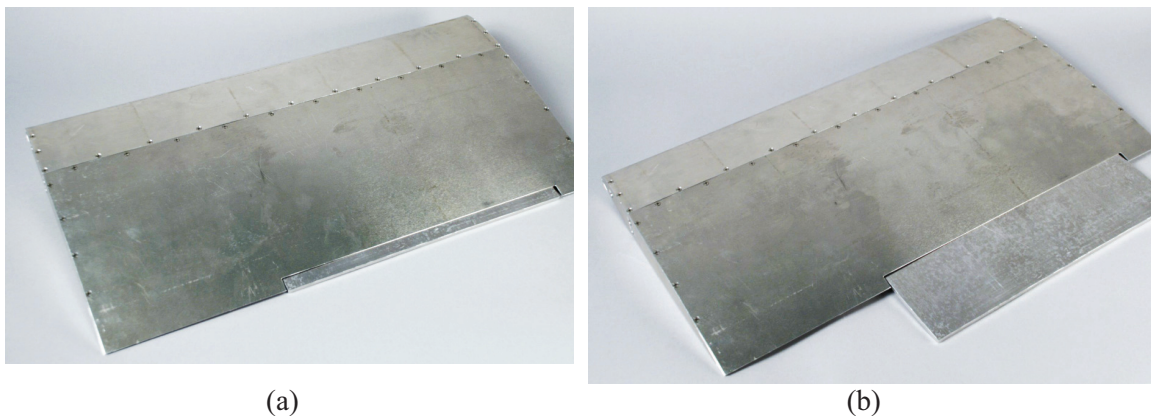
Figure 5: Assembled prototype with SETE in (a) fully retracted and (b) fully extended configurations. [6]

In this work, the same concept was further developed by considering a blade section whose 60% portion in chord (also referred to as "active" portion in this article) can undergo up to 50% shape change in length, for a total of 30% blade chord increase, as

illustrated in Figure 6, while carrying aerodynamic loads. In this case, the BO-105 blade is made of a suitably designed continuous cellular structure, able of 1D morphing and representing the main blade load-carrying structure, in conjunction with a pre-strained rubber skin. The shape change is supposed to take place by adopting variable RPM (centrifugal force) as actuation system, that allows for a minimum weight and complexity increase.

NACA 0012
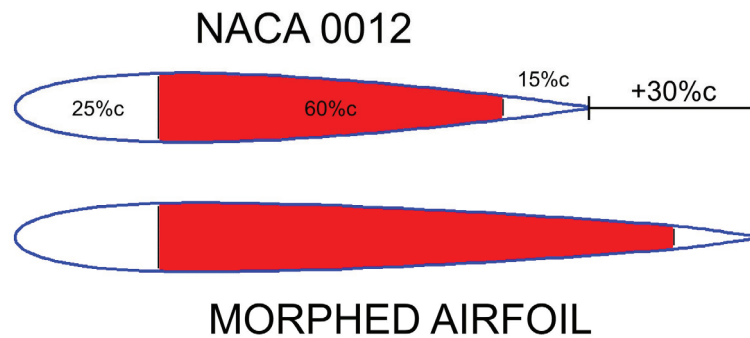
Figure 6: Initial and morphed airfoil geometry (highlighted is the "active" portion).

2 AERODYNAMIC ADVANTAGES OF CHORD MORPHING FOR FIXED WING AIRCRAFTS

Chord morphing can be adopted also for fixed wing aircrafts, to increase its surface and, so, its lifting capability. This is extremely interesting and something similar already happens for high lift devices on transportation aircrafts, where the typical single/double slotted solution for trailing edge flaps allow not only to increase wing curvature, but also its chord (that is, wing area) [7].
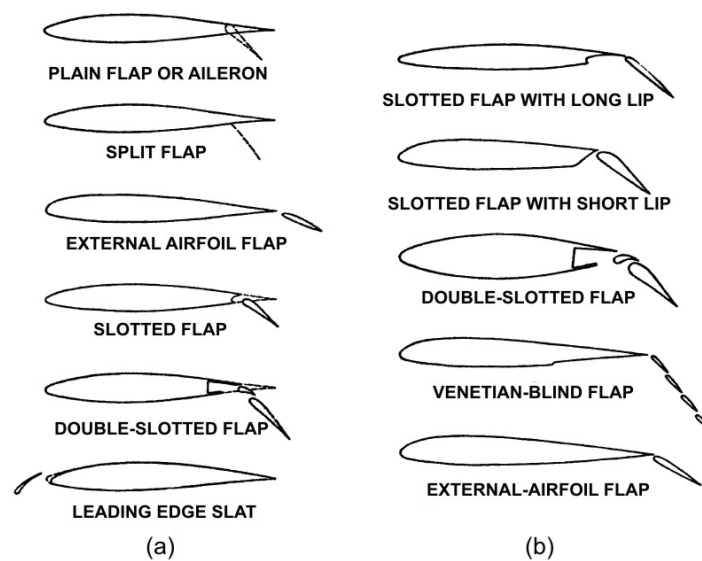
Figure 7: Typical high-lift devices (a) and several types of slotted flaps (b). [7]

However, the possibility to match the greater aerodynamic efficiency of a morphing flap (as illustrated in previous chapters) with an airfoil morphing chord can produce significant aerodynamic benefits.

Some preliminary studies have been carried out for a NACA 23012 airfoil, whose aerodynamic characteristics of the basic airfoil and in presence of both single and double slotted flap are well documented in literature [7]. These performance have been compared to similar morphing solutions, obtained as a combination of trailing edge camber morphing and chord morphing of a selected airfoil section.

The first step involved the introduction of chord morphing on the basic NACA 23012 airfoil (Figure 8): by means of a Matlab code, the airfoil geometry has been suitably modified to accommodate a 50% chord increase of the portion comprised in between airfoil coordinate located at 0.6 and 0.75 of chord. Only this part, representing the 15% of total chord, undergoes chord increase (50% of its length): this choice has been done

to keep unmodified the typical main load-bearing structural rigid box (represented by the front and rear spar) of a fixed wing, while introducing a feasible chord morphing (according to the results that will be discussed later in this chapter).
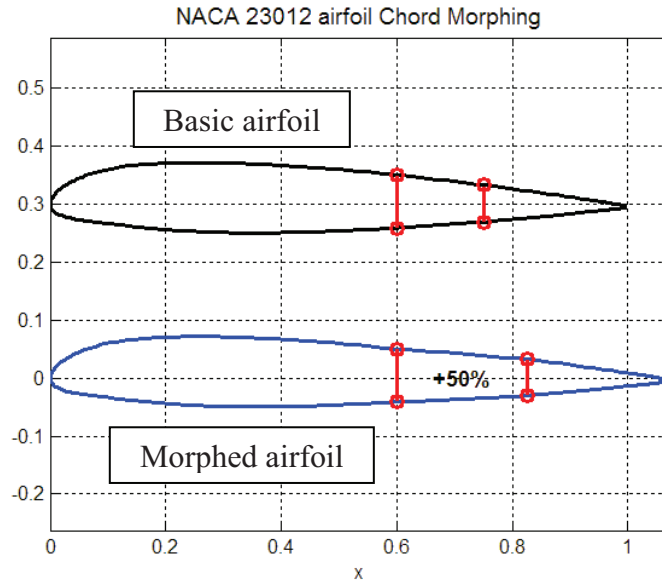
Figure 8: NACA 23012 airfoil chord morphing.

Then, the resulting airfoil has been morphed in camber with the same procedure already discussed in previous chapters, considering as a morphing portion the aft part only of the airfoil (after the chord stretched part, at the trailing edge). As a comparison, Figure 9 shows the same NACA 23012 airfoil with a camber only morphing at trailing edge (left) and a combined camber and chord morphing (right).
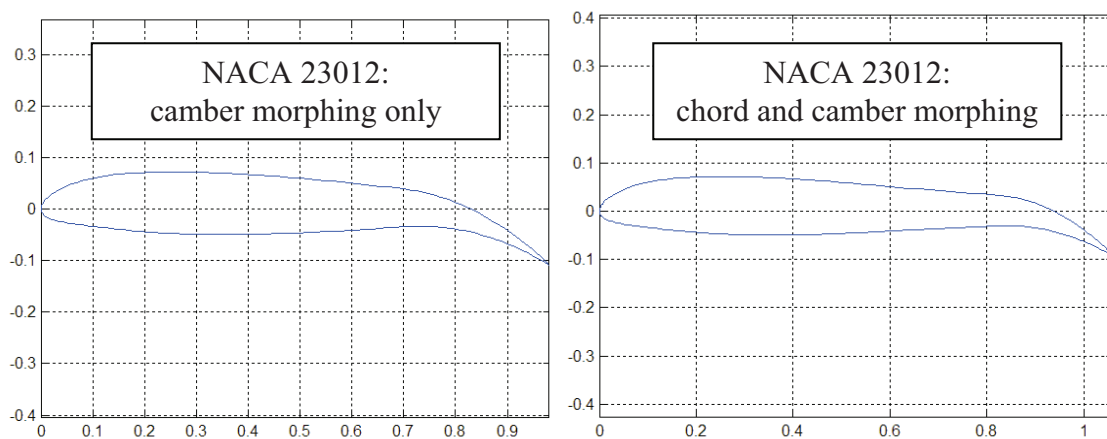
Figure 9: NACA 23012 airfoil morphing: camber only (left) and camber and chord (right).

It can be noticed that in Figure 9 the morphed solution on the left has a larger deflection at trailing edge than the one on the right: this is due to the greater airfoil portion that is

available to camber morphing only, while in the combined case the morphing actions have to share the same limited airfoil portion; this also makes evident that the best performing solution could be a seamless morphing, both in chord and camber, of the same available airfoil part (concurrent chord and camber morphing).

Using the same aerodynamic approach already described in great detail in paragraph 2 of Chapter 7, lift coefficient for a fixed angle of attack (α = 8 deg) of morphing solutions has been compared to its equivalent for traditional slotted flaps.

As shown in Figure 10, morphing solutions can be competitive with traditional slotted and double slotted flap solutions in terms of achievable lift coefficient, while requiring lower deflection angles (with the expected aerodynamic and structural advantages): further investigations are still ongoing.

NACA 23012 - Alpha = 8 deg
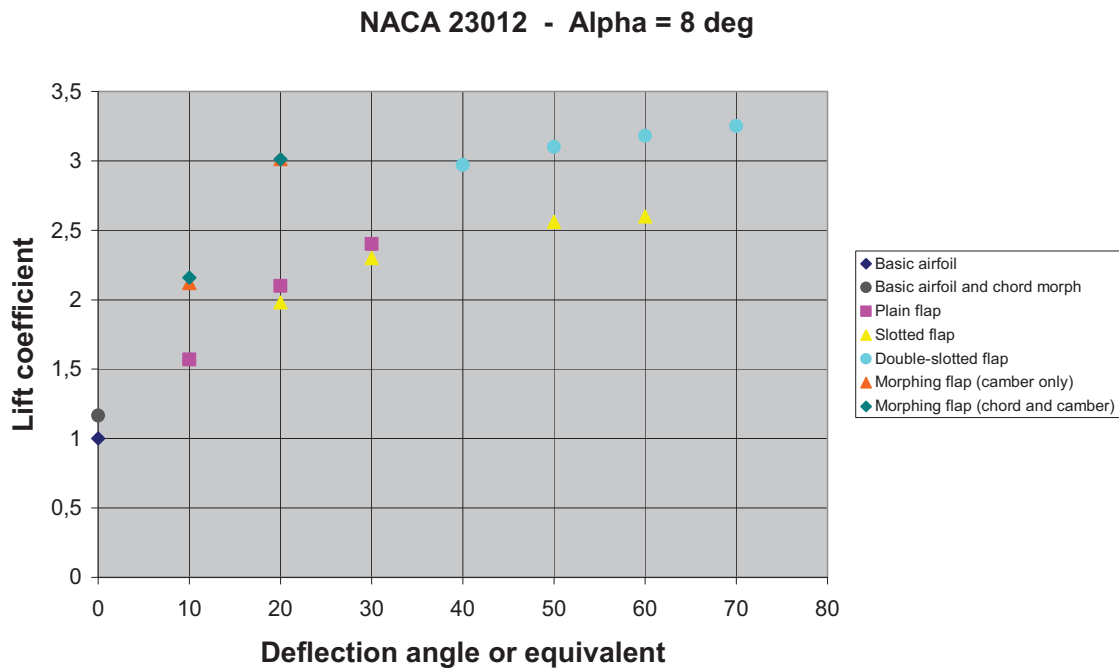
Figure 10: Lift coefficient (at a fixed α = 8 deg) vs deflection angle for several traditional and morphed solutions based on NACA 23012 airfoil.

3 ANALYSIS

In this chapter, the methodology and numerical simulations carried out to find a suitable solution for the chord-wise morphing blade are presented.

After evaluating the external loads that the morphing blade has to be able to withstand, within given requisites for both out-of-plane displacements and rotations of the cellular structure and the skin, the FE analyses carried out with MSC/Nastran software are shown.

As it will be illustrated briefly, the numerical simulation of the entire cellular structure has been suitably simplified, referring to the single cells and the single row of cells studies, without losing of generality.

Some analogies will be presented with current literature on "morphing skins", based on the use of sandwiched skins made of flexible face-sheet and a cellular core, that would be capable of undergoing large deformations, require little energy to morph and have a high out-of-plane flexural bending stiffness: in this work, the honeycomb substructure represents the main load carrying structure of the blade, with the elastomeric skin attached to it.

Aerodynamic loads estimate

A NACA 0012 airfoil was selected as the baseline airfoil for chord increase because it is simple, symmetric, and its aerodynamic properties are well documented [7].

The pressure distribution of a two-dimensional airfoil has been calculated using a Vortex Lattice Method: this 2D panel method includes the effects of the airfoil thickness, angle of attack, and mean camber line in the calculation of the aerodynamic pressure distribution [8]. A sample non-dimensional pressure distribution calculated using a NACA-0012 airfoil at an angle of attack of 5 deg is shown in Figure 11. The figure shows the pressure coefficients c_p corresponding to the top and bottom surfaces.

The aerodynamic force acting on the skin elements is calculated from the coefficient of pressure distribution. The dimensional pressure on the i-th skin element can be calculated using

$$p_i = \frac{1}{2} \rho V_\infty^2 c_{pi} \tag{1}$$

where c_{pi} is the pressure coefficient, V_∞ is the free-stream velocity, and ρ is the air density. A velocity of 200m/s (Mach=0.6) is selected as the reference free-stream velocity for the aerodynamic load calculations.
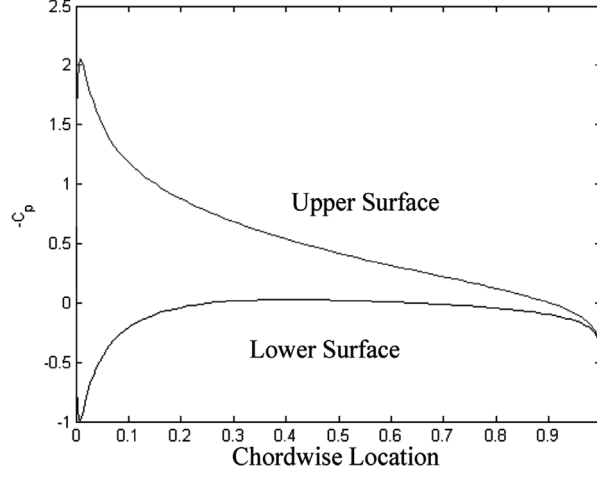
Figure 11: Pressure coefficient for a NACA 0012 airfoil at 5-deg angle of attack.

The aerodynamic load f_i on each skin element is then given by

$$f_i = p_i w_i l_i \tag{2}$$

where l_i is the length of the element along the airfoil cross section and w_i is the width along the span. From the distributed aerodynamic load on each skin element, the finite element nodal loads are calculated as

$$f_{air}^i = L^T \left[0, \frac{f_i l_i}{2}, \frac{f_i l_i^2}{12}, 0, \frac{f_i l_i}{2}, -\frac{f_i l_i^2}{12} \right] \tag{3}$$

where the transformation matrix L, required to account for the orientation of the skin elements, is defined as

$$L = \begin{bmatrix} c & s & 0 & 0 & 0 & 0 \\ -s & c & 0 & 0 & 0 & 0 \\ 0 & 0 & 1 & 0 & 0 & 0 \\ 0 & 0 & 0 & c & s & 0 \\ 0 & 0 & 0 & -s & c & 0 \\ 0 & 0 & 0 & 0 & 0 & 1 \end{bmatrix} \tag{4}$$

and c and s are the direction cosines determined from the nodal coordinates x_1, x_2, y_1 and y_2:

$$c = \cos\theta = \frac{x_2 - x_1}{l} \qquad s = \sin\theta = \frac{y_2 - y_1}{l} \tag{5}$$

The aerodynamic loads have been evaluated for both the original NACA 0012 airfoil and its morphed equivalent, obtained by expanding the "active" portion (60% in chord, between the fixed leading edge and the trailing edge geometry) by 50%.

These external loads have been applied in the F.E. simulations to estimate the out-of-plane displacements and rotations, as reported in the next paragraphs, for both the single cell simulations (in this case, as concentrated forces) and the entire row of cells in the span-wise direction model in presence of the skin (and in this case was possible to apply the appropriate pressure load). However, a conservative study has been carried out in all the simulations: the applied aerodynamic load (on both the single cell and the single row simulations) is always referred to the worst case, that is, the simulation of the most loaded portion of "active" part near the leading edge zone. Details about the applied pressure loads, for both the original airfoil and its morphed (expanded in chord) equivalent, are reported in Table 1.

Pressure	Original NACA 0012 airfoil	Morphed (expanded) airfoil
Airfoil Upper part	16700 Pa – 348.78 psf	15800 Pa – 329.99 psf
Airfoil Lower part	363 Pa – 7.58 psf	-424 Pa – -8.85 psf
NOTE: Positive pressure values are for the upward direction		

Table 1: Applied pressure loads evaluated near the leading edge, for both the original and the morphed airfoil.

Finally, it has to be noted that the absorption of the aerodynamic loads in the single row of cells simulation is mostly demanded to the lateral constraints on which the cellular structure can slide (see next paragraphs for details): this is actually well approximating the real behaviour of the morphing structure, which is supported on both sides by the classical fixed-geometry blade, and allows for greatly reducing the required out-of-plane stiffness of the cellular structure (and, so, total weight).

Reference cell identification

The blade morphing concept presented in this work is mainly based on a suitably designed continuous cellular structure, able of undergoing 1D chord-wise length variation without reaching local critical stresses or failure. As already illustrated in this article, a constant NACA 0012 airfoil is taken into account for the considered blade span-wise section.

A rigid D-spar serves as the primary load-carrying member and is located in the region extending from the leading edge to the quarter-chord. The rigid D-spar is assumed to

undergo no chord-wise deformation under any loading conditions considered in this work. This condition is enforced in the analysis by assuming the compliant section aft of the spar to be clamped at the quarter-chord. As a result, the design domain for the "active" cellular structure is defined as the region enclosed by the airfoil geometry between the quarter-chord and the trailing edge, for a total of 60% in chord length (see Figure 6). Having chosen a target of 30% length increase for the whole blade chord, the "active" cellular structure has to be able to stretch by 50% of its length, as easily calculated in (6).

$$0.6c \cdot x = 0.3c \Rightarrow x = \frac{0.3c}{0.6c} = 0.5 \qquad (6)$$

Considering in this study a chord length of 10.75in for a BO-105 blade, the final chord length is expected to get 13.97in long; the "active" portion, occupied by the cellular structure, has to undergo a length change from 6.45in to 9.67in.

Therefore, according to this estimate, the cellular structure has to be able to accommodate up to 50% strain in the chord direction, possibly without noticeable Poisson effects in the other plane direction (given our interest in 1D morphing). In Figure 12 are summarized some possible configurations for the honeycomb core which have been extensively studied by Olympio and Gandhi [9].

Through the combination of regular cells (with positive cell angle) and auxetic cells (with negative cell angle) it is possible to develop zero Poisson's ratio hybrid and accordion cellular honeycombs: it can observed that the axial stiffness in the morphing direction will not increase when the skins are restrained in the non-morphing direction, making these solutions ideal for use as cores in flex-skins for one-dimensional morphing applications [9].

Therefore, the accordion cellular structure solution has been selected for this work as main load carrying structure: however, instead of using an analytical approach based on the Cellular Material Theory [10], this study follows a Finite Element approach, which comes at hand for the exploration of more complex geometries for the elastic cells (based on curves and splines).

So, the cellular structure behaviour can be estimated by studying its essential basic element, that is the single elastic cell. Indeed, the accordion honeycomb-like structure is characterized by the suitable repetition and disposition in both plane directions of the same single cell, calling for a similarity with a "n by m matrix" of equal elements: the number "n" of rows actually corresponds to the number of elastic cells in the chord-wise

direction, while the number "m" of columns to the cells in the span-wise direction, as illustrated in Figure 13. The "m" cells in each "n-th" row are connected together by means of rigid "spars" (black continuous horizontal lines in Figure 13), which play an important role in increasing the out-of-plane rigidity of the accordion under pressure loads, and allow for considering the whole structure as an array of "m" parallel springs connected to "n" springs in series.

(a) Regular Honeycomb Core   (b) Auxetic Honeycomb Core

(c) Hybrid Honeycomb Core   (d) Accordion Cellular Honeycomb
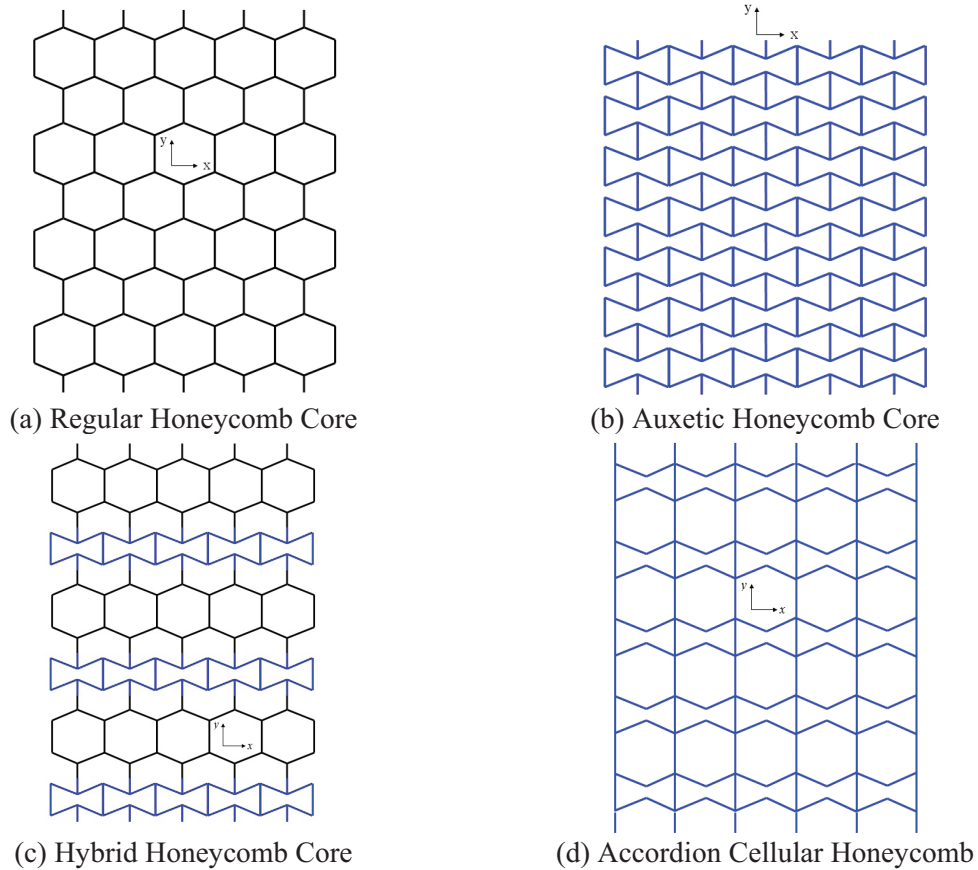
Figure 12: Comparison of (a) regular, (b) auxetic, (c) hybrid and (d) accordion cellular structures. [9]
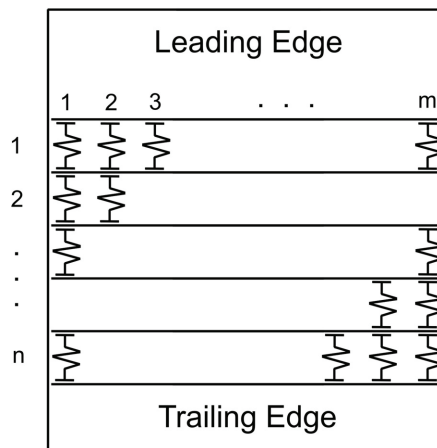
Figure 13: Top view of the considered blade section: accordion honeycomb-like structure detail, in which each spring is representative of a single elastic cell.

While the number "m" of cells can be almost freely set according to the length of the considered blade section in the span-wise direction, the volume occupied by each single cell (to avoid reciprocal interference) and other design parameters (f.i., the required rigidity to pre-strain the rubber skin, as reported in the next sections), the number of cells in the chord-wise direction has more stringent constraints due to the airfoil shape. Considering only the "active" portion of the selected NACA 0012 airfoil, the thickness plays an important role in the number of rows that can be arranged, as shown in two cases illustrated in Figure 14. The maximum thickness is 12% of chord at 30% in chord: for the BO-105 blade, assumed in this work, the "active" portion maximum thickness results to be 1.29in near the leading edge, while getting a minimum value of 0.42in at the trailing edge.

Let's note that the current proposed solutions for the cells chord distribution are arbitrary and follow just two different design philosophies, among almost "infinite" possibilities: in Figure 14(a), a constant chord-wise length is assumed for all the cells and its number depends on the considered dimension (in this case, the authors decided to put only five rows chord-wise to have a very simple geometry, which has been adopted for the experimental prototype); in Figure 14(b), a square aspect ratio design is chosen for all the cells and, then, its number is fixed by the airfoil thickness. Other possibilities are, for example, more dense cellular structures (smaller cells) which would be more similar to traditional honeycombs and less sensitive to the airfoil geometry, but also increase the total weight: in this work, the cells are elastic elements with a required flexibility and rigidity (to pre-strain the skin), which calls for metallic materials.

(a)

(b)
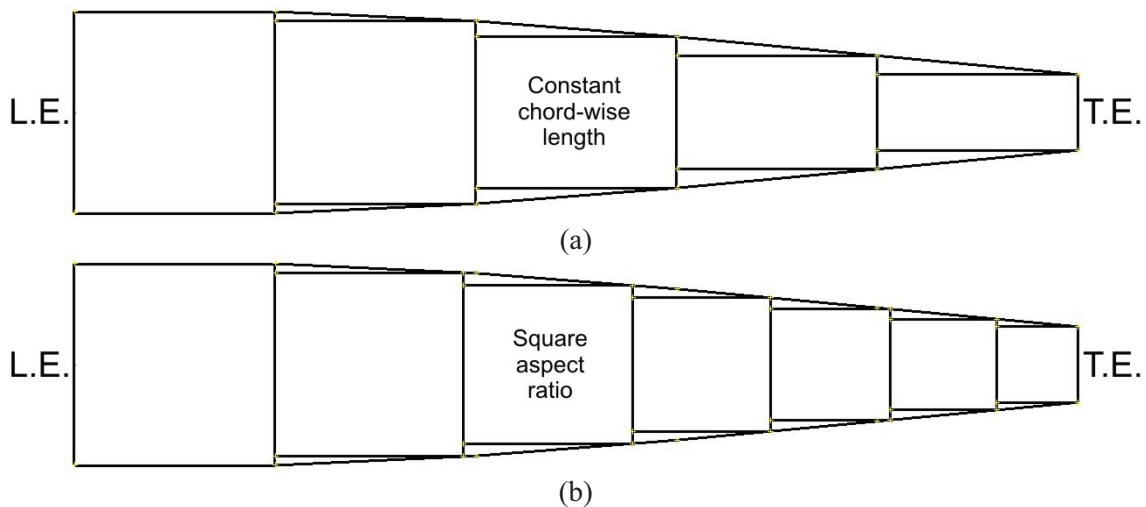
Figure 14: Possible chord distribution of the accordion cells in the "active" portion of the original NACA 0012 airfoil: (a) constant chord-wise length, (b) square aspect ratio.

In this work, the square aspect ratio solution has been selected from the authors as the best compromise for numerical simulations, taking into account cells with a constant aspect ratio that can be easily scaled to several dimensions (to fit best the airfoil); instead, for the realization of a working prototype, able to demonstrate the feasibility of this study, the authors selected the constant chord-wise length design (as illustrated in the next chapter), in order to minimize the complexity of the cellular structure, reducing also weight and manufacture costs.

According to this design choices, the selected reference cell dimensions for an embedded cell in this honeycomb-like accordion structure would have dimensions of 0.787in (L) x 1.574in (W) x 0.787in (H) when considering the original non-morphed airfoil geometry, having a square aspect ratio between chord (L) and thickness (H) dimensions and a span-wise size (W) assumed to be twice the length, as shown in Figure 15: as it will be demonstrated in the next paragraphs, the span-wise dimension can only be "assumed" at this moment to be a certain value, but it will be the result of the final selected geometry for the elastic cell; moreover, when considering an entire row (in the span direction) of cells, the number of elastic elements "m" can be increased or decreased according to the rigidity requirements of the overall structure, having only as maximum limit the volume interference among all the elements. The assumed dimensions have been selected as a mean value between the maximum and minimum cell sizes that can be accommodated in the airfoil (cell positioned in the middle in Figure 14(b)), trying to evaluate a "mean structural behaviour" for all the different cells; then, the selected square aspect ratio design allows for an easy scaling and adaptation to the several cells dimensions which can be housed in the blade. However, when scaling the reference cell to different sizes, it has to be kept in consideration that the stiffness is going to be different for each row of cells in the chord-wise direction (smaller cells, near the trailing edge, will presumably have lower stiffness than bigger ones, positioned near the leading edge), needing some adaptation for the elastic element of each cell. This is extremely important when taking into account the actuation system: if a constant force is going to be applied to the entire accordion structure, less stiff cells will stretch more when compared to stiffer ones, invalidating the entire "mean behaviour" and scaling concept adopted in this work. Of course, this can be overcome by applying at least two different, not exclusive approaches, which give some degree of freedom in the whole design process:

1) during the cell dimensions scaling, the parameters of the elastic element of the cells (f.i., shape or thickness) have to be tuned to keep the actuation force to a common constant value for all the single cells and, thus, for the entire honeycomb;

2) during the assembly of each n-th row, the number "m" of elastic cells that can be accommodated may be changed to pursue the goal of a common stiffness (and thus, actuation force) for each row of the accordion structure.
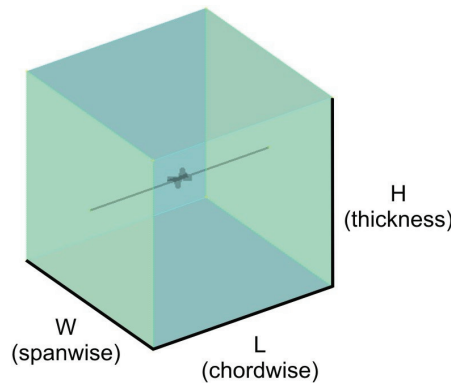
Figure 15: Reference cell geometry.

Furthermore, having the reference elastic cell a chord-wise length (L) of 0.787in and given the requisite of a 50% morphing capability in this direction, it is necessary to design an appropriate configuration capable of obtaining a 0.393in length increase without reaching cell failure or critical stresses within the material, to address the proposed morphing target. Let's note that this goal can be attained in at least three different ways:

1) the reference cell has an initial length (L) of 0.787in and can be expanded to 1.180in;

2) the reference cell has an initial length (L) of 1.180in and can be compressed to 0.787in;

3) the reference cell has an initial length (L) of 0.983in and can be expanded/compressed by 0.196in to reach both the 0.787in (compressed) and the 1.180in (expanded) position.

The last option seems to be the least demanding from a structural point of view, given that the reference cell is actually stretching only by 25% in length in both expansion/compression directions (instead of 50% in only one direction), thus reducing the stress levels within the material; this gives some benefits also for the actuation system, which has to stretch each elastic cell only by 25% instead of 50%, requiring a

lower actuation force/energy. However, option (3) requires a two-way actuator, able of both expanding and compressing the elastic cell (and, so, the entire accordion structure), while the first two options only need a one-way system: more details on this will be presented in the next appropriate paragraph.

Finally, it has to be pointed out that when simulating the reference cell behaviour under the external pressure loads, this is always referred to the worst loading case (cells positioned near the front spar, as already illustrated in the aerodynamic load estimate paragraph), leading to a conservative study about the cell rigidity and skin pre-strain requirements for all the other cells which are distributed along the chord (and are subject to lower loads). Anyway, large part of the load carrying ability of the accordion structure comes from the presence of the lateral sliding constraints, which allows for greatly reducing the required out-of-plane rigidity for each cell and gives more freedom in the optimisation of its elasticity in the chord-wise morphing direction; intermediate spars within the accordion structure are delegated to the role of transferring the pressure loads to the sliding constraints, and can be suitably designed and optimised for this function.

Preliminary cell studies

The study of the accordion structure started with the identification of a suitable elastic cell shape, capable of large global deformations (50% in chord-wise length) without reaching a critical stress within the material or failure: in particular, desiring to have a cyclic actuation capability of the accordion structure with an appropriate fatigue life, designs having a lower maximum local strain and stress levels within the elastic range of the material were preferred.

The main goal has been the development of a continuous elastic structure manufactured with the adoption of aeronautical materials. For this reason, an Al7075T6 alloy has been selected for the accordion honeycomb core, being an high strength material used for highly stressed structural parts (having an higher elastic stress limit when compared to other aluminium alloys): Table 2 summarizes the main features of this material.

A Finite Element approach has been adopted for the structural behaviour evaluation of the conceived cell shapes: this method has been chosen in spite of the analytical approach, based on the Cellular Material Theory [10], due to the complex geometries (curves and splines) explored for the elastic elements, which would have made difficult to identify many parameters required by the analytical analysis. The commercial

MSC/Nastran software has been used for the investigations: a static geometrically non-linear analysis (SOL 106 card) was conducted on each elastic cell, modelled through CQUAD elements on a suitable mesh; each cell has been clamped on one side, to simulate the connection with the preceding intermediate spar; cell displacements, required actuation force and maximum stress and strain were evaluated during the cell contraction/extension.

Al 7075-T6		
Density	2.81 kg/m^3	0.102 lb/in^3
Modulus of Elasticity	71.7 GPa	10400 ksi
Poisson's ratio	0.33	
Ultimate Tensile Strength	572 MPa	83000 psi
Tensile Yield Strength	503 MPa	73000 psi
Elongation at Break	11 %	
Fatigue Strength*	159 MPa	23000 psi
Shear Modulus	26.9 GPa	3900 ksi
Shear Strength	331 MPa	48000 psi
* = 500.000.000 cycles completely reversed stress; RR Moore machine/specimen		

Table 2: Main features of the Al7075T6 alloy adopted for the accordion honeycomb.

The authors interest has been focused towards elastic cells having a curved shape, as a way to further reduce stress and strain concentration at the edges of typical accordion cells, as illustrated in Figure 16.

(a)	(b)
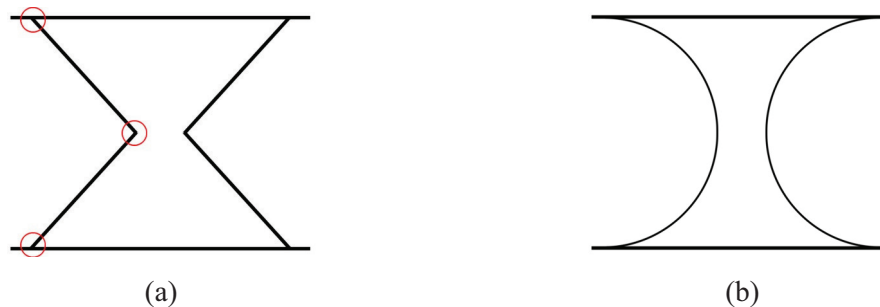
Figure 16: Accordion cell shape: (a) typical (edges are highlighted), (b) curved (investigated in this work).

During the preliminary analysis, attention has been paid to the best shape for the elastic element capable of minimizing local stress and strains: so, geometric parameters were kept in consideration and modified, taking into account also the elastic element thickness, which was properly tailored from 0.00787in to 0.0196in. At this stage, several simulations were carried out, for each solution, for different displacement options, trying to evaluate the possibility to use all of the three configurations illustrated

in the previous paragraph about cell actuation (50% expansion, 50% compression and +/-25% combined expansion/compression from the initial condition).

Numerical results about all the preliminary investigated solutions will not be reported in this paper, given that none of them has been selected for the final design: some of them did not meet stress limit requirements, others strain/displacement needs. In any case, this preliminary study has been necessary to asses the best geometrical configuration, unknown before of it, as reported at the end of this paragraph.

Considering the reference cell dimensions assumed in the previous paragraph, the first simulations have been done with the simplest curved shape: the semi-circular one, as illustrated in Figure 17. The left face of the cell is supposed to be clamped (connected with the previous, chord-wise, row of cells) while the right one is free to move; the initial geometry is shown in grey; the contour is representative of the local strain.
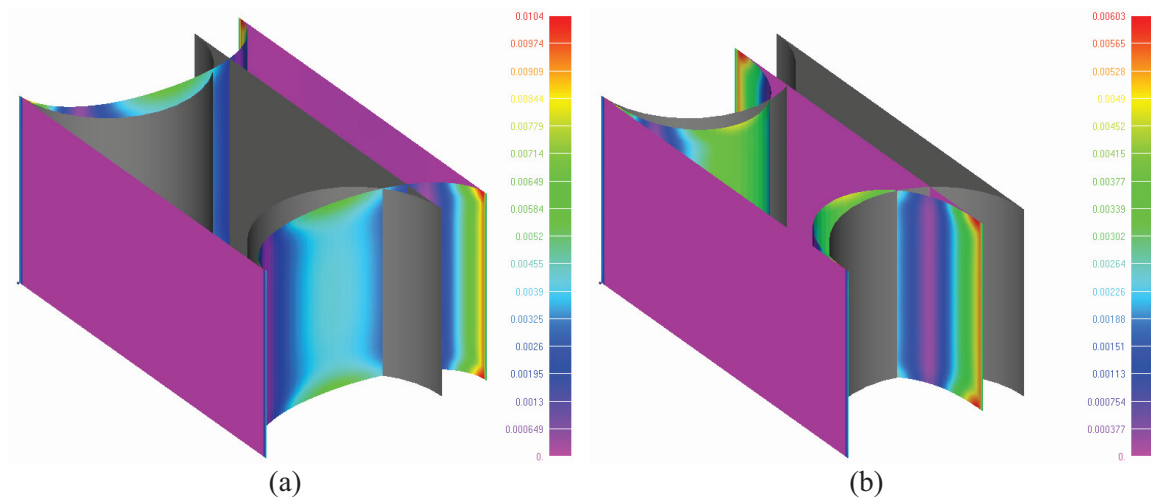
Figure 17: Preliminary elastic cell simulations: semi-circular shape for (a) 25% in length expansion and (b) 25% in length compression (left cell face is constrained, right one is free; initial geometry is shown in grey; contour is representative of local strain).

Although the maximum local strain is very low (1% in the expanded configuration), the maximum VonMises stress is well over the yield strength of the material, principally concentrated at the bonding of the elastic semi-circular element with the spars.

Bubert et al. [11] observed that it was possible to minimize the in-plane stiffness (and, so, the required actuation force) of the accordion honeycomb by reducing the angle at the connection between the spars and the elastic element, assumed to be similar to the one illustrated in Figure 16(a). However, in the case of curved elastic cells used in this work (Figure 16(b)), this solution leads to a stress/strain concentration at the bonding: the curved element is well performing its role of spreading the deformation along all its

length, but then the concentration of stress on the remaining edges is unavoidable and excessive.

For this reason, another design has been conceived, starting from the semi-circular shape (see Figure 18(a)) and characterized by a double curvature (see Figure 18(b)), with the aim of increasing the number of "fictional edges". However, this solutions led to similar results in terms of local stress/strain, with the only exception of the required actuation force, increased with respect to the previous case (this could be expected given that articulations increase the structural stiffness).

The best solution to reduce the stress/strain increase near the bonding between the spars and the elastic elements, while keeping the in-plane stiffness low, has been the design of additional curved junctions able to link the elastic element perpendicularly to the spars (see Figure 18(c)), thus accommodating the required chord-wise deformation of the cell. Again, a circular shape has been selected for these junctions.

| (a) | (b) | (c) |
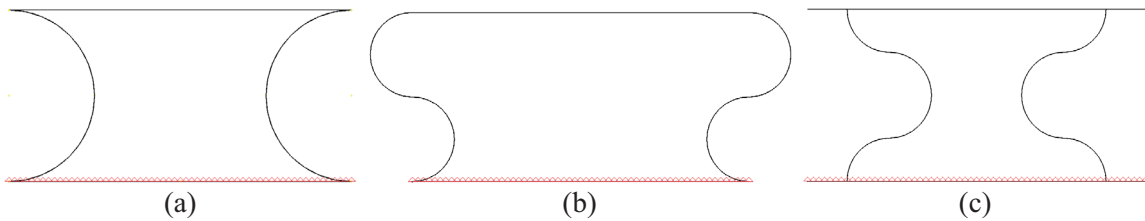
Figure 18: Preliminary simulations with a semi-circular elastic cell shape: top view of (a) the single curvature solution, (b) the double curvature solution and (c) the single curvature with perpendicular junctions solution.

Simulation results, as illustrated in Figure 19, showed a reduction of almost 50% in local strain/stress and required actuation force when compared to the initial solution (while keeping all the other parameters constant): the adoption of this kind of perpendicular junction has been kept for all the new designs studied in this work.

However, the maximum VonMises stress reached in this last configuration is still too high (almost the yield stress of the considered aluminium alloy) and it is attained for just a +/-25% expansion/ compression configuration: this means that it is impossible with this kind of elastic cell to reach 50% chord-wise strain (in one direction) without the cell failure.

To find a solution, the authors explored the possibility to change the assumed curved shape for the elastic cell: other than the semi-circular profile, also semi-elliptical and hyperbola outlines have been investigated, as illustrated in Figure 20. Of course, having assumed a given law for the elastic profile, it is still possible to change some geometrical parameters (f.i., for the ellipse case, the ratio between the two axis): some

simulations have been carried out for different cases, showing that the semi-elliptical solution leads to the best performance.
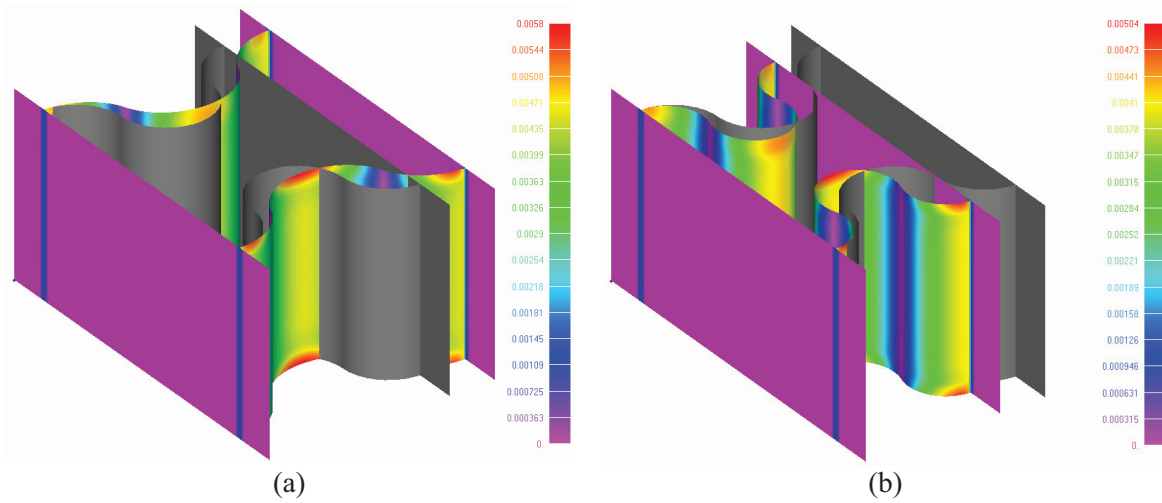
Figure 19: Preliminary elastic cell simulations: semi-circular shape with perpendicular junctions for (a) 25% in length expansion and (b) 25% in length compression (left cell face is constrained, right one is free; initial geometry is shown in grey; contour is representative of local strain).
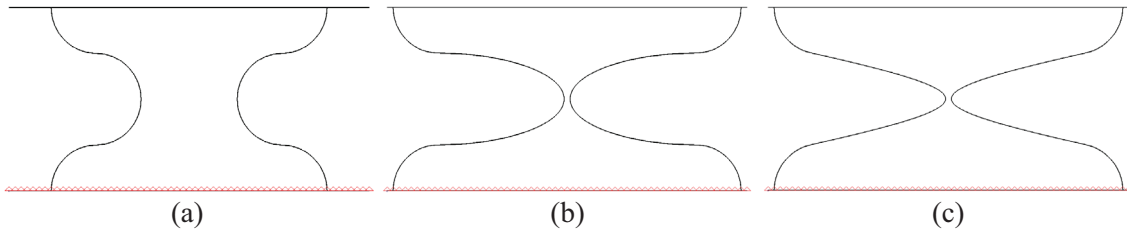
Figure 20: Preliminary simulations based on a single curvature solution with perpendicular junctions: top view of (a) the semi-circular case, (b) the semi-elliptical case and (c) the hyperbola case.

In particular, for an aspect ratio of 3:1 between the major and minor axis, the semi-elliptical solution allows for 50% deformation in both expansion and compression from its initial position while reaching a local maximum strain of 0.4% and a maximum VonMises stress in the linear elastic range of the selected material. Moreover, the actuation force required to deform by 50% the elastic cell resulted to be less than the half of the one previously calculated for the semi-circular solution with perpendicular junctions (and undergoing only 25% strain). In any case, it can be anticipated that the low level of force attained for this solution will not be completely functional to the final design: the presence of a pre-strained skin will require an elastic cell stiff enough to be able to find an equilibrium condition, and still be able to deform by 50% in length. This need will lead to the increase of the number of elastic elements for single cell, whose curved shape geometry will be then constrained due to reciprocal interferences, to

withstand the skin pre-strain with the necessary pre-load level and with a cell deformation as low as possible (to keep untouched the 50% allowable deformation).

So, it can be concluded that lower in-plane stiffness and stress levels within the elastic cell can be achieved by increasing the cell width, to accommodate elastic elements which have a larger extension in the direction orthogonal to the morphing one: similar conclusions have been reported also by Bubert et al. in [11], based on an analytical approach for simpler geometries (linear bending elements) and lower bending member angles between the spars and the elastic cell.

This solution has been selected as starting point for the development of the final design of the accordion structure: more details about the numerical results will be presented in the next paragraphs.

Skin requirements

The primary challenge in developing a morphing skin suitable as an aerodynamic surface is balancing the competing goals of low in-plane actuation requirements and high out-of-plane stiffness. In order to make the skin viable, actuation requirements must be low enough that a reasonable actuation system within the aircraft can stretch the skin to the desired shape and hold it for the required morphing duration. At the same time, the skin must withstand typical aerodynamic loads without deforming excessively (e.g., rippling or bowing), which would result in degradation to the aerodynamic characteristics of the airfoil surface.

With maximum strains above 100%, low stiffness, and a lower degree of risk due to their passive operation, elastomeric materials are ideal candidates for a morphing skin [12]. Isotropic elastomer morphing skins have been successfully implemented on the MFX-1 UAV [13]: this UAV employs a mechanized sliding spar wing structure capable of altering the sweep, wing area, and aspect ratio during flight; sheets of silicone elastomer connect rigid leading and trailing edge spars, forming the upper and lower surfaces of the wing. The elastomer skin is reinforced against out-of-plane loads by ribbons stretched taught immediately underneath the skin, which proved effective for wind tunnel testing and flight testing (a requirement of less than 0.1in of out-of-plane displacement, under aerodynamic pressure, was assumed for the skin; this same requisite will be used in this study).

However, suitable improvements over this skin, such as anisotropic fiber reinforcement and a better developed substructure for out-of-plane stiffening, are desired for a fully

functional morphing skin. Research activities with flexible matrix composite (FMC), made of a thin silicon elastomer sheet with highly anisotropic carbon fiber reinforcement, can be found in [14-15]: in any case, reinforcing carbon fibers controlling the major axis Poisson's ratio of the sheet would limit the FMC to 1-D shape change, which is still acceptable for this study (having to pay attention to the fiber orientation and the desired morphing direction).

However, this study will be mainly focused on the adoption of a thin sheet of silicone rubber, simpler to manufacture, less expensive and with lower actuation requirements. This last design parameter is of great interest, given that the skin pre-strain will be given by the accordion structure (and must not be confused with the morphing actuation system, which allows for the blade chord increase and decrease).

For a given skin typology, pre-strain requirements increase in proportion to the skin thickness, t_s, while out-of-plane stiffness is proportional to t_s^3 by the second moment of the area: to alleviate these competing factors, the accordion honeycomb substructure has to be capable of handling out-of-plane loads without greatly adding to the in-plane stiffness; this allows a thinner skin which, in turn, reduces pre-strain requirements.

As it will be exposed more in detail in the paragraph concerning the actuation system, the best solution found by the authors is to have an accordion structure which is nominally in the expanded shape (extended blade chord, morphed airfoil) and can be compressed, by means of the morphing actuation system, to fit into the original airfoil (nominal blade chord): with this solution, the one-way actuation system is highly simplified, given that it works always in traction, not needing rigid extendable members going through the blade chord.

On the other hand, this solution requires that the accordion structure must be able to pre-strain the skin to the desired amount, while keeping its morphing ability: an equilibrium condition must be found between the skin and the substructure, as illustrated in Figure 21(b), and this represents the extended morphing blade configuration (for reference, the morphed blade shape with a +30% chord increase); then, the actuation system brings the cell, with the skin attached to it, to the compressed condition (for reference, the initial non-morphed blade shape), as shown in Figure 21(c). Another way to think about the same equilibrium condition is given in Figure 22. In this plot, the dashed curve represents the elastic cell stiffness, which applies a decreasing force during its extension and, at the complete extended status, expresses a null force: the linear behaviour is qualitative, given that the cell is supposed to work in the elastic

range of the material (to avoid yielding and allow for cyclic actuation) and for low local strains. The solid curve, instead, gives the force required to strain the skin, for a given material and thickness: also in this case the trend is supposed linear, given the relatively low strain values for the elastomeric material. Where the two curves intersect determines the equilibrium point (maximum strain capability of the morphing system); the amount of cell extension which is on the right of the equilibrium condition is the extra cell strain necessary to guarantee the skin pre-strain, while the force level at the equilibrium point is the force necessary to pre-strain the skin to a certain amount. Both quantities can be determined only after fixing all the design parameters; no relevant numbers are reported in the plot because it has just a qualitative purpose.

Undeformed, free cell (no skin)   Skin - cell equilibrium condition   Actuation condition

(a)   (b)   (c)
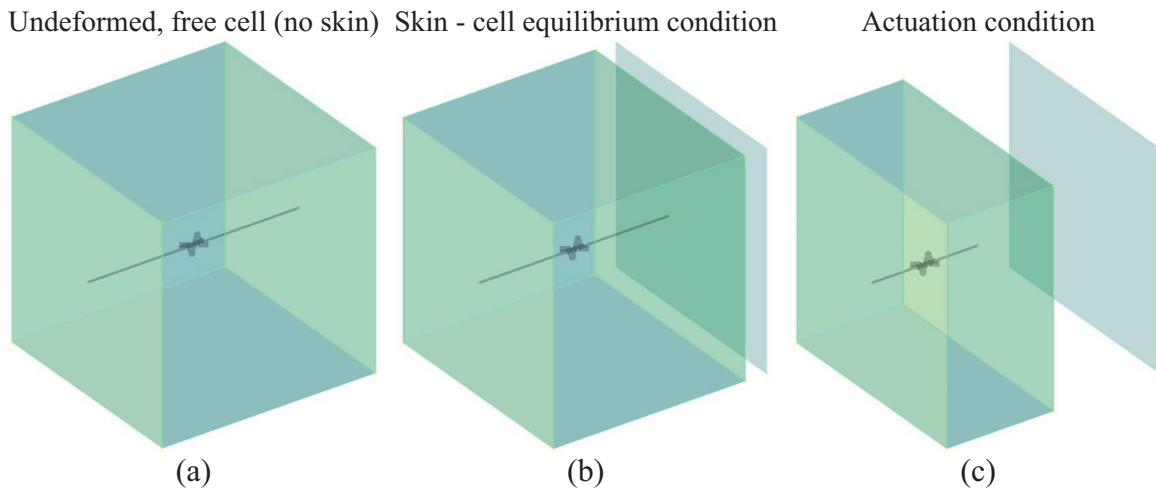
Figure 21: Schematic view of a single cell of the accordion honeycomb: (a) undeformed, extended cell (no skin), (b) equilibrium condition between the elastic cell and the pre-strained skin, (c) actuation condition (cell and skin).
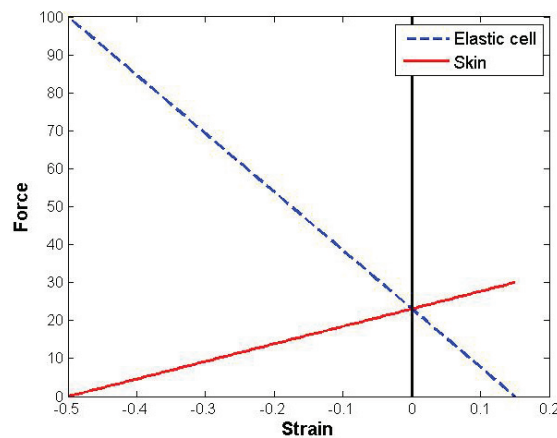
Figure 22: Equilibrium condition prediction between the elastic cell stiffness and the skin pre-strain.

Three observations have to be made at this point:

1) in the skin-cell equilibrium condition, which corresponds to the extended blade shape, the accordion structure has to able to pre-strain the skin to its maximum desired value;

2) the actuation condition is the worst case for the skin, given that it corresponds to the minimum pre-strain condition, and the out-of-plane requirements under aerodynamic loads have to be verified;

3) the maximum extended state for the accordion + skin set is given by the equilibrium condition: thus, this state can be limiting the whole morphing performance.

As a result of the third observation, it is not sufficient for the elastic cell to be able to undergo a 50% chord-wise length deformation to guarantee a 30% in chord blade morphing, given that a certain amount of its deformation capability will be "lost" by the skin pre-straining need. The only way to avoid this loss of morphing performance is to have an accordion structure whose elastic cells are able of accommodating, without reaching a critical or failure condition, a $(50 + X)\%$ in length compression, where X is the amount needed for the skin pre-strain.

Unfortunately, this amount cannot be easily predicted, but an iterative procedure must be adopted, as shown in Figure 23: of course, one would be interested in minimizing this extra strain required to the cell (which induces higher stress/strain levels). While assuming a given skin material, skin thickness, and a cell geometry, the skin pre-strain is related to the out-of-plane displacement under aerodynamic loads (to fit the requirements), the amount of extra cell strain available (other then the "basic" 50%) and the cell stiffness (which can be adjusted by changing the number of elastic elements).

In this study, this iterative procedure has been only partially adopted, given that other design constraints kicked in. For instance, the final design of the chosen elastic cell (reported more in detail in the next paragraph) only allowed for a maximum deformation of $(50\% + 15\%)$ of its initial length: desiring to keep untouched the 50% strain capability, the skin pre-strain had to be reached within the 15% cell deformation. Moreover, the cell stiffness can be varied by modifying the number of elastic elements which are present (f.i., it can be increased to reach an higher stiffness and, thus, be able to give an higher skin pre-strain within the 15% limitation): however, this can only be done by discrete steps (the number of elastic elements) and until reaching reciprocal interference among the cell volume. Details about the final design of the accordion structure can be found in the next paragraphs.

The main features of the selected skin material, TORR EL78, are reported in Table 3. A thickness of 0.019685in was assumed, basing on commercial sheets.
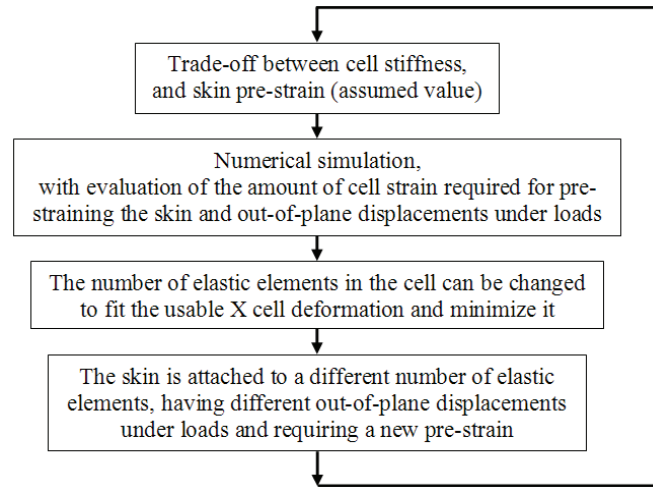
Figure 23: Iterative procedure needed to evaluate the amount of cell deformation, other than the 50% in length, to pre-strain the skin.

Silicone Rubber TORR EL78		
Specific gravity	1.10 with respect to water	
Modulus of Elasticity @ 25%	358 KPa	52 psi
Modulus of Elasticity @ 50%	503 KPa	73 psi
Modulus of Elasticity @ 100%	772 KPa	112 psi
Modulus of Elasticity @ 300%	2.234 MPa	324 psi
Elongation at Break	900 %	
Tensile Strength	10.34 MPa	1500 psi
Tear Strength	1.427 MPa	207 psi

Table 3: Main features of the TORR EL78 silicon rubber adopted for the skin.

According to these characteristics and the reference accordion cell (to which the skin will be bonded), some preliminary simulations have been carried out to evaluate the skin out-of-plane performance under aerodynamic load (only the maximum pressure load, 348.78 psf, was tested) for several pre-strain conditions, also evaluating the required force to stretch it. Results can be found in Table 4 and Table 5. The skin pre-strain has been imposed to different values in the two orthogonal in-plane directions: this way, the strain could be set to a lower value in the morphing direction, thus reducing the needed actuation force, while attaining higher values in the span direction, thus increasing the global skin pre-strain and out-of-plane stiffness. As illustrated in Figure 24, the silicone sheet was supposed to be bonded only to the accordion spars (fixed on both right and left sides), while having lateral constraints on the other two edges only to avoid Poisson effects.
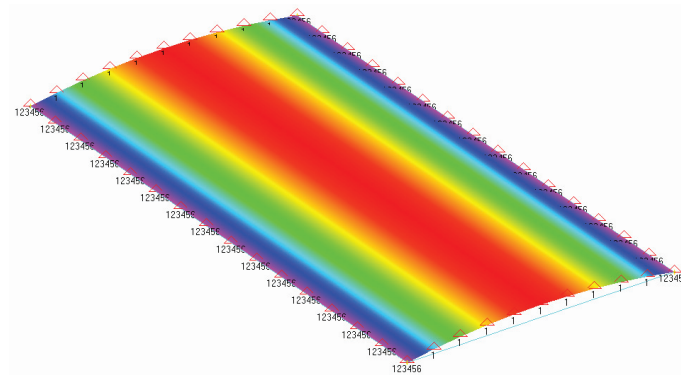
Figure 24: Preliminary simulations on the silicone sheet, under maximum pressure load, for several skin pre-strains in both morphing and span directions (the sheet is supposed to the bonded only to the accordion intermediate spars and has lateral constraints only to avoid Poisson effects).

Skin out-of-plane vertical displacement [in] under a pressure load of 348.78 psf					
Silicon sheet pre-strain in the span direction	Silicon sheet pre-strain in the morphing direction				
	50%	75%	100%	150%	200%
50%	0.181890	0.149213	0.119685	0.070472	0.042126
75%	0.111024	0.096850	0.083071	0.056693	0.037795
100%	0.073228	0.066929	0.059843	0.044882	0.032677
150%	0.035827	0.034252	0.032283	0.027165	0.022441
200%	0.020866	0.020079	0.019291	0.017717	0.015354

Table 4: Silicon skin simulations for the reference cell: out-of-plane displacement [in] under pressure loads.

As expected, increasing the skin pre-strain in both direction leads to lower out-of-plane displacements under aerodynamic loads; therefore, also the necessary actuation force increases accordingly. To satisfy the out-of-plane requirements (less then 0.1in displacement), at least two configurations seems sufficient (having the lower skin pre-strain values): the 150% x 50% and the 75% x 75% configuration, with a preference for the latter given its lower force value required for pre-straining.

However, taking into account also the tear strength of the silicone rubber material (207 psi), the number of feasible solutions reduces: as reported in Table 6, configurations with higher skin pre-strain values of 100% x 100% exhibit stress levels within the silicone sheet which are greater than this value, resulting not practicable.

So, the only viable solution seems to be the 75% x 75% configuration, which satisfies both the out-of-plane requirements and the tear strength limits. However, the actuation force needed to apply these skin pre-strain levels may result to be too high: it depends on the final design of the accordion elastic cell, its stiffness and the amount of cell strain available for the skin pre-straining (in excess to the 50% in length deformation, necessary for the morphing capabilities). The iterative procedure shown in Figure 23

has to be applied. Moreover, considering that the silicone skin will be attached not only to the accordion spars at both ends of each cell, but also to the elastic elements of the cell itself, then the out-of-plane requirements can be easily satisfied with lower skin pre-strain values (and these values have to be lower given that, after attaching the skin also to the elastic elements of each cell, the internal stress is going to grow due to the shape change during morphing, which additionally stretches the skin).

Required force [N] for skin pre-straining					
Silicon sheet pre-strain in the span direction	Silicon sheet pre-strain in the morphing direction				
	50%	75%	100%	150%	200%
50%	5.62	7.47	9.90	17.93	30.63
75%	10.80	12.64	14.98	22.57	34.22
100%	17.15	18.99	21.31	28.71	39.86
150%	36.02	37.91	40.23	47.48	58.07
200%	62.73	64.70	67.09	74.43	84.91

Table 5: Silicon skin simulations for the reference cell: required force [N] for skin pre-straining.

Max skin VonMises stress [psi]					
Silicon sheet pre-strain in the span direction	Silicon sheet pre-strain in the morphing direction				
	50%	75%	100%	150%	200%
50%	62.37	88.47	133.43	292.98	556.94
75%	82.67	104.43	140.69	288.63	530.84
100%	117.48	131.98	162.44	294.43	522.14
150%	239.31	243.66	258.17	348.09	536.64
200%	422.06	423.51	427.86	478.62	617.86

Table 6: Silicon skin simulations for the reference cell: max skin VonMises stress [psi].

As an anticipation of the final design, reported in the next paragraphs, the selected configuration for the silicone sheet skin (attached to both spars and elastic elements of the accordion structure) has been the one having a 100% pre-strain in the span direction, and a 26% to 39% pre-strain in the chord direction, according to the cell status: the equilibrium condition between the elastic cell and the skin is reached for the 39% pre-strain value, when considering the expanded cell geometry. The required force, given by the accordion cell in its expanded shape, to strain the skin to this value is 5.64N: however, let's note at this point that each cell has two skins, one on top and one on the bottom, and so has to be able to express a ~11N force value at equilibrium to pre-strain the skin. Then, during actuation, the cell compresses chord-wise, bringing the skin to a lower pre-strain value equal to 26%.

Of course, the out-of-plane requirements due to the pressure loads have to be satisfied in the worst case: having assumed a constant pressure load (the most loaded case, near the

leading edge), one could think that the actuation condition, with a 26% skin pre-strain, would be the worst loaded case. However, in the equilibrium condition, with a skin pre-strain of 39% (not a so greater value than the previous one), the pressure load is applied on a bigger surface (expanded cell shape), leading to higher out-of-plane displacements. Concluding, the worst estimated out-of-plane displacement resulted to be 0.018898in, well below the assumed requirements; instead, the maximum VonMises stress resulted to be 165.34 psi, below the tear strength.

Finally, in this numerical study the practical difficulties concerning the silicone skin (such as, the bonding technologies of the skin with the accordion structure, friction or manufacturing shortcomings, etc.) haven't been taken into account: however, the adoption of I-beams spars is also functional to increasing the surface of the accordion structure to which the skin can be attached.

Actuation system considerations

A morphing application is not only characterized by some adaptivity property within its working envelope (f.i., shape changing structures), but also by the adoption of a non-traditional actuation system, which should lead to advantages in terms of required force/energy or higher integration and lower weight; moreover, also passive actuation solutions are of great interest due to their automatic adaptation to an external changing parameter.

According to the authors' experience, various actuation systems could be adopted for the morphing blade concept (f.i., screws commanded by electrical motors or PZTs' worminches, for displacing the accordion structure, etc.): however, the typical small available volumes of helicopter blades together with the high centrifugal force acting on them led to the rejection of these designs. The idea of adopting variable RPM (centrifugal force) as actuation system for commanding the accordion shape change resulted to be particularly attractive: it allows for a minimum weight and complexity increase of the proposed morphing architecture while taking advantage of the high forces already available on an helicopter blade.

The designer can chose to deploy the chord-changing structure during both increasing or decreasing the RPM of the main rotor, as illustrated in the simple scheme of Figure 25: by putting the spring-mass system span-wise in the blade, before or after the accordion structure, it is possible to have both a pushing or pulling action when increasing the

RPM (of course, the opposite action is available when decreasing the RPM). This way, one is completely free to chose when to deploy the morphing structure.
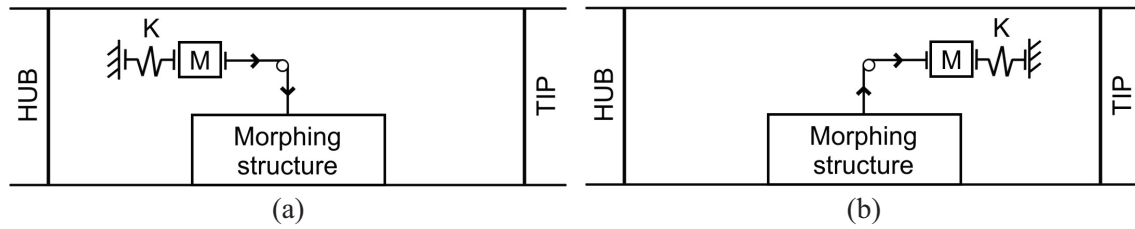
Figure 25: Actuation concept based on variable RPM: viewing the blade from top, (a) the arrangement of the spring-mass system before the accordion structure allows for a pushing (or releasing) force when increasing the RPM, (b) vice versa, a pulling action can be attained in the opposite configuration.

A suitable cornering system must be adopted to "rotate" the span-wise (centrifugal) force in the chord-wise direction as for the morphing application here presented: however, in case of a one-way actuation system, which should just apply a traction force to retract the accordion structure (if, as previously shown, the equilibrium condition between the cell and the skin is at the expanded shape), this cornering system could be simply a pulley, given that a wire should be sufficient for the purpose.

Therefore, among the initial proposed solutions about the nominal condition of the morphing structure, having an accordion structure which is nominally in the expanded shape (extended blade chord, morphed airfoil) and can be compressed by means of the variable RPM actuation system, to fit into the original airfoil (nominal blade chord), is highly recommended: with this solution, the one-way actuation system is highly simplified, given that it always works in traction, not needing rigid extendable members going through the accordion honeycomb "to push" it (which would then be a problem in the retracted configuration). So, there are two possibilities:

- if it is preferred to deploy the morphing structure when increasing the RPM, the solution illustrated in Figure 25(a) must be applied: the spring can be suitably designed to keep the accordion honeycomb in its compressed status until the centrifugal force, acting on the mass, increases and wins the spring stiffness;

- if the designer needs to deploy the morphing structure when decreasing the RPM, the solution shown in Figure 25(b) must be preferred: in this case the spring stiffness is calculated only to keep in place the mass during low rotation velocities while the centrifugal force allows for the accordion compression (increasing the RPM produces the original airfoil shape).

Let's note also that the initial proposed design of an elastic cell able to compress/expand by 25% in length, which minimizes the stress/strain levels, requires a two-way actuation system, making not feasible the adoption of wires to transfer the actuation force.

Anyway, the actuation system must be able to go through the accordion structure and connect to the last sliding spar (near the trailing edge) to apply the desired accordion expansion action: also in this case, the adoption of wires reduces the total weight and simplify the design; finally, with this solution a constant actuation force is applied to the accordion structure.

In the next paragraphs the final solution for the accordion structure will be shown to fit these considerations.

Cellular structure: single cell study

Following the results about the preliminary designs on the semi-elliptical cells, further investigations have been carried out to find the best compromise among all the expected cell properties, here summarized:

- ability to undergo a (50+X)% chord-wise global deformation without reaching critical or failure condition, where X is the amount of displacement necessary to pre-strain the skin;
- the nominal condition of the elastic cell must be the expanded shape, making it feasible to use a one-way actuator which always applies a traction force;
- ability of the elastic cell to reach the skin-cell equilibrium condition in its expanded shape, by expressing the necessary force level to pre-strain the skin;
- the force level necessary for the cell actuation in the chord-wise direction must be as low as possible while having high out-of-plane stiffness to withstand the applied aerodynamic loads, together with the lateral sliding constraints.

As previously illustrated, lower in-plane stiffness and stress levels within the elastic cell can be achieved by increasing the cell width, to accommodate elastic elements which have a larger extension in the direction orthogonal to the morphing one. To increase the geometric ratio between the semi-elliptical major and minor axis, it has been necessary to change the elastic element orientation (now pointing on the same side), making possible to further increase it (see Figure 26).

Several solutions have been studied for the elastic cell element shape, trying to increase both the thickness and the aspect ratio: increasing the aspect ratio allowed to lower the stress/strain levels inside the elastic elements and the maximum value has been limited

by the assumed cell span-wise width; increasing the elastic element thickness allowed to make the cell stiffer (especially having in mind the skin pre-straining), however also increased the stress level, calling for a compromise with the assumed cell shape. Also the number of elastic elements accommodated within a single cell has been object of evaluation, giving the ability to increase (of course, by discrete steps) the cell stiffness. Finally, the applied aerodynamic loads on the skin, and consequent out-of-plane displacements and rotations of the free edge of the elastic cell where also taken into account to chose the best performing configuration.

As a result of these considerations, various different solutions have been evaluated as a combination of all the discussed parameters: moreover, some other configurations have been studied considering also elastic elements made of Titanium Ti-6Al-4V, given its greater elastic range, or with variable thickness, to stiffen the cell for the out-of-plane displacements while keeping the in-plane high deformability; however, results will not be presented in this report, given that these solutions have been discarded due to excessive manufacture difficulties.

The final design for the adopted elastic cell is reported in Figure 26.
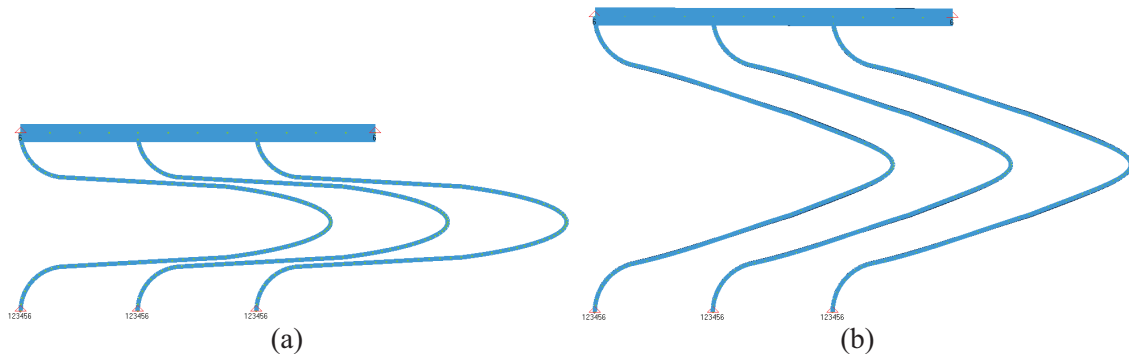
Figure 26: Final design of the elastic cell: (a) compressed shape and (b) expanded shape.

This configuration has been selected because it satisfies all of the expected properties previously exposed: the elastic elements, made of Al7075T6 alloy, have a semi-elliptical shape with a thickness of 0.019685in and a major/minor axis ratio of 6:1 (1.181102in and 0.196850in); rigid spars are 0.157480in thick; each cell has three elastic elements due to skin pre-strain requirements.

Let's note that the Finite Element model has only one rigid spar (up), while the one which is supposed to be fixed (down) is not represented and substituted by the equivalent constraint conditions; the rigid spar has also some lateral constraint that don't allow for rotations in the out-of-plane direction. Moreover, the semi-elliptic shape

of the elastic elements is the one in the compressed shape, which is the simulation starting point. The simulation is done as follows:

- the initial geometry "drawn" for the model is the compressed one (semi-elliptical);

- then, the expanded shape is evaluated by applying the desired in-plane actuation displacement: the evaluation of the expanded shape is done by applying to each node the numerical estimated displacements and rotations due to actuation;

- the expanded cell shape is then assumed as new initial geometry (that is equivalent to the real structural behaviour, which is nominally expanded): the stress/strain levels and required force to compress the elastic cell again are evaluated.
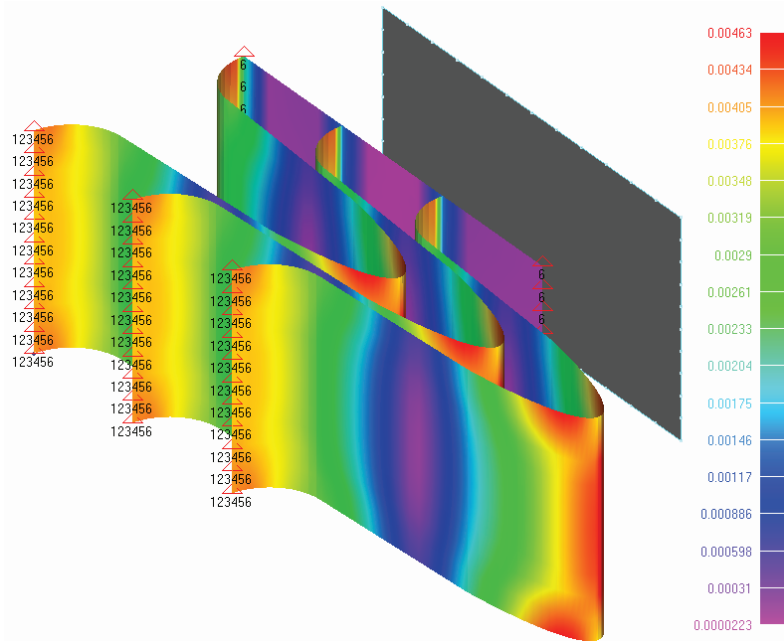
Figure 27: Final elastic cell simulation: maximum in-plane displacement and contour of local strains.

The cell performance are as follows (see Figure 27):

- maximum allowed displacement of 0.519024in over a compressed length of 0.787402in;

- maximum stress in the totally compressed shape of 69183psi (below the yield strength);

- required actuation force for the total displacement of 69N;

- maximum local strain of 0.46% for a global deformation of 65.9% in chord-wise length.

It is important to observe that due to the nature of the honeycomb design, relatively large global strains are achievable with only small local strains (ratio of 143:1); then, having low local strain is a benefit as it will increase the fatigue life of the honeycomb.

Moreover, the global deformation of the cell allowed by this design is equal to 65.9% of the initial chord-wise cell length: requiring a 50% morphing capability, the cell stiffness has been adjusted, by means of the three elastic elements, to allow the skin pre-straining within the remaining 15.9% cell deformation.

So, cell simulations with the attached silicone rubber skin and the aerodynamic loads have been carried out. As already illustrated, the equilibrium condition between the skin and the cell has been reached for a 15.9% initial cell deformation and a skin pre-strain of 100% in the span-wise direction and 39% chord-wise (skin thickness of 0.019685in): the equivalent force needed for the skin pre-strain is 5.64N, which means that the elastic cell is applying a total of ~11N when at the equilibrium, given that for each single cell there are an upper and lower skin.

The silicone rubber skin has been considered attached not only to the intermediate spars of the accordion structure, but also to the elastic elements of the cell: this has been necessary to withstand the out-of-plane requirements and could poses some practical issues when manufacturing a real demonstrator.

As illustrated in Figure 28, to effectively simulate the elastic cell with the skin attached to it, a two cell unit has been considered. Given that part of the three elastic elements hang out of the single cell, two consecutive cells have been simulated (six elastic elements) to have at least three elastic elements fully attached to the skin. This doesn't pose any serious problem when considering the entire row of cells, given that the number and position of elastic elements can still be modified and suitably fitted: actually it is the number of elastic elements to take into account the number of cells.

The constraints for the skin at both ends of the two cell row are only used to help convergence and avoid Poisson's effects. The contour of local strains shows mainly the strain concentration, during actuation, due to the reciprocal distance change between the elastic elements (to which the skin is attached): the values here reported are comprehensive of the skin pre-strain.

Finally, as illustrated in Figure 29, the out-of-plane displacements for the silicone skin have been evaluated under aerodynamic loads in both equilibrium and actuation condition: the contour reports the vertical out-of-plane displacement of the skin in millimeters. Let's note that the true skin displacements are only the one obtained in

between the elastic elements (zones outside the elastic elements are not representative of true displacements). In this case, as reported in Table 7, the out-of-plane requirements are fully satisfied (less than 0.1in).

(a)   (b)
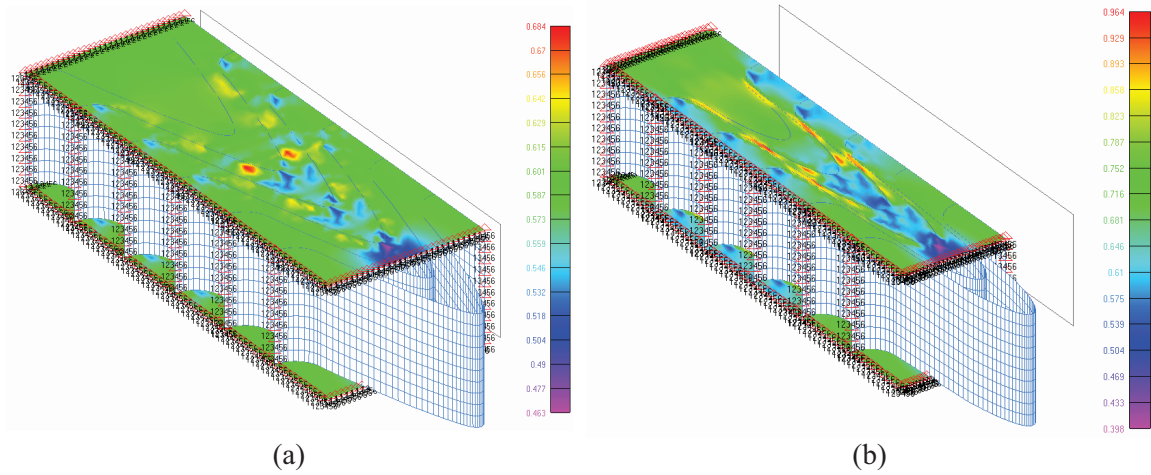
Figure 28: Final design of the elastic cell with the silicone rubber skin: (a) equilibrium condition and (b) actuated condition (contour of local strains, comprehensive of the skin pre-strain).

(a)   (b)
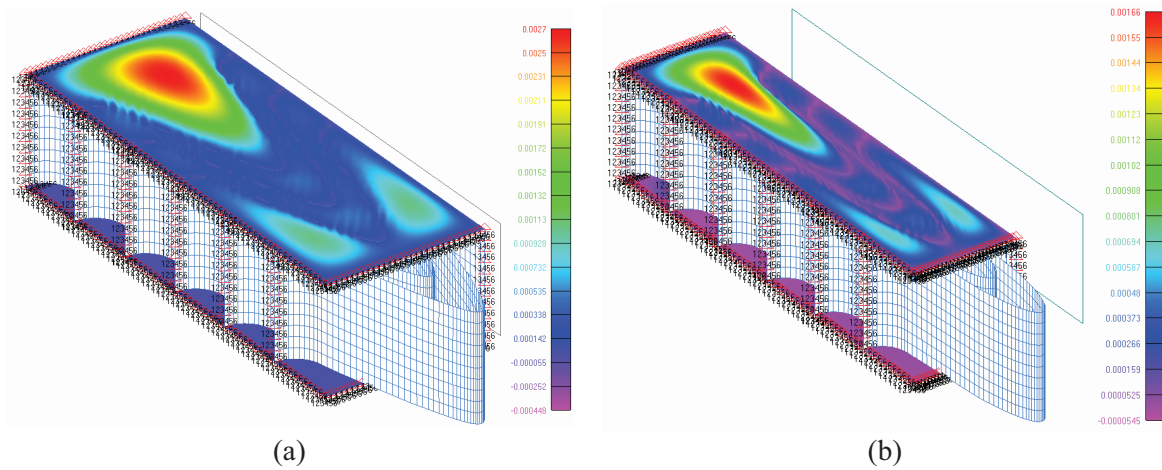
Figure 29: Final design of the elastic cell with the silicone rubber skin, under aerodynamic loads: (a) equilibrium condition and (b) actuated condition (contour of out-of-plane skin displacements in [mm]).

Silicone rubber skin performance under aerodynamic loads			
Condition	*Pre-strain*	*Out-of-plane displacement*	*Max VonMises Stress*
Equilibrium condition	39% x 100%	0.018898in	143.587 psi
Actuation condition	26% x 100%	0.016142in	165.343 psi

Table 7: Silicone rubber skin performance under aerodynamic loads.

Let's note that in these simulations the lateral constraints of the "free" spar (right spar in Figure 29) completely flatten unwanted out-of-plane rotations and displacement, and make this configuration comply with the proposed requirements (only the skin has to be checked): this will happen also for the entire row simulation, as reported in the next paragraphs, agreed that a sufficiently stiff spar is adopted (as already exposed

previously, in this case the aerodynamic loads are fully transferred to the lateral sliding supports).

Finally, the required force to actuate the single cell (three elastic elements together with the upper and lower skin) and make the transition between the equilibrium and the actuation condition is 61N (122N for the two cell configuration presented in Figure 29): this value is lower than the previously estimated 69N, but this can be explained by the presence of the silicone skins and their pre-strain.

Cellular structure: lateral constraint solutions

Lateral constraints play an important role in the absorption of the aerodynamic loads and stiffening of the structure in the out-of-plane direction. As previously presented, the accordion honeycomb structure is made of a sufficient number of elastic cells grouped in (chord-wise) rows which are all connected by means of intermediate spars: although the zero Poisson's configuration of the honeycomb already allows for lower in-plane stiffness when compared to the out-of-plane one, still the aerodynamic loads can be strong enough to generate unwanted out-of-plane displacements and rotations, above the admissible requirements. This can be particularly true when the final selected morphing solution has a quite large extension in the span direction, leading to non negligible bending effects in the middle due to the pressure loads.

In this case, the intermediate spar members can be suitably designed to withstand this kind of undesired effects: thus, by adopting correctly sized I-beams as spar members, the designer has another degree of freedom for increasing the out-of-plane stiffness of the accordion structure, while leaving completely unchanged the design of the elastic cells; vice versa, the number of spars chord-wise, which also affects the structure load bearing capability, is strictly related to the cells dimensions and chord extension (in this case, under a constant pressure load, having more spars leads to thinner I-beams: how to attain weight savings can eventually be evaluated on each single design case).

However, the increase of the structural stiffness by means of these intermediate spars can be attained if these elements are somehow connected to the fixed part of the blade, where the pressure loads can be relieved; furthermore, these spars have to move accordingly with the cellular structure expansion/ compression during chord morphing, and, when in the expanded configuration, still have some support from the "shorter" fixed blade structure.

The satisfaction of both requirements led to the general idea of sliding boundary conditions between the fixed blade part and the morphing section. Possible solutions for realizing this design from a practical perspective could be:

1) as shown in Figure 30(a), the adoption of a simple guide coming out of the fixed blade portion and on top of which the intermediate spars of the "active" portion can slide (the sliding guide has to be as long as possible, within the blade chord, and made of a stiff and slippery material, f.i. Teflon);

2) as shown in Figure 30(b), the adoption of friction or gear wheels connected to the fixed blade part as bearings on top of which the spars can slide (the vertical offset allows the wheels to rotate in opposite directions, actually facilitating the sliding in the same direction).

(a)

(b)
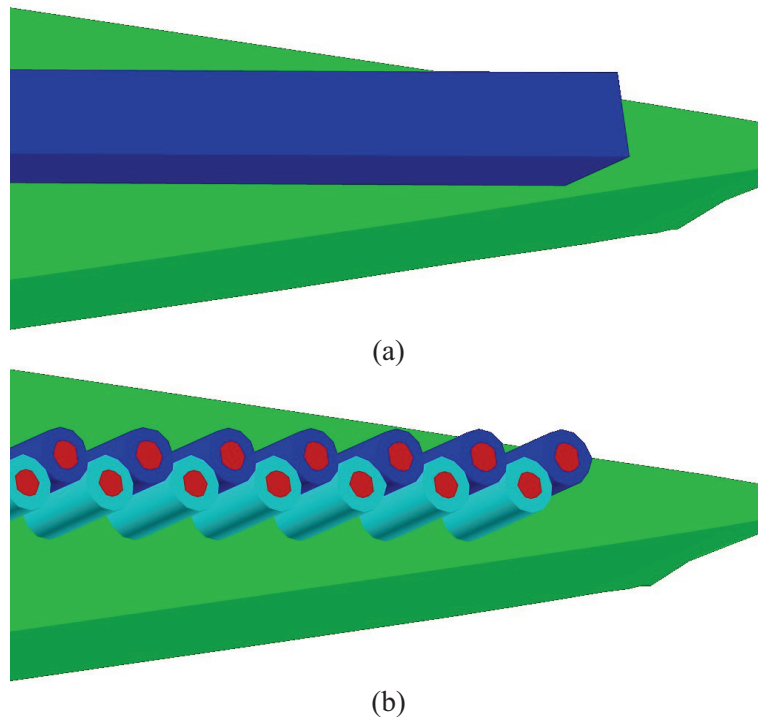
Figure 30: Possible solutions for the lateral supports: (a) solid sliding guide (f.i., made in Teflon), (b) friction or gear wheels as linear bearing.

The first solution has been adopted for the experimental prototype, given its simplicity, the small dimensions of the considered BO-105 blade and the absence of applied loads; the second solution seems to be a good candidate for "real" applications. It is not possible to use traditional bearings given that the sliding support is really thin (f.i., 0.118in for the prototype here developed) due to the airfoil thickness limits.

Several possible solutions have been evaluated, as illustrated in Figure 31 and Figure 32, all capable of allowing for the chord increase of the "active" part while keeping the

lateral constraint and support for the intermediate spars, and fitting within the airfoil thickness when in the compressed status: in dark grey is represented the fixed sliding guide (which has been split in several ones in some solutions); in different grey shading, instead, the various supports of the spars and the trailing edge on both sides of the fixed guide.

(a) Solution 1

(b) Solution 2

(c) Solution 3

Figure 31: Side view of possible sliding solutions for the 7 cells (6 spars) chord distribution, for both the original and morphed (extended) airfoil.

Two sets of possible solutions have been studied, considering both cases presented in Figure 10, with seven and five rows chord-wise respectively (this changes the actual number of spars and, then, supports needed on the sliding guide), according to the chosen chord distribution. The number of spars, which is spaced according to the cells dimensions, affects the solution needed near the trailing edge to guarantee the necessary support on the fixed blade portion: the smaller are the cells, the more is the number of spars which needs support at the trailing edge, making the solutions more difficult to implement (also because at the trailing edge the airfoil thickness is minimal). From the

F.E. simulation perspective, nothing is changing with the different proposed solutions: sliding constraints are applied to both sides of the single row of cells model.

(a) Solution 1

(b) Solution 2
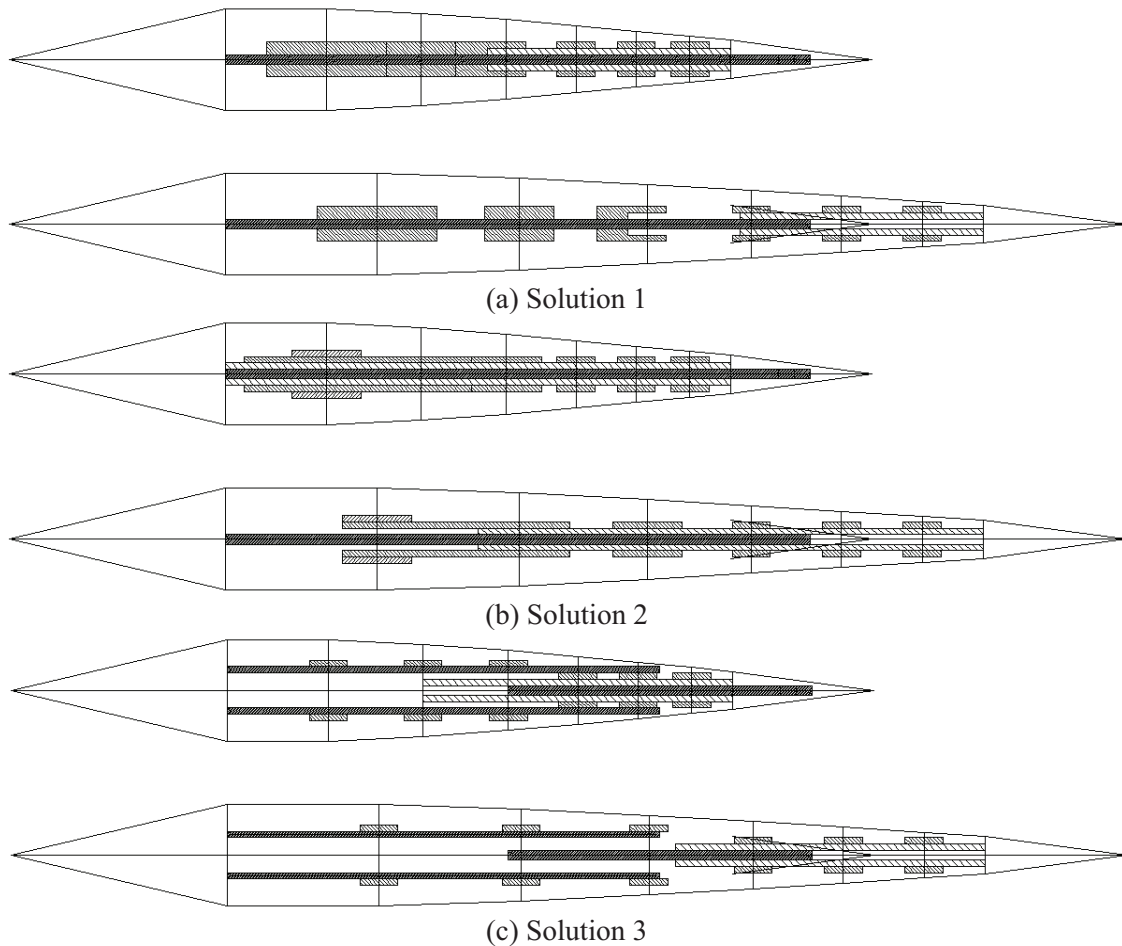
(c) Solution 3
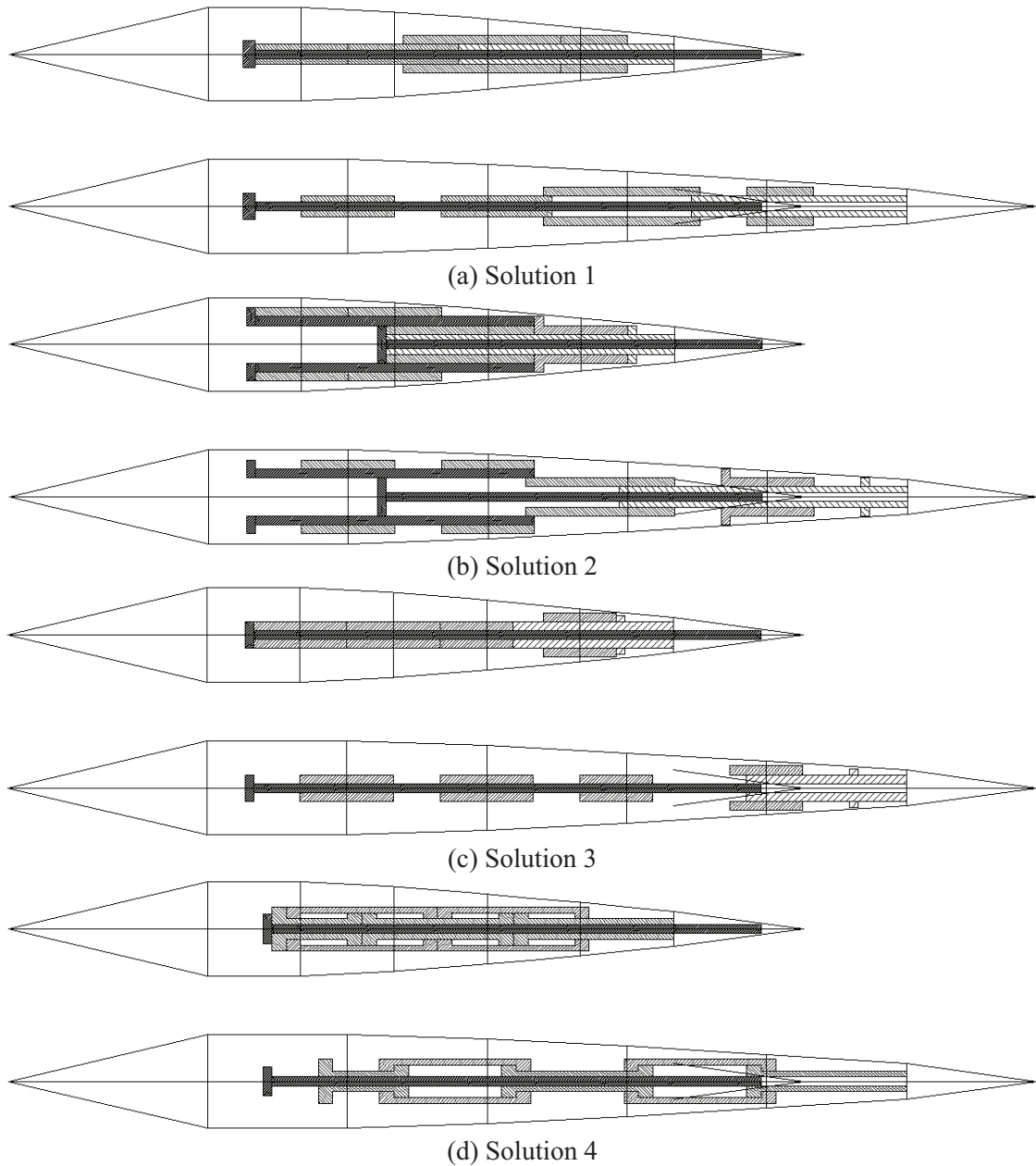
(d) Solution 4

Figure 32: Side view of possible sliding solutions for the 5 cells (4 spars) chord distribution, for both the original and morphed (extended) airfoil.

Cellular structure: single row study with loads

In previous paragraphs a suitable cell design has been presented, capable of undergoing a net 50% chord-wise morphing while having sufficient stiffness to pre-strain a silicon rubber skin to appropriate levels to keep the out-of-plane displacements within requirements: the single studied cell has reference dimensions of 0.787in (L) x 1.574in

(W) x 0.787in (H) when considering the original non-morphed airfoil geometry and is composed of three elastic Al7075T6 elements with a semi-elliptical shape and 0.019685in thick; the worst case pressure loads was applied on the skins.

As from Figure 13, the entire accordion honeycomb can be thought of as an "m by n" matrix: from a numerical point of view the study of the entire structure can be reduced to the single span-wise row, given that it can be repeated chord-wise to create the entire honeycomb and the worst aerodynamic load case has been already considered (conservative simulation). Of course, as from Figure 14(b), the cell dimensions could decrease chord-wise to fit the airfoil, but a constant aspect ratio has been chosen and this decreases the cell dimensions accordingly with decreasing external loads; moreover, the reference cell was chosen as an intermediate one, so the authors are not expecting its structural behaviour to change too much when scaling with different dimensions.

According to these considerations, the finite element model of the entire single row of the accordion structure has been assembled by taking into account the final cell design already presented. The objective of this simulation has been to check the out-of-plane displacements and rotations coming out from larger (span-wise) structures and to evaluate the total required actuation force for each row (given that the rows are in series, this force will be the same for all the accordion honeycomb). Let's note that the number of rows doesn't affect the actuation system but increasing their number (having smaller cells chord-wise) can be effective in diminishing the out-of-plane effects, given that a larger number of rigid spars can be used (of course, this increases also complexity and weight); the span-wise dimension of the rows affects instead the actuation force, which depends on the number of elastic elements packed in it.

Sliding constraints and rigid spars play an important role in this case to reduce unwanted out-of-plane effects: details about how practically reproduce these constraints and design suitably stiff spars have been already discussed in the previous paragraph.

However, another important design parameter in this context is the span-wise length of the morphing structure itself. If a large morphing blade section would lead to excessive out-of-plane displacements or excessive weight/complexity (due to a large amount of "big" spars), then the designer could decide to split it into multiple (span-wise) smaller ones: this approach, as illustrated in Figure 33, would also allow for an independent actuation of each morphing section, leading to a higher flexibility and the possibility of adapting the section deployment to several different RPM velocities or opposite

behaviour; finally, it reduces the actuation force for each section given that a smaller section can be filled with a lower number of cells (elastic elements).
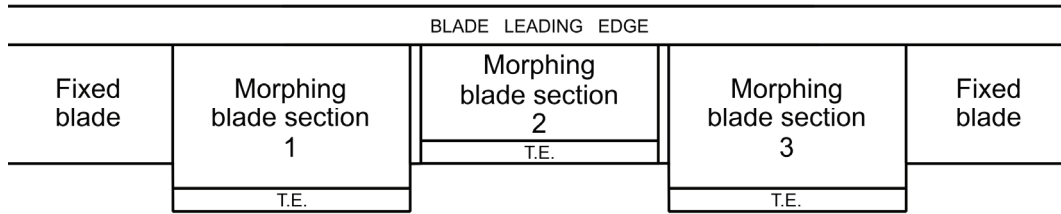

Figure 33: Schematic top view of an helicopter blade with 3 independent morphing sections.

In this work, the morphing section was chosen to be almost 1.5 chords long (16.5354in) in the span-wise direction, allowing to accommodate 10 reference cells (30 elastic elements) in the single row: a total actuation force for the single row (and, so, the entire honeycomb) of 610N has been estimated. Results of the single row simulation, in presence of aerodynamic loads, are illustrated in Figure 34.

(a)   (b)
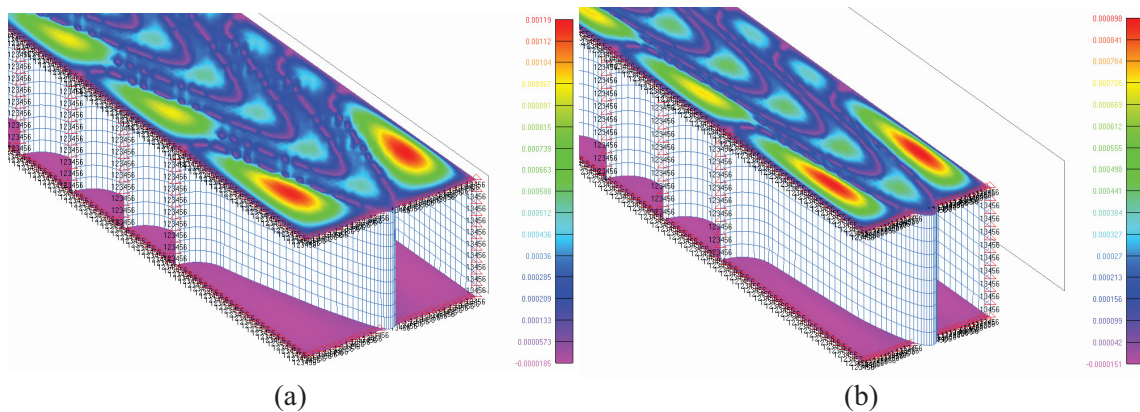
Figure 34: Single row simulation under aerodynamic loads: (a) equilibrium condition and (b) actuated condition (contour of out-of-plane skin displacements in [mm]).

As it can be noticed, the out-of-plane skin displacements (max value of 0.04685in for the equilibrium condition case) are well within the proposed requirements: of course, the final configuration presents some little bumps on the surface due to the elastic elements shape (to which the skin is attached), which cannot be avoided with the actual solution. Also the spar (made in aluminum, 0.15748in thick) has sufficient stiffness to avoid undesired bending or out-of-plane displacements/rotations of the free edge of the row: the measured rotation at the middle of the free spar is 0.05 deg, with a vertical displacement of less than 0.015748in. These values can be further diminished by considering as spar a suitable I-beam.

Moreover, the skin pre-strain together with the allowed formation of the little bumps on the surface doesn't produce any wrinkling due to the elastic elements relative displacements during actuation. The max VonMises stress in the skin, measured at the equilibrium condition, resulted to be 134.76psi, below the tear strength limit.

Finally, it has to be noted that the skin Poisson's effects at both lateral sides of the single row cannot be avoided as done in the simulation by means of lateral constraints. While the skin is fully attached to the spars and the elastic elements, on both sides of each row there aren't any supports: this unwanted effect can be hidden in part, for instance, by partially overlaying the morphing section at both lateral ends with rigid skin coming out from the fixed blade, which also helps the aerodynamic continuity.

4 PROTOTYPE DEVICE

This section describes the design and fabrication of a rotor blade section implementing the continuous cellular structure. Unlike fixed-wing aircraft in which the wing chord length and thickness are large enough to easily accommodate internal devices, the small size of a rotorcraft blade implies stringent space constraints. The baseline chord length has been selected to be 10.75 in, based on the BO-105 blade chord, and ensures that a morphing mechanism fitting within these dimensions would not present any problems when applied to larger rotorcraft (such as the UH-60).

As already illustrated in this paper, a NACA 0012 airfoil has been assumed, with a maximum thickness of 12% chord (1.29 in). The leading edge spar extended up to 25% in chord and the cellular structure has a 60% chord length: to achieve a 30% chord increase, the cellular structure has to expand by 50% of its initial length; so, the expected total "expanded chord" is 13.97in long, due to the "active" portion going from 6.45in to 9.67in (details are reported in the next paragraph).

The considered blade section has a span-wise dimension of 16.1417in (almost 1.5 chords). The blade front spar and the lateral fixed parts have been made of aluminum alloy. Solution 3 from Figure 32 has been selected for the lateral supports configuration (solid sliding guide, preferred due to the small dimensions of the prototype).

The design of the experimental device here presented has been optimized and simplified according to the authors interest in the manufacture of an early proof of concept only, capable of manual actuation and without skin and applied loads.

Cellular structure

In this work, the square aspect ratio solution has been selected from the authors as the best compromise for numerical simulations, as illustrated in the previous paragraphs; instead, for the realization of the working prototype, able to demonstrate the feasibility of this study, the authors selected the constant chord-wise length design, as illustrated in Figure 14(a).

According to this choice for the prototype, the chord-wise dimension (L) for the cells of the accordion structure has been selected to be 1.29in, allowing to fit up to five rows of cells in the "active" portion of the airfoil. This simplifies the design of the accordion structure, reducing the number of intermediate spars and supports for the lateral sliding constraints, thus reducing weight and manufacture costs. Moreover, the presence in

chord of cells with identical length and geometry also allows to get rid of the problem of the "optimization" of each row (having cells with different geometries) to deform of the same amount under a constant applied actuation force.

In the span-wise direction, 7 elastic cells have been fitted in each row (each cell has a width of 2.1653in): this choice has been done taking into account the material adopted for the accordion manufacturing and the desired actuation force.

As reported in Table 8, DELRIN has been used for the honeycomb: the accordion structure has been cut through water-jet starting from a solid sheet, commercially available, thick 0.3937in; for this reason, all the accordion honeycomb has a constant thickness fixed to this value.

DELRIN 100ST NC010		
Density	1340 kg/m^3	0.048 lb/in^3
Tensile Modulus	1400 MPa	203053 psi
Flexural Modulus	1050 MPa	152289 psi
Yield Stress	43 MPa	6237 psi
Yield Strain	30 %	
Nominal Strain at Break	> 50%	

Table 8: Main features of the DELRIN 100ST NC010 adopted for the accordion structure.

Assuming for the elastic element the same shape studied for the aluminium numerical model, a thickness of 0.07874in has been chosen as suitable for the new cell dimensions and material: the single cell resulted to require an actuation force of 4.21N from its expanded shape to be compressed by 50% in chord (let's note that in this case there isn't any amount of cell deformation necessary for the skin pre-strain, given that it is not present); consequently, the final accordion honeycomb, having 5 rows by 7 cells each, has an estimated required force of 29.5N for its total actuation, a suitable level chosen as compromise between a stiff enough structure and the manual actuation requirement for this prototype.

Figure 35 shows the simulation of the final accordion structure adopted for the experimental demonstrator: the elastic elements have been oriented all in the same direction and connected to the spars at the same position row after row to avoid any bending in the spars; for this reason, the four intermediate spars have been chosen to have a 0.23622in thickness; finally, the two external spars, which connect the accordion honeycomb to the rest of the structure, have been made 0.3937in thick.

Figure 36 shows a top view of the actuation results of the new designed honeycomb: the morphing structure is able of undergoing a 50% chord-wise deformation with a

maximum local strain of 1% (50:1 ratio) and a maximum local stress of 2835.49psi (well below the material capabilities).
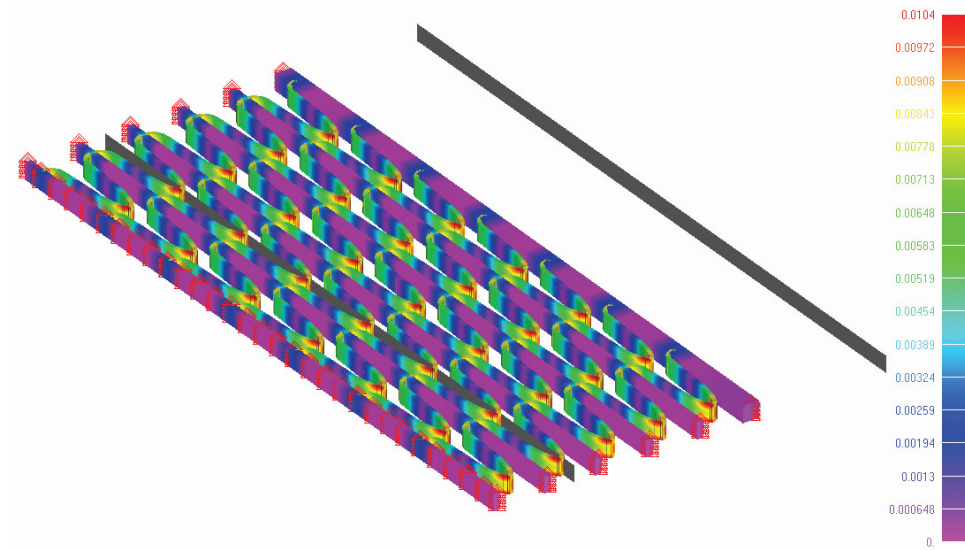

Figure 35: F.E. model for the final accordion structure adopted in the experimental prototype: compressed (actuated) shape with contour of the estimated local strain.
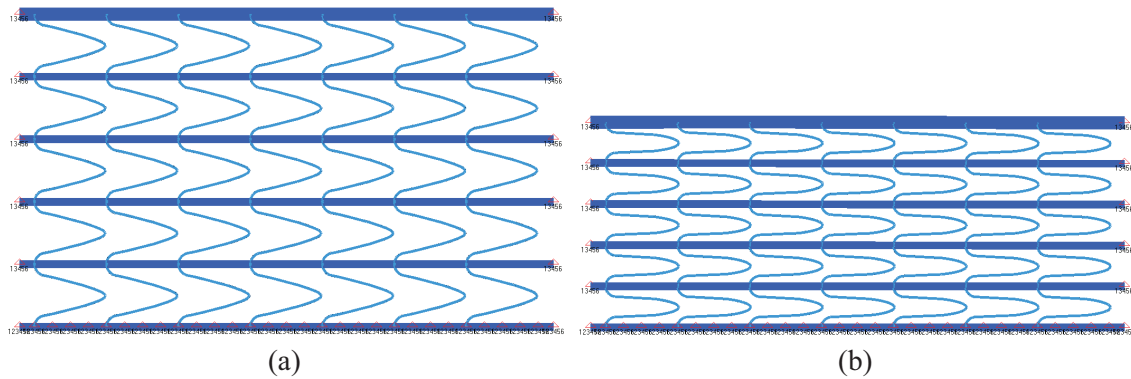

| (a) | (b) |

Figure 36: Top view of the F.E. model for the final accordion structure adopted in the experimental prototype: (a) extended (nominal) shape and (b) compressed (actuated) shape.

Blade section CAD model

A selection of computer generated drawings is presented in this section, to illustrate some design details of the prototype.

Figure 37 shows an exploded view of the main aluminium components of the blade section. The 2 lateral supports (green parts), which integrate the sliding guide solution, connect to the front spar (blue) by means of screws; another tubular element (magenta) is adopted to stiffen the structure (at torsion). The leading edge is covered by an aluminium skin (yellow), attached on both sides of the spar. Moreover, the spar also has a C section to accommodate the accordion structure in the middle and connect to it by

means of screws going through the thickness; finally, the spar has an hole on both sides to allow the actuation wire to pass through.
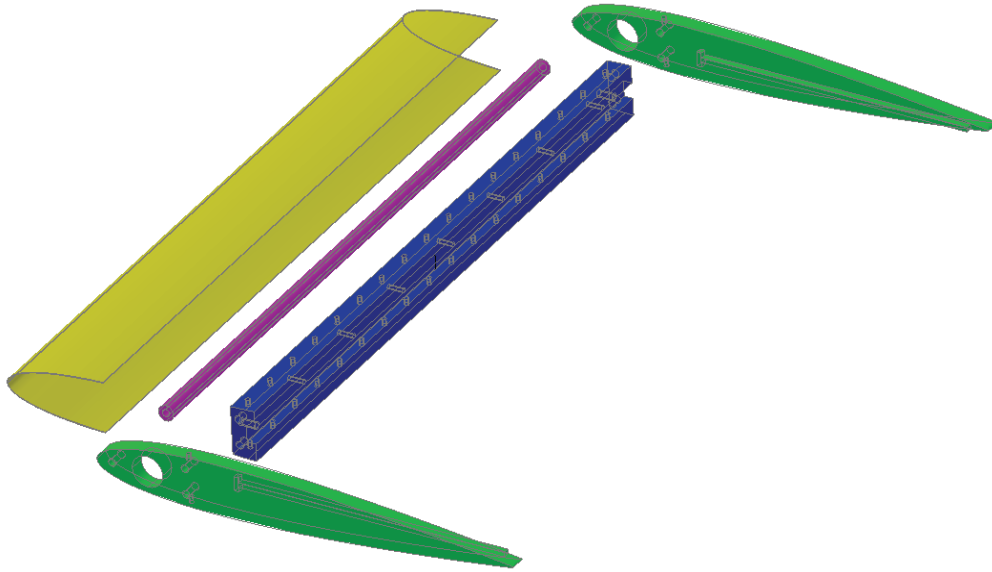

Figure 37: Exploded view of the CAD model for the experimental prototype: lateral supports in green, front spar in blue, tubular stiffener in magenta and leading edge skin in yellow.

Figure 38 shows the 3D model of the accordion structure as it will be cut, using water-jet, from the DELRIN sheet. It has been chosen to partially integrate the lateral sliding supports (which coordinate with the lateral fixed blade parts) to reduce the number of manufactured components; the last two intermediate spars (bottom of the figure) cannot have integrated supports due to the selected sliding solution.
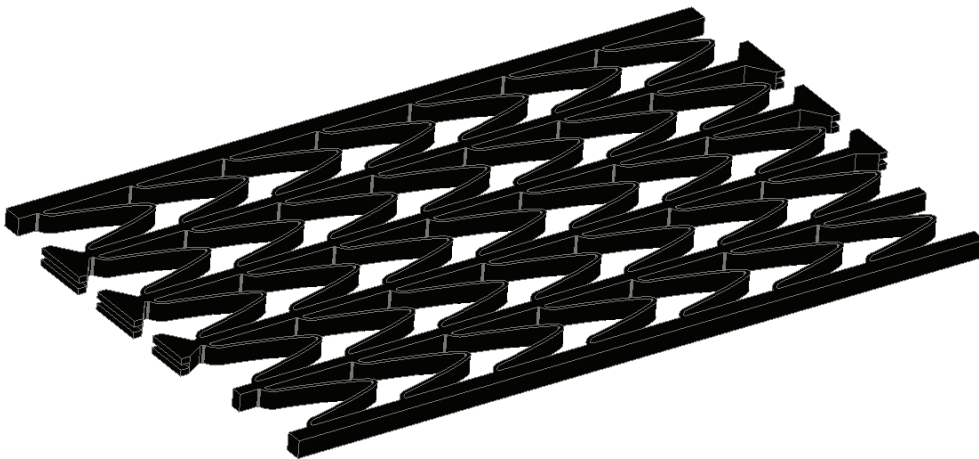

Figure 38: CAD model of the accordion honeycomb, with details about the integrated lateral sliding supports.

The complete assembled prototype is shown from Figure 39 to Figure 41 in several views.
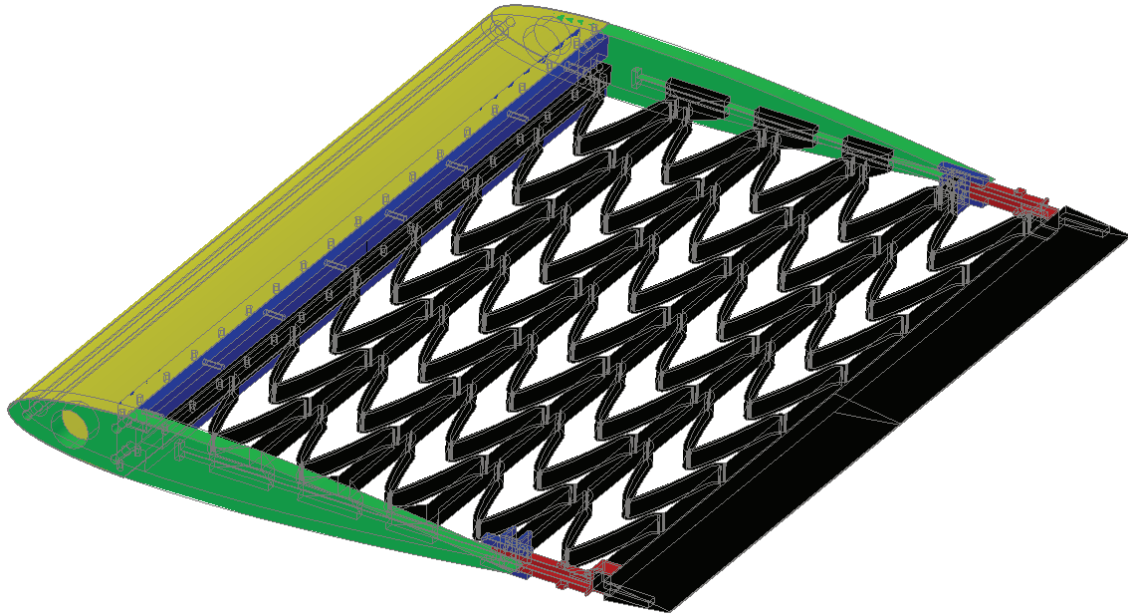
Figure 39: CAD model of assembled prototype.
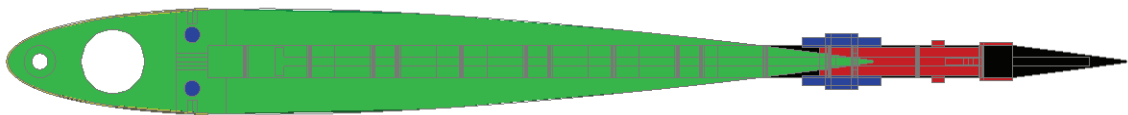

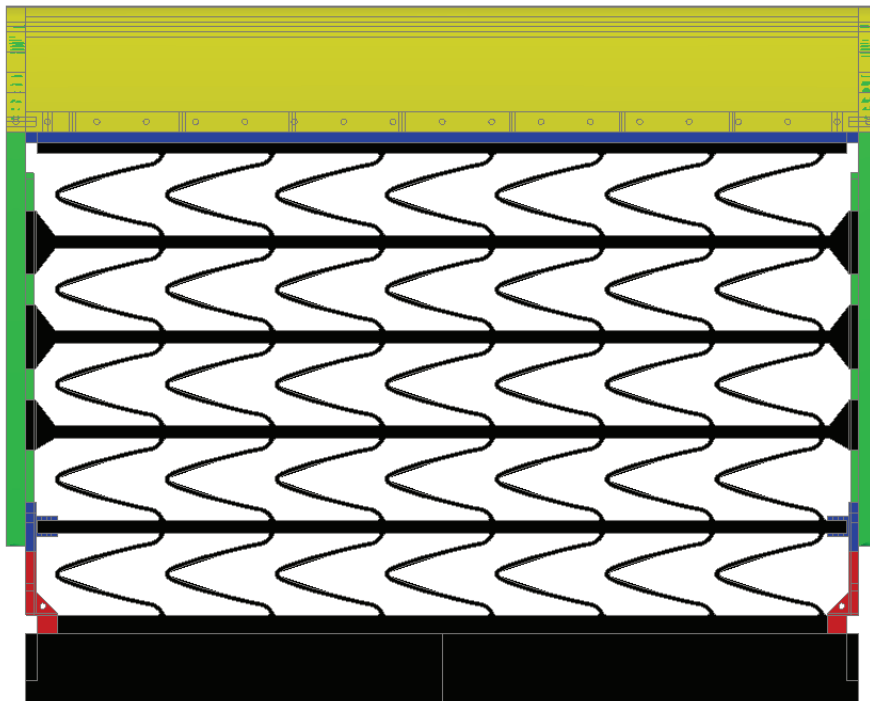**Figure 40:** CAD model of assembled prototype: lateral view.

Figure 41: CAD model of assembled prototype: top view.

The CAD model is presented in the expanded shape to show the efficacy of the selected sliding solution on supporting the trailing edge on the sliding guide also in the morphed condition. This has been attained by means of two specially designed pieces attached to

the last two spars of the accordion structure (near the trailing edge), shown in red and blue respectively in the figures. Actually the system works like this: the red piece is attached to the trailing edge spar and is long enough to be supported, also in the expanded shape, directly by the sliding guide of the fixed blade (once compressed, it doesn't interfere with other elements); the blue piece, instead, is supported by the red one in both the compressed and expanded condition (it couldn't be supported by the sliding guide directly due to the required length of the red element).

More close views of the lateral supports near the trailing edge are shown in Figure 42 and Figure 43.
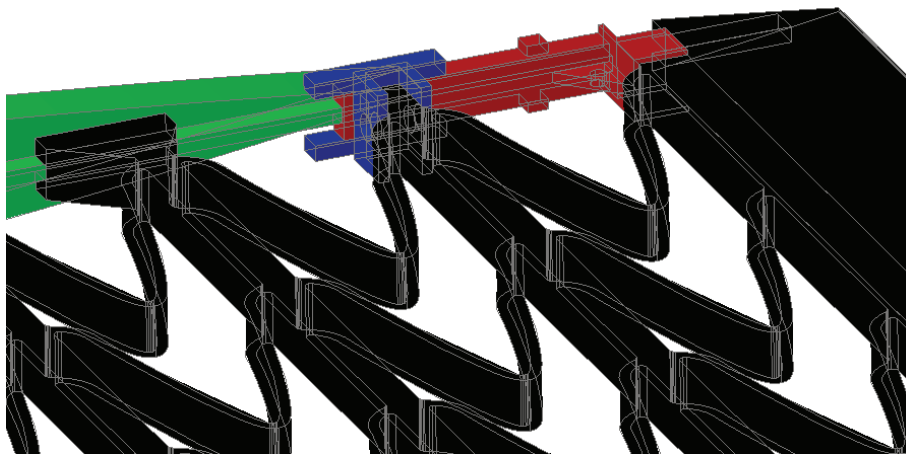

Figure 42: CAD model of assembled prototype: detail of the sliding supports near the trailing edge.
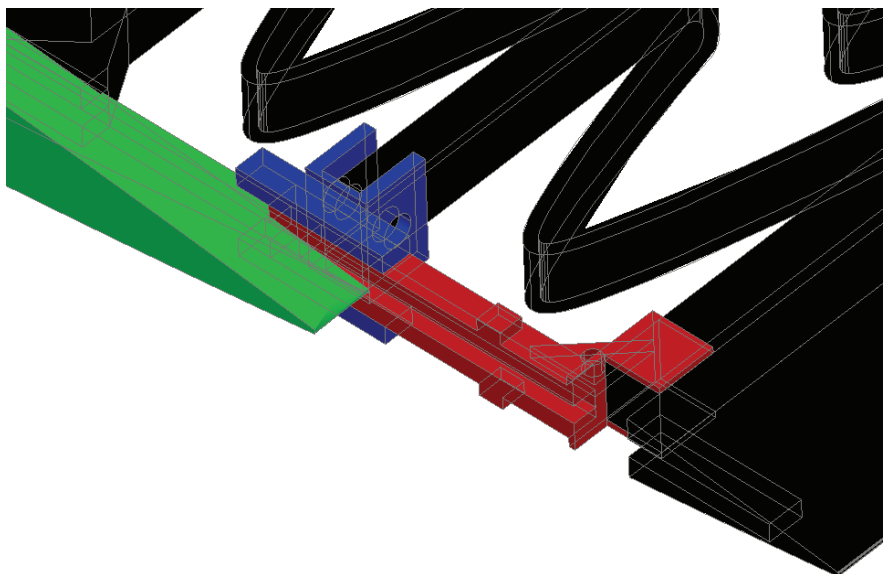

Figure 43: CAD model of assembled prototype: detail of the sliding supports.

The sliding supports (both integrated and separate ones) have been designed in such a way that, when the blade section is its compressed shape, they actually "touch" each

other, resulting in the end of the compressive action (no further deformation can be applied, that could lead to the accordion failure).

Let's note that the red piece has an hole in top of it (partially visible in Figure 43) to connect the actuation wire to the last spar near the trailing edge: photos in the next paragraph will clearly show it.

Experimental prototype

According to the executive drawing previously shown, the experimental demonstrator has been built. Figure 44 shows the accordion honeycomb as resulted immediately after the water-jet cutting.
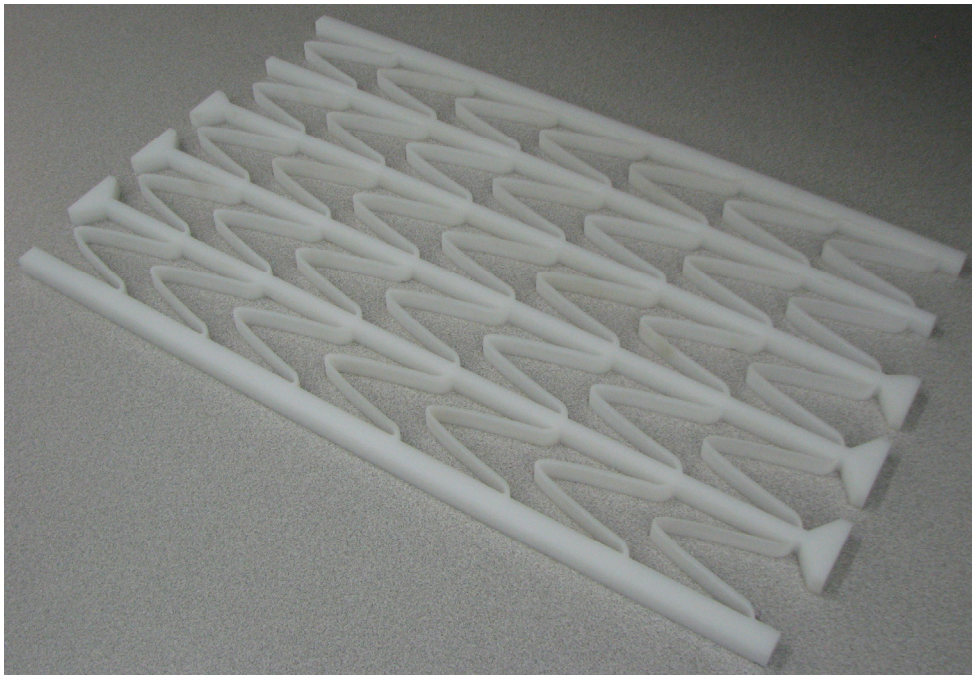
Figure 44: Accordion structure made through water-jet cutting a DELRIN sheet.

Then, Figure 45 shows the manufactured blade section fixed parts (16.1417in in span and 10.75in in chord), all made with aluminium alloy. The preliminary assembly is presented (without honeycomb), with details about the C-section of the front spar, where the accordion structure will be constrained, and the lateral sliding guide. It can be noticed the presence, near the front spar, of a dead end on the guide: it is used to stop the honeycomb sliding supports, during compression, from undergoing excessive displacements (more than the designed ones).

<div align="center">(a)   (b)</div>
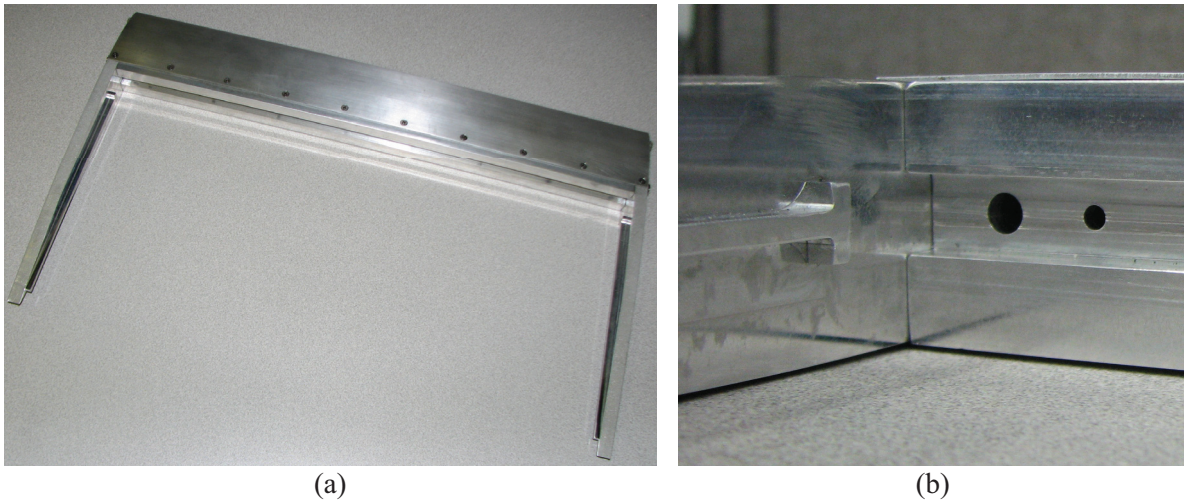
Figure 45: Airfoil structure: (a) preliminary assembly and (b) detail of the front spar and lateral sliding guide.

Figure 46 illustrates a detail of these sliding supports integrated within the accordion structure while supported by the sliding guide. The integrated supports have been carved to accommodate the guide in the middle.

Figure 46: Airfoil and accordion assembly: details of the sliding guide.

However, as already discussed, special supports had to be realized for the last two spars of the accordion honeycomb, near the trailing edge: Figure 47 shows the details of these manufactured pieces, made of aluminium. Figure 48, instead, presents the assembly of these parts with the rest of the prototype: in particular, in Figure 48(b), a detail of the actuation wire connection at the trailing edge is represented. One can notice also the C-section aluminium stiffener used at the trailing edge.

<div align="center">(a)</div>

<div align="center">(b)</div>
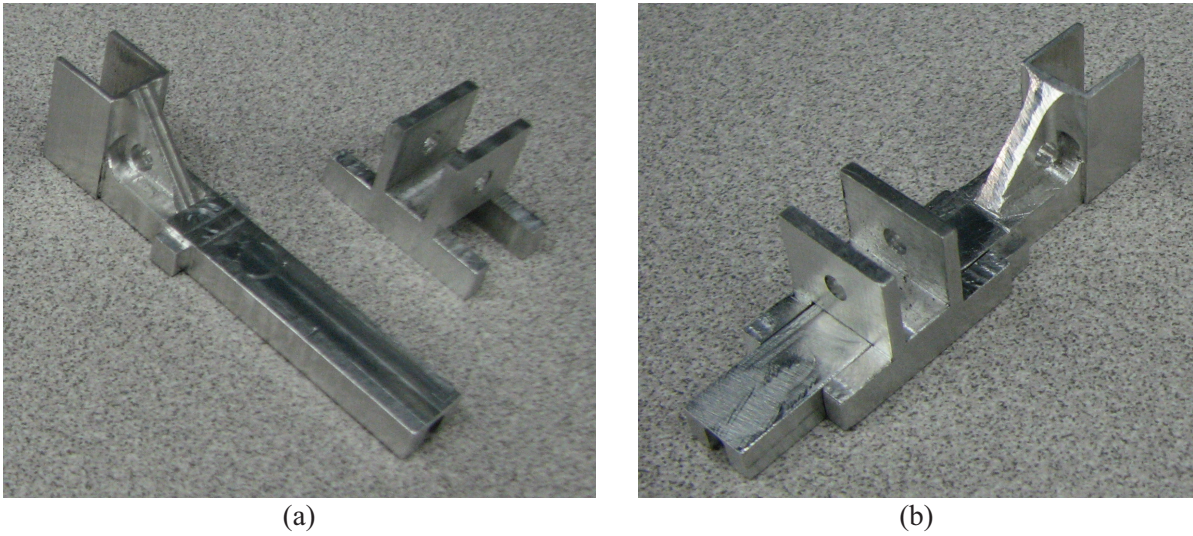
Figure 47: Prototype details: (a) last sliding guide parts and (b) how they are supposed to be assembled.

<div align="center">(a)</div>

<div align="center">(b)</div>
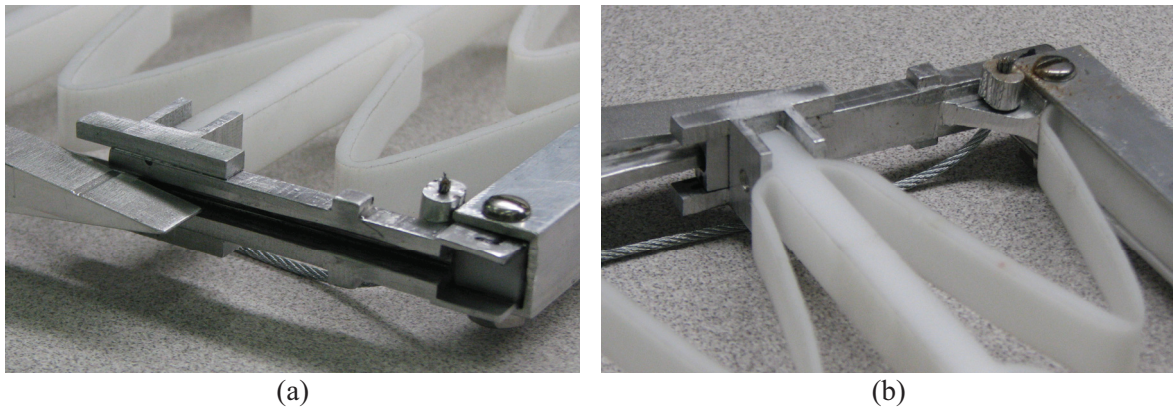
Figure 48: Prototype details (trailing edge zone): (a) final assembly; (b) the actuation wire connection.

Figure 49: Almost complete assembly: details of the actuation wire and the accordion connection to the front spar.

The almost complete prototype is presented in Figure 49: it can be noticed the actuation wire hanging out of the front spar. Finally, in Figure 50, the fully assembled demonstrator is shown, in both its expanded and compressed shape.
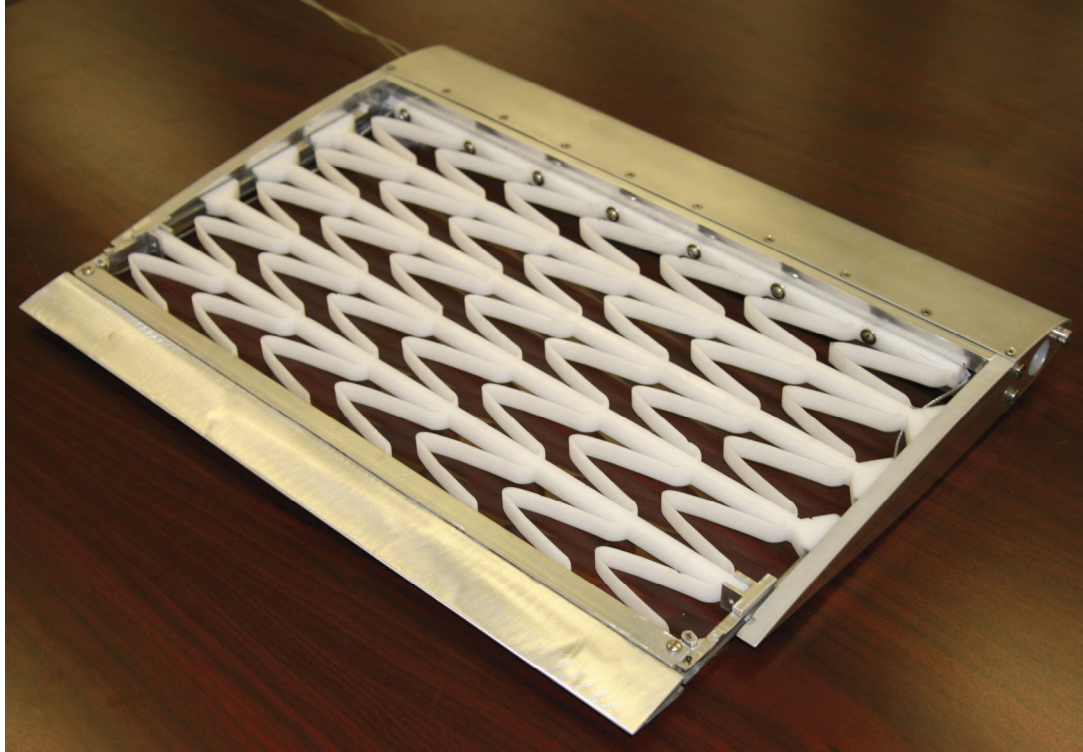
(a)
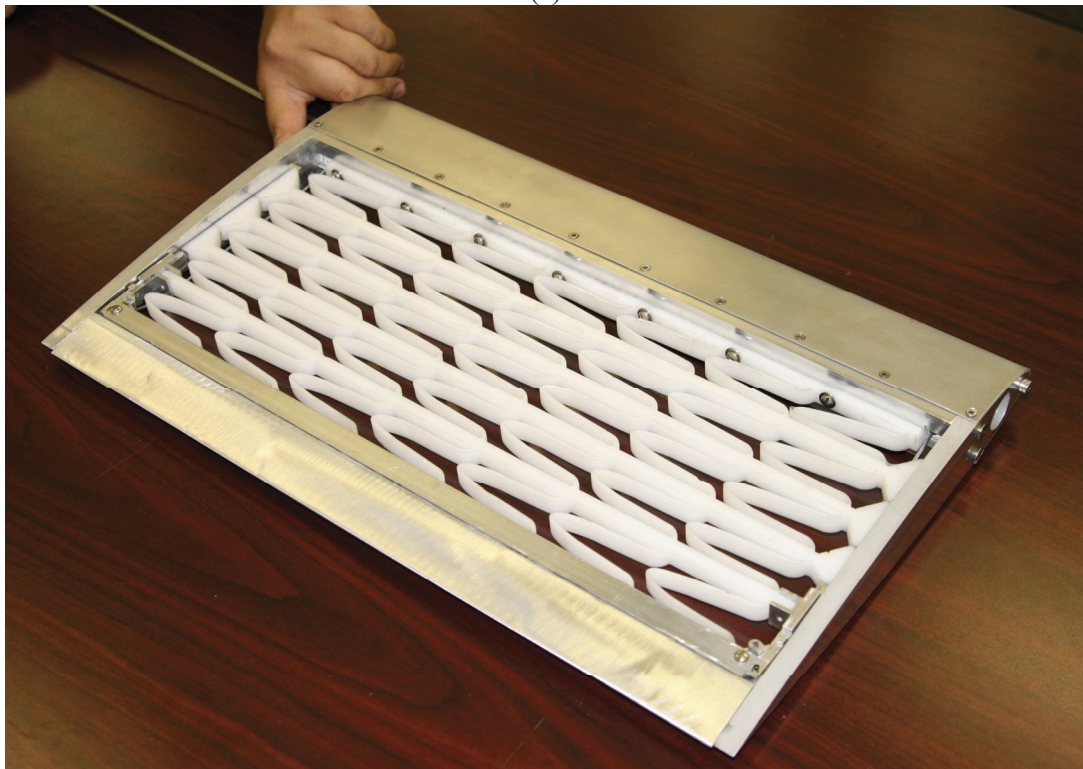
(b)

Figure 50: Fully assembled experimental prototype: (a) extended shape and (b) compressed shape.

After building the experimental demonstrator, its functionality has been successfully tested multiple times without failure of problems. The manual actuation system by means of wires also resulted effective: only some asymmetries during repeated cycles could be noticed due to not negligible friction on the solid sliding guide.

5 CONCLUSIONS

This study examined an implementation for quasi-statically increasing the chord over a section of the BO-105 blade through a suitably designed continuous cellular structure, able of 1D morphing and representing the main blade load-carrying structure, in conjunction with a pre-strained rubber skin. Benefits have been evaluated in a previous works, spacing from increase in maximum speed, altitude and gross-weight, and reduction in main rotor power near the envelope boundaries.

An accordion honeycomb has been suitably designed, made of aluminum alloy, able of undergoing up to 50% chord-wise deformation and allowing for a blade chord increase of 30%. The elastic cell shape has been properly conceived for sustaining large global deformations while attaining low local strains, which can help expected fatigue life. Some innovative and quite complex geometries have been analyzed through a Finite Element model, identifying the main parameters and features necessary to obtain the desired cell properties, that can be useful as a basis for further developments. This honeycomb-like structure represented the main load-carrying member for the blade, but these studies can actually be useful in the morphing skin field for bigger structures (f.i., area change for fixed wing aircrafts).

Also the influence of the rubber skin has been taken into account in the "integrated" design of the morphing blade section, resulting into a final project which meets the proposed aerodynamic requirements: further studies can be done considering flexible matrix composites (FMC) as alternative solution, which well meet the one-dimensional morphing necessities of the here presented study.

During the presentation of this work, the authors tried to point-out the main design criteria for the extendable chord morphing blade concept: however, the large amount of design parameters, many of which having several correlations and implications on others, didn't allow to fully explore all the possible configurations or surely to find the most efficient one. In some cases, these parameters have been assumed to be a fixed value basing on common sense or physical limits; in others, complexity or manufacture restrictions kicked in: in any case further optimizations are possible. For these reasons, the development of a multi-objective optimization process able of taking into account multiple of these features would be of great interest, especially to best suit this concept to several helicopters blade geometries and loads.

The idea of using a passive actuation system as variable blade RPM well suits the common desired characteristics from morphing structures of high efficiency and adaptability. The authors showed that it is possible to exploit the centrifugal forces with the proposed design while keeping a low general complexity, and many different implementations are achievable, also opposing ones.

An early proof-of-concept, real scale, experimental prototype has been built and tested, showing the feasibility of the proposed ideas and giving the alleged reason for solving some design and practical issues, as for the lateral sliding constraints design. Further improvements can be accomplished in a more complex future prototype, implementing the metal honeycomb structure, the bonded skin and the variable RPM actuation system: in this case, also dynamic and vibrations issues will be object of investigation.

6 REFERENCES

[1]   Yeo. H., 2008, "*Assessment of Active Controls for Rotor Performance Enhancement*" – Journal of the American Helicopter Society, vol.53, no.2, April 2008, pp.152-163

[2]   Maughmer, M., Lesieutre, G., and Kinzel, M., 2005, "*Miniature Trailing-Edge Effectors for Rotorcraft Performance Enhancement*" – AHS 61st Annual Forum, June 2005, Grapevine, TX

[3]   Bae, E.-S., Gandhi, F., Maughmer, M., 2009, "*Optimally Scheduled Deployment of Gurney Flaps for Rotorcraft Power Reduction*" – Proceedings of the 65th Annual Forum of the American Helicopter Society, May 27-29, Grapevine, TX

[4]   Liu, L., Friedmann, P. P., Kim, I., and Bernstein, D., 2008, "*Rotor Performance Enhancement and Vibration Reduction in Presence of Dynamic Stall Using Actively Controlled Flaps*" – Journal of the American Helicopter Society, vol.53, no.4, October 2008, pp.338-350

[5]   Liu, T., Montefort, J., Liou, W., Pantula, S.R., 2007, "*Lift Enhancement with Static Extended Trailing Edge*" – Journal of Aircraft, vol.44, no.6, November-December 2007, pp.1939-1947

[6]   Léon, O., Hayden, E., Gandhi, F., 2009, "*Rotorcraft Operating Envelope Expansion Using Extendable Chord Sections*" – Proceedings of the 65th Annual Forum of the American Helicopter Society, May 27-29, Grapevine, TX

[7]   Abbot, I.H., Von Doenhoff, A.E., 1959, "*Theory of Wing Sections*" – Dover, New York

[8]   Katz, J., Plotkin, A., 1991, "*Low-Speed Aerodynamics: From Wing Theory to Panel Methods*" – McGraw-Hill, New York

[9]   Olympio, K.R., Gandhi, F., 2007, "*Zero-v Cellular Honeycomb Flexible Skins for One-Dimensional Wing Morphing*" – 48th AIAA/ASME/ASCE/AHS/ASC Structures, Structural Dynamics, and Materials Conference, April 23-26, Honolulu, Hawaii, AIAA Journal 2007-1735

[10]   Gibson, L.J., Ashby, M., 1997, "*Cellular Solids: structures & properties*" – Cambridge University Press, 2nd ed.

[11]   Bubert, E.A., Kothera, C.S., Wereley, N.M., 2008, "*Design and Fabrication of a Passive 1-D Morphing Aircraft Skin*" – 49th AIAA/ASME/ASCE/AHS/ASC

Structures, Structural Dynamics, and Materials Conference, April 7-10, Schaumburg, IL, AIAA Journal 2008-2045

[12] Kikuta, M. T., 2003, "*Mechanical Properties of Candidate Materials for Morphing Wings*" – Master of Science Thesis, Virginia Polytechnic Institute and State University, Blacksburg, VA

[13] Flanagan, J., Strutzenberg, R., Myers, R., Rodrian, J., 2007, "*Development and Flight Testing of a Morphing Aircraft, the NextGen MFX-1*" – 48th AIAA/ASME/ASCE/AHS/ASC Structures, Structural Dynamics, and Materials Conference, April 23-26, Honolulu, Hawaii, AIAA Journal 2007-1707

[14] Murray, G., Gandhi, F., Bakis, C., 2007, "*Flexible Matrix Composite Skins for One-Dimensional Wing Morphing*" – 48th AIAA/ASME/ASCE/AHS/ASC Structures, Structural Dynamics, and Materials Conference, April 23-26, Honolulu, Hawaii, AIAA Journal 2007-1737

[15] Olympio, K. R., 2006, "*Design of a passive flexible skin for morphing aircraft structures*" – Master of Science Thesis, Pennsylvania State University

- *Chapter 9* -

Conclusions and Future Developments

The present dissertation proposes several solutions of structural morphing to improve aerodynamic performance by means of seamless wing shape adaptation, while reducing maintenance costs and structural weight too. To overcome penalties (weight, costs, etc.) usually introduced by morphing architectures, the conceived architectures have been integrated within the Smart Structures paradigm: Shape Memory Alloys have been preferred and adopted in many of them.

Thus, research focused on two main topics:

1) wing morphing, with particular reference to solutions suitable for a real scale aircraft for civil regional transportation;

2) smart materials, integrated both as actuators and structural load-bearing elements.

The research activities focused on three main airfoil geometric parameters:

- airfoil (upper) **bump**;

- airfoil **camber** at trailing edge (morphing flap);

- airfoil **chord**.

Several novel architectures have been investigated for each of those parameters; an SMA based actuator has been developed too. All these solutions are original and have been numerically simulated with a Finite Element approach; then, prototypes have been manufactured and tested in laboratory. An industrial partner (Alenia Aeronautica Spa) funded some of these activities and showed great interest in their future industrialization: an European patent (see Appendix) has been actually requested for the selected applications.

Given the multitude of the presented applications, this thesis has been arranged as a collection of independent papers (where possible) and reports of the research activities carried out on the morphing topic by the author: each of them is self-contained and complete, discussing in detail also the achieved results and conclusions. In this chapter,

only general conclusions and future developments of the research activities will be discussed.

In particular, based on the results the following conclusions can be drawn:

- the model adopted to simulate the thermo-mechanical behaviour of SMA and its integration procedure within the Finite Element approach (both in COMSOL Multiphysics and MSC/Nastran) has been validated by means of experimental tests campaigns on several prototypes, demonstrating an overall good correlation;

- several novel morphing architectures have been designed and simulated for each of the investigated wing geometry parameters: some solutions have been then selected and further optimized and / or prototyped, having to solve practical manufacturing issues;

- the full functionality against the requirements of these solutions has been demonstrated (only numerically in some cases, experimentally and in presence of static loads for others);

- experimental tests on solutions integrating Shape Memory Alloys showed their ability to work as actuators for static applications, also if thermal inertia still represents a concern (time required to cool down) and affects cyclic functioning;

- the conceived architectures well integrate with current perspectives on the design of future aircrafts, asking for low weight and noise, capable of wing adaptability to the mission requirements and based on the "all-electric" and "fly-by-wire" paradigm.

Some future work recommendations have been already discussed in each chapter. However, as a general overview, one can detect:

- studies could be carried out to implement a more sophisticated thermo-mechanical model for SMA and improve the numerical-experimental correlation;

- investigations on the presented architectures must be assessed to gain a better understanding of the aero-elastic phenomenology of such solutions;

- actual prototypes have shown the functionality of the proposed concepts but need to be suitably modified for industrialization purposes and performance optimization;

- activities concerning the variable camber of wing trailing edge could be extended to an aileron solution;

- the possible adoption of Shape Memory Alloys as actuators on airborne structures is strictly connected with the development of active control systems and the resolution of thermal inertia issues;
- research activities on the aeronautical morphing topic could be extended to other wing parameters (span, winglet, etc.) and the search for new configurations.

At the moment of writing, there are many opportunities to actually deploy these further studies due to the large amount of new projects and research activities going on:

- "TIAS" project inside Alenia Aeronautica Technological Program for the next generation Jet and Prop Regional Aircraft;
- "JTI Clean Sky" EU project, for the development of alternative morphing flap architectures;
- "Europa" project (EU and Alenia Aeronautica), for studies on adaptive winglets;
- "SADE" project (EU and CIRA), for the investigation of compliant LE and TE solutions.

- *Appendix* -

Patent

Barbarino, Silvestro

Via Amerigo Crispo 11
I-80033, CICCIANO (Napoli)
ITALIE

**For any questions about
this communication:**

Tel.:+31 (0)70 340 45 00

Date
11.09.09

Reference	Application No./Patent No.
	09165941.7 - 1254
Applicant/Proprietor	
Alenia Aeronautica S.p.A.	

Designation as inventor - communication under Rule 19(3) EPC

You have been designated as inventor in the above-mentioned European patent application. Below you will find the data contained in the designation of inventor and further data mentioned in Rule 143(1) EPC:

DATE OF FILING : 21.07.09

PRIORITY : IT/23.07.08/ ITA TO20080566

TITLE : An actuator device based on a shape memory alloy, and a wing flap assembly fitted with such an actuator device

DESIGNATED STATES : AT BE BG CH CY CZ DE DK EE ES FI FR GB GR HR HU IE IS IT LI LT LU LV MC MK MT NL NO PL PT RO SE SI SK SM TR

INVENTOR (PUBLISHED = 1, NOT PUBLISHED = 0):

1/Iannuzzo, Generoso/ Via Guerriero Augusto 36/I-83100, AVELLINO/IT
1/Riccio, Massimo/ Via Tedeschi 8/I-81100, CASERTA/IT
1/Russo, Salvatore/ Via G. Gigante 16/I-80010, QUARTO (Napoli)/IT
1/Calvi, Erika/ Via Municipio 95/I-83026, MONTORO SUPERIORE (Avellino)/IT
1/Pecora, Rosario/ Via Lago Patria 255 ("Parco Bellavista")/I-80014, GIUGLIANO (Napoli)/IT
1/Lecce, Leonardo/ Via San Giacomo dei Capri 125/SAC/I-80131, NAPOLI/IT
1/Barbarino, Silvestro/ Via Amerigo Crispo 11/I-80033, CICCIANO (Napoli)/IT
1/Concilio, Antonio/ Via F. Evangelista 27/I-81020, SAN NICOLA LA STRADA (Caserta)/IT
1/Ameduri, Salvatore/ Via G. Jannelli 220 ("Parco Vanna")/I-80131, NAPOLI/IT

DECLARATION UNDER ARTICLE 81 EPC:
The applicant(s) has (have) acquired the right to the European patent under an agreement dated 12.07.07

Receiving Section

EPO Form 1048 12.07

- 463 -